Seismic Strengthening of Deficient Exterior RC Beam-Column Sub-assemblages using Post-tensioned Metal Strips

A thesis submitted for the degree of Doctor of Philosophy in the Faculty of Engineering of the University of Sheffield

By

Yasser Helal

(BSc Structural Eng., Damascus University)

(MSc Earthquake Eng., The University of Sheffield)

Earthquake Engineering Group (EEG)

Department of Civil & Structural Engineering

The University of Sheffield

August 2012

To My family

for

their prayers, patience and love

ABSTRACT

Old reinforced concrete buildings are vulnerable to seismic actions as they were built in accordance with non-seismic code provisions and suffer from poor material quality and/or reinforcement detailing. Moreover, many buildings were constructed without even basic design code recommendations. Consequently, their structural components, in particular beam-column joints, suffer from a wide range of deficiencies. These joints may deteriorate severely under seismic actions leading to extensive damage and collapse.

The current study aims to develop an understanding of the behaviour of exterior beam-column joints with shear strength and anchorage deficiencies, and to examine a strengthening solution using post-tensioned metal strips in upgrading their performance.

A multiphase experimental programme was conducted including small and medium-scale beams with inadequate lap splices loaded in tension and deficient isolated full-scale exterior beam-column joints subjected to quasi-static cyclic loading.

In the beam tests, deficient splices were investigated under different confinement conditions, namely, unconfined, internally confined by steel stirrups, and externally confined by metal strips. Test parameters included concrete cover, confinement ratios, concrete quality, and bar diameter. Providing post-tensioned external confinement had a considerable impact on the behaviour, and resulted in sizable enhancements in strength and ductility. Parametric studies were conducted to identify the parameters most influencing the contribution of external confinement to bond. A bond stress-slip model is proposed that can be used to predict and simulate the behaviour of splices strengthened by post-tensioned metal strips. This model was implemented in FE models of beams and showed good correlation with the measured response.

In the joint tests, four full scale exterior RC beam-column joints were tested under cyclic loading. The joints experienced severe cracking and damage including a shear mechanism in the panel zone. The joints failed prematurely at about 50% of their nominal flexural strength. Strengthening the joints with post-tensioned metal strips led to an improved performance, higher energy dissipation and more controlled shear failure along with moderate damage in the beam.

An enhanced ACI-based strut-and-tie joint model is proposed and verified against the current test results and results by others. The model can be used for strengthened specimens as well as unconfined exterior joints and it accounts for different beam anchorage lengths.

A quad-linear shear stress-strain model is proposed to simulate the behaviour of strengthened joints. The model was implemented in a finite element panel-zone scissors model. The scissors model was incorporated in nonlinear static and cyclic analyses. The simulated response was found to represent the joint behaviour reasonably well.

A full-scale two storey reinforced concrete framed building was designed and tested on a shaking table, in cooperation with different researchers and academic partners. The building was substandard with a multiple range of deficiencies in the joint regions and connecting elements. The bare building suffered severe damage under small seismic intensities. Upgrading the structure with schemes of post-tensioned metal strips led to a considerably enhanced performance.

ACKNOWLEDGEMENTS

I would like to express my deepest gratitude to my supervisor and friend, Prof. Kypros Pilakoutas for his valuable and continuous support and inspiration during the completion of this work. His guidance was of a great help to successfully overcome all obstacles found in this project. In addition, his insights and professional opinions pushed me towards new limits.

I am really thankful to Dr. Maurizio Guadagnini for his valuable notes in completing this work appropriately.

I would like also to thank everyone in the research group (Yaser Jemma, Reyes Garcia Lopez, Tammim Macharkah, Sohaib Ahmad, Shaukat Khan, Rini Mulyani, Raudhah Ahmadi and others) with whom I shared memorable moments. In particular, I would thank my best friends Yaser Jemma and Reyes Garcia Lopez. The collaborative work we have done in the laboratory and the support we provided each other has deepened our friendship.

Having worked in the laboratory I have made many friends to whom I am indebted for their experience and technical support. I thank in particular:

- The supervisor of the laboratory Paul Blackbourn and the experimental officer Shaun Waters for their technical support and co-operation and their patience during my long hours in the laboratory and during testing.
- The technicians Kieran Nash, David Hobart and Chris Todd who provided me with their technical support when I mostly needed it.

I am deeply thankful to my family whose prayers have always helped and strengthened me to achieve this bench mark.

I am thankful to Prof. Mohammed Al-Samara for his support and encouragement throughout my study.

Finally, I would like to acknowledge the financial support offered by Damascus University during my study.

TABLE OF CONTENTS

LIST OF FIGURES

CHAPTER 1:

CHAPTER 2:

CHAPTER 3:

CHAPTER 4:

CHAPTER 5:

CHAPTER 6:

CHAPTER 7:

CHAPTER 9:

CHAPTER 10:

APPENDIX A:

APPENDIX B:

APPENDIX C:

APPENDIX D:

APPENDIX E:

APPENDIX F:

APPENDIX G:

APPENDIX H:

APPENDIX J:

APPENDIX K:

LIST OF TABLES

NOTATION

A_g = the column gross section area

A_j = the effective joint area

A_{str} = the minimum strut area

A'_{sc} = the area of column reinforcement in compression

A_{tr} = the area of one link in the splice region

a_b = the compressive zone depth of the beam cross-section

a_c = the compressive zone depth of the column cross-section

a_{str} = the strut width

α_j = the joint aspect ratio

$\alpha 1$ = the ratio of the ultimate biaxial compressive stress to the uniaxial compressive ultimate stress

$\alpha 2$ = the absolute value of the ratio of uniaxial tensile stress at failure to the uniaxial compressive stress at failure.

$\alpha 3$ = the ratio of the magnitude of a principal component of plastic strain at ultimate stress in biaxial compression to the plastic strain at ultimate stress in uniaxial compression

$\alpha 4$ = the ratio of the tensile principal stress value at cracking in plane stress, when the other nonzero principal stress component is the ultimate compressive stress value, to the tensile cracking stress under uniaxial tension.

b_s = strip width

b_j = the joint effective depth

β_d = bar diameter factor

β_s = concrete softening coefficient

C_b = bottom concrete cover of spliced bars

C_m = clear spacing between splices

c_{min} = the minimum concrete cover

c_{max} = the maximum of c_s and c_b

C_s = side concrete cover of spliced bars

c_s = the smaller of side cover or half the clear distance between bars + 6mm

c_b = the bottom cover

C_{PTMS} = the axial compressive force applied by the PTMS on a length equal to a_b

d_b = bar diameter

d_{sb} = the effective depth of the beam cross-section

d'_{sb} = the effective cover to compression reinforcement in a beam cross-section

DR = deflection ratio (beams), drift ratio (joints)

d_c = the distances of tension reinforcement in the column cross-sections measured from the outermost fibre in compression.

$d"_{sb}$ = the distance between compressive and tension longitudinal reinforcement of the beam

$d"_c$ = the distance between compressive and tension longitudinal reinforcement of the column cross-section

d_{sb} = the effective depth of the beam cross-section

δ_m = the deflection at the maximum load capacity

$\delta_{30\%}$ = the deflection at 30% drop in the maximum load capacity

E_c = concrete moduli of elasticity

E_s = steel moduli of elasticity

E_h = the amount of energy dissipation per cycle

E_{so} = the strain energy

ε_d = and ε_r the average principal strains

ε_o = the concrete cylinder strain

ε_s = steel strain

ε_y = yield steel strain

ε_u = ultimate steel strain

F_{max} = maximum load capacity

f_b = the strip stress

f_s = steel stress

f_y = yield steel stress

f_u = ultimate steel stress

f_{ce} = effective strut compressive stress

G_c = moduli of shear (concrete)

G_m = the secant shear stiffness at the maximum shear stress τ_m

γ_{res} = the shear strain at the residual shear stress τ_{res}

γ_m = the shear strain at the peak point τ_m

γ_b = a factor accounting for confinement by transverse beams and is equal to 1 for isolated exterior joints

H = column height

HSC = high strength concrete

h_c = column width

j = the effective beam lever arm ratio

k = the secant stiffness of the hysteretic cycle

L_s = splice length

L_b = the beam length up to the column interface

L = the beam length from the contraflexure point up to column centroid

l_d = the beam anchorage length within the joint area

l_{st} = the anchorage length participating in the tension force T_{SA}

LSC = low strength concrete

M_j = the beam moment at the column centroid

M_j = the moment of the shear spring

n = modular ratio, number of splices

N = number of strips along the splice

NSC = normal strength concrete

ν = Poisson ratio of concrete

p_c = the principal compressive stress on the core

p_t = the principal tensile stress on the core

P = the column axial load

P_{strip} = the force in the strip

PTMS = post tensioned metal strips

ρ and ρ' = tension and compression beam reinforcement ratios, respectively

PGA = peak ground acceleration

R_r = the relative rib area of the reinforcing bar

r_d = bar rib spacing

s = the link spacing

S_{Anch} = bar elongation component

s_e = slip at the post-splitting point

s_m = slip at the maximum bond stress

s_r = slip at the residual point

σ_d = the average principal stress of concrete

σ_{jv} = vertical joint shear stress

t = strip thickness

T = the bar force

T_b = the tension force at the beam anchorages

T_{SA} = the tension force of any beam reinforcement acting on the nodal zone

τ_{actual} = actual bond value

τ_{cr} = the initial shear cracking stress

τ_e = pre-splitting bond stress

τ_j = the shear stress

τ_{jh} = horizontal joint shear stress

τ_{norm} = normalised bond value

τ_{max} = maximum bond stress

τ_m = the maximum shear stress

τ_r = residual bond stress

τ_{res} = the residual shear stress

τ_s = post-splitting bond stress

θ = the strut angle

θ_j = the modified strut angle

u_0 = maximum amplitude of the hysteretic cycle

V_b = the lateral force applied at the beam flexural point

V_{cc} = the shear force applied along the compression part of the nodal zone

V_{jh} = horizontal shear forces within the core

V_{jv} = vertical shear forces within the core

ζ_{eq} = equivalent damping

Z_b = lever arm

ξ = softening coefficient

Chapter 1

INTRODUCTION

1.1 INTRODUCTORY REMARKS

It is well established that the vulnerability of existing reinforced concrete (RC) buildings in developing countries is very high (Ahmad, 2011). Most of these buildings were either constructed or designed according to non-seismic code provisions for reinforcement detailing, material quality or ductility requirements. The widespread damage and collapse of non-seismic non-engineered RC structures is often attributed to premature brittle failure mechanisms in connections or their adjoining elements (Hassan, 2011).

In reconnaissance reports from the Tehuacan, Mexico, earthquake of June 15, 1999 (EERI 1999a); the Izmit, Turkey, earthquake of August 17, 1999 (Sezen et al., 2000); the Athens, Greece, earthquake of September 7, 1999 (EERI, 1999b); the Chi-Chi, Taiwan, earthquake of September 21, 1999 (Uang et al. 1999, EERI 1999c); the M_w7.1 Erciş-Van, Turkey earthquake of October 23, 2011 (EERI, 2012); and the March 20, 2012, Ometepec, Mexico, earthquake

(EERI, 2012), it was indicated that severe damage in existing buildings was primarily due to inferior performance of beam-column connections.

The failure of a beam-column connection in a structural system causes local stiffness degradation resulting in large sidesway drifts and possibly occurrence of P-Δ effects. As a consequence, additional loads are transferred to columns leading to severe damage and loss of the axial load carrying capacity. This in turn can lead to instability of the global structural system and subsequently to partial or complete collapse (Mosier, 2000).

Some examples of partial and total collapses of substandard buildings due to connection failures are shown in Figure 1-1 through Figure 1-3.

Figure 1-1: Connection failure and partial building collapse in the March 13, 1992, Erzincan, Turkey, earthquake (Hassan, 2011)

Figure 1-2: Partial building collapse and beam-column failure in Chi-Chi, Taiwan, earthquake of Sep. 21, 1999 (Uang et al., 1999)

Figure 1-3: Total collapse of a three-story school in Turkey, partly due to rupture of joints (Erciş-Van, Turkey, earthquake of October 23, 2011)

Many surveys and studies were conducted to identify potential critical detailing affecting the performance of older designed beam-column connections. Moreover, some surveys were conducted so as to revise reinforcement detailing provisions found in older design codes of practice. Pessiki et al. (1990) and Beres et al. (1991, 1992, 1996), among others, identified seven joint critical details which could jeopardise the integrity of gravity-loaded designed buildings (GLD) during earthquakes. These details include low reinforcement ratios, inadequate splices, discontinuous beam bottom bars in connection regions (short anchorages), construction joints below and above beams, widely spaced transverse reinforcement, discontinuous column steel ties into the connection region, and strong beam-weak column design. Existing joints with such details are categorised to be deficient or substandard. A schematic view of potential deficiencies is shown in Figure 1-4. Similar findings were also identified by Naseer et al. (2010) while investigating damage of non-seismic buildings in the aftermath of Kashmir earthquake (2005). However, the presence of poor construction materials was an additional prominent

observation reported during the investigation. The use of poor construction materials was also reported by Koru (2002), Mohamed and Clark (1992), Ilki et al. (2008), Bedirhanoglu et al. (2010), Lin and Nagasaka (2005), Ahmad (2011), and EERI special report (2012) "*the March 20, 2012, Ometepec, Mexico, Earthquake*".

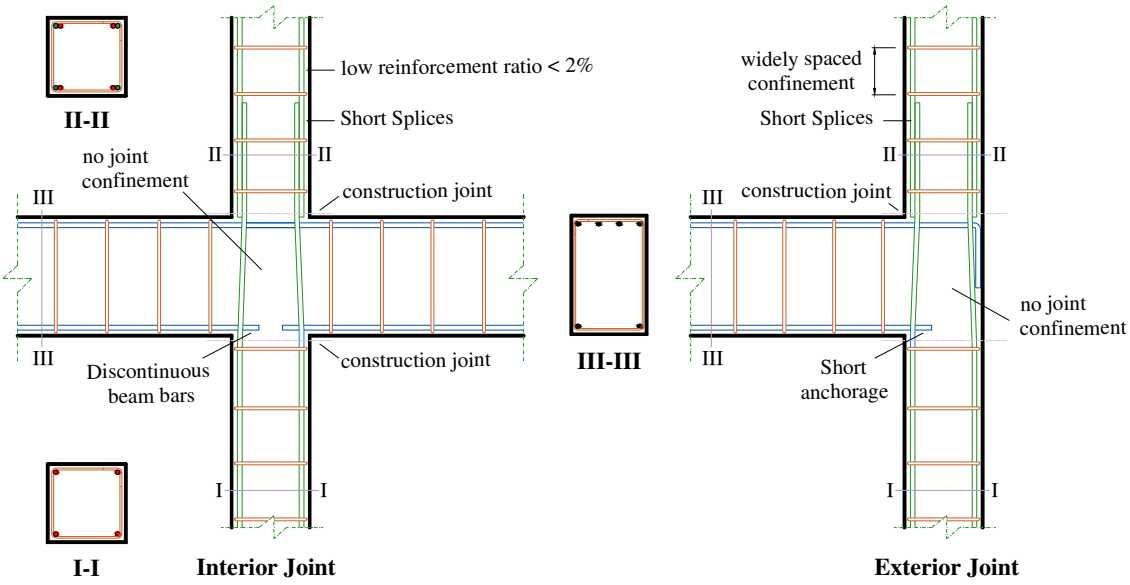

Figure 1-4: Deficiencies observed in substandard RC connections (Beres et al., 1996)

1.2 JOINT-SHEAR AND BEAM-ANCHORAGE DEFICIENCIES

In the last three decades, two prominent joint deficiencies, namely, insufficient joint transverse reinforcement and/or inadequate beam anchorages within the joint region were investigated and shown to have a significant influence on the joint behaviour [Hassan (2011), Pantelides et al. (2002), Clyde et al. (2000), Sharma (2011), Bedirhanoglu et al. (2010), Pampanin et al. (2003), Ehsani and Wight (1985), El-Amoury and Ghobarah (2002), Ghobarah and Said (2001), Park and Mosalam (2009), Sezen et al. (2000), among others]. Failure modes related to joints with such detailing were due to joint shear failure and/or bond-slip failure.

A major cause of joint damage during many previous seismic events such as the 1999 Tehuacan, Mexico earthquake, the 2005 Kashmir earthquake, and Haiti (2010) was found to be related to the presence of unconfined joint regions or substandard beam anchorages. Many cases were also reported where joints with light lateral confinement or moderately short anchorages had sustained severe deterioration in the lateral load capacity resulting in significant damage and even failure [Moehle and Mahin (1991); Pantelides et al. (2002)]. What's more, in some cases, even when the amount of confinement or anchorage detailing were close to those specified by current code provisions, failures also occurred [Moehle and Mahin (1991), Wong (2005)]. Figure 1-5 through Figure 1-7 show a close-up view of some local failures in substandard beam-column connections during different earthquakes.

Figure 1-5: Reinforced concrete beam-column joint damage due to inadequate detailing in a) the June 15, 1999 Tehuacan, Mexico earthquake (Pantelides et al. 2002), b) the Athens, Greece, earthquake of September 7, 1999 (EERI 1999b), and c) a corner joint (Hassan, 2009)

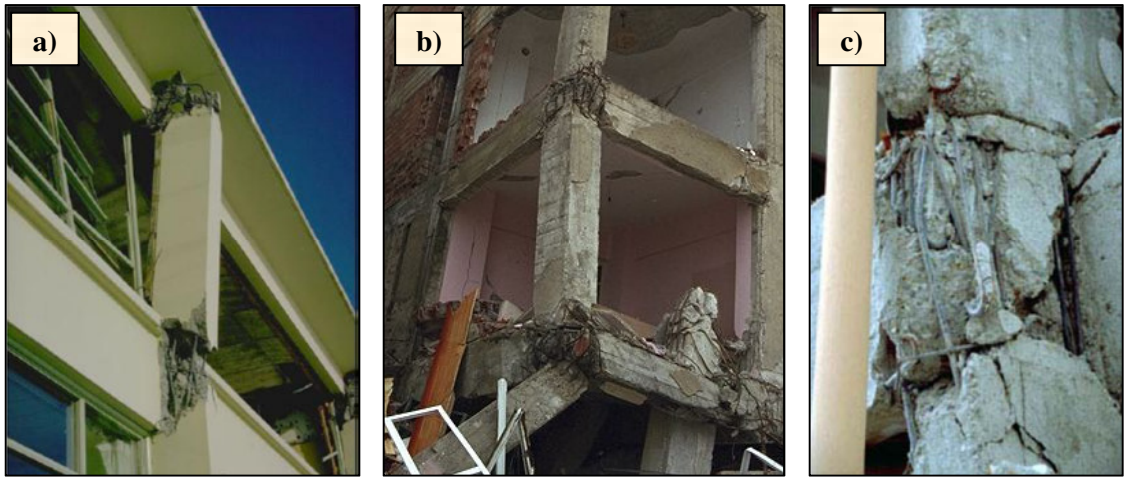

Figure 1-6(a): Severe exterior joint damage, (Lehman et al., 2002)
Figure 1-6(b) & (c): Joint failures during the 1999 Kocaeli, Turkey, earthquake (Sezen et al., 2000)

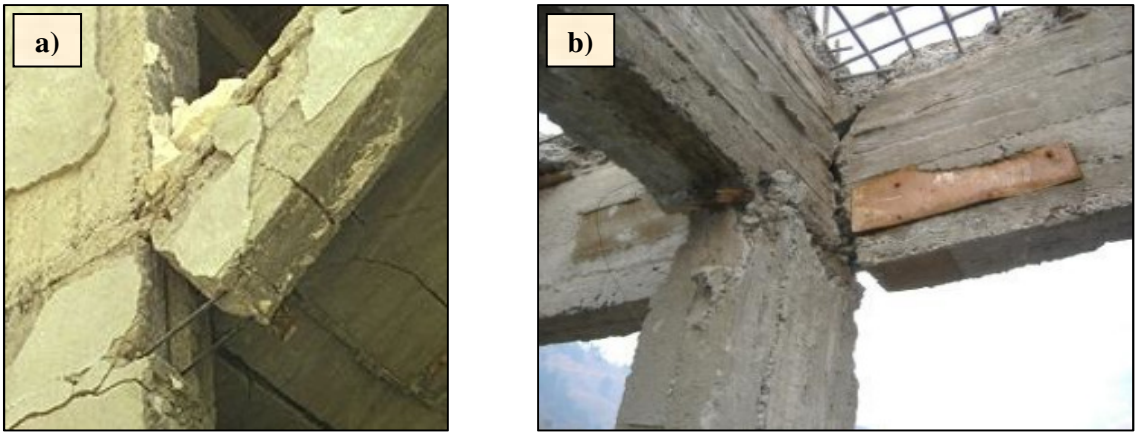

Figure 1-7: Beam anchorage failure a) Sezen (2000), and b) Ahmad (2007)

Different locally-applied rehabilitation solutions such as steel and reinforced concrete (RC) jacketing [Migliacci et al. (1983), Corazao and Durrani (1989), Estrada (1990), Beres et al. (1992), Alcocer and Jirsa (1993), Prion and Baraka (1995), and Biddah (1997)], and FRP composites [Said and Nehdi (2004), Pantelides et al. (1997, 1999, 2008), Castellani et al. (1999), Tsonos and Stylianidis (1999), Gergely et al. (2000), Mosallam (2000), Ghobarah and Said (2001), Amoury and Ghobarah (2002), Prota et al. (2003), Antonopoulos and Triantafillou (2003), Mukherjee and Joshi (2005), Smith and Shrestha (2006), Salloum and Almusallam (2007), Almusallam and Salloum (2007), Shrestha and Smith (2007), Karayannis et al. (2008), Karayannis and Sirkellis (2008), Ilki et al. (2008, 2011), Shrestha (2009), Engindeniz et al. (2005), Engindeniz (2008), Bedirhanoglu (2009), Bousselham (2010)] have been widely used to upgrade the shear strength as well as to control the beam anchorage failure of deficient RC joints in the past. Also, many repair measures were developed to fix damaged joints. For most rehabilitation options, joint failures were partially or totally supressed resulting in improved inelastic deformations. Nevertheless, most of these methods have disadvantages relating to their practical application, constructability, artful detailing and most importantly cost efficiency.

1.3 COLUMN SPLICE DEFICIENCY

Column splices are also critical and could jeopardise the integrity of the joint and its connecting elements. Splices are normally located above the column footing or above the joint area. In old practice, splices were commonly designed in compression, and thus, they were relatively short (20 to 24 times the bar diameter). Moreover, they were provided only with light transverse reinforcement (Melek et al., 2003). Given the fact that bond strength in tension is low, compression splices were observed to perform poorly under load reversal caused by seismic loading. Failure of a splice assembly may cause severe degradation in strength and stiffness at column hinging zones. As a result, the ability of the column to sustain the axial load deteriorates and this, in turn, may cause serious partial collapses [Forell and Nicoletti (1980), Melek et al. (2003)]. Figure 1-8 shows failures which occurred at poorly detailed splice regions. Also, Figure 1-9 shows the measured response of two columns tested by (Chai et al., 1991) in which one column (column 1) is provided by splices of 20 times the bar diameter and one column (column 3) with continuous bars. It is clear that the presence of inadequate splices resulted in much deteriorated response due to loss of bond between concrete and steel.

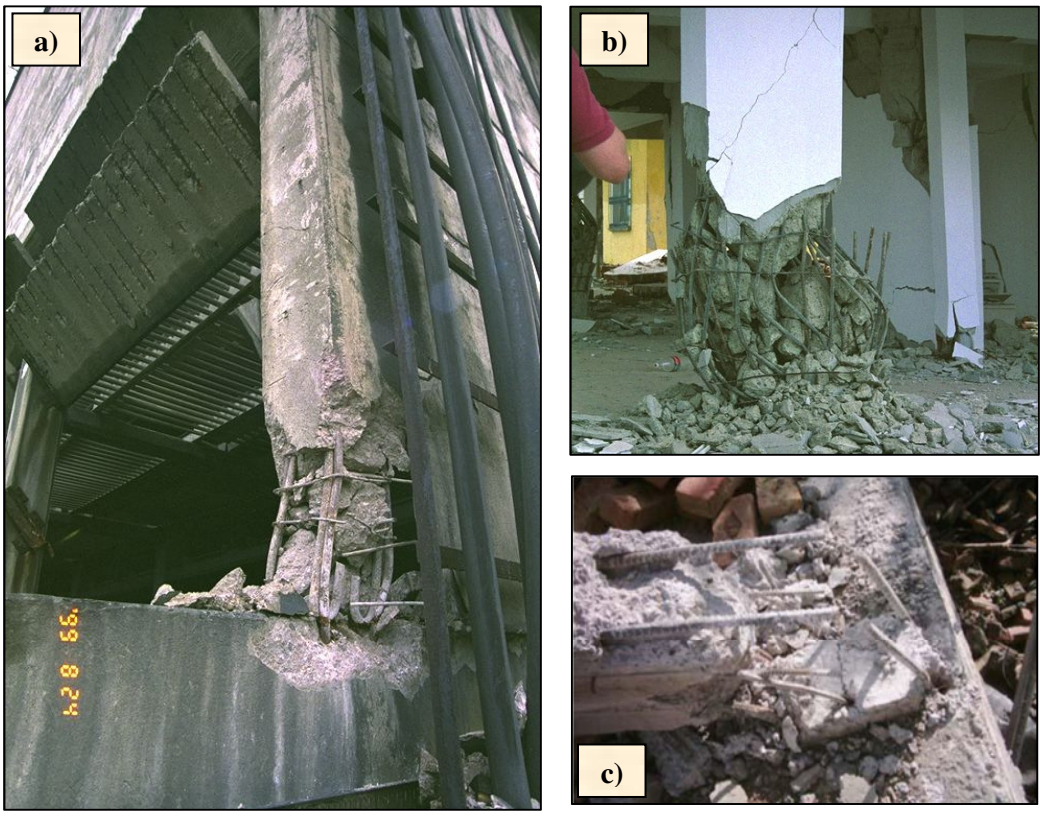

Figure 1-8: a) splice detailing and damage in a column hinging zone (Sezen, 2000), b) axial load failure and bar buckling at column splice region (Sezen, 2000), c) splice failure (Ahmad, 2011)

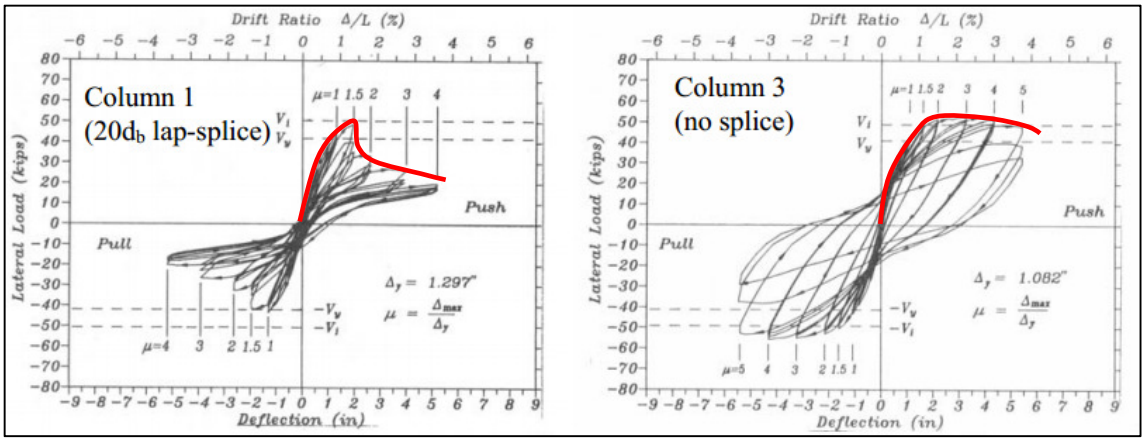

Figure 1-9: Lateral Load capacity of columns with and without splices (Chai et al., 1991)

Several splice-strengthening measures were investigated in the past including the addition of external and internal steel ties, or the use of jackets (for example: steel angles with straps, steel-plate jackets with and without through bolts, steel wires, FRP composites, and fibre reinforced concrete "FRC"). In most methods, the brittle nature of splice failures was retarded and some inelastic behaviour was developed at the local level prior to any deterioration in the lateral load capacity. Despite the noticeable enhancement in behaviour, the rehabilitation methods are typically accompanied by high cost due to disruption to the building function and possibly displacement of the occupants. Thus, strengthening of splices may be impractical unless less disruptive and more cost-efficient methods are considered.

1.4 A NEW STRENGTHENING TECHNIQUE

Previous research at the University of Sheffield [Frangou (1992, 1996), Frangou et al. (1995), Gunja (2005)] and at Sharif University [Moghaddam et al. (2007-2010)] had led to the development of the Post-Tensioning Metal Strapping strengthening technique (PTMS). The technique entails the pre-tensioning of ductile metal strips around the element cross-section and sealing them by means of metal clips. The technique was first developed for its simplicity (it is easy to apply), economy (the use of cheap materials makes it affordable for cases with low-cost existing buildings), and efficiency (the pre-tensioning state induced in the metal strips increases the effectiveness of confinement).

The introduction of the PTMS technique has created the necessity for the development of design specifications which will allow engineers to rehabilitate or upgrade existing deficient RC structures using this technique. Consequently, research has to be done on all aspects of its structural behaviour. Past investigations involved strengthening of under-designed or damaged RC members in flexure, compression and shear [Frangou (1992, 1996), Moghaddam et al. (2010)]. Figure 1-10 and Figure 1-11 present some applications of the technique to deficient RC beams and columns.

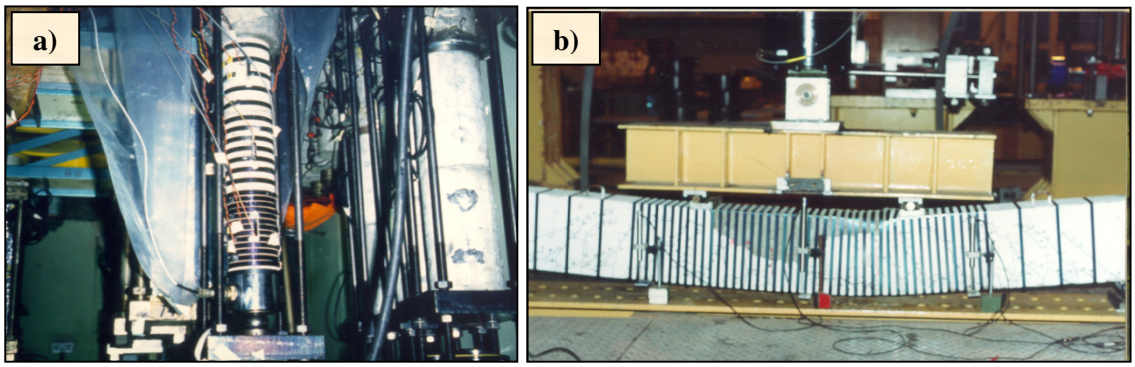

Figure 1-10: Retrofitted Medium scale RC elements a) columns, b) beams (Frangou, 1996)

Figure 1-11: Deficient RC columns strengthened by PTMS (Moghaddam et al., 2010)

The outstanding success of previous strengthening applications, as well as its suitability for developing countries, encouraged the author to further investigate the technique on different structural aspects including deficient exterior RC connections and column splices.

1.5 RESEARCH AIM AND METHODOLOGY

This study aims to contribute towards understanding the behaviour of poorly detailed exterior beam-column sub-assemblages in substandard existing RC buildings. The sub-assemblage details targeted include no joint transverse hoops, improper anchorages of beam longitudinal bars within the joint area and inadequate lap splices above the joint area or the column footing. Also, the study aims to develop economical and effective rehabilitation schemes to upgrade the strength of deficient beam-column sub-assemblages.

Ultimately, the above mentioned aims target the development of a bond stress-slip model for PTMS confined column splices, the development of proper and applicable rehabilitation schemes by means of PTMS to enhance the performance of deficient exterior beam-column sub-assemblages failed due to shear, the proposition of a shear-stress strain model for predicting the shear capacity as well as shear deformations of deficient or PTMS strengthened beam-column sub-assemblages and finally providing a computer-based model to simulate the behaviour of such sub-assemblages.

To achieve these goals, the following methodology has been adopted:

1. Reviewing the fundamentals of joints including potential failure mechanisms, shear transfer mechanisms, mechanics of exterior joints and compression softening phenomenon.
2. Conducting a literature investigation on a) cyclic tests concerned with the performance of poorly detailed joints, b) shake table tests on deficient RC buildings and c) key parameters affecting the joint behaviour.
3. Reviewing the behaviour of substandard column splices as well as strengthening techniques used to upgrade their performance.
4. Establishing an understanding of the bond behaviour of reinforcing bars embedded in reinforced concrete and its key influence parameters.
5. Reviewing the current models for joint panel zones suitable for computer-based analyses.
6. Reviewing the current research on developing strengthening measures of deficient joints.
7. Reviewing recent experimental and analytical advances relating to the PTMS technique.
8. Conducting a multiphase experimental programme including tests on deficient column splices in tension and substandard exterior beam-column joints under cyclic loading.

9. Evaluating the accuracy of existing bond equations to predict the enhancement in bond strength due to PTMS.
10. Conducting a parametric study to examine the parameters affecting the contribution of PTMS to bond strength.
11. Developing a generalised bond stress-slip relationship to predict the contribution of PTMS to bond strength.
12. Introducing a FE analytical modelling technique to simulate splices in RC elements and to verify its suitability to predict the experimental results.
13. Developing different strengthening strategies to upgrade the performance of poorly detailed joints using the PTMS technique along with the use of better quality materials and welding.
14. Evaluating the performance of strengthened joints by making comparisons with control deficient specimens.
15. Evaluating joint seismic performance provisions in existing building assessment document such as ASCE/SEI 41-06 in addition to a recent strut-and-tie joint model.
16. Developing a simplified strut-and-tie model to predict the shear strength of unconfined and PTMS-confined exterior joints.
17. Proposing a constitutive finite element joint model for simulating the behaviour of PTMS-confined exterior joints.
18. Conducting static as well as cyclic analyses using a suggested computer-based panel zone model to simulate the behaviour of the tested joints.
19. Investigating the capability of the PTMS technique to upgrade the performance of a real full-scale substandard RC framed structure subjected to shake table tests.

1.6 THESIS STRUCTURE

Chapter 2, on literature review, is divided into four parts. The first part starts by reviewing the fundamentals and mechanics of beam-column joints, experimental research efforts conducted worldwide on deficient joints, shake table tests on deficient RC structures, and it ends with a brief description of parameters influencing joint behaviour. In the next part, the behaviour of substandard splices in columns is demonstrated through experimental works. In addition, comments on some key rehabilitation methods for splices are given. In the third part, the up-to-date computer-based panel zone models suitable for simulating joint behaviour are presented. In the last part, an overview of advantages and disadvantages relating to strengthening and repair methods of deficient RC joints is given. This part also introduces the PTMS technique.

Chapter 3 introduces the test programme which comprises three test series. In the first (I) and second (II) series, twelve small scale and twelve medium scale RC beams with lapped steel bars i) unconfined, ii) internally confined with steel stirrups or iii) externally confined by PTMS

were tested in four-point bending. The beams were designed to fail in the splice region due to splitting-type failure. In the third stage, four substandard RC beam-column connections were tested under cyclic loading. The joints were designed to fail in shear within the connection region due to the absence of transverse reinforcement. Moreover, different anchorages of beam bottom bars in the connection region are examined. The failed joints were then strengthened using strengthening schemes of PTMS and tested again.

In chapters 4 and 5, the experimental results from test series I and II are reported, interpreted and analysed. The mode of bond failure of differently confined specimens is examined and compared with the respective failure of unconfined specimens. The influence of various parameters on bond development is also evaluated. The splitting-type of bond failure in splices is investigated. The strain and bond stress distributions over the spliced bars are reported, as well as the contribution of the shear links and PTMS to the bond splitting strength of reinforcing bars. Furthermore, the bond splitting strength developed over the splice assembly is calculated and discussed. Based on the observed failure modes and responses, a behavioural bond stress-slip model is identified which simulates deficient splices confined by PTMS. Finally, an elastic approach based on cracked sectional analysis is used to predict the bond strength. Predictions are compared to the test results and conclusions are drawn.

In chapter 6, the test results on four bare exterior joints are described and the key structural characteristics including strength and stiffness degradation, and energy dissipation capacities are presented. Modes of failure of the test units are explained, and the progress of damage is detailed.

In Chapter 7, different rehabilitation schemes using PTMS are examined to upgrade the strength of the deficient joints. Before strengthening, the damaged core was replaced by new better-quality concrete. The strengthening schemes included vertical and horizontal meshes of strips, as well as diagonal meshes along the joint region. The results of cyclic tests on the rehabilitated joints are also presented. Failure modes are described and the response components are quantified. Furthermore, performance of the repaired joints is compared to that of the bare joints in terms of stiffness degradation, strength and deformation capacities, ductility, and energy absorption capacity.

Chapter 8 presents analytical work on bond behaviour. Enhancement in bond strength due to the presence of PTMS is first compared to predictions from state-of-the-art model equations and current codes of practice. Conclusions and discussions are given based on the comparisons. In the second part of the chapter, parametric studies are used to identify the parameters affecting the bond strength of strengthened specimens. Based on the trends observed, multivariable nonlinear regression is carried out to develop a bond strength model accounting for the enhancement due to the use of PTMS.

Chapter 9 reports on the FE modelling of beams with splices. ABAQUS 6.9 finite element (FE) package is used to model the bond between steel bars and concrete for the test specimens of Phase I&II. The smeared crack approach is used to model the concrete material. The bond interaction is simulated by using non-linear springs with characteristics based on the type of confinement provided in the splice zone. The analytical results including modes of failure, strength and deformation capacities are compared with the experimental results.

In Chapter 10, the shear stress-strain curves of the beam-column joints tested in this study are produced and compared to recent models of unconfined joints. A quad-linear shear stress-strain model is proposed to simulate the behaviour of PTMS confined joints. Also, the strut-and-tie ACI model for unconfined joints is enhanced to incorporate PTMS confinement and different beam anchorages. The shear stress-strain joint model is implemented in a scissors panel-zone model and nonlinear static and cyclic analyses are performed using DRAIN-2DX. The simulation results are compared with the measured responses and conclusions are given.

Chapter 11 presents the preliminary results of a shaking table test programme conducted on a full scale two-story RC framed building. A brief description of the building design including reinforcement detailing, material qualities, beam-column joint details, and results at different seismic intensities is given. In addition, general comments on the damage states of the bare and strengthened structures are presented. Furthermore, the time history results of a DRAIN-2DX model of the bare structure are presented.

In the final chapter, general conclusions drawn from the present study are given, together with recommendations for further research.

Chapter 2

LITERATURE REVIEW

This literature review is separated into four parts:

1) Deficient beam-column joints
2) Substandard column splices
3) Computer-based joint models
4) Strengthening of beam-column joints

PART I: DEFICIENT BEAM-COLUMN JOINTS

This part reviews briefly a) fundamentals and mechanics of joints, b) experimental work conducted on substandard beam-column connections typical of those found in existing GLD buildings, b) shake table tests done on RC framed structures built with deficient joints, and c) parameters affecting the joint behaviour.

2.1 BEAM-COLUMN JOINTS: A CRITICAL COMPONENT

The joint, defined as the portion of the column framing with the beam depth (see Figure 2-1), is an essential structural component responsible for load transfer among adjoining elements. Moreover, its integrity is an important requirement to develop inelastic behaviour and hinging in the adjoining elements. The behaviour of joints in seismic regions is still a controversial issue when dealing with the assessment of existing frames or design of ductile frames [Ruitong and Park (1987), Priestley and Calvi (1991), Sasmal (2009), and Hassan (2011)].

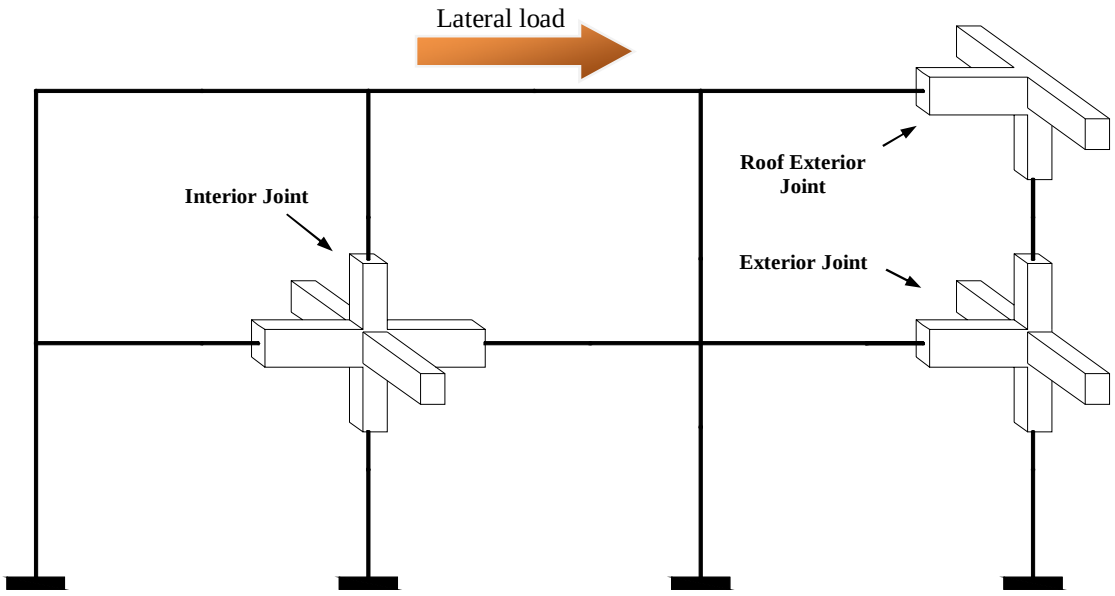

Figure 2-1: A typical interior RC frame with different types of beam-column joints

Seismic loads applied to structures impose large demands and forces on joints. As a result, complex mechanisms develop within the joint area involving bond and shear [Paulay and Priestley (1992), Paulay and Park (1984), Park and Paulay (1975), and Hakuto et al. (2000)]. Moreover, many parameters tend often to act simultaneously [Hassan (2011), and Park and Mosalam (2009)]. Figure 2-2 depicts the forces applied to exterior and interior joints. As can be seen from the figure, the compression and tension forces of beams and columns are transferred through the joint and develop diagonal tensile and compressive stresses. Many factors such as reinforcement detailing, joint aspect ratio, axial load, confinement, and beam-column design ratio influence the development and spread of these stresses.

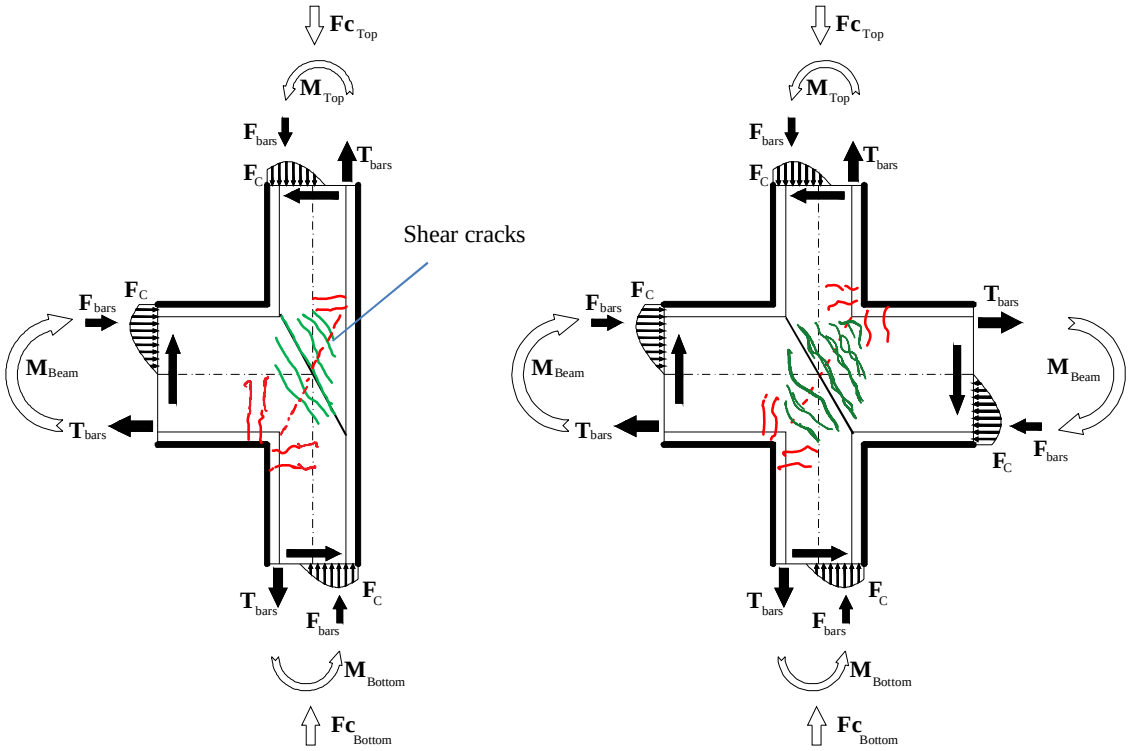

Figure 2-2: Exterior (left) and interior (right) beam-column joints under seismic loading

Based on extensive research works and experience from past seismic events, the failure of beam-column connections can be attributed to the following modes [Schofield et al. (2006), Dutta and Mander (2001), Beres et al. (1992), and Engenidiz et al. (2005)]:

1. Bond failure inside the joint area due to inadequate anchorages of bottom beam bars.
2. Bond failure of splices at the end of the column (short splices).
3. Shear failure mechanism within the joint area.
4. Buckling of column longitudinal bars inside the joint area due to lack of confinement or fracture of confining hoops.
5. Concrete failure in compression due to insufficient confinement or fracture of transverse reinforcement.
6. Shear or flexure-shear failure modes outside the plastic hinge zones.
7. Failure due to low cycle fatigue of longitudinal bars.

The above mentioned failure modes are considered to be weak sources of energy dissipation and should be avoided. A combination of these modes could occur resulting in complicated force transfer mechanisms and possibly more severe damage. It is reported that in exterior as well as corner connections, these failure modes are more pronounced and severe [Hassan (2011), Sasmal (2009) and Sharma et al. (2011)].

2.2 JOINT SHEAR TRANSFER MECHANISMS

Figure 2-3(a) shows forces acting on the joint area of an exterior beam-column connection. When the seismic load is applied to the joint area, the forces are initially transmitted through incomplete struts embraced by beam and column reinforcement along with development of minor shear cracks in the core. As the seismic load increases, major diagonal shear cracks form in the core and the joint shear resistance is attributed to two main transfer mechanisms, namely, the strut mechanism and truss mechanism [Paulay et al. (1978), and Park and Paulay (1975)].

In the strut mechanism, shear forces acting on the joint surfaces are transferred through a diagonal concrete strut in compression with an angle close to the core diagonals. This mechanism develops at loading stages before large flexural rotations take place which lead to high strains in reinforcement and wide cracks. The diagonal strut is activated by concrete compressive forces at the opposite corners and bond forces transmitted from beam and column reinforcement, as shown in Figure 2-3(b). It is reported that, in this case, a minimum amount of joint transverse reinforcement would provide effective confinement level within the joint.

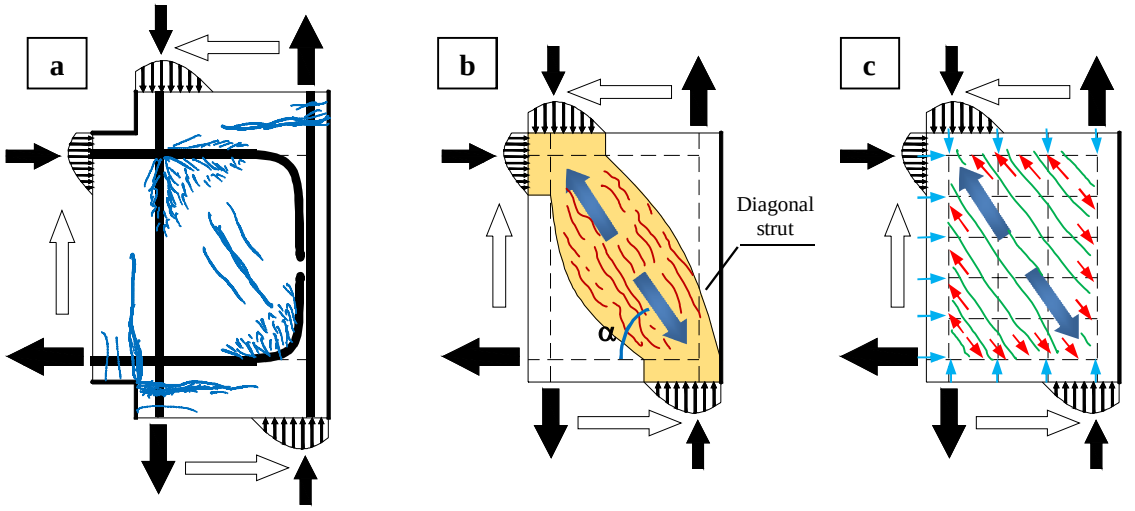

Figure 2-3: a) Lateral forces, b) strut mechanism and c) truss mechanism

The truss mechanism, on the other hand, develops usually at high load levels when large inelastic strains in reinforcement and bond deterioration take place. In this case, the joint shear resistance is due to contributions from horizontal (in the form of joint hoops) and vertical reinforcement (in the form of column intermediate bars) within the joint area. The truss mechanism is postulated as a distributed shear flow forming a network of small compression struts with tensile forces due to horizontal and vertical reinforcement, as shown in Figure 2-3(c). Although large cracking exists in this case, an adequate amount of joint confinement can activate a diagonal compression field able to sustain and transmit the bond forces. It should be mentioned that this mechanism is not activated in cases where no joint hoops exist such as those found in substandard older RC frames.

2.3 MECHANICS OF EXTERIOR JOINTS

Due to high seismic demands, large sidesway deformations are applied to frames which in turn lead to high shear stresses within the joint region. Figure 2-4(a) illustrates forces acting on an exterior beam-column sub-assemblage when the force V_b is applied in the upward direction. Forces acting on the joint region of an exterior joint are shown in Figure 2-4(b).

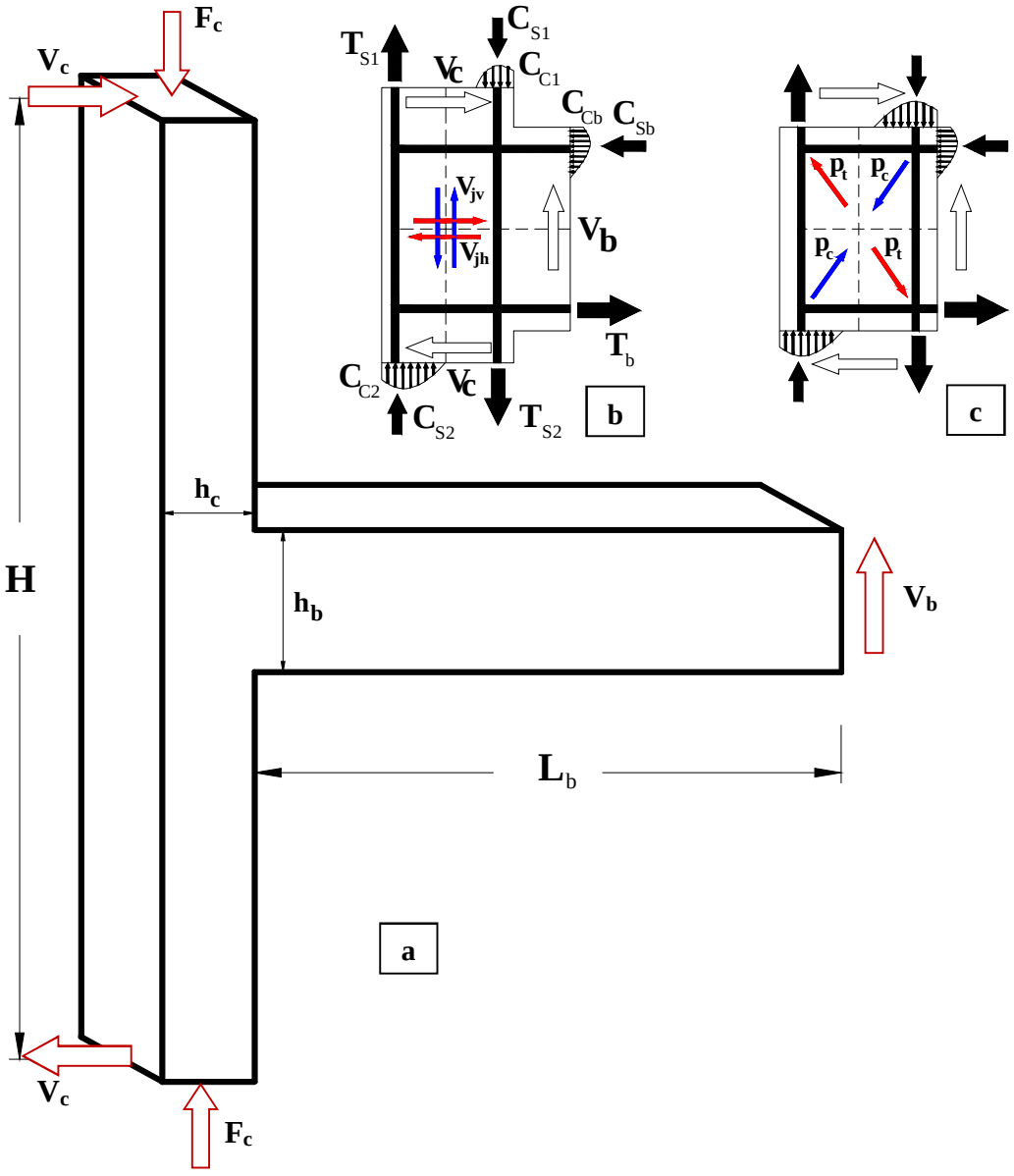

Figure 2-4: Mechanics of exterior joints subjected to seismic loads

As can be seen from the figure, the external moment and shear forces acting on the joint result in horizontal (V_{jh}) and vertical (V_{jv}) shear forces within the core. From equilibrium, the horizontal shear force on the joint V_{jh} can be calculated from the following:

$$V_{jh} = T_b - V_c \tag{2-1}$$

The tension force at the beam anchorages can be given by the following:

$$T_b = M_b/Z_b = V_b L_b/Z_b \quad (2\text{-}2)$$

where M_b is the beam moment at the interface with the column; V_b is the lateral force applied at the beam flexural point; Z_b is the lever arm and it is estimated as $Z_b = d_{sb} - d'_{sb} \cong 0.875 d_{sb}$, in which d_{sb} is the effective depth of the beam and d'_{sb} is the effective cover to compression reinforcement. L_b is the beam length up to the column interface.

Also, by imposing equilibrium on the external forces on the beam-column sub-assemblage, the resultant shear force in the column can be calculated as:

$$V_c = V_b(L_b + h_c/2)/H \quad (2\text{-}3)$$

in which H and h_c are the column height and width, respectively.

Substituting equations (2-2) and (2-3) into (2-1), the horizontal shear force V_{jh} is calculated by the following expression:

$$V_{jh} = V_b \left[\frac{L_b}{Z_b} - \frac{L_b + h_c/2}{H}\right] \quad (2\text{-}4)$$

Therefore, the joint shear stress τ_{jh} can be calculated using the following expression:

$$\tau_{jh} = \frac{V_{jh}}{h'_c b'_c} \quad (2\text{-}5)$$

in which h'_c and b'_c are the width and effective depth of the joint area.

Similarly, the vertical shear stress σ_{jv} on the core is obtained as:

$$\sigma_{jv} = \frac{V_{jv}}{h'_c b'_c} \quad (2\text{-}6)$$

in which V_{jv} is the vertical shear force acting on the core and can be calculated using the joint aspect ratio α as [Paulay and Park (1984), EC8-1 (1998), Park and Paulay (1975), and Tsonos (2007)]:

$$\frac{V_{jv}}{V_{jh}} = \frac{h_b}{h_c} = \alpha \quad (2\text{-}7)$$

Thus, the principal compressive and tensile stresses on the core, see Figure 2-4(c), can be obtained as (Tsonos, 2007):

$$p_{c,t} = \frac{\sigma_{jv}}{2} \pm \frac{\sigma_{jv}}{2}\sqrt{1 + 4\frac{\tau_{jh}^2}{\sigma_{jv}^2}} \quad (2\text{-}8)$$

In the case of considering the axial load effect, an additional axial stress of $\sigma_a = F_c/A_g$ should be added; where F_c is the column axial load, and A_g is the column cross-section area. For example,

Priestley and Hart (1994) use the following expression to calculate the principal tension stress of a joint region:

$$p_t = -\frac{\sigma_a}{2} + \sqrt{\tau_{jh}^2 + \left(\frac{\sigma_a}{2}\right)^2} \tag{2-9}$$

2.4 COMPRESSION SOFTENING PHENOMENON

It is well established that cracked concrete in compression within the joint area of a beam-column connection exhibits lower strength and stiffness than conventional concrete under uniaxial compression (see Figure 2-5). This occurs due to development of compression and tension fields within the joint area. The softening effect of concrete was quantified by several investigations such as Stevens et al. (1991a), Vecchio and Collins (1993), Belarbi and Hsu (1995), Zhang and Hsu (1998), and Park and Mosalam (2012) which led to better understanding of the shear problem in beam-column connections.

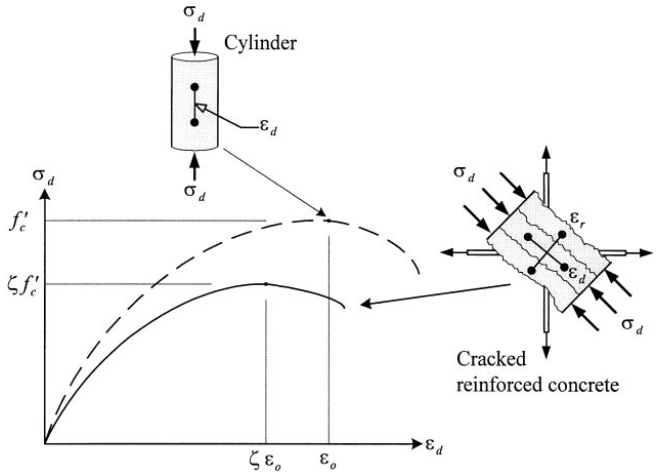

Figure 2-5: Softened behaviour of cracked concrete in compression (Hwang and Lee, 1999)

Several models were proposed to describe the behaviour of softened concrete in compression. For example, Hwang and Lee (1999) proposed the following equations for the softened concrete:

$$\sigma_d = \xi f_c' \left[2\left(\frac{\varepsilon_d}{\xi \varepsilon_o}\right) - \left(\frac{\varepsilon_d}{\xi \varepsilon_o}\right)^2\right] \quad for \left(\frac{\varepsilon_d}{\xi \varepsilon_o}\right) \leq 1 \tag{2-10}$$

$$\xi = \frac{5.8}{\sqrt{f_c'}} \frac{1}{\sqrt{1 + 400\varepsilon_r}} \leq \frac{0.9}{\sqrt{1 + 400\varepsilon_r}} \tag{2-11}$$

$$\varepsilon_o = -0.002 - 0.001\left(\frac{f_c' - 20}{80}\right) for\ 20 \leq f_c' \leq 100\ MPa \tag{2-12}$$

where σ_d is the average principal stress of concrete, ξ is the softening coefficient; f'_c is the compressive strength of a conventional concrete cylinder; ε_d and ε_r are the average principal strains, respectively; and ε_o is the concrete cylinder strain corresponding to f'_c.

2.5 PERFORMANCE OF NONSEISMICALLY DEFICIENT BEAM-COLUMN JOINTS

In the past three decades, a considerable amount of experimental research has been devoted to investigating behaviour of poorly detailed interior and exterior joints [Pantelides et al. (2002), Hakuto et al. (2000)]. Exterior joints, in general, are more vulnerable to seismic loading due to the sudden discontinuity of geometry and, as a consequence, the large demand imposed by the seismic load (Pampanin et al., 2003). Tests conducted on joints covered many parameters including different joint geometries, beam reinforcement ratios and anchorage details, column axial load ratios, joint shear stress demands, splices, and joint confinement.

Durrani and Wight (1985) and Ehsani and Wight (1985) tested interior and exterior joints, respectively, designed according to the recommendations of ACI-ASCE Committee 352 (1976). The results were compared to ductile joints to investigate the effect of joint hoops on strength, stiffness and energy dissipation capacity, and also to examine bar slippage inside the joint area. It was concluded that: a) the damage level in the joint can be deemed acceptable if the joint shear stress is below a certain limit ($\sqrt{f'_c}$ for exterior and $1.25\sqrt{f'_c}$ for interior); b) although bar slippage results in undesirable failures, joints with minor slippage and pullout failures showed good performance; and c) joint hoops improved the performance considerably but their effect was more pronounced on shear strength than reducing stiffness degradation. The final cracking mode observed for an interior joint is presented in Figure 2-6.

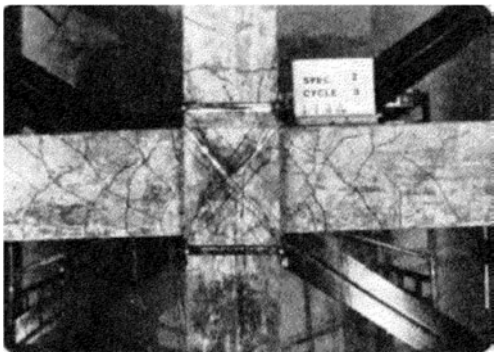

Figure 2-6: Crack pattern of an interior joint tested by Durrani and Wight (1985)

Aycardi et al. (1994) investigated 1/3 scale interior and exterior joints designed, according to ACI 318-89 (1989), to resist gravity loads only. The joints had transverse beams from both sides and a slab. The tests results showed that damage in exterior joints initiates at the anchorage region due to pullout of beam bottom bars and then it progresses towards the columns. In these specimens, a weak beam-strong column mechanism was evident and the maximum shear stress calculated was $0.87\sqrt{f'_c}$. The damage on the interior joints, on the other hand, was concentrated in columns with minor cracking in beams. In addition, a weak column-strong beam mechanism

occurred and the maximum shear stress in the joints was calculated at $1.04\sqrt{f'_c}$. For both the interior and exterior joints, the maximum capacity was reached at drifts between 2 to 3%.

Hakuto et al. (2000) tested joints that did not conform to NZS 3101 (1995). The joints investigated included inadequate beam anchorages and insufficient amount of joint hoops. Hakuto et al. considered in their investigation the details from a GLD seven-story RC building built in New Zealand in the late 1950s. When compared to design requirements of ductile frames as those found in NZS 3101 (1995) and ACI 318 (1995), the building had a) low column longitudinal reinforcement ratios, which in turn prevents achieving strong column-weak beam mechanisms, b) short splices at plastic hinge zones, c) inadequate beam and column lateral reinforcement for shear resistance and ductility requirements, d) no joint transverse hoops, e) poorly anchored reinforcement in the joint area, and f) beam hooks bent outside joint area in the case of exterior joints. The test results showed that i) interior joints with no joint hoops will receive severe damage if the horizontal shear stress in the core exceeds a certain value ($0.17f'_c$); ii) failure of the core occurs when the nominal shear stress in the core exceeds $0.07f'_c$; iii) the behaviour of exterior joints with little joint reinforcement was affected by the way the beam bars anchored into the core; iv) both exterior joints failed in shear at nominal shear stresses of $0.31\sqrt{f'_c}$ (bars bent inside the core) and $0.25\sqrt{f'_c}$ (bars bent outside the core), however, the joint with bars bent into the core allowed plastic hinges to develop in the beams. Figure 2-7 displays damage observed and crack patterns from the tests.

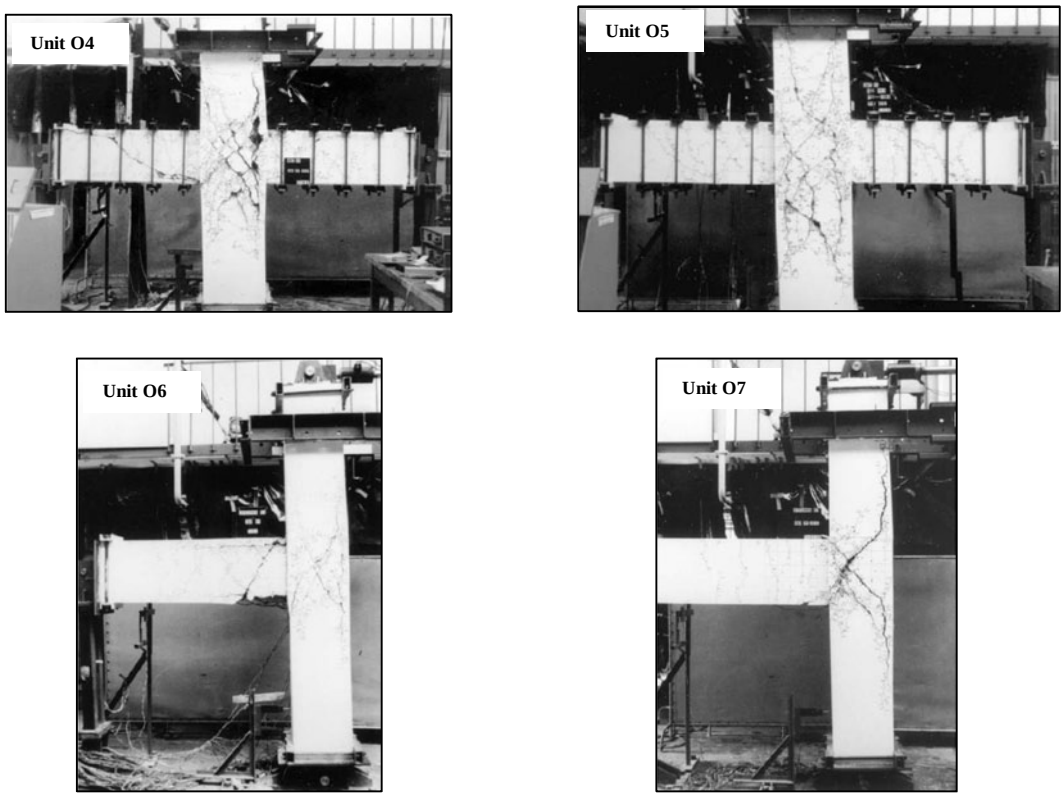

Figure 2-7: Observed damage from joints tested by Hakuto et al. (2000)

Clyde et al. (2000) reported on the performance of exterior joints with deficient detailing. Two column axial loads were investigated. Two specimens were tested with an axial load equal to 10% of f'_cA_g, and two were tested with an axial load equal to 25% of f'_cA_g, where A_g is the column cross-section area. Damage and crack patterns in the specimens were similar to those found in previous tests on exterior joints. In the tests, five performance levels were identified based on story drift, crack width and joint shear strength factor. In most of the specimens, the performance levels were reached at small storey drifts, large crack widths, and high shear strength factors. The final damage observed in the test units is shown in Figure 2-8.

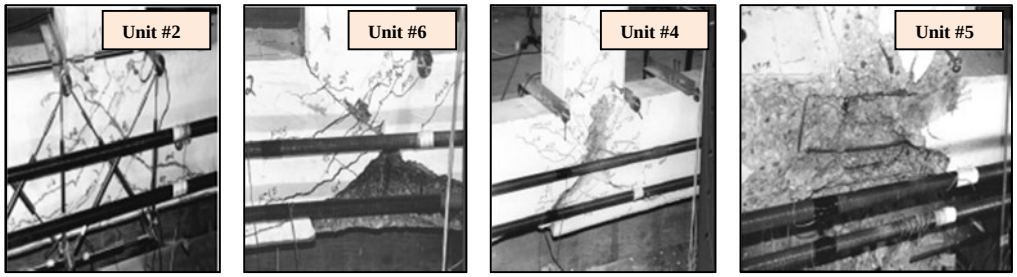

Figure 2-8: Crack patterns of tested joints at V performance level (Clyde et al., 2000)

Walker et al. (2002) tested seven GLD interior joints so as to investigate the effect of different joint shear demands and displacement histories on the behaviour of the joints. The specimens were designed to achieve strong column-weak beam mechanisms. To achieve this, beam bottom bars passing through the joint were made continuous, and as a result, the bond demand on the beam bars reduced. Two shear stress demands were investigated including 0.75 and $1.29\sqrt{f'_c}$. In addition, four different loading histories were applied. Cracking in the joints was observed to occur at a drift of 0.5% and a joint shear stress of $0.5\sqrt{f'_c}$. Damage in the core occurred after yielding of the beam bars taking place at 1.1% and 1.5% drifts for low and high shear demands, respectively. The joint damage due to shear initiated in the centre of the core at drifts of 3% (low shear demand) and 2% (high shear demand); whereas failure occurred at drifts of 4% and 3%, respectively. Failure was followed by bucking of column longitudinal bars. The tests also showed that half-symmetric displacement cycles were less damaging than full symmetric cycles. Walker et al. (2002) differentiated five performance levels based on the story drifts applied.

Pantelides et al. (2002) tested six substandard full scale exterior joints typical of those found in the United States pre-1970s buildings. Specimens were designed to fail in shear within the joint area. Thus, no joint hoops were provided in this area. In addition, beam bottom bars were inadequately anchored in the joint for four of the specimens. Moreover, details and amount of confinement did not conform to the design criteria of ACI 352 (1991). Two levels of axial loads were used similar to those by Clyde et al. (2000). The two main failure modes observed from the tests were joint shear failure and anchorage failure. The axial load level was noted to influence the joint shear strength coefficient. It was also noted that, in general, the joint shear strength coefficient γ=0.041 MPa given in FEMA 273 (BSSC 1997) was very conservative.

Also, one of the findings of this study is that joints with lower axial load level and failed in shear showed a 24% increase in the energy dissipation capacity compared to the corresponding specimen which failed in bond. However, at higher axial load levels, both types of joints showed the same energy dissipation capacity. In this investigation, five performance levels were also defined similarly to those by Clyde et al. (2000) and Walker et al. (2002). Plastic rotations, however, were additionally used to delineate between the performance levels. Figure 2-9 displays the crack patterns observed in the tested units at performance level V (loss of gravity load).

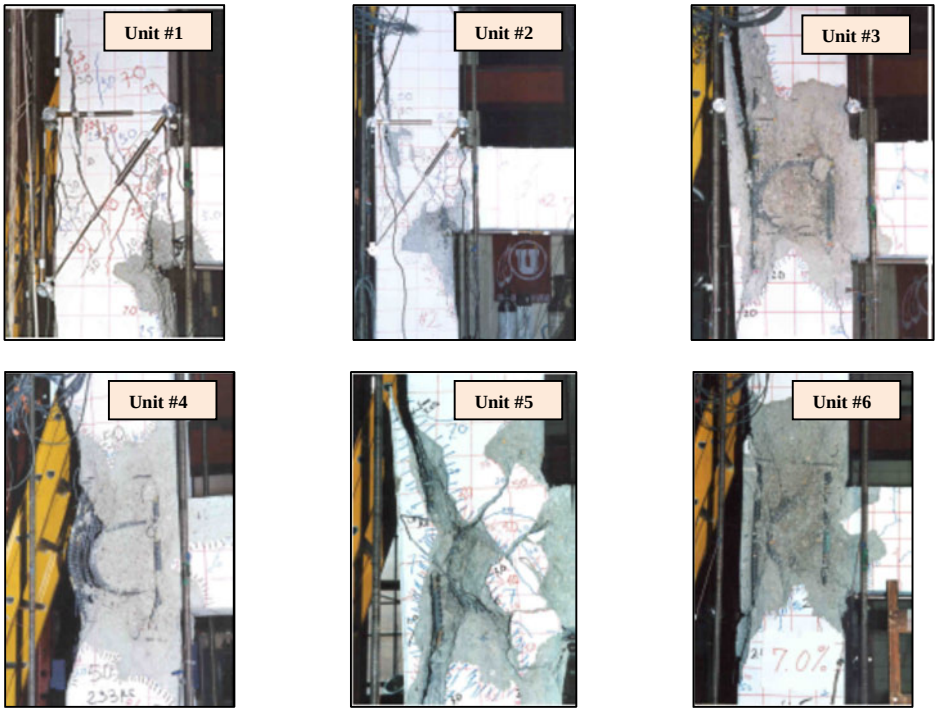

Figure 2-9: Crack patterns of tested joints at V performance level (Pantelides et al., 2002)

Pampanin et al. (2002) tested six joints including two knee, two exterior and two interior specimens. The joints were designed for gravity loads only with structural deficiencies typical of those found in the 1970s before the introduction of seismic provisions for detailing and materials. In the specimens, smooth longitudinal bars were used with end-hook anchorage detailing in the joint area. In addition, column reinforcement ratios were kept low. The test results showed that exterior joints experienced severe damage with high bar slippage and spalling of concrete at the back of the joint due to the “concrete wedge” effect, which prevented the formation of shear mechanism in the core. Knee and interior joints, on the other hand, showed acceptable levels of ductility and the failure was dominated by damage in the columns ”soft story mechanism”. Also, in these joints, high beam bar slippage was observed. Figure 2-10 shows the final cracking occurring in the exterior joint due to the concrete “wedge” effect.

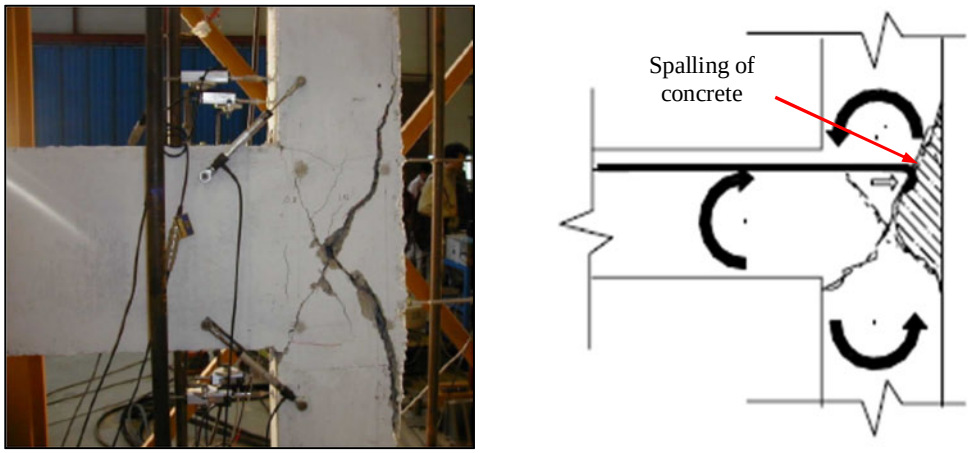

Figure 2-10: Failure of exterior joint due to concrete wedge effect (Pampanin et al., 2002)

Dhakal et al. (2005) tested six full scale RC joints designed, in accordance with British Standard BS8110 (1985), to sustain only gravity loads. No hoops were provided in the joint area. Key findings from the test results were: a) all joints failed due to shear mechanism in the core before formation of plastic hinges in the framing elements; b) shear strength of the GLD joints could be predicted safely using equations available in current seismic codes for ductile joints; and c) severe damage in the joint took place when 80% loss in the initial shear stiffness occurred. Figure 2-11 shows joint detailing and final damage observed in some of the specimens.

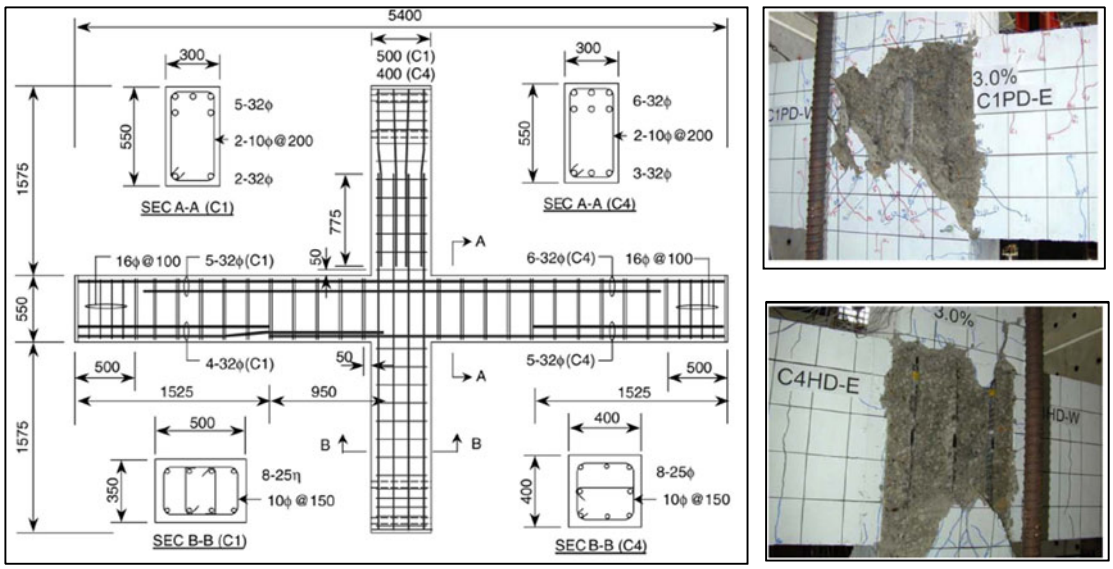

Figure 2-11: Specimens tested by Dhakal et al. (2005)

Kuang and Wong (2005) investigated the effect of beam bar anchorages on beam-column joint hysteretic behaviour. Five exterior joints were tested with different anchorage details including bars bent inside and/or outside the core and one specimen with lap splices. No transverse hoops were provided into the joint area in all units. The joints were built to simulate those in as–built RC framed buildings designed according to BS 8110 (1997). On the basis of the test results it was found that beam bar anchorages have a significant effect on the joint shear capacity as well

as on the hysteretic behaviour. Some of the joints failed at 50% of the nominal maximum capacity. Joints with beam bars bent away of the joint showed poorer behaviour and were recommended to be excluded from code design provisions. The presence of lap splices in the columns did not appear to have an effect on the joint shear strength. The final crack patterns and damage which occurred in the joints are shown in Figure 2-12.

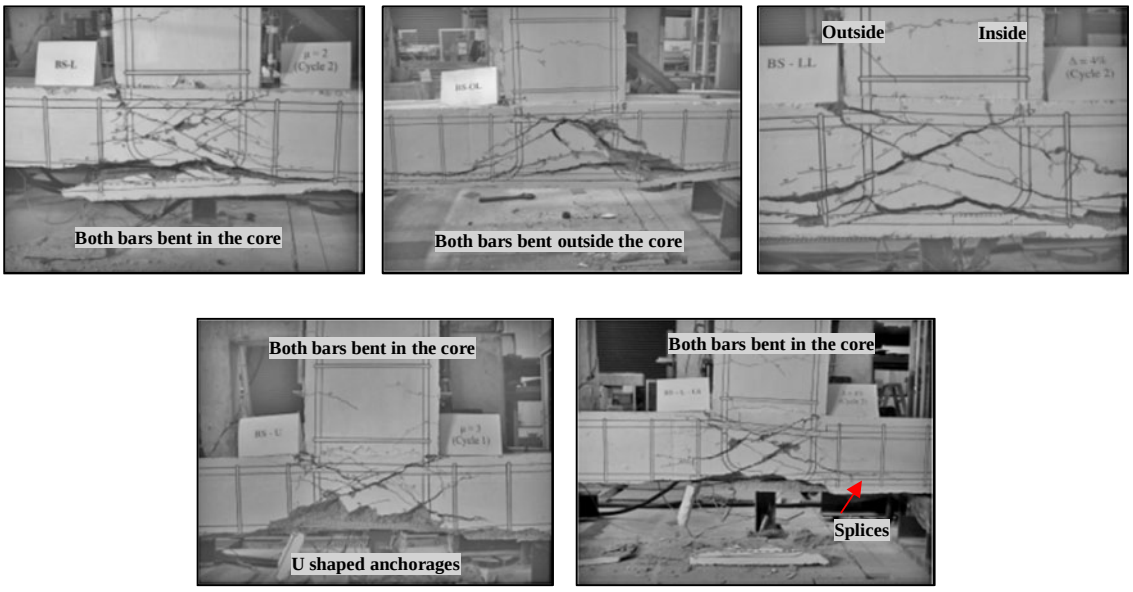

Figure 2-12: Failure modes of joints tested by Kuang and Wong (2005)

Bedirhanoglu et al. (2010) conducted two test series including nine beam-column joints built with reinforcement detailing and concrete qualities typical of those in Turkey. The specimens were constructed with very low strength concrete of 8.3MPa and plain round reinforcing bars (16*mm* as longitudinal and 8*mm* as transverse). Only two of the specimens were provided with transverse hoops within the joint area. Other parameters investigated included displacement history and axial load (0 to 50% of the column strength in compression). All specimens had a transverse beam and slab, except one specimen. Also, in two of the specimens, the beam top hook was welded to the bottom anchored bars. The test results showed that: 1) all specimens experienced joint failure before yielding; 2) specimens with welded hooks-to-anchorages had improved shear strength (about 35% higher) in comparison to those specimens without welding which exhibited a considerable bar slippage that limited their capacities; 3) welding was not sufficient to allow the beam and column to reach their nominal strengths; 4) specimens with higher axial load showed higher energy dissipation capacity. Figure 2-13 shows the cracking patterns and damage of the specimens at a drift of 4%.

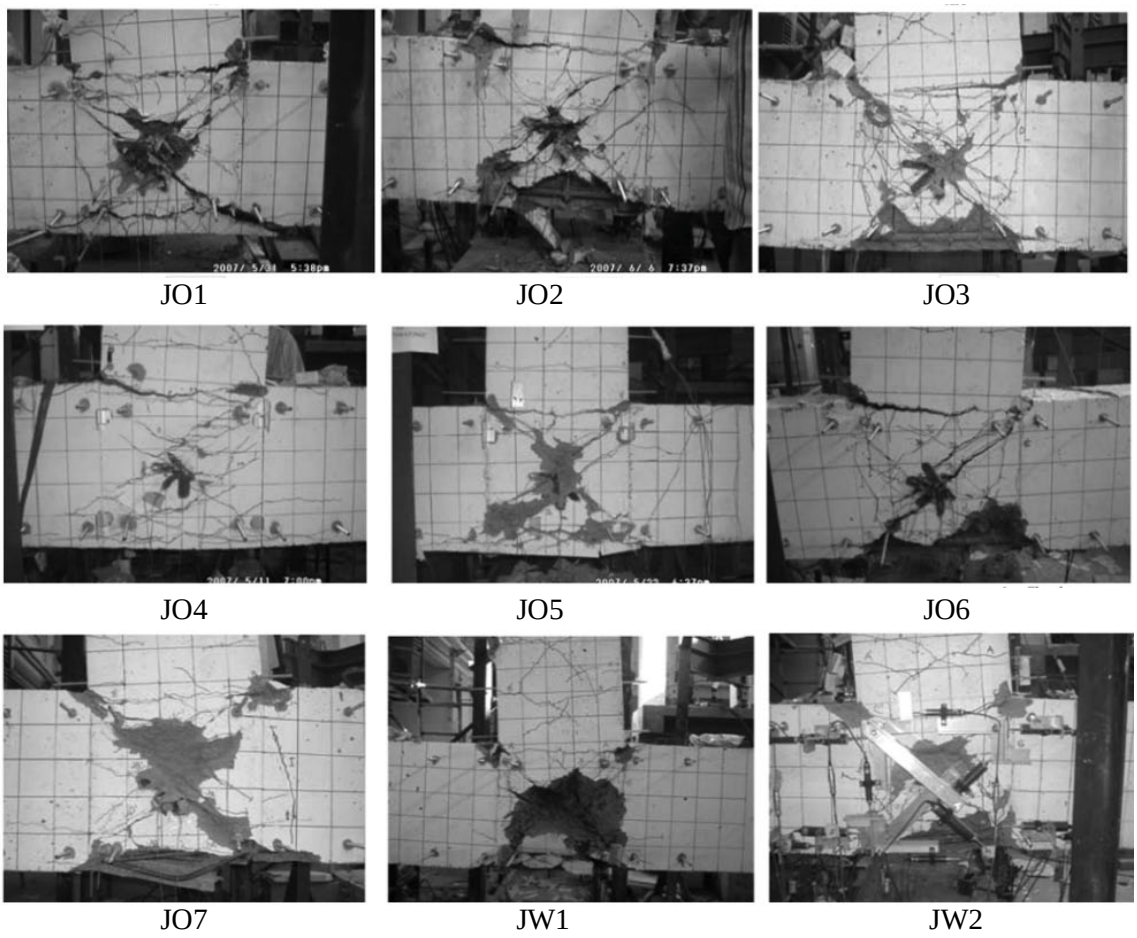

Figure 2-13: Cracking patterns and damage state of the tested specimens at a drift of 4% (Bedirhanoglu et al., 2010)

Recently, Hassan (2011) conducted an experimental programme at the University of California, Berkeley which included four full-scale corner joints. The joints were substandard with pre-1971 detailing and having no transverse hoops in the core. Test parameters investigated were the beam reinforcement ratio, beam aspect ratio (1 and 1.67), axial load ratio, and loading history (unidirectional and bidirectional). The joints were three-dimensional with a slab and full story column height. All specimens failed due to severe shear mechanism in the joint area along with buckling of column longitudinal reinforcement. However, failure in three of the specimens occurred before yielding of beam longitudinal bars (J failure), whereas one specimen failed after beam yielding (BJ failure). From the results, it was found that the axial load only affected joints with J type failure; where an increase in shear strength occurred when the axial load level was higher than $0.2f'_cA_g$. The test results also showed that biaxial loading resulted in early joint cracking, more severe stiffness degradation and higher post-peak pinching. In addition, the increase in beam reinforcement ratio did not appear to affect the joint shear strength of specimens with J type failure mode; however, joint shear strength was proportional to beam reinforcement for the BJ-Failure mode. Figure 2-14 shows failure modes of two tests units under unidirectional (U-J-1) and bidirectional (B-J-1) loadings.

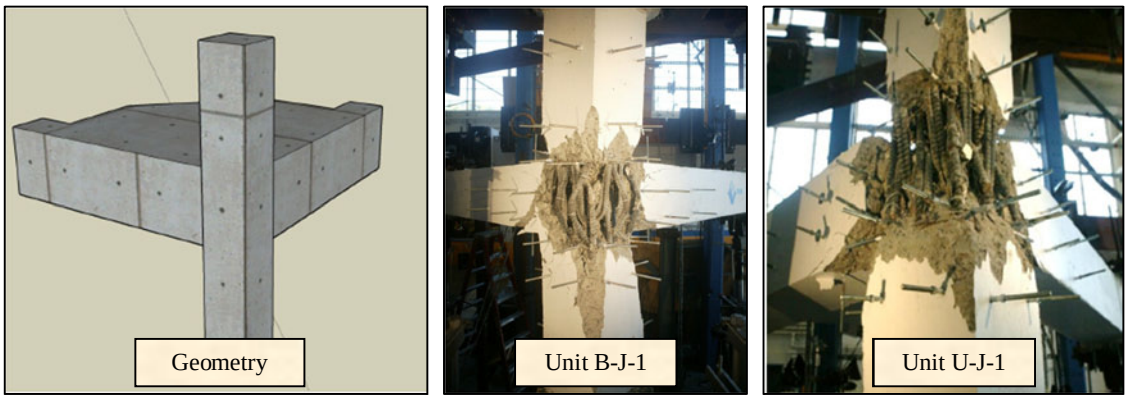

Figure 2-14: Specimen isometric geometry of test specimens and failure modes of some specimens (Hassan, 2011)

In addition to the investigations reported above, several studies are available in the literature in which the performance of poorly detailed joints was examined to evaluate the enhancement due to a specific strengthening scheme [for example: French et al. (1990), Beres et al. (1992), Filiatrault and Lebrun (1996), Karayannis et al. (1998), Tsonos (2001), Alcocer and Jirsa (1993), Choudhuri et al. (1992), Ghobarah et al. (1997), Biddah et al. (1997), Hoffschild et al. (1995), Antonopoulos and Triantafillou (2002, 2003), Ghobarah and Said (2002), Gergely et al. (1998, 2000), Pantelides et al. (1999), Prota et al. (2001, 2002), El-Amoury and Ghobarah (2002), Tsonos and Stylianidis (2002), Karayannis and Sirkelis (2002), Dogan et al. (2000), Shannag et al. (2002), Adin et al. (1993), and Pantelides and Gergely (2002), Sasmal et al. (2011)]. These studies attributed the need for joint upgrading to: a) shear failure mechanism in the joint area and spalling-off concrete, b) a combined shear-bond failure within the joint area along with pullout of anchored beam flexural reinforcement, c) spalling-off of concrete at the back of the joint area of exterior joints, c) buckling of column bars within the joint area due to spalling off concrete, and d) inferior beam and/or column capacities (Engenidiz et al., 2005).

2.6 SHAKE TABLE TESTS ON SUBSTANDARD STRUCTURES

Many experimental studies have been conducted on RC beam-column connections with poor reinforcement detailing and material qualities, but the damage was mainly investigated at the local level (i.e. joint level). Moreover, several analytical panel-zone models have been developed to simulate the behaviour of beam-column connections [Sharma et al. (2011), Hassan (2011)]. However, further validation on a full-scale structure is still necessary. This is due to the fact that the use of these models may lead to significant changes in dynamic characteristics of the structure such as the study by Favatta et al. (2008). Thus, shake table tests are essential for verification of findings of local-level experimental tests, calibration of existing numerical joint models, and to develop practical cost-efficient modelling strategies for full-scale deficient structures.

Scarce data are available on shaking table tests on full-scale deficient structures. Beres et al. (1992), for example, tested a 1/8 scaled three story building with light reinforcement. Based on the results it was concluded that lightly reinforced buildings suffer from high deformability and P-Δ effects. It was also found that the presence of slabs may increase significantly the beam capacity and stiffness and, as a consequence, a soft story mechanism is most likely to occur.

El-Attar et al. (1991) tested a 1/6 scaled one-bay two-story GLD office building designed according to ACI 318-89 (1989). The same building with close details was tested at the University of California-Berkeley at a 7/10 scale (Blondet et al., 1980). The test aimed to provide an insight into the behaviour of simple lightly reinforced GLD buildings. Based on the test results, it was found that although beam anchorages were critical regions and suffered significant damage compared to columns, they could not cause failure of the building even at high seismic intensities (0.75g). However, considerable reduction in stiffness was evident from the test.

Bracci et al. (1995) evaluated the performance of 1/3 scaled three story building using the results by Aycardi et al. (1994) on exterior joints. The model was tested on the shaking table of the State University of New York (SUNY) by Bracci et al. (1992). The main conclusions from the shaking table tests were that: a) lightly reinforced structures suffer from weak column-strong beam mechanisms, b) moderate earthquakes may cause severe damage to these buildings along with sidesway deformations higher than code recommendations, and c) the structural behaviour can be captured reasonably if sufficient knowledge about the modelling components is available.

At ITU Earthquake and Structural Engineering, Turkey, Erol et al. (2006) conducted an experimental test programme on seven ½ scale two-storey one bay RC frames under constant vertical load and reversed cyclic lateral loads. Some of the frames were built with and some without splices at column ends. The study aimed to give an insight into the behaviour of CFRP strengthened infilled RC frames experimentally and collect data to be used in theoretical work. The test results showed that strengthening infill walls with CFRP composites in a diagonal direction improves significantly lateral strength and stiffness. This work fills, to some extent, a gap on the performance of deficient frames with infills.

In 2004, the Concrete (CI) and Earthquake Engineering research groups (EEG) at the University of Sheffield (UoS) supported by the European Union (ECOLEADER PROJECT No 2 - SEISMIC TESTS ON A REINFORCED CONCRETE BARE FRAME WITH FRP RETROFITTING, 2004) took part in the seismic shaking table tests on a two-storey full-scale RC framed building. The seismic tests were carried out at the Mechanical Seismic Studies Laboratory EMSI (Etudes de Mecanique Sismique) at CEA research centre (Commissariat à l'Energie Atomique) in Saclay, Paris (Chaudat, 2005). The framed building was designed for no

seismic loading and with poor reinforcement detailing. However, joint regions were provided by transverse hoops, beam top and bottom reinforcement were anchored into the joint area in the form of hooks, and no column splices were used. The bare building was initially subjected to seismic intensities up to PGA=0.4g to cause severe damage. Initial damage and yielding occurred at a seismic intensity of PGA=0.2g. After that, the building was strengthened by different applications of CFRP sheets in order to assess their efficiency to upgrade the capacity. The strengthening was successful and improved the performance significantly. Figure 2-15 shows the tested 2004 Saclay building.

Figure 2-15: General view of the 2004 Saclay building (Chaudat et al., 2005)

From the previous work on shaking table tests it is noted that: a) tests conducted on full-scale deficient structures are very limited, and the main focus was only on structures with lightly reinforced elements; b) the tested buildings did not address all possible deficiencies such as very poor concrete quality, short beam anchorages and column splices, and no transverse hoops in the joint region; c) no data are available on cost-effective methods to upgrade such structures.

Thus, the performance of deficient buildings under seismic actions is still questionable. The presence of multiple deficiencies simultaneously in a building, which is very common in Mediterranean countries, may cause severe collapses and this needs further investigation. Moreover, the development of strengthening measures that can be cheap, effective and easy to apply on real buildings with minimum disruption to building functionality is still needed.

2.7 PARAMETERS AFFECTING JOINT BEHAVIOUR

Based on the previous literature on beam-column joints, it can be noted that many parameters affect the joint behaviour. These parameters include beam anchorages, column splices, axial load, load history, joint dimensions, presence of concrete slabs and transverse beams, joint confinement, and column intermediate bars. In the following subsections, the parameters of interest are summarised. A detailed review on all parameters can be found in the study by Hassan (2011).

2.7.1 Beam anchorages

Figure 2-16 shows examples of typical anchorages of beam bars within the joint area of older joints with substandard details. As can be seen from the figure, beam flexural bars in the old practice were anchored into the joint area in different ways which, in turn, influence the force transfer mechanism within the joint (see Figure 2-17). The joint strength as well as the general hysteretic behaviour depends primarily on the development of resisting shear mechanism within the core. If the beam flexural bars are anchored adequately in the core, then two mechanisms can be recognised, namely, secondary-strut (in the case of bars bent inside the core) or extended-strut mechanism (in the case of bars bent outside the core). In the first case, a virtual strut mechanism develops along the diagonal of the core and it is enclosed by a bearing force due to anchored beam bars (see Figure 2-17a). The bearing resistance is produced through bond action between bar lugs and surrounding concrete (Hassan, 2011). In the other mechanism, the strut developed within the core tends to extend to the first column shear link forming a long but unstable strut mechanism (see Figure 2-17b). In both cases, reduced and severely degraded joint shear strength is obtained [Hakuto et al. (2000), Kuang and Wong (2005)]. For joints with such detailing, a maximum joint shear stress of about $0.34\sqrt{f'_c}$ is expected [Pampanin et al. (2002) and Hakuto et al., (2000)]. Kuang and Wong (2005) reported a maximum shear strength of $0.45\sqrt{f'_c}$.

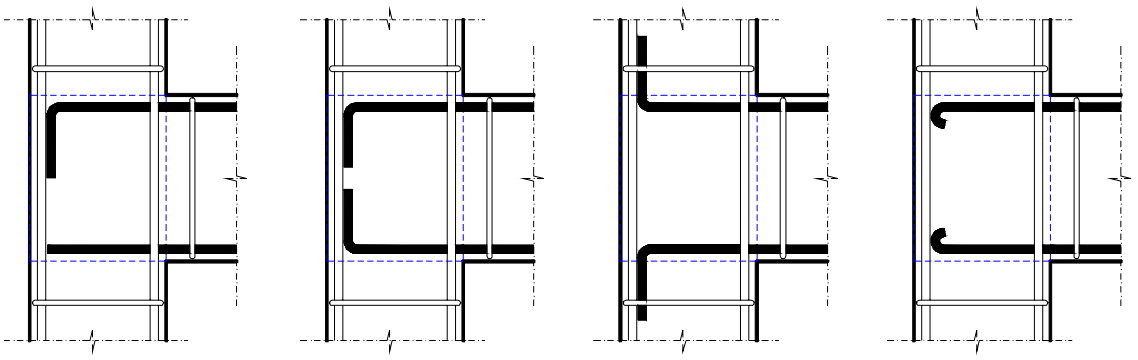

(a) (b) (c) (d)

Figure 2-16: Examples of beam bar anchorages within the joint region of older design connections

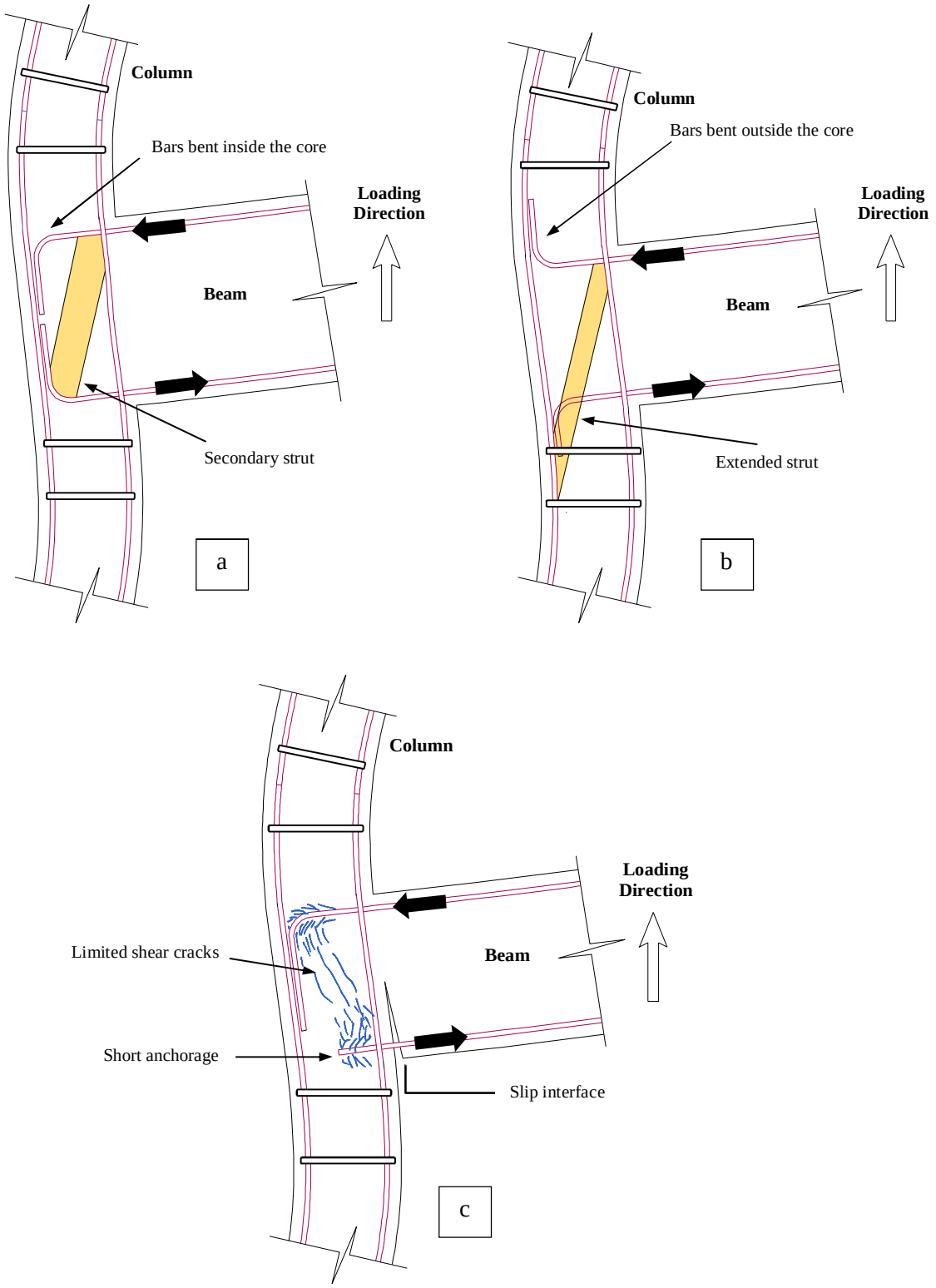

Figure 2-17: a) Secondary strut mechanism, b) extended strut mechanism and c) short beam bottom bar anchorages

When the beam bottom bars are inadequately anchored within the core, as shown in Figure 2-17(c), the joint strength is governed by the premature pullout mechanism developed at the beam/joint interface. A reduction in the joint strength of about 25-50% is expected (Hassan, 2011), depending on the length of the embedded bars. In such case, the strut mechanism will not be fully developed due to the absence of a sufficient support when loading in the upward

direction (bottom bars in tension). The slip at the beam/joint interface is also reported to jeopardise the joint strength in the downward loading direction due to opening of large cracks (Hakuto et al., 2000). Furthermore, large bar slippage will lead to excessive sidesway drifts which may, in turn, result in unstable failure mechanisms. Thus, ensuring a sufficient and appropriately anchored beam bars within the joint region is important to prevent premature failures and to develop proper shear transfer mechanisms within the joint.

2.7.2 Column lap splices

The effect of column splices on the joint shear strength was investigated by Wong (2005), Wong and Kuang (2008) and Beres et al. (1992) based on experimental observations on beam-column joints. Accordingly, it was observed that column splices only influence the joint shear strength in the case of low column flexural capacity. The developed splitting cracks along the column splices in addition to yielding of column reinforcement tend to reduce the shear strength of the joint.

2.7.3 Load history

For a conventional quasi-static loading protocol comprising two to three cycles in each loading step, the shear strength is only slightly affected by the load history (Hassan, 2011). Within the elastic range, no effect of the load history on the maximum shear strength is observed unless a large number of cycles is applied.

The use of complicated loading histories could result in severely deteriorated post-peak response [Engindeniz (2008), Priestley and Hart (1994), and Hassan (2011)]. Hassan (2011) reported that bidirectional loading leads to lower initial cracking, less effective stiffness, faster stiffness degradation, higher pinching, earlier shear cracking initiation, and less drift ratio at the peak shear strength.

In terms of load history type, Bedirhanoglu et al. (2010), for example, reported that no effect is observed from using unidirectional loading histories with 66 or 10 cycles. Walker et al. (2002) showed that half-symmetric displacement cycles were less damaging than full symmetric cycles. An actual seismic load is also well-established to result in higher joint shear strengths in comparison to quasi-static load histories due to the dynamic effect.

2.7.4 Axial load

Despite the numerous investigations, the effect of axial load on the joint shear strength is still controversial. In some studies, such as that by Vollum (1998), no effect of the axial load on the shear strength was reported. Other studies such as that by Pantazopoulou and Bonacci (1992) indicated a decrease in the joint shear strength with increase in the axial load. While some studies such as those by Barnes and Jigoral (2008), Clyde et al. (2000), Pantelides et al. (2002), Bedirhanoglu et al. (2010) reported an increase in the shear strength as the axial load increases

but with faster degradation in strength. Hassan (2011) reported that the axial load results in enhanced shear strength for J-type joints.

It is recognised, however, that joints with weak column-strong beam design will exhibit higher shear strengths with increase in the axial compressive load due to reduction in tensile strains penetrating through the joint panel zone [Barnes and Jigoral (2008), Kim and LaFave (2009)]. It is also reported that the axial compressive load has a favourable effect on joints with inadequately anchored bars, where it improves the general behaviour due to enhancement in bond strength [Hassan (2011), Pantelides et al. (2002)].

Chapter 2

PART II: SUBSTANDARD COLUMN SPLICES

2.8 INTRODUCTION

Many older RC columns were designed primarily for gravity loads with little or no considerations for seismic loading. Thus, their reinforcement details such as transverse reinforcement and lap splices are not adequate to provide satisfactory performance in seismic events. This was evident from the severe damage and collapses observed in previous earthquakes such as the 1994 Northridge, 1999 Izmit, and 1999 Chi-Chi, earthquakes. Therefore, knowledge of the behaviour of these "non-ductile" columns under earthquake loads is necessary to develop efficient and reliable rehabilitation measures.

This part reviews briefly the performance of RC columns with substandard splices. Works conducted to evaluate the response of lap splices in members subjected to earthquake cyclic

loads, as well as techniques to improve the performance of inadequate lap splices are summarised.

2.9 COLUMN SPLICES: DEFICIENCY AND STRENGTHENING

Paulay et al. (1981) investigated the behaviour of inadequate column splices with different confinement contents. Twelve columns with either (406.4 mm x 304.8 mm) or (406.4 mm x 406.4 mm) cross-sections and lap lengths of 82% to 95% of that required to achieve yield were tested. The outcome of this study revealed the importance of confinement on the cyclic response of RC columns with inadequate splices. The use of closely spaced ties delayed splitting cracks and flexural hinging was achieved. Also, it was observed that increasing the amount of confinement is more favourable than increasing the lap length. These important findings encouraged further research on confinement as a repair measure for deficient splices.

Chai et al. (1991) conducted cyclic tests on circular columns with pre-1970 construction details. No axial load was applied to the columns. The as-built specimens had a splice length of 20 times the bar diameter. Steel jackets were used to repair and strengthen the substandard specimens. The tests demonstrated that the unconfined specimens experienced bond splitting failure accompanied by significant degradation in load and stiffness before reaching yielding in the flexural reinforcement. The use of steel jackets resulted in an improved cyclic behaviour even in the case of repair. Figure 2-18 shows the response of a column specimen before and after retrofitting.

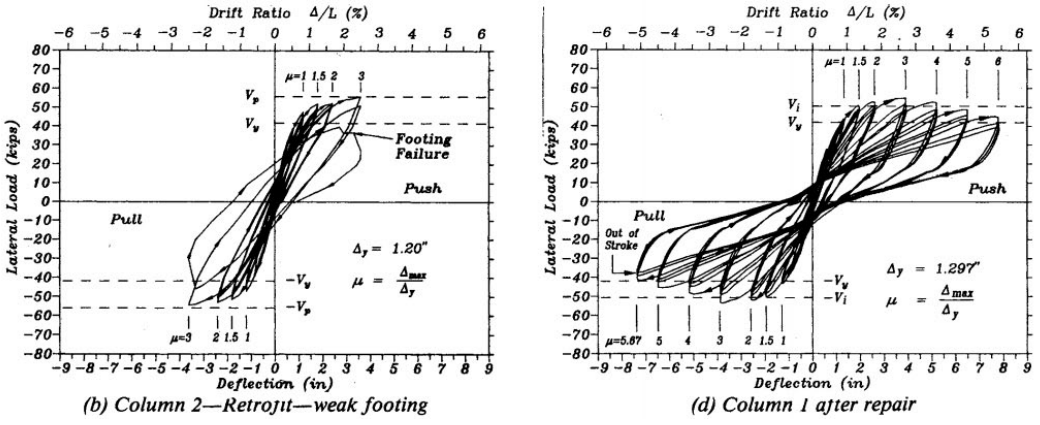

(b) Column 2—Retrofit—weak footing (d) Column 1 after repair

Figure 2-18: Hysteretic response of columns with lapped starter bars (Chai et al., 1991)

Coffman et al. (1993) tested four half-scale circular columns with details used in the 1950s-to-1970s. The columns were built with lap splice lengths of 35 times the bar diameter. Prestressed external steel ties were used to confine the splices. The amount and spacing of the steel ties varied between the specimens. Tests were performed under reversal cyclic loading with the axial load held constant at 10% of the column strength in compression. The unconfined specimens failed due to flexure hinging at the splice zone, reaching a displacement ductility of

four. The externally confined specimens showed only improvement in ductility and a larger number of cycles was sustained at the maximum load. Thus, the addition of external ties was not truly effective due to the fact that the reference specimens performed well. Figure 2-19 shows the response of a reference specimen as well as the response of a specimen strengthened by four prestressed hoops spaced at eleven inches.

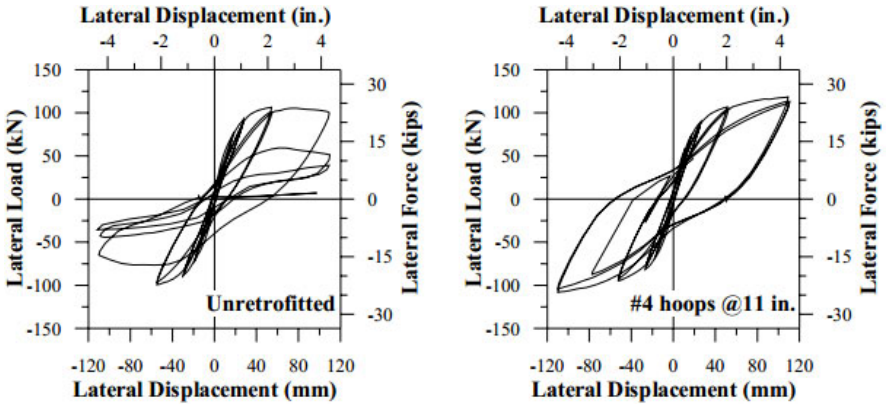

Figure 2-19: Comparison of Test Results (Coffman et al., 1996)

Valluvan et al. (1993) tested twelve third-scale columns under cyclic axial loads. The specimens were built with a lap length of 24 times the bar diameter. Various rehabilitation measures including (i) steel angles and straps, (ii) internal or external ties, or (iii) welds along the spliced bars were used to confine the splice region. The unconfined specimen failed prematurely due to splice failure at about 2/3 of the nominal flexural capacity of the column. The use of steel angles and straps or external ties resulted in a significantly improved behaviour. However, the improvement due to strengthening required the use of grout to ensure a proper bond between the existing concrete and the additional steel confinement. The use of internal ties was less efficient in enhancing the performance. This was due to the fact that removal of the concrete cover to install the ties might have caused an internal micro-cracking that compromised the bond capacity. Welding of splices to ensure continuity of bars was found to be an effective measure; however, internal ties were required to prevent reinforcement out-bursting and buckling.

Aboutaha et al. (1996) used steel jackets to confine inadequate lap splices of building columns with square and rectangular cross-sections. Thin steel jackets fixed by adhesive anchor bolts were used along the splice length. In some cases, the strengthening was extended beyond the splice end. No axial load was applied to the column during the tests. The test results showed that the retrofit approach can be effective at improving the performance of the column. It is also found that the use of anchor bolts resulted in stiffening of the steel plates leading to better behaviour; and this was important as the column width increased. Aboutaha et al. (1996) reported that a proper strengthening using the steel jacket requires the extension of the jacket above the splice length along with the use of adhesive bolts on opposite sides of the column. Figure 2-20 shows a typical steel jacket repair of a rectangular cross-section.

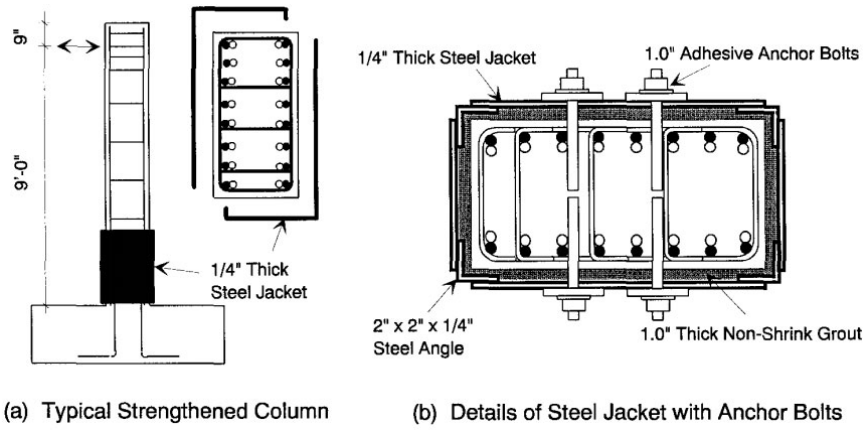

Figure 2-20: Steel jacket repair measure for lap splices (Aboutaha et al., 1996)

Lynn (1996) conducted a study on columns with pre-1970s construction detailing. Three of the columns were built with spliced bars of 20 to25 times the bar diameter and tested under cyclic load conditions and a constant axial load of 12% or 35% the column strength in compression. The presence of splices was noted to affect the performance in the post-peak stage. More degradation in the response after yielding was observed in the case of splices and low axial load in comparison to continuous bars, as shown in Figure 2-21. For columns with high axial loads, splices did not affect the performance.

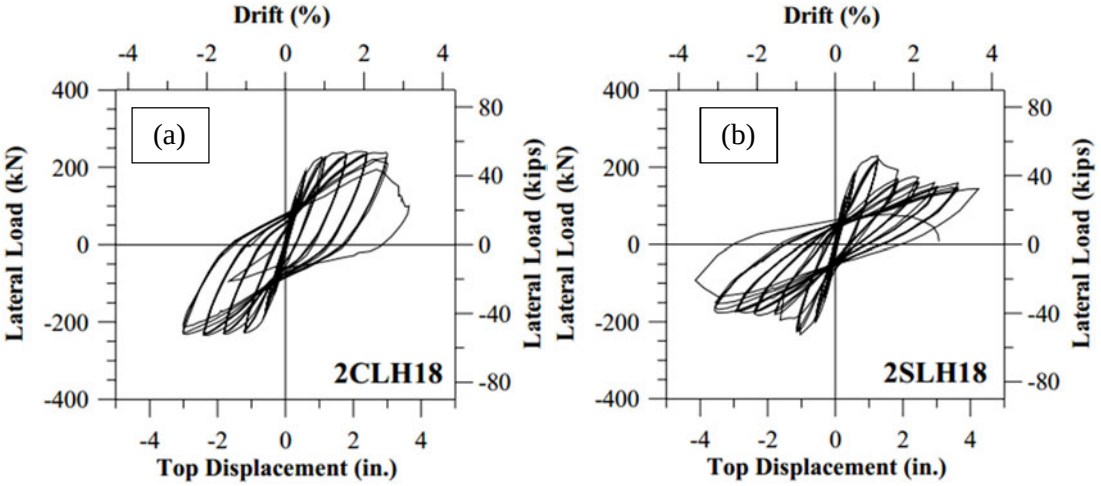

Figure 2-21: Response of tested specimens a) no splices, and b) with $20d_b$ splice length and 0.12 axial load ratio (Lynn, 1996)

Melek et al. (2003) tested six RC columns with pre-1960s details. Variables investigated included the level of axial load (10%, 20% and 30% the column capacity), the ratio of moment to shear (0.67 to 0.93), the load history on column behaviour, and a splice length of $20d_b$. All specimens behaved unsatisfactorily under cyclic lateral load and degradation in the response initiated prior to bar yielding. The degradation in the lateral strength was due to bond deterioration; however, the rate of degradation was dependent on the axial load level, the moment to shear ratio, and the load history. The increase in the axial load ratio resulted in loss of column axial capacity at high drifts. However, this effect was absent at lower axial loads.

Figure 2-22 and Figure 2-23 show an example of the severe damage occurred in the tested specimens and the degradation in lateral strength due to deficient splices.

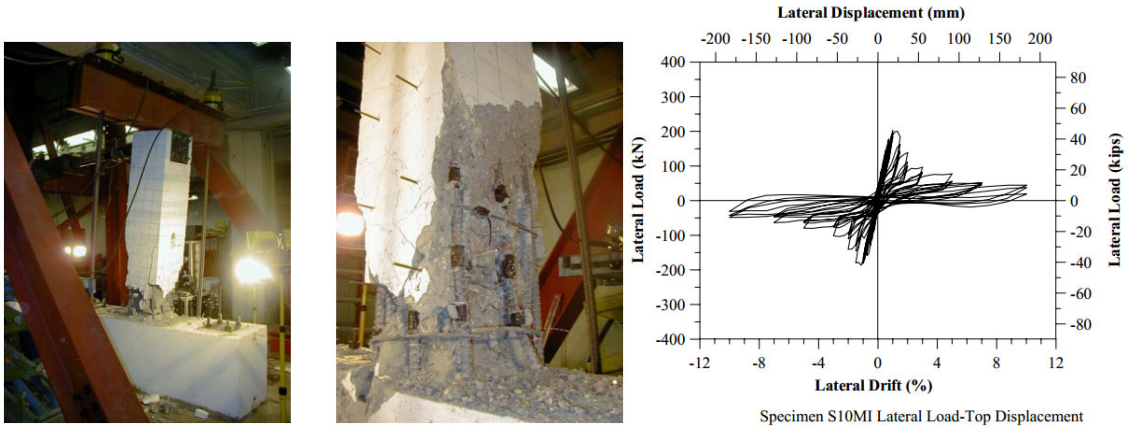

Figure 2-22: Specimen S10MI at 10% drift – axial load capacity maintained (Melek et al., 2003)

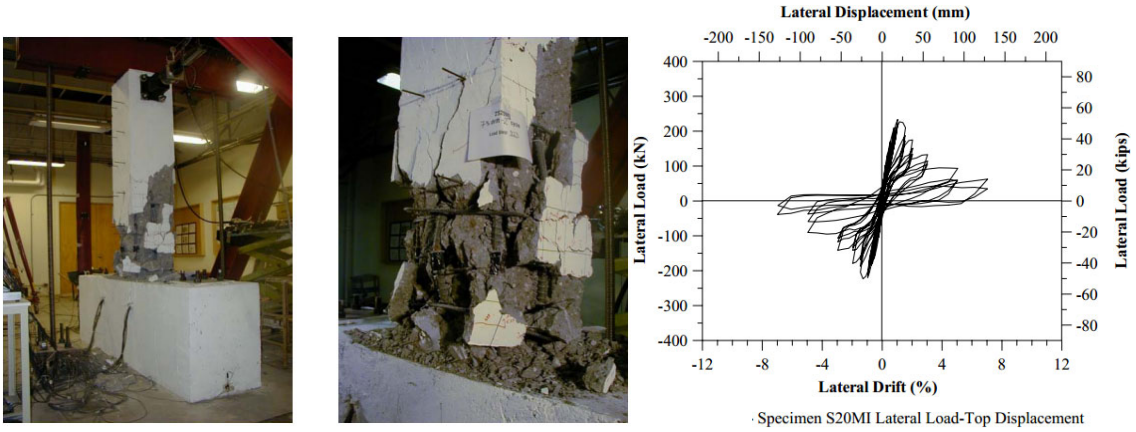

Figure 2-23: Specimen S20MI at 7% drift – axial load capacity lost (Melek et al., 2003)

Harries et al. (2006) tested full-scale building columns built with $22d_b$ lap lengths located at the hinging zone. In this study, all the as-built specimens demonstrated poor performance accompanied by rapid loss of stiffness and lateral strength due to splice failure. Specimens retrofitted with external jackets of CFRP exhibited improved ductility and capacity. However, the improvement in ductility was limited by the onset of bar slippage. In fact, the retrofit jackets provided were insufficiently stiff to control the large slip of the splices. Harries et al. (2006) reported that the amount of CFRP materials required to control such large bar slippage will be expensive and impractical.

Breña et al. (2007) tested six circular columns with details conforming to the 1960s. The details included short lap splices (24 times the bar diameter) at the base and widely spaced transverse reinforcement. Two of the specimens were tested in the unconfined conditions; while four specimens were rehabilitated using one transverse layer of FRP jackets of carbon and aramid along the splice region. Figure 2-24 shows the reinforcement detailing and strengthening of the tested columns. Results of the cyclic tests showed that the failure of unconfined specimens was

due to lap splice failure at the base of the columns after reaching yielding. Degradation in the response occurred at a displacement ductility of 2 while failure occurred at a displacement ductility of 3. The rehabilitated specimens, on the other hand, were able to maintain their lateral strength at moderate displacement ductilities between 4 to 5. Enhancement in lateral strength, which amounted up to 40% in some specimens, was also achieved.

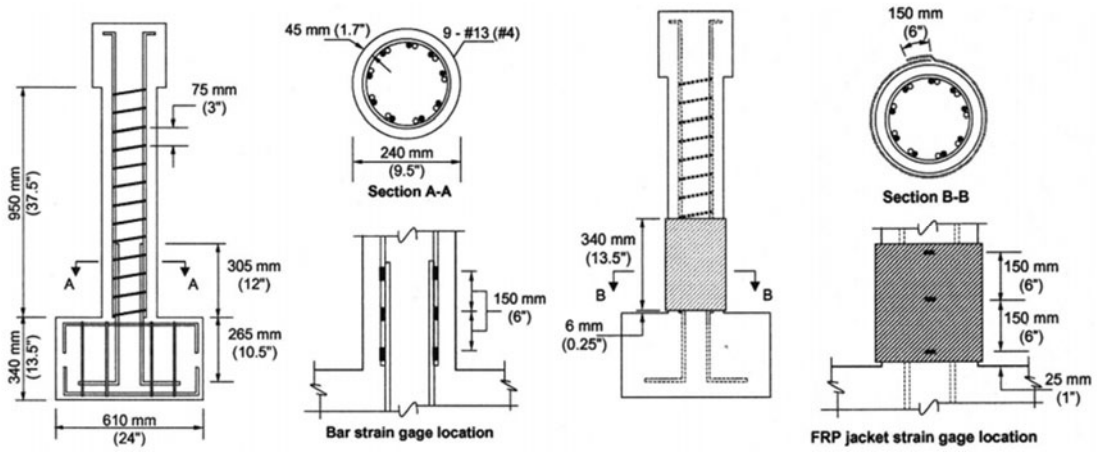

Figure 2-24: Reinforcement detailing and FRP strengthening of the tested columns (Breña et al., 2007)

Harajli et al. (2008) tested full-scale columns built with $30d_b$ lap splice at the column base. One or two layers of CFRP were used for strengthening. The as-built specimens failed prematurely before yielding due to splitting cracks along the splices (see Figure 2-25a). This failure resulted in significant deterioration in the lateral load resistance and severe degradation in stiffness. The degradation was more pronounced for columns with smaller concrete cover to bar diameter ratios. The CFRP strengthened columns, on the other hand, failed due to partial or complete loss of splitting strength (see Figure 2-25b). The increase in the lateral strength ranged between 9% to 60%. Harajli et al. (2008) reported that the increase in the lateral capacity was limited by bar yielding; and the improvement could be higher if smaller concrete covers and larger amounts of CFRP were used.

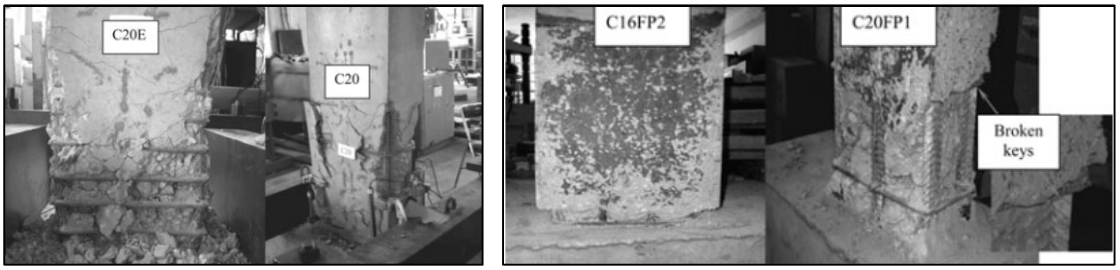

Figure 2-25: a) failure of unconfined and earthquake resistant columns and b) failure mode of FRP repaired specimens after removing the FRP sheets (Harajli et al., 2008)

Endeshaw (2008) tested columns with construction details typical of those in the 1950's and 1960's. The tests were conducted on 40% scaled specimens. The columns were designed with flexural and lap splice deficiencies. The lap splice length was 35 times the column longitudinal

bar diameter (d_b). Two specimens (AB-1 and AB-2) were tested in the as-built condition. One specimen (SJ) was retrofitted with oval-shaped steel jacket (see Figure 2-26), and five specimens were retrofitted using CFRP composites (see Figure 2-27).

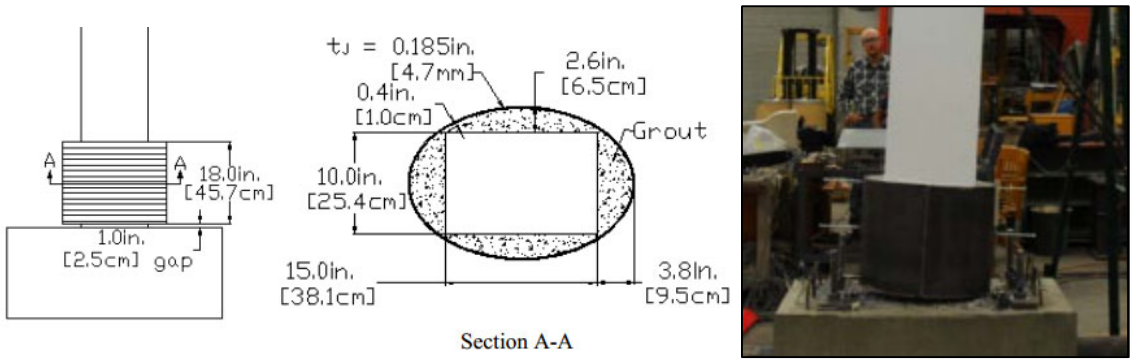

Figure 2-26: Steel jacketing repair measure (Endeshaw, 2008)

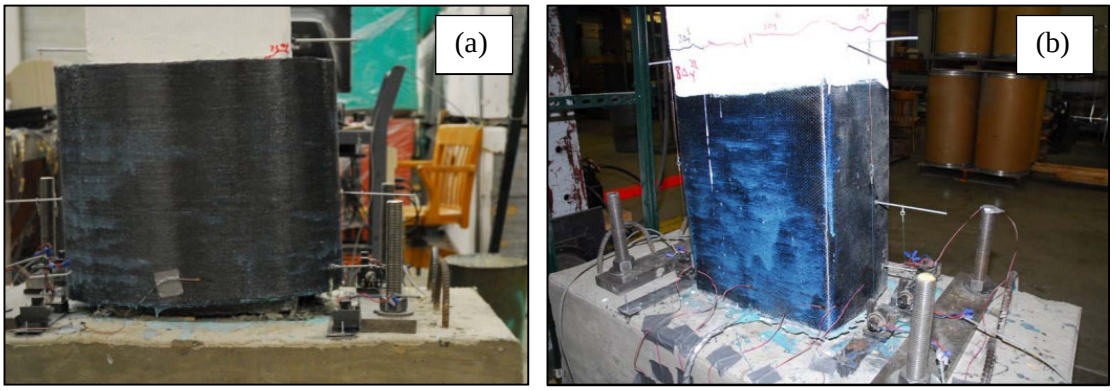

Figure 2-27: a) Oval shaped and b) rectangular shaped CFRP measures (Endeshaw, 2008)

Failure of the unconfined specimens was due to spalling of concrete at the hinging zone accompanied by buckling of longitudinal reinforcement and splice failure. However, yielding and flexural hinging was achieved. A displacement ductility level of 6 was reached. The specimen retrofitted with an oval-shaped steel jacket showed a slight improvement in performance, reaching a displacement ductility of 7. Similar performance was achieved by the FRP specimen with the oval-shaped jacket. Other CFRP specimens with rectangular-shaped jackets experienced more flexural hinging, achieving displacement ductilities of 7 or higher. No actual bar slippage occurred during testing. Figure 2-28 summarises the performance of the tested specimens. Thus, in this study, the strengthening measures were capable of achieving modest improvements in the flexural behaviour due to the relatively good performance of the as-built specimens.

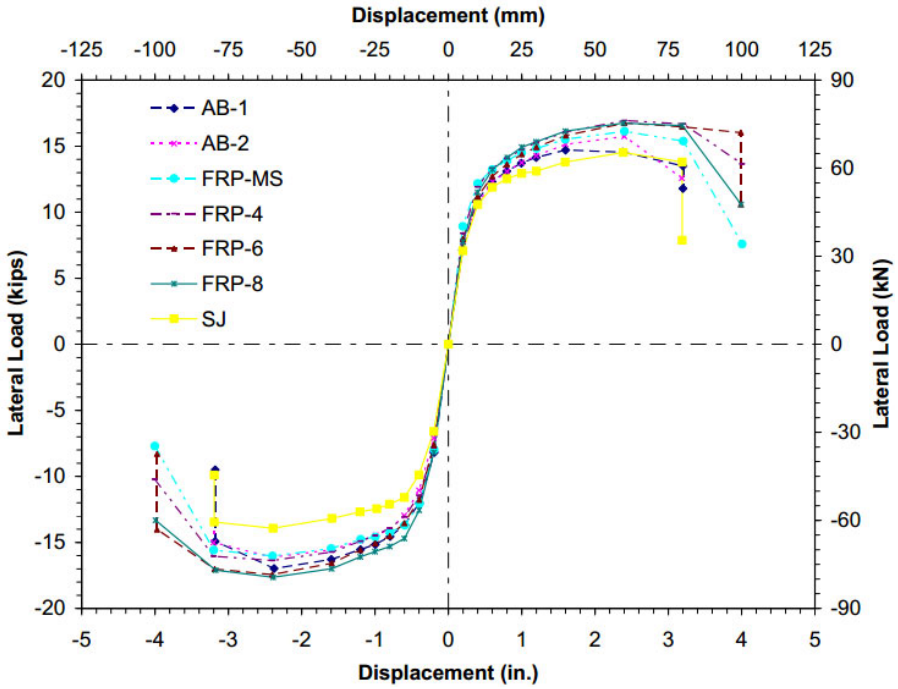

Figure 2-28: Envelope curves for tested specimens (Endeshaw, 2008)

In addition to the previous investigations, many studies such as those by Orangun et al. (1977), Sozen and Moehle (1990), Zuo and Darwin (1998-2005), and Harajli et al. (2002-2010) incorporated experimental tests on beams with deficient lap splices. In these studies, many strengthening measures were examined including steel stirrups and wires, FRC, and FRP laminates. On average, the enhancement in bond strength in comparison to unconfined splices ranged from 48%-65% for steel stirrups (2 to 3 links), 44%-80% for FRC (volume fraction of fibre from 0.5% to 2%) and 30%-70% for FRP (1 to 2 layers). Results from these tests were used to develop equations for bond capacity and to recommend spliced lengths of deformed bars in tension under cyclic and monotonic loading. In addition, many bond-stress slip models were developed to provide proper simulations of RC columns with substandard splices and strengthened by these materials. The results were also used to improve existing code provisions for reinforcement detailing in bond critical regions. Furthermore, the parameters influencing bond capacity were identified. These parameters included development/splice length, concrete strength, bar diameter and geometry, concrete cover, bar stress, and amount and type of transverse reinforcement (confinement) [ACI Committee 408 (2003), fib Bulletin 10 (2000)].

2.10 CONCLUSIONS

From the previous review, it can be concluded that:

a) Column splices are common deficiencies in existing older RC framed buildings and may cause severe degradation in the performance and collapses.

b) The performance of lap splices of column longitudinal reinforcement can be improved by several techniques such as removal of cover concrete and welding overlapped bars, confining the splice by steel or RC jackets, providing new longitudinal reinforcement in a jacket, and the use of FRP composite jackets.

c) Most of the previous strengthening methods are applied in a passive way such that improvement in bond strength is mobilised as load increases. In addition, the enhancement in bond and performance is obtained due to enlargement of the element cross-section which delays the spread of splitting cracks.

d) Not much work has focused on the importance of transverse pressure to increase bond strength of splices. This is due to the fact that any method involving external pressure requires heavy steel works, skilled workers to apply, welding works, and above all time which adds significantly to the total cost. What's more, in cases where external pressure was applied, no significant improvement in the behaviour was obtained due to the good performance of the unconfined specimens. Thus, the importance of transverse pressure on bond was not well appreciated and development of proper techniques was limited.

A method that can offer easy and rapid application, time- and cost-efficiency and, above all, effectiveness can be summarised by the PTMS technique. The use of PTMS entails the application of transverse compressive force along the element cross-section. According to CEB Bulletin 151 (1982), transverse compression delays the onset of splitting failure in a plane perpendicular to the direction of compressive stresses and also increases the frictional force applied to the concrete-to-steel failure surface. The presence of transverse pressure leads to an increase in the peak bond strength and a reduction in the associated slip.

In recognition of the previous conclusion, a preliminary experimental programme was conducted on short splices (10 times the bar diameter) in tension and the results were remarkable. Based on the results, an extensive experimental programme was planned on splices and this is presented in the next chapter.

As the work on splices and confinement requires knowledge about the bond problem, a brief review relating to the state-of-knowledge on bond behaviour of reinforcing bars embedded in reinforced concrete is given in Appendix A. Also given in the appendix are the key parameters most relevant to the current work.

Chapter 2

PART III: COMPUTER-BASED JOINT MODELS

This part reviews the up-to-date models for joint panel zones suitable for computer-based analyses.

2.11 INTRODUCTION

Many analytical models were developed to predict the behaviour of beam-column joints. These models include strut-and-tie models, shear strength models, bond strength models, FE continuum models, empirical models, mathematical-based models, strength degradation models, and computer-based spring models. A critical review of these models is presented in recent studies conducted by Park and Mosalam (2009) and Hassan (2011). The study by Hassan (2011), however, included comparisons with extensive databases of unconfined joints. From the comparisons, Hassan (2011) found that a large scatter in model predictions existed.

Recent studies such as those by Sharma (2011), Hassan (2011), and Shin and LaFave (2004) showed more interest in computer-based models and suggested different methods for joint simulations in a RC frame. By definition, computer-based joint models are panel-zone frame elements connected using multi- rotational and/or translational springs which represent joint shear and slip deformations. This research study is concerned with providing a suitable joint model of a beam-column connection strengthened by PTMS. Thus, a brief review of up-to-date computer-based joint models is presented in the following section.

2.12 SIMULATION METHODS OF BEAM-COLUMN JOINTS

2.12.1 Pampanin et al. (2003)

Pampanin et al. (2003) developed a single rotational spring model for exterior/interior joints. In the model, the total interstory drift was decomposed into three components including a) beam contribution, b) column contribution, and c) a panel zone contribution, as illustrated in Figure 2-29.

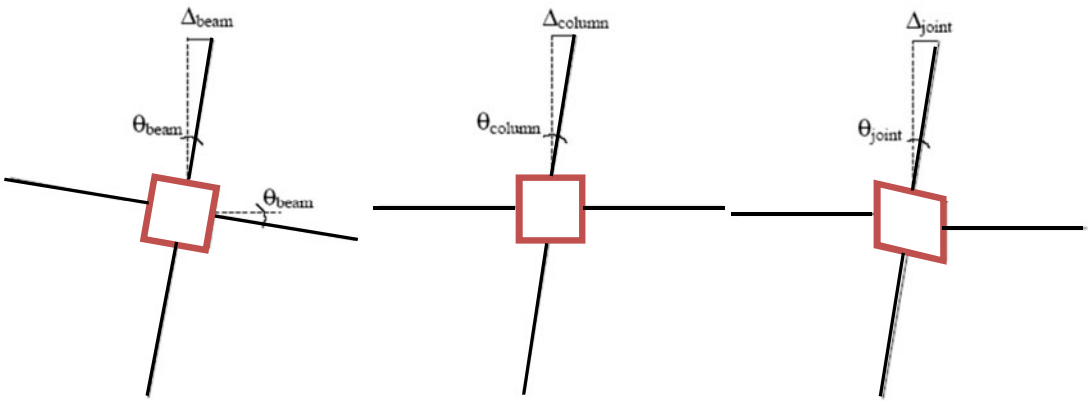

Figure 2-29: Contribution of beams, columns and joints to total interstory drifts (Pampanin et al., 2003)

The model proposed by Pampanin et al. (2003) consists of an equivalent moment-rotation spring having a moment equal to the sum of beam or column moments, and with a rotation corresponding to the joint shear deformations. The shear hinge mechanism is assumed to activate due to shearing of the joint area and affects the relative rotation of beams and columns, as shown in Figure 2-30(a). The joint panel is modelled as rigid elements connected by a rotational spring (Figure 2-30(b)). The rotational hinge properties can be used for monotonic as well as cyclic analyses with hysteretic rules for pinching behaviour (see Figure 2-31). However, the model does not consider a post-peak degrading response. In comparison with experimental responses of exterior and knee joints, the model resulted in satisfactory predictions of the response, as shown in Figure 2-32.

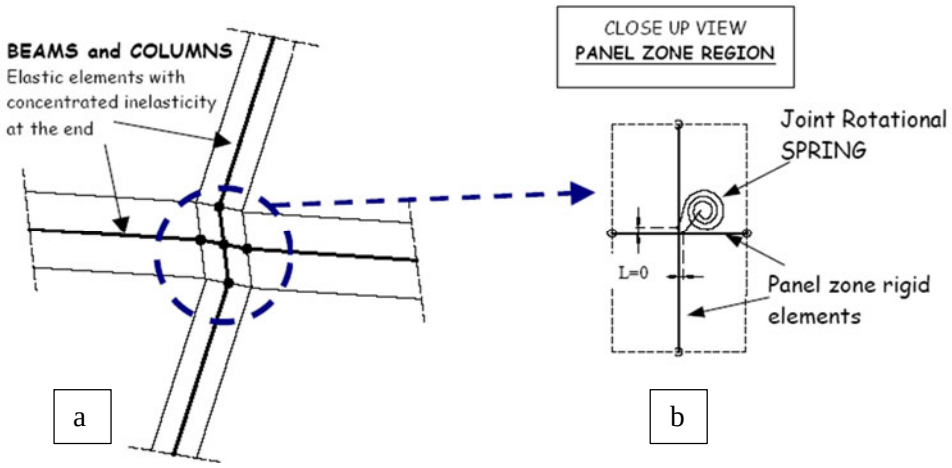

Figure 2-30: Rotational spring model proposed by Pampanin et al. (2003)

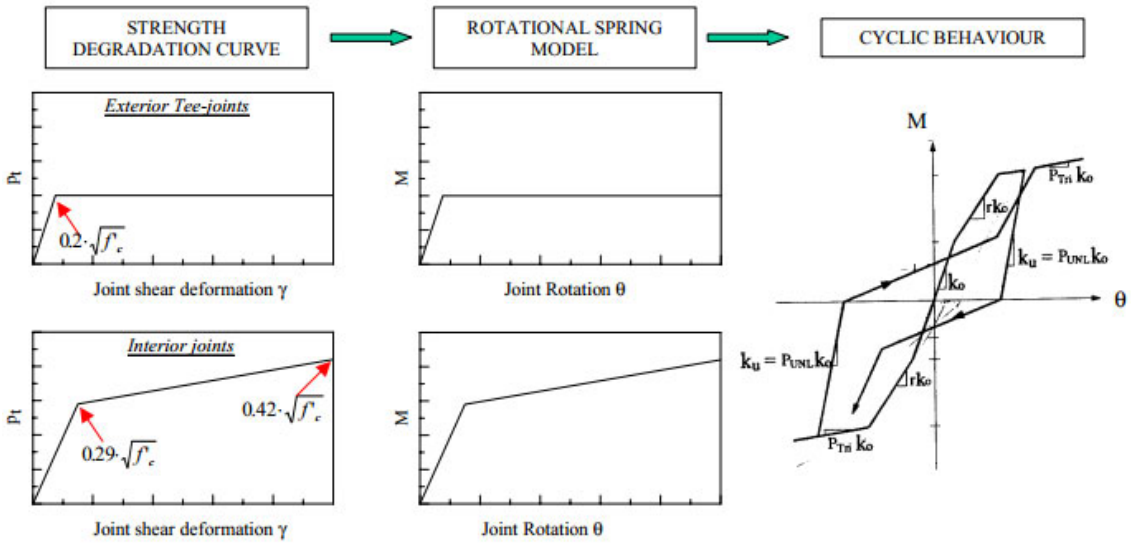

Figure 2-31: Behaviour of the shear hinge (Pampanin et al., 2003)

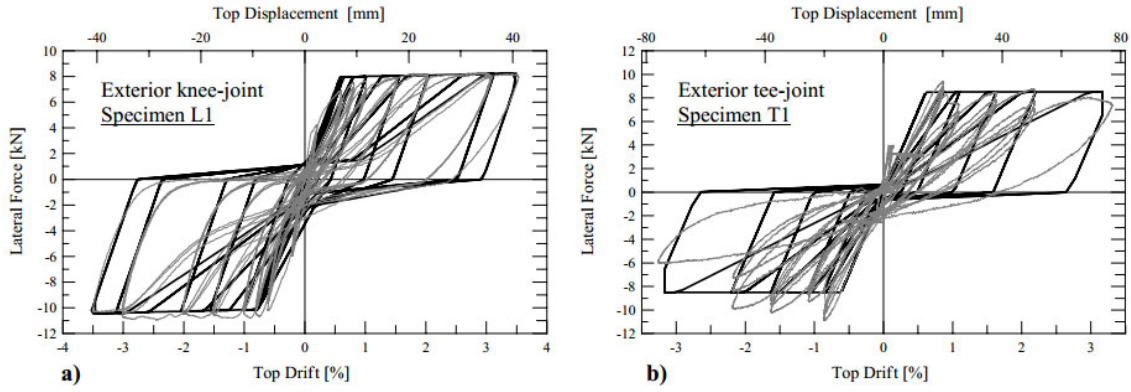

Figure 2-32: Comparisons of simulations to measured responses (Pampanin et al., 2003)

2.12.2 Celik and Ellingwood (2008)

Celik and Ellingwood (2008) presented a critical review with regard to existing models developed for dynamic analysis of beam-column joints. Those models are presented in Figure 2-33.

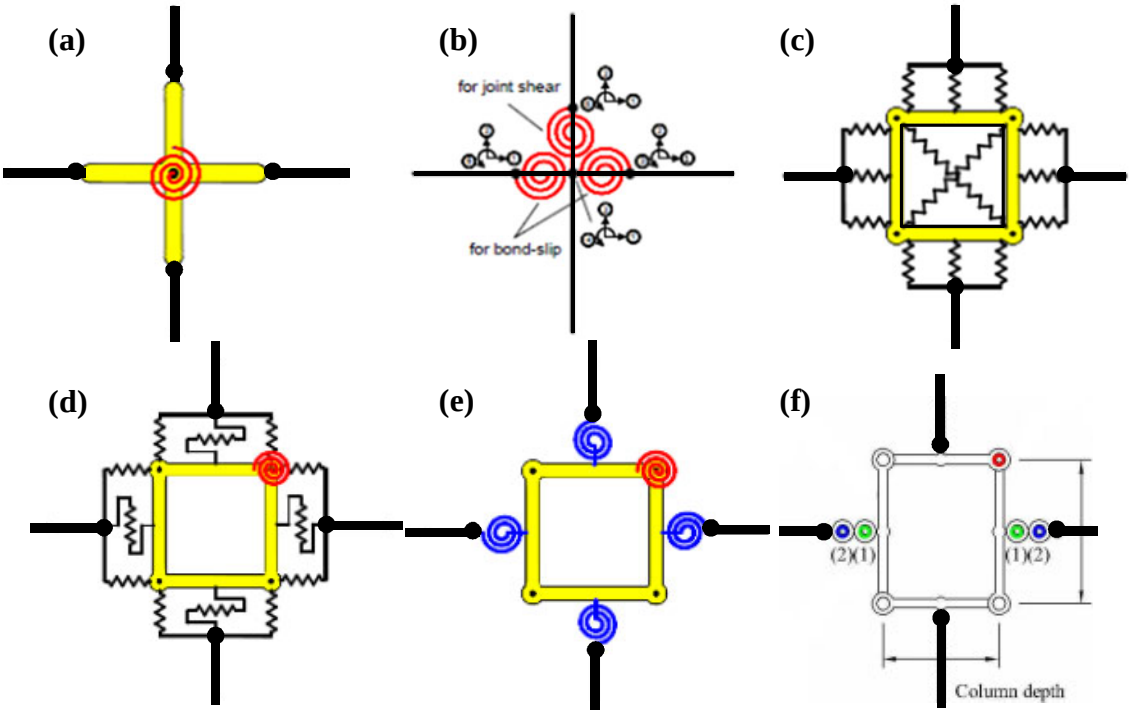

Figure 2-33: Existing beam-column joint models: (a) Alath and Kunnath (1995), (b) Biddah and Ghobarah (1999), (c) Youssef and Ghobarah (2001), (d) Lowes and Altoontash (2003), (e) Altoontash (2004), and (f) Shin and LaFave (2004); (Celik and Ellingwood, 2008)

Celik and Ellingwood implemented four of the models in OpenSees FE platform and compared simulated results with those measured from experiments. Test results reported in Pantelides et al. (2002) for exterior joints were used for comparisons. The implemented models included a rigid panel zone model, a single rotational spring model with no rigid links, a single rotational spring with rigid links (Scissors Model, as by Alath and Kunnath (1995)), and a simplified joint model proposed by Altoontash (2004) which is developed from the model in Figure 2-33(d), as shown in Figure 2-34. The joint model characteristics are defined to simulate the experimental joint shear stress-strain relationships. However, the effect of rotations due to bond-slip is taken into consideration by reducing the envelope characteristics of the joint shear stress-strain relationship rather than using an additional bond-slip rotational spring.

It was found that the conventional rigid joint model (Figure 2-34a) was inappropriate to simulate the highly pinched experimental responses; this in turn revealed the significance of considering joint shear and bond-slip in modelling of GLD RC frames. All other models led to better predictions of the measured behaviour in comparison to the conventional rigid joint model. The scissors model with rigid end zones, in particular, produced accurate predictions of

the experimental responses. Consequently, it is deemed more appropriate for simulating the seismic response of GLD RC frames for performance-based earthquake engineering.

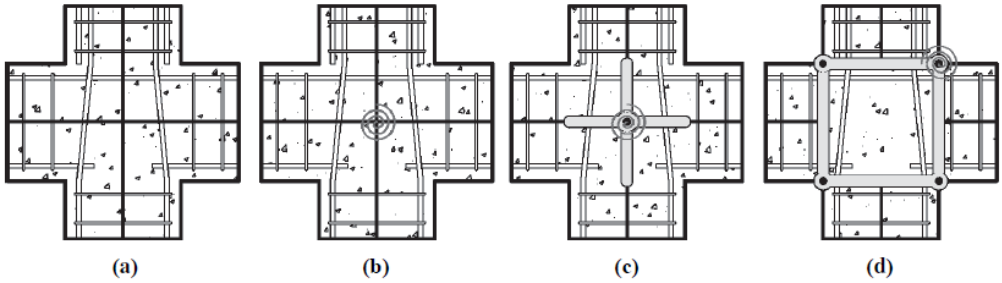

Figure 2-34: (a) Conventional rigid joint model; (b) the scissors model without rigid links; (c) the scissors model with rigid links; and (d) the Joint2D model (Celik and Ellingwood, 2008)

2.12.3 Favatta et al. (2008)

Favatta et al. (2008) introduced a zero-length rotational spring (a Scissors-type model) to simulate the behaviour of exterior beam-column joints, as shown in Figure 2-35. Based on the critical failure mechanism state of the joint, criteria were introduced to determine the flexural strength of the spring. The failure mechanisms included: a) yielding of beam flexural reinforcement for joints where strength is limited by the beam strength, b) joint shear strength for joints with beam reinforcement hooked inside the core, c) pullout failure in joints with insufficiently anchored beam reinforcement.

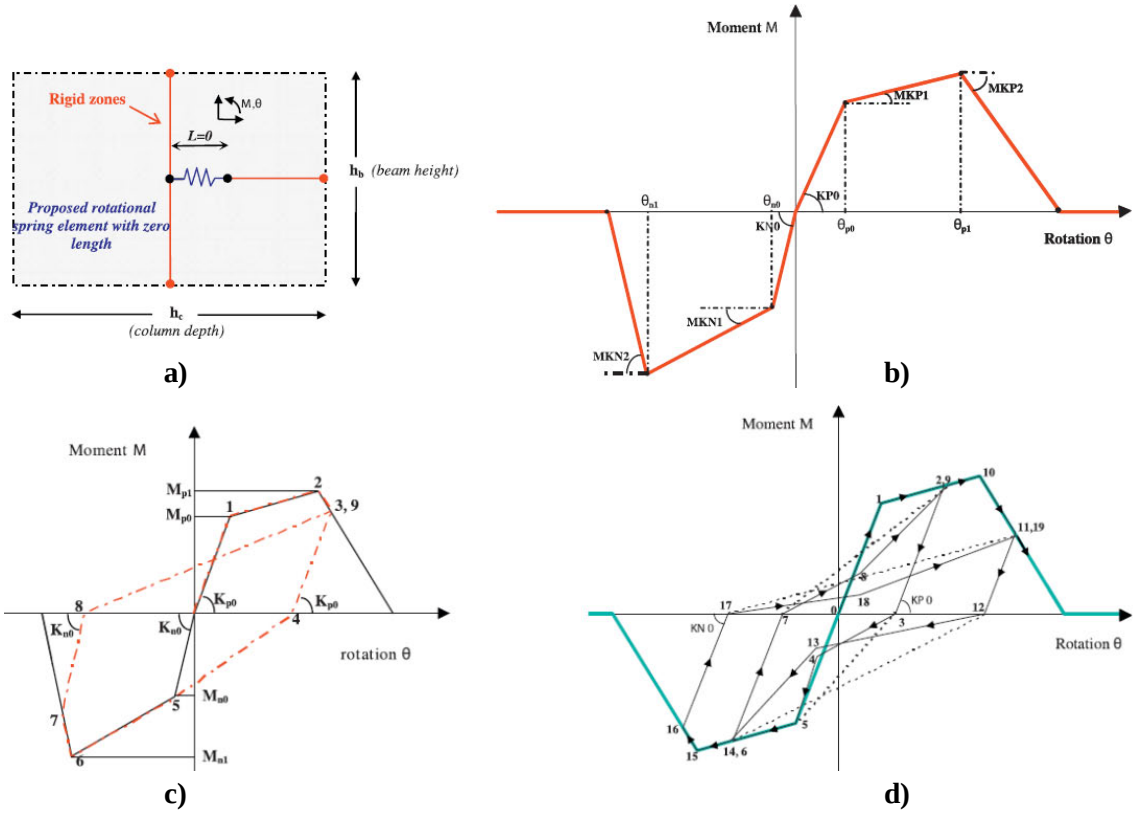

Figure 2-35: Proposed panel zone model for simulating exterior RC beam-column joints: (a) Analytical model-partial elevation view of a joint region; (b) envelope curve of the proposed model; (c) response model during a typical hysteretic cycle; and (d) hysteretic response of the proposed model including pinching effect (Favatta et al., 2008)

The Favatta et al. model was used to simulate the behaviour of exterior joints tested by Karayannis et al. (2006), Tsonos and Papanikolaou (2003), and Ehsani and Wight (1985), as shown in Figure 2-36(a), (b) and (c), respectively. In comparison to the use of conventional rigid link model, the proposed model showed good predictions of the experimentally measured responses.

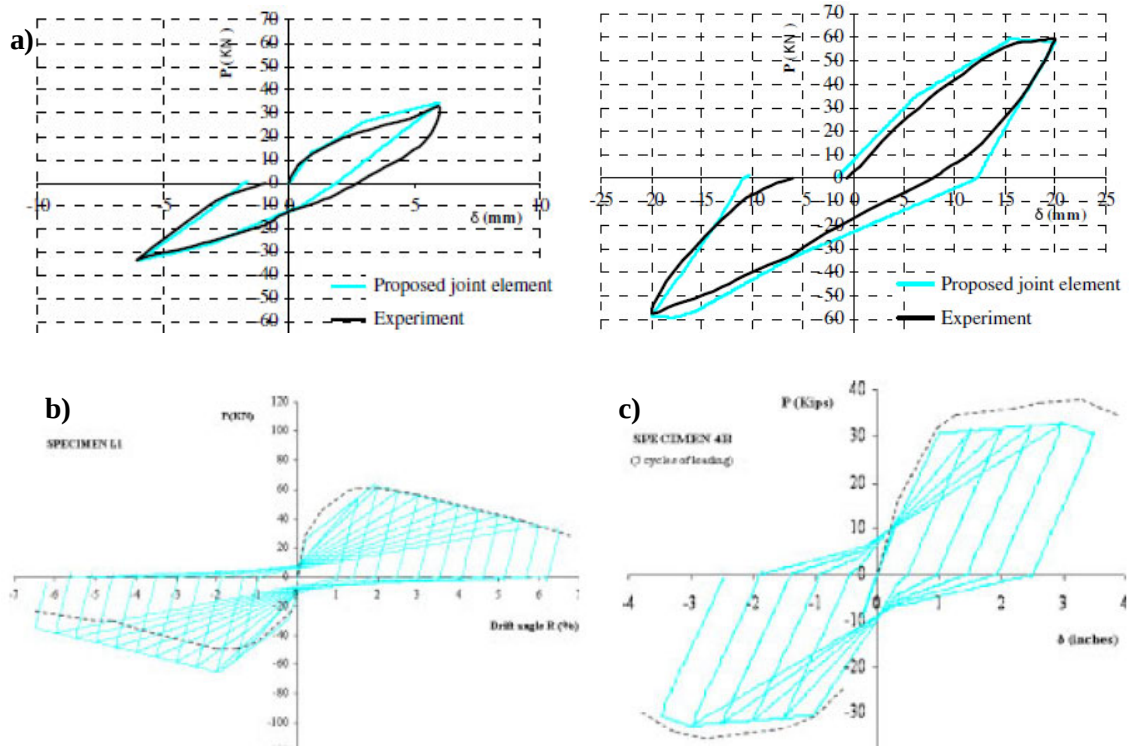

Figure 2-36: Comparison of analysis results with measured responses (Favatta et al., 2008)

The model was also used to simulate the seismic response of an eight-story GLD building with unconfined joints. The analysis results using this model, as shown in Figure 2-37(a) or (b), indicate a change in the dynamic characteristics of the building such as failure mechanism and plastic hinge locations, maximum drift storey, and maximum ductility demand of the 1st storey columns. In general, higher drifts and lower ductility demands were obtained by the model.

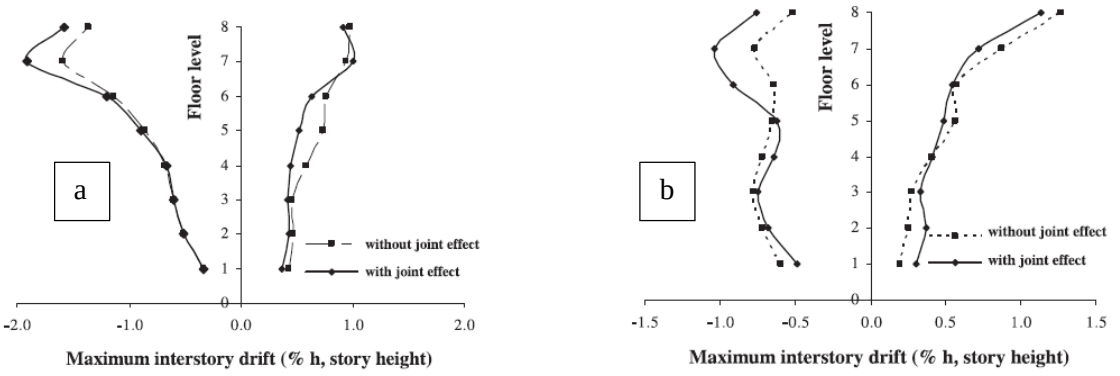

El Centro, 1940 earthquake Thessaloniki, Greece, 1978 earthquake

Figure 2-37: Dynamic analysis results for 8 story RC frame using rigid links and rotational spring model (Favatta et al., 2008)

2.12.4 Sharma et al. (2011)

Sharma et al. (2011) proposed a shear stress-strain model to simulate the behaviour of poorly detailed beam-column joints without lateral reinforcement in the core. The model requires the use of principal tensile stresses as a failure criterion of the joint panel zone. By utilising the mechanics of exterior joints and considering the effect of axial load, Sharma proposed the following equation to calculate the principal tensile stresses, p_t:

$$p_t = \frac{\sigma}{2} - \frac{\sigma}{2}\sqrt{1 + 4\frac{(\sigma - \sigma_a)^2}{\alpha^2\sigma^2}} \tag{2-13}$$

where σ is the vertical joint shear stress, given by equation (2-14); α is the joint aspect ratio given by equation (2-7); and σ_a is the axial stress of the column.

$$\sigma = \frac{V_{jh} + P}{b_c h_c} \tag{2-14}$$

In the development of the model, two joint failure types were considered based on the beam bar detailing within the joint area as follows: a) the beam bars are bent into the joint area as hooks producing a well stabilised compressive strut, and b) the beam bottom bars are anchored as short straight anchorages ≤ 150 mm and the failure is due to pullout of beam bars. For the first case, Sharma used tests conducted by Clyde et al. (2000), Pantelides et al. (2002), and Pampani et al. (2002); whereas for the other case, tests conducted by Pantelides et al. (2002), Murty et al. (2003), El-Amoury and Ghobarah (2002) and Genesio et al. (2010) were used. The principal tensile shear stress-strain curves of both cases are shown in Figure 2-38 and Figure 2-39. As can be seen from the figures, a maximum tensile stress of $0.42\sqrt{f'_c}$ was used when the beam bars are hooked into the core; while a reduced value of $0.19\sqrt{f'_c}$ was used in the case of short beam anchorages. Also, it can be noted that the maximum resistance was represented by a flat plateau with increasing rotations of (0.003 rad). The rotation at the residual point was assumed to be constant and equal to 0.025 and 0.015 rad for the case of hooks and straight bars, respectively.

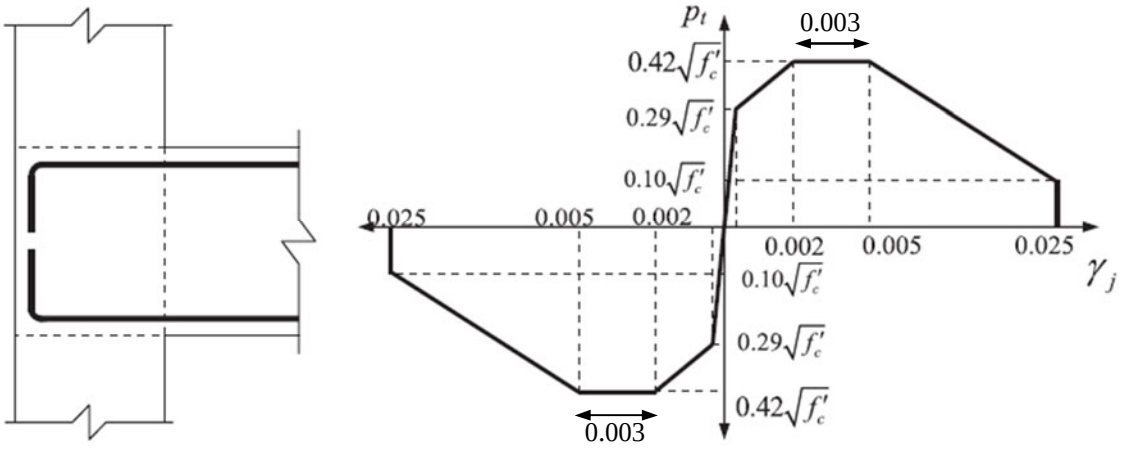

Figure 2-38: Proposed principal tensile stress–shear deformation relationship for joints with hooks (Sharma et al., 2011)

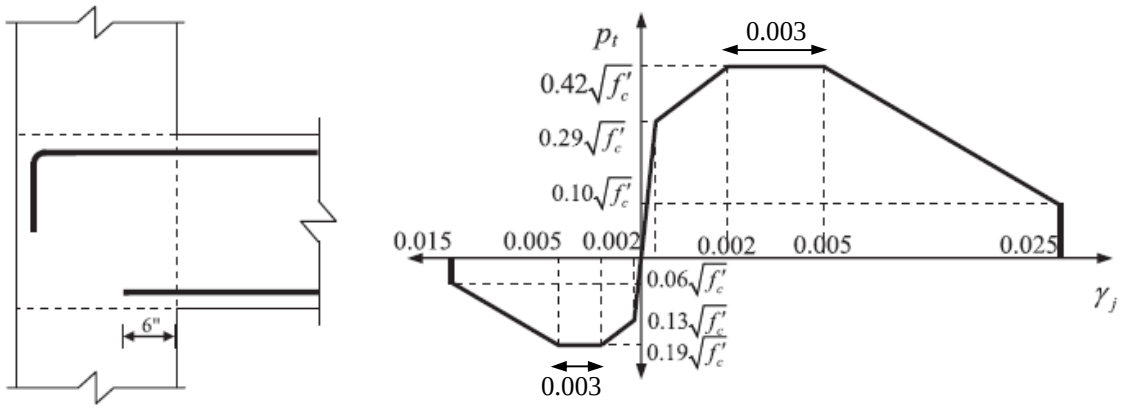

Figure 2-39: Proposed principal tensile stress–shear deformation relationship for joints with short beam-anchorages (Sharma et al., 2011)

The shear stress-strain curve was implemented in a joint model through a single rotational spring at the beam-to-joint interface and two translational springs at the column-to-joint interfaces, as shown in Figure 2-40. In the determination of spring characteristics (beam moment-rotation and column shear-translation) an iterative procedure was used.

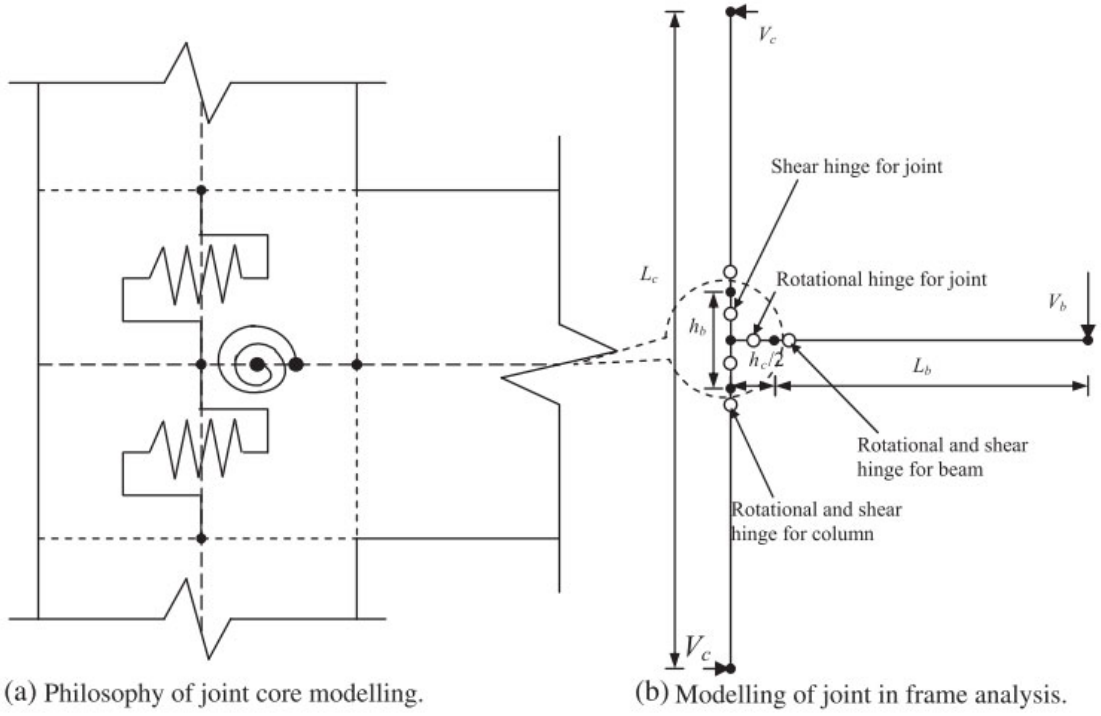

Figure 2-40: Joint-modelling philosophy proposed by Sharma et al. (2011)

The model was employed in static analyses of joints and showed good predictions of the response, as shown in Figure 2-41. Sharma suggested that the model is also suitable for dynamic analyses.

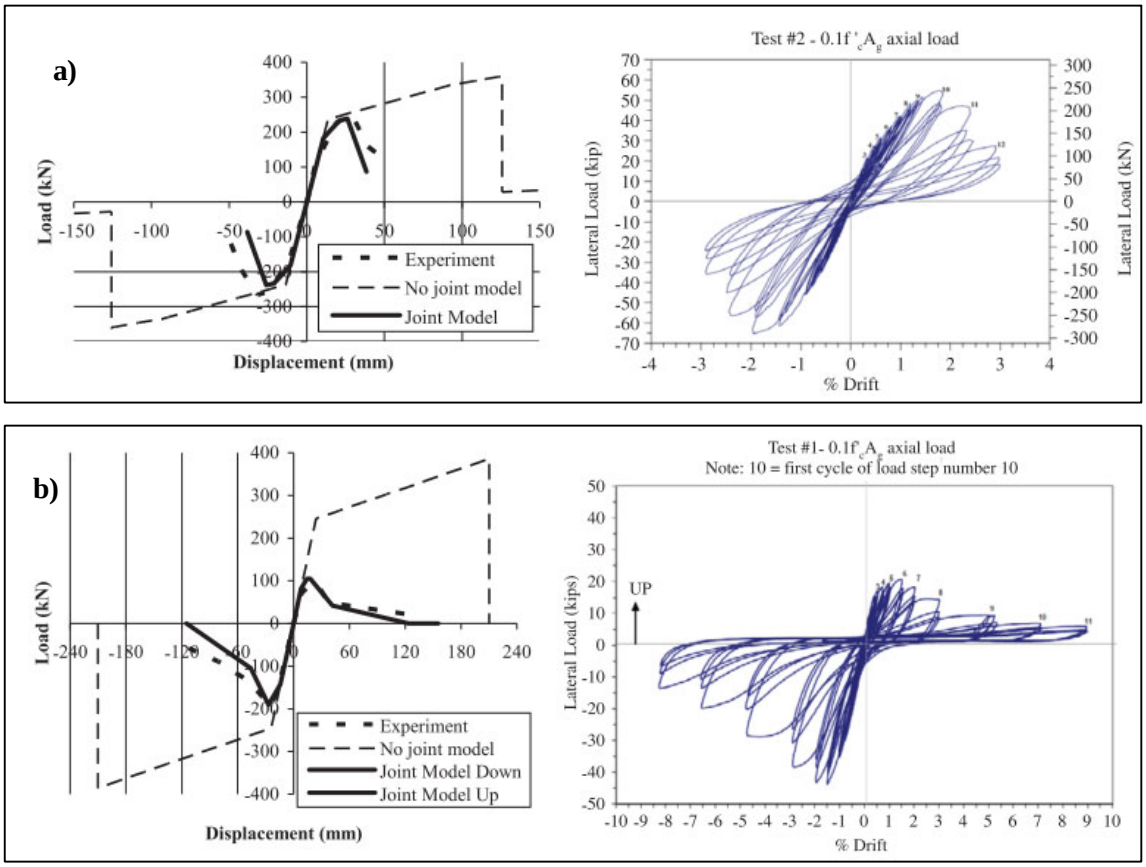

Figure 2-41: Validation of model by Sharma with tests performed by a) Clyde et al. (2000) and b) Pantelides et al. (2002).

2.12.5 Hassan (2011)

Hassan (2011) developed a quad-linear shear stress-strain model to simulate the behaviour of unconfined beam-column joints, as shown in Figure 2-42(a). The model is proposed based on a predefined quad-linear moment-rotation curve, as shown in Figure 2-42(b). The transformation from the horizontal shear stress to moment is achieved using equation (2-15).

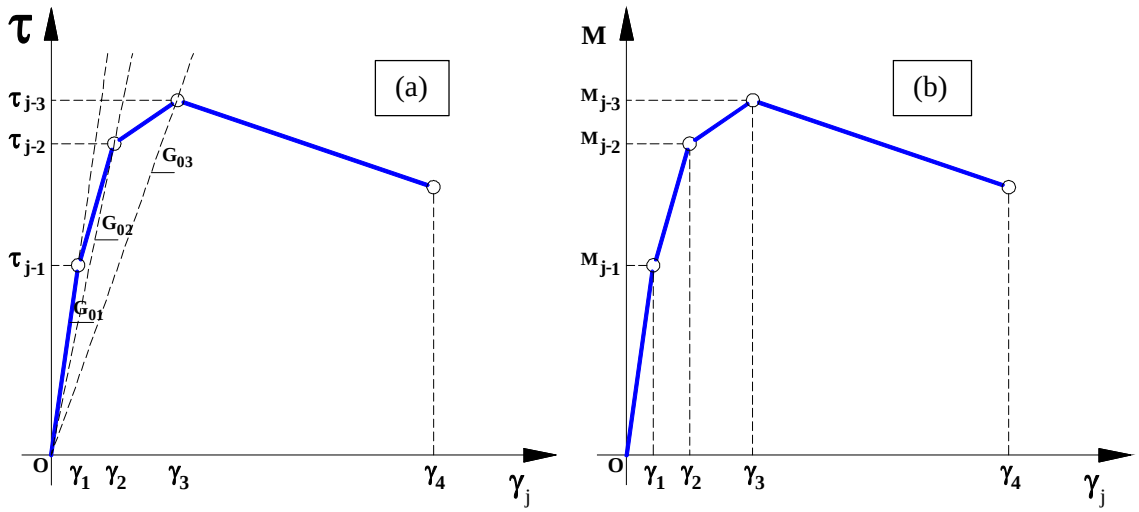

Figure 2-42: Shear stress-strain model proposed by Hassan (2011)

$$M_j = \tau_j A_j \frac{L}{\frac{L - 0.5h_c}{jd_{sb}} - \frac{L}{H}} \quad (2\text{-}15)$$

where M_j is the beam moment at the column centroid; τ_j is the shear stress; A_j is the effective joint area; L is the beam length from the contraflexure point up to column centroid; h_c is the column width; H is the column height; d_{sb} is the effective depth of the beam; and j is the effective beam lever arm ratio = 0.875 for J-type failure and 0.9 for BJ-type failure.

The model distinguishes four damage states as explained below:

- *Cracking point (τ_{j-1}, γ_1)*

This point represents hairline cracking within the joint area. To calculate the cracking stress, Hassan suggested the use of the equation by Uzumeri (1977) for beam-column joints which accounts for the effect of axial load. The equation used by Uzumeri is given by:

$$\frac{\tau_{j-1}}{\sqrt{f_c'}} = 3.5\sqrt{1 + 0.002\frac{P}{A_j}} \quad \leq 0.6\frac{\tau_{j-3}}{\sqrt{f_c'}} \quad in\ psi^{0.5} \quad (2\text{-}16)$$

where P is the column axial load; and A_j is the effective joint area.

Based on tests conducted by Hassan (2011), the initial stiffness was taken as ½ the modulus of rigidity G_c.

- *Pre-peak "yielding" point (τ_{j-2},γ_2)*

During this stage, multiple major and small diagonal cracks form within the panel zone. In the BJ-type failure, this point represents yielding of the beam bars.

For the J-type failure, the secant joint shear modulus of rigidity G_{02}, was approximated by $0.1G_c$, in both loading directions; whereas the shear strain was taken as 0.0025 and 0.002 for upward and downward loading, respectively. In the case of BJ-failure type under high axial loading ($>0.3f_c'A_j$), the joint shear strain corresponding to point 2 was taken as 0.0002; whereas the shear stress was taken as 90% of the maximum value. In all cases, a lower bound of 90% of the maximum stress was set on the shear stress.

- *Maximum point (τ_{j-3},γ_3)*

To determine the shear stress at this stage, Hassan proposed an ACI 318-08 (2008) based strut-and-tie model as well as an empirical shear strength model. The proposed strut-and-tie model is shown in Figure 2-43. Accordingly, a well stabilised single compressive strut is assumed to transfer the forces within the joint area. The compressive strut is embraced by the beam reinforcement in the core. The strut-and-tie model, however, was considered stable due to the presence of well anchored beam reinforcement in the form of a hook able to support the

compressive force imposed by the strut. Thus, the strut width is assumed to be constant and determined by the depth of beam and column compressive zones.

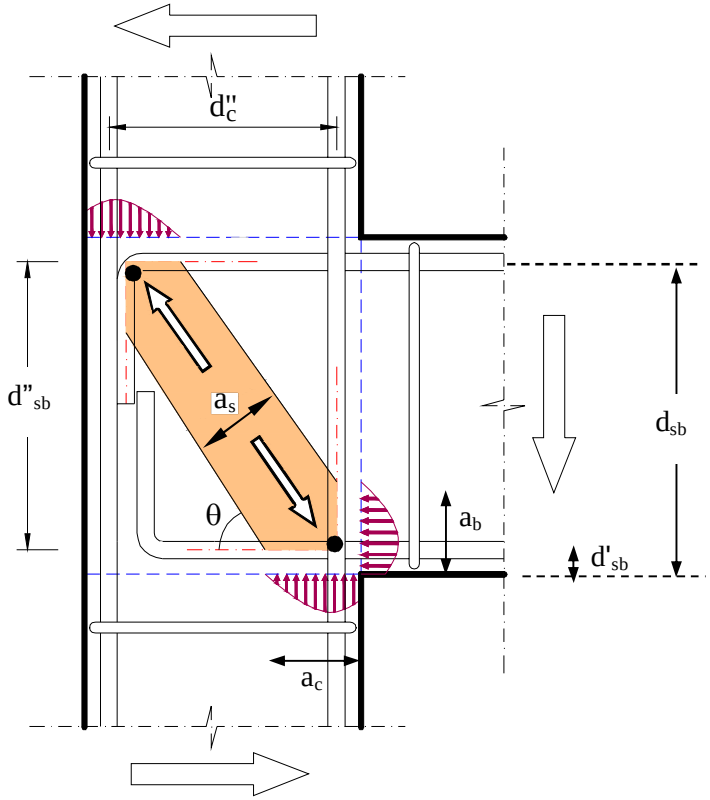

Figure 2-43: Strut-and-tie model proposed by Hassan (2011)

The nominal compressive strength of the strut can be calculated as:

$$D = A_{str} f_{cu} \quad (2\text{-}17)$$

where A_{str} and f_{cu} are the effective strut area and stress, respectively, and determined by the following expressions:

$$f_{cu} = 0.85\beta_s f_c' \quad (2\text{-}18)$$

$$A_{strut} = a_{str} b_j \quad (2\text{-}19)$$

$$a_{str} = \beta_1 \sqrt{a_b^2 + a_c^2} \quad (2\text{-}20)$$

$$\beta_1 = 1 - 0.05(f_c' - 4) \quad (2\text{-}21)$$

$$a_b = k d_{sb} \quad (2\text{-}22)$$

$$k = \left[(\rho - \rho')^2 n^2 + 2\left(\rho + \rho' \frac{d'_{sb}}{d_{sb}}\right) n\right]^{0.5} - (\rho + \rho') n \quad (2\text{-}23)$$

$$n = E_s / E_c \quad (2\text{-}24)$$

$$a_c = \left[0.25 + 0.85 \frac{P}{f_c' A_g}\right] h_c \leq 0.4 h_c \quad (2\text{-}25)$$

where β_s is a concrete softening coefficient taken equal to 0.6 for unconfined joints; a_{str} is the strut width; a_b and a_c are the compression beam and column zone depths, respectively; The

value a_c is estimated using the equation suggested by Paulay and Priestley (1992); β_1 is a factor accounting for a further reduction in beam and column stress block height associated with concrete strengths higher than 4 ksi (27.2MPa); d_{sb} and d'_{sb} are the depths from extreme compression fibre to centroids of beam longitudinal reinforcement in tension and compression, respectively; n is the modular ratio; E_c and E_s are the modulus of elasticity of concrete and steel, respectively; ρ and ρ' are tension and compression beam reinforcement ratios, respectively; P is the column axial load and A_g is the column gross section area.

Thus, the joint shear strength considering the unconfined diagonal strut capacity is:

$$V_{jh} = D \times cos\theta_j \tag{2-26}$$

where θ is the strut angle and calculated by the following expression:

$$\theta_j = tan^{-1}\left(\frac{d''_{sb}}{d''_c}\right) \tag{2-27}$$

where d''_{sb} and d''_c are the distances between compressive and tension longitudinal reinforcement of the beam and column, respectively.

The shear stress τ_{jh} is calculated by the following expression:

$$\frac{\tau_{jh} = \tau_{j-3}}{\sqrt{f'_c}} = \frac{V_{jh}}{h_c b_j \sqrt{f'_c}} \tag{2-28}$$

where b_j is the joint effective depth.

Furthermore, Hassan proposed equation (2-29) to calculate the shear strength of unconfined joints accounting for parameters most influencing the joint shear strength, namely, joint aspect ratio and axial load ratio.

$$\frac{\tau_{jh}}{\sqrt{f'_c}} = 11.25\left[1 + (0.86 - 0.31\alpha_j)\left(\frac{P}{f'_c A_g} - 0.15\right)\right]\frac{b_j h_c}{\sqrt{\alpha_j}} \tag{2-29}$$

in which α_j is the joint aspect ratio determined by equation (2-7).

Hassan (2011) highlighted two differences in the proposed strut-and-tie model compared to the soft strut-and-tie model (SSTM) by Hwang and Lee (1999). In, the SSTM model, the beam contribution to the strut width is ignored which is not the case for joints with J-type failure. The other difference between the two models is the determination of the cracked concrete strength in compression at failure of the diagonal strut.

- *Residual point*

This point represents the axial load failure in the case of joints under high compressive loads. In the case of low axial load, this point represents instability of the concrete frame due to large shear cracking. The degradation curve is determined by a stress of $0.7\tau_m$ and a shear strain equal

to the strain at the maximum strength and a value of 0.02 for high axial load and 0.025 for low axial load cases.

In the case of BJ-failure, Hassan suggested the following procedure to determine the joint shear stress demand:

Step 1: Calculate the nominal beam yielding capacity M_{by} using the conventional sectional analysis method. In the presence of a slab, the yielding flexural capacity should be calculated considering an extended compressive flange and slab reinforcement.

Step 2: Calculate the tension force in the beam bars at yield T_{by}. The tension force can be taken from a sectional analysis or can be approximated as:

$$T_{by} = \frac{M_{by}}{0.9 d_{sb}} \tag{2-30}$$

where d_{sb} is the effective depth of tension bars measured from the outermost compressive fibre.

Step 3: Calculate the column shear force V_{cy} corresponding to the beam yielding moment M_{by}. Using joint equilibrium, the column shear force can be given by

$$V_{cy} = \frac{M_{by}}{L_b} \times \left[\frac{L_b + h_c/2}{H}\right] \tag{2-31}$$

in which L_b is the beam length measured from the point of contraflexure up to the column face; H is the column height.

Step 4: Compute the joint shear force at yielding using the following equation:

$$V_{jy} = T_{by} - V_{cy} \tag{2-32}$$

Step 5: Calculate the normalised joint shear stress corresponding to beam yielding:

$$\frac{\tau_j}{\sqrt{f_c'}} = \frac{V_{jy}}{h_c b_j \sqrt{f_c'}} \tag{2-33}$$

The proposed rotational spring was introduced between duplicate nodes at the intersection of beam and column centrelines, as shown in Figure 2-44(a). The scissors joint model was used to simulate the panel zone. The bond slip was modelled in two ways: a) explicitly as a separate rotational spring at the beam-to-column interfaces (Figure 2-44(b)), and b) as a combined spring with the shear spring, Figure 2-44(c). The bond-slip model proposed by Lehman and Moehle (2000) was used. The joint model was incorporated in cyclic analyses using OpenSees software (2010) and showed good predations of the response, as shown in Figure 2-45.

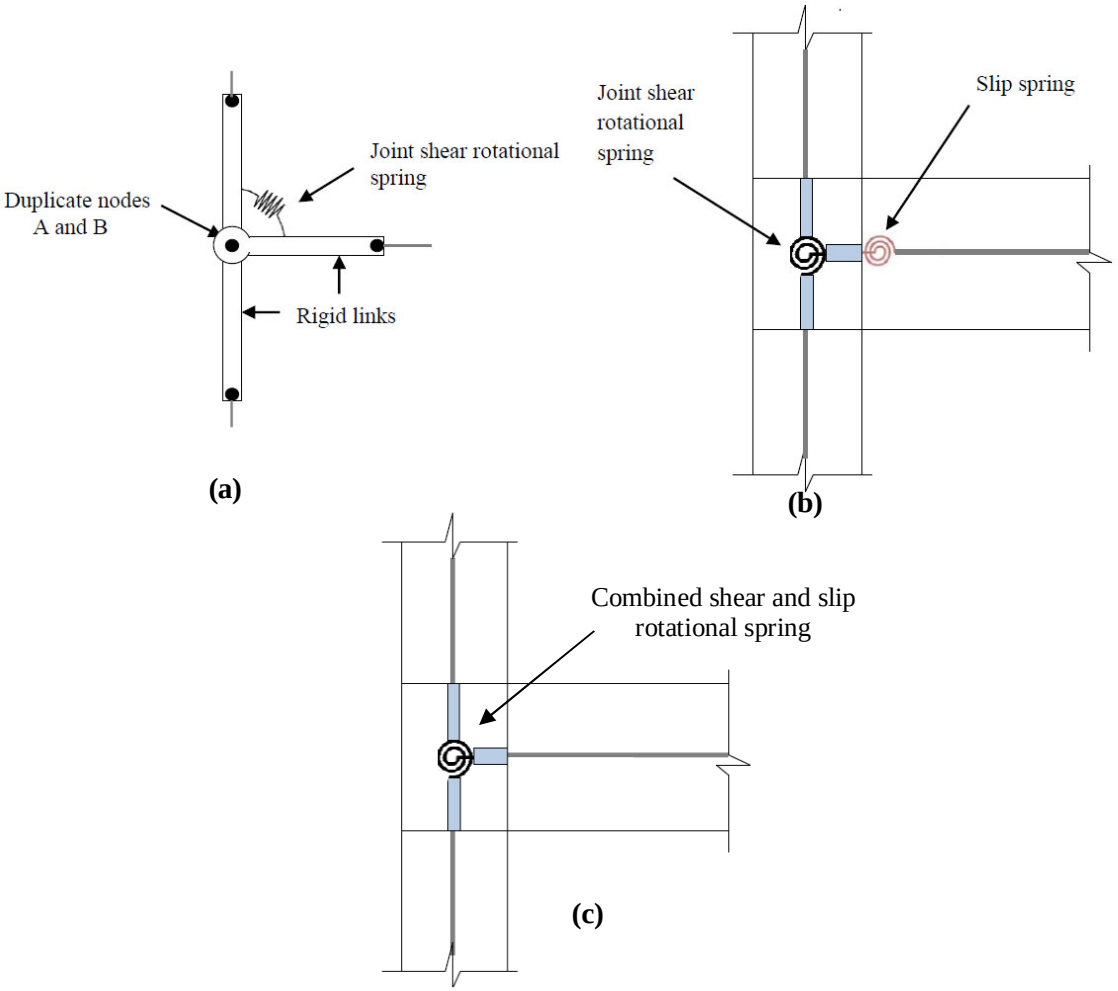

Figure 2-44: (a) Panel zone model – explicit bond spring, (b) scissors model, and c) combined shear and slip spring (Hassan, 2011)

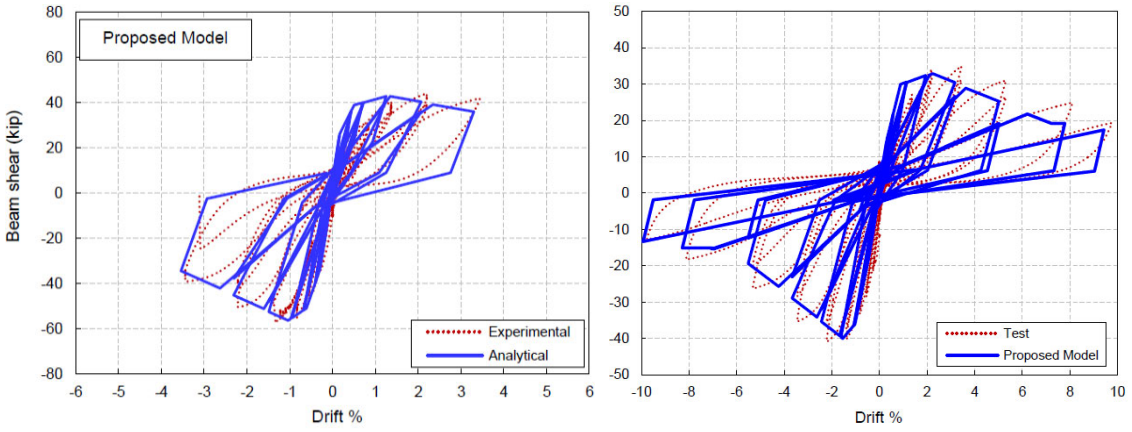

Figure 2-45: Simulation results of specimen U-J-2 (left) and U-J-1 (right), (Hassan, 2011)

2.12.6 ASCE/SEI 41-06 (2006) and ACI 369 (2011) RECOMMENDATIONS

In the modelling of joints, ASCE/SEI 41-06 (2006) and ACI 369 (2011) propose the use of rigid element connections in the panel zone for linear analyses. The joint shear deformations in this case are ignored. However, reinforcement slippage of beam bars at the joint interface is accounted for by reducing flexural stiffness of the beam. In the case of nonlinear static and

dynamic analyses, ASCE/SEI 41-06 (2006) and ACI 369 (2011) suggest the use of an envelope curve, as shown in Figure 2-46, for simulating the shear behaviour of beam-column joints. However, there is no clear method to implement this curve in a specified panel zone model.

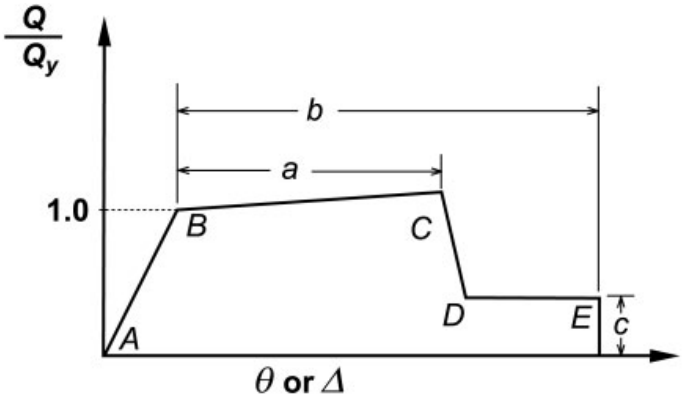

Figure 2-46: Generalised deformational curve for concrete elements and components [ASCE 41-06 (2006), ACI 369 (2011)]

The ASCE model was used in many studies to predict the shear strength of beam-column joints such as those by Hassan (2011), Clyde et al. (2000), and Pantelides et al. (2002). The comparisons indicated that the recommended ASCE shear strength values could be used as a lower bound for joint strength predictions. In general, the ASCE results were very conservative in comparison to the experimental results. The modelling parameters for joint shear strength coefficient and plastic shear strains are shown in Table 2-1 and Table 2-2.

Table 2-1: Joint shear strength coefficient γ recommended by ASCE 41-06 (2007)

	Value of γ (units: $MPa^{0.5}$)				
ρ"	Interior joint with transverse beams	Interior joint without transverse beams	Exterior joint with transverse beams	Exterior joint without transverse beams	Knee joints
< 0.003	1	0.83	0.67	0.5	0.33
≥ 0.003	1.67	1.25	1.25	1	0.67

ρ" = volumetric ratio of horizontal confinement in the joint; knee joint = self-descriptive (with transverse beams or not)

Table 2-2: Modelling parameters and numerical acceptance criteria for nonlinear analyses - RC beam-column joints

			Modeling Parameters[4]			Acceptance Criteria[4]				
						Plastic Rotation Angle, radians				
						Performance Level				
			Plastic Shear Angle, radians		Residual Strength Ratio		Component Type			
							Primary		Secondary	
Conditions			a	b	c	IO	LS	CP	LS	CP
i. Interior joints[2, 3]										
$\frac{P}{A_g f'_c}$	Trans. Reinf.	$\frac{V}{V_n}$ [3]								
≤ 0.1	C	≤ 1.2	0.015	0.03	0.2	0.0	0.0	0.0	0.02	0.03
≤ 0.1	C	≥ 1.5	0.015	0.03	0.2	0.0	0.0	0.0	0.015	0.02
≥ 0.4	C	≤ 1.2	0.015	0.025	0.2	0.0	0.0	0.0	0.015	0.025
≥ 0.4	C	≥ 1.5	0.015	0.02	0.2	0.0	0.0	0.0	0.015	0.02
≤ 0.1	NC	≤ 1.2	0.005	0.02	0.2	0.0	0.0	0.0	0.015	0.02
≤ 0.1	NC	≥ 1.5	0.005	0.015	0.2	0.0	0.0	0.0	0.01	0.015
≥ 0.4	NC	≤ 1.2	0.005	0.015	0.2	0.0	0.0	0.0	0.01	0.015
≥ 0.4	NC	≥ 1.5	0.005	0.015	0.2	0.0	0.0	0.0	0.01	0.015
ii. Other joints[2, 3]										
$\frac{P}{A_g f'_c}$	Trans. Reinf.[1]	$\frac{V}{V_n}$								
≤ 0.1	C	≤ 1.2	0.01	0.02	0.2	0.0	0.0	0.0	0.015	0.02
≤ 0.1	C	≥ 1.5	0.01	0.015	0.2	0.0	0.0	0.0	0.01	0.015
≥ 0.4	C	≤ 1.2	0.01	0.02	0.2	0.0	0.0	0.0	0.015	0.02
≥ 0.4	C	≥ 1.5	0.01	0.015	0.2	0.0	0.0	0.0	0.01	0.015
≤ 0.1	NC	≤ 1.2	0.005	0.01	0.2	0.0	0.0	0.0	0.0075	0.01
≤ 0.1	NC	≥ 1.5	0.005	0.01	0.2	0.0	0.0	0.0	0.0075	0.01
≥ 0.4	NC	≤ 1.2	0.0	0.0	–	0.0	0.0	0.0	0.005	0.0075
≥ 0.4	NC	≥ 1.5	0.0	0.0	–	0.0	0.0	0.0	0.005	0.0075

1. "C" and "NC" are abbreviations for conforming and nonconforming transverse reinforcement. A joint is conforming if hoops are spaced at ≤ $h_c/3$ within the joint. Otherwise, the component is considered nonconforming.
2. P is the design axial force on the column above the joint and A_g is the gross cross-sectional area of the joint.
3. V is the design shear force and V_n is the shear strength for the joint. The design shear force and shear strength shall be calculated according to Section 6.5.2.3.
4. Linear interpolation between values listed in the table shall be permitted.

Chapter 2

PART IV: STRENGTHENING OF BEAM-COLUMN JOINTS

2.13 INTRODUCTION

In GLD buildings, many collapses were attributed to column failures "weak column-strong beam design" and/or joint failures. However, strengthening of columns only by increasing the strength capacity could move failure to the joint area as it will be the next deficient location due to either lack of joint hoops, anchorage detailing or geometrical design inconsideration. Over the years, strengthening of deficient joints has been a challenging task to many investigators to provide practical strengthening applications as well as to eliminate undesirable failure modes. In many strengthening strategies, the presence of a floor slab and transverse beams in actual RC framed buildings poses an additional big challenge to confine the limited joint area (Engenidiz et al., 2005). Other considerations and concerns during strengthening include labour cost, complex detailing, installation time, and disruption of building functionality.

Current investigations on strengthening beam-column joints involved RC/steel/or prestressed jacketing, use of external steel elements, epoxy repair, concrete removal and replacement, and FRP composite applications (Engenidiz et al., 2005). The following sections present a brief review on advantages and disadvantages observed from using these techniques in real strengthening applications. Details of the most well-known strengthening techniques on deficient beam-column joints are presented in Appendix B.

2.14 EPOXY REPAIR

Epoxy repair is a very beneficial rehabilitation measure when the damaged joint is hard to access or large cracks need repairing. However, this technique requires high skill levels to provide satisfactory applications which, in turn, are limited by the ambient temperature (ACI 224.1R-93, 1998). Some other advantages of using epoxy and which make it desirable to use are adhesion, versatility, chemical resistance, rapid hardening, and moisture resistance. Two methods of epoxy repair are used including pressure injections and vacuum impregnations (Engindeniz et al., 2005).

2.15 CONCRETE RENEWAL

In the aftermath of earthquakes, severe damage and concrete spalling are expected to take place in GLD connections due to inappropriate design detailing or construction deficiencies. Moreover, buckling of longitudinal reinforcement and rapture of steel ties might also occur. Consequently, repair of the connection by partial or complete removal of damaged concrete is essential for any further rehabilitation measures. In addition, placement of new transverse and/or longitudinal bars might also be necessary [UNDP/UNIDO PROJECT RER/79/015 (1983), Engindeniz et al., (2005)]. Better concrete qualities with high strength and minimum shrinkage characteristics can be used for renewal. Special care also must be taken to ensure good bond conditions between old and new concrete surfaces. Some studies used the concrete replacement repair along with additional strengthening schemes.

It should be mentioned that the use of the concrete removal and replacement repair depends on other factors such as accessibility of the damaged connection and cost of shoring. Exterior and corner joints are usually more accessible than interior joints. It is also reported that, in some cases where only beams are the accessible elements, their sole repair may shift damage to the column or joint region (Lee et al., 1977).

2.16 RC JACKETING

RC jacketing has been used widely in practice for several decades. Applications included strengthening of partial or complete parts of framed structures. The technique involves casting

of a new better-quality concrete along the strengthened parts as well as placement of additional transverse and longitudinal reinforcement. However, removing part of the slab at the connection location is necessary. The technique is considered expensive due to intensive work required, particularly if joint hoops and beam hooks are provided. Other disadvantages of the technique are enlargement of the cross-section, disruption of building functionality and change in dynamic characteristics of the building [Engindeniz et al. (2005), Bracci et al. (1995)]. Nevertheless, the technique did improve the performance in most of the applications.

2.17 STEEL JACKETING

This beam-column joint rehabilitation technique involves the use of different configurations of steel elements including flat or corrugated steel plates and tubes, in addition to welding works. Conventionally, steel elements are attached to confine elements by using bolts, adhesives and/or connecting rolled sections. Main disadvantages of using the steel jacketing technique are: a) enlargement in cross-section and loss of floor space, b) corrosion, c) difficulty in handling heavy steel formworks, d) complex detailing, and e) difficulty in installing beam formworks due to the presence of slabs (Engindeniz et al., 2005). Nonetheless, steel jacketing was proven to enhance the performance considerably even when it is only used for lateral confinement purposes; however, some unexpected failure mechanisms may occur (Hoffschild et al., 1995). Moreover, in comparison to RC or masonry jacketing techniques, the steel jacketing technique has the advantage of rapid application due to the use of prefabricated steel works (Engindeniz et al., 2005).

2.18 FRP COMPOSITE APPLICATIONS

Huge amount of research has been devoted in the last two decades to investigate the efficiency of FRP laminates and sheets to upgrade the performance of substandard joints. Different forms of FRP have been used including flexible sheets and strips, and near surface mounted rods or plates. Despite the high material cost, it is reported that other advantages such as light weight, ease of application, corrosion resistance, high strength, minimum structure disruption, flexibility, no significant enlargement in element cross-section, and low labour cost justifies the use of FRP widely in normal applications [Engindeniz et al. (2005), and Bousselham (2010)]. Due to large and appreciated successes of FRP applications, findings have entered design guidelines such as ACI Committee 440 (2008), Canadian Standards Association S806 (2002), and recommendations by fib-TG9.3 (2001). Most of the research on FRP, however, was devoted to strengthening columns (Saatcioglu, 2003), beams, and infill masonry walls [Saatcioglu (2006), El- Gawady et al. (2005)]. Applications to beam-column joints are still limited. A brief review of most FRP applications on joints is given in Appendix B. Based on this review, it is found that the use of FRP composites resulted, in most cases, in significant improvement in

performance. However, to obtain a very ductile behaviour and flexural hinging in the beam, considerable amounts of FRP materials are required. Some applications of the FRP jacketing were aimed to restore the original performance but with improved ductility. Other applications also included the use of FRP composites along with other more economical techniques such as RC jacketing (Sasmal, 2009) or steel rods or plates (Ghobarah and El-Amoury, 2005) so as to reduce the cost.

Despite the success of using the FRP technique on joint applications, it is thought that other issues such as the need for skilled workers, careful surface preparations and a space for work application will increase the expenses significantly when strengthening of substandard low-cost buildings is of concern.

2.19 POST-TENSIONING METAL STRAPPING TECHNIQUE (PTMS)

The post tensioning metal strapping technique (PTMS) involves tensioning of ductile metal strips around the member cross-section using standard tensioning machines similar to those used in the packaging industry. Strips are secured in place by means of metal clips using sealing machines. Metal strips can be available in different widths, thickness and strengths based on the ease of handling, bending and the tensioning process. A maximum thickness and width of about 1 *mm* and 30 *mm*, respectively, are found easily workable (Frangou, 1996). Strengths can be available based on the required confining stress. Metal clips are also available in different types based on the required fastening efficiency. Metal clips can be punched through single or double notches to be secured in place. Single notch is easier to apply, but less efficient than the double notch. Figure 2-47 shows the materials used for the technique.

(a) (b) (c)

Figure 2-47: The materials used for the technique a) metal strips, b) trimmed metal strips, c) metal clips

The tensioning of the strips and securing them in place by metal clips can be achieved either by using hand-operated or hydraulic tensioning and sealing machines. The hand-operated machines are used for small applications where the strip width is less than 13mm. The confinement level in this case depends on the amount of force put on the lever arm of the tensioning machine, and

thus, it is variable. Figure 2-48 shows the hand-operated machines used in the Heavy Structure Laboratory of the University of Sheffield. Also shown in the same figure is the strengthening of a cylindrical specimen.

Figure 2-48: Hand-operated tensioning and sealing machines

The hydraulically operated tensioning and sealing machines, on the other hand, are used for larger applications including columns, beams and joints. Confinement level is controlled by the air pressure provided by an air pump. Figure 2-49 shows the hydraulically operated machines available in the Heavy Structure Laboratory of The University of Sheffield. It should be mentioned that both types of machines are easy to use.

Figure 2-49: Hydraulically-operated tensioning and sealing machines

The efficiency of the clips is normally assessed by testing a metal strip sealed with a clip and monitoring the strain applied to the strip, as shown in Figure 2-50. Failure may occur either due to strip rupture, slipping of the strip or failure of the metal joint. Failure due to strip rupture is most desirable as this utilises the full strip capacity. The other two failures are brittle in nature and may cause a premature failure of the structural element.

Figure 2-50: Testing of the clip efficiency

In comparison to the strengthening techniques typically used in practice, the use of the PTMS technique has many beneficial effects. These are summarised in the following:

- Full utilisation of the strengthening material due to pre-stressing
- Economical due to the use of low-cost strengthening materials
- Less time consuming (three hours to retrofit a column while two days are needed using RC jacketing technique (Frangou, 1996)
- No additional formwork is needed to apply this technique

The technique can also:

- Enhance the flexural and shear capacity of the member.
- Enhance bond strength and prevents buckling of longitudinal reinforcement.

In previous research works, the PTMS technique was utilised mainly to upgrade the strength of small and medium scale RC elements in compression [Frangou (1996), Gunja (2004), Moghaddam et al. (2007)] and in shear (Frangou, 1996). Tests included over-reinforced beams, lightly reinforced columns with bar buckling deficiency, shear-deficient beams, and concrete cylinders in compression. In all applications, researchers complimented on the positive effect of using post-tensioning. In some cases in which post-tensioned metal strips were used to confine concrete cylinders, the enhancement in concrete compressive strength reached more than twice the original value (Gunja, 2004). The analytical work on the technique only involved the development of a stress-strain model for concrete confined by PTMS (Moghaddam et al., 2007).

All previous developments and applications related to the PTMS technique are summarised in Appendix C.

Further research on the technique is still underway. The technique has potential to offer practical, cheap and effective solutions to many problems in substandard buildings such as the deficient joint assembly. In contrast to the sole strengthening of beams and/or columns, strengthening of joints is much more complicated and work is still needed to develop an appropriate and easy-to-apply strengthening methodology for actual joints.

Chapter 3

EXPERIMENTAL METHODOLOGY

3.1 INTRODUCTION

Experimental simulation is considered fundamental for gaining insight into the behaviour of structural components under real loading events, such as earthquakes. Simulating the effect of such events on those components, however, requires some simplifications for most problems of interest. This chapter provides details of a multi-phase experimental programme designed to simulate deficient structural elements with insufficient internal reinforcement detailing and poor construction materials. More specifically, the experimental programme aims to investigate elements with bond critical regions and deficient reinforced concrete beam-column connections with poor reinforcement detailing. The work was done in three phases.

In the first phase, twelve small-scale RC beams with short lap splices at the mid-span were tested in four-point bending. In the second phase twelve medium-scale RC beams with long lap splices at the mid-span were also tested in four-point bending. The first and second phases of the programme represent an idealisation for different conditions of splicing the extension of

bottom column reinforcement to the top storey column reinforcement. The splice lengths were selected as 10 and 25 times the bar diameter so as to capture the different trends in behaviour and also for test limit, where the production of additional splice lengths, although it is desirable, would require long execution periods. In these two phases, the measurement of slip at the end of the bars as well as predictions of splice bond capacities is essential to produce an appropriate bond stress-slip relationship (τ, s), which can be used to simulate the performance and deformational behaviour of PTMS-confined column splices in a joint assembly.

The third phase of the experimental programme, on the other hand, included testing of four deficient full-scale RC beam-column connections having inadequate anchorage length of beam bottom bars into the core and no shear links within the core. The joints were designed with the strong beam-weak column concept. This phase ultimately aims to investigate the performance and characteristics of deficient joints including energy dissipation, stiffness, load and deformation capacities and most importantly the contribution of joint deformations to the total behaviour. By examining these deficient characteristics, rehabilitation measures by means of PTMS are designed to improve the joint performance characteristics. Moreover, predictions of the PTMS-strengthened joint behaviour from instrumentation provided (see Sec 3.3.4) is essential to propose a shear stress-strain model (τ_j, γ_j) for the confined joint area, which can be used for simulating such joints.

In this chapter, the choice of test parameters, mechanical properties of construction materials, specimen design and preparation, test setup, instrumentation, loading protocol and loading systems are presented.

3.2 PHASE I & II: BEAM TESTS

3.2.1 General

This phase of the experimental programme deals with splitting bond strength using flexural beam specimens. Under flexural conditions, splitting of concrete in the tension zone is a common mode of bond failure.

This method of testing is considered to be more representative of bond conditions in an actual connection than the conventional pullout test. This is due to the fact that it simulates loading conditions, cracking patterns and failure mechanisms similarly to those in real structures. In addition, the splitting failure occurs at lower bond values than pullout conditions and is accompanied by spalling of the concrete cover, which is not commonly observed in pullout failures. Furthermore, strain profiles along splices are influenced by cracking patterns under different loading combinations.

Therefore, to understand this type of failure in poor quality beams and to measure the enhancement provided by PTMS confinement, a series of tests on small and medium scale beams were conducted in this phase.

3.2.2 Phase I- Small Scale Beams in Tension

3.2.2.1 Specimen Description

The test specimens consisted of (150 x 200 mm^2 cross-section and 1.2 m length) simply supported rectangular beams. The clear span between supports was 1.1m with a shear span to total depth of 1.75. The test beams are separated into three groups as shown in Table 3-1. Figure 3-1 shows a schematic view of the test specimens with reinforcement detailing.

Table 3-1: Summary of test parameters of beam specimens – Phase I

Group	**Specimen Notation**	**Type of Loading**	C_s* *mm*	C_b* *mm*	C_m* *mm*	f'_c *MPa*
Group I	SC10-D12-Ctrl	Monotonic	13	13	50.0	22.5
$C_s=C_b=10mm$	SC10-D12-S	Monotonic	12	12	51.0	22.5
$d_b=12mm$	SC10-D12-PTMS1	Monotonic	12	12	51.0	22.5
$L_d=120mm$	SC10-D12-PTMS2	Cyclic	17	12	32.5	37.2
Group II	SC20-D12-Ctrl	Cyclic	17	17	31.5	37.2
$C_s=C_b=20mm$	SC20-D12-S	Cyclic	19	22	30.5	37.2
$d_b=12mm$	SC20-D12-PTMS1	Cyclic	20	24	31.0	37.2
$L_d=120mm$	SC20-D12-PTMS2	Cyclic	18	22	30.0	37.2
Group III	SC27-D16-Ctrl	Cyclic	24	26	12.5	37.2
$C_s=C_b=27mm$	SC27-D16-S	Cyclic	26	25	15.5	37.2
$d_b=16mm$	SC27-D16-PTMS1	Cyclic	29	26	15.5	37.2
$L_d=160mm$	SC27-D16-PTMS2	Cyclic	22	27	16.0	37.2

C_s is the side cover, C_b is the bottom cover, and C_m is ½ the clear distance between spliced bars

L_d is the splice length and d_b is the bar diameter

* It should be mentioned that the actual side and bottom covers deviated from the nominal designed values (as stated in the first column) due to lab conditions such as casting process, concrete vibration or mould imperfections.

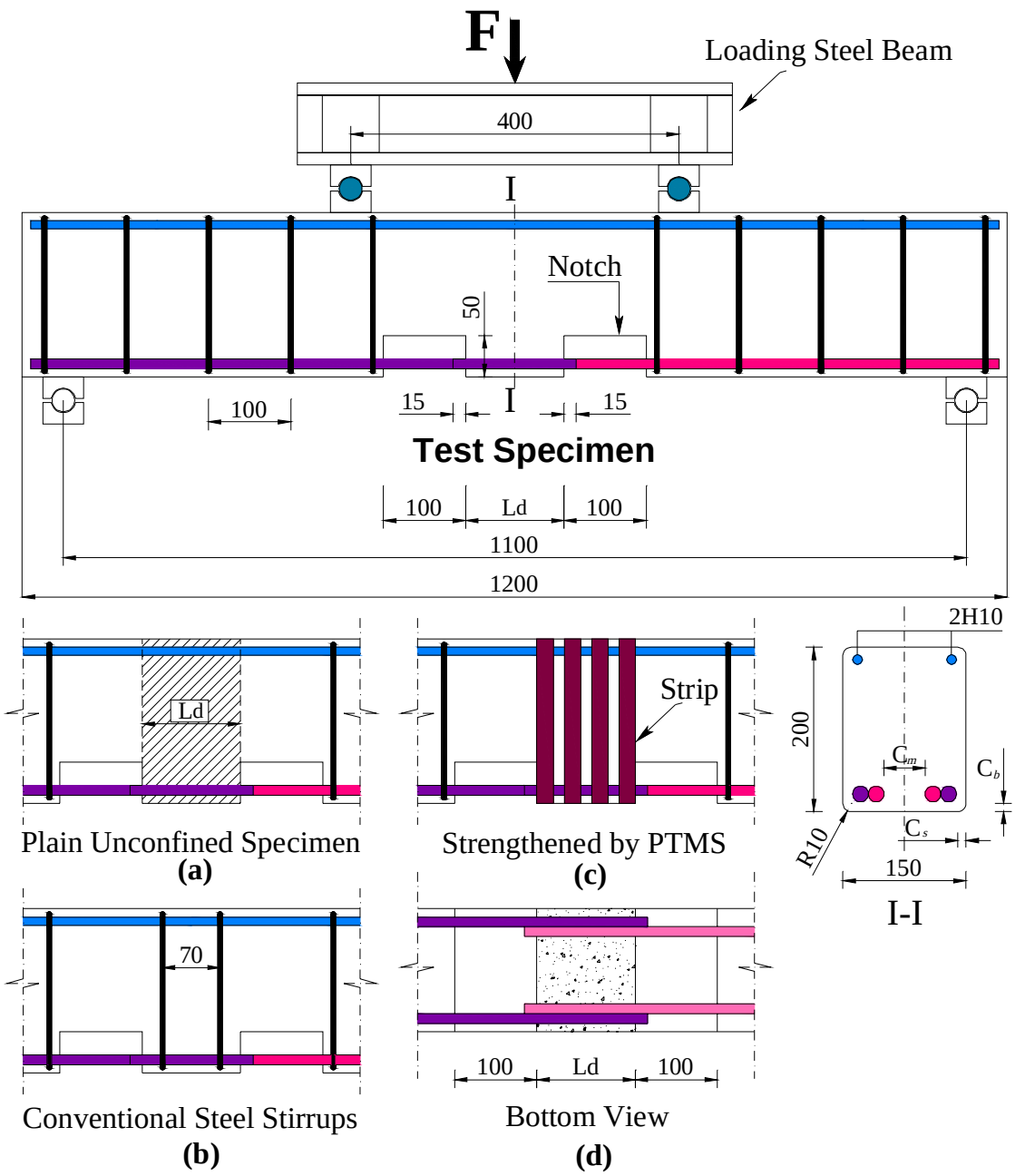

Figure 3-1: Schematic view of the small scale test specimens

Each group contained a control (unconfined) specimen, an internally confined specimen by conventional steel stirrups and two externally confined specimens by PTMS. The bottom reinforcement is spliced at mid-span with a splice length L_p of $10d_b$, where d_b is the reinforcing bar diameter. The specified lap length was selected so that splitting-type failure takes place before the attainment of yield stresses. Nevertheless, the short splices allowed a reasonable number of bar lugs to participate in bearing the bar tensile strength through bond action. The width of the beam and number of splices were designed to produce two different concrete cover ratios c/d_b. To achieve this, the concrete side cover and bottom cover were kept identical for each group.

The spliced bars consisted of steel ribbed bars. The clear distances between the ribs r_d were 8 and 10 *mm* for the 12 and 16 *mm* bars, respectively as shown in Figure 3-2.

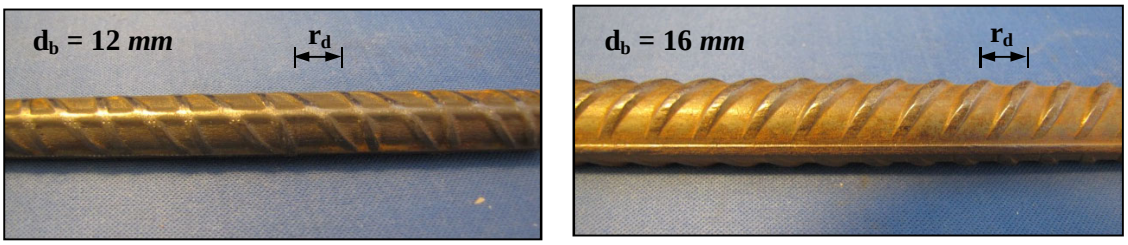

Figure 3-2: Geometry and types of reinforcing bars used in the beams

Rectangular (100*mm* width × 50*mm* height × 150*mm* depth) notches were made at the bottom of the beams for slip measurement at splice free-ends. In addition, a 15*mm* bond-free length of spliced bars was extended through the notches to enable mounting a mechanical gauge at the splice free-ends. For the PTMS strengthened specimens, the cross-section corners at the splice location were rounded to an approximate 10*mm* radius to enhance the confining efficiency of PTMS. For the steel confined specimens, the area and spacing of steel stirrups were selected to produce practical values of $\frac{A_{tr}}{\mathrm{sn}d_b}$ between 0.011 and 0.12, in which A_{tr} is the area of one link in the splice region, s is the link spacing, n is the number of spliced sets of bars (2 in the studied case), and d_b is the bar diameter. Two steel stirrups were provided within the splice length at spacing of 70 mm to be uniformly distributed.

The lateral reinforcement located outside the splice length was designed using 6 *mm* closed ties spacing at 100 *mm* so that any potential shear failure preceding bond failure is avoided. Continuous top reinforcement using two 10 *mm* diameter bars was provided in all specimens so as to resist shrinkage, keep steel links in place during casting, improve the concrete compressive strength at the top of the beam, and prevent collapse which may cause damage to instrumentation set at the bottom of the beam.

3.2.2.2 Test Parameters

Many parameters affect the splitting bond strength, as explained in chapter 2. The selection of the test parameters was based on the most critical conditions found in typical existing buildings including small concrete cover, low confinement ratio, poor concrete quality, bar diameter and seismic loading. In this study, the parameters considered include:

- The diameter of spliced bars d_b (12*mm* and 16*mm*)
- Nominal concrete cover to bar diameter ratio c/d_b (0.83, 1.67)
- Concrete compressive strength f'_c (22.48 and 37.22 MPa).
- Type of loading (monotonic and unidirectional cycles).

- $\frac{A_{tr}}{\mathrm{sn}d_b}$ ratio of 0.025 to 0.034 for steel confined specimens and 0.034 to 0.053 for the PTMS confined ones.

Table 3-1 provides a summary of specimen designations and test variables.

It should be mentioned that use of different concrete strength values in this test phase was due to inability of the external provider to achieve low concrete strengths. The target concrete compressive strength f'_c was ordered between 15 - 20 MPa. This strength was selected to replicate the quality of concrete generally used in the construction of substandard RC structures.

3.2.2.3 Specimen Preparation

3.2.2.3.1 Preparation of reinforcement cages

The reinforcement was cut and bent according to the specified lengths at the Heavy Structure laboratory of the University of Sheffield. Steel cages were prepared and formed into the required shapes using plastic ties. The splice length at the mid-span L_d was ensured by using polystyrene blocks with made-holes to insert the splices as shown in Figure 3-3. The polystyrene blocks were also used to form voids at the splice free-ends for slip measurement. The cages were labelled and positioned in steel moulds using plastic spacers to ensure the required concrete covers. This was essential due to the fact that the concrete cover was considered to be a main parameter in this study. Figure 3-4 shows the preparation and formation of the reinforcement cages.

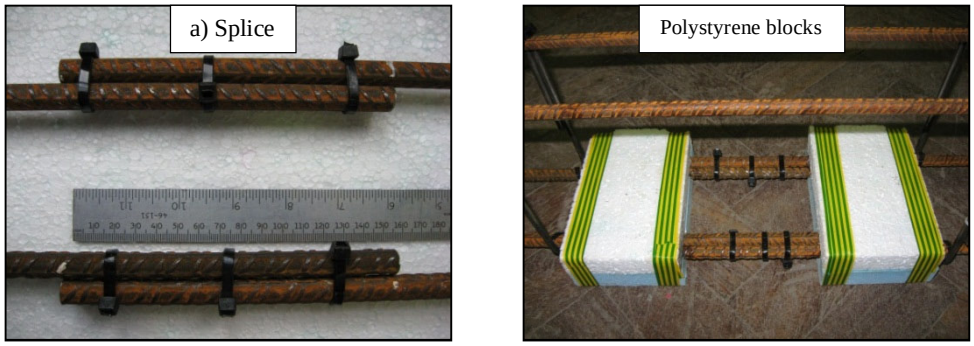

Figure 3-3: Splice formation at the mid region of the test specimen

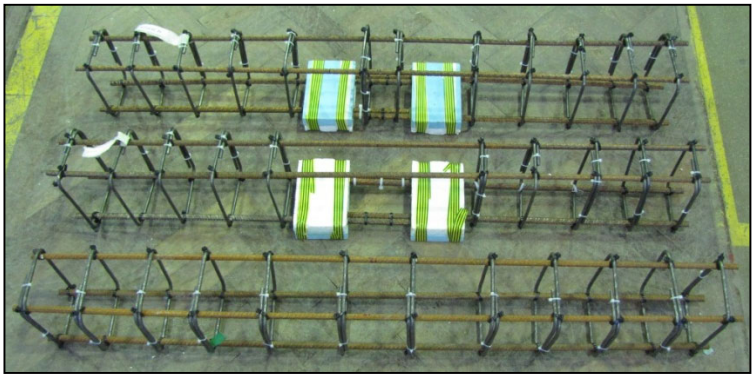

Figure 3-4: Steel cages of the test specimens

3.2.2.3.2 Mould preparation

The moulds used for casting were made of steel channel sections and mounted on wooden bases. The moulds were formed to produce 150*mm* × 250*mm* cross-section and 2.5*m* length specimens. An additional wooden spacer of 50*mm* height was used to reduce the specimen height to 200 *mm*. In addition, steel dividers of (100 *mm* width and 250 *mm* height) were used at mid-length to shorten the length to 2 × 1.2 *m*. The inner sides of the moulds were cleaned carefully, and silicon was used to seal all inside edges. A thin layer of oil was applied to the inner surfaces prior to casting to facilitate de-moulding of the RC specimens. Each steel mould enabled the production of four specimens. Four steel moulds were used for casting. Figure 3-5 shows a steel mould with reinforcement cages before casting.

Figure 3-5: Steel moulds with reinforcement cages before casting

3.2.2.3.3 Casting and curing

The cast concrete was provided by an external ready-mix supplier. The beams were cast in two batches. In the first batch, three beams were cast using two steel moulds whereas nine beams were cast in the second batch. For each batch, nine standard (150 *mm* diameter and 300 *mm* height) cylinders were cast to determine the concrete compressive strength at the age of testing. Six (100 *mm* diameters and 200 *mm* height) cylinders along with six (100x100*mm* cross-section and 300*mm* length) concrete beams were cast to determine the concrete tensile strength at the age of testing. After casting, the concrete was slightly vibrated using a small electrical poker vibrator and then levelling was imposed to the top surface of the specimen to minimise geometric irregularities. The cast beams, cylinders and concrete beams were covered by plastic sheets to prevent dehydration. The specimens were de-moulded one week after casting and stored in the lab until the day of testing. Figure 3-6 shows the beams during casting.

Figure 3-6: Casting of the small scale beams

3.2.2.4 Material properties

3.2.2.4.1 Concrete

Two ready-mix concrete batches were used to cast the beams. The target concrete compressive strength f'_c ranged between 15 - 20 MPa. This strength was selected to replicate the quality of concrete generally used in the construction of substandard RC structures.

The actual concrete compressive strengths, determined using standard (150 × 300 *mm*) cylinders, were 22.5 MPa (standard deviation SD=1.67 MPa) and 37.2 MPa (SD=1.28) for the first and second batches, respectively. The tensile strength of the concrete was determined from splitting tests performed on six cylinders (100 × 200 *mm*) and the flexural testing of six prisms (100 × 100 × 500 *mm*) according to BS 1881-117 (1983b) and BS 1881-118 (1983c), respectively. Accordingly, the concrete tensile strengths were found to be 2.6 MPa (SD=0.16 MPa) and 2.8 MPa (SD=0.2 MPa) for the first and second batches, respectively. The modulus of elasticity E_c was derived according to ACI 318 (2008) and was found to be 22.3 and 27.8 GPa for the first and second mixes, respectively. The full results of the compressive and tensile strength derived from the tests are reported in Appendix D.

3.2.2.4.2 Reinforcement

The main reinforcement consisted of deformed 12 and 16*mm* bars and the top reinforcement consisted of deformed 10*mm* bars. In addition, shear reinforcement consisted of plain bars with a nominal diameter of 6*mm*. Direct tension tests (referred to as coupon tests) were carried out to determine the mechanical properties of the bars. Thus, for each bar diameter, three segments of 600*mm* length were machined down at mid-length with 200*mm* length. Strain gauges were then attached to the bar surface to monitor strains during the test, as shown in Figure 3-7. Table 3-2 shows details of the mechanical properties of both main and transverse reinforcement. The average values were derived from the coupon tests.

Figure 3-7: Direct tension test on steel deformed rebars

Table 3-2: Average mechanical properties of reinforcing bars

Bar diameter mm	**Yield stress f_y MPa**	**Ultimate stress f_u MPa**	**Yield strain ε_y**	**Strain hardening strain ε_{sh}**	**Ultimate strain ε_u**
	Main reinforcement E_s=200 GPa				
d_b= 12 *mm*	470	570	0.0028	0.020	0.09
d_b= 16 *mm*	470	570	0.0028	0.020	0.09
	Top reinforcement E_s=200 GPa				
d_b= 10 *mm*	533	688	0.0025	0.030	0.10
	Shear reinforcement E_s=200 GPa				
d_b= 6 *mm*	360	420	0.0018	0.009	0.10

3.2.2.4.3 Metal Strips and Clips

Metal strips of 25*mm* width and 0.8*mm* thickness were used to strengthen two specimens of each group. Hydraulically operated sealing and tensioning machines were used to secure strips in place. The average yield and ultimate stresses were 760 and 1100 MPa, respectively. The average yield and ultimate strains were 0.0027 and 0.073, respectively. Clips were secured in place using double notches. Moreover, the double notches ensured full utilisation of strip strength and no clip failure was observed during tests.

The amount of strips required along the splice region was designed to give multiple values of the (A_{tr}/snd_b) ratio of corresponding internally confined specimens. This allowed comparisons between the effect of internal and external confinement on bond strength.

3.2.2.5 Test Procedure and Instrumentation

The test specimens were tested in a four column universal testing machine with a 1,000 kN capacity dynamic actuator. A steel beam was used to support the specimen with a clear spacing of 1.1*m*. The test specimens were loaded symmetrically using two point loads at a distance of 400*mm*, to produce a constant moment region over the splice length. The load was applied to the specimen through a rigid steel beam positioned at the centre of the specimen and reacting against the specimen. The test specimens were subjected to two types of loading regimes in this series. Both loading regimes were applied in displacement (deflection) control. In the first loading regime, three specimens were subjected to monotonically increasing displacements at a loading rate of 0.1*mm/min*. The second loading regime involved testing nine specimens under a sequence of complete unidirectional cycles using the loading history shown in Figure 3-8. The loading/unloading rate used was 0.2*mm/min*. The deflection ratio DR% was defined as the percentage of mid-span deflection to the half specimen length between supports (equal to 0.55*m*).

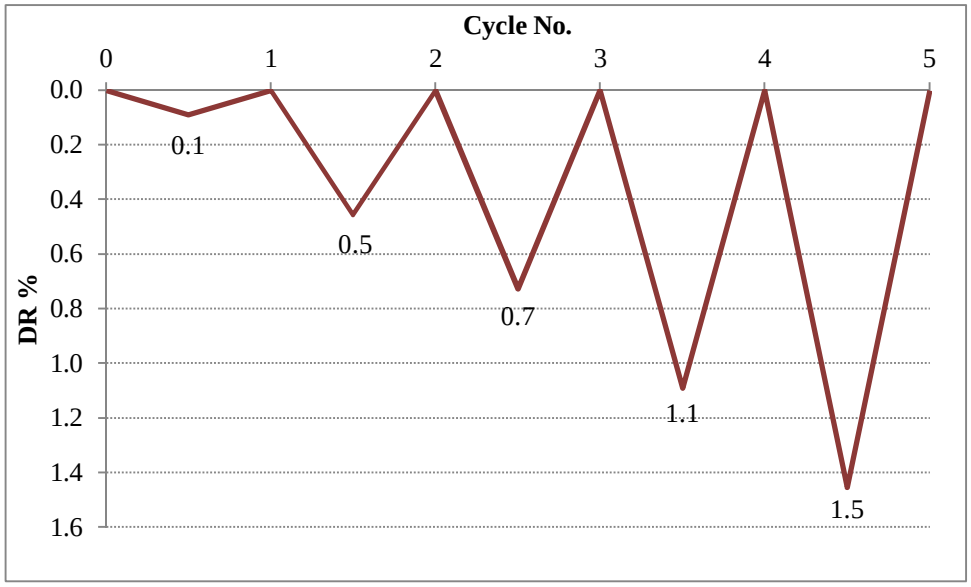

Figure 3-8: Cyclic load history used in the test of small scale beams

The deflection of the beam was monitored at each load increment using two Linear Variable Differential Transducers (LVDTs) placed at the centre of the beam. Two LVDTs were also used to monitor support movements. The steel strains of spliced bars were measured using electric resistance strain gauges attached to the exposed surface of the bars at notch locations. In addition, electric strain gauges were bonded to steel strips to measure the variation in the confining pressure during the test.

Particular attention was given to measuring slip values of spliced bars in these tests. Slip readings at splice free-ends were taken using small LVDTs of 10 *mm* capacity mounted on the extension of spliced bars into the notches. The readings were taken with reference to the

surrounding concrete, at the splice location, to record pure slip measurements. In doing so, a steel frame was constructed to hold the small LVDTs and was mounted at the centre of the beam using steel screws. The locations of steel screws were selected to be situated on intact parts of the concrete in the splice zone. Figure 3-9 presents the instrumentation used for strain and slip measurement. In addition, Figure 3-10 shows a test specimen with the instrumentation installed.

Capturing the cracking progress during the test was very important in this test. For this reason, the sides of the beam were white-washed before the day of testing. This facilitated locating and marking of the cracks as the test progressed.

At each loading stage, deflection readings were taken at the centre of the beam and the cracking patterns were monitored. All data were collected and stored automatically using a data acquisition system.

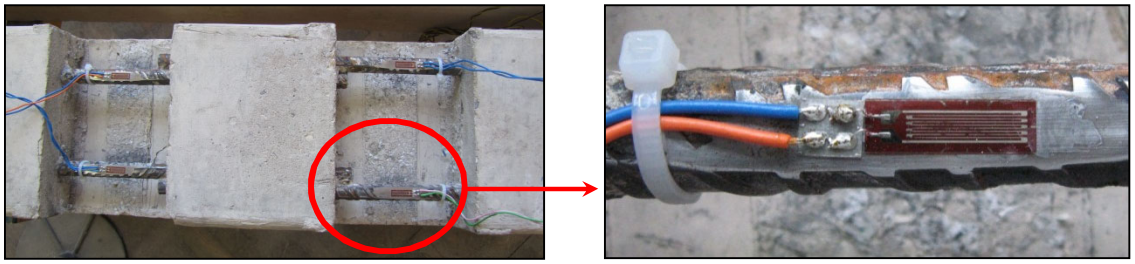

(a) Strain gauges on the exposed part of splices

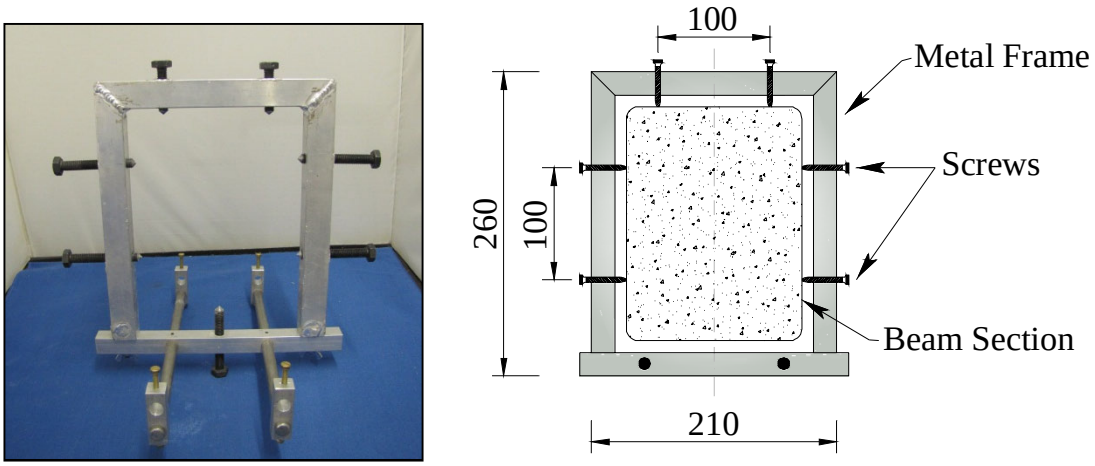

(b) Metal frame for slip measurement

Figure 3-9: Instrumentation of test specimens a) strain gauges and b) LVDTs

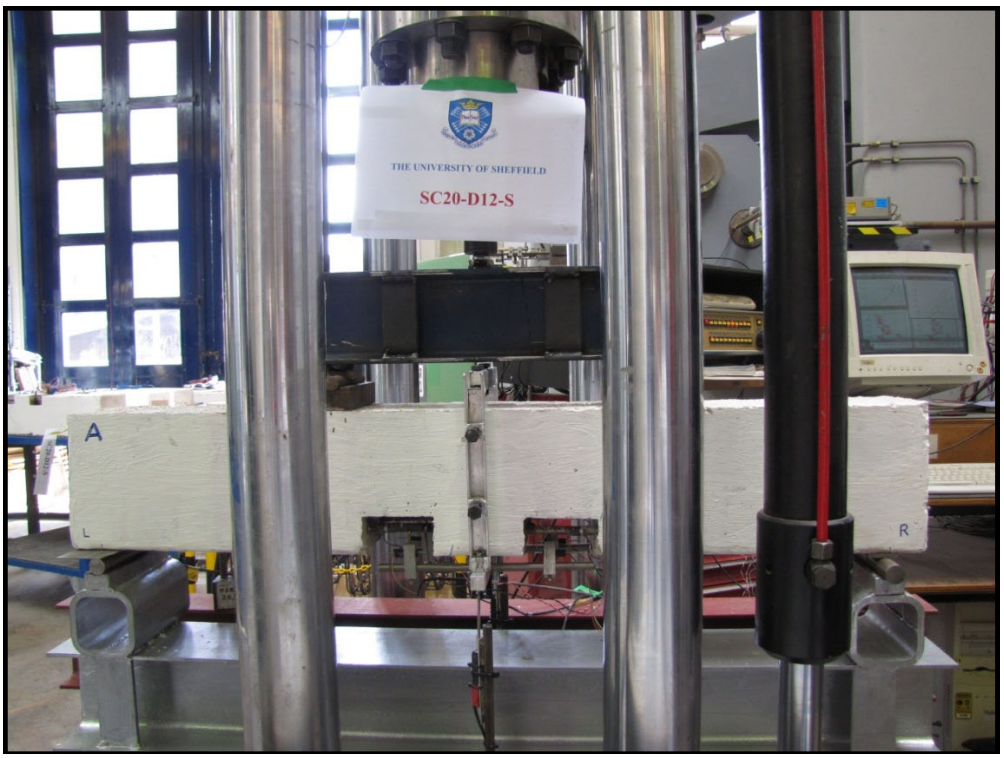

Figure 3-10: A test Specimen with instrumentation installed.

3.2.2.6 Designation

Because of the various parameters investigated in this study, it was necessary to provide a designation that reflects the main test variables, including the splice length, the type of confinement used in the splice region, bar diameter, and cover concrete. Therefore, the use of a compact four-part notation was adopted to indicate these variables. Accordingly, in the specimen code, the first letter refers to the splice length (S-short $10d_b$ and L-long $25d_b$); the second letter and the following number refer to the nominal side and bottom concrete cover (C10,20,27 represents side concrete cover equal to 10, 20 and 27*mm*, respectively); the third letter and following number refer to the spliced bar diameter (D12, 16 represents 12 and 16*mm* bar diameter, respectively); the fourth letter/word refers to the confinement used along the splice length (Ctrl for the bare unconfined specimen; S for the internally confined by steel stirrups; and PTMS for the externally confined by post tensioned metal strips); an additional number 1 or 2 in the designation of PTMS specimens was used to represent the sequence of specimen in the group, and the number 2 refers to higher PTMS confinement.

For Example:

- SC10-D12-Ctrl: Short splice $10d_b$ – concrete cover 10mm – bar diameter 12mm – control unconfined specimen.
- SC27-D16-PTMS1: Short splice $10d_b$ – concrete cover 27mm – bar diameter 16mm – PTMS confinement (specimen 1)

3.2.3 Phase II- Medium Scale Beams in Tension

3.2.3.1 Specimen Description and Design

In this phase, twelve medium scale RC beams were constructed to simulate long insufficiently confined anchorages/splices that exist in older existing buildings. The test specimens consisted of (150 x 250 mm^2 cross-section and 2.5 m length) simply supported beams. The clear span between supports was 2.3m with a shear span to total depth of 3.1. Similarly to Phase I, the specimens were categorised into three groups based on the thickness of the external concrete cover as shown in Table 3-3. A schematic view of the test specimens is presented in Figure 3-11.

Table 3-3: Summary of test parameters of beam specimens in Phase II

Group	**Specimen Notation**	$\mathbf{A_{tr}/\,snd_b}$	$\mathbf{C^*_{sa}}$ *mm*	$\mathbf{C^*_{sb}}$ *mm*	$\mathbf{C^*_b}$ *mm*	$\mathbf{C^*_m}$ *mm*	f'_c *MPa*
Type of loading: complete unidirectional cycles							
Group I	LC10-D12-Ctrl	-	12	13	11	39.5	28.6
C_s, C_b=10*mm*	LC10-D12-S	0.047	11	16	13	40.5	28.6
d_b=12*mm*	LC10-D12-PTMS1	0.048	12	12	12	51.0	28.6
L_d=300*mm*	LC10-D12-PTMS2	0.067	17	17	12	32.5	28.6
Group II	LC20-D12-Ctrl	-	27	22	17	27.5	24.9
C_s, C_b=20*mm*	LC20-D12-S	0.047	26	21	20	28.0	24.9
d_b=12*mm*	LC20-D12-PTMS1	0.048	23	16	22	32.0	24.9
L_d=300*mm*	LC20-D12-PTMS2	0.067	24	14	17	31.0	24.9
Group III	LC27-D16-Ctrl	-	24	30	21	15.5	26.5
C_s, C_b=27*mm*	LC27-D16-S	0.031	30	28	27	14.5	26.5
d_b=16*mm*	LC27-D16-PTMS1	0.031	27	27	27	15.5	26.5
L_d=400*mm*	LC27-D16-PTMS2	0.063	26	30	22	16.0	26.5

C_{sa} is the side cover on side A of the beam; C_{sb} side cover on face B; C_b is the bottom cover; and C_m is ½ the clear distance between spliced bars; Face B of the beam corresponds to the side with spliced bars strain-gauged.

* It should be mentioned that the actual side and bottom covers deviated from the nominal designed values (as stated in the first column) due to lab conditions such as casting process, concrete vibration or mould imperfections.

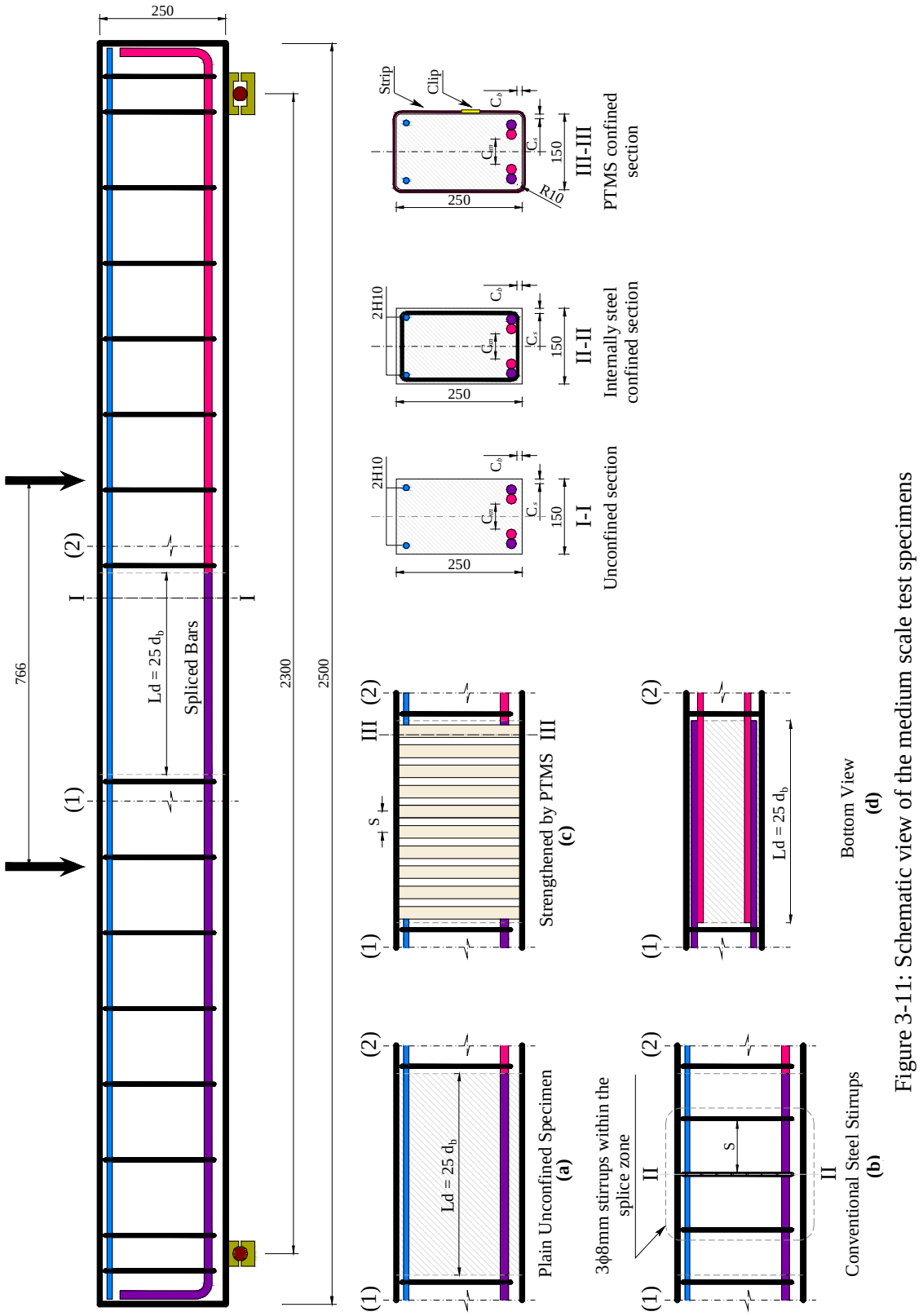

Figure 3-11: Schematic view of the medium scale test specimens

Each group comprised a bare (unconfined) specimen, a steel confined specimen with internal steel stirrups, and two specimens externally confined with PTMS. The specimens of each group were similar in terms of flexural reinforcement, concrete strength, cover concrete thickness and splice length. The bottom reinforcement was spliced at mid-span with a splice length L_p of $25d_b$, where d_b is the reinforcing bar diameter. The specified lap length was long enough to enable splitting-type failure at the tension splice zone after reaching yield stresses. For the purposes of this study, the lap length was selected so that it does not conform to the requirements of current codes of practice but represents old practice detailing. The spliced bars consisted of high tensile steel ribbed bars. The clear distances between the ribs r_d were 8 and 10 *mm* for the 12 and 16*mm* bars, respectively. The width of the beam and number of splices were designed to produce two different concrete cover to bar diameter ratios c/d_b of nominal values (0.83 and 1.67).

Strain gauges were attached to the spliced bars to monitor strain profiles along the splices during loading. In addition, strain gauges were attached to the confining material to measure its resistance to splitting. The application of strain gauges is described in detail in section 3.2.3.3.

For the steel confined specimens, the area and spacing of steel stirrups were selected to produce a value of $\frac{A_{tr}}{\mathrm{sn}d_b}$ ranging from 0.03 to 0.047 which corresponds to a value of $\alpha\omega_\omega$ equal to 0.089. Accordingly, three closed ties were added within the splice zone at spacing, s, of 90*mm* for specimens LC10-D12-S & LC20-D12-S and 100*mm* for specimen LC27-D16-S. The selection of these spacings is only to ensure uniform distributions of lateral reinforcement along the splice length. The external confinement of PTMS confined specimens was designed to produce multiple values of the aforementioned ratio ranging from 0.03 to 0.067 corresponding to values of $\alpha\omega_\omega$ of 0.10 to 0.128. The cross section corners of the PTMS confined specimens were rounded, prior to pre-tensioning, to an approximate 10*mm* radius.

Closed ties spaced at 100*mm* were provided in the shear span to prevent shear failure. Top reinforcement of 10*mm* diameter was also provided to all beams for the same reasons mentioned in 3.2.2.1.

3.2.3.2 Test parameters and specimen designation

Analogously to Phase I, the test parameters investigated in this phase were

- The diameter of spliced bars d_b (12*mm* and 16*mm*)
- Nominal concrete cover to bar diameter ratio c/d_b (0.83, 1.67)
- Compressive strength f'_c ranged between 20 to 30 MPa.
- $\frac{A_{tr}}{\mathrm{sn}d_b}$ ratio (ranging from 0.03 and 0.047 for steel confined specimens; and 0.03 to 0.067 for the PTMS confined specimens).

Also, in this test phase, the target concrete compressive strength f'_c was ordered between 15 - 20 MPa to replicate the quality of concrete generally used in the construction of substandard RC structures. However, the external provider could not produce such low concrete strength although the trial mixes he produced indicated it is achievable.

The designation of the specimens in this series is similar to Phase I. For Example:

- LC10-D12-Ctrl: Long splice $25d_b$ – Concrete cover 10*mm* – Bar diameter 12*mm* – Control unconfined Specimen.

3.2.3.3 Specimen preparation

The steel reinforcement was cut and bent according to the specified lengths by a commercial steel supplier. The steel cages were assembled and constructed in the Heavy Structures Laboratory of the University of Sheffield. Before the construction of the steel cages, strain gauges were installed on the main and transverse reinforcement within the splice region. The locations of the strain gauges were marked appropriately on the main reinforcement. The logic behind the arrangement of strain gauges is explained in detail in section 3.2.3.6.1. The marked locations on the bars were ground carefully and then sanded to provide a flat surface for the strain gauges. Strain gauges were attached by means of cement glue and connected to wires through a connecting station. A high performance Araldite adhesive was used to cover the strain gauges to provide a waterproof protection and to protect the gauges from aggregate impact during casting. The strain gauges used were foil type electrical resistance gauges of two specific sizes; 10 × 3 *mm* and 5 × 2 *mm*. The bigger size was used on the 12 and 16*mm* diameter bars and on the metal strips, whereas the smaller ones were used on the 8*mm* steel stirrups within the splice zone.

For the construction of the reinforcement cages, plastic ties were used to hold the bars and shear links in their positions. Figure 3-12 shows the reinforcement configuration within the splice region for a steel confined specimen and bare specimen. In addition, completed cages are shown in Figure 3-13.

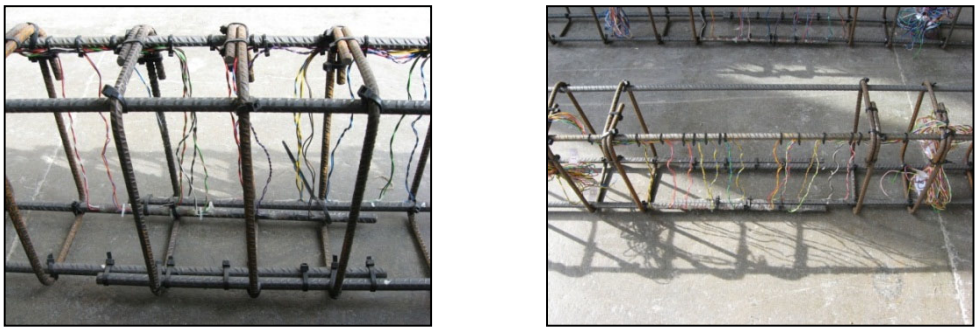

(a) (b)

Figure 3-12: Reinforcement detailing in the splice zone for a) steel confined specimen, b) unconfined specimen

Figure 3-13: Completed reinforcement cages

After they were built, the cages were placed in the steel moulds. The same procedure and preparations as in Phase I (see section 3.2.2.3.2) were considered and followed. Plastic spacers were used to provide the appropriate concrete cover. Figure 3-14 shows the reinforcement cages positioned in the mould just before casting.

Figure 3-14: Beams ready for casting

Each group of six specimens was cast with a different batch due to the limitation of moulds. Therefore, three batches were used to complete all specimens. The given mix proportions were 10 *mm* maximum aggregate size, cement type CIIIA with an average slump of 50*mm* and a water cement ratio of 0.8. The same procedure and considerations for casting were taken as

explained in section 3.2.2.3.3. The curing of the beams was stopped after the first week and the specimens were de-moulded and stored under standard laboratory conditions (about 20˚C and 80% humidity) until the day of testing. For each batch, six standard (150 *mm* diameter and 300 *mm* height) cylinders were cast to determine the concrete compressive strength at the age of testing. In addition, six (100 *mm* diameters and 200 *mm* height) cylinders along with three (100x100*mm* cross-section and 300*mm* length) concrete prisms were cast to determine the concrete tensile strength at the age of testing. Figure 3-15 shows the beams during curing.

Figure 3-15: Curing of beam specimens

3.2.3.4 Material Properties

3.2.3.4.1 Concrete

The actual concrete compressive strengths at the age of testing, determined using standard (150 × 300 *mm*) cylinders according to BS EN 12390-3 (2009), were 28.6 MP a (SD = 0.97 MPa), 24.9 MPa (SD = 0.95 MPa) and 26.5 MPa (SD = 1.03 MPa) for group I, II and III, respectively. The tensile strength of the concrete was determined from splitting tests performed on three (100 × 200 *mm*) cylinders and the flexural testing of three prisms (100 × 100 × 500 *mm*) according to BS EN 12390-6 (2000) and BS EN 12390-5 (2000), respectively. Accordingly, the concrete tensile strengths were found to be 2.45 MPa (SD = 0.22 MPa), 2.2 MPa (SD = 0.12 MPa) and 2.21 MPa (SD = 0.41 MPa) for group I, II and III, respectively. The full results of compressive and tensile strength are reported in Appendix D.

3.2.3.4.2 Steel

The mechanical properties of the reinforced bars were determined in direct tension. Strain gauges were attached to the bar surface to monitor strains during the test. Table 3-4 shows details of the mechanical properties of both main and transverse reinforcement.

Table 3-4: Mechanical properties of reinforcing bars

Bar diameter mm	**Yield stress f_y MPa**	**Ultimate stress f_u MPa**	**Yield strain** ε_y	**Strain hardening strain** ε_{sh}	**Ultimate strain** ε_u
	Main reinforcement E_s=210 GPa (d_b=12mm) and 240 GPa (d_b=16mm)				
d_b= 12 *mm*	530	677	0.0025	0.020	0.10
d_b= 16 *mm*	555	690	0.0023	0.020	0.10
	Top reinforcement E_s=210 GPa				
d_b= 10 *mm*	533	688	0.0025	0.030	0.10
	Shear reinforcement E_s=230 GPa				
d_b= 8 *mm*	630	760	0.0027	0.030	0.12

3.2.3.4.3 Metal Strips

The clips, tensioning and sealing machines, notching of clips and calibration methods used in Phase I were utilised in this phase as well. However, High ductile strips were used with yield and ultimate strength of 930 and 1030 MPa, respectively. The modulus of elasticity of the material was 202 GPa.

3.2.3.5 Experimental set-up and preparations before testing

A week before the testing, the corners of the beam cross-section at splice region were rounded using a small electrical concrete grinder. Afterwards, the beam surfaces were cleaned by an air compressor to eliminate debris and fine particles due to the grinding.

The day before the testing, the sides of the beam were white-washed and a 100*mm* × 100*mm* grid was drawn over the whole surface. The reason for this preparation was to facilitate locating and following the growth of cracks from photos after testing.

The test beam was positioned in a rigid steel frame system as seen in Figure 3-16. Figure 3-17 shows a typical beam in the test rig. In the frame, the beam was simply supported over a clear span of 2.3*m* through two steel rollers. The left support allowed both rotation and horizontal movements while the right one only allowed rotation.

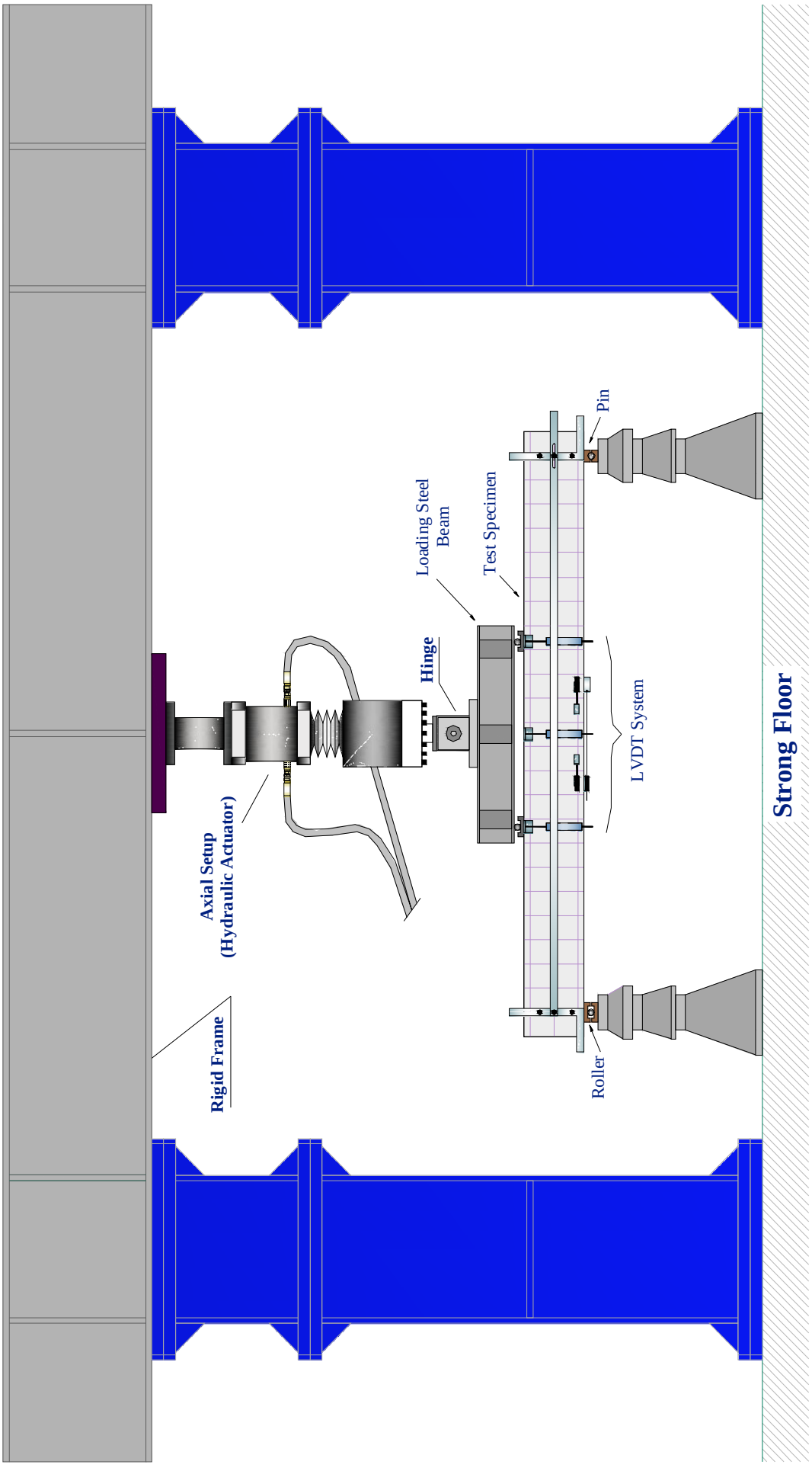

Figure 3-16: test rig of the medium scale beams

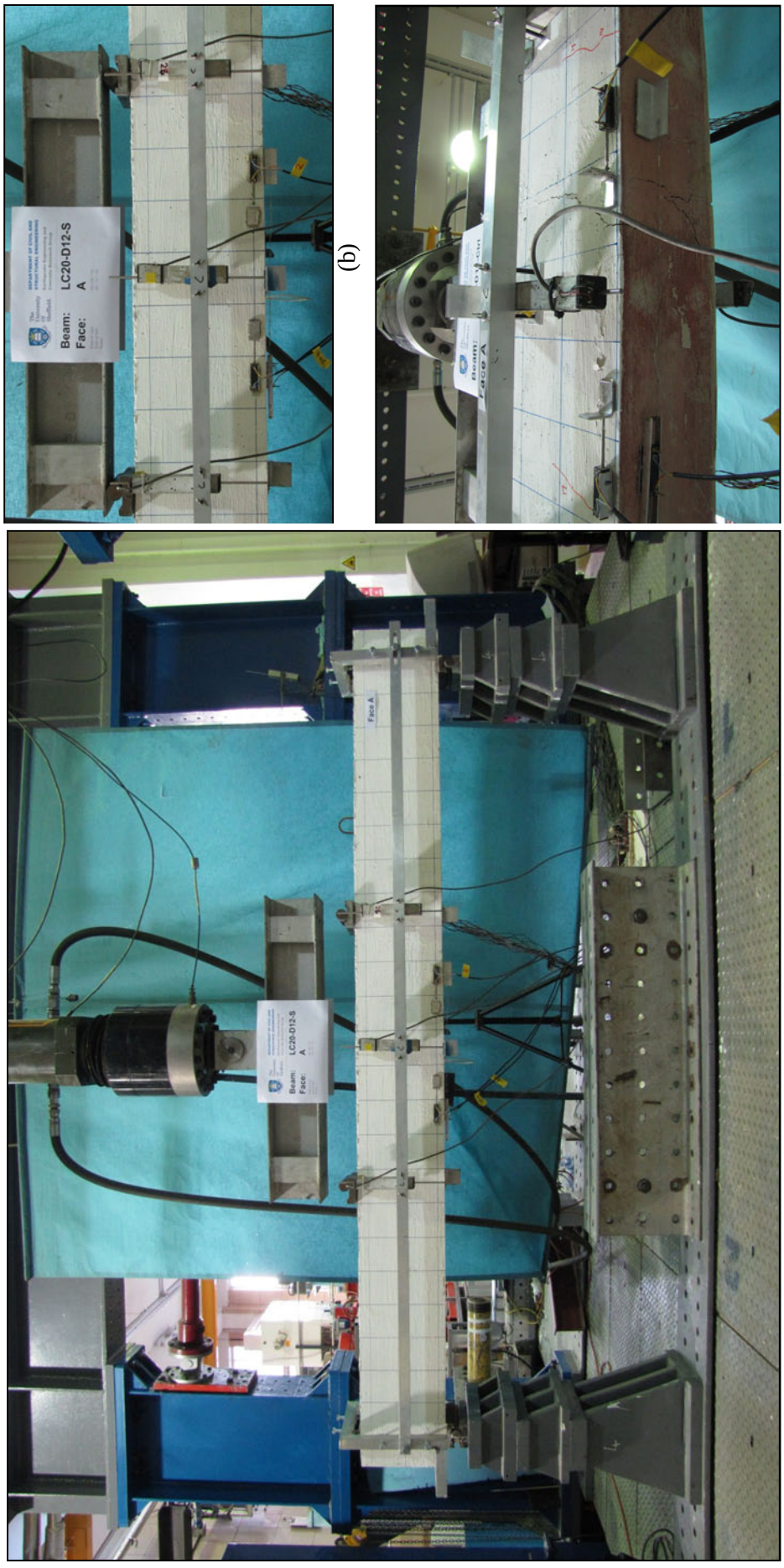

Figure 3-17: (a) Test specimen in the test rig with instrumentation installed b) & c) side and isometric view of the setup at the splice zone

The load was applied through a 500 kN servo-controlled hydraulic actuator. The actuator could be controlled either in load or displacement mode. The latter method was selected for this test series. The maximum stroke of the actuator was 150*mm*, which was more than adequate for the deflections expected in the beams. The actuator was controlled by an Electronic Control Unit connected to a data acquisition system (ORION) connected in turn to a PC. The applied load was transferred to the test specimen through a rigid steel beam reacting against the specimen over a distance of 766*mm*. This distance ensured a constant moment along the splice zone.

Before each test, the wires of the installed strain gauges were connected to the data acquisition system through a connection station. In addition, a special LVDT system was installed on the specimen body to measure the deflection of the beam and slip of the splices as illustrated in detail in section 3.2.3.6.2.

3.2.3.6 Instrumentation

3.2.3.6.1 Strain gauge arrangement on reinforcing bars and shear links

The use of strain gauges on the surface of reinforcing bars and transverse reinforcement within the splice region is essential since it enables monitoring the strains developed on the splices during the test and therefore the calculation of bond stresses. Moreover, the variation in the confining stress provided by the transverse reinforcement and its contribution to the bond splitting strength can be quantified.

The distribution of strain gauges along the splices was based on the expected strain trend along the splice length. In this phase, the splice length was designed to induce splitting cracks simultaneously with reaching yielding in the bars. Accordingly, the splice length was divided into two segments as shown in Figure 3-18. In the first segment L_y, extending from the bar free-end to the location of yield strain, the strain profile is expected to be approximately linear. On the other hand, in the second segment L_u, extending from the yield point up to the splice face, the bar is expected to experience yielding and strain hardening. Based on calculations using bond strengths from phase I and considering the new splice length L_d, this segment is estimated at 0.25 L_d. Thus, six strain gauges, distributed as illustrated in Figure 3-18, were found to be sufficient to capture the expected strain profile. The selected number and specific distribution took into consideration the possibility of strain gauges malfunctioning during casting, yet the number was minimised so that it did not disturb the bonded area. Despite the best efforts to minimise this effect, some reduction in the bonded area is expected due to the installation of strain gauges. This reduction, however, is found to be less than 2.3% of the total bonded area, and thus, it is neglected during calculations of bond stresses.

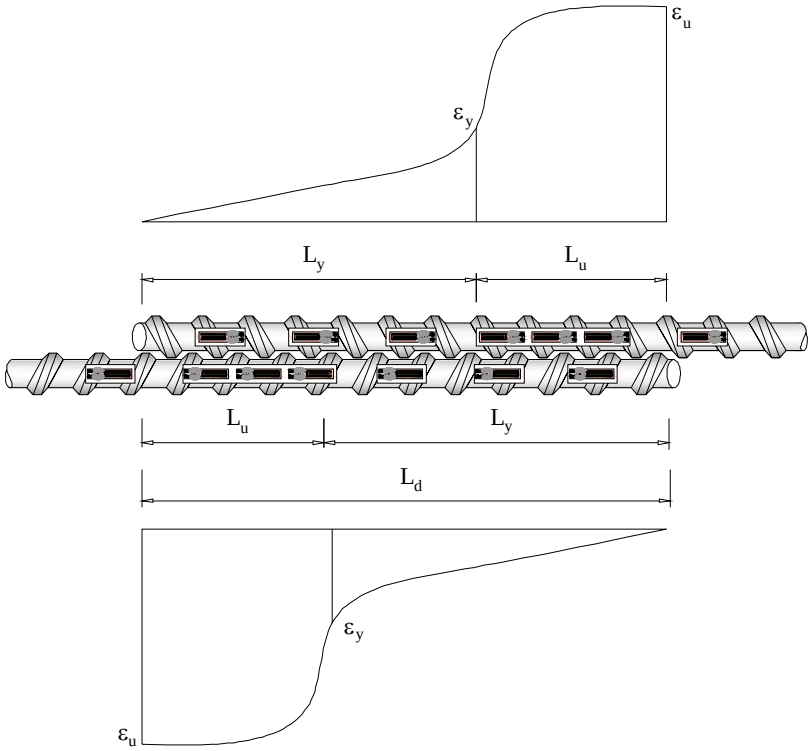

Figure 3-18: Arrangement of strain gauges along the splice bar

3.2.3.6.2 Arrangement of LVDTs on the beam

Four 100*mm* LVDTs were used in each beam test to measure the deflections at specific locations as schematically shown in Figure 3-19. The locations include the loading and mid-span points. In this phase, a yoke support system is constructed to be fitted on the beam body. The system enables elimination of support deflections as well as any torsion that may disturb the readings. In this system, the LVDTs are mounted on a metal bar that is supported by two metal frames fixed at supports. The bar is only able to rotate at both ends and slide at one end.

Two additional 20*mm* LVDTs were placed at the splice interfaces over a length of 50*mm* for slip measurement, as shown in Figure 3-19(a). The LVDTs were positioned at the level of the spliced bars on the side of the beam. In addition, a 20*mm* LVDT was placed at the bottom of the beam over a length of (L_d + 50*mm*) to measure the crack openings along the entire splice, as shown in Figure 3-19(b).

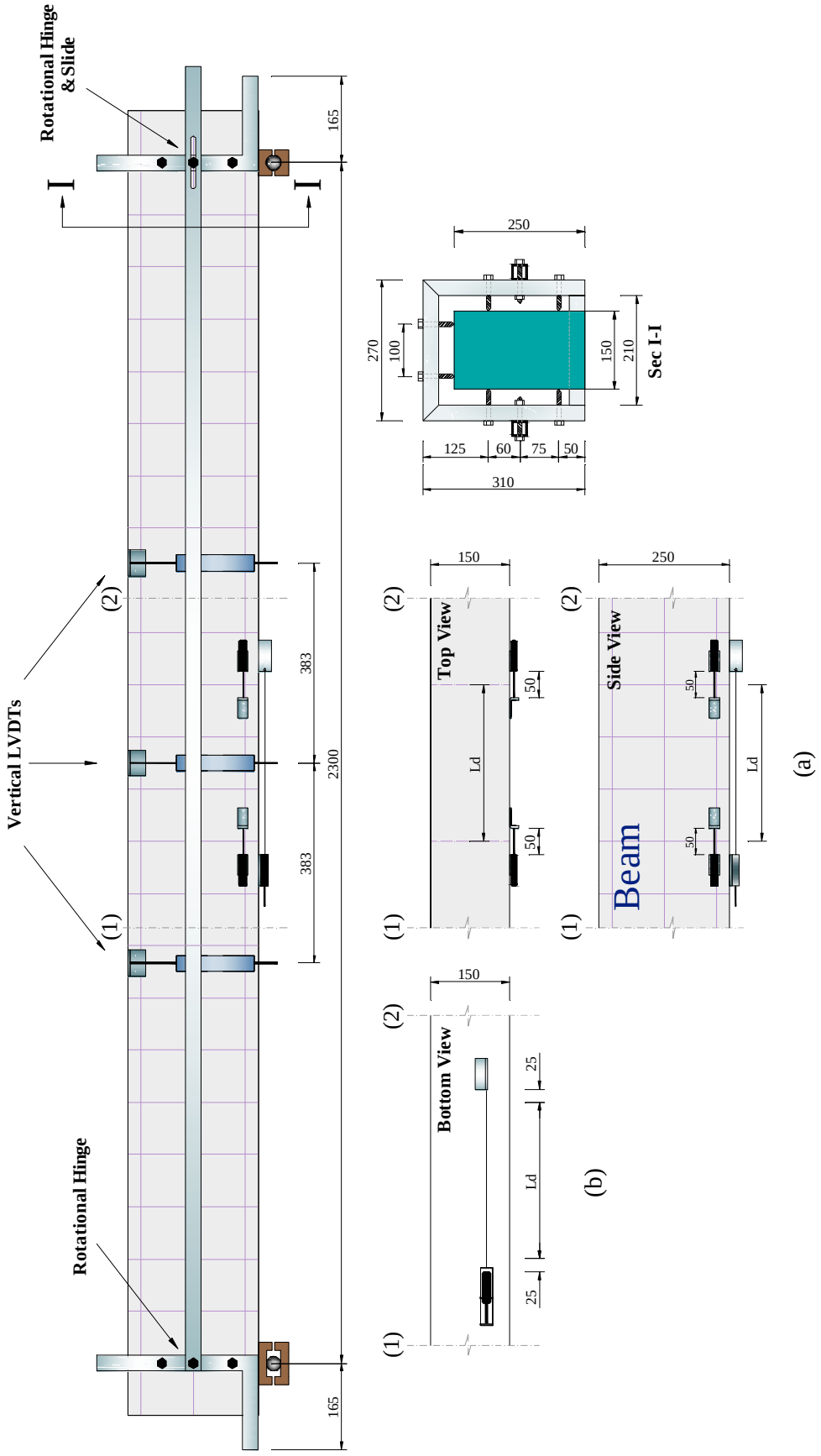

Figure 3-19: LVDT system installed on the test specimen

3.2.3.7 Testing procedure

The loading regime followed in the testing comprised two phases. In the first phase, one cycle was applied at approximately 50% (~20 kN) of the estimated maximum load resistance of the bare specimen to check the test setup and to ensure that all data acquisition channels were functioning properly. The specimen subsequently was loaded until the maximum load resistance was reached. In the second phase, the beam was subjected to three complete unidirectional cycles according to the loading scheme and associated deflection ratios DR% illustrated in Figure 3-20. The selection of DR% at the beginning of the second loading phase was dependant on the behaviour of the test specimen at the maximum load of the first phase. The cycles were imposed at constant increments of DR of 0.35%. The loading, unloading and reloading were performed at a rate of 0.1*mm*/min that resulted, on average, in a test period of four hours for each specimen.

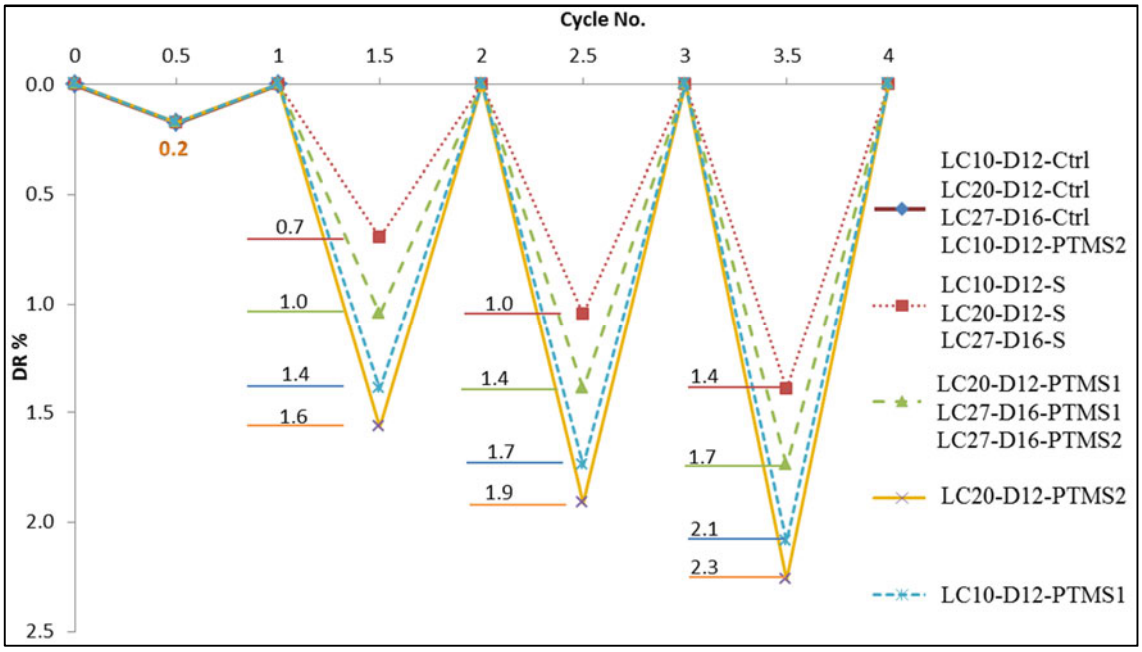

Figure 3-20: Loading history of the medium scale beams

During the test, the developed cracks on the side faces were marked. Photographs were also taken during each loading stage.

After the completion of each test, a closer examination of the mode of failure was conducted. The PTMS confined specimens were stripped out of the metal strips and the failure cracking patterns were observed and further photos of the damaged zone were taken.

3.3 PHASE III: TESTS ON DEFICIENT FULL-SCALE RC BEAM-COLUMN CONNECTIONS

The aim of this test phase was first to provide an understanding of the behaviour of deficient beam-column connections and then to develop effective selective rehabilitation schemes using PTMS. Exterior joints were selected as they are more vulnerable to damage and failure. Four full scale RC exterior beam-column connections were constructed to represent existing concrete joints with shear strength and bar anchorage deficiencies. The connections were tested under reversed quasi-static cyclic loading. Different design methodologies for the rehabilitation schemes will be proposed. The goal of the rehabilitation is to upgrade the shear strength of these joints such that the brittle failure mode can be delayed or eliminated.

It should be mentioned that the test units are a part of three research projects in which 7 units were constructed to be tested as control specimens and then rehabilitated using PTMS and/or CFRP. Each two units were designed as a pair similar in reinforcement detailing in the core and different in the axial load level applied to the column. The pairs differed in terms of reinforcement detailing in the core. The first unit, however, was designed as a reference specimen for preliminary testing and was strengthened using PTMS then by CFRP. The other units tested for this study represented a specimen of each pair.

The subsequent sections describe the design, construction, casting and strengthening of the test units, as well as the setup of the test rig along with installation of instrumentation including strain gauges, LVDTs and displacement transducers.

3.3.1 Specimen description and design

A typical exterior beam-column joint isolated from the Saclay building (Chaudat et al., 2005), which replicates a reinforced concrete structure built according to old practice, was chosen as the model for this phase of study, as shown in Figure 3-21.

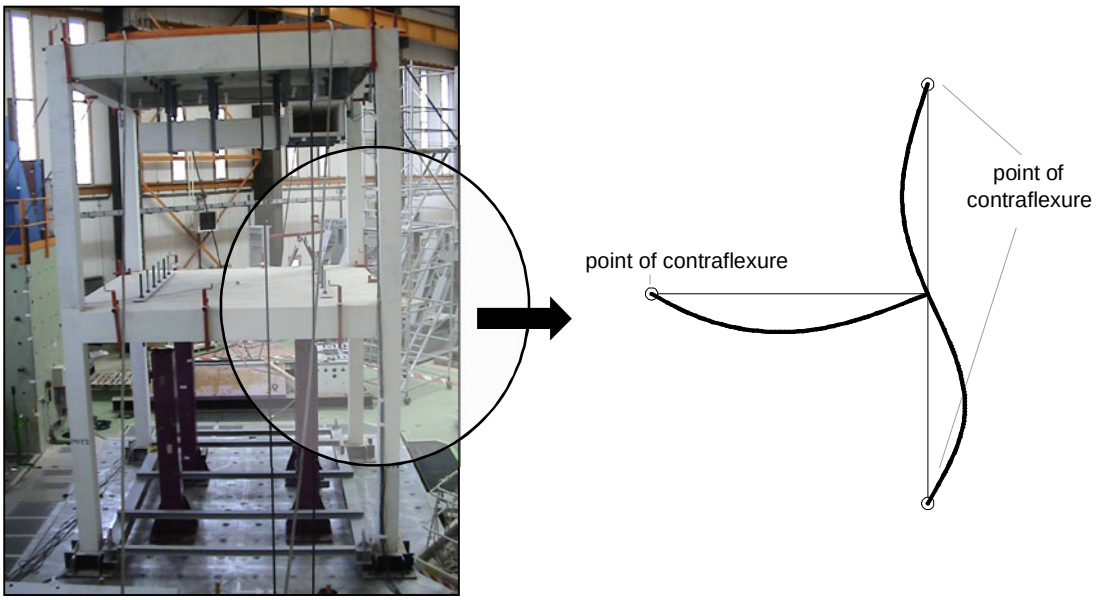

Figure 3-21: Full scale RC frame tested in Saclay, France (Chaudat et al., 2005)

The four test units, designated as JA-1, JA-3, JB-1 and JC-1, are full scale models of the joints with dimensions and lengths as illustrated in Figure 3-22. The column's height is 2700*mm* with cross-section dimensions of 260×260*mm*. The beam's length is 1650*mm* from the face of the column to the free end, with a cross-section of 260×400*mm*.

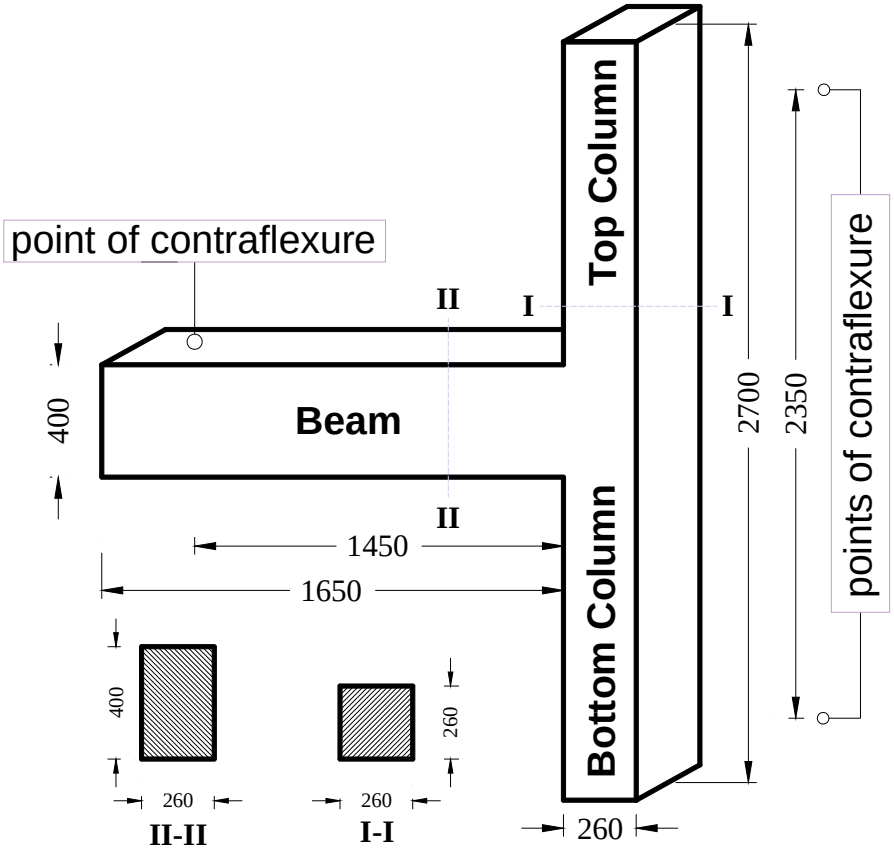

Figure 3-22: Specimen geometry and dimensions

Both the beam and columns have symmetrical compression and tension reinforcement of 16*mm* diameter bars. The bottom column is reinforced with (3H16*mm*) bars as a top and bottom reinforcement along with 2H16*mm* in the middle with the exception of joint JA-1; whereas the top column is reinforced with (2H16*mm*) in compression and in tension. The bottom column and top column reinforcement are spliced with a length of $25d_b$, where d_b is the bar diameter. The beam is reinforced with 4 bars of 16*mm* diameter as top and bottom longitudinal bars. Figure 3-23 shows typical reinforcement and detailing of a test unit. The beam longitudinal reinforcement is anchored in the joint area with lengths and shapes as illustrated in Figure 3-24. The transverse reinforcement of the beam and columns consists of single closed ties of 8*mm* diameter. The ties start at around 60*mm* from the interfaces and spaced at 150*mm* ending with spacing of 50*mm* at supports. Following the old practice found in non-seismic RC buildings, no transverse reinforcement is provided in the beam-column core.

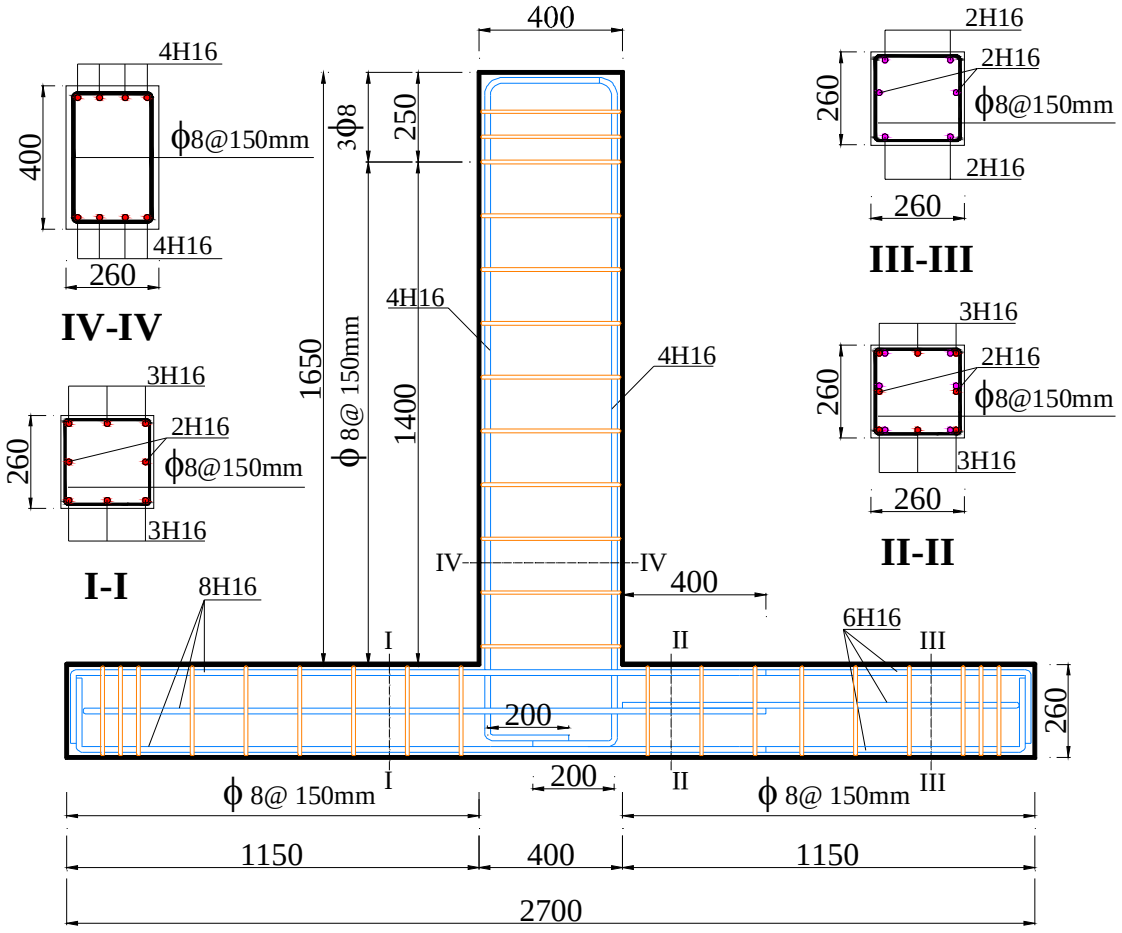

Figure 3-23: Reinforcement detailing of the test unit JC-1

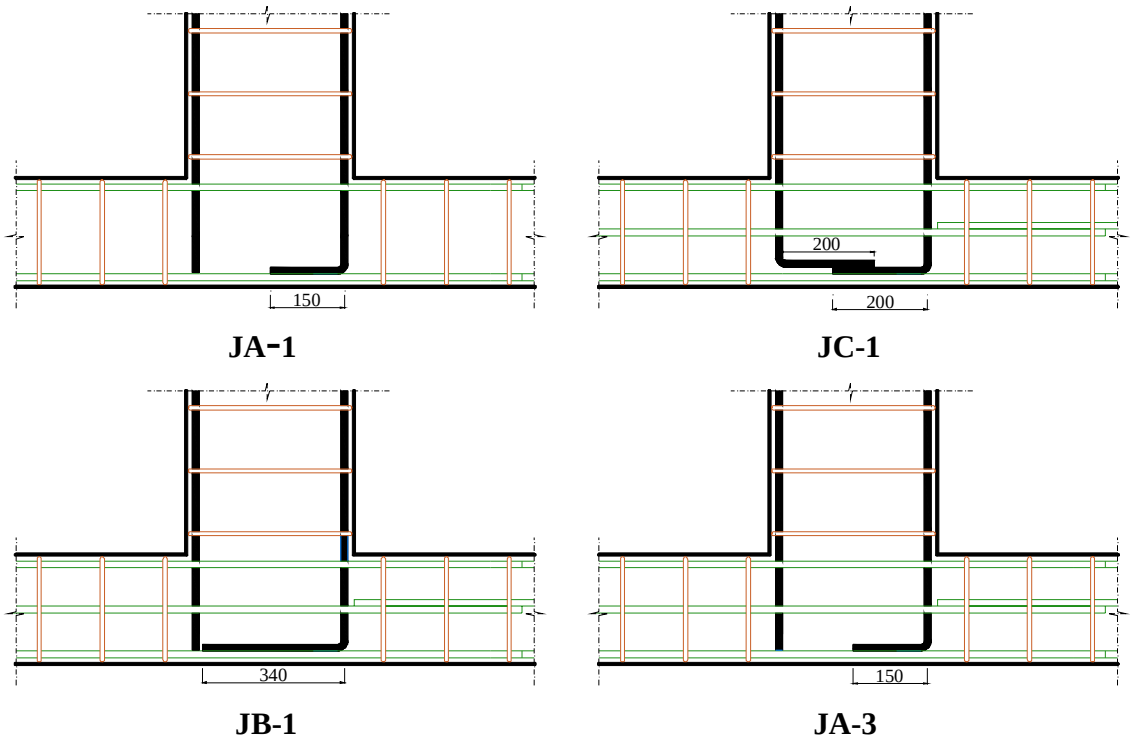

Figure 3-24: Anchoring details of beam longitudinal reinforcement in the joint area

The theoretical beam flexural capacity is estimated to be 144kN.m, whereas the column flexural capacity is estimated to be 72kN.m under an axial load of 150kN. This design, together with the absence of shear reinforcement in the joint area, should ensure that the beam-column assemblage will fail due to shear in the joint area before the moment-resisting capacity of the columns or beam is reached.

3.3.2 Construction of specimens

All four beam-column specimens tested for this study have identical dimensions, but different reinforcement detailing. The reinforcing bars were cut and bent according to the specified lengths by an external provider. The steel cages were assembled and constructed in the Heavy Structures laboratory of the University of Sheffield. Before the construction of the steel cages, a total of 35 strain gauges were installed on the main and transverse reinforcement as discussed in Sec 3.3.4. Plastic ties were used to assemble the cages.

Three wooden formworks were manufactured and assembled in the laboratory. The reinforcement cages were tied inside the formwork and positioned in place using plastic spacers. Clamps were used to maintain the design dimensions of columns and beams during casting. The inner side of the mould was oiled to facilitate de-moulding. Moreover, a bolt of 10*mm* diameter and 150*mm* length was provided at the top of the beam to provide a lateral movement restraint to the joint during testing. The moulds were sealed by means of waterproof silicon to prevent leakage. Figure 3-25 shows the cages tied in the moulds and ready for casting. Also Figure 3-26

(a) shows the bolt fixed at the tip of the beam, and Figure 3-26(b) shows the spacers used to maintain the required cover concrete. The specimens were cast in the horizontal position.

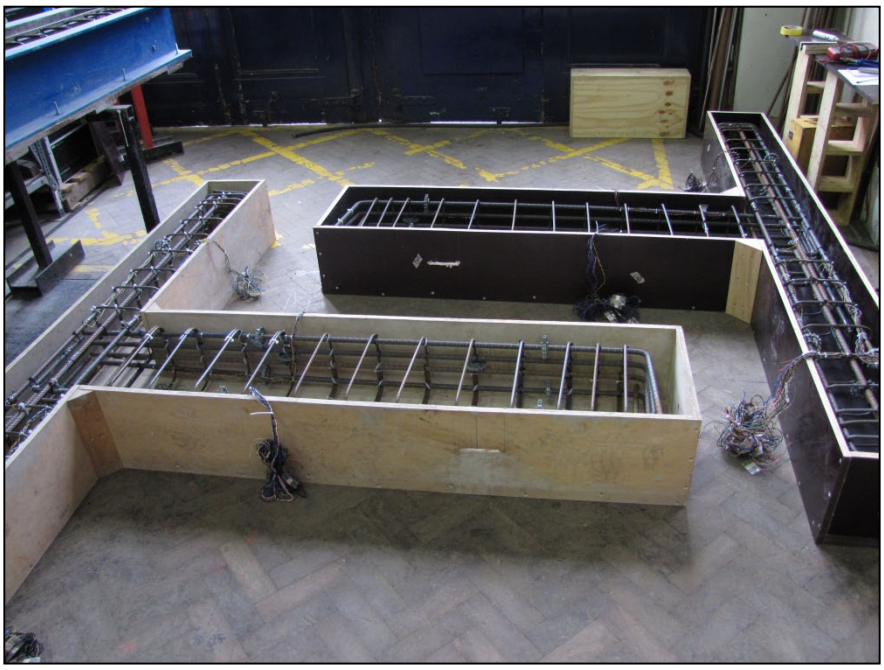

Figure 3-25: The cages positioned and tied in the formwork

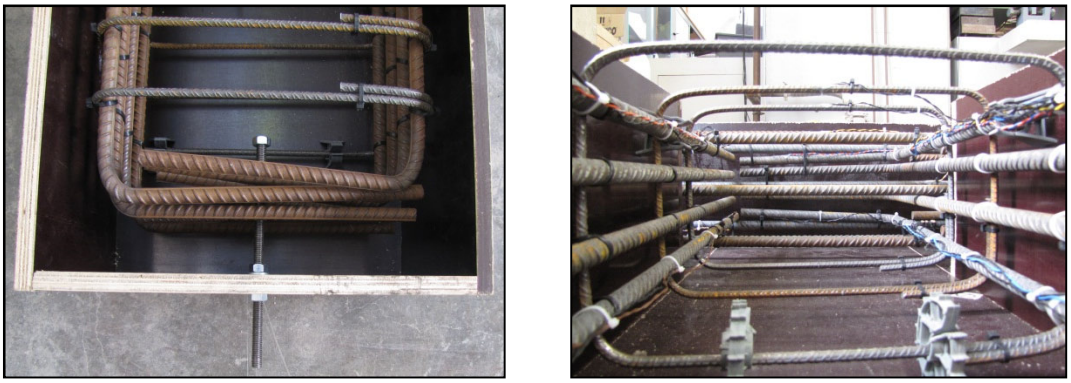

(a) (b)

Figure 3-26: a) bolt at the beam tip, b) the use of spacers to maintain the cover thickness

The test units were cast in three batches with a target concrete compressive strength of 15-20 MPa. The maximum aggregate size was 10*mm* and target slump between 70-100*mm*. The water/cement ratio was 0.8 to obtain poor quality concrete. The concrete was cast in two layers of approximately the same thickness and vibrated slightly using a large electrical poker vibrator. After casting, levelling was imposed on the top surface of specimens to remove irregularities in geometries, as shown in Figure 3-27. Standard (150 *mm* diameter and 300 *mm* height) cylinders were cast to determine the concrete compressive strength at the age of testing. In addition, standard (100 *mm* diameters and 200 *mm* height) cylinders along with (100x100*mm* cross-

section and 300*mm* length) concrete prisms were cast to determine the concrete tensile strength at the age of testing.

Figure 3-27: Casting and levelling of the specimen

After casting, the specimens were covered with plastic sheets and cured for one week before removing the formwork. The specimens were then stored under standard laboratory conditions until testing. Figure 3-28 shows a specimen after casting and during curing.

Figure 3-28: Curing of the cast specimen

3.3.3 Material properties

3.3.3.1 Concrete

The concrete was ordered with a target compressive strength of 15-20 MPa. However, the total amount of concrete ordered was just over $1m^3$ and for that reason it was difficult for the ready mix company to achieve the specified strength required. Three standard ($100\times100\times100mm^3$) cubes were tested after 7days which indicated that the target strength was exceeded. The

concrete compressive and tensile strengths at the age of testing were determined by testing nine (150*mm*×300*mm*) cylinders under compression along with six (100*mm*×200*mm*) cylinders under indirect tension and three (100×100×500) prisms in flexure. Table 3-5 presents the average concrete strengths from the tests. Complete results obtained from the tests on the cylinders and prisms are presented in Appendix D.

Table 3-5: Average concrete compressive and tensile strength of specimens

Specimen	f'_c **MPa**	f_t **(cylinders) MPa**
JA-1	22.5	2.63
JA-3	31.4	2.40
JB-1	28.6	2.45
JC-1	28.6	2.45

3.3.3.2 Reinforcement

The main longitudinal and transversal reinforcement consisted of 16*mm* and 8*mm* diameter deformed bars, respectively. The mechanical properties of these bars were similar to those used in Phase II

3.3.4 Instrumentation and measurement of loads, strains and displacements

3.3.4.1 Strain Gauges

A total of 35 strain gages were attached to the longitudinal and transversal reinforcement of each test unit. The same procedure, considerations and precautions stated in Sec 3.2.3.3 were followed. The locations of strain gauges were selected to be at the hinging zone, splices, anchorages, and shear links. The strain gauge wires were gathered into bundles and exited out of the formwork in four places. Figure 3-29 illustrates the strain gauge location and numbering followed for specimen JC-1. Figure 3-30 shows specimen JC-1 in the wooden formwork after the installation and protection of strain gauges.

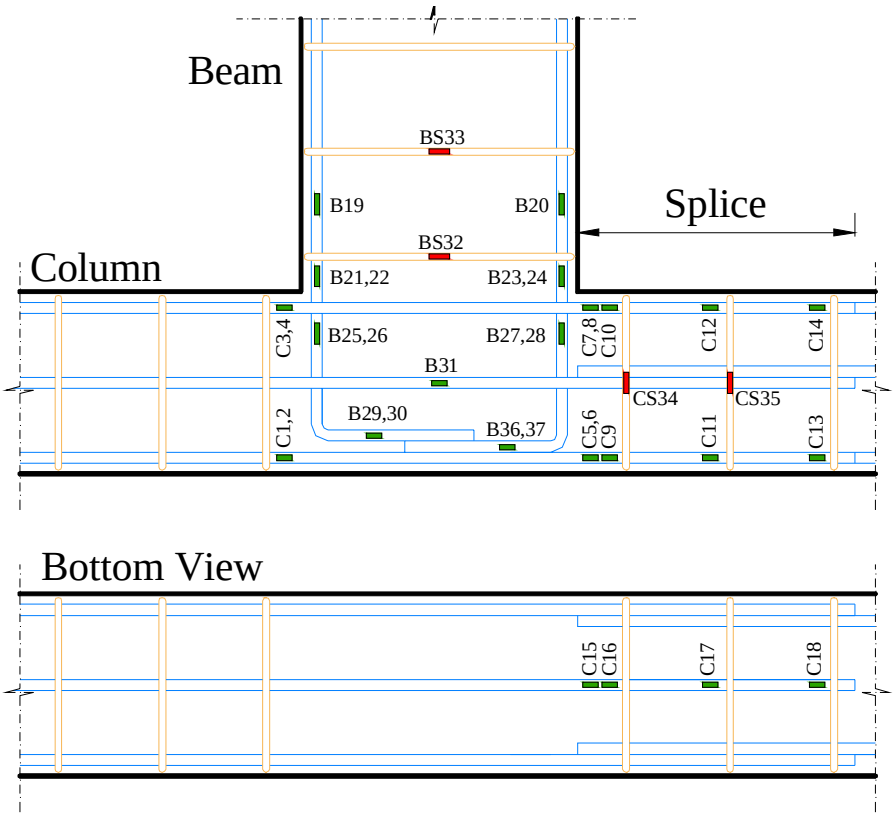

Figure 3-29: Strain gauge distribution on the longitudinal and transverse bars of the test unit JC-1

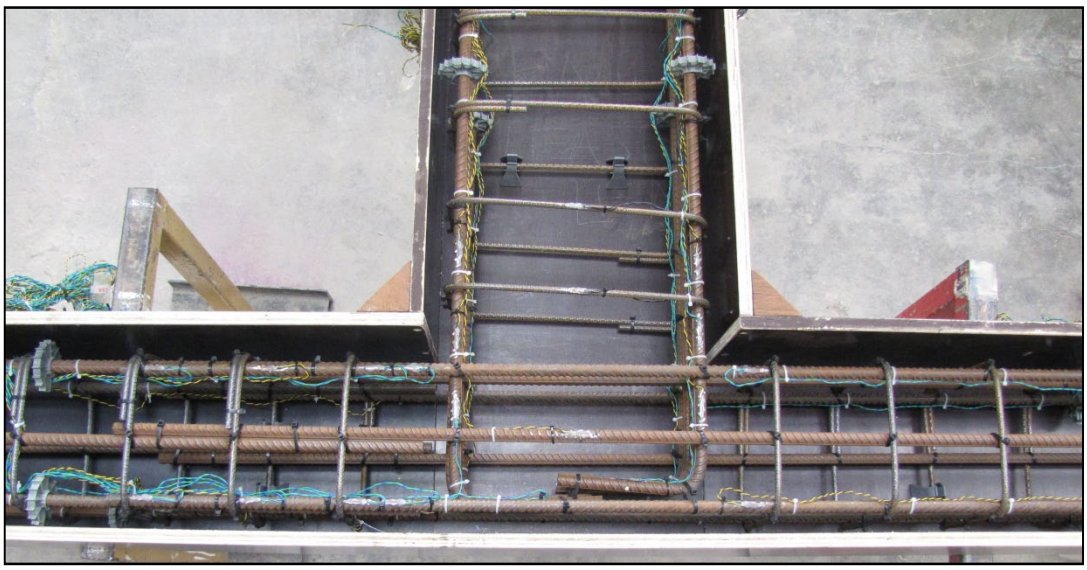

Figure 3-30: The specimen JC-1 with strain gauges installed on bar surfaces

3.3.4.2 Potentiometers

A configuration of sixteen potentiometers was mounted on the joint area, lap splice region and the beam hinging zone, as illustrated in Figure 3-31. The positioning enables capturing the expected deformations due to slip at the beam-column interfaces along with capturing core movement. 30 *mm* potentiometers were used for the configuration, which were connected

through wires to hinges made of metal rods fixed to the concrete. Figure 3-32 shows the test unit with the potentiometer configuration mounted on the front side.

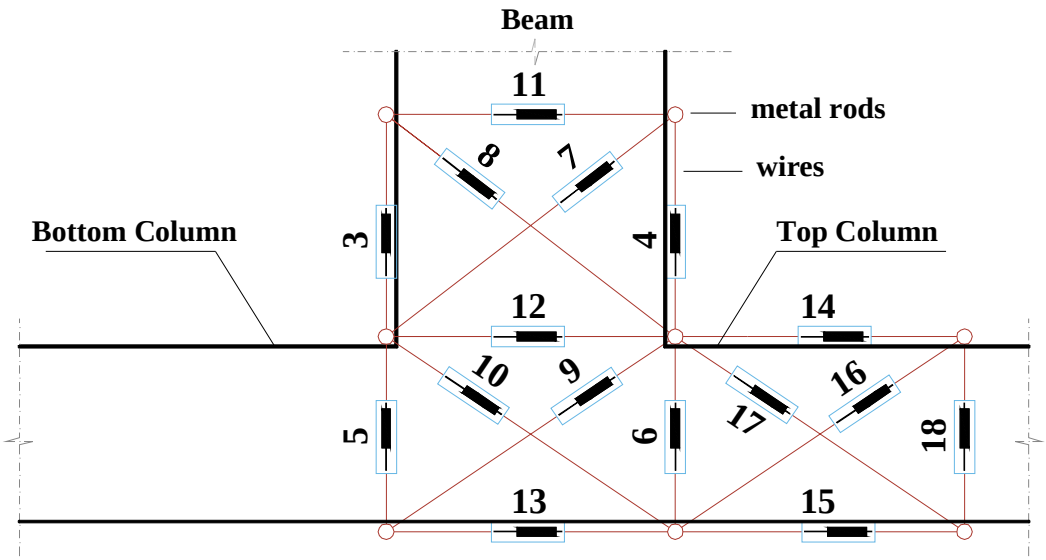

Figure 3-31: LVDT configuration

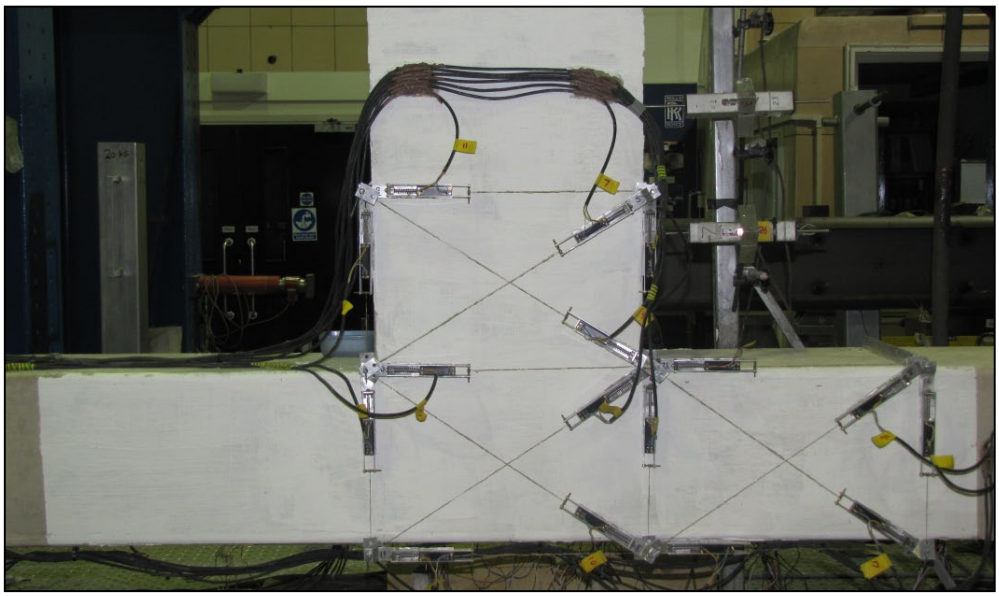

Figure 3-32: A test unit with the LVDT configuration installed

3.3.4.3 Displacement Transducers

A total of ten 100*mm* Linear Variable Differential Transducers (LVDTs) were attached to the specimen to measure deflection at the tip of the beam, support movements, curvature along the beam, rotation of the joint and reaction frame movement. Figure 3-33 shows a schematic view of the test specimen with the location of the displacement transducers.

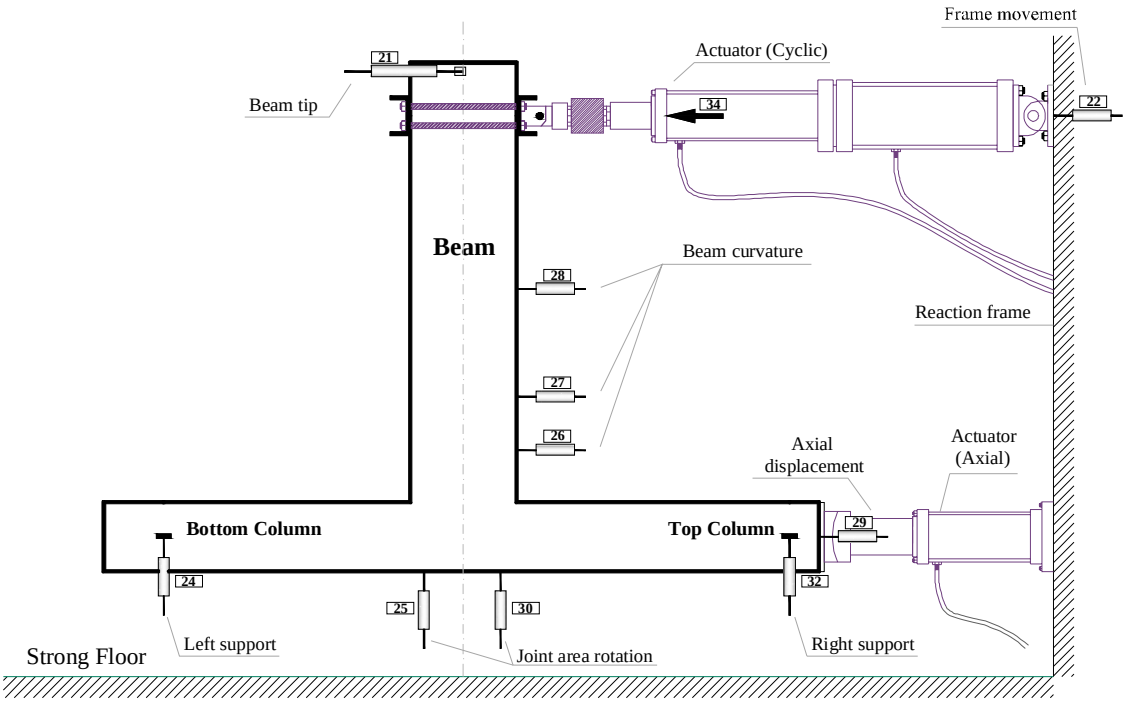

Figure 3-33: Schematic view of the test specimen with instrumentation installed

3.3.5 Loading apparatus

Figure 3-34 shows a schematic view of the test unit inside the reaction frame and with the loading apparatus mounted. As seen from the Figure, the test specimens are loaded in the horizontal position and the column is mounted horizontally with pinned supports at both ends. The loading is applied by means of two hydraulic actuators that allow the application of axial and reversed quasi-static cyclic loading. An actuator of 250 kN capacity is fixed to the steel frame and reacting against the end of the column to apply the axial load. The axial load transferred to the column is reacted by a roller mounted on the steel frame at the other end. The cyclic load is applied at the end of the beam through a two-hinged actuator of 150 kN capacity and 300*mm* stroke. The actuator is mounted horizontally and reacts against a steel frame from one end and applies the load through a steel collar, fixed at the beam tip, at the other end. The actuator is connected to the steel collar through a load cell to measure the load applied to the beam. The reaction of the actuator against the very rigid frame system is required in this case so as to avoid any additional deformations. The two hinges coupled at the actuator ends permit rotations and avoid bending of the actuator. To prevent any out-of-plane movement of the joint, a lateral movement holder is mounted on the top of the reaction frame and a steel rod was embedded into the top of the joint. Both actuators are connected to a data acquisition system through loading control unit that allowed manual operation during the test. Figure 3-35 shows a view of a test unit with the loading actuators mounted at the beginning of testing.

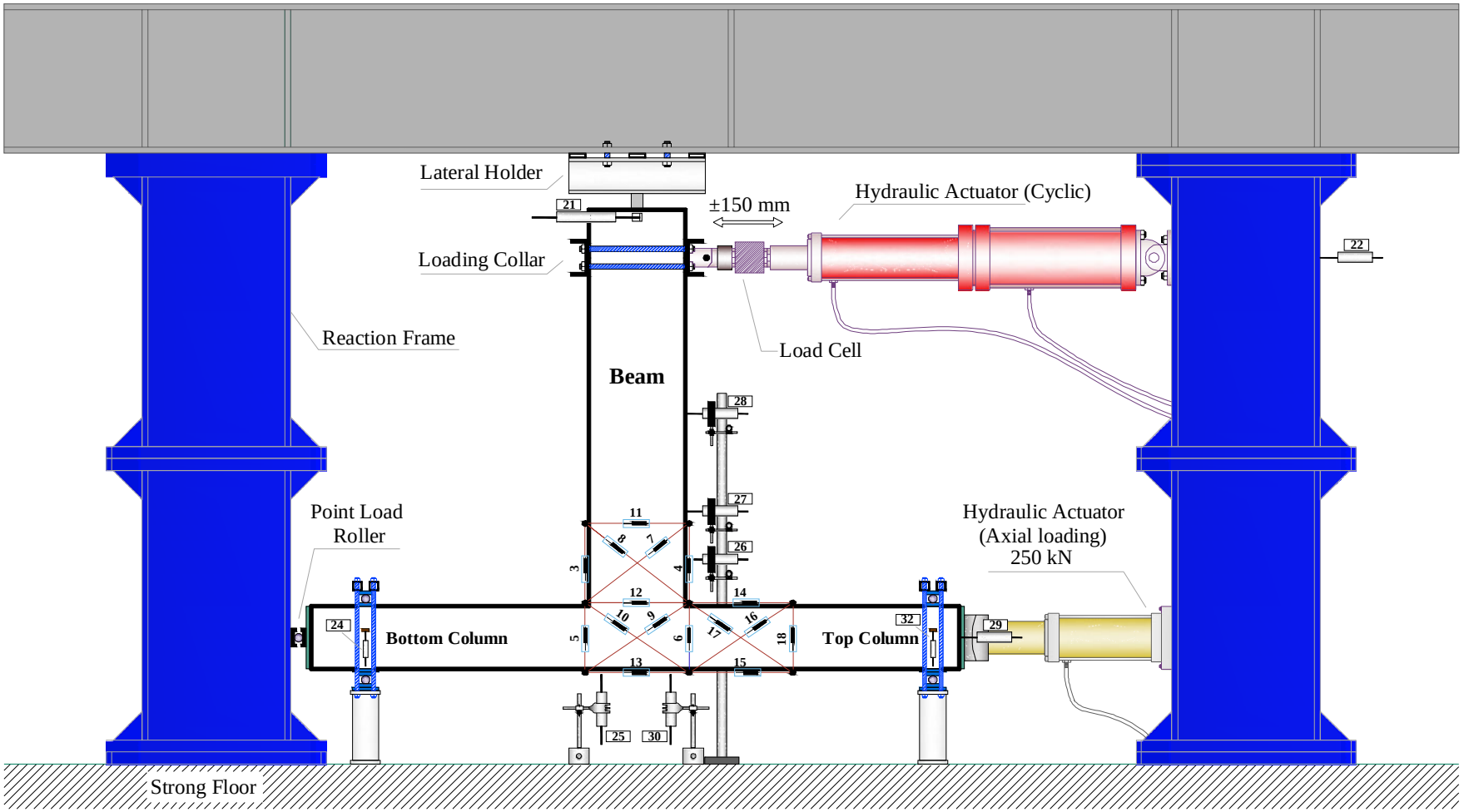

Figure 3-34: Schematic view of a test unit in the test rig

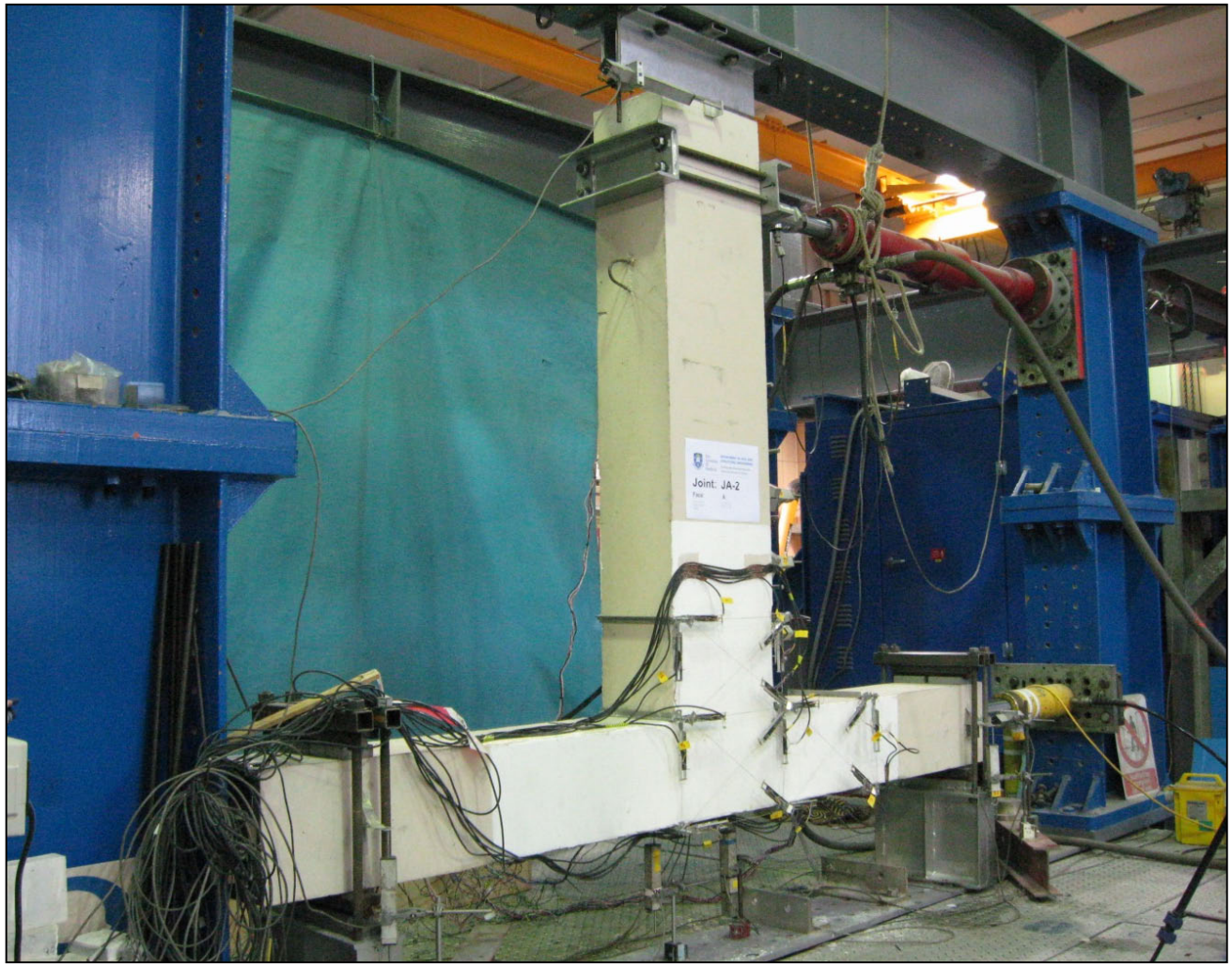

Figure 3-35: Test unit in the test rig and instrumentation installed and loading apparatus mounted

3.3.6 Test procedure

Before the test, the joint area was white-washed to facilitate marking the growth of cracks during testing. The potentiometers and LVDTs were connected to a data acquisition system (ORION) of 80 channel capacity. Moreover, the strain gauges were connected to the (ORION) through a connection station of 50 channel capacity. The top actuator was controlled by a loading control unit connected to the ORION. Figure 3-36 shows the ORION (on the right) and the loading control unit (on the left) used in the test.

Figure 3-36: The ORION (on the right) and loading control unit (on the left) used for the test

The test was initiated by applying an axial load through slow and balanced loading steps until reaching the appropriate level specified in Table 3-6. The amount of axial force in the column was maintained at the required level by manually adjusting the hydraulic pressure imposed by the actuator. The lateral load was applied to the system, at the top of the beam, in a quasi-static fashion through the loading collar. The loading protocol recommended by PEER (Pantelides et al, 2002) was adopted in these tests. Accordingly, the loading protocol consisted of a sequence of cycles, in displacement-control steps, with target drift reversals expressed as a function of drift ratio (DR %) according to the loading history shown in Figure 3-37. The DR% is defined as the percentage of lateral drift at the tip of the beam to the length of the beam. Therefore, in each test, loading steps with drift ratios (DR%) beginning at a 0.1% followed by steps of 0.25%, 0.50%, 0.75%, 1.0%, 1.5%, 2.0%, 3.0%, 5.0%, 7.0%, and 10.0% were applied. Each loading step was composed of three equal cycles of push and pull with a loading rate of 0.4*mm*/*min*. The actuator stroke was sufficient to cause severe damage in the strengthened joint. Typically, the loading of the strengthened joint to failure required 6-to-7 hours. The test was concluded when the drop in the resistance was less than 50% of the maximum load.

Table 3-6: Levels of axial load applied to the units

Specimen	**Axial load P (kN)**	**$P/A_g f'_c$ (%)**
JA-1/PTMS	150	9.1
JA-3/PTMS	250	11.4
JB-1/PTMS	150	7.2
JC-1/PTMS	150	8.2

A_g is the column cross-section; and f'_c is the concrete compressive strength

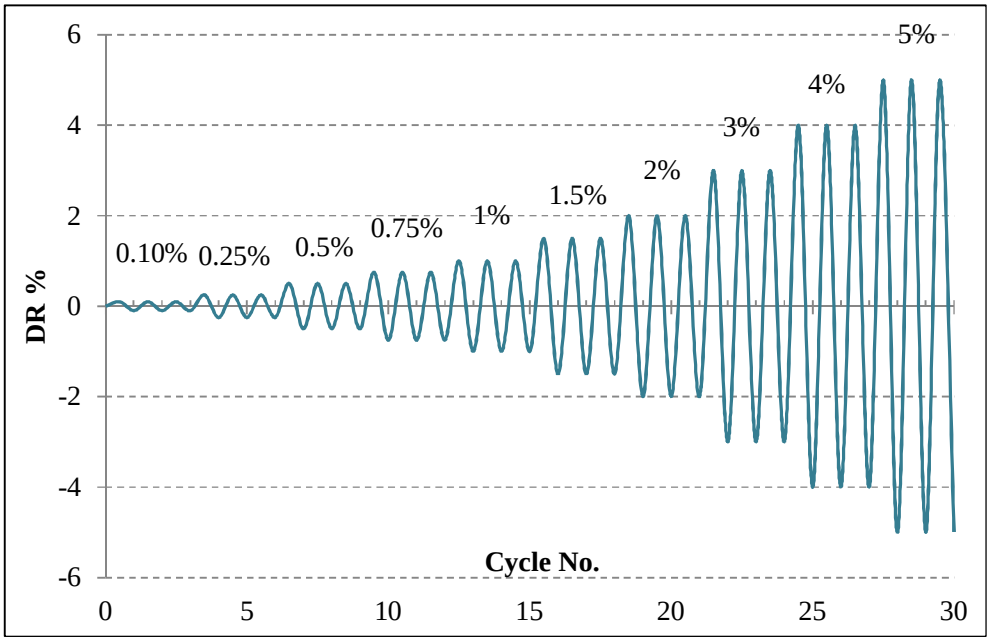

Figure 3-37: The proposed loading scheme of the test units

Chapter 4

SMALL SCALE BEAMS: TEST RESULTS, OBSERVATIONS AND DISCUSSION

4.1 GENERAL

A summary of the experimental results from fifteen beam tests is presented in this chapter. In addition to the categorisation adopted in the previous chapter, the test specimens are separated into three families depending on the type of confinement provided in the splice zone. Thus, the first family comprises the bare (unconfined) specimens; the second comprises the internally confined specimens; and the third comprises the PTMS confined specimens. The behaviour of the specimens in each family is examined in terms of damage progress, load-deflection, deformability as well as slip of reinforcement. A comparison between the behaviour of each family is also performed. A unique bond stress-slip relationship is derived for the individual test specimens, and accordingly, a basic behavioural bond-slip model is identified.

4.2 GENERAL BEHAVIOUR AND MODES OF FAILURE

As the load was applied, all specimens tended to develop flexural tensile cracks at the notch locations within the constant moment area, as shown in Figure 4-1. The average measured cracking loads were 17, 14 and 23 kN for group I, II and III, respectively.

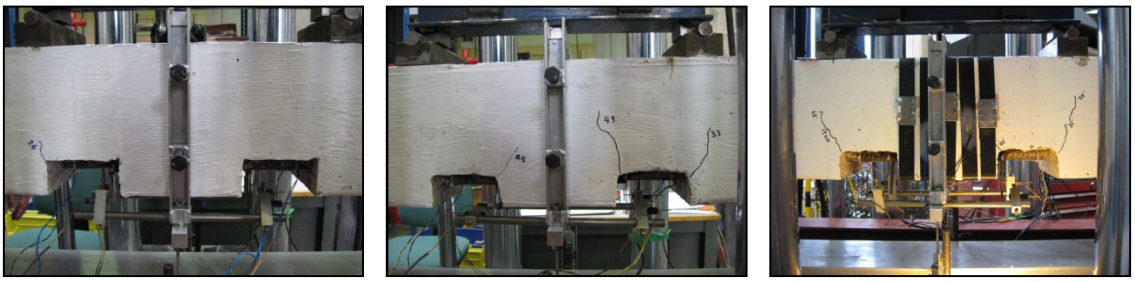

SC27-D16-Ctrl SC27-D16-S SC27-D16-PTMS1

Figure 4-1: Typical initial flexural cracking patterns in the beams

As the load was increased beyond flexural cracking, splitting cracks started to form in the splice zone. In all specimens, formation of splitting cracks was observed when the load reached (80-90%) of the maximum capacity. That was accompanied by a slight change in stiffness. The propagation of splitting cracks and the nature of crack formation varied in relation to the type of confinement and its content in the splice zone. Nevertheless, horizontal and vertical splitting cracks along splices were observed in all specimens as the maximum tensile strength was attained. All specimens failed due to loss of bond strength that resulted in a drop in the load resistance.

In the following sections, the behaviour of each family after the formation of the first splitting crack is described.

4.2.1 Control unconfined specimens

Horizontal side and bottom splitting cracks developed suddenly along the splice length accompanied by rapid loss in load resistance. Figure 4-2 shows the nature of failure in these specimens at the maximum load. Further loading beyond the initial splitting cracks resulted in widening of the splitting cracks which in turn caused spalling of the concrete cover surrounding the splice, as shown in Figure 4-3. No flexural cracking was observed within the splice zone during loading. Because the splice length was short, the specimens experienced bond failure before the attainment of yield in the bars. Hence, the test specimens behaved in an inelastic manner while the strains in the bars remained elastic throughout the test.

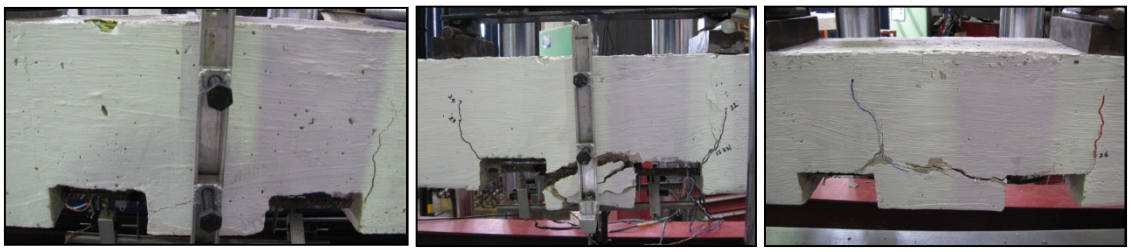

SC10-D12-Ctrl SC20-D12-Ctrl SC27-D16-Ctrl

Figure 4-2: Splitting bond failure in the bare (unconfined) specimens

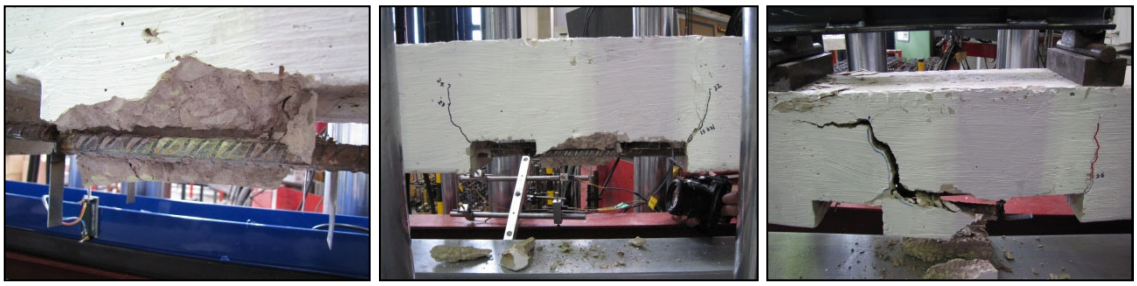

SC10-D12-Ctrl SC20-D12-Ctrl SC27-D16-Ctrl

Figure 4-3: Widening of splitting cracks and spalling-off of the concrete cover (bare specimens)

4.2.2 Internally confined specimens

The splitting cracks initiated at the splice ends and propagated vertically and horizontally along the splice resulting in a horizontal side and bottom splitting failure, as shown in Figure 4-4. Multiple splitting cracks were noticed to form at splice zones compared to the control unconfined specimens. The rate of propagation of splitting cracks was slower than that in the control specimens, but cracks spread on a larger-scale along the tension splice zone. Flexural cracks were also observed to develop at stirrup locations during the loading and interfered with the splitting cracks. That caused partial spalling-off of the concrete cover at the splice zone, as shown in Figure 4-5. After reaching the maximum splitting strength, splitting cracks along with flexural cracks started widening and steel stirrups were exposed in all specimens, as shown in Figure 4-5.

The amount of damage in the splice zone was less than that of the associated control specimens, which experienced complete loss of the concrete cover. The development of multiple cracks resulted in a more ductile bond failure compared to the sudden and brittle failure occurred in the control specimens.

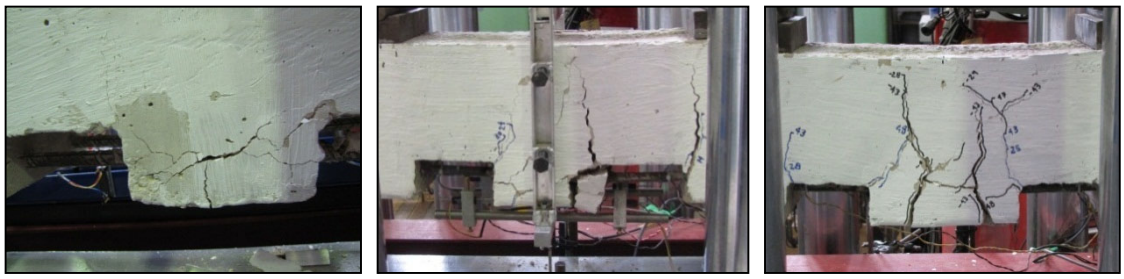

SC10-D12-S SC20-D12-S SC27-D16-S

Figure 4-4: Splitting bond failure in the steel confined specimens

SC10-D12-S SC20-D12-S SC27-D16-S

Figure 4-5: Spalling-off of concrete cover due to spitting and flexural cracking

4.2.3 PTMS confined specimens

Splitting cracks were observed to develop at the end of splices as the loading was reaching the maximum splitting strength. Visual observations of the growth of splitting cracks showed that these cracks tended to form initially in a diagonal manner towards the corners of the notch, as shown in Figure 4-6. With further increase in loading, these cracks propagated along the entire splice length, as seen in Figure 4-7.

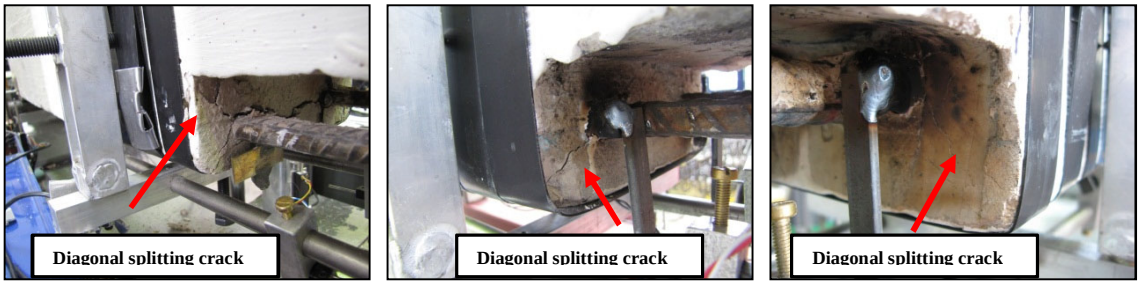

SC10-D12-PTMS1 SC20-D12-PTMS2 SC27-D16-PTMS1

Figure 4-6: Diagonal splitting cracks developing at the corners

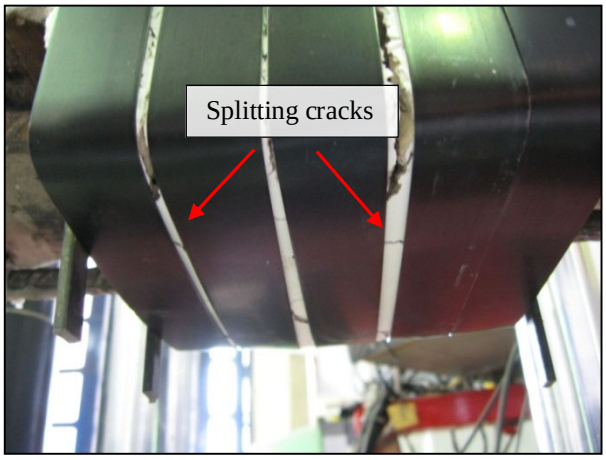

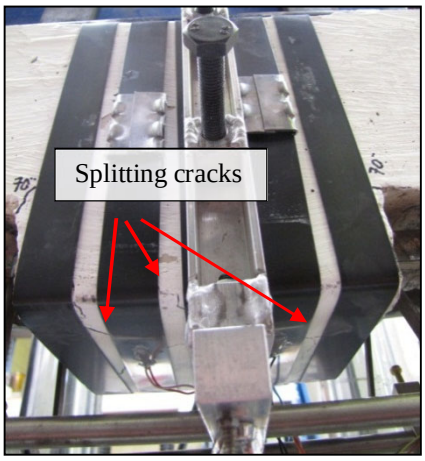

SC20-D12-PTMS2 SC27-D16-PTMS1

Figure 4-7 : Propagation of splitting cracks along the entire splice length

Splitting cracks were also observed (after the end of the test and removing of the strips) to form between splices and propagated vertically towards the bottom side of the beam, as shown in Figure 4-8. The evolution stage of these cracks was related to the c_m/c_s ratio; where c_m denotes half the distance between the splices and c_s denotes the minimum value of the bottom and side covers. As the ratio was < 1, as in group III, the splitting cracks between splices were the first to develop followed by side splitting cracking; whereas in group I and II, where the ratio was > 1, these cracks formed after the side splitting cracking initiated.

Figure 4-8: Formation of vertical splitting cracks and propagation along the splice (SC27-D16-PTMS1)

Flexural cracks also developed within the splice zone in all specimens. They initiated at the first stage of loading and tended to interfere with splitting cracks resulting in severe damage at the edges of the splice zone, as shown in Figure 4-9. These cracks developed among the strips and increased in number with reduced spacing between strips.

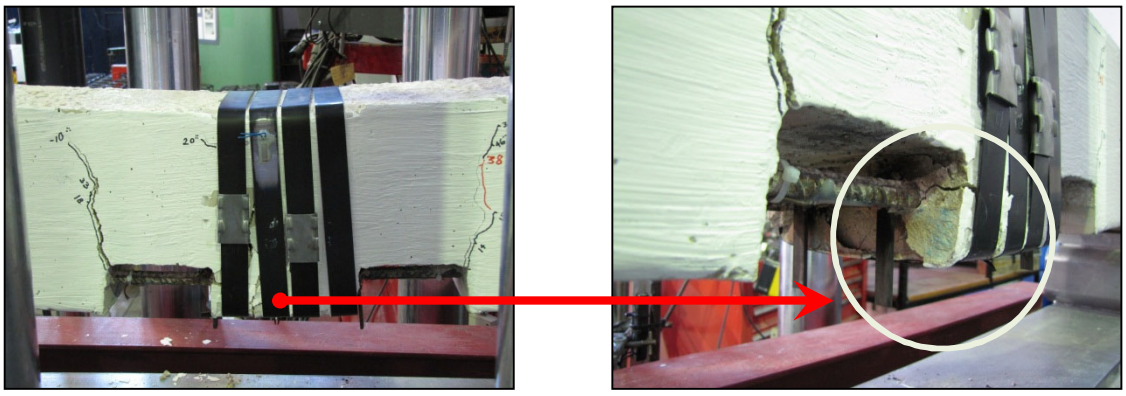

Figure 4-9: Damage due to the interference of flexural and splitting cracks (SC20-D12-PTMS1)

Crack patterns and modes of failure occurring in the splice zone are also shown in Figure 4-10 after stripping the PTMS off the splice zone. During removal of the strips, the concrete cover of some specimens, particularly the fully confined, spalled-off and the reinforcing bars were exposed, as shown in Figure 4-11.

SC10-D12-PTMS2 SC27-D16-PTMS1

Figure 4-10 : Cracking patterns and modes of failure

SC20-D12-PTMS2 SC27-D16-PTMS2

Figure 4-11 : Spalled off concrete cover of the fully confined specimens

The amount of damage and cracking propagation within the splice zone was dependent on the amount of confinement provided. In other words, the increase in the amount of confinement resulted in a higher load resistance accompanied by the formation of multiple cracks and higher deflections. Throughout the test, no strip rupture occurred. That prevented any potential spalling of the concrete cover, and therefore, improved the performance.

4.3 LOAD-DEFLECTION RESPONSE

The load-midspan deflection curves of the confined specimens in group I, II and III are compared to those of the bare (unconfined) specimens in Figure 4-12, Figure 4-13 and Figure 4-14, respectively. All load responses are normalised by a ratio of $(37.2/f'_c)^{1/4}$. The selection of this ratio is explained later in chapter 8. It should be noted that during testing the specimen SC20-D12-S a malfunction occurred that caused a sudden failure during the unloading of first post-peak cycle.

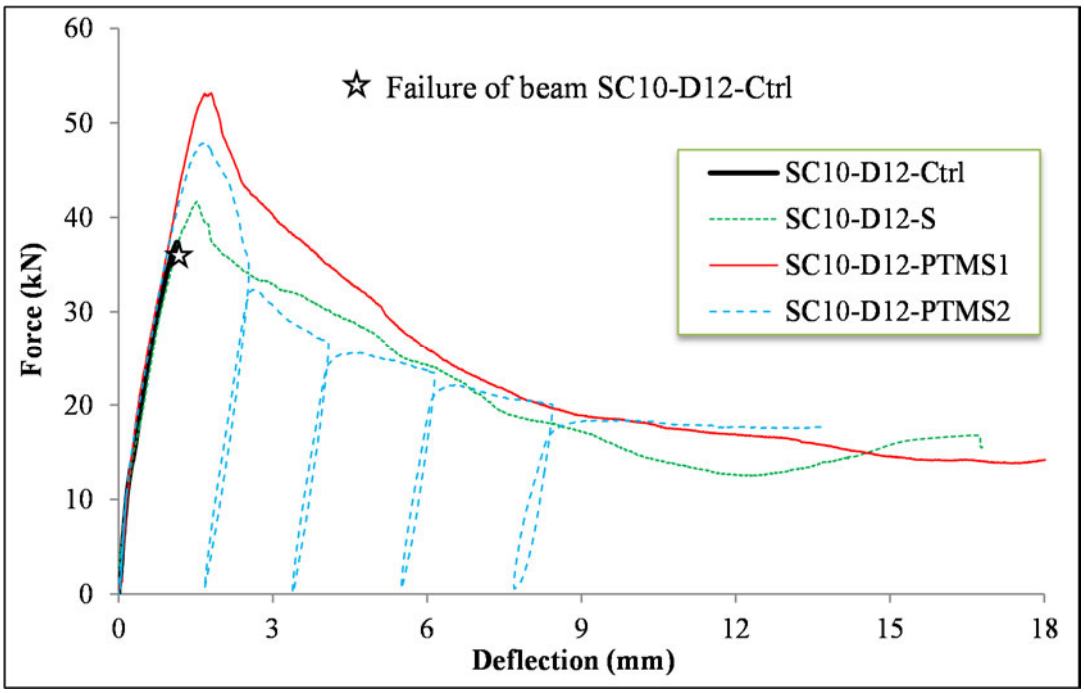

Figure 4-12: Load-deflection curves of test specimens in Group I

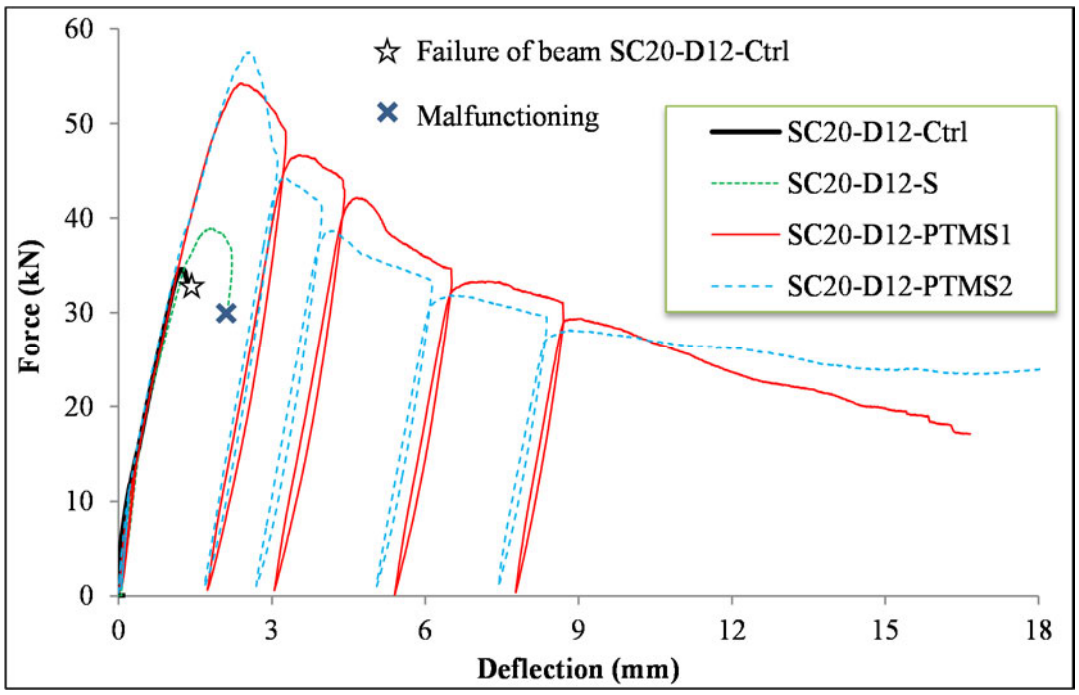

Figure 4-13: Load-deflection curves of test specimens in Group II

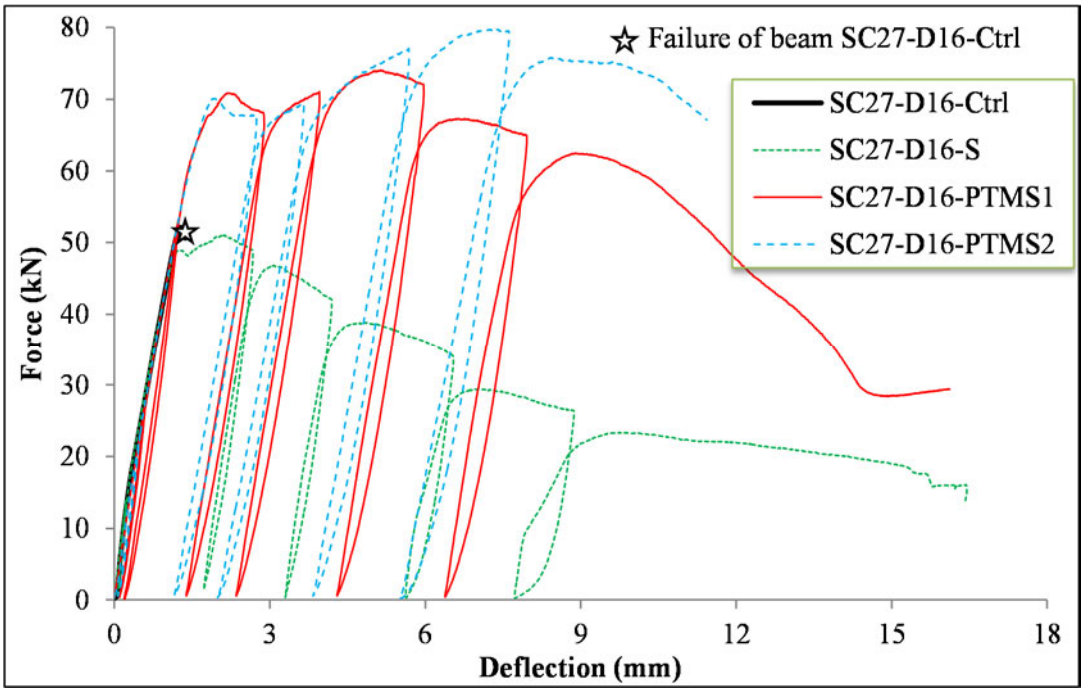

Figure 4-14: Load-deflection curves of test specimens in Group III

From the figures it is observed that all beams behave linearly, with a slight change in the stiffness at the flexural cracking point, until reaching the first splitting cracking at about 80-90% of the maximum load. The response afterwards was as follows:

For the control (unconfined) specimens, a sudden and dramatic drop in the post-peak response and almost complete loss of flexural stiffness occurred. That was due to splitting in the splices.

The maximum load and corresponding deflection ratios achieved were 33, 35 and 52 kN and 0.21%, 0.22% and 0.23% for the control specimens in group I, II and III respectively.

For the internally confined specimens, a slight change in the stiffness occurred until reaching the maximum load that was almost identical to those of the control specimens. Hairline splitting cracks tended to appear at this stage. The response afterwards tended to diminish gradually along with the formation of multiple splitting cracks. That allowed for more energy to dissipate and therefore improved substantially the deformability of the specimens in the post-splitting range. Although many splitting cracks developed during this stage, the response remained stable until it levelled off after reaching high deflection values. The maximum load and corresponding deflection ratios achieved were 37, 39 and 51 kN and 0.28%, 0.33% and 0.38% for the specimens in group I, II and III respectively.

For the PTMS confined specimens, the stiffness changed slightly until reaching the maximum capacity. Afterwards the stiffness in group I and II tended to decline in a similar way to the corresponding internally confined specimens, but after reaching higher values. In group III, however, the load decreased slightly at about a deflection of 2*mm* (DR of 0.4%) but with increasing the displacement, an additional strength was attained until the fourth post-peak cycle was reached. The response thereafter degraded in a linear manner and levelled off at a deflection of 15*mm*. This trend in the response was also observed in the corresponding internally confined specimen but the strength degraded before starting the first post-peak cycle. The maximum load and corresponding deflection ratios achieved were 47 kN and DR 0.30% (PTMS1), 48 kN and DR 0.30% (PTMS2) in group I; 54 kN and DR 0.44% (PTMS1), 58 kN and DR 0.46% (PTMS2) in group II; 74 kN and DR 0.93% (PTMS1), 80 kN and DR 1.34% (PTMS2) in group III.

In comparison with the unconfined and steel confined specimens, the PTMS specimens did not only mobilise larger loads, but also larger deflections, higher energy absorption and dissipation capacities and experienced less damage at a given loading stage. The increase was more pronounced and significant as the exterior concrete cover to bar diameter ratio c_e/d_b increased. That was due to the prevention of the spalling-off of the concrete cover and the positive effect of confining pressure where the splices tended to be more confined as the c_e/d_b ratio increased as schematically illustrated in Figure 4-15.

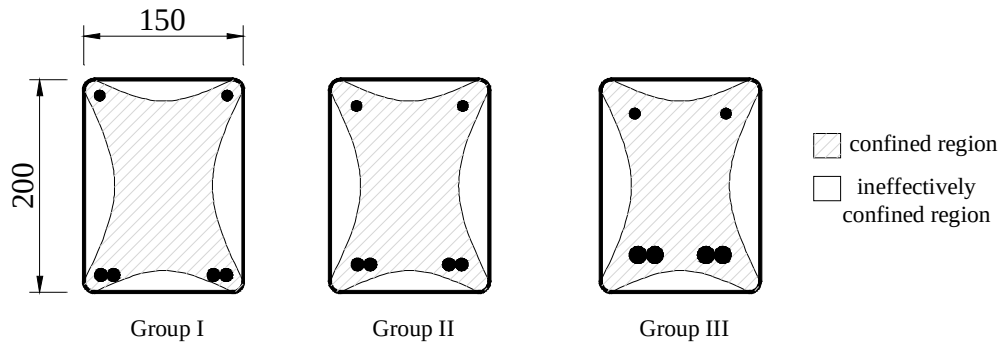

Figure 4-15: Location of splices within the effectively confined region

It should be noted that the flexural stiffness was almost identical for the beams in each group. In other words, the lateral confinement provided in the splice zone did not influence the flexural stiffness or cracking load of the specimens. All confined specimens in each group showed a consistent improvement in the maximum load and corresponding mid-span deflection compared to the unconfined ones. That highlighted the favourable effect of confinement on the performance of the specimens. In comparison to the unconfined specimens, the maximum load of the confined specimens in group I increased by 12% (steel), 42% (PTMS1) and 45% (PTMS2). Similarly, the improvement for group II was 11% (steel), 54% (PTMS1) and 66% (PTMS2). Group III showed an increase of 42% (PTMS1) and 54% (PTMS2) while no improvement was observed in the internally confined specimen. Table 4-1 shows the maximum loads and corresponding midspan deflections for all specimens. As seen from the table, the deflections of the confined specimens at the maximum load increased considerably in comparison to the bare specimens and reached a ratio of 5.76 for a full PTMS jacket (SC27-D16-PTMS2) with respect to the corresponding control specimen (SC27-D12-Ctrl).

In order to investigate further the enhancement in the deformability of the test specimens due to the use of confinement, a new indicator is introduced in this study called deformability ratio. This ratio $\delta_{-30\%}/\delta_m$ represents the deflection at 30% drop in the load capacity to the deflection at the maximum load capacity. The deformability ratios of the test specimens are presented in Table 4-1.

From the table, it can be noted that the deformability ratio of the unconfined specimens are zero as they failed directly after the load reaches the maximum capacity. For the internally and PTMS confined specimens, it can be noted that the internally confined specimen show almost identical deformability in comparison to the first PTMS specimen. The error in loading of specimen SC20-D12-S during the first post-peak cycle was the reason for zero deformability.

A sizable enhancement in the deformability can be noted in group III, where failure occurred in a pullout-like manner. In this group, the PTMS specimens showed considerable enhancement in deformability in comparison with the internally confined specimen. This enhancement was more than twice the value of the internally confined specimen.

Table 4-1: Summary of test results - small-scale beams

Group	**Specimen Notation**	**F_{max}** kN	δ_m *mm*	**DR%**	**DR/DR_{ctrl}**	$\delta_{30\%}/\delta_m$	**A_{tr} / Snd_b**
Group I	SC10-D12-Ctrl	33	1.14	0.21	1	0	NA
C_s=10mm	SC10-D12-S	37	1.52	0.28	1.34	2.3	0.034
d_b=12mm	SC10-D12-PTMS1	47	1.68	0.3	1.47	2.3	0.053
L_d=120mm	SC10-D12-PTMS2	48	1.67	0.3	1.47	2.6	0.053
Group II	SC20-D12-Ctrl	35	1.22	0.22	1	0	NA
C_s=20mm	SC20-D12-S	39	1.82	0.33	1.49	-	0.034
d_b=12mm	SC20-D12-PTMS1	54	2.4	0.44	1.96	2.3	0.053
L_d=120mm	SC20-D12-PTMS2	58	2.54	0.46	2.08	1.7	0.067
Group III	SC27-D16-Ctrl	52	1.28	0.23	1	0	NA
C_s= 27mm	SC27-D16-S	51	2.08	0.38	1.63	2.7	0.025
d_b=16mm	SC27-D16-PTMS1	74	5.14	0.93	4.02	5.5	0.037
L_d=160mm	SC27-D16-PTMS2	80	7.36	1.34	5.76	7.0	0.05

δ_m and DR are the mid-span deflection and deflection ratio at the maximum load Fmax, respectively; A_{tr}/Snd_b is the confinement ratio; $\delta_{30\%}/\delta_m$ is the deformability ratio representing the deflection at 30% drop in the load capacity to the deflection at the maximum load capacity.

4.4 LOAD VERSUS UNLOADED-END SLIP

The load-average slip of test specimens in Group I, II and III are shown in Figure 4-16, Figure 4-17 and Figure 4-18, respectively. Because the failure of beams is due to bond, the resultant load-slip response is found to be similar to the load-deflection response.

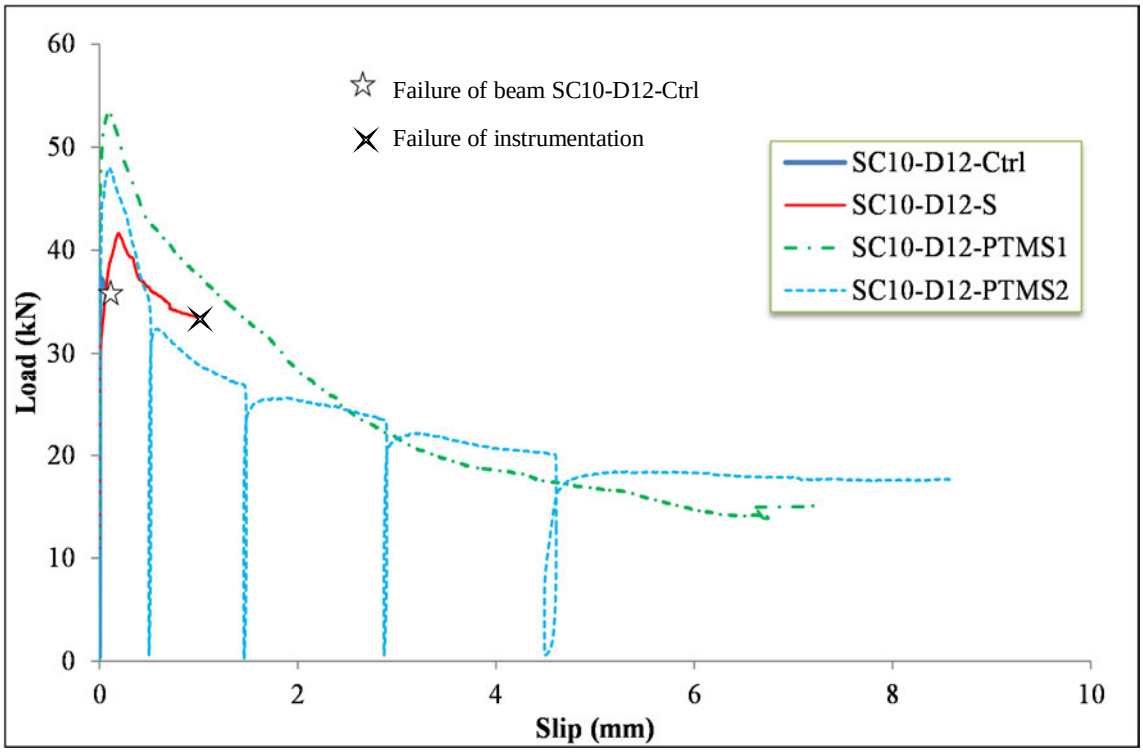

Figure 4-16: Load-slip curves of test specimens in Group I

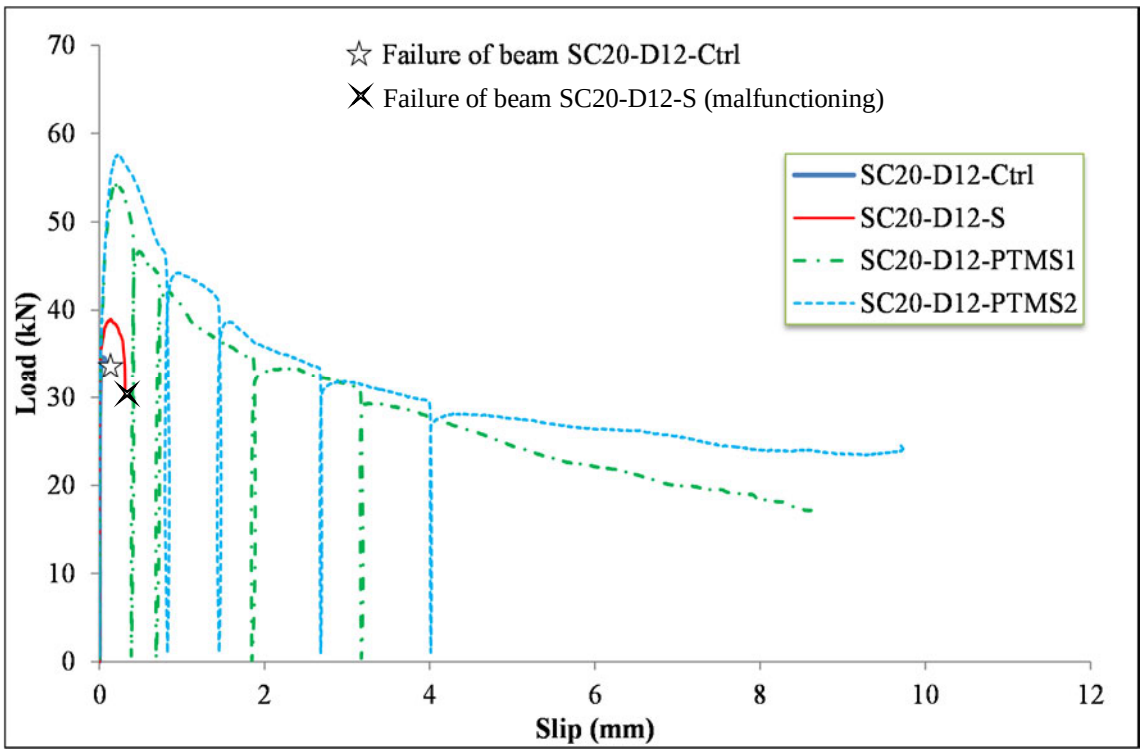

Figure 4-17: Load-slip curves of test specimens in Group II

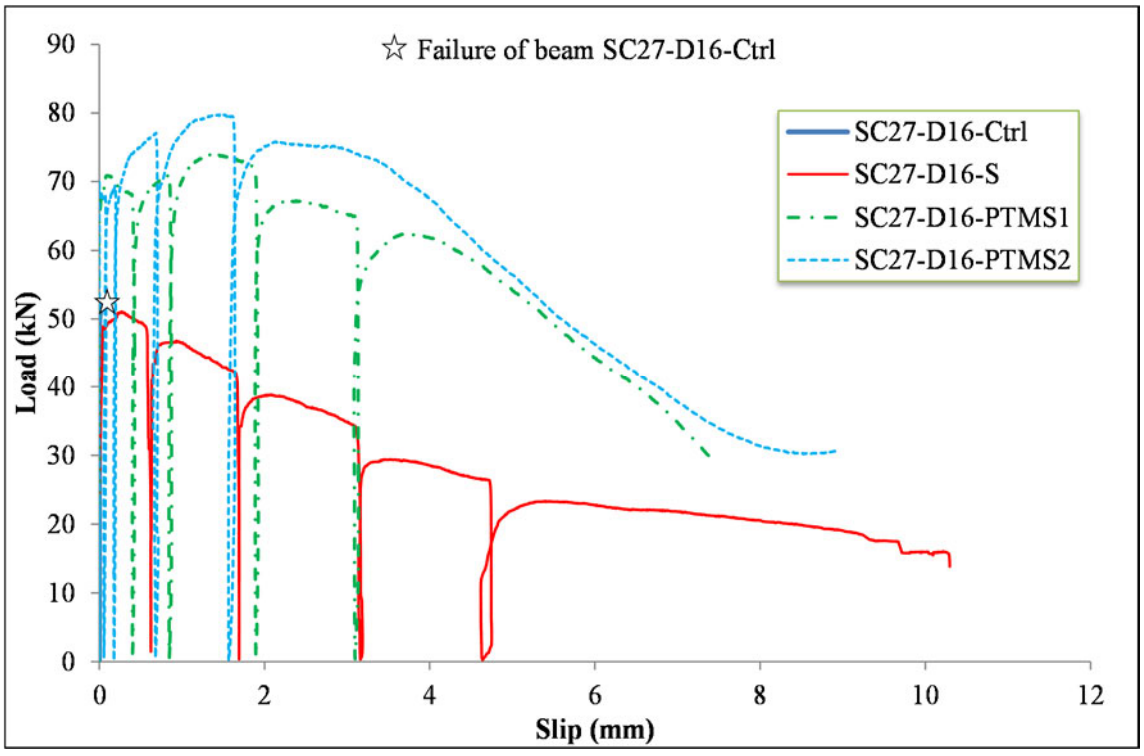

Figure 4-18: Load-slip curves of test specimens in Group III

As can be seen from the figures, slip values are almost insignificant until the loading reaches 80-90% of the maximum load that corresponds to first splitting in splices. The response afterwards is noted to have a slight change in stiffness due to bar slippage. This was also the reason for the reduction in stiffness of the load-deflection response as explained in Sec 4.3. It is

also evident from the figures that the type of confinement and its content within the splice zone has a significant influence on the load-slip response which is described in the following:

4.4.1 Control unconfined specimens

Once the maximum splitting strength is reached, the bars are pulled out and the resistance drops to zero. That takes place at very small slip values of approximately 0.04 *mm*. During the loading stage, a splitting crack occurs prior to failure. This allows for the development of only a very small load beyond this value. In these specimens, the absence of confinement along splices is responsible for the rapid and sudden growth in splitting cracks. The small slip values occurring in the bars are also the reason for the small corresponding deflections of these specimens. The slip at the maximum load is measured at 0.05, 0.04 and 0.03 *mm* for the specimens in Group I, II and III, respectively. These values represent 0.625%, 0.5% and 0.3% of the distance between the bar lugs, that is reported in the literature to be the maximum value before the concrete keys between the lugs to shear-off.

4.4.2 Internally confined specimens

Multiple splitting cracks are observed to form before reaching the maximum splitting strength. That causes more slip in the bars during this stage and at the maximum load. As a result, the deflections of these specimens are higher in comparison to the unconfined ones. During the post peak loading stage, more splitting cracks form along splices and result in very high slip values in the bars. Despite the large slip achieved, a complete loss in the load resistance does not occur. In fact, the residual load resistance accounted for ~50% of the maximum load compared to the complete loss which occurred in the unconfined specimens. Although the presence of confinement in the splice zone does not improve much the load resistance, reaching higher slips and deflections is considered essential during a seismic event. The slip values at the maximum load were measured at 0.19, 0.14 and 0.28 *mm* for the specimens in Group I, II and III respectively. The presence of lateral confinement modified the peak slips by 280%, 250% and 830%, respectively, relative to the unconfined specimens.

4.4.3 PTMS confined specimens

Analogous to the internally confined specimens, multiple splitting cracks are observed to form within the splice zone before reaching the maximum strength. The formed splitting cracks, however, are larger in number and the specimens show higher slips and higher deflections at the maximum load when compared with the internally confined specimens. The slip values measured are 0.24*mm* (PTMS1) and 0.18*mm* (PTMS2) in Group I; 0.19*mm* (PTMS1) and 0.22mm (PTMS2) in Group II; and 1.41mm (PTMS1) and 1.5mm (PTMS2) in Group III. It can be noted that the slip values of specimens in Group I and II are very close to those of the companion internally confined ones but occur at higher loads. The difference, however, becomes sizable for the specimens in Group III and reaches a ratio of 5.0 (PTMS1) and 5.34

(PTMS2) when compared with that of the companion internally confined specimen. At the post peak stage, the load resistance is found to level off at about an average slip of 8*mm* with 50% residual strength. This value of slippage coincides with the bar lug spacing which confirms the available findings about the shearing-off of concrete keys between bar lugs.

It is important to note that in all specimens, during unloading and reloading stages in the post-peak stage, as the load dropped, the slip did not recover indicating permanent loss of bond due to the excessive splitting cracking along the splices.

The effect of cyclic load on the response is examined by comparing the load-slip relation of specimens SC10-D12-PTMS1&2. From Figure 4-16, it is clear that the use of cyclic loading regime resulted in somewhat faster degradation in the post splitting response. However, as the loading (displacement) progressed, the difference diminished which is expected as the load levels off. It should be indicated, however, that the use of more severe cyclic regime is expected to make a significant change in the response. This can be done in a further study.

4.5 BOND STRESS-SLIP RELATIONSHIP

The bond stress-slip relationship is developed based on the test measurement of strains on the bars and slips at splice ends. Strain gauge readings are given in Appendix E. At each loading increment, the average bond stress τ (as schematically illustrated in Figure 4-19) is the calculated load on the bar F_s divided by the product of splice length l_d and the bar perimeter ρ as shown below:

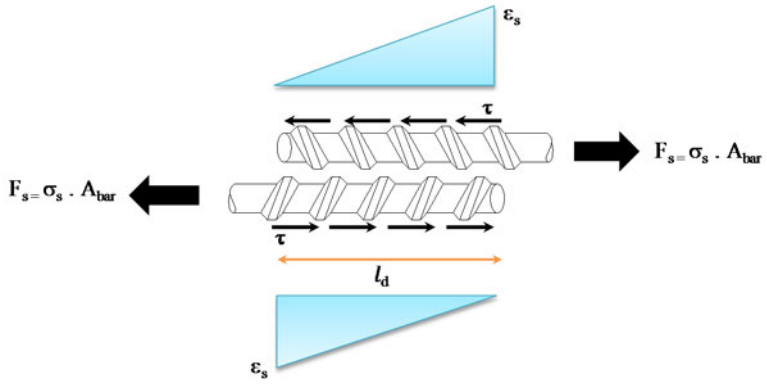

Figure 4-19: Bond and strain distribution along the splice length

$$[F_s = (f_s.A_{bar})] = \tau.\rho.l_d \quad \Rightarrow \quad f_s.\pi.\frac{d_b^2}{4} = \tau.\pi.d_b.l_d \quad \Rightarrow \quad \tau = (f_s/l_d) \times (d_b/4) \quad \Rightarrow$$

$$\boldsymbol{\tau = (E_s.\varepsilon_s/l_d) \times (d_b/4)} \qquad (4\text{-}1)$$

where σ_s is the bar stress, d_b is the nominal bar diameter, A_{bar} is the bar area, E_s is the modulus of elasticity of steel bars, and ε_s is the strain at the end of the splice.

Because the resulting bond-slip relationships are found to be comparatively similar in the specimen, the average curve is calculated. Table 4-2 presents the average bond stress, bond ratio τ_{norm}/τ_{bare}, bar stress and slip of all test specimens at the maximum load. The bond ratio in each group is the normalised bond stress with confinement divided by that of the companion beam with no confinement. The bond stress-slip curves for group I, II and III are presented in Figure 4-20, Figure 4-21 and Figure 4-22, respectively.

Table 4-2: Test results and bond stresses

Group	*Specimen Notation*	F_{max} *kN*	τ_{actual} *MPa*	f_s *MPa*	*s mm*	τ_{norm}/τ_{bare}
Group I	SC10-D12-Ctrl	33	3.80	155	0.05	1.00
C_s=10*mm*	SC10-D12-S	37	4.33	170	0.19	1.14
d_b=12*mm*	SC10-D12-PTMS1	47	5.53	221	0.09	1.46
L_d=120*mm*	SC10-D12-PTMS2	48	5.75	230	0.11	1.33
Group II	SC20-D12-Ctrl	35	4.41	177	0.04	1.00
C_s=20*mm*	SC20-D12-S	39	3.87	155	0.14	0.88
d_b=12*mm*	SC20-D12-PTMS1	54	6.71	268	0.19	1.07
L_d=120*mm*	SC20-D12-PTMS2	58	6.97	279	0.22	1.58
Group III	SC27-D16-Ctrl	52	4.03	161	0.03	1.00
C_s= 27*mm*	SC27-D16-S	51	3.82	153	0.28	0.95
d_b=16*mm*	SC27-D16-PTMS1	74	5.49	219	1.41	1.36
L_d=160*mm*	SC27-D16-PTMS2	80	6.21	248	1.50	1.54

τ_{actual} ,τ_{norm}, f_s and s are actual bond values, normalised bond by $(37.2/f'_c)^{1/4}$, average steel stress and average slip at the maximum load F_{max}, respectively.

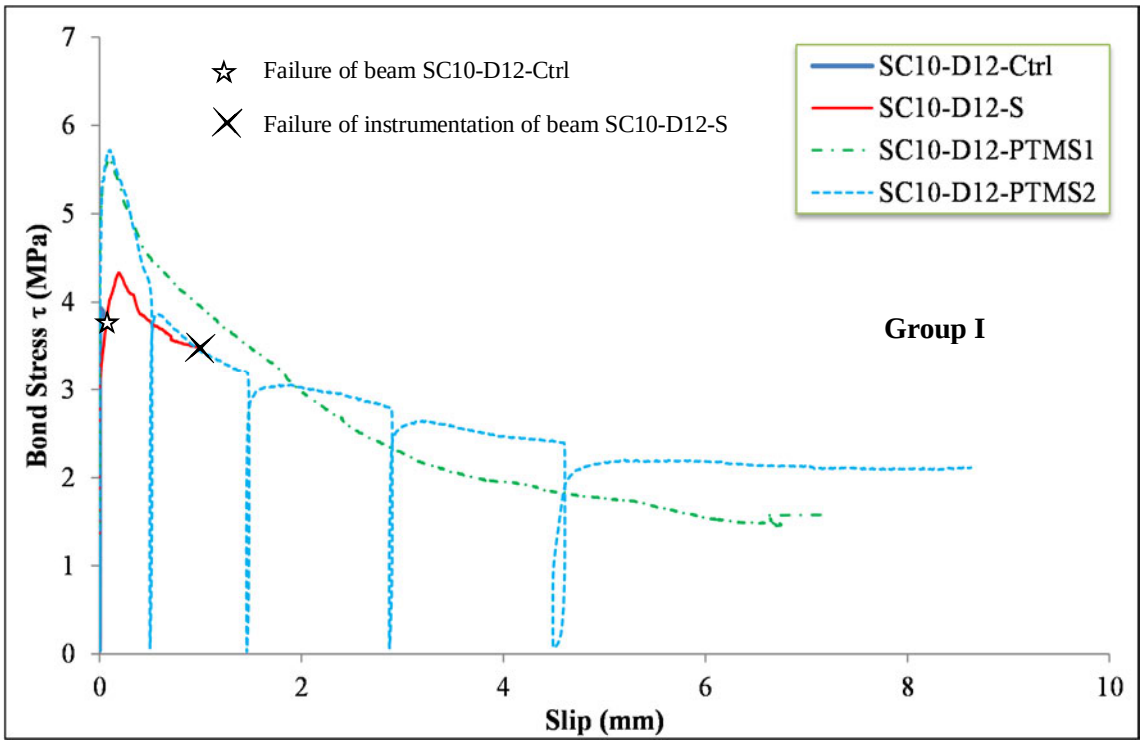

Figure 4-20: Comparison of bond test results with unconfined concrete and concrete confined with steel stirrups or PTMS – Group I

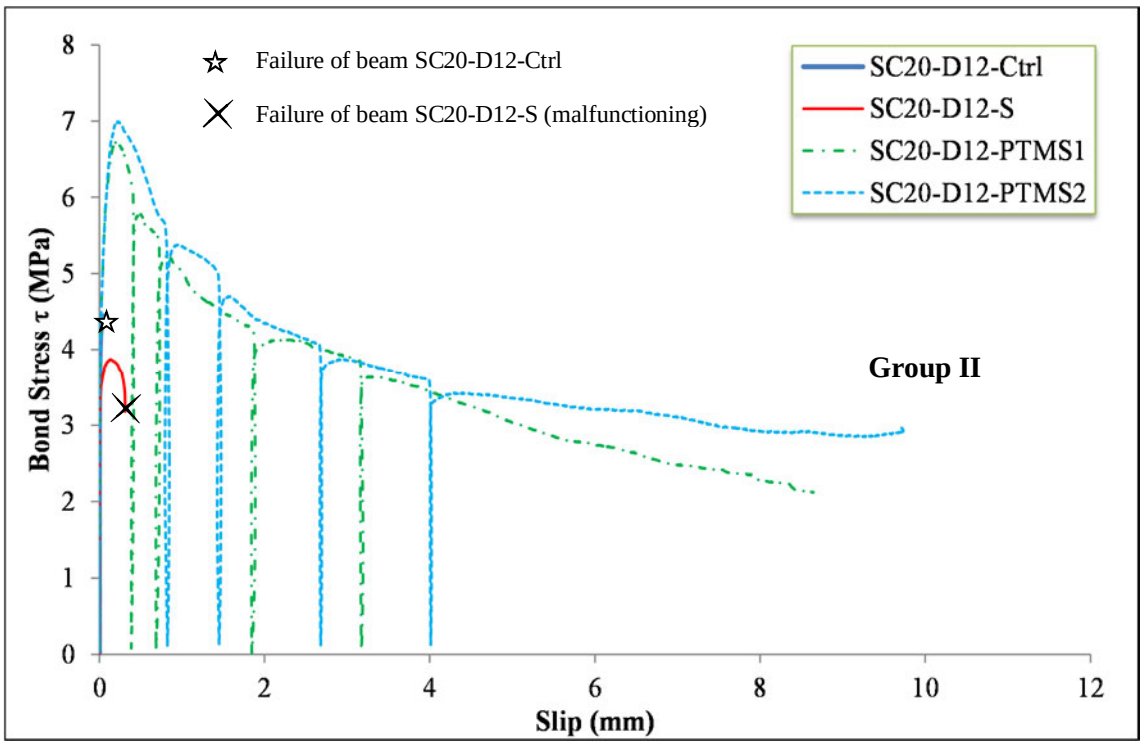

Figure 4-21: Comparison of bond test results with unconfined concrete and concrete confined with steel stirrups or PTMS – Group II

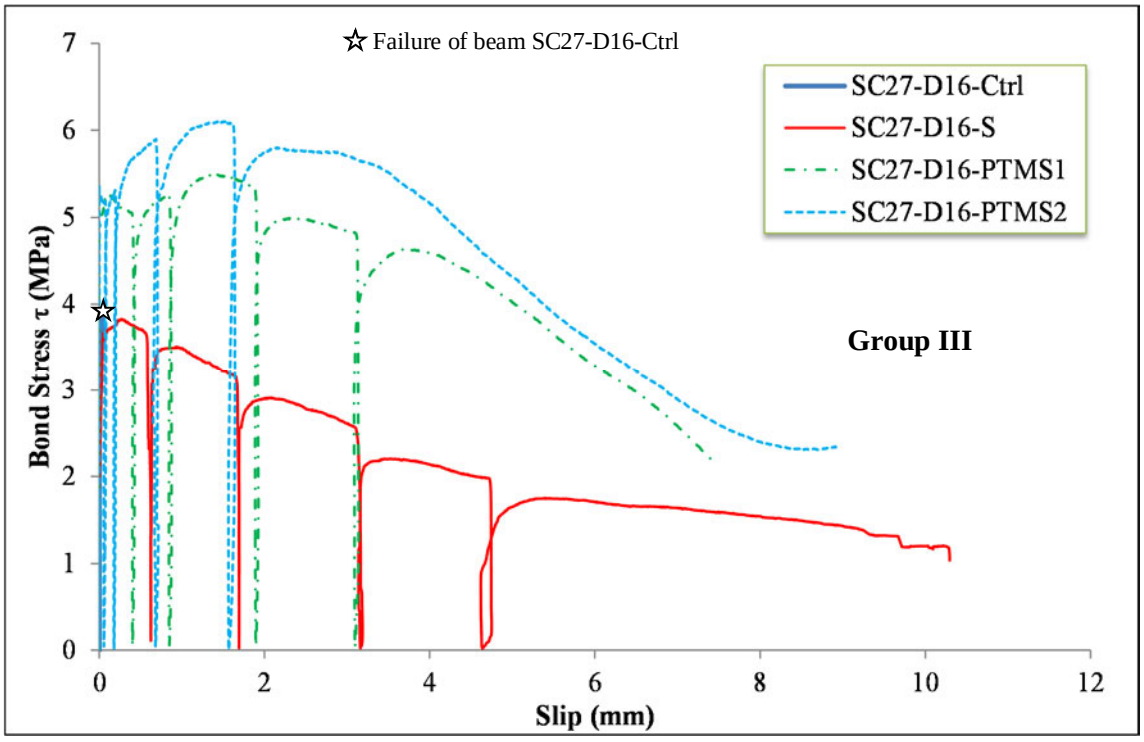

Figure 4-22: Comparison of bond test results with unconfined concrete and concrete confined with steel stirrups or PTMS – Group III

From Figure 4-20 to Figure 4-22, the following observations can be made:

- The unconfined splice zones have complete loss of bond strength immediately after the peak.
- The confinement by steel stirrups does not show a significant influence on bond strength, however, it mobilises larger deformability when compared to the original unconfined specimens.
- Confining the splice zone with PTMS results in significant increase in the peak bond strength as compared to plain unconfined concrete.
- The general bond stress-slip response after splitting shows similar behaviour irrespective of the type of confinement used.
- The amount of confinement within the splice zone reduces bond degradation in the post-splitting stage leading to more ductile behaviour.

Another important observation from the bond-slip response is that the unloaded end slip remains practically zero until the bond stress reaches quite high values close to the bond strength. The experimental results show that the ratio of the bond at which the unloaded end starts to slip to the maximum value is around 0.82, 0.69 and 0.71 for the unconfined, internally confined and externally confined specimens, respectively. Figure 4-23 shows these bond ratios for all specimens.

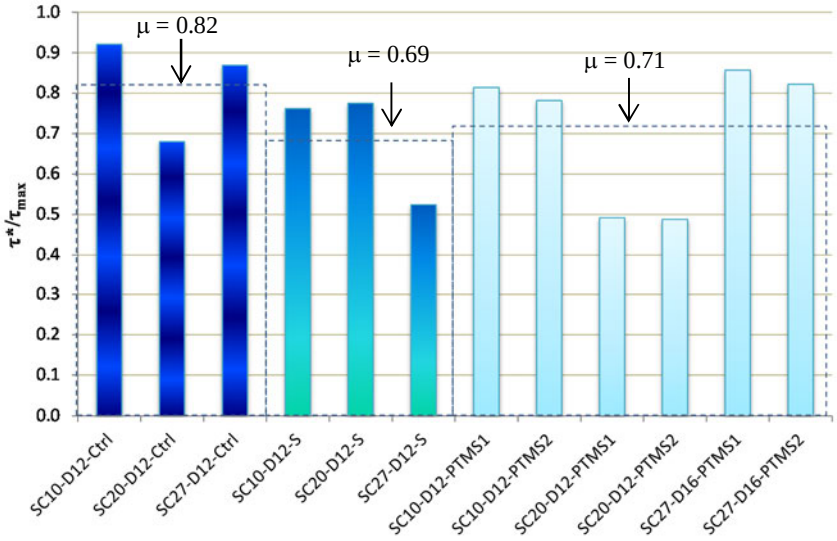

Figure 4-23: Ratio of bond stress when unloaded end starts to slip to maximum bond strength for all specimens

The bond-slip response of the confined specimens can be divided into five distinct stages of behaviour. These stages are shown schematically in Figure 4-24 and are described as follows:

- Initial stiff bond-slip response associated with no measurable slip such that the force is transferred through chemical adhesion, as shown in Figure 4-25(a).
- Soft pre-splitting behaviour due to partial loss of chemical bond associated with formation of circumferential tensile cracks around the spliced bars until the maximum tensile strength is attained, as shown in Figure 4-25(b), and where the load is transferred partially through adhesion and mainly through mechanical bearing. Hairline splitting cracks tend to form along the splice due to propagation of some of the circumferential tensile cracks outwards to the concrete cover, as shown in Figure 4-25(c)
- Sudden drop in the bond-slip response at the first post-splitting stage due to splitting and rapid cracking in the concrete matrix around the bar along with the propagation of some splitting cracks along the spliced bars, as shown in Figure 4-25(d), and such that the residual force is transferred through mechanical bearing.
- Gradual degradation in the bond-slip response associated with widening of splitting cracks and resulting in considerable bar slippage. The residual force is transferred mainly by mechanical bearing as well as friction, as shown in Figure 4-25(e).
- Constant bond-slip behaviour where the concrete keys between lugs is sheared-off and such that the bond resistance is only due to friction, as shown in Figure 4-25(f). Figure 4-11 shows the sheared-off concrete between bar lugs of a PTMS confined specimen after the removal of strips and concrete cover.

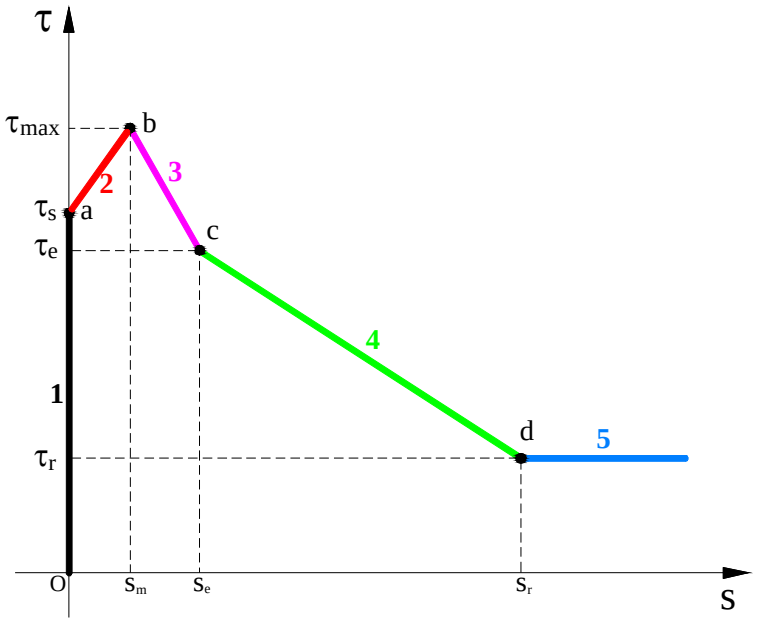

Figure 4-24: Idealised bond stress-slip response of plain and confined concrete

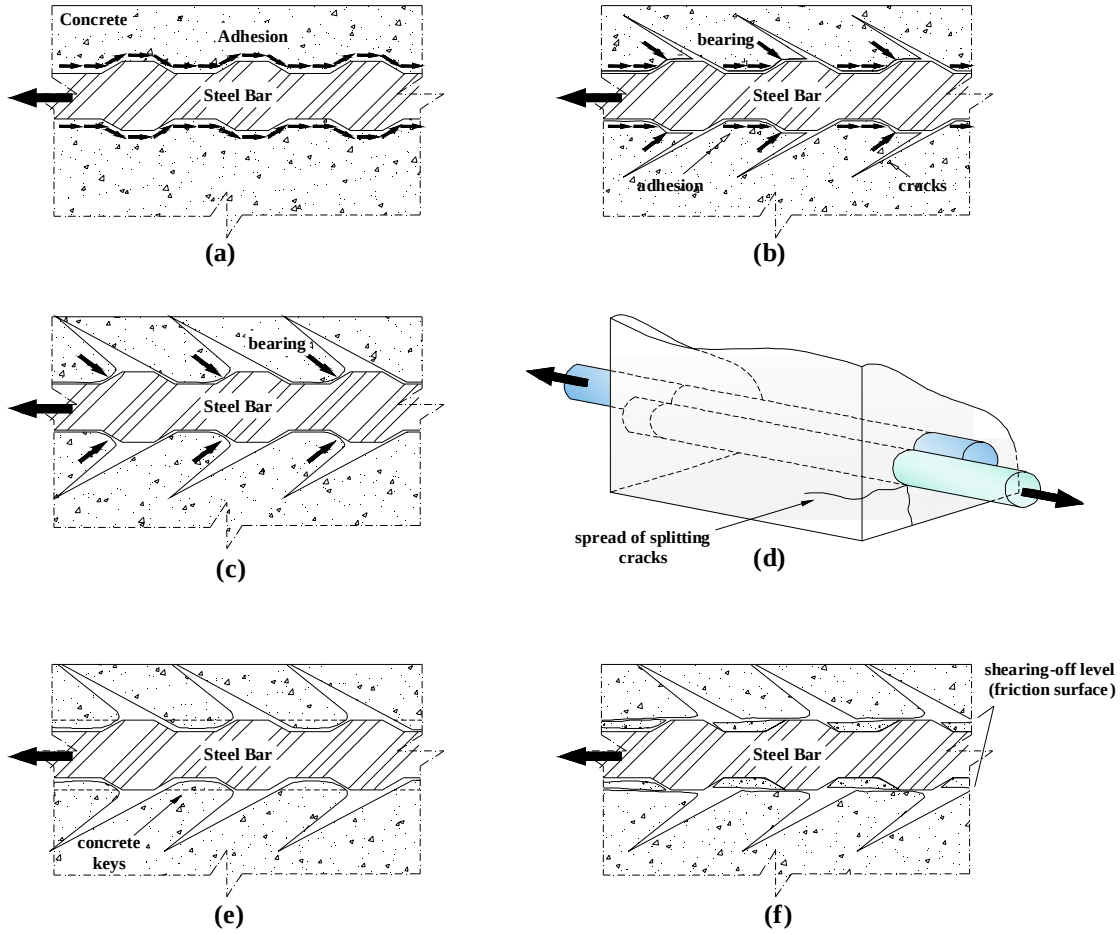

Figure 4-25: Mechanism of bond transfer during the different stages of response

The values that identify the curve are given in Table 4-3 for each specimen. Those values will be used to propose a bond-slip relation that can describe the behaviour, as explained in chapter 8. It should be mentioned that some of the values at the post-peak stage could not be measured due to failure of some of potentiometers.

Table 4-3: Characteristics of bond stress-slip curves of the test specimens (Series S)

Group	Specimen	τ_s MPa	τ_{max} MPa	τ_e MPa	τ_r MPa	s_m mm	s_e mm	s_r mm
I	SC10-D12-Ctrl	3.50	3.80	N/A	N/A	0.05	N/A	N/A
	SC10-D12-S	3.20	4.33	3.50	-	0.19	0.80	-
	SC10-D12-PTMS1	4.20	5.53	4.60	1.80	0.09	0.43	5.10
	SC10-D12-PTMS2	4.30	5.75	4.50	2.17	0.11	0.45	5.00
II	SC20-D12-Ctrl	3.60	4.41	N/A	N/A	0.04	N/A	N/A
	SC20-D12-S	3.20	3.87	-	-	0.14	-	-
	SC20-D12-PTMS1	4.00	6.71	4.90	2.90	0.19	1.05	5.40
	SC20-D12-PTMS2	4.00	6.97	5.00	3.30	0.22	1.30	5.30
III	SC27-D12-Ctrl	3.50	4.03	N/A	N/A	0.03	N/A	N/A
	SC27-D12-S	3.00	3.82	3.70	2.40	0.28	3.10	6.00
	SC27-D16-PTMS1	4.80	5.49	4.00	2.20	1.41	5.00	8.00
	SC27-D16-PTMS2	5.10	6.21	4.30	2.30	1.42	4.90	8.00

4.6 ANALYTICAL PREDICTIONS OF BAR FORCES

As some of the specimens did not have strain gauges installed on the steel bars, bar forces are calculated based on moment curvature analysis. This approach has been verified by Zuo and Darwin (1998) to give more realistic results in comparison to the working stress and strength approaches. Moreover, this approach is used by ACI Committee 408R-03 (2003) to determine the average bar force at the time of failure.

In this section, bar forces are evaluated for all specimens. Conventional sectional analysis, as illustrated in Figure 4-26, is first performed using the computer programme XTRACT (XTRACT, 2004) to calculate the moment-curvature curves of the cross-section. Typical characteristic steel and concrete material models implemented in the programme are shown in Figure 4-27. The confined concrete model proposed by Moghaddam et al. (2010) is adopted for the PTMS confined sections. Typical moment-curvature curves are plotted in Figure 4-28. Since bond failure took place before yielding, the pre-yield part of the curves is only utilised. At each loading step, strains in the bars and as a result bar forces are calculated. Figure 4-29 shows a comparison between the predicted and experimental bar forces at maximum loading. Strain gauge readings were used to calculate the experimental values. Based on the calculated bar forces, the average bond stress can be evaluated using Equation 4.1.

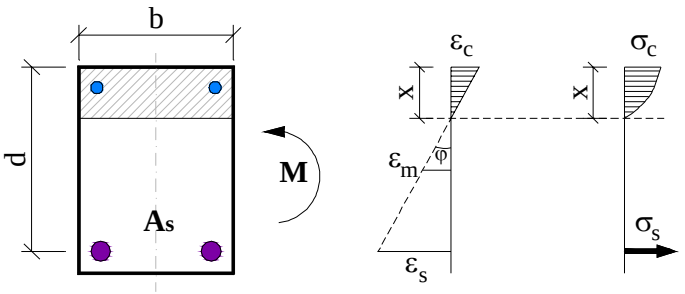

RC section strain distribution stress distribution

Figure 4-26: Conventional Cracked sectional analysis (CSA)

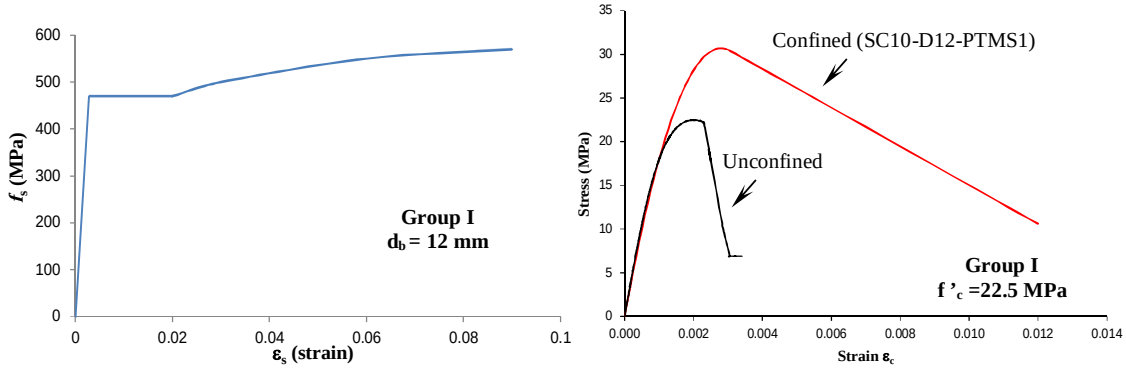

Figure 4-27: Typical steel stress-strain model (left) and concrete compressive strength (right) used for the sectional analysis

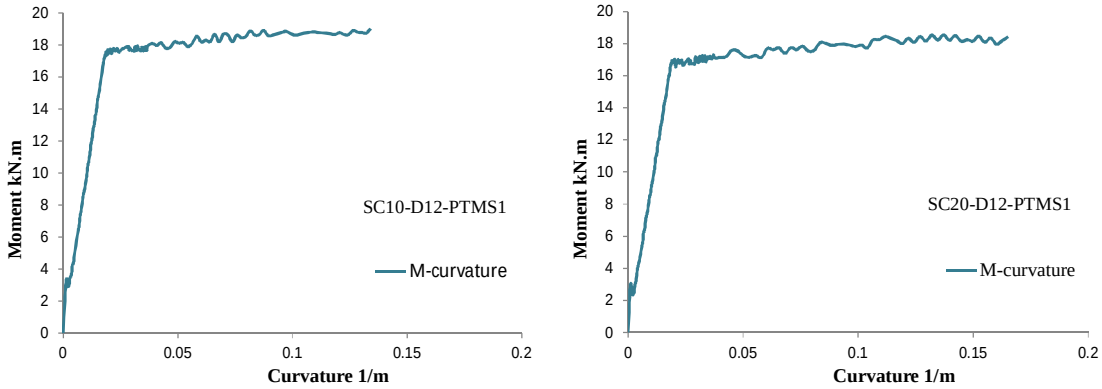

Figure 4-28: Typical moment-curvature relations calculated from XTRACT

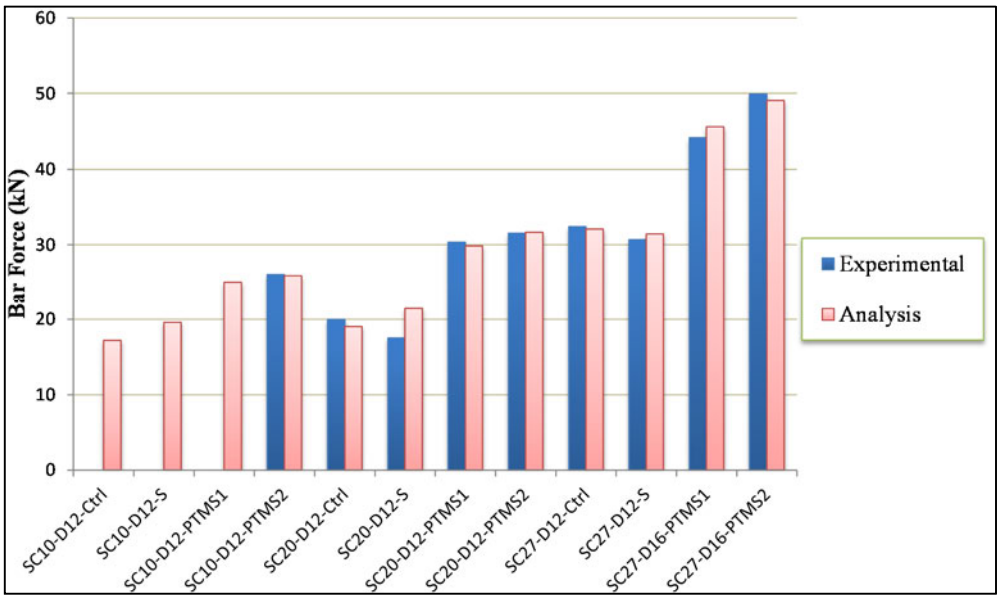

Figure 4-29: Comparison of predicted and experimental bar forces at maximum load

From Figure 4-29, it is evident that the cracked sectional analysis can accurately predict the maximum bar force.

4.7 VARIATION OF STRESSES IN STRIPS

The variation in stress within the strips is monitored by using strain gauge readings. The strain gauges were installed on the side and bottom parts of the tensioned strips as shown in Figure 4-30(a). Figure 4-31 shows typical strain gauge readings of a PTMS confined specimen.

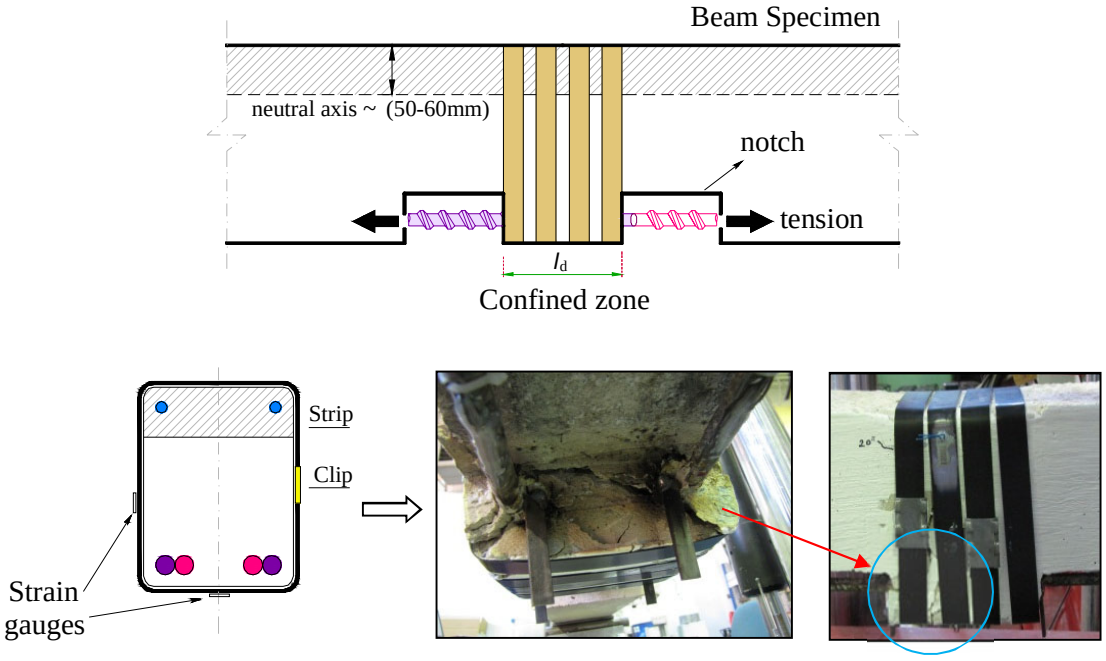

(a) PTMS Confined section

(b) Cracked concrete underneath strips

Figure 4-30: Effect of cracking on confinement of strips

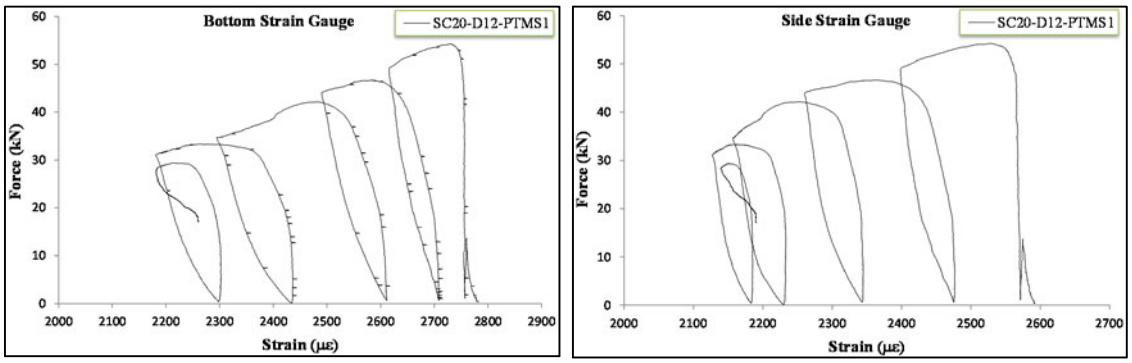

Figure 4-31: Strain gauge readings of specimen SC20-D12-PTMS1

Based on strain gauge readings, it was observed that the stress on strips remained more or less constant until the first splitting crack. The stress, thereafter, reduced slightly until the maximum capacity was reached. The reduction accelerated as slip developed. During the test it was observed that a large number of splitting cracks occurred which caused severe damage and deformations in the concrete cover, as shown in Figure 4-30 (b), and as result relaxation in the strips.

The initial average pre-strain applied to the strips was around 0.003 which represents around 80% of the nominal yield strain or 10% of the nominal ultimate strain of strip. At the conclusion of the test, the average reduction in strains was found to be around 17% of the initial value.

4.8 RESTRAINING EFFECT OF STRIPS

The restraining effect of the strips is found to delay the formation of splitting cracks and as a result bar slippage. This effect can be explained by analysing the external forces acting on the confined section, as shown in Figure 4-32.

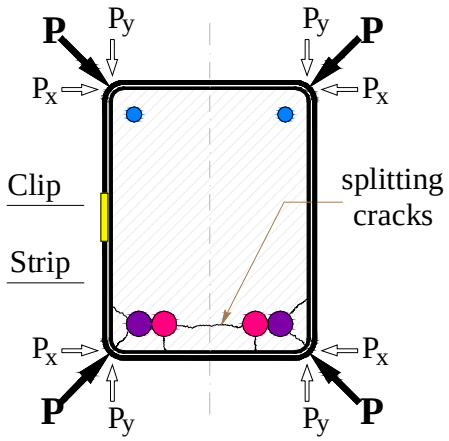

Figure 4-32: PTMS confined section and pressure components

As can be seen from Figure 4-32, the horizontal and vertical parallel components of the pressure creates a reaction restraint against the formation of splitting cracks. It should be noted that, from

the elastic theory, the weakest plane for splitting is now the diagonal. This explains the initial formation of splitting cracks in a diagonal manner as explained in SEC 4.2.3. It is important to point out that this phenomenon is absent in the internally confined specimens because the external cover is not confined, and therefore, the horizontal and vertical splitting planes represent the shortest paths for cracking. From the bond perspective, the restraining effect as a result of the PTMS confinement improves the bond action and enhances the load-slip response when compared with the unconfined specimens.

4.9 CONCLUSIONS

This chapter presented the experimental results of a research on the effect of PTMS confinement on bond strength enhancement of spliced bars embedded in normal strength concrete. All specimens were designed and constructed with insufficient splice length of $10d_b$ and small concrete cover thickness ranging from 0.8 to $1.6d_b$. The following conclusions were drawn:

1. All specimens, confined or non-confined, failed by splitting type of bond failure leading to considerable concrete damage within the spliced zone and loss in flexural strength. Splitting initiated when the load reached 80-90% of the maximum load.
2. The absence of confinement in the splice zone resulted in a sudden and brittle failure immediately after the maximum load was reached.
3. PTMS confinement resulted in bond strength enhancement in all specimens regardless of the concrete strength, bar diameter, c_d/d_b ratio and the amount of PTMS confinement in the section.
4. The number and orientation of splitting cracks in the radial direction, starting from the reinforcing bar and ending at the nearest concrete free surface, are altered by the application of PTMS confinement. While splitting cracks in specimens reinforced with internal links formed conventionally in a horizontal and vertical manner, in the PTMS specimens they initially started in a diagonal manner (V-notch). These splitting cracks are attributed to the clamping force resulting from the PTMS confinement.
5. The use of PTMS confinement improves the small concrete cover and splice length deficiencies by means of strengthening the cracked concrete matrix which lies between the reinforcing bars and concrete cover.
6. The PTMS specimens experienced excessive splitting and flexural cracking that led to a sizable enhancement in the deformability compared to the counterpart unconfined specimens.
7. The presence of steel stirrups in splice zones is mainly beneficial in terms of deformability rather than increasing the splice strength.
8. The bond stress-slip responses are found to be similar to the load-deflection responses.

9. The load-deformation characteristics are described in terms of an idealised bond-slip relationship. The characteristics and limitations of this relationship are discussed in chapter 8.

Chapter 5

MEDIUM SCALE BEAMS: TEST RESULTS, OBSERVATIONS AND DISCUSSIONS

5.1 INTRODUCTION

In this chapter, the experimental results of twelve medium scale beams subjected to flexural loading described in chapter 3 are presented. Due to the large volume of test results, only the most relevant are presented herein. The full results are included in Appendix F. Similarly to Phase I, the test specimens are categorised into three families depending on the type of confinement provided in the splice zone. Based on measured test data, visual observations and photos, the behaviour of specimens in each family is examined in terms of cracking and propagation of cracks, load-deflection, strain profiles along splices, deformability as well as slip of reinforcement. A comparison between the behaviour of each type of confinement is also performed. An evaluation of the derived test data including bond values and bar stresses follows.

5.2 GENERAL BEHAVIOUR, MODES OF FAILURE AND LOAD CAPACITY

At the beginning of loading, all specimens tended to develop flexural cracks randomly within the constant moment area on the tension side of the beam, as shown in Figure 5-1. These cracks were observed to initiate outside the splice zone and occurred at similar loading levels for each group. The average flexural cracking load was measured at 14, 13 and 15 kN for specimens in Group I, II and III, respectively, as shown in Table 5-1.

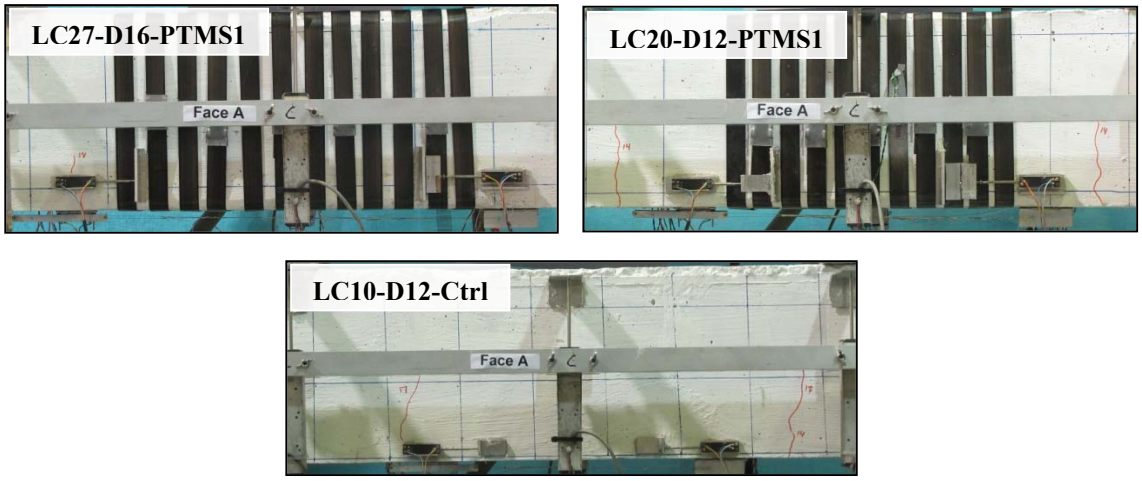

Figure 5-1: Typical flexural cracking of test specimens

Table 5-1: Test results of the tested specimens

Group	Specimen Notation	F_{cr} kN	F_{max} kN	δ_m *mm*	DR%	δ/δ_{ctrl}	$\delta_{.30}/\delta_m$	A_{tr} / Snd_b
Group I	LC10-D12-Ctrl	14.0	36.2	4.2	0.55	1.00	0	NA
C_s=10mm	LC10-D12-S	17.0	46.1	7.3	0.96	1.74	1.6	0.047
d_b=12mm	LC10-D12-PTMS1	12.0	65.7	11.1	1.45	2.63	2.3	0.048
L_d=300mm	LC10-D12-PTMS2	12.0	68.6	16.1	2.1	3.80	2.3	0.067
Group II	LC20-D12-Ctrl	13.5	39.4	6.1	0.8	1.00	0	NA
C_s=20mm	LC20-D12-S	14.0	35.5	6.5	0.85	1.06	1.8	0.047
d_b=12mm	LC20-D12-PTMS1	14.0	55.2	10.7	1.4	1.76	1.5	0.048
L_d=300mm	LC20-D12-PTMS2	12.0	62.5	15.9	2.07	2.60	1.7	0.067
Group III	LC27-D16-Ctrl	15.0	60.9	6.4	0.83	1.00	0	NA
C_s= 27mm	LC27-D16-S	14.0	65.4	7.1	0.93	1.12	1.2	0.031
d_b=16mm	LC27-D16-PTMS1	14.0	87.2	10.9	1.43	1.72	1.2	0.031
L_d=400mm	LC27-D16-PTMS2	15.0	80.7	9.1	1.19	1.43	1.3	0.063

δ_m and DR are the mid-span deflection and drift ratio at the maximum load F_{max}, respectively; A_{tr}/Snd_b is the confinement ratio; $\delta_{.30\%}/\delta_m$ is the deformability ratio representing the deflection at 30% drop in the load capacity to the deflection at the maximum load capacity.

As loading increased beyond flexural cracking, multiple flexural cracks developed along the beam until the point of first splitting was reached. The splitting pattern differed for each specimen based on the type of confinement within the splice zone and reinforcement detailing within the cross-section. That resulted in distinct stages of behaviour for the different specimens. In the following sections, the behaviour is discussed for each family separately and any deviations from the general pattern are explained.

5.2.1 Control unconfined specimens

At the splitting point, longitudinal side and bottom splitting cracks formed rapidly along splices leading to a sudden, brittle and loud failure. Figure 5-2 shows the failure of these specimens. As can be seen from the figure, splitting cracks developed on the side cover adjacent to the bar location along with the formation of slip interfaces. Few flexural cracks were observed to develop inside the splice region and these mostly appeared after failure.

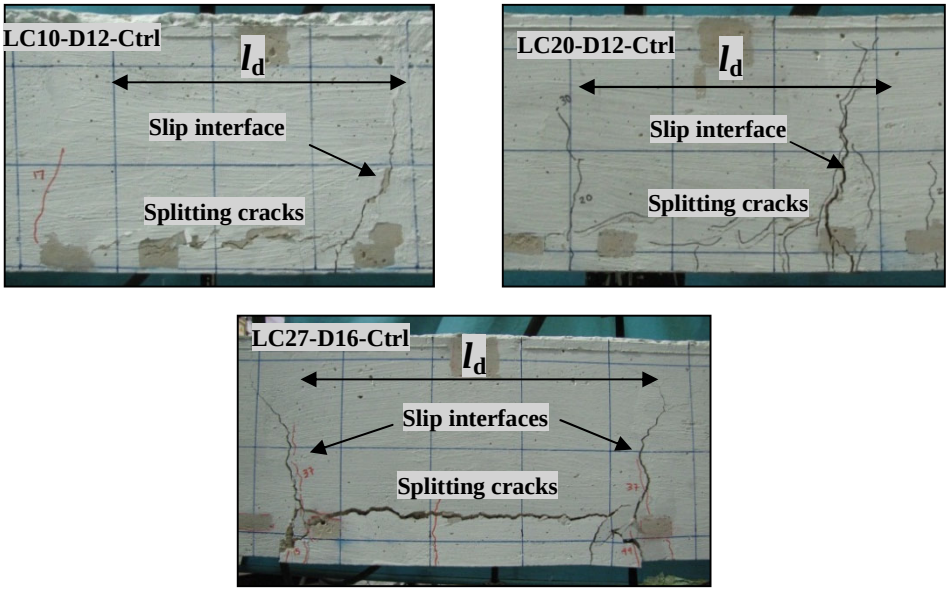

Figure 5-2: Modes of failure in the control unconfined specimens

The splitting cracks propagated mainly in a horizontal direction on the side of the beam ending with a flexural crack. On the underside of the beam, diagonal splitting cracks were also observed. These cracks led to detachment of the entire concrete cover. In specimen LC27-D16-Ctrl, the concrete cover between splices spalled-off instantly after splitting, as shown in Figure 5-3.

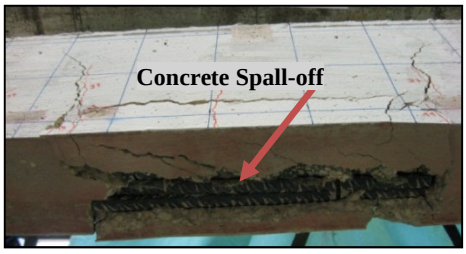

Figure 5-3: Spalling-off of the concrete cover in Specimen LC27-D16-Ctrl

The load resistance of the unconfined specimens was lost completely immediately after splitting. That indicated a complete loss of bond action between the reinforcing bars and the surrounding concrete. However, no collapse occurred in the beams after splitting due to the presence of the top flexural reinforcement.

During removal of the bottom cover concrete and revealing the splitting plane, it was observed that the failure of these specimens was caused by the sudden loss of bond between the bars and concrete such that both splices failed simultaneously, as shown in Figure 5-4.

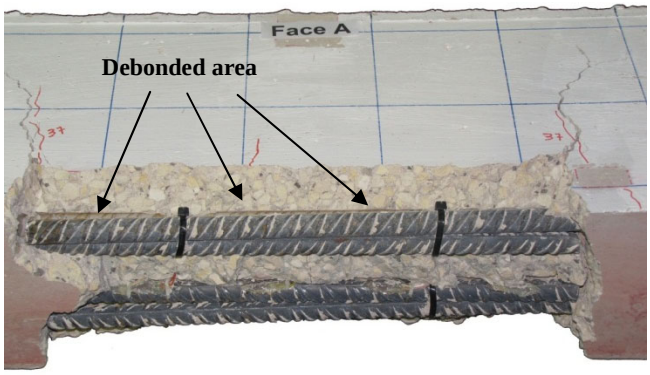

Figure 5-4: Loss of bond between steel bars and surrounding concrete of specimen (LC27-D16-Ctrl)

5.2.2 Internally confined specimens

After initial flexural cracking, splitting cracks were observed to initiate at one end of the splice and with further increase in loading they propagated along its entire length. At the post-peak stage, specifically after the third cycle, the splitting cracks started to widen and slip interfaces formed. These interfaces were noted to form at the end of the splice in specimen LC10-D12-S, see Figure 5-5. In specimen LC20-D12-S and LC27-D16-S, however, the interfaces were shifted to the stirrup location within the splice zone due to the flexural cracking at that location. Flexural cracks were more frequent, in general as well as in the splice zone, in these beams compared to the unconfined ones. Figure 5-5 and Figure 5-6 show the typical splitting cracks at the maximum load and at failure of these specimens, respectively.

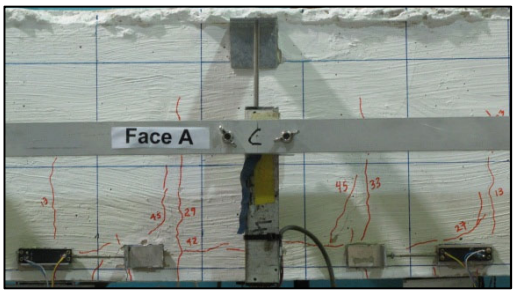

a) Side View

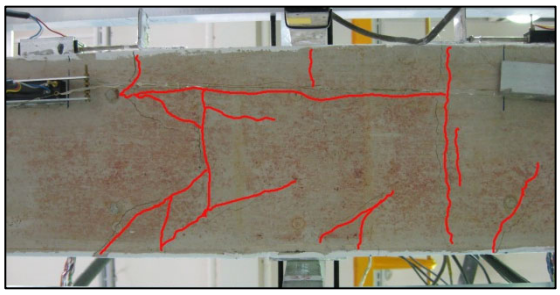

b) Bottom View

Figure 5-5: Typical splitting cracking at the maximum of the internally confined specimens, LC10-D12-S

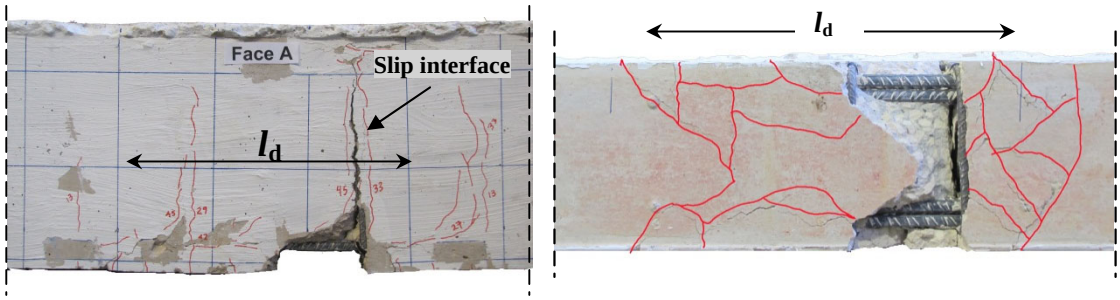

a) Side View b) Bottom View

Figure 5-6: Typical splitting cracking at failure of the internally confined specimens, LC10-D12-S

In this family, severe damage and many splitting cracks were observed to develop near the slip interface. That caused spalling of the concrete cover at that location as shown in Figure 5-6. Although the final mode of failure was due to side and bottom splitting of the cover, failure developed gradually and was more ductile compared to the unconfined specimen and was accompanied by the formation of multiple splitting cracks.

Unlike the unconfined specimens, failure of the internally confined beams was predominantly caused by pullout of one of the spliced bars, namely, internal or external bars. This was evidenced by the formation of a splitting plane on one side of the splices; and second by complete loss of bond action of slipping bars with the surrounding concrete after the cracked cover was removed. In specimen LC10-D12-S and LC20-D12-S, the failure occurred due to slip of the external spliced bars. The concrete bond with the internal bars was observed to be almost intact (see Figure 5-7). Specimen LC27-D16-S, on the other hand, failed due to slip of the internal spliced bars. The reason for this could be attributed to the fact that the minimum concrete cover to bar diameter ratio results from the distance between the spliced bars which was almost half the side or bottom ratio. That caused splitting of the concrete between the internal bars first, and as a result, slippage of those bars. A typical example of interconnection conditions of steel bars with concrete after exposing the bars is shown in Figure 5-7.

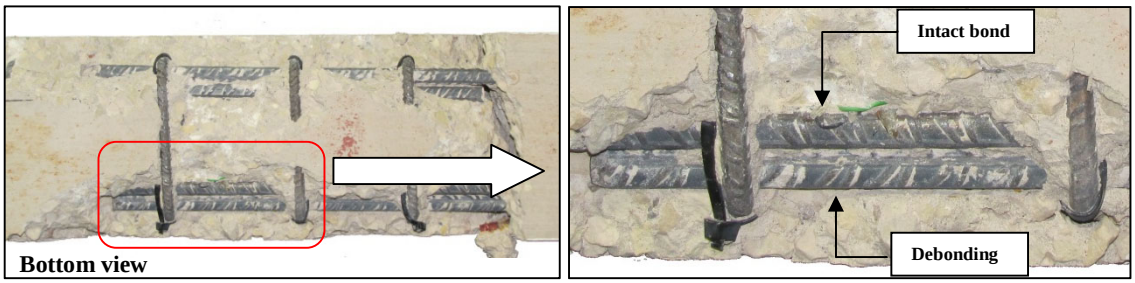

Figure 5-7: Loss of bond between concrete and steel bar of specimen LC20-D12-S

5.2.3 PTMS confined specimens

As the loading was increased after flexural cracking, it was observed that the width of the flexural cracks inside the splice region and their propagation along the depth of the cross-section

were noticeably less than the width and propagation of cracks outside the region. That is due to the fact that before splitting, there is twice as much of reinforcement in the splice zone as compared to outside. In most specimens, splitting cracks started as longitudinal cracks along the splices at the bottom side of the beam. With increase in loading, the cracks propagated to the entire splice length. After the maximum load was reached, the load dropped gradually in a rather ductile manner and this was accompanied by widening of the cracks. The resistance of beam LC10-D12-PTMS2, confined with a full jacket, however, dropped suddenly after bar yielding with a loud noise and this led to wide cracking at the slip interface. The reason for this is that the bars slipped suddenly after yielding in a pull-out manner. After the sudden drop, the resistance continued to diminish gradually with increasing deflections. No failure occurred in the strips or metal clips for any specimens. That prevented any spalling-off of the concrete cover in the splice region. Figure 5-8 shows a typical failure in this family.

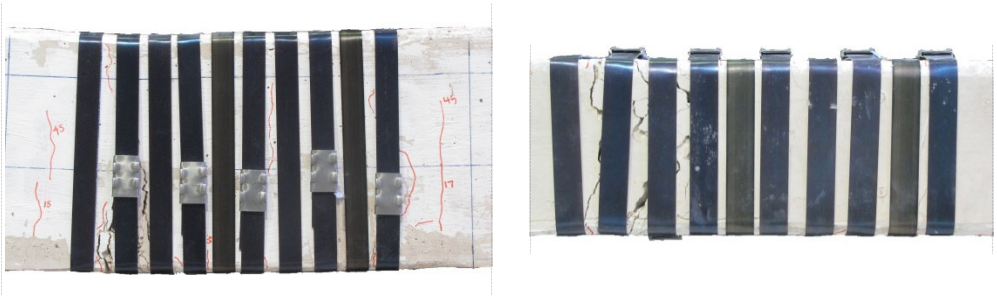

b) Side View b) Bottom View

Figure 5-8: Typical cracking patterns and failure modes of the PTMS confined specimens, LC10-D12-PTMS1

After the test was concluded, the strips were cut and removed from the splice zone to inspect better the mode of failure. The cracked cover was also removed to reveal the failure plane in the splice zone. Figure 5-9 shows a typical cracking mode after removing the strips. Figure 5-10 shows the failure surface after removing the cover concrete for the same specimen

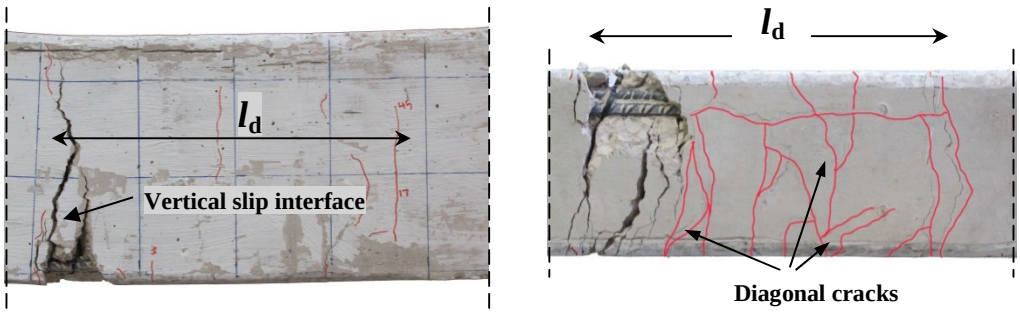

a) Side View b) Bottom View

Figure 5-9: Typical cracking patterns and failure modes after removing the confining PTMS, LC10-D12-PTMS1

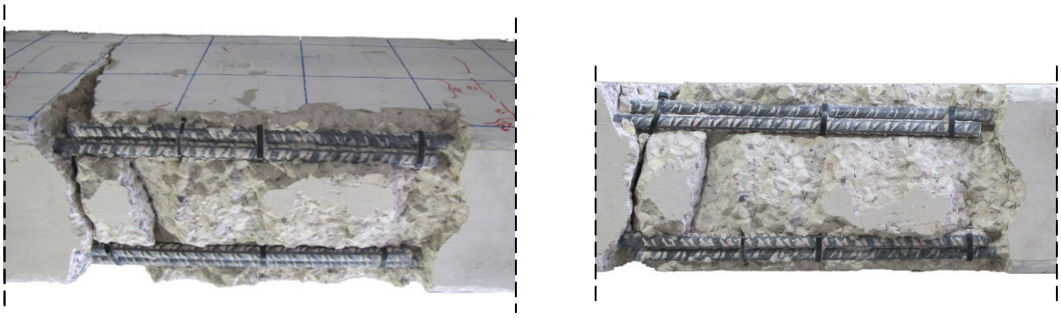

a) Isometric View b) Bottom View

Figure 5-10: Typical splitting plane after removing the cover concrete, LC10-D12-PTMS1

Based on observations from Figure 5-9 and Figure 5-10, the following conclusions were drawn for the PTMS confined specimens: 1) the cracking patterns were similar in all specimens regardless of the amount of confinement, concrete cover or bar size. This pattern was characterised by bottom splitting cracks along splices; 2) Splitting interfaces formed at the end of splices (i.e. at the vertical slip plane); 3) Severe damage occurred at the tension side of the splice interface resulting in spalling-off of the concrete cover at that location immediately after cutting the strips; 4) During the process of revealing the longitudinal splitting plane along the splices, it was observed that the damage due to splitting stopped in most specimens at the splice edges, as shown in Figure 5-10(a) and schematically explained in Figure 5-11. This indicates that the splitting cracks propagated in a diagonal manner along with bottom splitting; 5) The side cover of the spliced bars was relatively free of splitting cracks in most specimens; 6) Diagonal splitting cracks formed on the underside of the splice region, as shown in Figure 5-10(b); 7) The failure of all specimens was caused by pullout of internal lapped bars, and as a result, the slip interface always formed at the loaded end of those bars.

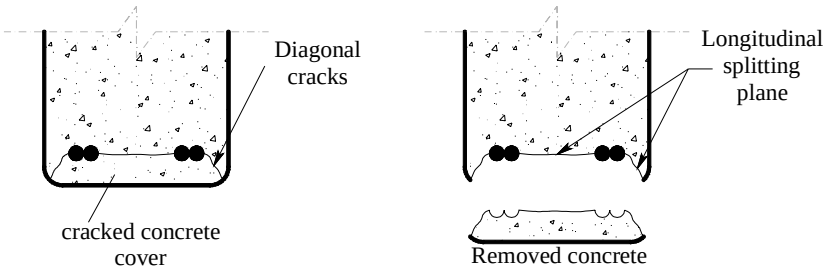

Figure 5-11: Horizontal splitting plane of a PTMS confined specimen

5.3 LOAD-DEFLECTION RESPONSE

The load-midspan deflection curves of the confined specimens in group I, II and III are compared to the companion unconfined ones in Figure 5-12, Figure 5-13 and Figure 5-14, respectively. As can be seen from the figures, a change in stiffness occurred at the point of first flexural cracking which was almost identical in each group. Thus, the presence of confinement within the splice zone did not influence the cracking load or flexural stiffness of the beams.

Also, from the same figures, it can be observed that the specimen response remained identical until the point of first splitting. Thereafter, softening in the response took place in all beams. The nature of the post-splitting response was dependent on the type of confinement within the splice zone and can be described as follows.

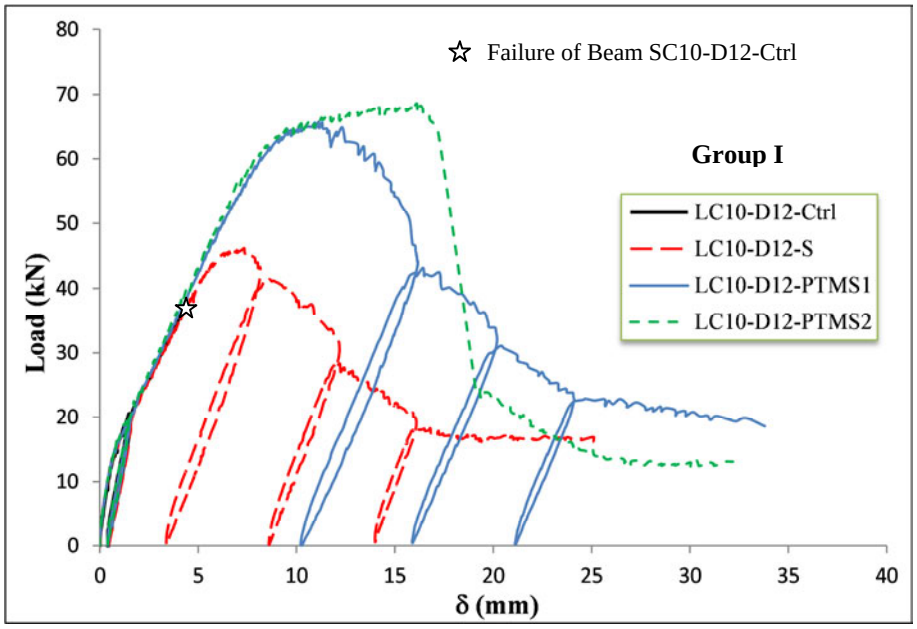

Figure 5-12: Load-deflection response of specimens in Group I

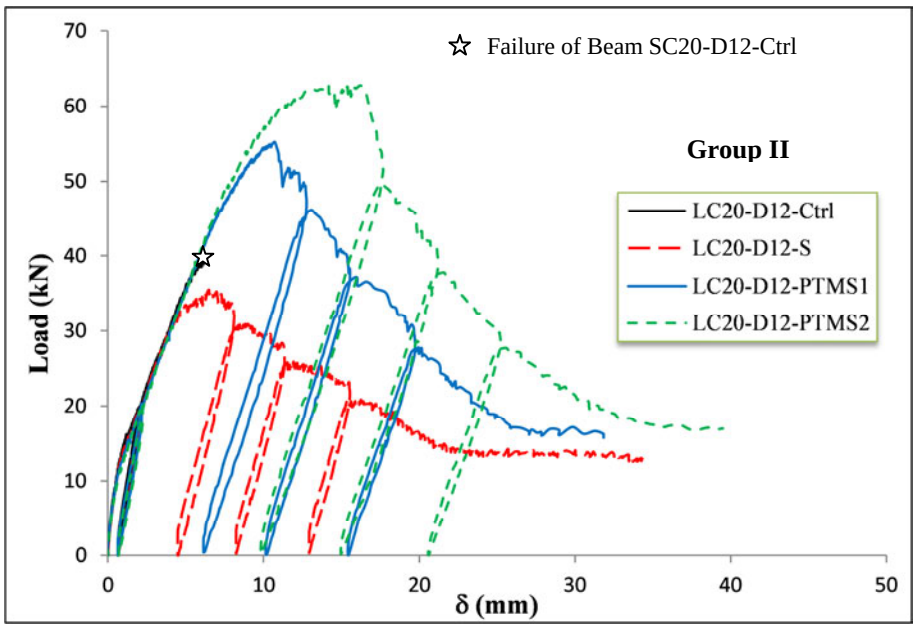

Figure 5-13: Load-deflection response of specimens in Group II

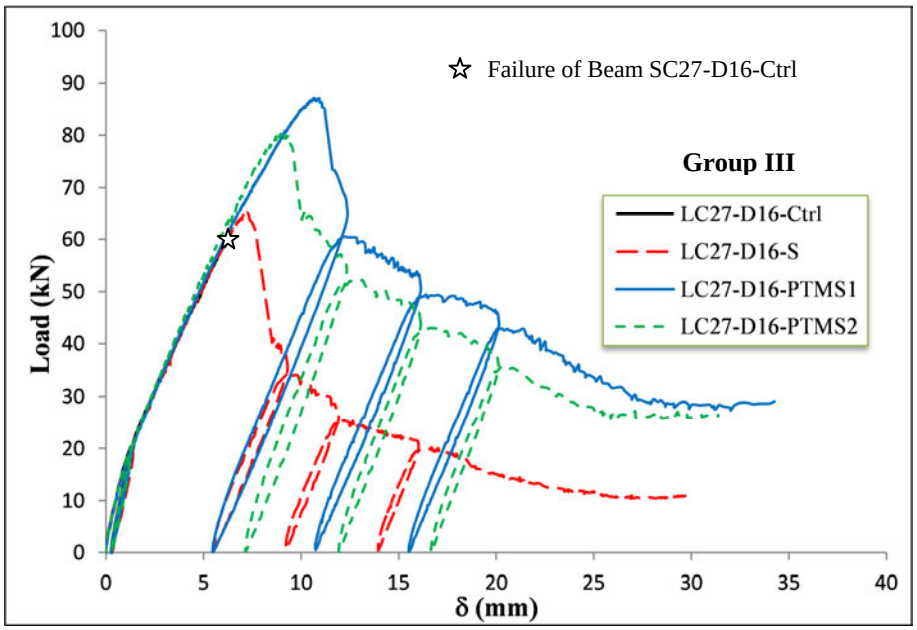

Figure 5-14: Load-deflection response of specimens in Group III

For the control unconfined beams, a sudden drop in stiffness along with a complete loss of load resistance occurred immediately after first splitting. The absence of confinement in the splice zone did not allow a gradual formation of cracks in the splice zone resulting in brittle behaviour. In these specimens, the failure is found to be related to the minimum concrete cover as it will be discussed in chapter 8. The measured maximum load capacities and corresponding deflection ratios were 36.2 kN and 0.55% for the specimen in Group I; 39.4 kN and 0.8% for the specimen in Group II; and 60.9 kN and 0.83% for the specimen in Group III.

For the internally confined specimens, the addition of stirrups in the splice zone resulted in higher load capacities (with the exception of specimen LC20-D12-S), higher deflections at the maximum load and more splitting cracks. The contribution of steel stirrups was more pronounced for the specimens with the smaller concrete cover to bar diameter ratio c_d/d_b. In groups I and III where the c_d/d_b ratio was 0.83 and 1, respectively, the stirrups inhibited the growth of early splitting cracks, and therefore, a noticeable improvement in the load resistance and deflections was observed compared to the unconfined specimens. In specimen LC20-D12-S, however, where the c_d/d_b ratio was 1.66, the stirrups did not increase the load resistance. Instead, the stirrup contribution was mainly in terms of deformability in the post-peak stage. In comparison to the unconfined specimens, the increase in maximum load was 27%, -10% and 7.4% for the specimens in Group I, II and III, respectively. The corresponding increases in midspan deflections at the maximum load were 74%, 6% and 12%.

For the PTMS confined specimens, the external confinement delayed the growth of splitting cracks which resulted in a substantial increase in load and deflection capacities and allowed for the gradual degradation in the post-peak response until large deflections were reached. In

comparison to the companion unconfined specimens, the increase in the maximum load was 81% (PTMS1) and 90% (PTMS2) in Group I; 40% (PTMS1) and 59% (PTMS2) in Group II; and 43% (PTMS1) and 32.5% (PTMS2) in Group III. The corresponding increases in deflections with respect to the unconfined specimens were 163% (PTMS1) and 280% (PTMS2) in Group I; 76% (PTMS1) and 160% (PTMS2) in Group II; and 72% (PTMS1) and 43% (PTMS2) in Group III. Although the first PTMS confined specimen of each family had the same A_{tr}/snd_b ratio of the companion internally confined specimen, the improvement in the load capacity and deflections was considerable. The increases were 42.5% (load) and 52% (deflection) for the PTMS1 specimen in Group I; 56% and 56% for the PTMS1 specimen in Group II; and 33% and 28% for the PTMS1 specimen in Group III. In comparison to the PTMS1 specimen, the increase in A_{tr}/snd_b ratio by 40% for the PTMS2 specimens in Group I and II comparatively improved the load capacity and increased substantially the deflections at maximum. This increase accounted for 4.4% (load) and 45% (deflection) for the PTMS2 in Group I; and 13.2% (load) and 50% (deflection) for the PTMS2 in Group II. In Group III, the PTMS2 specimen was doubly reinforced by strips at the same strip spacing of the PTMS1 specimen, yet no improvement was noticed. The reason is that the initial stress applied to double strips was less than that of the single strip due to the tensioning mechanism of the strip. Furthermore, the deformation on the tension side of the beam did not allow the mobilisation of strips to restrain the growth of the splitting cracks. Consequently, the use of single strips along the entire length was more effective than double strips. It also should be noted that the PTMS2 specimen in Groups I and II underwent yielding of the main flexural reinforcement. This highlights the effectiveness of the PTMS confinement since the splitting failure was altered to a pullout failure induced by splitting cracks.

Similarly to Phase I, the enhancement in the deformability of the test specimens due to the use of confinement was examined using deformability ratio. This ratio $\delta_{-30\%}/\delta_m$ represents the deflection at 30% drop in the load capacity to the deflection at the maximum load capacity. In case of yielding, the deformability ratio represents the deflection at 30% drop in the load capacity to the deflection at first yield. The deformability ratios of the test specimens are presented in Table 5-1.

From the table, it can be noted that the deformability ratio of the unconfined specimens are zero as they failed directly after the load reaches the maximum capacity. For the internally and PTMS confined specimens, it is interesting to note that the internally confined specimen show very close deformability compared to the PTMS specimens. This is attributed to the fact that the response of the internally confined specimens degraded equally or in a more gradual manner compared to the PTMS specimens, which showed fast degradation in the post-splitting stage. The PTMS specimens in group I, however, showed better enhancement in the deformability compared to the internally confined specimens due to yielding. In group III, it is clear that the

degradation rate of the all confined specimens are more or less similar resulting in almost equal deformability ratios.

To conclude, the confined specimens showed more ductile behaviour in the post peak stage. The ductility as well as deformability achieved by the PTMS confined specimens was somewhat more significant when compared to the internally confined specimens with the same A_{tr}/snd_b ratio.

Table 5-1 presents the test results including maximum loading F_{max} along with the corresponding deflections δ_{max}, deflection ratios DR%, δ/δ_{ctrl} ratio (deflection of the confined specimen to that of the companion unconfined one), and the A_{tr}/snd_b ratio.

5.4 DEFORMATIONS OF SPLICE ZONE

Measurement of crack widths at splice interfaces and along the entire lap length was done using potentiometers. Cracking, at least locally, means that slip deformations between reinforcement and surrounding concrete take place. Accordingly, the crack width measured at slip interfaces represents the total slip of a splice which includes pure slip due to bar slippage, as well as elongation of the bar. Therefore, bar elongation is subtracted from the total slip and the results are plotted versus load in Figure 5-15 through Figure 5-17. For comparison, the load was also normalised by the ratio of $(25/f'_c)^{1/4}$. It should be noted that failure of some potentiometers during the test prevented capturing the full response of some specimens. The load-total slip curves are given in Appendix F.

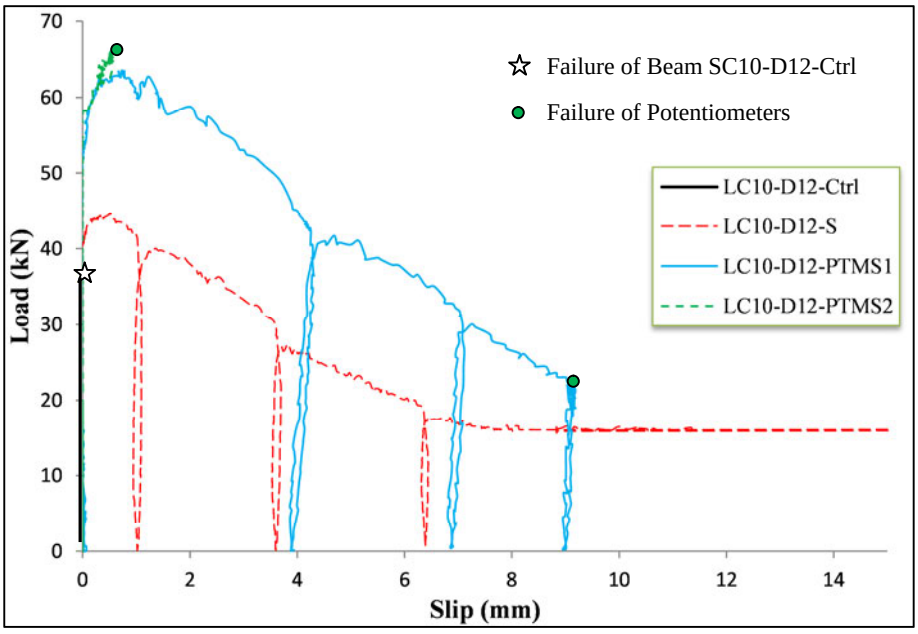

Figure 5-15: Load-pure slip of specimens in Group I

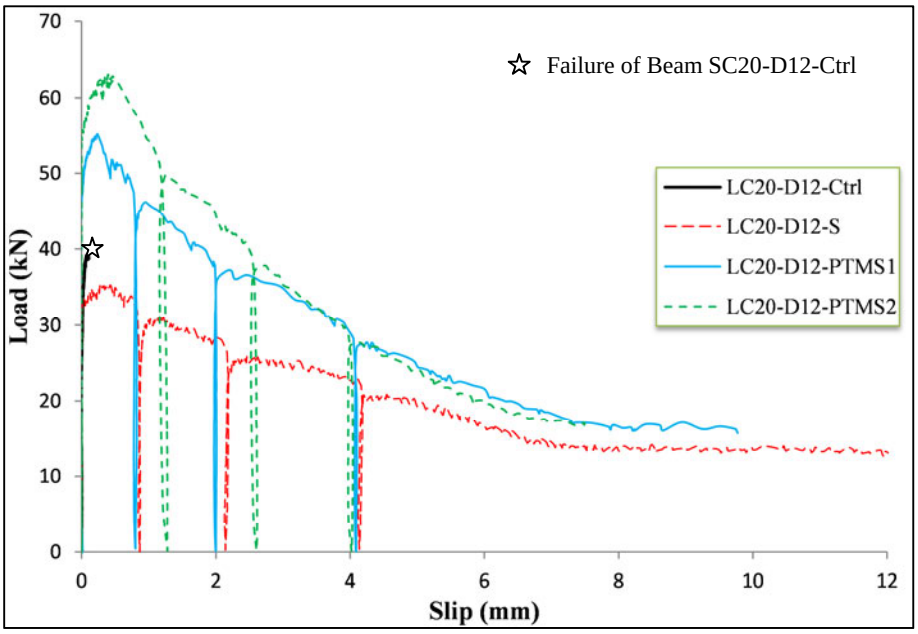

Figure 5-16: Load-pure slip of specimens in Group II

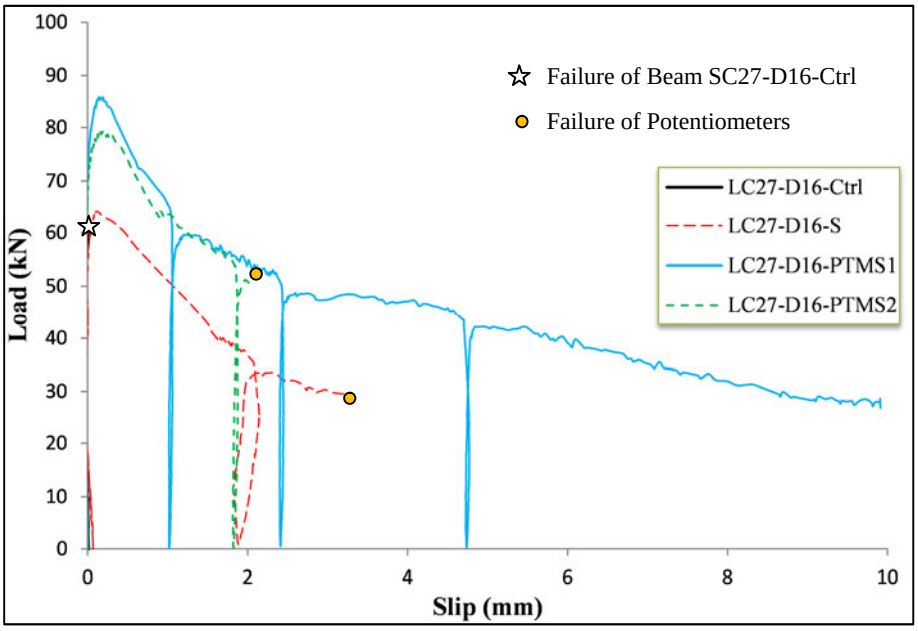

Figure 5-17: Load-pure slip of specimens in Group III

As can be seen from the figures, the load-slip response is, in general, analogous to the load-deflection response. The initial response is very stiff with practically zero slip values until the initiation of splitting cracking. Afterwards, the unconfined specimens tend to fail at practically zero slip values. Such behaviour would be expected in those beams as the absence of confinement does not allow the formation of gradual splitting cracks, which are the cause of bar slippage. The internally and PTMS confined specimens, on the other hand, show a reduction in stiffness accompanied by formation of multiple splitting cracks, and as a result, bar slippage. After the maximum load, bar slippage of those specimens increases rapidly due to excessive

splitting cracks in the splice zone. That is accompanied by a comparatively rapid drop in the load resistance. Afterwards, the load-slip response degrades gradually until it levelled off at high slip values which are found to be almost equal to bar spacing. An important observation is that the PTMS2 specimens of group I and II show a threshold at the maximum load before the degradation initiates. The slip values of the test specimens at the maximum load are presented in Table 5-2.

It is important to note that in all specimens and similarly to test Phase I, during unloading and reloading stages in the post-peak stage, as the load dropped, the slip did not recover indicating permanent loss of bond due to the excessive splitting cracking along the splices.

Table 5-2: Bond stress results of the test specimens

Group	***Specimen Notation***	F_{max} ***(kN)***	τ_{actual} ***(MPa)***	f_s ***(MPa)***	***s*** ***(mm)***	τ/τ_{bare}
Group I	LC10-D12-Ctrl	36.2	2.46	248	0.00	1.00
C_s=10*mm*	LC10-D12-S	46.1	3.76	348	0.52	1.53
d_b=12*mm*	LC10-D12-PTMS1	65.7	5.18	530	0.78	2.11
L_d=120*mm*	LC10-D12-PTMS2	68.6	5.75	527	1.16	2.19
Group II	LC20-D12-Ctrl	39.4	3.47	376	0.11	1.00
C_s=20*mm*	LC20-D12-S	35.5	3.40	281	0.50	0.98
d_b=12*mm*	LC20-D12-PTMS1	55.2	4.78	478	0.24	1.38
L_d=120*mm*	LC20-D12-PTMS2	62.5	5.31	530	0.39	1.53
Group III	LC27-D16-Ctrl	60.9	3.69	367	0.00	1.00
C_s= 20mm	LC27-D16-S	65.4	4.60	417	0.12	1.25
d_b=12mm	LC27-D16-PTMS1	87.2	4.97	494	0.19	1.35
L_d=160mm	LC27-D16-PTMS2	80.7	4.92	492	0.20	1.33

τ_{actual}, f_s and *s* are the actual bond values, average steel stress and the pure slip at the maximum load F_{max}, respectively.

5.5 BOND STRESS ALONG SPLICES

The calculation of average bond stresses (τ) along the splice length was based on strain readings from the strain gauges attached on the bar surface. By investigating the change in bar stresses over a finite length, *dl* between two points (i) and (i+1), of a spliced length, as illustrated in Figure 5-18 (a) and (b), it can be found that

$$(\sigma + d\sigma)A_{bar} = \sigma.A_{bar} + \tau.\pi.d_b.dl \quad \Rightarrow d\sigma.A_{bar} = \tau.\pi.d_b.dl \quad \Rightarrow$$

$$d\sigma.\pi.\frac{d_b^2}{4} = \tau.\pi.d_b.dl \Rightarrow \tau = (d\sigma/dl) \times (d_b/4) \Rightarrow \tau = E \times (d\varepsilon/dl) \times (d_b/4) \Rightarrow$$

$$\boldsymbol{\tau = E_s \times ((\varepsilon_{i+1} - \varepsilon_i)/dl) \times (d_b/4)} \quad 5\text{-}1$$

in which τ is the average bond stress, d_b is the nominal bar diameter, A_{bar} is the bar area, σ is the stress in the bar and E_s is the modulus of elasticity of the steel bars. The value of *dl* can be taken as the distance between two consecutive strain gauges, as illustrated in Figure 5-18(c).

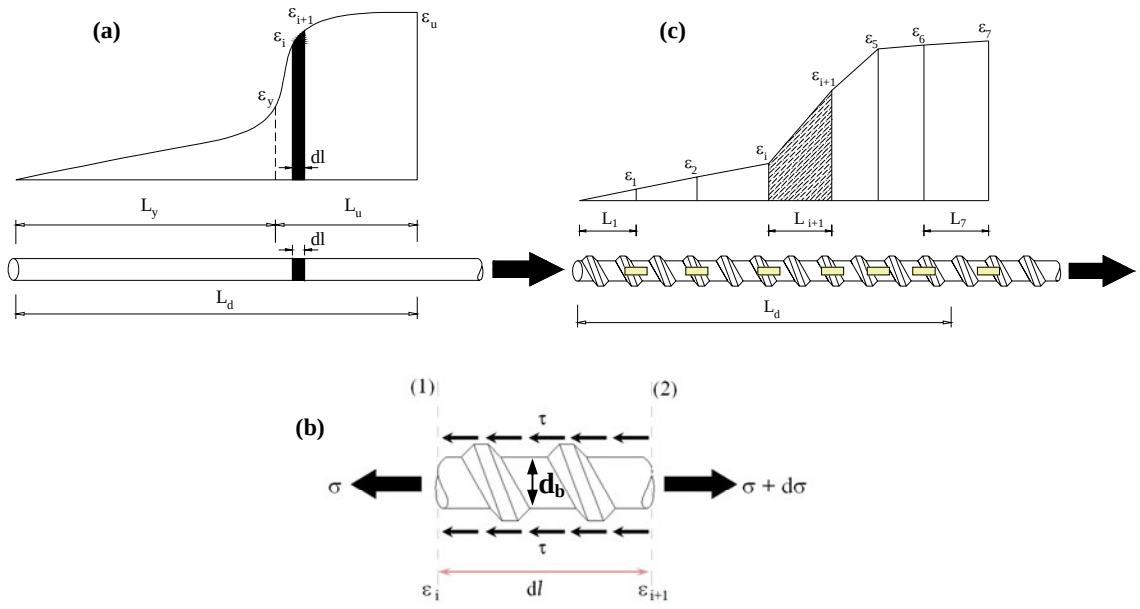

Figure 5-18: a) Typical strain profile along a spliced bar with a length of L_d, b) change of bar stresses along an finite length *dl* of the reinforcing bar and c) strain profile considering strain gauge readings

From equation (5.1), it can be deduced that the bond stress distribution along the bar is dependent on the strain profile as well as the steel stress-strain relationship.

The calculated bond values from Equation (5-1) were assigned to the mid-distances between the strain gauges. Accordingly, bond stress distributions along splices were derived and are described in the next section. Based on these distributions, the average bond stresses overall the splice length, bond ratios and steel stresses at maximum were calculated and are presented in Table 5-2. The bond ratio τ/τ_{bare} is the bond stress of the confined specimen divided by that of the companion unconfined one.

5.6 STRAIN AND BOND STRESS DISTRIBUTIONS OVER THE SPLICED LENGTH

For clarity, the strain and bond stress profiles over the spliced length are plotted for load increments of about 10 kN, up to the failure load. It should be noted that some strain gauges failed before or during the test and those were excluded from calculations. The strain gauge failure can be due to various reasons such as:

• Disconnection of the wire from the terminals of the strain gauge during casting.

• Damage of the strain gauge during casting due to the vibration process.

• Detachment of strain gauges or wires due to bar slippage or excessive cracking along the gauge or the connection terminal.

Strains at the unloaded end are assumed to be zero during the calculations. Readings from the strain gauge situated outside the splice length are used to determine the force at the loaded end. It is important to note that the recorded strains were affected by the crack pattern along the splice. In general, a strain gauge located close to a crack indicates higher strain values than a strain gauge positioned in the middle of the distance between cracks. This difference becomes more prominent at higher load levels.

The strain gauge numbers on the spliced bars and steel stirrups are illustrated in Figure 5-19. It should be mentioned that the strain-gauged splice is always located on face B of the beam.

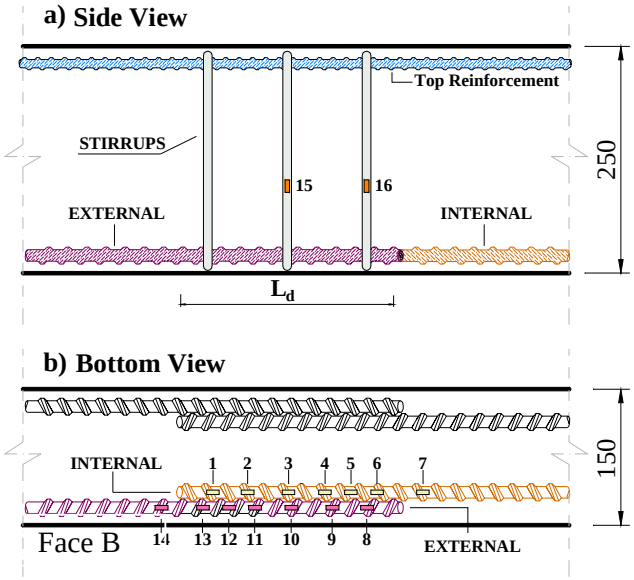

Figure 5-19: Arrangement of strain gauges on the splice and stirrups

- **Influence of flexural cracks on strain and bond distributions along spliced and anchored bars**

In order to produce appropriate strain and bond distributions for the spliced bars at midspan, the influence of main flexural cracks on these distributions should be understood. An expected profile for strain distribution between successive cracks along a single bar for a normal beam in flexure is shown schematically in Figure 5-20(a). Each end of the bar can be considered to be subjected to a pullout force. The higher force (F_s+dF_s) is normally located at the section closer to the midspan of the beam. These forces are expected to create strain and stress distributions prior to yield as shown in Figure 5-20(a-(i)). The distributions are similar to that of two single pullout bars acting separately, as explained in sec 5.5. The resultant normal stress and strain

distributions along the bar between cracks are the summation of both strain profiles along the bar, as shown in Figure 5-20(a-(ii)).

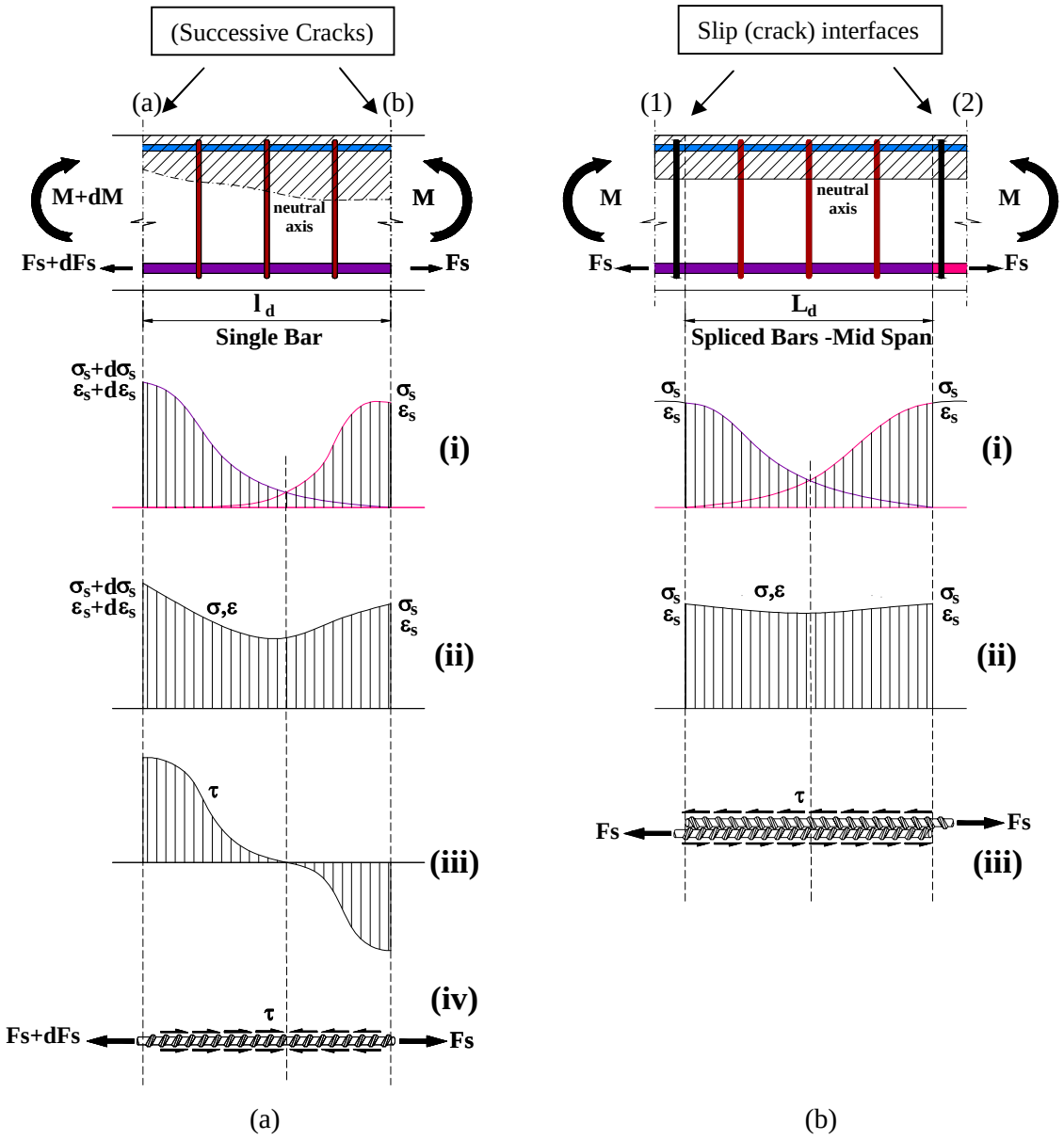

Figure 5-20: Typical strain and bond stress distributions between successive flexural cracks of a) single bar, and b) spliced bars at mid span

The bond stress distribution can be deduced from the stress distribution (provided the σ–ε characteristics of the steel material are known) as it is proportional to the rate of change of stress. Profile (iii) in Figure 5-20(a) shows an indicative bond stress distribution between successive cracks. As can be seen from the figure, the bond distribution includes positive and negative values. This is due to the fact that the bond stress acts in different directions at the two ends of the bar so as to resist the pullout forces, as shown in profile (iv) in Figure 5-20(a). The average bond stress along the bar between cracks is defined as the area between the bond curve and the bar axis and it is always lower than the peak values.

The behaviour of splices is more complicated compared to that of a single bar. In lap splices, both bars interact with each other to form a complex force transfer mechanism. In this study, the spliced bars are located at the midspan with symmetrical loading on both sides. In most of the test beams, main flexural cracks were located at the end of the bars as explained previously in sec 5.2. Moreover, due to the large stress demand adjacent to the cracks, imposed by the difference in the cross-sectional properties, cone-type cracking was found to develop locally at the very end of the splice.

The expected profile of strain and bond stress distributions of a typical lap splice is shown schematically in Figure 5-20(b). Both spliced bars are subjected to the same pullout forces which should produce symmetrical normal strain distributions (profile (i) of Figure 5-20(b)) along the lap length. It is important to note, however, that the concrete contribution of the lapped bars in a splice assembly differs slightly which in turn causes a slight difference in strain and bond stress distributions.

In this investigation, the behaviour of a splice is examined based on the strain and bond distributions of the single bars. It should be noted though that the distributions are somewhat affected by the number of strain gauges considered along the spliced length. In the following sections, strain and bond stress distributions of each family are explained and compared. Moreover, average bond stresses over the splice length of the single bars are calculated and compared during the different loading stages. Comparisons between the families are also made.

5.6.1 Control unconfined specimens

As explained previously in SEC 5.2.1, the control specimens failed due to loss of bond resistance at an early stage prior to yield. Moreover, failure was due to splitting which occurred suddenly. No flexural cracks appeared until just before failure. The flexural cracks were mostly located close to the splice ends.

5.6.1.1 Specimen LC10-D12-Ctrl

The characteristic normal strain distributions along the internal and external bars are plotted in Figure 5-21(a). The external bar seemed to be slightly more stressed than the internal bar and this may be attributed to the concrete contribution. The failure occurred at strains of 1090 με (internal bar) and 1267 με (external bar) recorded at the loaded end of the bar. These values correspond to stress values of 229 MPa and 266 MPa, respectively. At low load levels, the strains are very small but evenly distributed along the bar. As the load increases, the strains at the loaded end increase rapidly. The rate of change in strains is higher close to the loaded end. Near failure, the strain profiles tend to be linear with slightly lower strain rate of change close to the loaded end. No sudden change in strain profiles occurred, because the splice zone is almost void of flexural cracks. The rate of change at the unloaded end area was also noted to be high due to the interaction of the spliced bars.

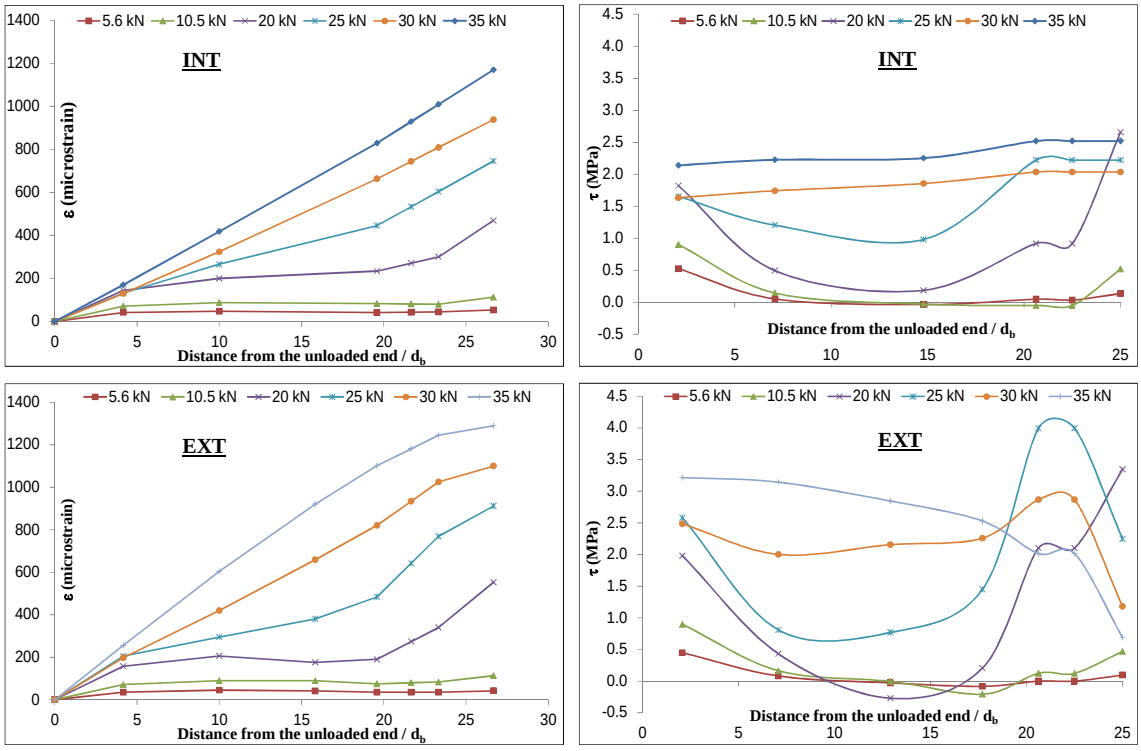

(a) (b)

Figure 5-21: (a) Normal strain and (b) bond distributions along the single bars of specimen LC10-D12-Ctrl

The bond stress distributions along the spliced bars are shown in Figure 5-21(b). As the strain profiles of the internal bar were nearly linear, their resulting bond distributions were more uniform compared to those of the external bar. However, the bond profiles of both bars had the same tendency during loading. At the beginning of loading, the peak bond value tended to form at both bar ends, as expected, whereas the middle part had almost zero bond stresses. With increase in loading, the peak bond at the loaded end started to migrate towards the middle of the lap length. This migration was limited by the sudden failure of the specimen. Thus, the peak value formed at a distance of about $4d_b$ from the loaded end where the slip interface formed suddenly.

From visual observation, it was found that the slip interface formed towards the loaded end of the external bar. As can be seen from Figure 5-21(b), the highest bond stresses were located close to the loaded end of the external bar exactly where the failure took place. However, near failure, the bond stress at that location dropped considerably.

Figure 5-22 shows the average bond stresses over the lap length versus the load up to failure for both spliced bars. As can be seen from the figure, after the cracking load is reached, the splice zone tends to attract bond stress at a higher rate until a load of 25 kN where the rate reduces slightly until failure. The external bar has higher average bond values throughout the different loading stages compared to those of the internal bar. The average bond strength at failure is calculated at 2.29 and 2.66 MPa for internal and external bars, respectively.

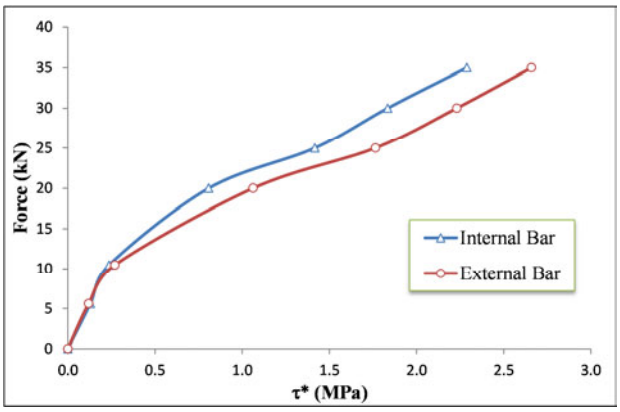

Figure 5-22: Average bond stress along the internal and external bars

5.6.1.2 LC20-D12-Ctrl

The characteristic normal strain distributions along the internal and external bars are plotted in Figure 5-23(a). Unlike the first control specimen, at low load levels, the internal bar is more stressed than the external one. However, as the load increases, more strain develops along the external bar. The maximum strains achieved were 1594με (internal bar) and 1688με (external bar) recorded at the loaded end of spliced bars. These values correspond to steel stresses of 334 MPa and 351 MPa, respectively. The higher rate of change in strains always occurs at the loaded end. Near failure, the strain profiles along the bar are more or less linear. It is expected in this specimen that the splice failure is due to bond failure of external bars as the concrete contribution is less compared to that of the internal ones.

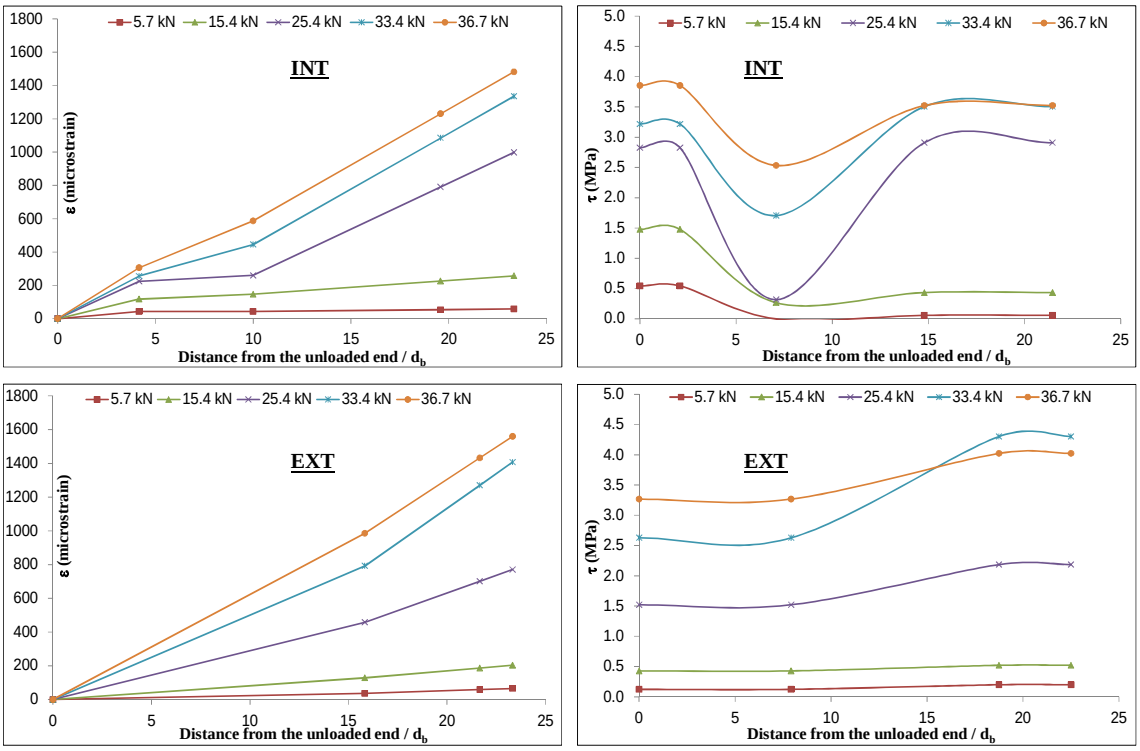

(a) (b)

Figure 5-23: (a) Normal strain and (b) bond distributions along the single bars of specimen LC20-D12-Ctrl

The corresponding bond stress distributions along the bars are plotted in Figure 5-23(b). As can be seen from the figure, the external bar has more uniform distributions compared to those of the internal one, which could be attributed to the number of strain gauges considered. The unloaded end of the internal bar appears to attract more bond stresses at the beginning of loading which is probably due to local cracking. The external bar, on the other hand, has uniform bond distribution at low load levels. With increase in loading, higher bond values develop at the loaded end.

In this specimen, the slip interface at failure is located at the loaded end of the external bar. The bond stress at that location is found to have a peak at around 4.5 MPa. Before failure, however, the loaded end of the internal bar attracts higher bond stresses.

The average bond stresses over the lap length of both bars are shown in Figure 5-24. The characteristics of the curves are found to be similar to those of the first specimen. It is clear though that the increase in concrete cover, compared to LC10-D12-Ctrl, has influenced the interaction mechanism between the bars such that the internal bar contributed more to the splice strength. As the external bar had less bond capacity, the bar showed rapid increase in bond stresses near failure reaching its maximum value and causing the failure of the splice assembly. The average bond stress developed at the maximum loading was calculated at 3.34 MPa and 3.52 MPa for the internal and external bars, respectively.

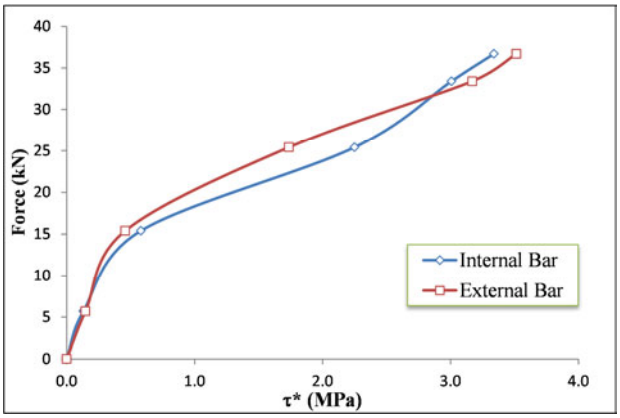

Figure 5-24: Average bond stress along the internal and external bars

5.6.1.3 LC27-D16-Ctrl

The normal strain distributions along the spliced bars are shown in Figure 5-25(a). At low load levels, both bars have the same stress level. Moreover, the strain distributions are similar along the bars. The external bar attracts somewhat more stresses as the load increases. Near failure, the loaded end tends to be highly stressed for a distance of about $5d_b$. In addition, the unloaded end of both bars has the highest rate of change. It should be mentioned that the difference between the strain profiles of the two bars is due to the number of strain gauges considered. The maximum strains achieved at the loaded end are 1484με (internal bar) and 1608με (external bar)

corresponding to steel stresses of 356.2 MPa and 385.9 MPa, respectively. In this specimen, the minimum cover to bar diameter ratio results from the external bar. However, the ratio was very close to the internal one. Thus, as expected the external bar reached higher stresses than the internal one.

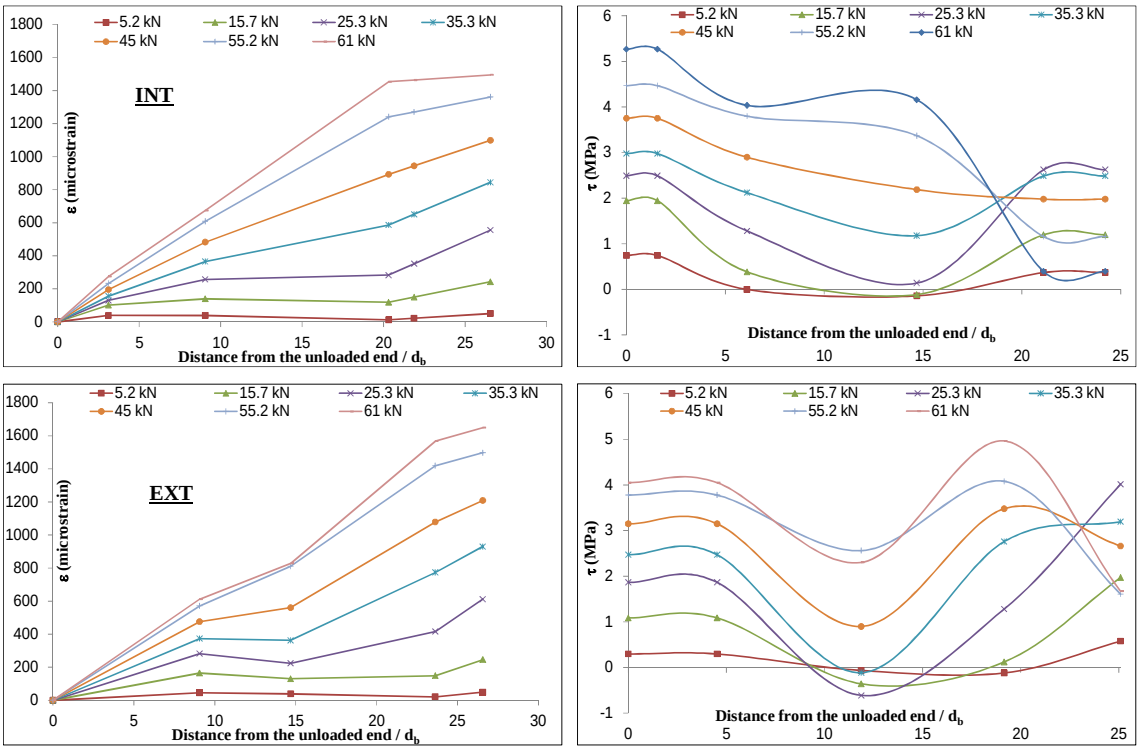

(a) (b)

Figure 5-25: (a) Normal strain and (b) bond distributions along the single bars of specimen LC27-D16-Ctrl

The bond stress distributions of internal and external bars are plotted in Figure 5-25(b). At low load levels, the peak bond develops at both ends of the bars with zero values along the middle part. With increase in loading, the peak bond is located at the unloaded end while the peak of the loaded end tends to migrate towards the middle. Near failure, it is found that the bond at the slip interfaces of both bars reduces considerably. The failure in this specimen, based on visual observations, takes place at both bar ends simultaneously where the bond deteriorates the most.

The average bond stresses over the splice length of both bars are plotted in Figure 5-26 versus the load. As can be seen from the figure, both bars have the same bond values until the cracking point. After that, the external bar tends to attract more loading. The average bond strength at the maximum load is calculated at 3.56 MPa and 3.85 MPa for the internal and external bars, respectively.

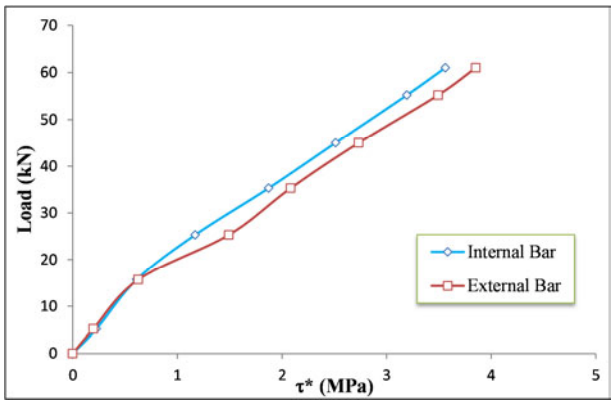

Figure 5-26: Average bond stress along the internal and external bars

5.6.1.4 Comparison of unconfined specimens

The average bond stresses over the spliced bars of the unconfined specimens are plotted versus load in Figure 5-27. The calculated average bond values are 2.47, 3.43 and 3.71 MPa for specimens in group I, II and III, respectively. Normalising these values to a concrete strength of 25 MPa, by a ratio of $(25/f'_c)^{0.68}$ in line with the latest finding by Sohaib (2011) for unconfined anchored bars, results in values of 2.26, 3.43, and 3.56 MPa, respectively. It is clear that specimen LC10 had failed at lower bond stresses as it had the lowest c_d/d_b ratio of (0.92) among the unconfined specimens. Specimen LC27, on the other hand, showed the highest bond strength among the unconfined specimens although it had c_d/d_b of 1.31, which is less than 1.42 of specimen LC20. The increase in c_d/d_b ratio of specimen LC20 by 54% compared to LC10 led to an increase in the bond strength of 52%, which is almost the same ratio. In addition to the increase in c_d/d_b ratio, the increase in bar diameter in specimen LC27 seemed to have more influence on bond strength, which was enhanced by 58% and 4% compared to that of specimen LC10 and LC20, respectively. The load-bond curves of all specimens have the same characteristics. Further comparisons are discussed later with regard to bond-slip relationships.

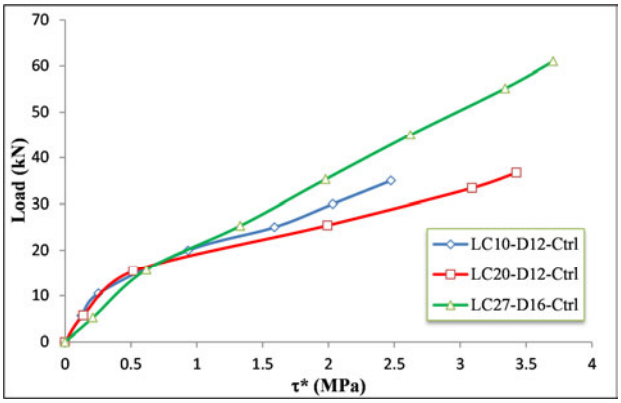

Figure 5-27: Actual average bond stresses of control specimens

5.6.2 Internally confined specimens

The splitting cracks in these specimens developed initially at the very end of the splice and as the load increased, they propagated along the entire lap length. The beam specimens failed due

to splitting prior to yield. The flexural cracks initiating at link locations at early loading stages caused slip interfaces to shift to these locations in some specimens.

5.6.2.1 LC10-D12-S

The slip interface of this specimen formed towards the loaded end of the external bar but shifted to the first link location. In such specimen, where the concrete cover is very small and the stirrups are located near the surface, flexural cracks most likely tend to form first at stirrup locations and as a result shift the slip interface. The characteristic normal strain distributions of the internal and external bars are plotted in Figure 5-28(a). In general, at early loading stages the strain profiles are more or less uniform. With increase in loading, the loaded end regions tend to be more stressed with high rate of change. The unloaded end region of the bars, however, had lower strains but high rate of change due to the interaction of the coupled spliced bars. The mid area seems to be evenly stressed until loading levels above 60% of the maximum load. At this loading level, the external bar starts to experience higher strains than those of the internal one due to the formation of splitting cracks at the loaded end of the bar. Near failure, the external bar has almost linear strain distribution with comparatively constant rate of change. The internal bar, on the other hand, is stressed with slow rate of change to a length of $15d_b$ from the loaded end. Afterwards, the strains decrease rapidly up to the unloaded end with constant but higher rate. The higher strains achieved at the loaded end at failure are 1663με (internal bar) and 1865με (external bar) corresponding to steel stresses of 349.1 MPa and 391.6 MPa, respectively.

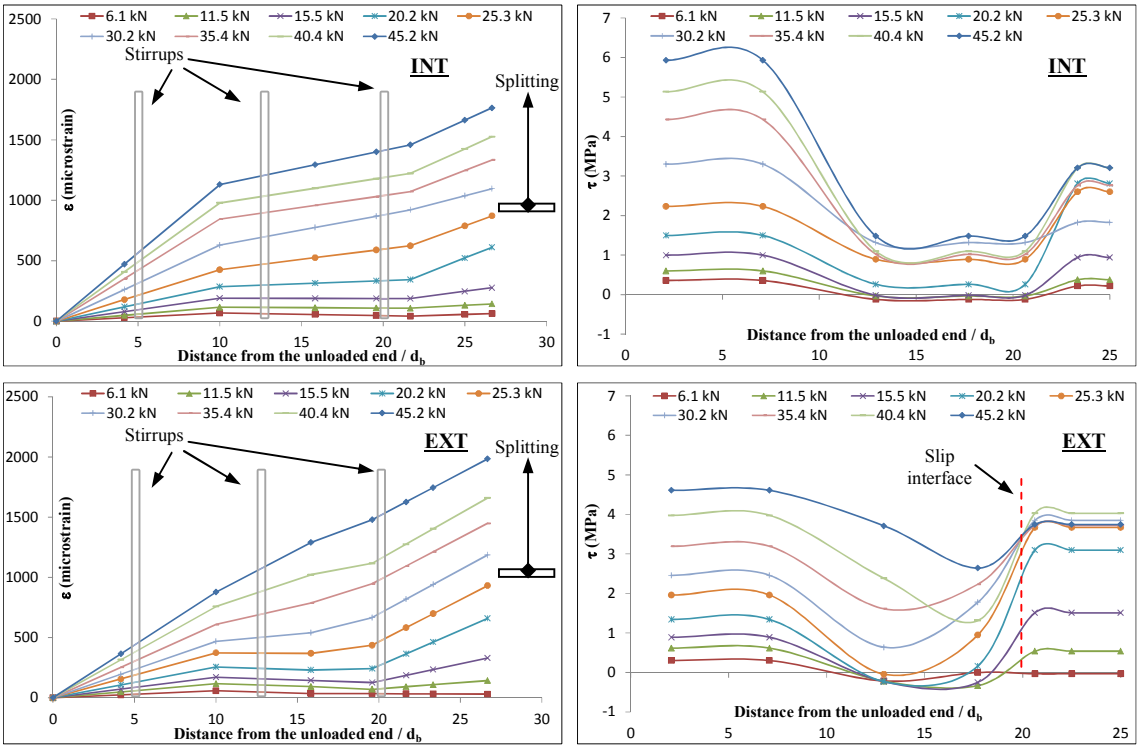

(a) (b)

Figure 5-28: (a) Normal strain and (b) bond distributions along the single bars of specimen LC10-D12-S

Bond stress distributions along both bars are shown in Figure 5-28(b). It is clear that both bars experience the same trend during loading such that higher bond develops at the bar ends and less bond at the middle region. However, the external bar appears to develop higher and more uniform bond values than those of the internal bar. This could be attributed to cracking of the concrete matrix surrounding the external bar due to splitting cracks. The region between the loaded end of the external bar and slip interface (which is also the region between the unloaded end of the internal bar and slip interface) had high and almost uniform bond values. Near failure, the bond stress degraded slightly at the loaded end of the external bar.

The calculated average bond stresses over the lap length are plotted in Figure 5-29 for both bars. It is clear that after a load of 42 kN (or bond of 3.2 MPa), where splitting cracks tended to propagate rapidly along the splice accompanied by initiation of bar movement, the bond strength increased less rapidly towards its maximum. At the maximum load, the average bond strength was calculated at 3.5 and 3.92 MPa for the internal and external bars, respectively.

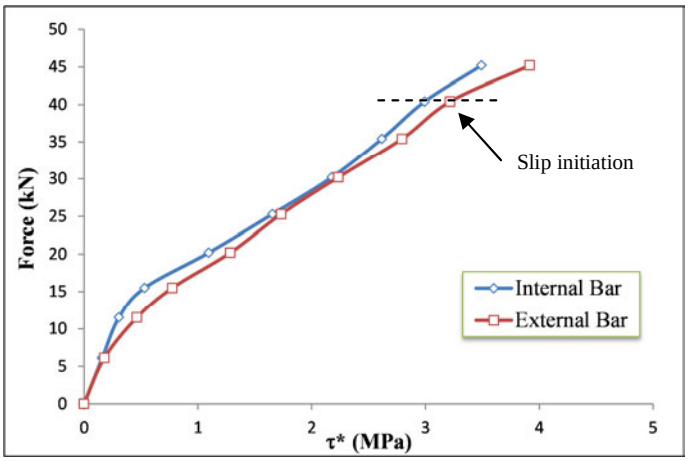

Figure 5-29: Average bond stress along the internal and external bars

5.6.2.2 LC20-D12-S

In this specimen, the slip interface formed at the loaded end of the external bars. However, the slip interface extended to the first link location causing moderate damage near failure. Flexural cracks in the splice zone initiated first at the end of the external bars at a load of 22.5 kN. Flexural cracks also appeared subsequently at the other link locations. Splitting cracks appeared at a load of 34 kN and spread rapidly along with slip of the external bars. The normal strain profiles along the splices are plotted in Figure 5-30(a). The behaviour of the internal bar is similar to that of the first specimen. The external bar, however, differs because of the use of only three strain gauges along the splice length. This affects slightly the distribution of strains along the mid area such that the rate of change becomes higher, starting from the unloaded end until the first strain gauge. In general the external bar has relatively lower strains as well as rate of change compared to that of the internal one. The maximum strains recorded at the loaded end

of the bars were 1433με and 1331με for the internal and external bars, respectively. These values correspond to steel stresses of 301 MPa (internal bar) and 279.4 MPa (external bar).

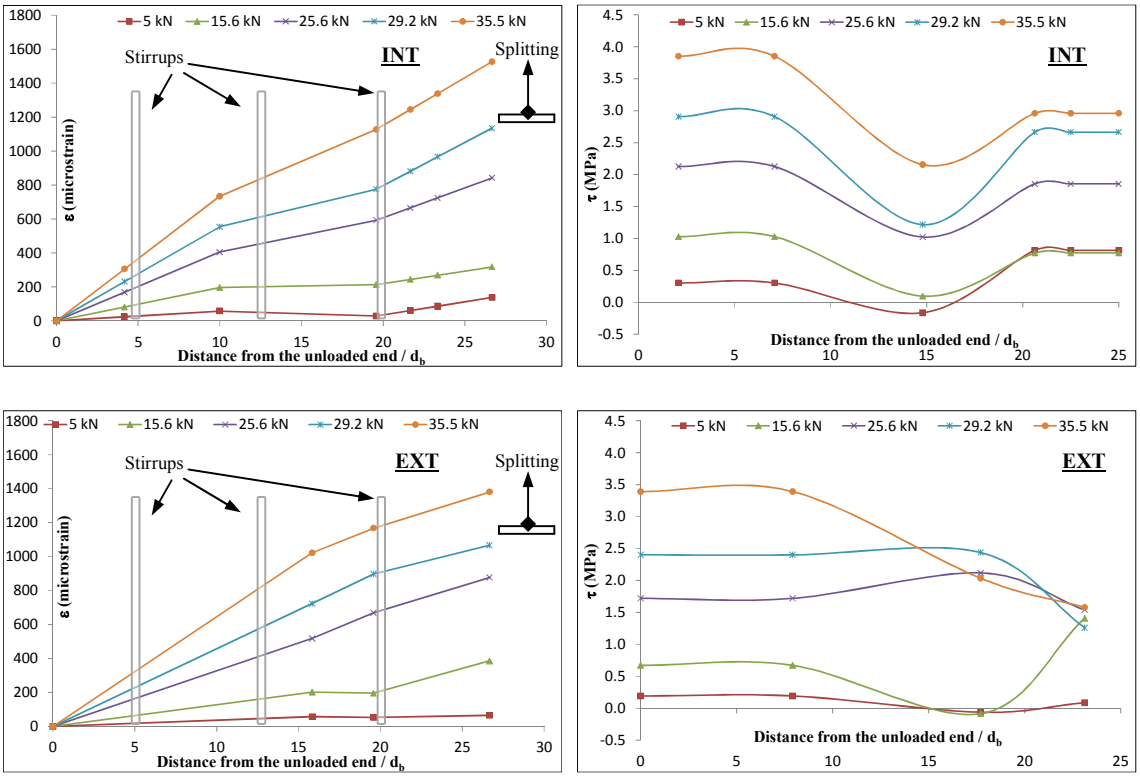

(a) (b)

Figure 5-30: (a) Normal strain and (b) bond distributions along the single bars of specimen LC20-D12-S

Figure 5-30(b) shows the corresponding bond stress distributions along the spliced bars. For the internal bar, the peak bond formed locally at both ends whereas the mid segment had lower bond values as expected. As the loading continued, the peak started to propagate along the mid segment of the bar. The external bar profile shows a similar trend to that of the internal one; but with increase in loading, the peak at the loaded end remained more or less constant.

The average bond stresses of both bars are plotted in Figure 5-31. Both bars showed comparatively similar capacity up to a load of 34 kN. At this load, corresponding to a bond stress of 2.6 MPa, slip of the external bars occurred. The average bond at the maximum load was calculated at 3.0 and 2.79 MPa for the internal and external bars, respectively. It can be noted that the internal bar showed a higher bond value at the maximum load than the external one but it did not fail. This can be attributed to the fact that the internal bar did not slip.

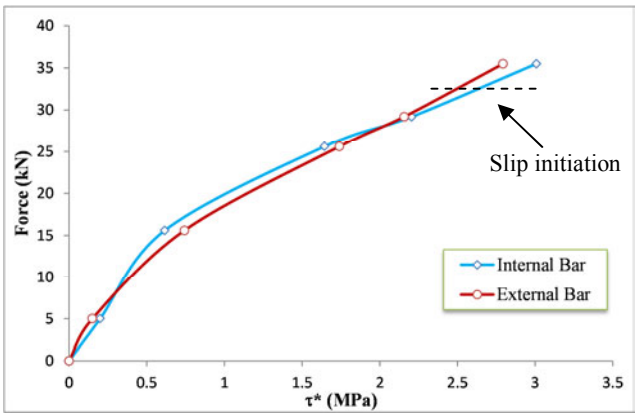

Figure 5-31: Average bond stress along the internal and external bars

5.6.2.3 LC27-D16-S

Similar to specimen LC10-D12-S, the slip interface was shifted to the location of first link, but the one adjacent to the loaded end of the internal bars. Flexural cracks initiated first at the end of internal bars. With increase in loading, flexural cracks appeared at the other splice end and at the link location closest to the end of external bars. Splitting cracks appeared first between the end of the internal bars and the adjacent link location at a load of 60 kN then spread very rapidly along the splice length. The characteristic normal strain distributions along the bars are plotted in Figure 5-32(a). The maximum strains recorded at the loaded end of the internal and external bars are 1608 με and 1878 με, respectively. The corresponding steel stresses are calculated at 386 MPa and 450.8 MPa, respectively.

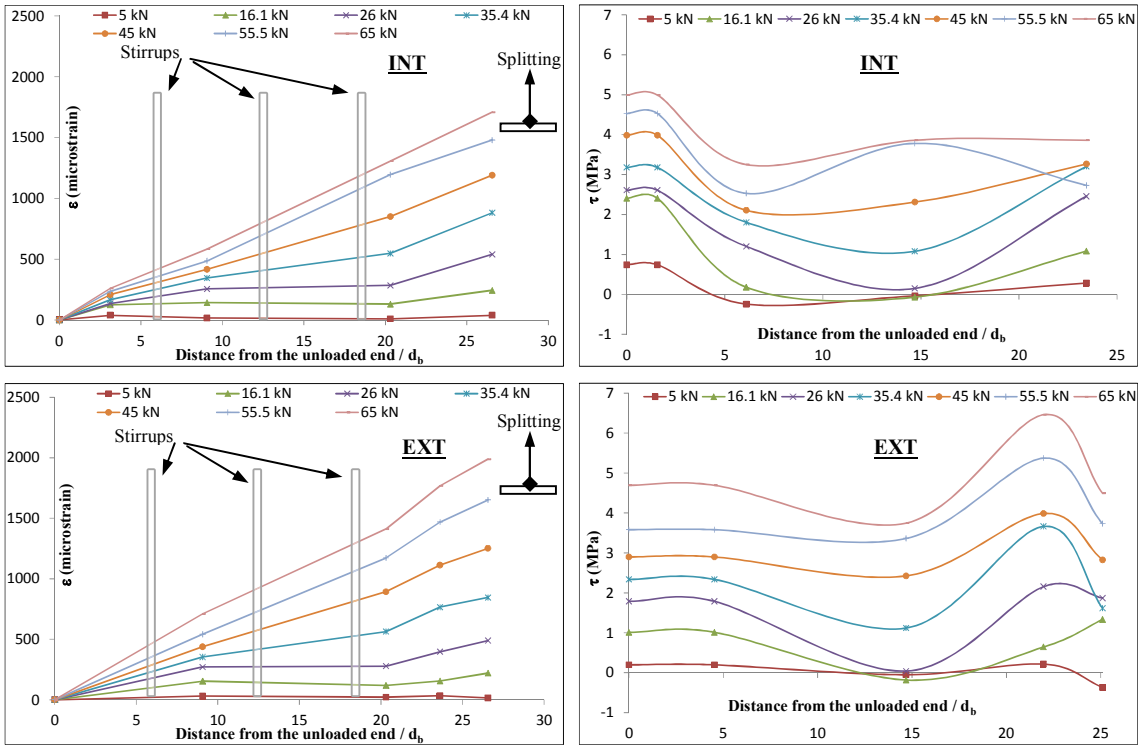

(a) (b)

Figure 5-32: Normal strain distributions along the single bars of specimen LC27-D16-S

The average bond stresses along the spliced bars are plotted in Figure 5-32(b). The peak bond formed locally at both bar ends. The bond at the mid segment was low at the first stages of loading until some local flexural cracking took place in the splice zone (up to load of 26 kN). Afterwards, the bond increased rapidly and uniform distributions resulted along most of the lap length.

The average bond stress over the spliced bars is plotted versus load in Figure 5-33. The bond stresses at the maximum load was calculated at 3.86 MPa and 4.49 MPa for the internal and external bars, respectively. Apparently, the internal bars had lower bond capacities than the external ones. This is expected in this specimen due to the fact that the minimum c_d/d_b ratio results from the spacing between the internal bars which in turn reduces the concrete contribution. It was observed that a slight softness in bond occurred after the internal bars started to slip (around a bond value of 3.5 MPa) due to the rapid growth of splitting cracks along splices. In this specimen, as the main part of the splitting plane is located between the splices, no significant contribution from stirrups is expected on bond strength.

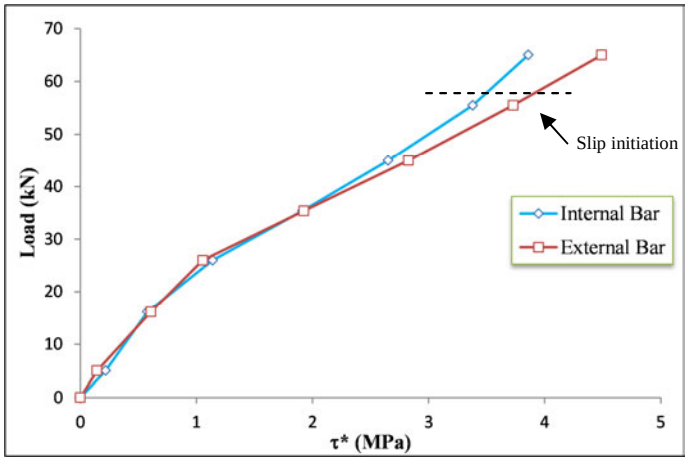

Figure 5-33: Average bond stress along the internal and external bars

5.6.2.4 Comparison of internally confined specimens

The average bond stresses of the internally confined specimens are plotted versus load in Figure 5-34. The bond strengths are also plotted versus those of the unconfined specimens in Figure 5-35. The actual bond stresses at the maximum load are calculated at 3.70, 2.90 and 4.18 MPa for specimens in group I, II and III, respectively. Normalising these values to a concrete strength of 25 MPa, by multiplying with the ratio of $(25/f'_c)^{1/4}$ in line with the results by Darwin et al. (1996b), yields 3.58, 2.90 and 4.12 MPa, respectively. For the same confinement ratio (A_{tr}/snd_b = 0.047) of specimens LC10 and LC20, it is found that steel stirrups contribute more to bond strength as the concrete cover to bar diameter ratio c_d/d_b becomes lower. Conversely, in specimen LC27 (A_{tr}/snd_b = 0.031), splitting cracks, and as a result the splitting plane, form first between splices then propagate to the external cover. For this reason, the presence of stirrups

seems to inhibit slightly the spread of splitting cracks towards the external sides and, as a result, the contribution to bond was limited.

All specimen showed improvement in bond strength in comparison to the counterpart unconfined ones except specimen LC20 which reached -15% of that of the control specimen. This cannot be taken as a cause of the steel stirrups. In fact, loading conditions, curing, casting as well as vibration are all possible causes for such a reduction in the bond strength. It should be mentioned though that the presence of stirrups had caused the growth of multiple flexural cracks along the splice before the maximum load.

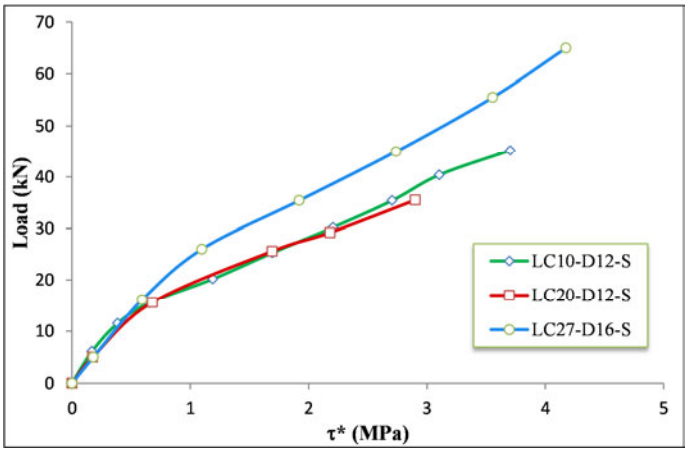

Figure 5-34: Average bond stresses of the internally confined specimens

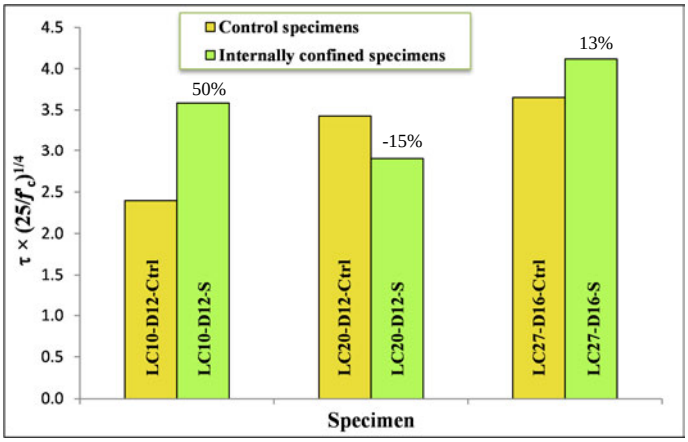

Figure 5-35: Average bond strength of unconfined vs. internally confined specimens

5.6.3 PTMS Confined Specimens

The PTMS confined specimens failed in a more ductile manner compared to the unconfined or internally confined specimens. The main damage, flexural cracking and bar slippage took place mostly at splice interfaces due to bar deformations. Splitting cracks tended to form at one end and spread along the splice as the load increased. In all specimens, the failure was caused by pullout of the internal bars as they were less confined. The external bars, on the other hand, had

almost complete intact bond with the surrounding concrete. As a result, the slip interface was always located at the loaded end of the internal bars.

Readings from strain gauges attached on the spliced bars show that some specimens undergo yield before the response degrades. Specimens intensely confined with PTMS (spacing=0) show a more prominent yield threshold. The bond stress and strain distributions of PTMS specimens are examined in detail in the following sections. This is deemed essential so as to determine the contribution of the bar elongation component to the total slip, as will be explained later.

5.6.3.1 LC10-D12-PTMS1

The maximum capacity of this specimen was reached shortly after the yield strain was attained. The strain at the maximum loading achieved was 2984με ($1.18\varepsilon_y$). The characteristic normal strain distributions along the internal bar in the pre- and post-yield stages are shown in Figure 5-36. The yield length at the maximum load was calculated to be as small as 0.5*mm*. At low load levels, the strains were evenly distributed along the length and the peak was located at the loaded end. At high load levels, the strains showed linear distributions. As the maximum load was approached, the strains adjacent to the loaded end tended to accelerate giving higher rate of change. Compared to the counterpart internally confined specimen, the strain distributions were more consistent (refined). This can be attributed to the uniform application of external confinement along the splice. The increase in strains after yield was limited by reaching the maximum capacity due to spread of multiple splitting cracks along the splice.

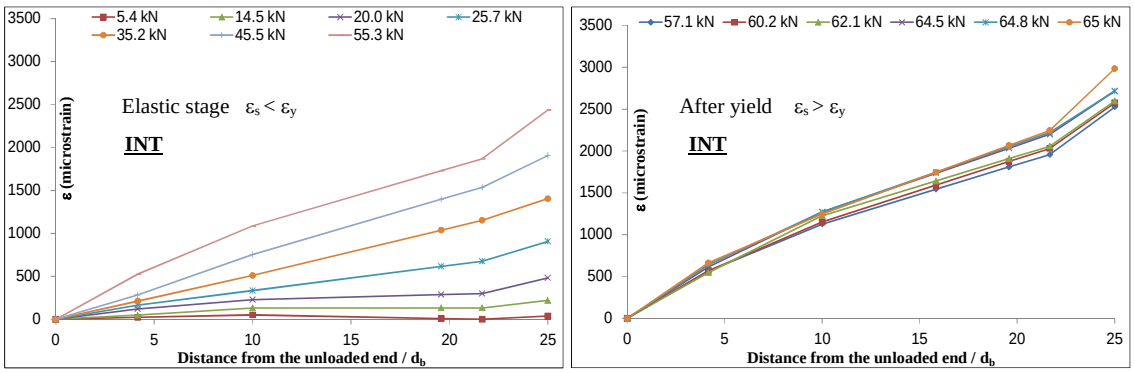

Figure 5-36: Normal strain distributions along the internal bar of specimen LC10-D12-PTMS1

Bond stress distributions before and after yielding are shown in Figure 5-37. Before yield, the bond was distributed uniformly along the bar with local peaks at the loaded end. As the yielding was approached, the unloaded end of the bar started picking up higher strains due to interaction with the other spliced bar and, as a result, higher bond values (almost equal to those at the loaded end) were reached. At yield, high local bond was calculated, which reached 9 MPa and spread along a distance of $4d_b$. After yielding, the bond stress at the loaded end started to degrade very rapidly due to local damage and multi-cracking in that area, whereas it continued to increase slightly at the unloaded end.

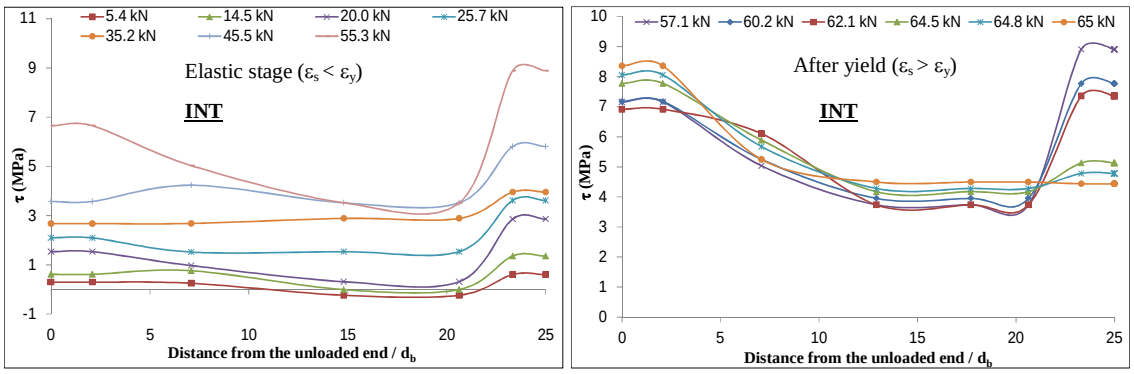

Figure 5-37: Bond stress distributions along the internal bar of specimen LC10-D12-PTMS1

The average bond stress over the lap length is plotted versus load in Figure 5-38. As can be seen from the figure, the bond accelerated after the cracking point was reached until the load corresponding to yield was attained at 57 kN. Afterwards, the increase in bond decelerated severely and the force increased slightly. The average bond at yielding was calculated at 5.30 MPa, whereas the average bond at the maximum was calculated at 5.31 MPa corresponding to a load of 65 kN. Splitting cracks appeared at a bond value of 4.0 MPa, while the bar started to slip at 4.4 MPa.

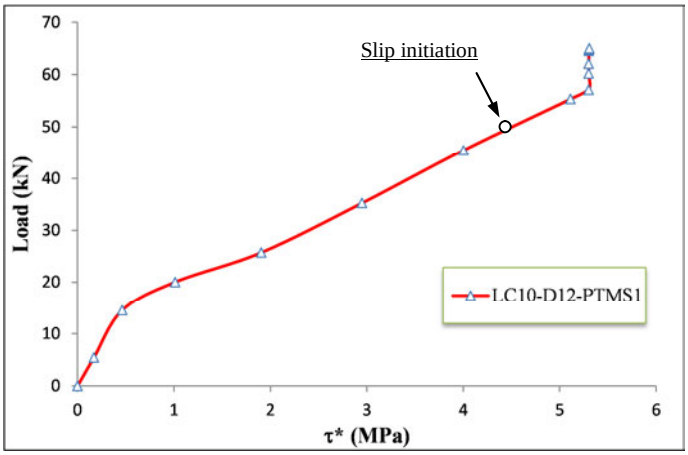

Figure 5-38: Average bond stress along the internal bar

5.6.3.2 LC10-D12-PTMS2

This specimen was intensely confined by PTMS (spacing between strips s = 0) and yielding was reached at a load of 60 kN. Yielding took place first in the external bar then shortly after that the internal bar underwent yielding. The yield length was calculated at 40*mm* (internal bar) and 41*mm* (external bar). Basically, this specimen had a sudden pullout-like failure and the force dropped significantly after the internal bars pulled out. The characteristic normal strain distributions along the internal and external bars in the pre- and post-yield stages are shown in Figure 5-39. In general, the strain distributions of the internal bar are similar to those of the PTMS1 specimen in this group. The internal bar showed slightly higher strains than the external one until the load at first splitting was approached (≈56 kN). After that, the strains at the

external bar increased rapidly causing yielding of the bar. This can be attributed to the fact that the external bars are more confined than the internal ones. The strain distributions after yielding were usually smooth similar to those within the elastic range. The penetration of yield strains along the spliced bar was limited due to spread of splitting cracks along the splice that deteriorated the splice capacity. The strains at the maximum load were 3894με ($1.54\varepsilon_y$) and 14827με ($5.9\varepsilon_y$) for the internal and external bars, respectively.

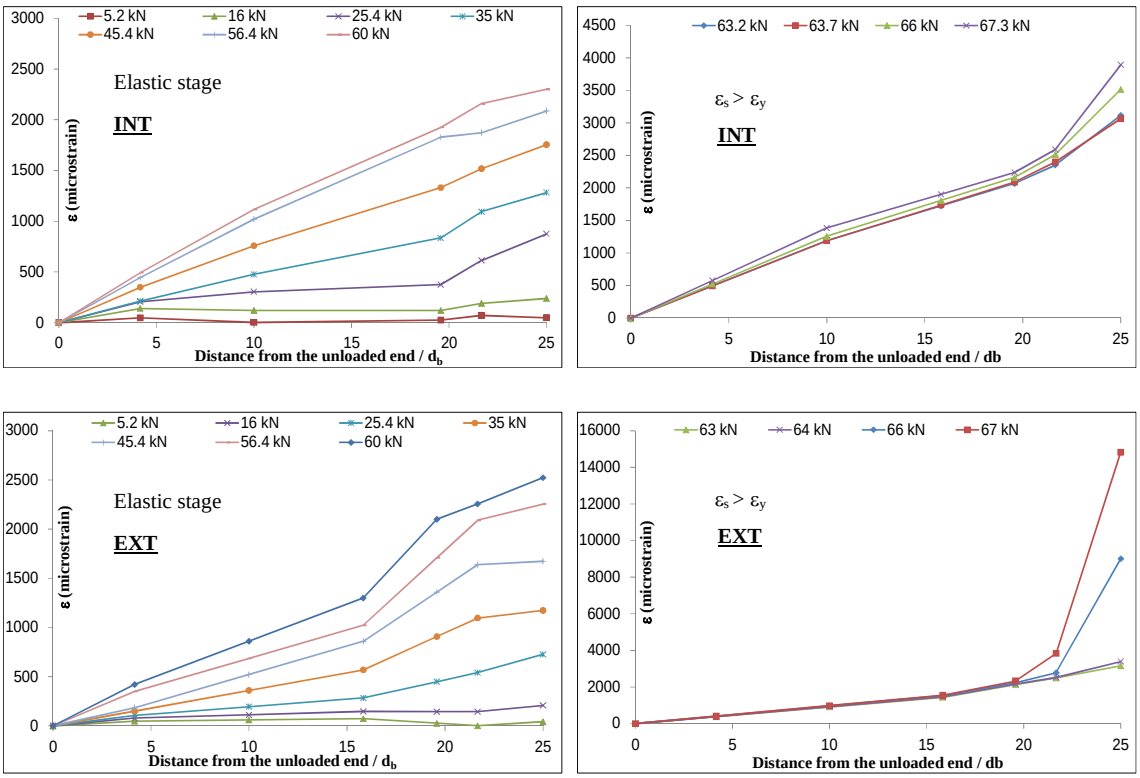

Figure 5-39: Normal strain distributions along the single bars of specimen LC10-D12-PTMS2

The bond distributions along the internal and external bars in the pre- and post-yield stages are plotted in Figure 5-40. The behaviour can be divided into two stages namely, pre- and post-yield as follows.

Before yield:

The internal bar developed higher bond values at the bar end as well as at a distance of about $5d_b$ from the loaded end. The external bar, on the other hand, developed high bond values at both bar ends, and as the load increased, the peak bond at the loaded end started migrating towards the mid length of the bar. The reason for these peaks could be attributed to local flexural cracks at those locations which could not be observed during the test because of confinement. After removing the strips, it was found that flexural cracks formed at those locations.

After yield:

At yielding, a severe drop in bond occurred at the loaded end such that it was near zero where yielding took place. As the external bar maintained its bond capacity, the bond continued spreading as yielding progressed, and the peak value was migrating towards the mid length. For the internal bar, the bond at the loaded end increased slightly. After that, the peak bond at the yielding region started diminishing rapidly as the bar pulled out. The pullout mechanism prevented penetration of yield along the bar.

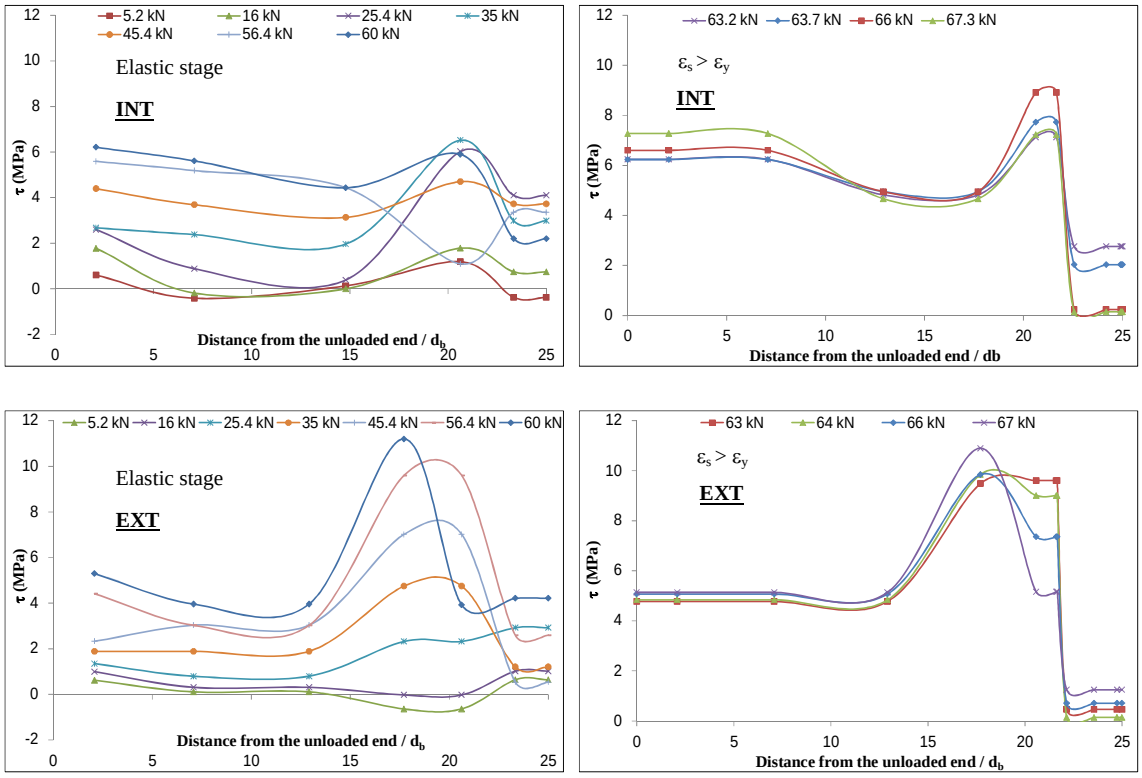

Figure 5-40: Bond stress distributions along the single bars of specimen LC10-D12-PTMS2

The average bond stresses calculated over the lap length are plotted versus load in Figure 5-41. It can be seen that both spliced bars behaved similarly in most of the loading stages. After yield, the bond increased slightly along with the spread of splitting cracks along the splice. Bond failure (or ultimate splice strength) was attained when the bar was unable to resist any additional forces due to penetration of yield strains into the splice length along with excessive splitting cracking. The average bond stresses at yield were 4.8MPa and 5.34MPa for the internal and external bars, respectively. At the maximum load, the average bond stresses were 5.32MPa for the internal bar (10 % increase), and 5.57MPa for the external bar (4.3% increase). It can be noted from the figure that after yielding, the load capacity increased slightly because of the increase in bond resistance of the external bar while the internal bar was slipping.

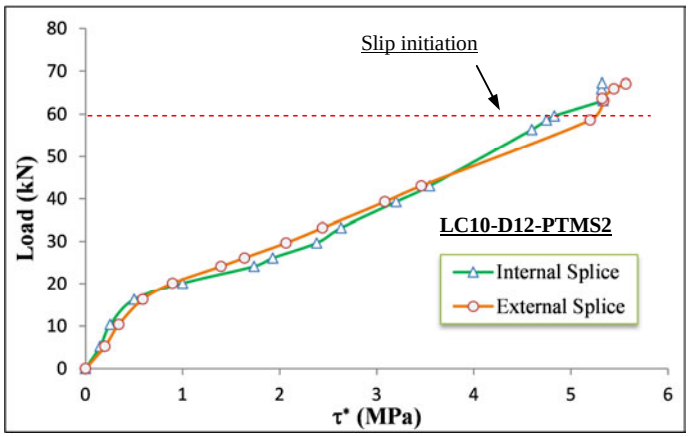

Figure 5-41: Average bond stress along the internal and external bars

5.6.3.3 LC20-D12-PTMS1

This beam failed in the elastic stage at a load of 55 kN. Most of strain gauges were damaged before the test and consequently the behaviour was examined based only on two strain gauge readings (at $10d_b$ and $22d_b$ from the unloaded end). The characteristic normal strain distributions of the internal bar are shown in Figure 5-42. The calculated bond stress profiles are shown along the spliced length in the same figure. As can be seen from the figure, the peak bond stress developed close to the unloaded end of spliced bars. As the load increased, almost uniform distributions seemed to develop along the bar. Near the maximum, the peak bond took place at the unloaded end. The average bond stress versus load is plotted in Figure 5-43. At the maximum load, the average bond was calculated at 4.26 MPa.

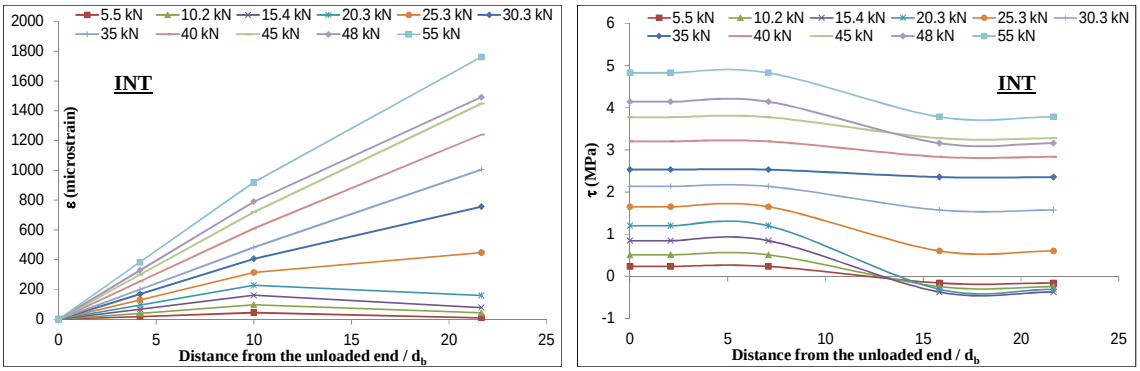

Figure 5-42: Normal strain and bond distributions along the internal bar of specimen LC20-D12-PTMS1

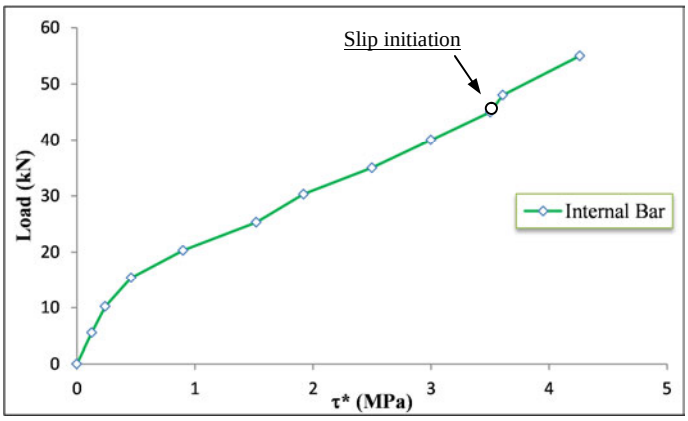

Figure 5-43: Average bond stress along the internal bar

5.6.3.4 LC20-D12-PTMS2

This beam was confined by strips with spacing of (s=0). Strain gauges on the external bar were failed and, thus, only readings from gauges on the internal bar were considered. The yield was reached at a load of 60 kN. The yield length is calculated at 40 mm from the splice end. The characteristic normal strain distributions along the splice length at the elastic and yield stages are shown in Figure 5-44. As can be seen from the figure, the peak strains developed at the loaded end. High rate of change occurred at both bar ends. As the load increased, the strain profiles were more or less linear. At the maximum load, the strain developed at the loaded end was measured at 2977με (1.18ε_y). It is clear that after yield, the high rate of change was closer to the unloaded end. This is expected because the splice capacity is reached shortly after the bar yields.

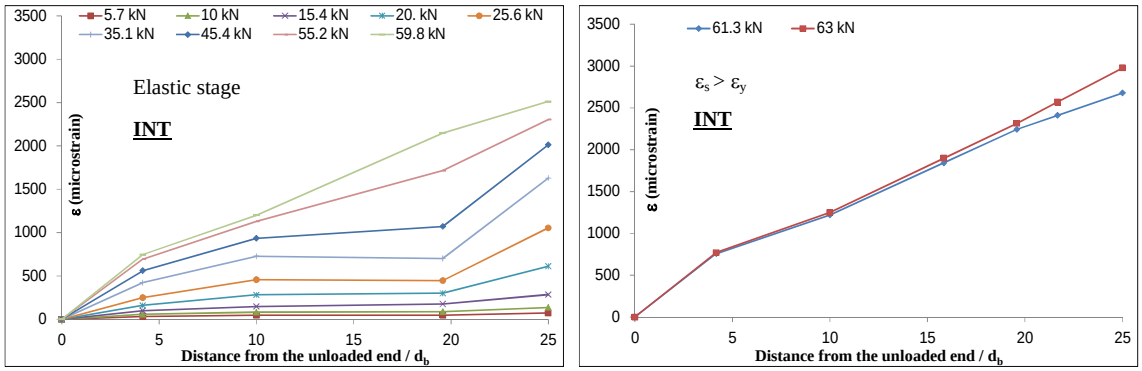

Figure 5-44: Normal strain distributions along the internal bar of specimen LC20-D12-PTMS2

The corresponding bond stresses along the splice length are shown in Figure 5-45. At low load levels, the bond is high at the ends as expected, and the mid segment has almost zero bond values. As the load increases, the bond at the mid segment increases. As yielding is approached, the bond at the loaded end tends to degrade rapidly reaching almost zero values. As a result, the peak bond tends to migrate towards the mid segment. At the unloaded end high bond values are reached at yield.

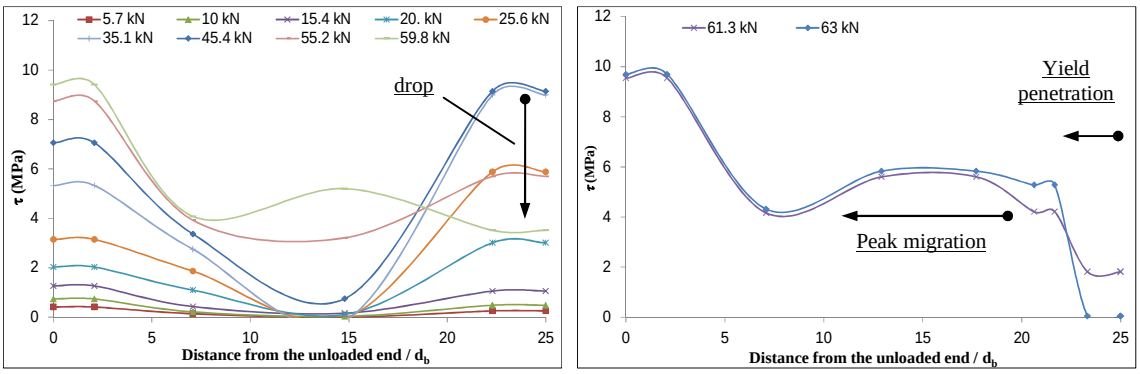

Figure 5-45: Bond stress distributions along the internal bar of specimen LC20-D12-PTMS2

The average bond stress over the splice length is plotted versus load in Figure 5-46. After yield, there was a slight increase in bond capacity that resulted in a small increase in the load resistance. The average bond at yield and at maximum load is calculated at 5.28 and 5.31 MPa, respectively.

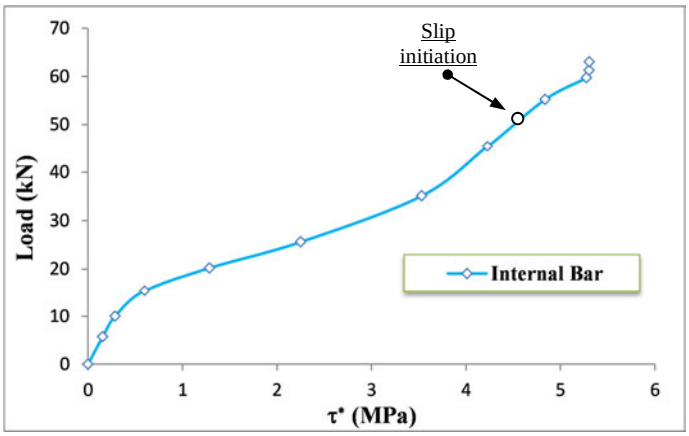

Figure 5-46: Average bond stress along the internal bar

5.6.3.5 LC27-D16-PTMS1

This specimen failed in the elastic stage due to splitting. The characteristic normal strain distributions along the external bar are shown in Figure 5-47. The calculated average bond stresses are shown in the same figure. Strain gauges of the internal bar were found damaged before the test. From the beginning of loading it was clear that the peak strains are located at the loaded end of the bar and with uniform distributions along the lap length. After the initiation of splitting cracks at a load of 75 kN, more strains tend to develop closer to the loaded end resulting in less rate of change at that region. The propagation of splitting cracks along the splice length results in higher strains along the mid segment of the bar. At the maximum load, the strain developing at the loaded end is measured at 2047με.

At low load levels, the bond profiles have local peaks at both bar ends. The mid length, on the other hand, has low but uniform bond distributions. As the load approaches the maximum resistance, the peak bond at the loaded end tends to migrate towards the mid length along with a

rapid drop in the bond value at the end. The drop is accompanied by multiple spitting cracks at both splice ends which is believed to be the cause of the deterioration. The calculated average bond stress over the external bar is plotted versus load in Figure 5-48. At the maximum load, the average bond is calculated at 4.91 MPa.

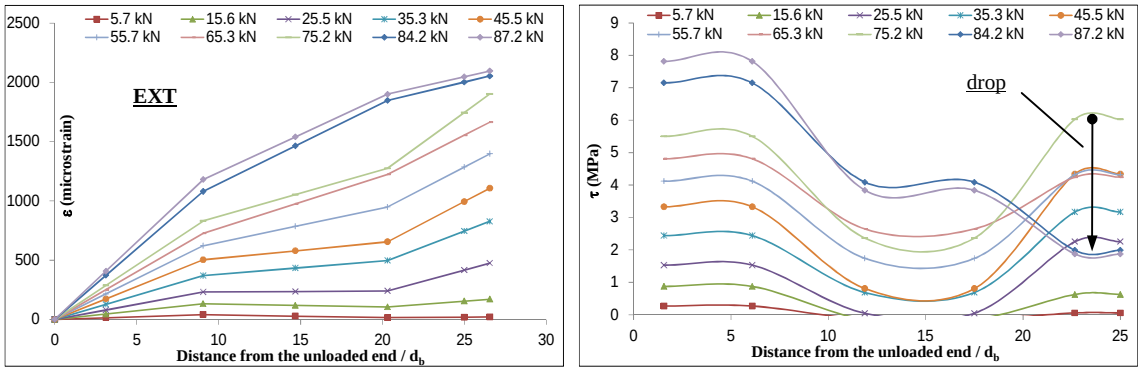

Figure 5-47: Normal strain and bond distributions along the external bar of specimen LC27-D16-PTMS1

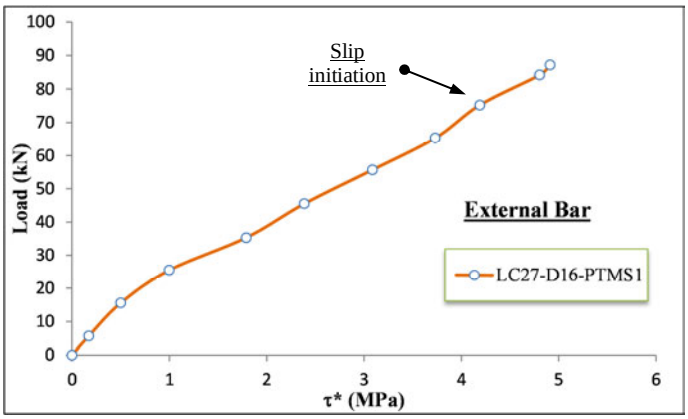

Figure 5-48: Average bond stress along the external bar

5.6.3.6 LC27-D16-PTMS2

Similar to the previous specimen, this beam failed in the elastic stage at slightly lower load capacity. The characteristic normal strain distributions along the spliced bars are shown in Figure 5-49. The strain profiles of the internal bar are produced based on the strain gauge at the loaded end and as a result the profiles are linear. For the external bar, the peak strain develops at the loaded end, whereas the mid segment has more uniform distributions similar to the first PTMS specimen (LC-27-D16-PTMS1). At the maximum load, the strains developed at the loaded end are measured at 1754με and 2136με for the internal and external bars, respectively.

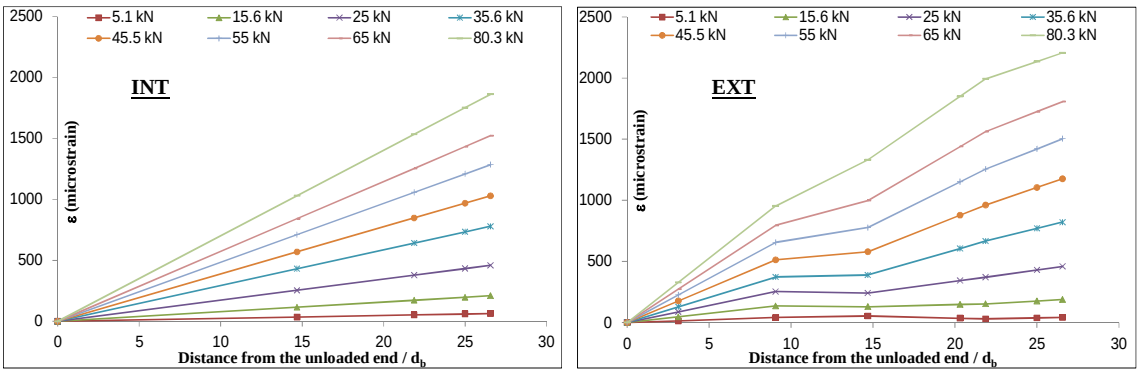

Figure 5-49: Normal strain distributions along the single bars of specimen LC27-D16-PTMS2

The calculated average bond distributions along the spliced bars are shown in Figure 5-50. For the internal bars, the profiles are uniform due to the use of one strain gauge at the unloaded end. For the external bar, at low load levels peak bond values formed locally at both bar ends. With increase in loading and initiation of splitting cracks at both bar ends, the bond at the loaded end deteriorated, migrating towards the mid segment.

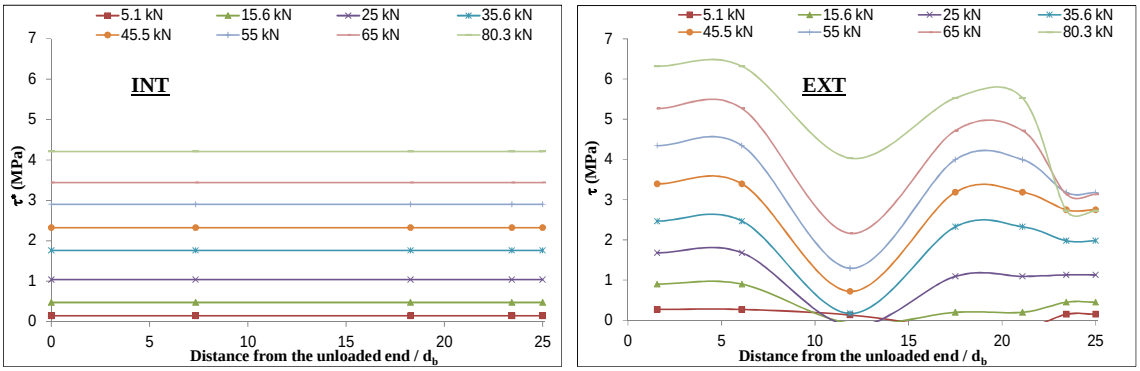

Figure 5-50: Bond stress distributions along the single bars of specimen LC27-D16-PTMS2

The calculated average bond stresses over the splice length are plotted versus load in Figure 5-51. At the maximum load, the average bond was calculated at 4.21 and 5.13 MPa for the internal and external bars, respectively. The response was limited by pullout of the internal bars.

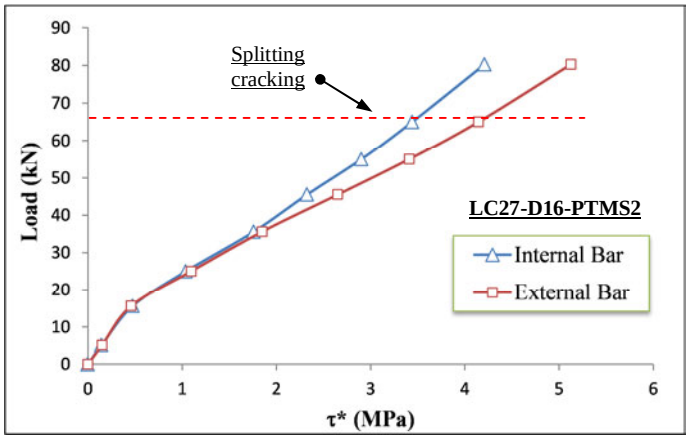

Figure 5-51: Average bond stress along the internal and external bars

5.7 BOND STRESS-SLIP RELATIONSHIP

Refined bond stress-slip relationships were produced for all specimens based on the average bond distributions and corresponding slips. The average bond stress versus pure slip curves of the test specimens are plotted in Figure 5-52 through Figure 5-54. For comparison reasons, the bond stress is normalised to a concrete strength of 25 MPa by the ratio of $(25/f'_c)^{1/4}$, as justified later in chapter 8.

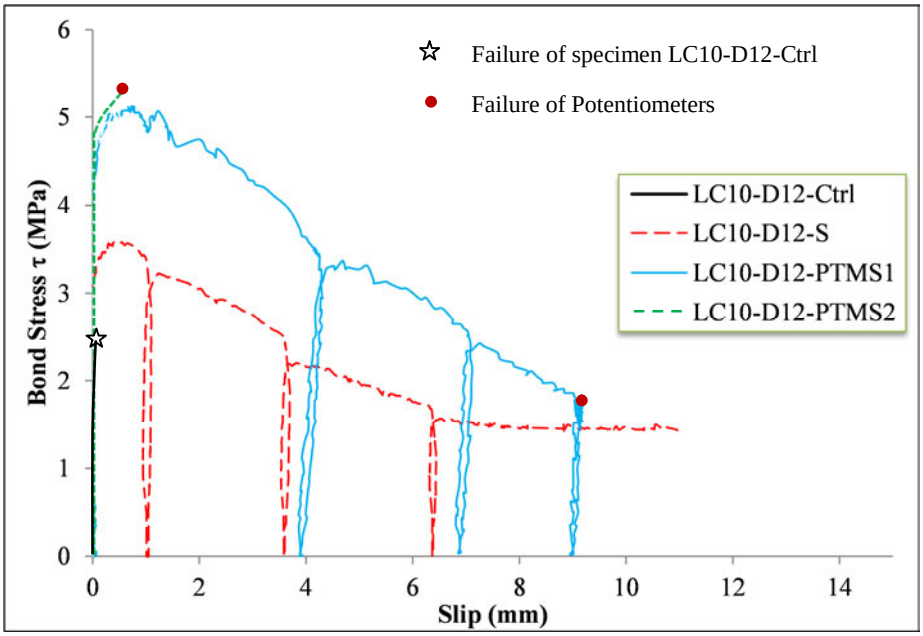

Figure 5-52: Average bond stress-slip response of specimens in Group I

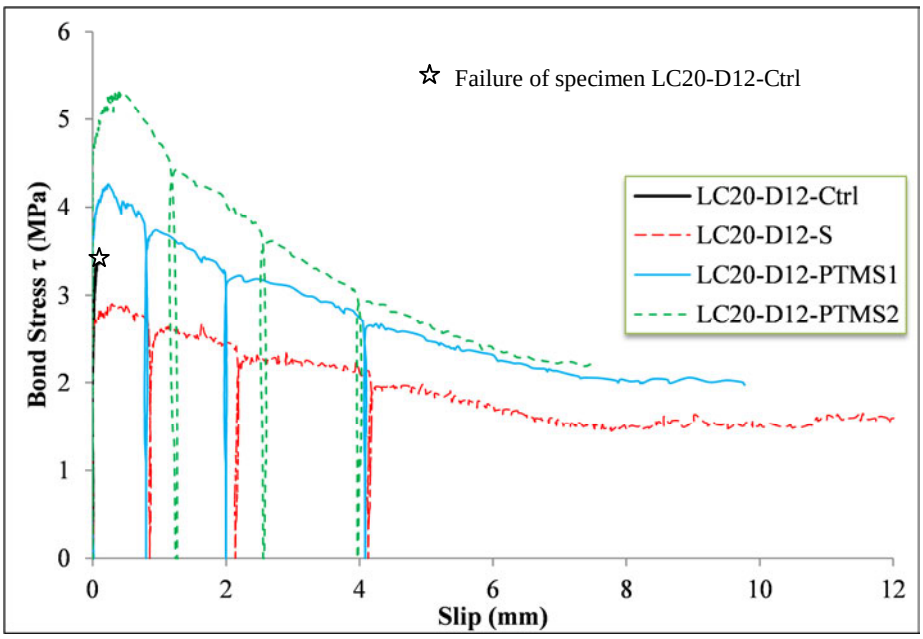

Figure 5-53: Average bond stress-slip response of specimens in Group II

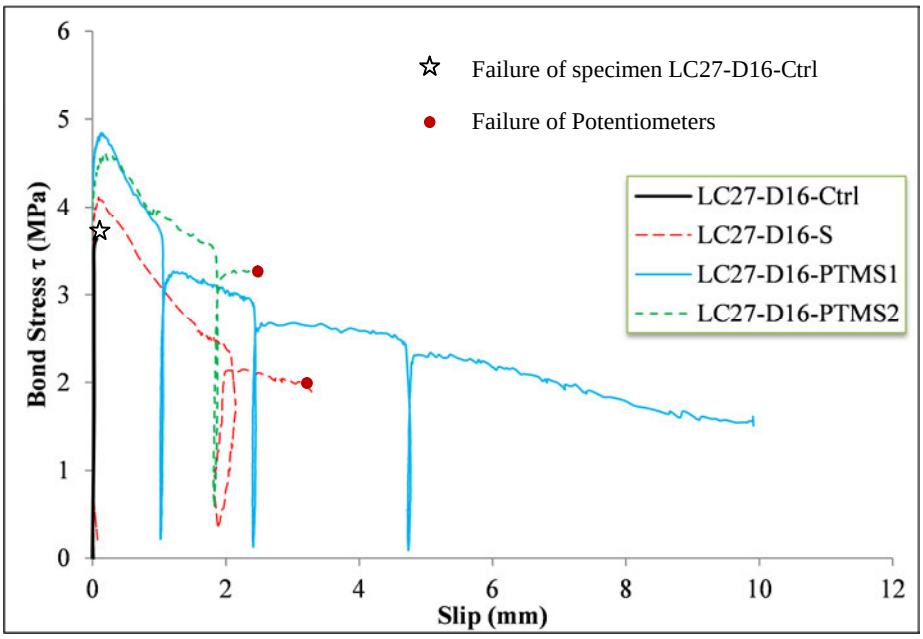

Figure 5-54: Average bond stress-slip response of specimens in Group III

As can be seen from the figures, the bond slip response is similar to the load-slip response with the same characteristics. The bond strength of the unconfined specimens was observed to diminish completely shortly after the bar started slipping. The use of PTMS was very effective at increasing the bond strength and deformability of bond failure. In most of the PTMS specimens, the resulting bond strength caused yielding of the spliced bars and resulted in a pullout-like response for those specimens with full PTMS jacket (strip spacing =0). The use of double strips in specimen LC10-D12-PTMS2 was not as efficient (as expected) to mobilise higher bond strengths. Confinement by steel stirrups, on the other hand, had limited bond strength improvement. The deformability of bond failure, however, was enhanced considerably.

The residual bond strength of the PTMS confined specimens was noted to be higher in specimens with higher concrete cover to bar diameter ratios. The same conclusion was reached for internally confined specimens. However, the residual strength of PTMS specimens was in average 34% higher than those of internally confined specimens. It should be mentioned though that the least improvement in residual bond strength was in the PTMS1 specimen of group I which had an increase of only 15% compared to that of corresponding internally confined specimen. The reason could be attributed to the small concrete cover that was excessively cracked near failure.

The post peak response, in general, shows an accelerated bond degradation part directly after the peak followed by gentle bond degradation up to failure. It was observed that the PTMS confinement was most efficient in specimens of group I where the concrete cover was the least (10 mm). This is expected as the corresponding unconfined specimen failed at a lower bond value compared to those of other groups, and as a result, the confinement contribution to bond

strength was higher. The peak bond stresses of PTMS confined specimens in comparison with the counterpart unconfined and internally confined specimens are plotted in Figure 5-55. All values are normalised by the ratio of $(25/f'_c)^{1/4}$. The bond enhancement in comparison to those of unconfined specimens was calculated at 114% (PTMS1) and 120% (PTMS2) of specimens in group I; 24% (PTMS1) and 55% (PTMS2) for specimens in group II; and 33% (PTMS1) and 26% (PTMS2) for specimens in group III. For the internally confined specimens, a noticeable improvement in bond strength of 50% was achieved in specimen LC10-D12-S compared to that of the unconfined specimen. The enhancement of other specimens was found to be 0% and 13% of specimens in group II & III, respectively. This indicates, along with the results from PTMS specimens, that the confinement, in general, is more efficient in specimens with smaller concrete cover.

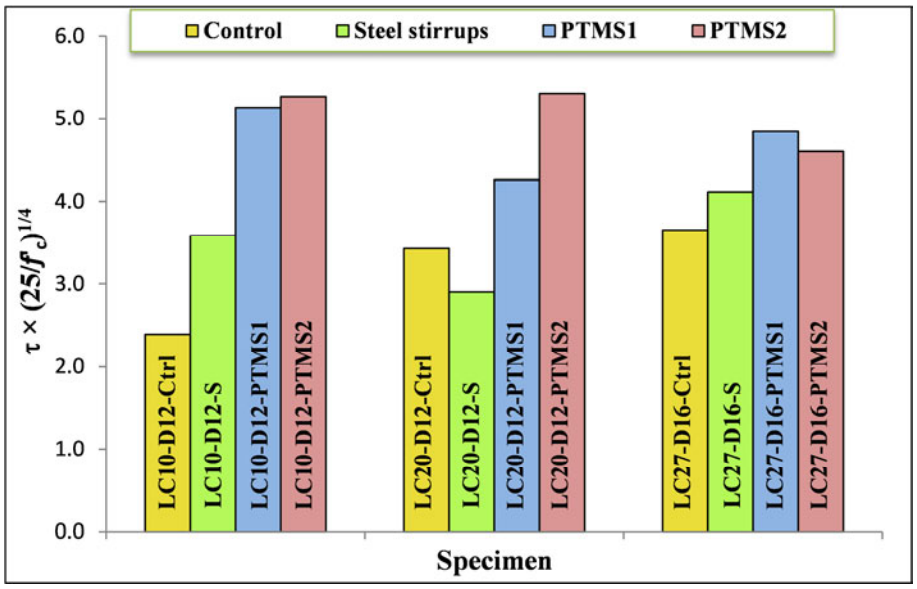

Figure 5-55: Average bond strength of unconfined, internally and PTMS-confined specimens

Similarly to the behaviour of specimens tested in phase (I), five stages of behaviour are identified in the bond slip response. The values that identify the curve are given in Table 5-3 for each specimen. At the post-peak stage, some values could not be measured due to failure of some potentiometers.

Table 5-3: Characteristics of bond stress-slip curves of the test specimens (Series L)

Group	Specimen	τ_s	τ_{max}	τ_e	τ_r	s_m	s_e	s_r
		MPa	**MPa**	**MPa**	**MPa**	**mm**	**mm**	**mm**
I	LC10-D12-Ctrl	2.47	2.47	N/A	N/A	0	N/A	N/A
	LC10-D12-S	3.2	3.70	-	1.58	0.52	1.15	7.01
	LC10-D12-PTMS1	4.4	5.31	4.28	1.83	0.73	3.0	9.10
	LC10-D12-PTMS2	4.7	5.45	-	2.04	0.96	-	-
II	LC20-D12-Ctrl	2.3	3.43	N/A	N/A	0.09	N/A	N/A
	LC20-D12-S	2.6	2.90	2.60	1.58	0.29	0.92	6.90
	LC20-D12-PTMS1	3.5	4.26	3.5	2.0	0.24	0.92	7.21
	LC20-D12-PTMS2	4.6	5.31	4.55	2.10	0.39	1.5	7.23
III	LC27-D12-Ctrl	3.6	3.71	N/A	N/A	0.02	N/A	N/A
	LC27-D12-S	3.5	4.18	2.57	1.20	0.12	1.56	-
	LC27-D16-PTMS1	4.3	4.91	3.3	1.65	0.14	1.18	9.0
	LC27-D16-PTMS2	4.1	4.67	4.0	2.22	0.20	0.90	9.0

5.8 ANALYTICAL EVALUATION OF BOND STRESS RESULTS

The average bond stress at the maximum load is calculated by using the cracked section analysis approach similar to that of phase (I). The computer software XTRACT is also utilised for this series. The moment-curvature curves of the cross-section are first produced. Excel spreadsheets are used to computerise CSA based on the results of XTRACT. One-dimensional concrete and reinforcement models are used based on the experimental results given in chapter 3. The strains along the spliced bar are assumed to be linear resulting in uniform bond distributions. The analytical bond predictions at maximum are compared to the experimental results in Figure 5-56.

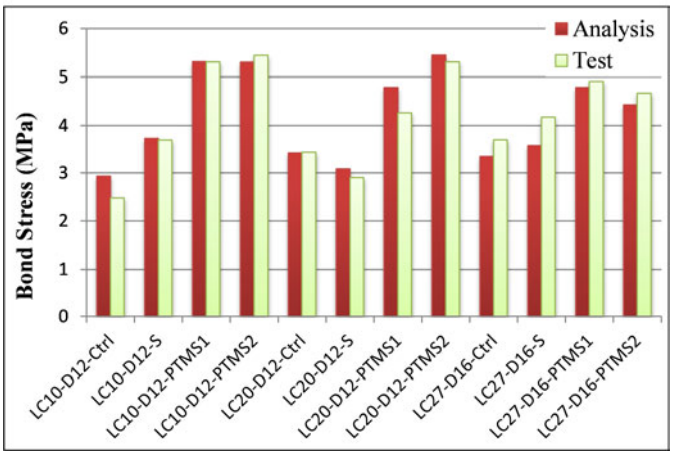

Figure 5-56: Comparison of predicted and experimental bond stresses at the maximum load

As can be seen from the previous figure, the CSA can predict the experimental results with very good accuracy. The comparison also implies that the assumption of a uniform bond distribution along the splice before yielding leads to an acceptable solution for bond.

5.9 VARIATION OF STRAINS WITHIN THE CONFINING STRIPS

A typical variation of the strains within the confining PTMS during the test is shown in Figure 5-57. As can be seen from the figure, no reduction in the strain occurred until the load reached the maximum load. Afterwards, the pressure tended to decrease as the load decreased (displacement is increasing). At the end of the test, the reduction in strain was calculated at 25% of the initial state. Similarly to Phase I, this indicates that the performance of splices in tension in flexural elements is directly related to the initial strain applied to the strip. The average strain initially applied in the confining strips was 0.0015 which represents 32% of the yield strain.

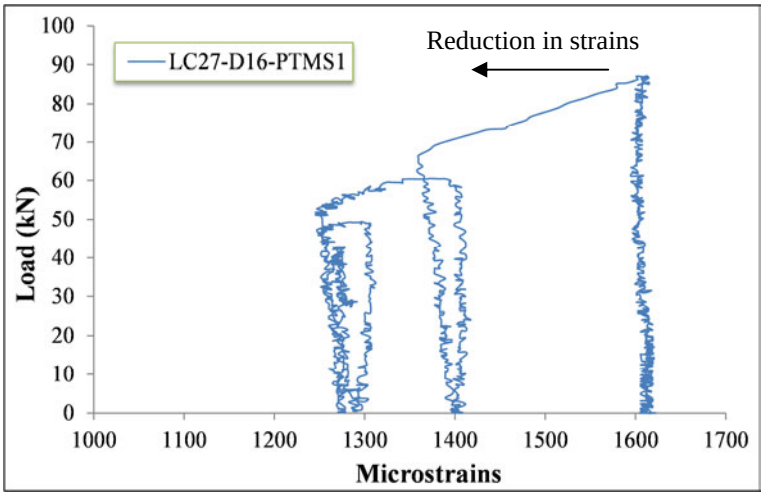

Figure 5-57: A typical variation in the strain of strips from test specimen LC27-D16-PTMS1

5.10 STRAINS IN THE STEEL STIRRUPS

The contribution of steel stirrups of the internally confined specimens to bond strength was calculated by monitoring the strains within the stirrups. The strain gauges were attached to one vertical leg of the mid and side stirrups within the splice region (see Figure 5-58a). Figure 5-58(b), (c) and (d) shows the load versus the strain occurring in the steel stirrups of the internally confined specimens.

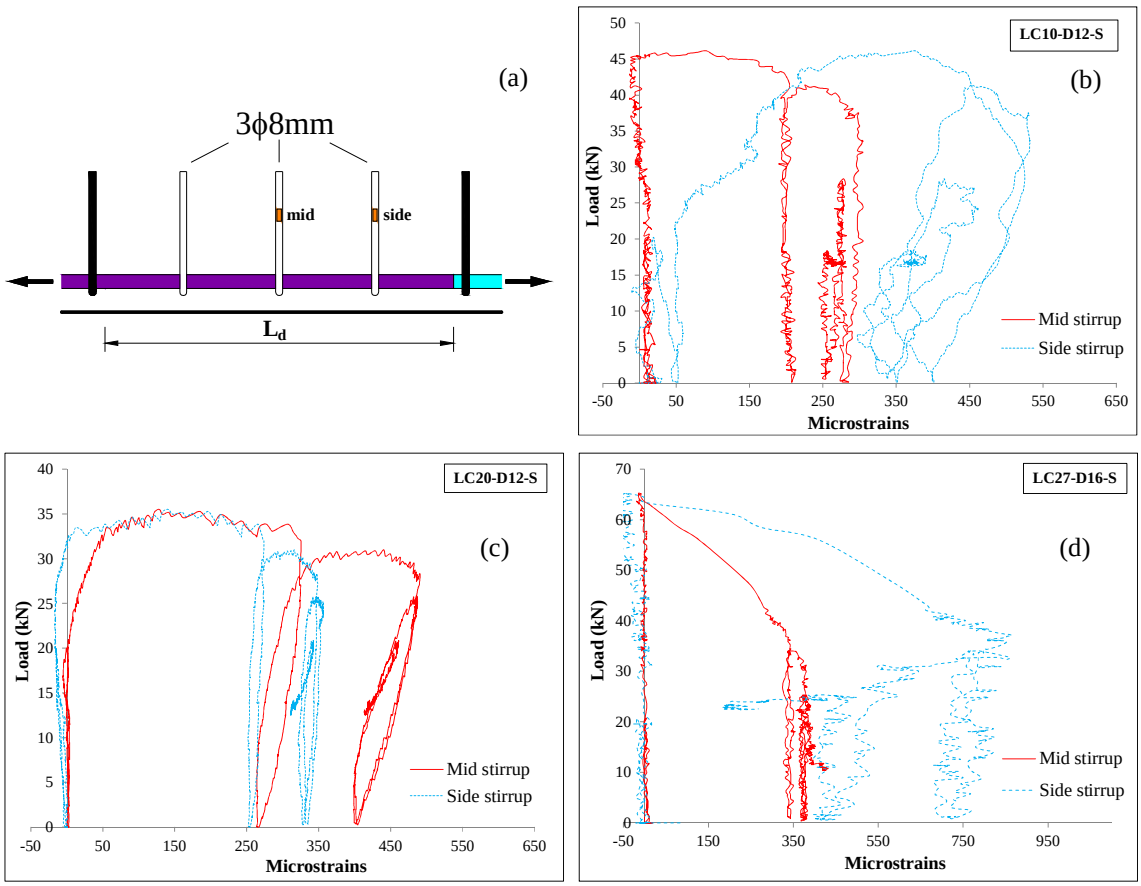

Figure 5-58: Strains recorded in steel links within the spliced region of the internally confined specimens

The contribution of stirrups to bond resistance is found to be somewhat related to the evolution stage of splitting cracks and their propagation along the splice. Although the development of splitting cracks is similar in all specimens, their propagation differs from one specimen to another as follows:

- **LC10-D12-S**

In this specimen, visual observations of cracking progress showed that the first splitting cracks initiated at the side of the splice at a load of 27 kN. As can be seen from Figure 5-58 (b), the side stirrup tended to react to the formation of splitting cracks at a load of 25 kN. At the maximum capacity, the initial splitting cracks propagated to the entire lap length rapidly, and concurrently, the mid stirrup started to react. The stress of stirrups at ultimate loading was calculated at 57 MPa and 105 MPa for the mid and side stirrups, respectively.

- **LC20-D12-S**

In this specimen, visual observations showed that the first splitting crack appeared at the end of the splice at a load of 34 kN and then rapidly propagated along the entire lap length. Figure 5-58(c) shows that both stirrups started to react to the formation of splitting cracks at a load of

20 kN (mid stirrup) and 26 kN (side stirrup). A rapid increase in the recorded strain values starts after the load reaches 33 kN. The stresses in the links at the ultimate loading were 100 MPa and 70 MPa for the mid and side stirrups, respectively.

- **LC27-D16-S**

In this specimen, the splitting cracks first appeared at a load of 61 kN. These cracks were observed to form at the splice end and with further increase in loading they propagated to the entire lap length. As a result, the side stirrup tended to be stressed more than the mid one. It is clear from Figure 5-58(d) that none of the links appear to react to the formation of splitting cracks until the maximum was reached at a load of 65 kN. The stress of stirrups at ultimate loading was calculated at 75 MPa and 160 MPa for the mid and side stirrups, respectively. These values, however, do not appropriately represent the actual contribution of the stirrups because the main splitting cracks developed at the bottom side of the splices where no strain gauges were attached.

5.11 CONCLUSIONS

- All specimens confined or unconfined failed due to splitting-type of bond failure within the splice zone. Splitting cracks initiated at a load level of 80-90% of the maximum load.
- All unconfined specimens experienced brittle-nature failure due to sudden and complete loss of bond between steel bars and concrete within the splice zone. This failure occurred directly after splitting cracks initiated and became more severe as concrete cover decreased.
- Specimens confined by internal steel stirrups exhibited noticeable enhancement in deformability (up to74% in the deflection at the maximum load compared to the unconfined condition, along with large post-peak DR up to 3%) due to gradual formation of multiple splitting and flexural cracks along the splice zone. Enhancement in strength, on the other hand, was only significant for lower concrete cover values (an increase of 50% compared to that of the unconfined value in specimen LC10-D12-S).
- In comparison to the unconfined specimens, confinement of splices by PTMS resulted in superior enhancement in strength (up to 90% in load) and deformability (up to 280% in the deflection at the maximum load, and post-peak DR up to 3%) and allowed the spliced bars to develop post-yield strains when full PTMS jackets were used. Yielding in the PTMS confined specimens, however, was limited by spread of splitting cracks in the concrete matrix along the spliced bars.

- In cases where full PTMS jackets were used, enhancement in bond strength led to pullout-like failure type such that steel bars pulled out of the concrete matrix along with shearing-off of the concrete keys between bar lugs.
- Near the maximum load, strain profiles resulting from strain gauge readings along the spliced bars were more or less linear in all specimens.
- In contrast to PTMS specimens of Phase I, a decrease in the concrete cover of spliced bars had positive influence on the bond strength. This was due to the decrease in concrete contribution to bond as the lap length increased.
- The bond stress-pure slip behaviour of the PTMS specimens can be described in a similar way to that of specimens in Phase I.

Chapter 6

DEFICIENT BEAM-COLUMN JOINTS: TEST RESULTS, OBSERVATIONS AND DISCUSSIONS

6.1 INTRODUCTORY REMARKS

This chapter presents the experimental results of four deficient RC beam-column connections tested under cyclic loading conditions.

The behaviour of the test units is discussed including crack patterns and modes of failure. Furthermore, plots of measured responses are presented in terms of applied displacement and load configurations. In addition, plots of strains on flexural reinforcement, the energy dissipation and stiffness degradation characteristics are also produced and examined to evaluate the performance.

6.2 GENERAL DEFINITIONS AND CONSIDERATIONS

Some key definitions, considerations and calculations of behavioural structural characteristics are given in this section:

- Selection of test units

In this study, the test units represent a specimen selected from each test pair, as indicated in chapter 3. As a consequence, several parameters are included in each test unit, which might have some effect on the comparisons. However, as the purpose of this test phase is to examine the applicability and efficiency of PTMS technique on joint applications, this issue is overlooked. An extension of this study should focus on using the PTMS technique on test units considering the change of one parameter.

- Envelopes

The envelope of a hysteretic response is defined as the curve enclosing the maximum cycles of the different loading steps. Each loading step comprises three complete cycles at the same loading rate.

- Axial load

Each test unit was tested under a specific level of axial compressive load as stated in chapter 3. In order to evaluate the variation in the axial load with cyclic loading, it was decided to present the deviation in load. These values are referred to as the axial load ratio. The initially applied load is set at 0%, while +5% means a 5% increase in the compressive load. It should be noted that the actuator used to apply the load was not servo-controlled and the load was applied through a hydraulic pump and was monitored by the ORION system. The lack of continuous control caused some difficulties in maintaining the load at the same level throughout the test due to the nature of applied cyclic loading in the system, which also caused some relaxation in the supports. The loss in the axial load in most cases was restored by changing the pressure in the pump.

- Energy dissipation

Energy dissipation is an important structural characteristic that strongly influences the response of a structure to seismic loads. The total energy within a structure is dissipated through 1) steel reinforcement, b) friction between concrete surfaces of an existing crack, and c) formation of new cracks (El-Amoury and Ghobarah, 2002).

The energy dissipation of a test unit is calculated from the enclosed area under the load-displacement hysteresis at each cycle, as illustrated in Figure 6-1. The cumulative energy is

calculated by summing up the energy dissipated in consecutive load-displacement cycles throughout the test.

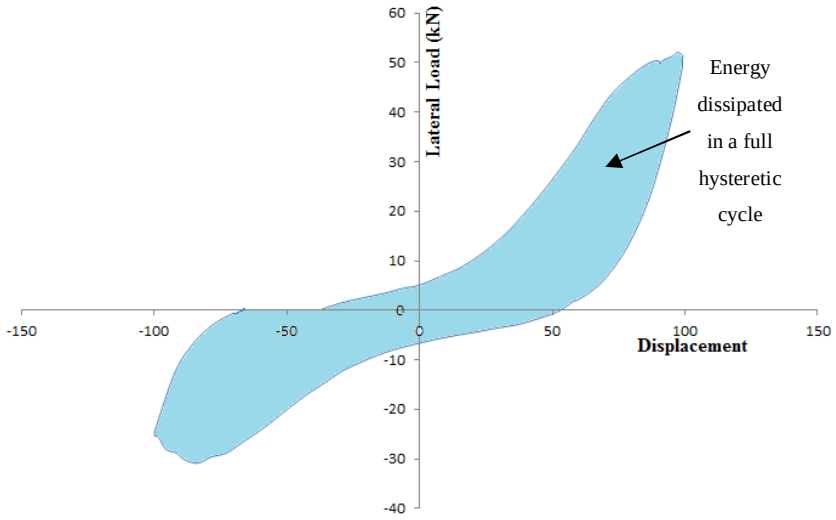

Figure 6-1: Calculation of energy dissipation from load-displacement hysteresis

- Stiffness degradation

Experimental investigations show that stiffness degradation is attributed to various factors such as nonlinear deformations, cracks and cracking in flexure and shear, bond deterioration and bar slip, loss of concrete cover and deformation of the joint area (El-Amoury and Ghobarah, 2002).

The stiffness of a test unit is evaluated based on a) the peak-to-peak stiffness (secant stiffness) of the beam-tip load-displacement relationship, as illustrated in Figure 6-2 and b) zero-to-peak load stiffness for each loading direction separately. In the figure, the secant stiffness is calculated for two consecutive cycles (n) and (n+1).

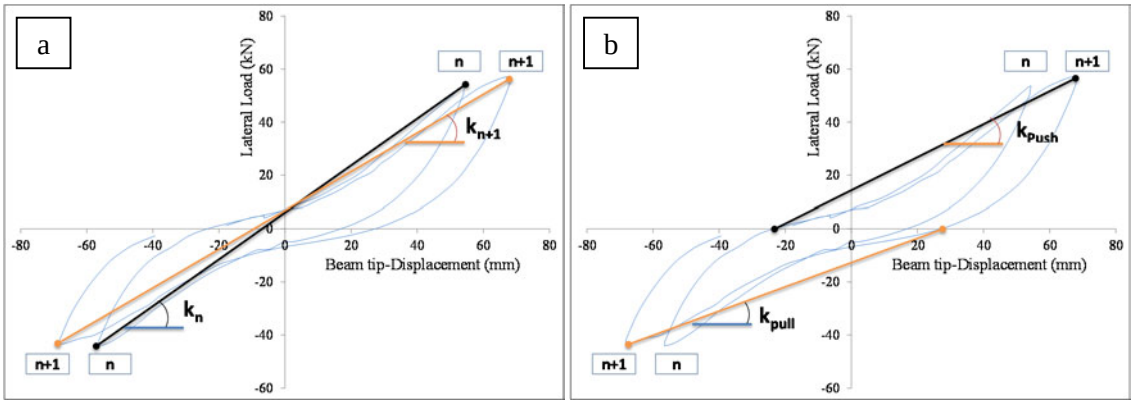

Figure 6-2: a) Peak-to-peak stiffness degradation and b) stiffness of a loading direction

- Strain gauge readings

The strain gauge readings mainly referred to in this chapter are considered at the beam and column interfaces, as shown schematically in Figure 6-3. For example, ST1 refers to the strain gauge on the anchorages, whereas ST5 refers to the strain gauge on the bottom spliced bars.

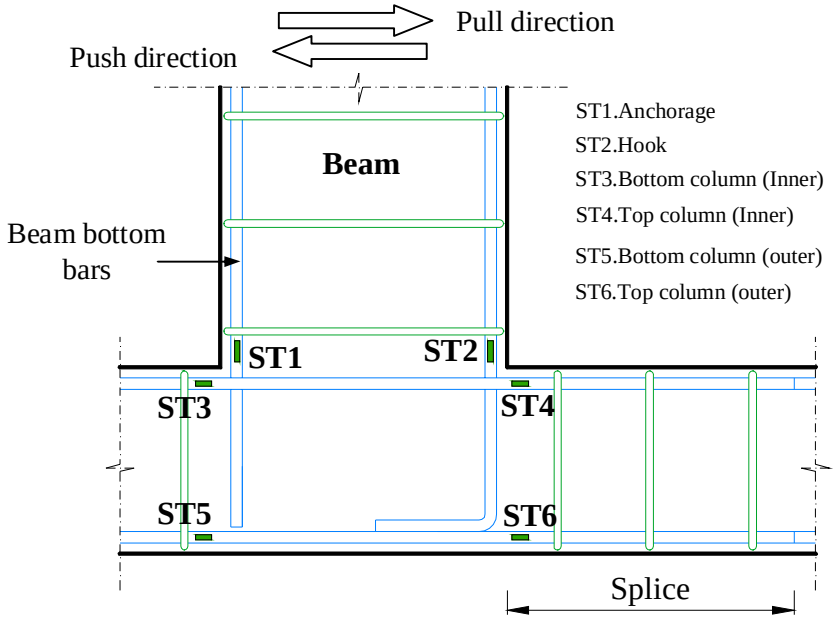

Figure 6-3: Locations of key strain gauges in beam-column joints

- Drift ratio (DR%)

The drift ratio DR% is defined as $(\Delta l / l_b) \times 100$, where Δl and l_b are the applied displacement at the beam tip and the length of the beam from the column face, as defined earlier.

- Loading Directions

The strong direction of a joint corresponds to the state where the top beam bars are in tension. This direction also corresponds to the state where the actuator pushes the beam (push direction), and it represents the positive values on the load-displacement curve. On the other hand, the weak direction corresponds to the state where the beam bottom bars are in tension (pull direction), and it represents the negative values on the load-displacement curve.

6.3 BEHAVIOUR OF THE CONTROL UNITS

A brief description of the performance of each control unit and the key behavioural characteristics is given in the following sections. Also, a comparison is made between these units along with a general discussion.

6.3.1 UNIT JA-1

The unit was tested under load control until the maximum strength in the strong direction was reached which corresponded to a displacement of +10mm. The loading, thereafter, was continued in displacement control until failure. The use of load control in the first phase of this pilot test was to control the damage at the maximum load as the joint capacity and general behaviour were unclear. The switch to displacement control thereafter was only to damage the joint. The adopted loading strategy in this joint enabled the use of only a displacement control regime in the later joint tests as the behaviour and damage could be controlled.

Figure 6-4 illustrates the loading regime applied throughout the test. The loading regime comprises three loading steps in load control (±5, ±10 and ±20kN), then one cycle in displacement control at each loading direction to cause failure.

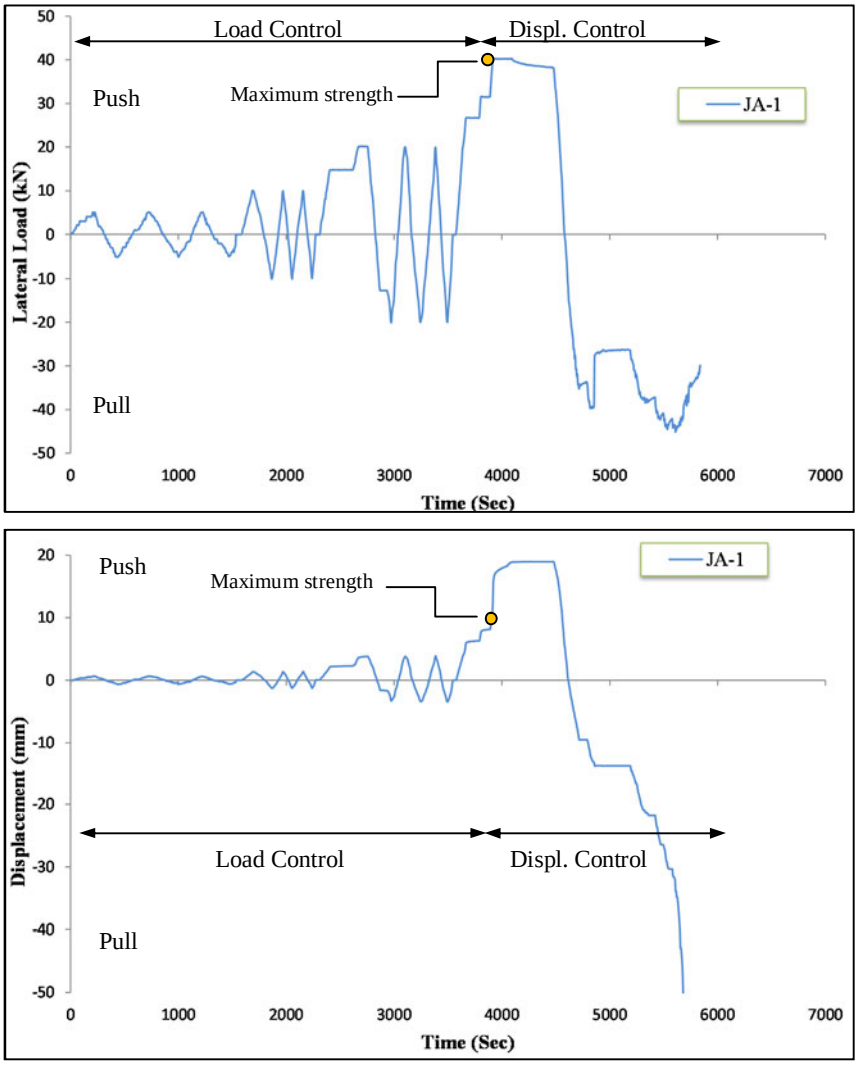

Figure 6-4: Loading regime used during testing of Joint JA-1

The compressive axial load applied to the column of this unit was set at 150 kN (7% of column squash capacity). Figure 6-5 shows the variation of axial load applied throughout the test. It can

be noted that a variation in the axial load of approximately (+5 and -12 kN) occurred despite an effort to maintain it at the same level. As can be seen from the figure, all drops in the axial load occurred in the pull direction. In this case, the upper actuator is applying a load that loosens the load imposed by the axial load actuator. On the other hand, the increase in the axial load occurs when loading in the push direction. However, it can be noted that the variations in the axial load, especially the drop, occur for short periods and therefore are deemed insignificant.

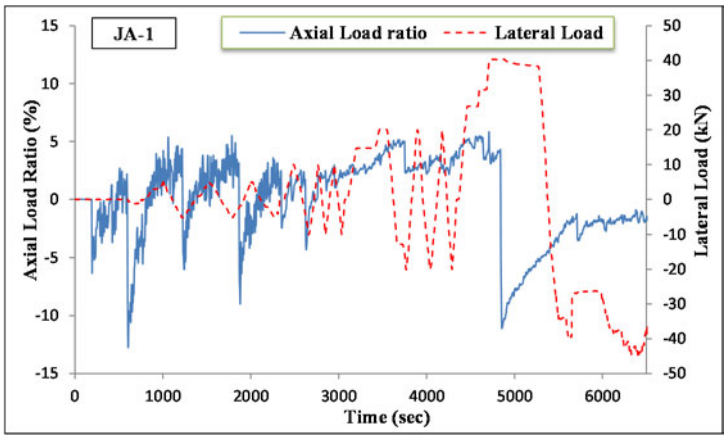

Figure 6-5: Variation of axial load throughout the test of unit JA-1

The lateral loading was initiated with small load steps of about 5 kN (0.7 mm or 0.04% DR). At this loading rate, readings from all instrumentation including LVDTs, strain gauges and potentiometers were checked to test their functionality. A schematic representation of the cracking progress along with the final damage state of the test unit is shown in Figure 6-6. First cracking was observed at the third load step at a load of +18 kN and displacement of +3.8 *mm* (DR% = +0.23%). The crack occurred along the first shear link location of the beam, as shown in Figure 6-6(a). Similar cracks appeared on both sides due to the cyclic nature of the applied load. With further increase in load, more flexural cracks appeared along the beam also at shear link locations, see Figure 6-6(b). The first cracks in the core appeared at a load of +30 kN (DR% = +0.42%), as shown in Figure 6-6(c). These cracks initiated at the corner of the core and propagated along the beam and column longitudinal reinforcement. When the maximum capacity of the unit was reached at a load of +40 kN (DR% = +0.65%), a sizable diagonal shear crack appeared, as shown schematically in Figure 6-6(d). In addition, flexural cracks appeared at the exterior tension side of the bottom column. The application of loading, thereafter, was switched to displacement control and the assembly was pushed to a DR% of +1%. When cycling in the other direction, multiple diagonal shear cracks appeared in the core and an X-shaped failure mechanism formed, as shown in Figure 6-6(e), which led to the deterioration of the joint resistance. As the displacement was increased above the DR of -2%, the cracks widened and the load diminished gradually. The test was stopped when reaching -100 mm displacement (DR% =- 6%). The final damage state and cracking pattern are shown in Figure 6-6(g).

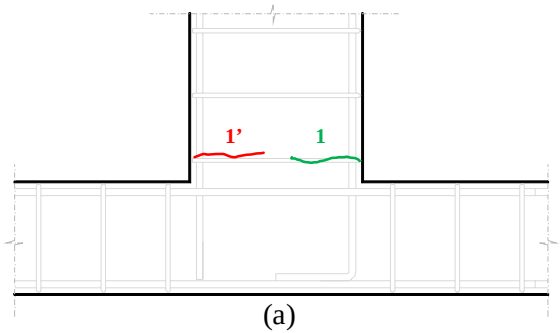

(a)

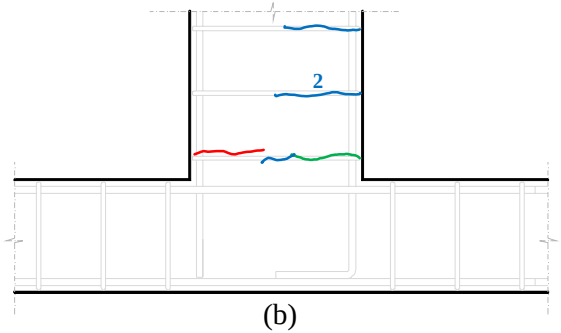

(b)

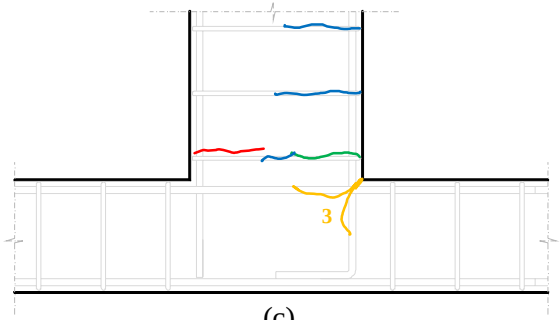

(c)

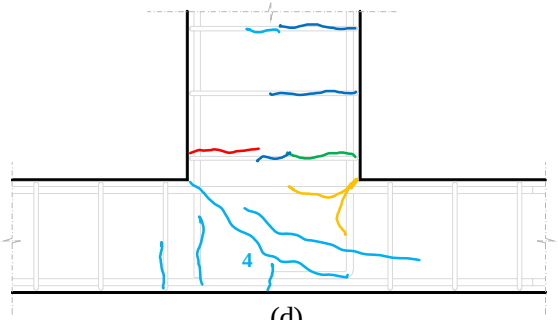

(d)

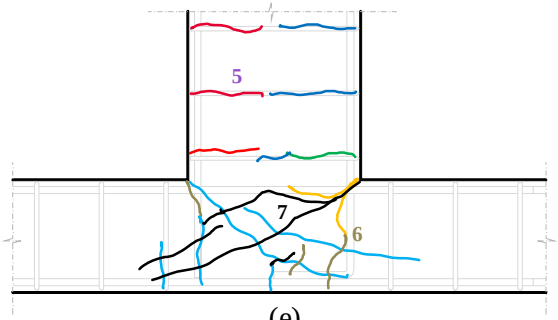

(e)

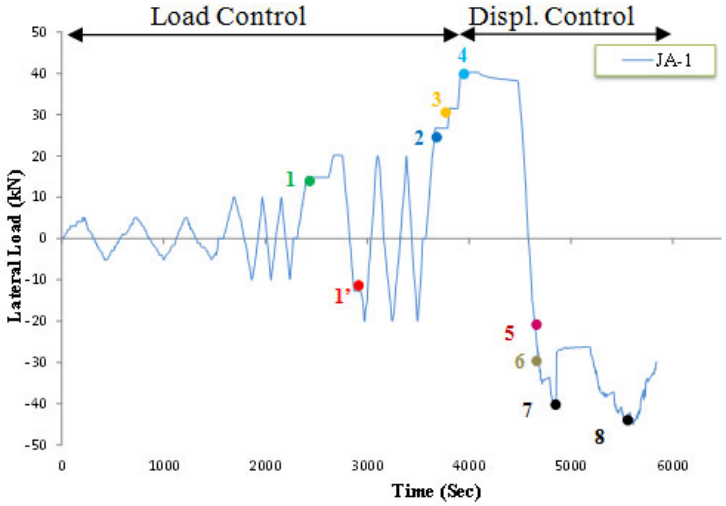

(f) Load Regime

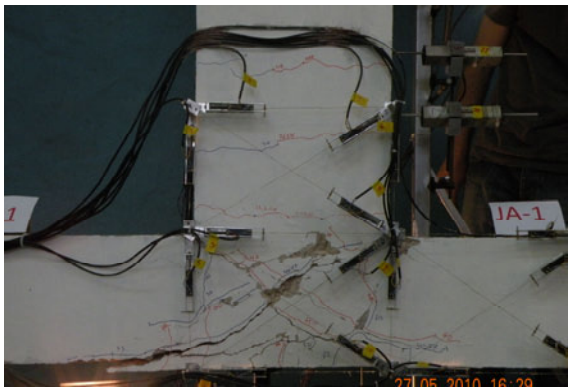

(g) Final Cracking Pattern

Figure 6-6: Cracking patterns and progress of damage of the test unit JA-1

The beam load- tip drift response of unit JA-1 is shown in Figure 6-7. As can be seen from the response, the joint was subjected to only one cycle in the post-peak stage, and therefore, the key characteristics such as stiffness degradation, pinching effect, anchorage strength and energy dissipation cannot be determined. The maximum strength achieved was +40.4 kN (push direction) and -45.1 kN (pull direction), corresponding to displacements of +19 (DR of +1%) and -33.9 mm (DR of -2%), respectively. A sudden drop in the load occurred at a displacement of -19 mm (DR of -1%) due to the formation of diagonal shear crack in the core. However, with further increase in displacement the load recovered reaching its maximum resistance and then declined at a gentle rate. At the end of the test, it was noted that the joint did not completely lose its strength. In fact, a residual strength of about -30 kN (34% reduction with respect to the maximum resistance) was achieved at a displacement of -100 mm (DR% =- 6%).

It should be mentioned that the degradation in the pull (weak) direction was not as severe as it was expected, which could be due to the use of one cycle, where the drop in the resistance was mainly due to the formation of one major diagonal crack along the core.

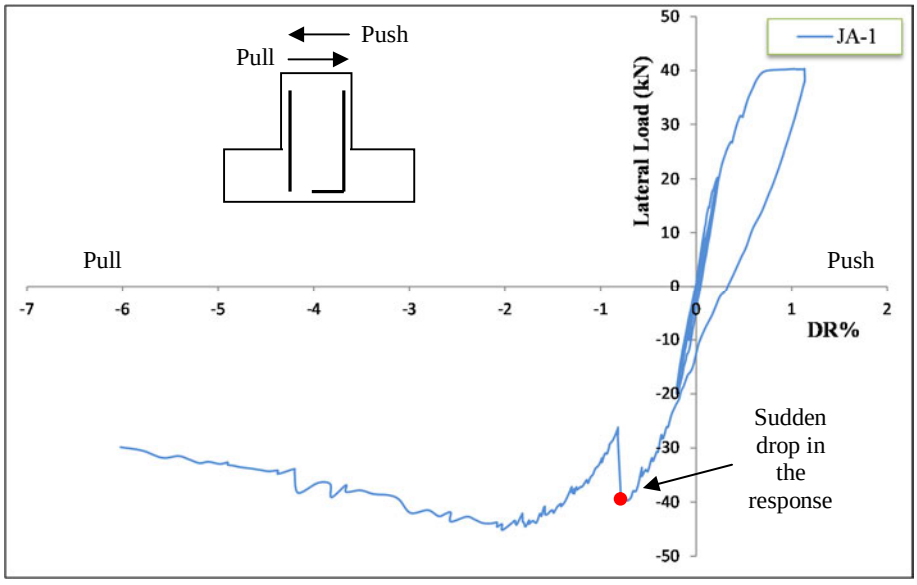

Figure 6-7: The hysteretic response of the test unit JA-1

Readings from the strain gauges attached to the reinforcing bars show that the strains in the bars remained elastic throughout the test. The maximum strains achieved at the maximum loading of the beam and columns in both directions are presented in Table 6-1. Figure 6-8 shows the strain history of the beam anchored bars and top column splices. From the figure, it can be noted that the strains in the anchored bars remained linear until first cracking in the core initiated (4^{th} loading step). In the splices, on the other hand, the strains in the push direction became nonlinear (elastic) after the first diagonal cracking in the unit; whereas in the pull direction, strains remained elastic until the maximum load was reached. During the last cycle and after the maximum load was reached, large positive (tension) strains in the splices and anchors were

recorded. The strains in splices started from an initial value of -300με because of the compressive axial load applied to the column.

Table 6-1: Strains at beam and column reinforcement at maximum loading (JA-1)

Lateral Force		**δ_{max} Deflection**	**Beam**		**Top column**		**Bottom Column**	
Direction	Value		ε_s (με)		ε_s (με)		ε_s (με)	
	kN	*mm*	ST1	ST2	ST4	ST6	ST3	ST5
Push	40.4	19.0	333	1012	1326	-646	186	1400
Pull	-45.1	-33.9	1733	-135	317	964	895	909

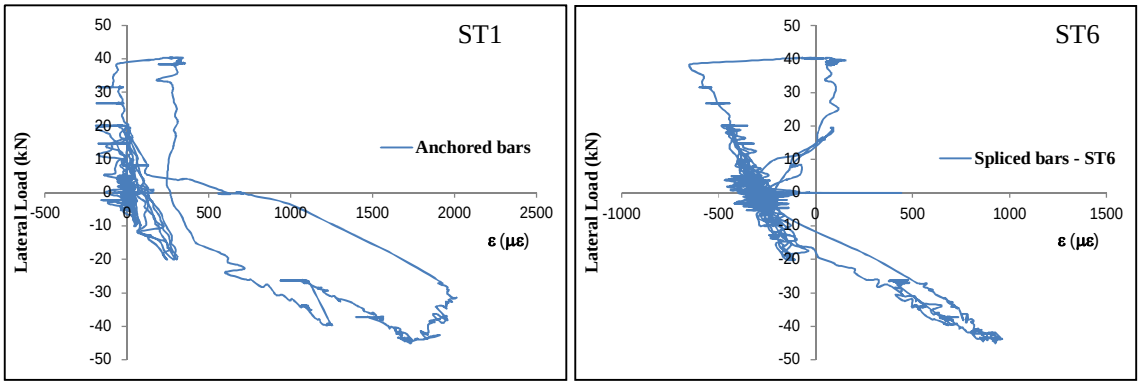

Figure 6-8: Strain history of anchored and spliced bars of the unit JA-1

The cumulative energy dissipated in this unit is shown in Figure 6-9. As can be seen from the figure, the energy dissipation mostly occurred during the last and single post-peak cycle. In addition, the energy dissipation took place in the joint area due to the severe cracking in this region; no plastic hinges formed at the adjoining elements. At the end of the test, the joint had dissipated a total energy E_{JA-1} of around 3kN.m.

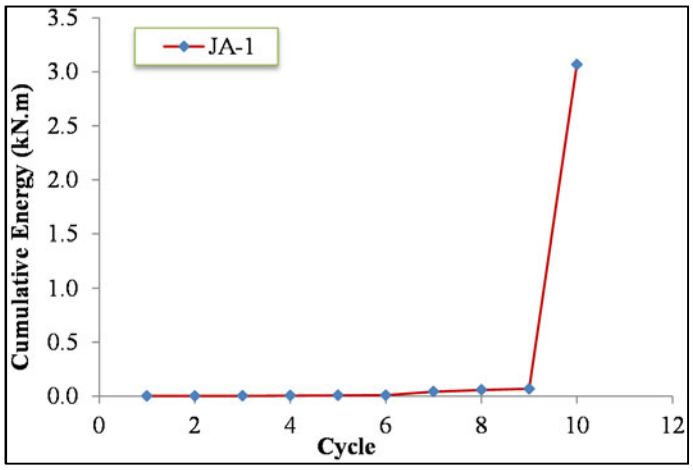

Figure 6-9: Cumulative energy dissipation of the test unit JA-1

6.3.2 UNIT JA-3

This unit was tested under displacement control, as illustrated in Figure 6-10. The loading regime comprised seven loading steps at drifts of ±0.25%, ±0.5%, ±1%, ±1.5%, ±2%, ±3%, ±4% and one cycle at +5%. An additional half cycle was performed during the 5th loading step because of an error that caused the hydraulic pump of the top actuator to lose pressure.

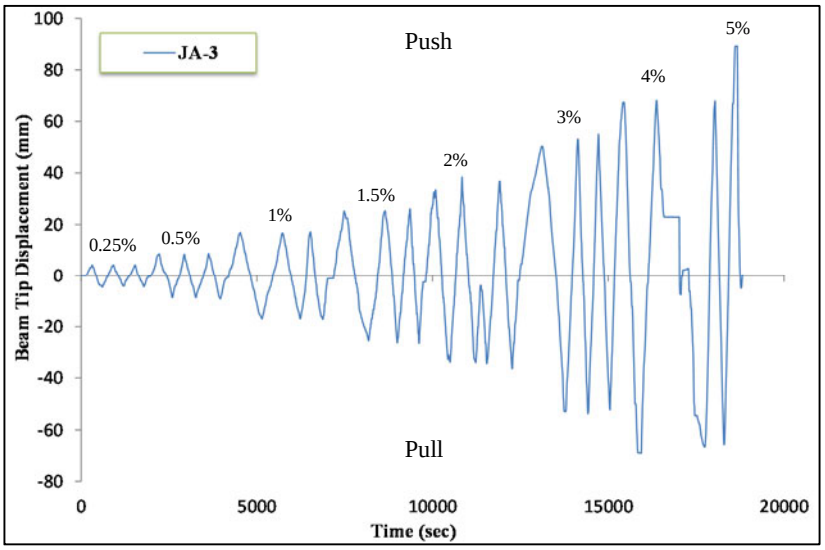

Figure 6-10: Loading regime of the control unit JA-3

The column of this test unit was subjected to a compressive axial load of 250 kN representing 8.6% of the cross-section capacity in compression. Figure 6-11 shows the fluctuation of the axial load as the specimen was subjected to the various loading cycles. As the loading increased, the axial load tended to decrease and reached 206 kN (18% reduction) at a DR of 0.5%. Thus, the loading was removed and the axial load was reapplied at the desired level. With further loading, the axial load continued to fluctuate slightly. An increase in the axial load occurred during the 6th loading step and continued until it reached +12% at the end of loading. The variation in the axial load for most of the main part of the response was low, and therefore, it can be considered insignificant.

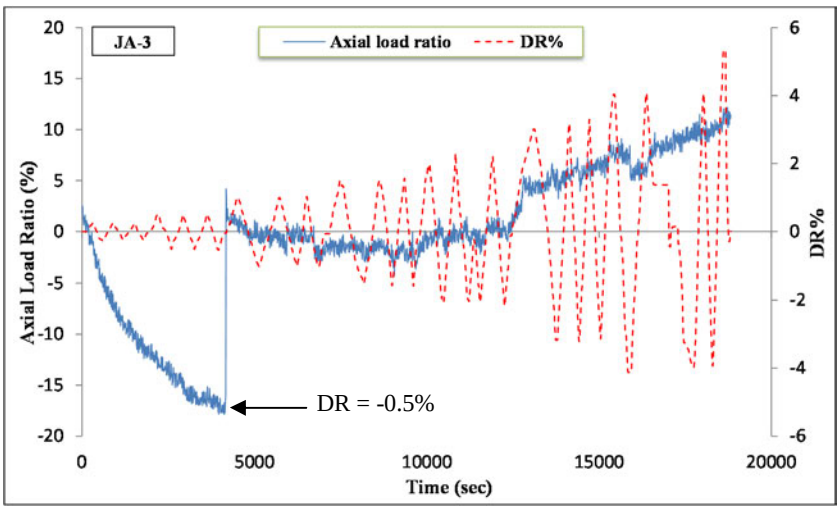

Figure 6-11: Fluctuation of the column axial load throughout the test

The test initiated with small loading steps of a DR ±0.25%. In this cycle, readings from all instrumentation including LVDTs, strain gauges and potentiometers were checked to test their functionality. The first crack was observed to develop at shear link locations of the beam hinging area, as shown in Figure 6-12(a). These cracks formed on both sides during the repetitive cycle. With further increase in loading to a DR of ±0.5%, the first cracks in the joint area were recorded at the beam interface with the column. These cracks formed in a diagonal manner and propagated along the inner longitudinal reinforcement of the column and beam bars, as shown in Figure 6-12(b). With increase in loading above DR of ±0.75%, multiple diagonal shear cracks formed in the joint area in both loading directions forming an X-pattern, as shown in Figure 6-12(c) for DR=±1%. These cracks extended outside the joint area to the back of the column along the longitudinal reinforcement. Flexural cracks also appeared at column interfaces with the core as seen in the same figure. After the maximum load was reached at about a DR of ±1.5%, the main shear crack in the joint area widened, and when additional cycles were performed, a failure mechanism started to form. Loading beyond the peak resulted in widening of the formed cracks and the appearance of multiple small diagonal shear cracks in the core. At a DR of ±4%, severe cracking also occurred in the outer (external) side of the core. The assembly after that was pushed to a DR of +5% to damage the core further and inspect more clearly the failure mechanism.

Ultimately, the joint failed in a classical shear failure pattern such that a cracked triangular section formed at the bottom part of the joint area. The failure triangle extended up to the splice end of the top column and along a distance of 300 mm of the bottom column. It was also observed that at the column interfaces with the core, there were multiple cracks extending from cracks in the core. The final cracking pattern of the joint is shown in Figure 6-12(g).

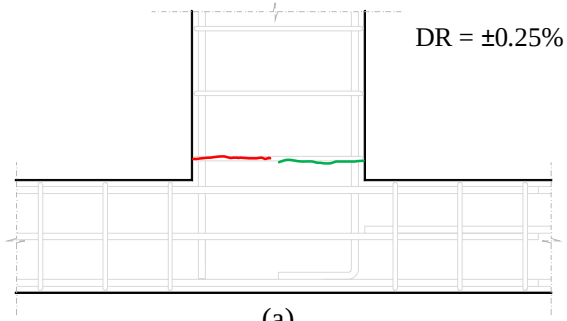

(a)

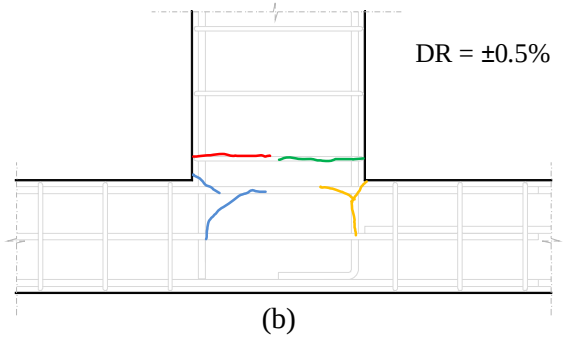

(b)

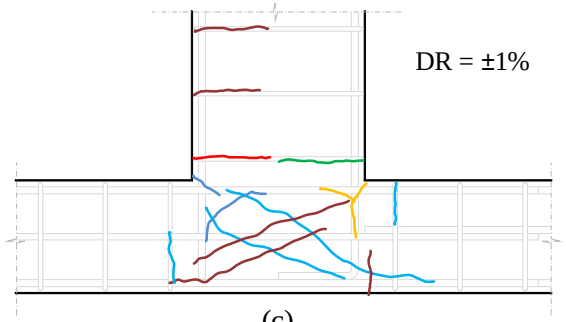

(c)

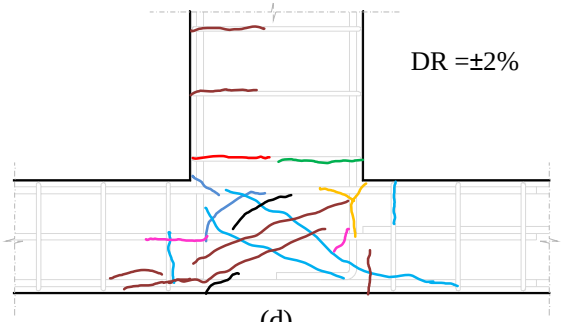

(d)

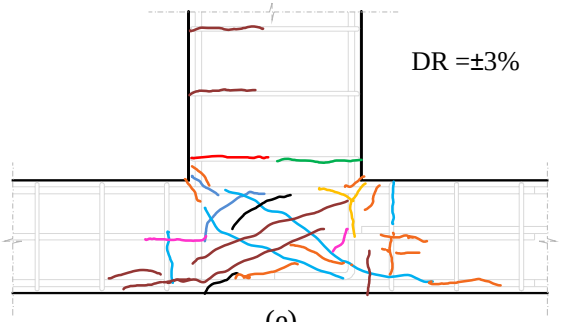

(e)

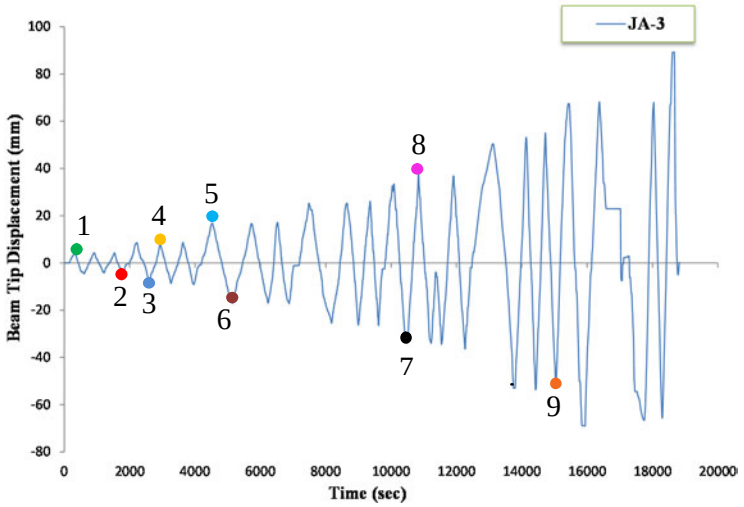

(f) Loading Regime (Displacement Control)

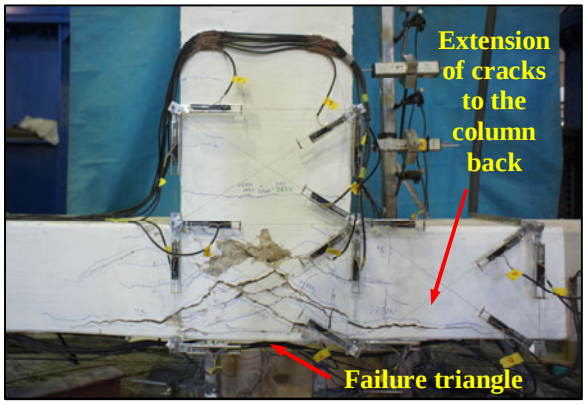

(g) Final Crack Pattern

DR (±5%)

Figure 6-12: Cracking patterns and damage progress of test unit JA-3

The beam load- tip drift of the control unit is shown in Figure 6-13. It is clear that the pull direction resistance is deficient because of the inadequate anchorage of the beam bottom bars (only 230mm into the core). It can also be observed from the figure that a sudden drop in the load occurred accompanied by the formation of diagonal shear cracks in the core at a DR% of -0.5% during loading from +1% towards -1% (DR). Afterwards, the response recovered with no sudden drops. In fact, the degradation occurred in a relatively gradual manner. After a DR ±4%, the load sustained by the assembly dropped below 50% of the maximum load and the test was halted. The maximum load sustained by the bare joint in both directions was +56 kN and -52 kN, corresponding to DR of +1.5% and -1.5%, respectively.

It can also be noted from the response that the joint, within each cycle in the post-peak stage, had almost completely lost its stiffness near the zero-displacement loading due to opened cracks, as shown in Figure 6-14. The figure shows the crack opening in the core at a DR of -3% and at a DR of 0% (return from DR of -3%). Due to these wide cracks, the pinching effect was significant in this joint.

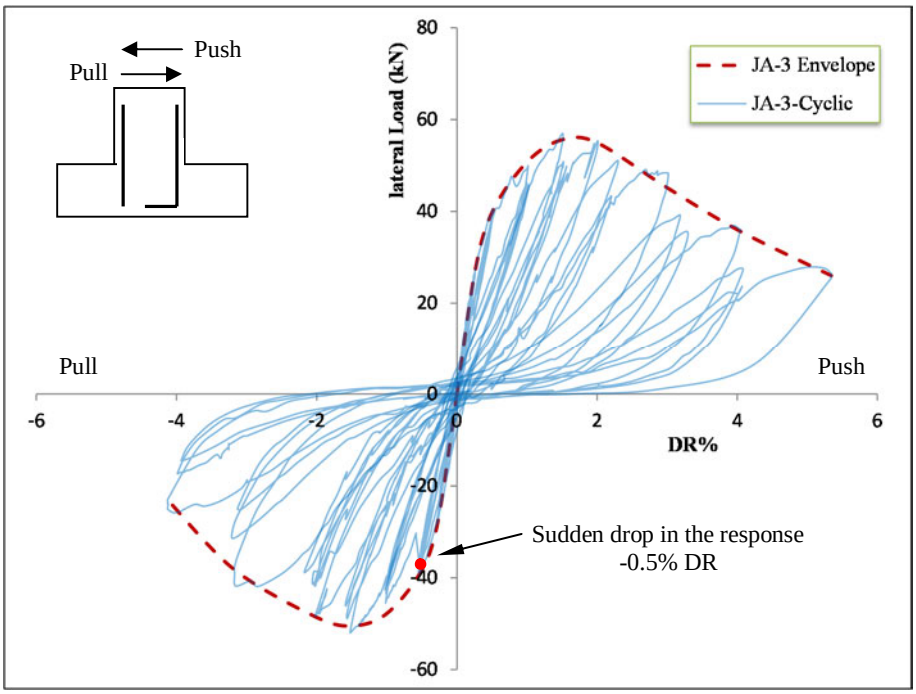

Figure 6-13: The hysteretic response of the test unit JA-3

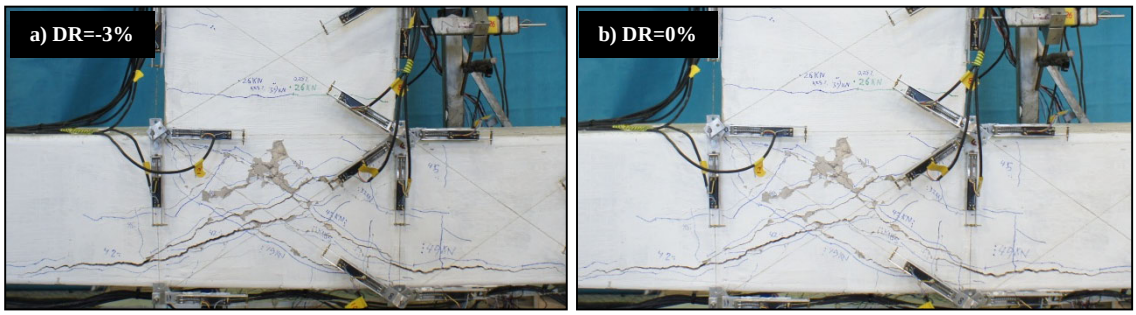

Figure 6-14: Joint JA-3 at a DR of -3% (Left) and at zero load displacement 0% (Right)

In order to determine the stage at which the bottom beam bars (anchorages) started to influence the resistance of the joint, the beam-tip load at the pull and push directions were plotted at each load step in Figure 6-15(a). The ratio of the load at the push to pull direction, referred to as the resistance factor RF in this study, is also plotted in Figure 6-15(b). From the figure, it can be noted that the anchorage effect was noticeably recognised after the sudden drop in the resistance occurring when the loading was going towards a DR of -1%. Although the first shear crack in the joint initiated first in the strong direction at a DR of +1% (+43kN load), no drop in the load resistance occurred. The reason for this drop is discussed later in this chapter, see Sec 6.3.5.

The difference in load values of both directions was calculated at 10% (RF=1.1) at the maximum load (DR=±1.5%) and reached 60% (RF=1.6) at a DR of ±4%. Thus, the anchorage effect was significant mostly in the post peak stage when the joint area was damaged and a failure mechanism formed.

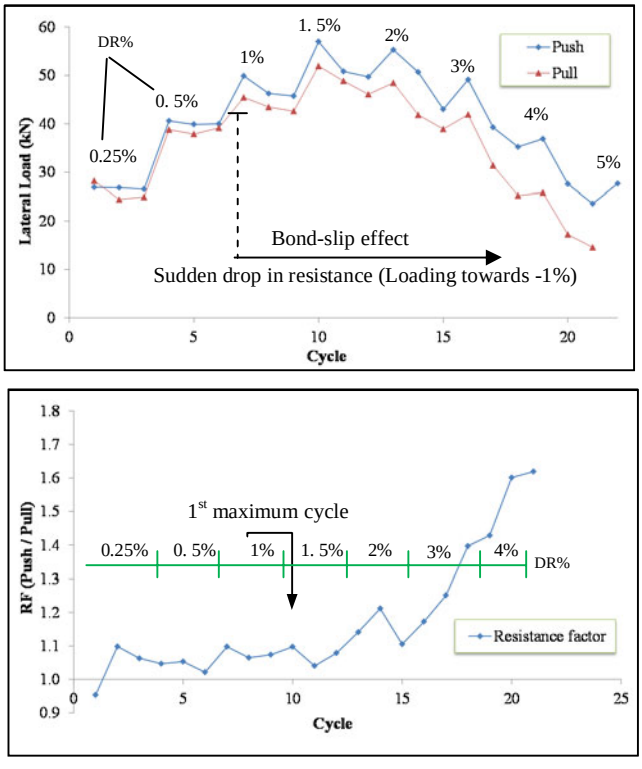

Figure 6-15: a) variation of beam tip load during cycling, b) resistance factor

Stiffness degradation of the test unit is shown in Figure 6-16 for both loading directions and also for each complete cycle K_{secant}. At the beginning of loading, the behaviour was stiff and as a result, both loading directions had the same stiffness (with the exception of the initial cycle). In the third loading step, the 1st diagonal crack formed in the core and, as a consequence, severe drop in stiffness occurred (to 2/3 of the initial value). As loading progressed, the stiffness diminished gradually. At the end of the test, the joint lost around 95% of its initial stiffness. It is clear from the figure that the strong direction had slightly higher stiffness, in particular after the formation of the diagonal shear crack in the core. Also, it can be noted that the secant stiffness was slightly higher than that of the push direction. However, after the core started failing in shear, the stiffness's were almost equal.

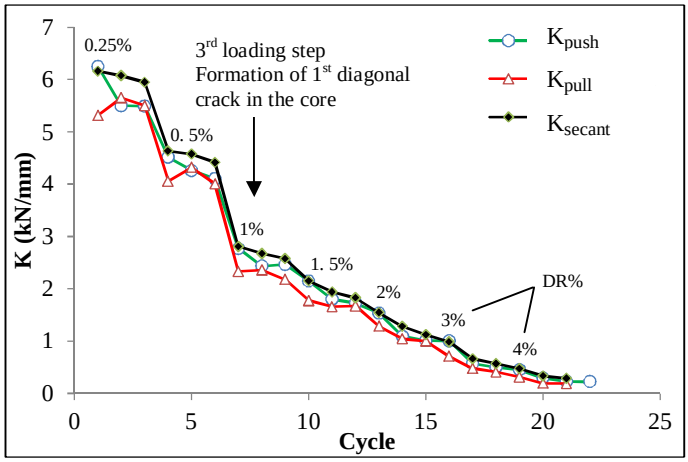

Figure 6-16: Stiffness degradation of test unit JA-3

At the maximum loading, the strains developed in both the beam and column longitudinal reinforcement are presented in Table 6-2. It is clear from the table that strains in the bars remained elastic during the test. The strain history of beam anchorages and column splices is shown in Figure 6-17. The strains in the anchorages and splices remained linear until a DR of ±1% (core cracking). The strains recorded at the maximum load were +1522με at a load of -51.9 kN in the anchored bars; and 1023με at the same load in the spliced bars. These values correspond to an average bond stress (τ) of 6.9 MPa and 2.15 MPa, respectively.

Table 6-2: Strains at beam and column reinforcement at maximum loading (JA-3)

Lateral Force		**δ_{max}**	**Beam**		**Top column**		**Bottom Column**	
Direction	Value		ε_s (με)		ε_s (με)		ε_s (με)	
	kN	*mm*	ST1	ST2	ST4	ST6	ST3	ST5
Push	55.7	25.2	193	1858	-	-340	1480	602
Pull	-51.9	-25.5	1522	289	-	1023	-84	-303

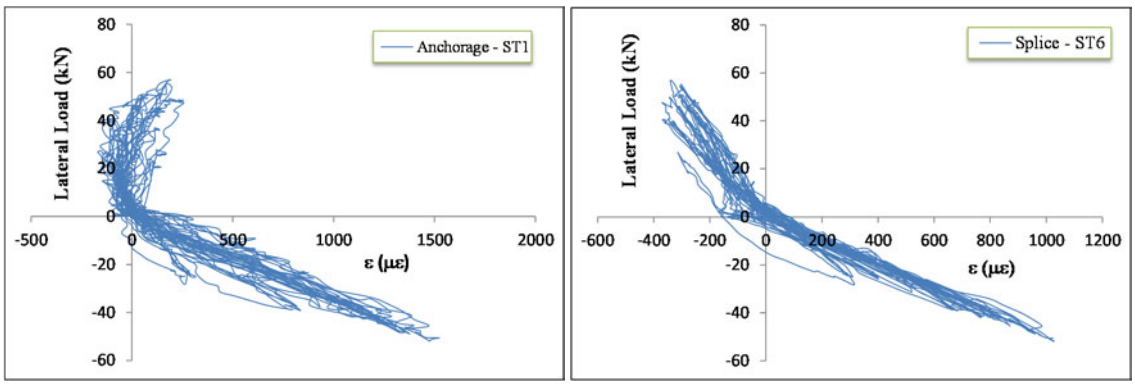

Figure 6-17: Strain history of anchored and spliced bars of the unit JA-3

The amount of energy dissipated in the joint at each cycle, along with the cumulative energy dissipation is shown in Figure 6-18. At low load level up to a DR of ±1%, the energy dissipation was noted to be small and slow. In the third loading step, when the first diagonal crack initiated, the energy absorption started to accelerate. Most absorption occurred during the first cycle of the last two loading steps when large deformations and severe loss in stiffness took place. By the end of the test, the joint had dissipated a cumulative energy E_{JA-3} of 9.6 kN.m. The joint had dissipated 10% of the total energy at ±1% drift, 24% of the energy at ±1.5% drift (maximum load), and 100% of the energy at ±4% drift. It is interesting to note that the energy dissipation is higher during the first cycle of each loading step, while it reduces with cycling. This can be attributed to strength deterioration along with pinching of the hysteretic loops.

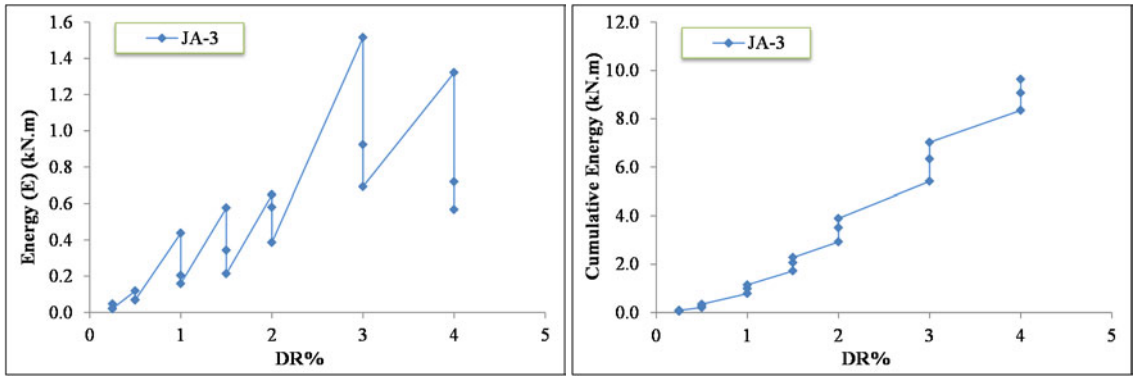

Figure 6-18: Energy dissipated at each cycle (Left) and cumulative energy dissipated (Right) of the test unit JA-3

To better examine the energy dissipation components, two additional indicators were examined. The first indicator relies on normalising the energy dissipated to the strain energy of an equivalent linear system to calculate the equivalent viscous damping ζ_{eq}. In this case, the energy will be normalised with respect to the square of the amplitude of the cycle. It is shown experimentally by Caughey (1962) and analytically by Chopra (2006) that the energy loss is proportional to the square of the amplitude. The equivalent damping was calculated according to Chopra (2006), using the following equation:

$$\zeta_{eq} = \frac{1}{4\pi}\frac{E_D}{E_{so}} \quad (6\text{-}1)$$

in which ζ_{eq} is the equivalent damping; E_D is the amount of energy dissipation per cycle; E_{so} is the strain energy and can be approximated as $E_{so}=ku^2_0/2$, where k and u_0 are the secant stiffness and maximum amplitude of the hysteretic cycle, see Figure 6-19.

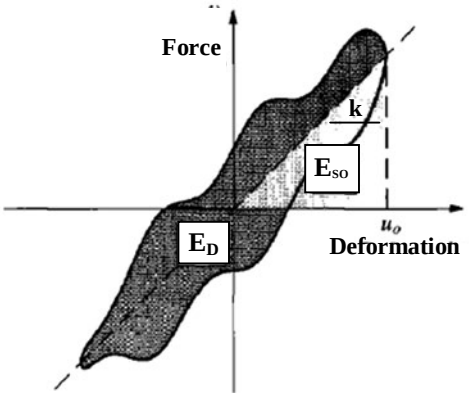

Figure 6-19: Per-cycle energy dissipated E_D and strain energy E_{so} of a hysteretic loop, Chopra (2006)

Figure 6-20 shows the equivalent viscous damping versus the drift of the test unit. It is clear from the figure that up to a DR of ±2%, the damage occurring in the core resulted in a comparatively constant damping value of about 4.2%. This value is typical for such RC elements (3-5%) in which the strains developed within the elements are around half the yield stress and considerable cracking takes place (Chopra, 2006). The formation of the diagonal crack in the core (1st cycle at DR of ±1) led to a severe drop in the energy dissipated; the damping dropped from 9% to 4.2%. During the last two loading steps, more energy was dissipated due to formation of more cracks; however, crack opening and bar slip reduced the damping when repeating the loading. On average, damping at the last loading steps was calculated at 8.5%.

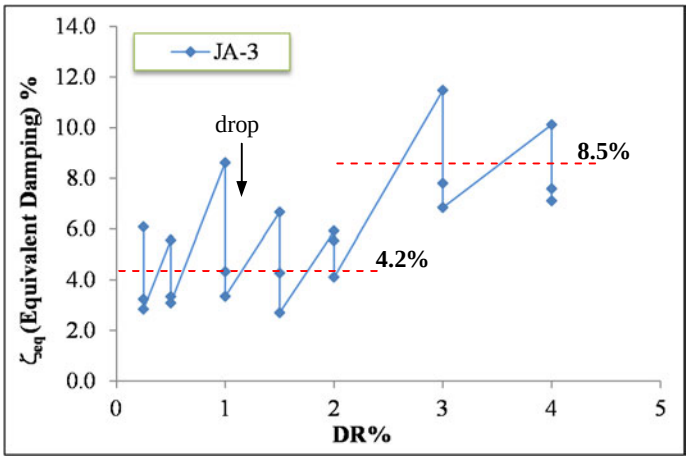

Figure 6-20: Equivalent viscous damping of test unit JA-3

The second indicator uses the per-cycle dissipated energy (E) normalised to the area enclosed by a perfect un-pinched hysteretic response (E_h), as shown in Figure 6-21. The area of the perfect response is limited by the maximum loads (from +positive to -negative) of the cycle and has unloading/reloading stiffness's equal to the initial secant stiffness of the hysteretic response. This indicator (E/E_h) is important to give an insight into the amount of pinching occurring during each cycle. Furthermore, the ratio gives an idea on the plastic damage taking place per cycle. It is worth mentioning that pinching of the hysteresis loops due to opening and closing of cracks or due to bar slippage was believed for many years to be an undesirable characteristic of the hysteretic behaviour, and lead to large inelastic deformations. However, it is shown that the hysteretic pinching does not produce undesirable behaviour unless it is accompanied by significant strength deterioration (Huang et al., 2009).

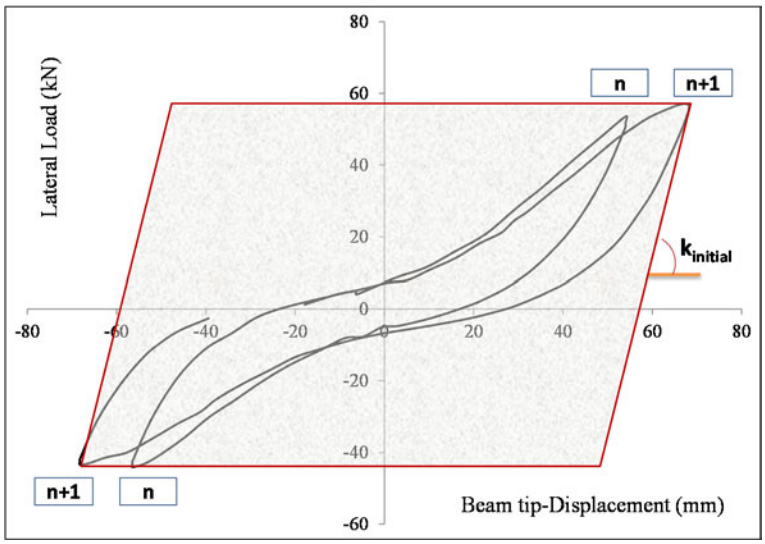

Figure 6-21: Calculation of energy dissipation of a hysteretic cycle

Figure 6-22 shows the normalised per-cycle energy (E) with respect to E_h. At the first loading step, the unloading and reloading behaviour of the unit is somehow linear with few flexural cracks; therefore, the ratio was > 1. However, the importance of the ratio lies after significant cracking in the joint occurs (> DR of ±0.5% in this unit). As a result, values higher than 1 are ignored. From the figure, it can be noted that up to a DR of ±2% the amount of energy dissipated was relatively small, and as a result, the ratio decreased. An increase in the values occurred at the first cycle of DR ±3% and ±4% as the joint showed some resistance and many cracks were developing. Consequently, the ratio E/E_h increased. However, this increase reduced significantly within the loading step due to load deterioration and large loss of reloading stiffness. On average, the ratio in this unit was found to be 15%.

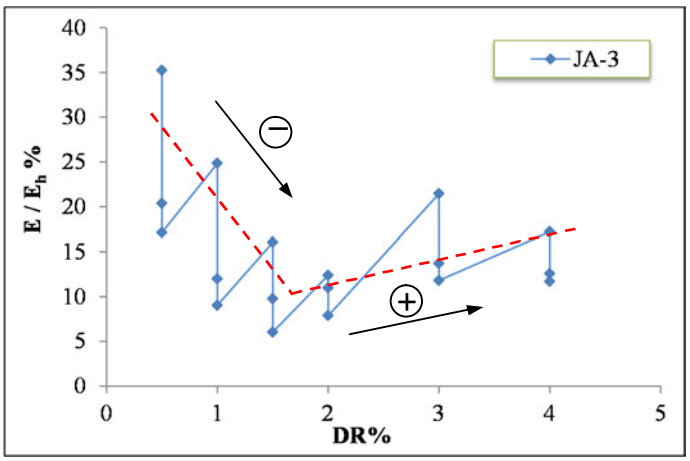

Figure 6-22: Ratio of per-cycle energy E to E_h of test unit JA-3

6.3.3 UNIT JB-1

This joint was subjected to a loading regime in displacement control as shown in Figure 6-23. The regime comprises eight loading steps corresponding to drift ratios (DR) of ±0.25%, ±0.5%, ±0.75%, ±1%, ±1.5%, ±2%, ±3% and ±4%.

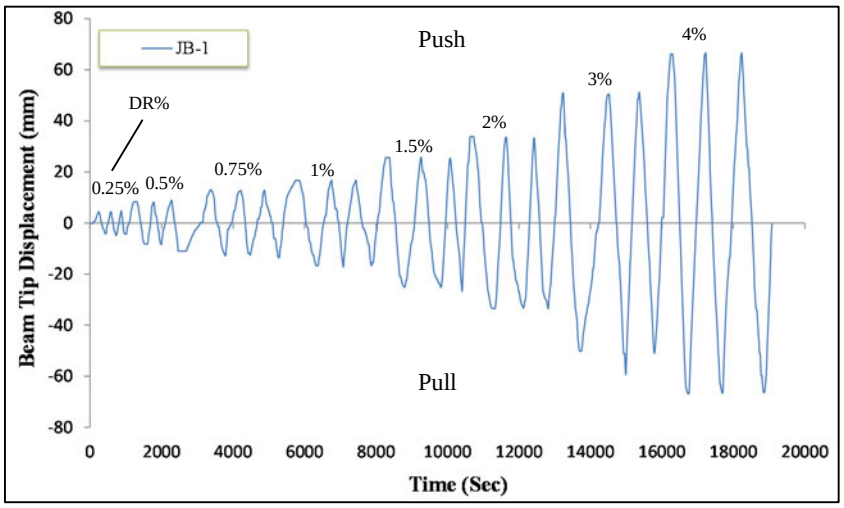

Figure 6-23: Loading regime of the test unit JB-1

The test unit was subjected to an axial compressive load of 150 kN or 5.4% of the column cross-section capacity in compression. The test results show, however, that the actual load imposed was 133.5 kN. Figure 6-24 shows the fluctuation of the applied axial load throughout the test. A reduction in axial load was occurring with loading until the end of the 4th loading step. The reduction, thereafter, settled at a load level of 127 kN representing a -5% reduction of the initial state or -15% of the design level.

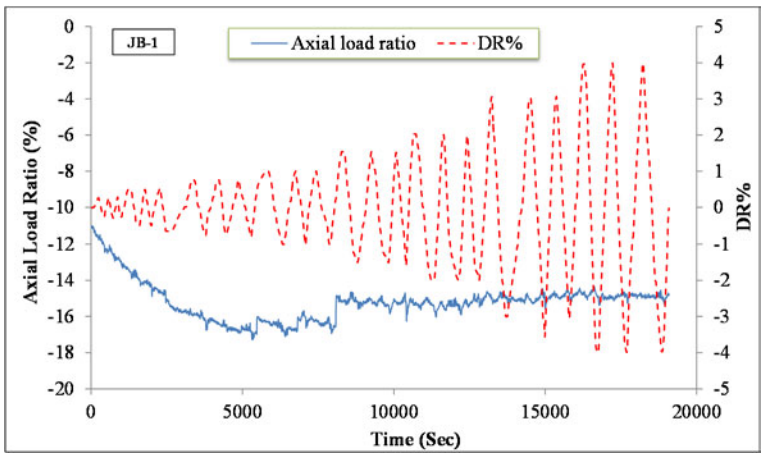

Figure 6-24: Fluctuation of the column axial load throughout the test

The loading on the assembly was initiated with a small loading step of DR ±0.25% to test the instrumentation and stability of the system. Similarly to the previous tests, in this loading step, some flexural cracks appeared at shear link locations of the beam, as shown in Figure 6-25(a). As the load increased to a DR of ±0.5%, cracks tended to form in the joint area at the beam interface with the column, as shown in the same figure. These cracks formed initially in a diagonal manner and then propagated along the beam and column longitudinal reinforcement. During the last cycle at DR of +0.5% to -0.5%, the applied displacement accidentally reached a DR of -0.64 and diagonal cracks appeared along the core. As the displacement was increased to a DR of ±0.75% diagonal shear cracks developed along the entire joint area in both loading directions. Some flexural cracks also appeared at the outer tension sides of the column. Figure 6-25(b) shows the cracking pattern at this stage. Increasing the loading to a DR of ±1% resulted in the formation of more flexural cracks in the column at the interface with the core. Multiple shear cracks appeared in the core in both directions when loading to a DR of ±1.5%. In addition, the main diagonal shear cracks extended to the back of the column along the longitudinal reinforcement, as shown in Figure 6-25(c). The increase in loading to a DR of ±2% resulted in widening of the formed cracks along with the formation of random hairline shear cracks within the core. An X-pattern shear failure mechanism clearly formed at the loading step of DR ±3% and caused spalling of concrete at the centre of the mechanism. Severe damage occurred during cycling at a DR of ±4% such that the shear cracks caused failure of the compression struts in the core leading to a considerable loss in the resistance. The test was stopped at this loading step (the load was below 50% of the maximum resistance). Figure 6-25(g) shows the final cracking pattern and damage state of the joint.

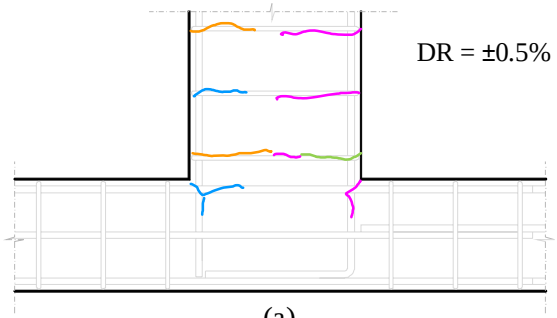

(a)

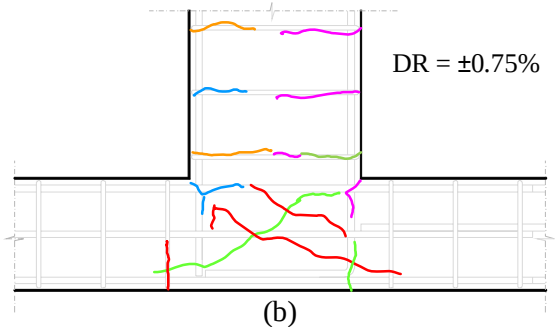

(b)

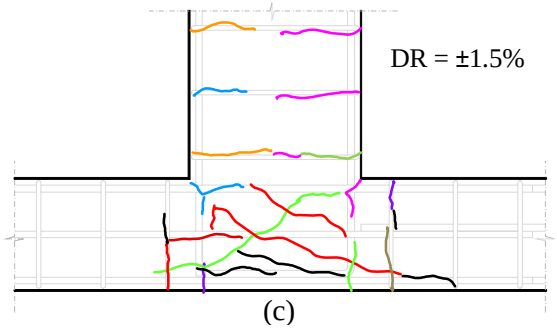

(c)

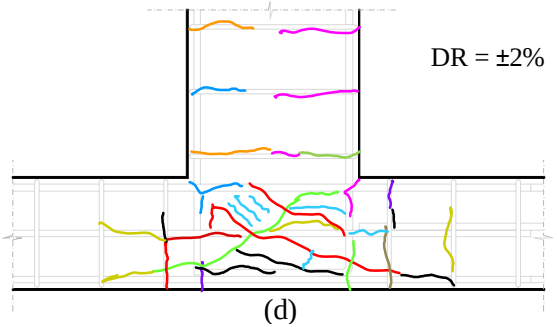

(d)

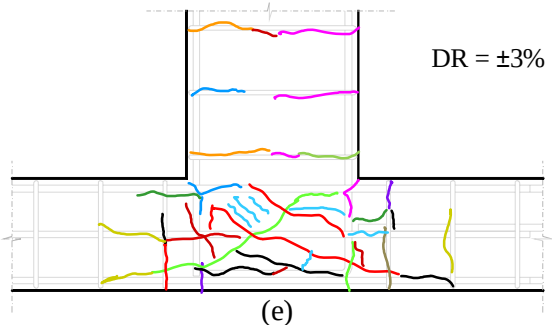

(e)

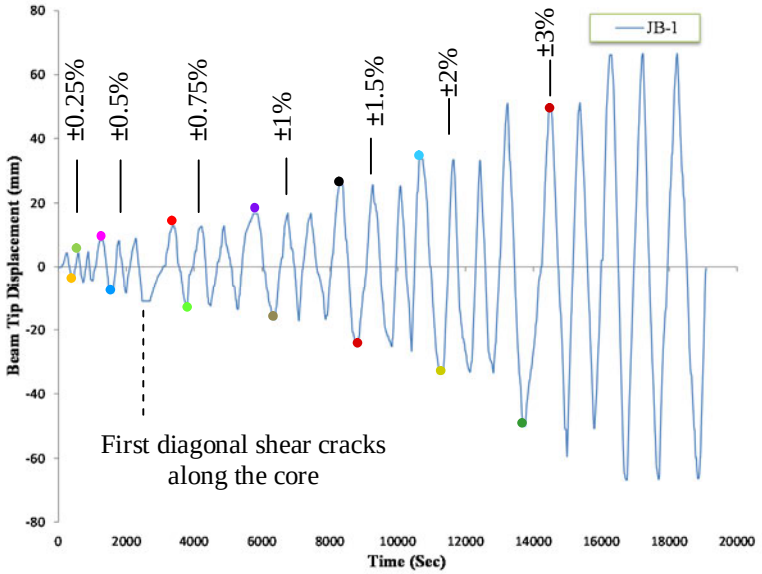

(f) Load Regime (Displacement Control)

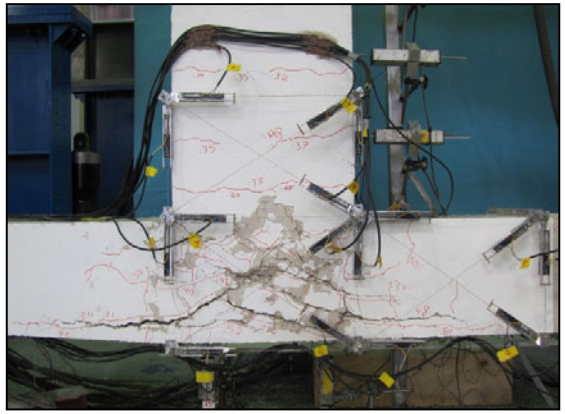

(g) Final Crack Pattern

DR = ±4%

Figure 6-25: Cracking patterns and damage progress of test unit JB-1

The load-beam tip drift hysteretic diagram of the test unit JB-1 is shown in Figure 6-26 along with the envelope curve. A sudden drop in the load of about 25% occurred at a DR of -0.64% that coincided with the formation of the 1st diagonal crack in the pull direction of the core. In the next loading step, this drop recovered partially without reaching the previous peak. As the loading continued, the response tended to diminish gradually until the end of the test. Before the sudden drop in the load, the response was degrading very gently. After that, a significant degradation in stiffness occurred. In the push direction, on the other hand, the response degraded gently with a slight loss of stiffness at the shear cracking point until the maximum was reached at a DR of +1.54%. That was accompanied by cumulative damage in the core. The maximum loads achieved in the unit were +50.8 (+1.54% DR) and -41.1kN (-0.64% DR). Hence, the ratio between the lateral load capacity in the push and pull directions is equal to 1.24.

The hysteresis loops of the post-peak response reveal that the joint experienced almost complete loss of its stiffness near the zero-displacement point because of the severe cracking in the core. Those cracks seemed not to recover directly after reloading in the reverse direction. Therefore, severe pinching is noticed in the response of this unit.

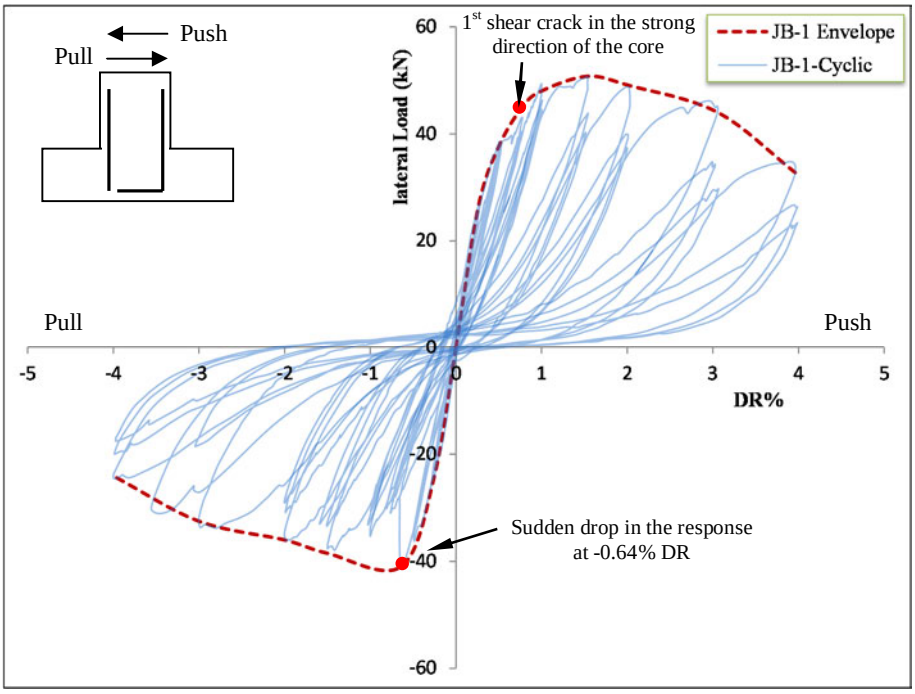

Figure 6-26: The hysteretic response of the test unit JB-1

Stiffness degradation of the test unit is shown in Figure 6-27. As can be seen from the figure, unlike test specimen JA-3, this unit had faster stiffness degradation in the first two loading steps. Moreover, after the formation of the 1st diagonal crack (end of 2nd loading step), the behaviour in the pull direction was noticeably affected. The unit had lost 60% of its initial stiffness at this stage. At the end of the test, the unit had lost 95% of its initial stiffness.

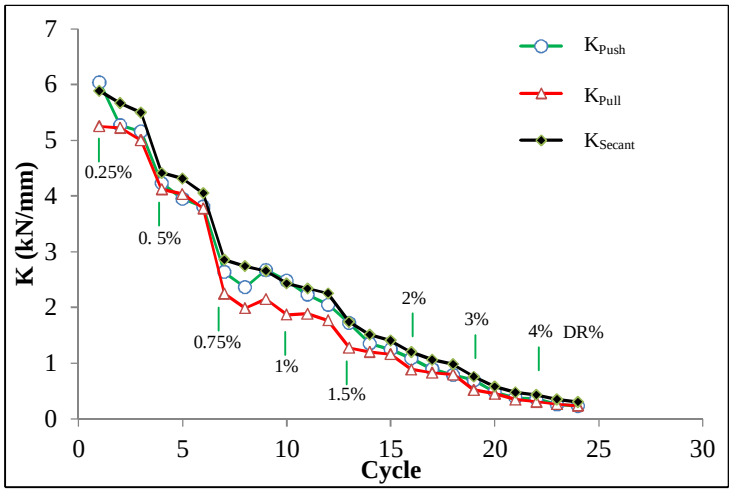

Figure 6-27: Stiffness degradation of test unit JB-1

The strains developed in both the beam and column reinforcement at the maximum load are presented in Table 6-3. These values represent 34%, 65% and 29% of yield strain at the beam, top column and bottom column, respectively. Moreover, Figure 6-28 shows the strain history of the anchored bars (ST1) and spliced bars (ST6). As expected, strains were approximately linear during the first loading steps until the diagonal cracks formed in the core. Afterwards, nonlinear (elastic) behaviour in strains was noted for the anchored and spliced bars. After the sudden drop in the resistance, strains increased slightly in the anchorages and reached a value of 1113 με ($\tau = 4$ MPa). In the splices, on the other hand, the strains reversed. This can be attributed to the formation of multiple flexural cracks along the interface of the column with the core as explained earlier. Also, the formation of the major cracks along the diagonals of the core up to the splices at the back of the column is most likely another reason for the change in the strain sign of spliced bars

Table 6-3: Strains at beam and column reinforcement at maximum loading (JB-1)

Lateral Force		**δ**	**Beam**		**Top column**		**Bottom Column**	
Direction	Value		ε_s (με)		ε_s (με)		ε_s (με)	
	kN	*mm*	ST1	ST2	ST4	ST6	ST3	ST5
Push	50.8	-10.7	21	damaged	1613	212	-292	722
Pull	-41.1	25.7	842	damaged	27	520	300	-806

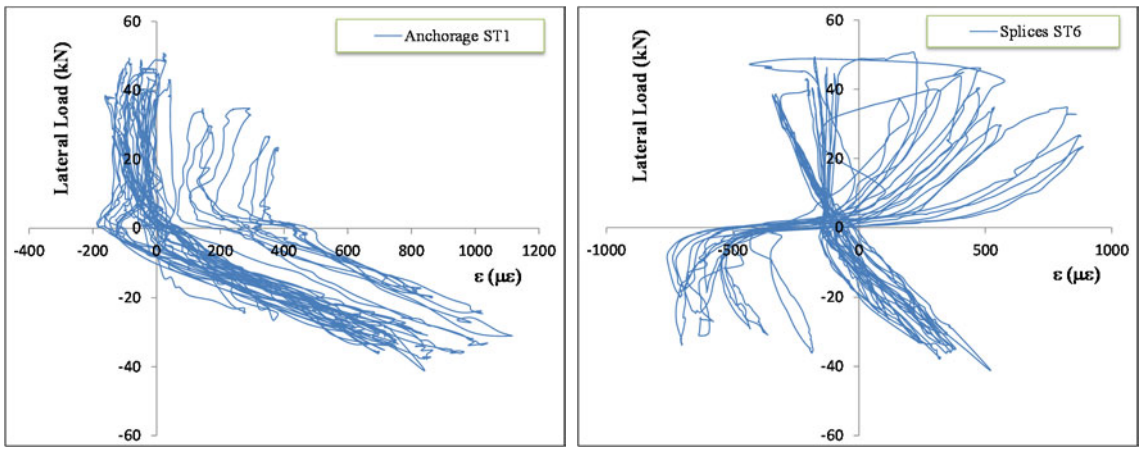

Figure 6-28: Strains at the beam bottom bars (Left) and at top column splices (Right)

The effect of anchorage failure on the resistance of the joint is demonstrated by plotting the load in the pull and push directions at each loading step, as shown in Figure 6-29. The resistance factor RF is plotted in the same figure. In the first and second loading steps, the difference was 5% (RF=1.05). After the drop in resistance occurred (at a DR of -0.64), the difference between the load values increased to 40% (RF=1.4). After reaching the maximum capacity at the push direction (DR=1.5%) where an X-shear mechanism in the core formed, the difference in RF reduced to 30%. The difference remained comparatively constant until the end of the test.

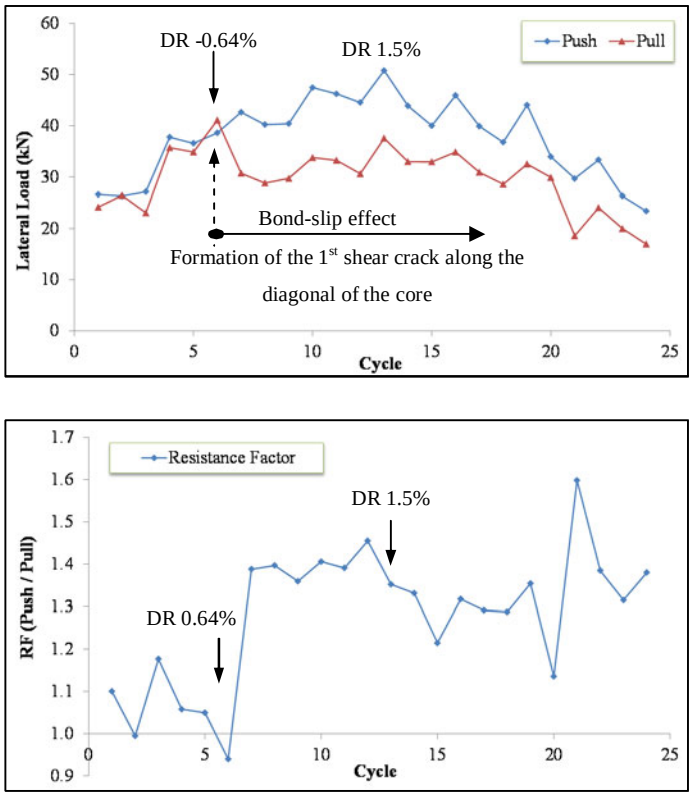

Figure 6-29: a) variation of beam tip load during cycling, b) resistance factor

The amount of per-cycle energy dissipated and the cumulative energy are shown in Figure 6-30. It can be noted that the energy dissipation is small and slow at low drifts. With increase in loading, the amount of energy absorbed at each loading step generally increased. The energy, however, was observed to diminish severely within the same loading step due to deterioration in load. The highest energy absorption in the joint occurred at a DR of ±3%. Ultimately, the beam-column joint dissipated a total energy E_{JB-1} of 9.2 kN.m at the end of the test (DR=±4%). The joint had dissipated 4.2% of energy at DR of ±0.64%, 21.4% of energy at DR of ±1.5%, 58% of energy at DR of ±2% and 100% at DR of ±4%.

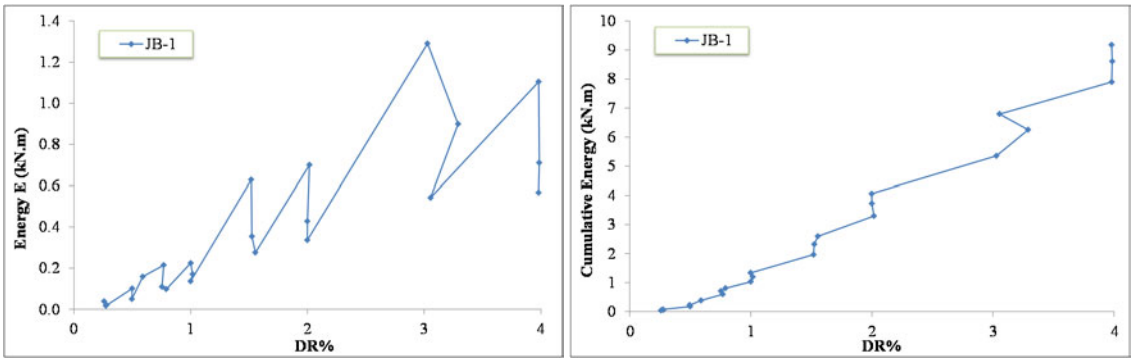

Figure 6-30: Energy dissipated at each cycle (Left) and cumulative energy dissipated (Right) of the test unit JB-1

The calculated equivalent viscous damping of this unit is plotted versus drift in Figure 6-31. As damage progressed, more energy was dissipated, and as a result, higher damping took place. A reduction in the damping, however, occurred during each loading step due to load deterioration and loss of stiffness, as it was observed from the hysteretic response. Up to a DR of ±2%, an average damping of 5% was found. In the subsequent stage (DR > ±2%), the unit had a damping of 8.2%.

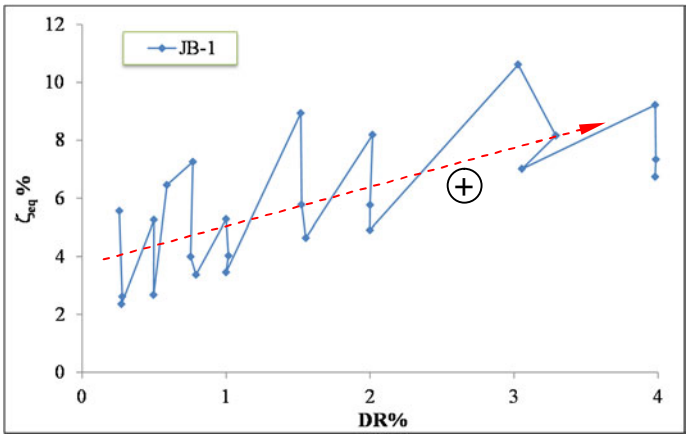

Figure 6-31: Equivalent viscous damping of test unit JB-1

The ratio of energy dissipated E to E_h of this unit is shown in Figure 6-32. After shear cracking initiated in the core, a 10% drop in the ratio occurred. An additional 10% drop also occurred at

the next cycle. After that (DR ≥ ±1%), the ratio increased only slightly with an average value of around 12.8%. It can be noted that the ratio decreases with cycling due to deterioration of the load.

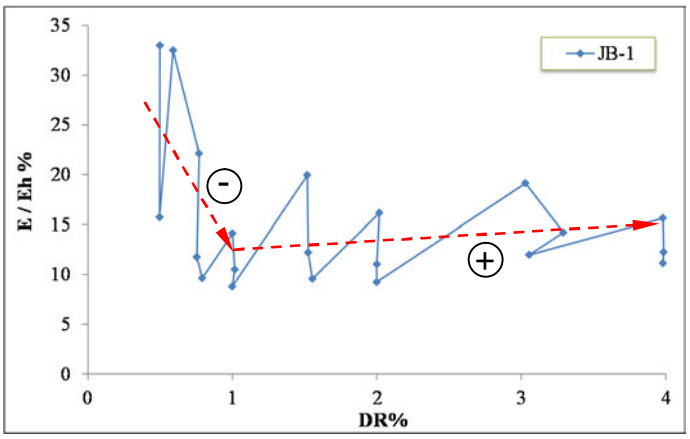

Figure 6-32: Ratio of per-cycle energy E to E_h of test unit JB-1

6.3.4 UNIT JC-1

In this unit, the beam longitudinal reinforcement had symmetrical detailing such that the bars are hooked into the core. The unit was subjected to a loading regime in displacement control, as illustrated in Figure 6-33. The regime comprised ten loading steps at drifts of ±0.1%, ±0.25%, ±0.35%, ±0.5%, ±0.75%, ±1%, ±1.5%, ±2%, ±3% and one cycle at ±4%.

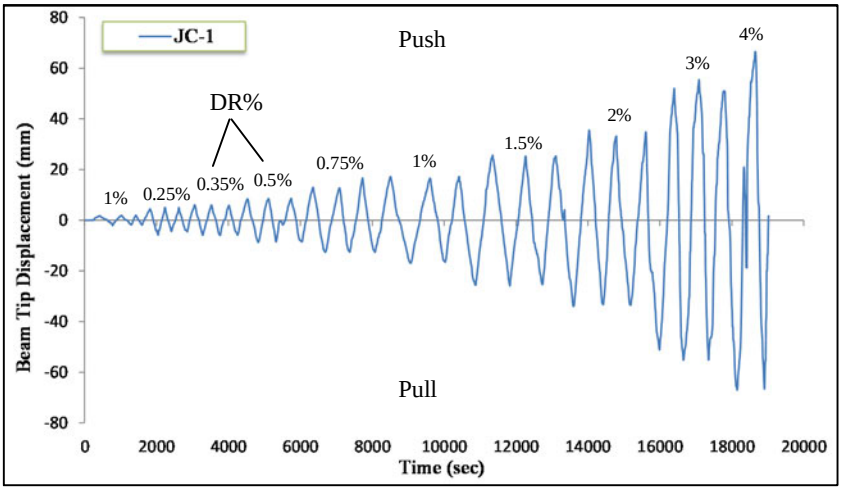

Figure 6-33: Loading regime of the test unit JC-1

The unit was subjected to a compressive axial load of 150 kN (6.1% of column cross-section capacity in compression). The results show that the actual axial load imposed on the column was 144 kN (-4% drop). Throughout the test, the axial load fluctuated about this value with a range of (±6 kN). This drop is very small and can be ignored.

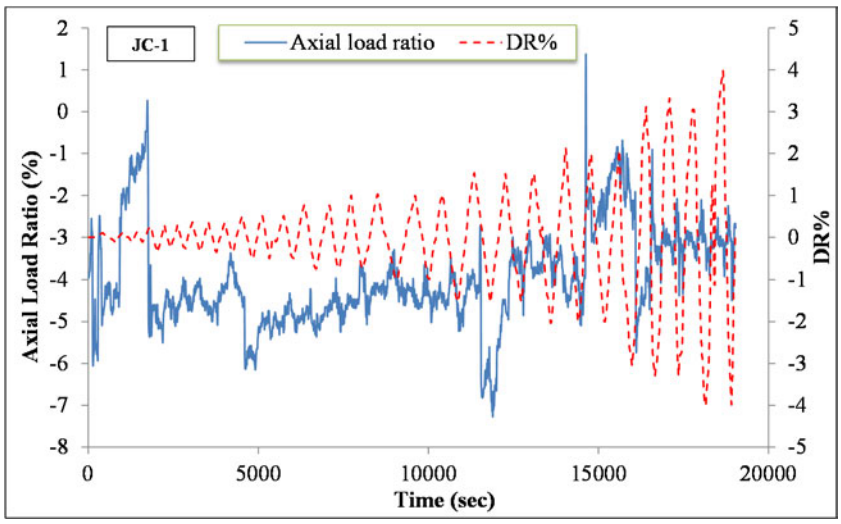

Figure 6-34: Fluctuation of the column axial load throughout the test

During loading up to a DR of ± 0.25%, flexural cracks initiated in the hinging area of the beam along the stirrup locations and at the interface with the column. Hairline cracks were also observed at the inner corners of the joint region, and they extended along the beam and column longitudinal bars, as shown in Figure 6-35(a). During loading to a DR of ± 0.5%, diagonal cracks initiated within the joint core region in both loading directions at a load of 34 kN. With further increase in loading up to a DR of ±2%, multiple shear cracks appeared in the joint region forming an X-shaped cracking pattern. These cracks were observed to extend to the back of the column along the longitudinal reinforcement. In addition, few flexural cracks appeared at the column interface with the core. During loading beyond DR of ±2%, the cracks widened and a triangular-shaped cracked section formed at the bottom part of the joint. This triangle spalled off at the back of the column by the end of the test and exposed the longitudinal reinforcement. Figure 6-35 shows the damage stages of the joint during the lateral loading. The joint ultimately failed at a displacement of 66 *mm* corresponding to a DR of ±4%.

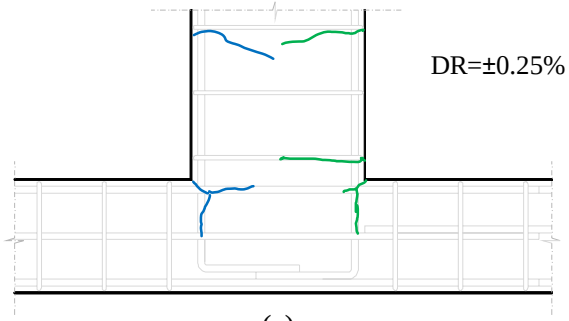

(a)

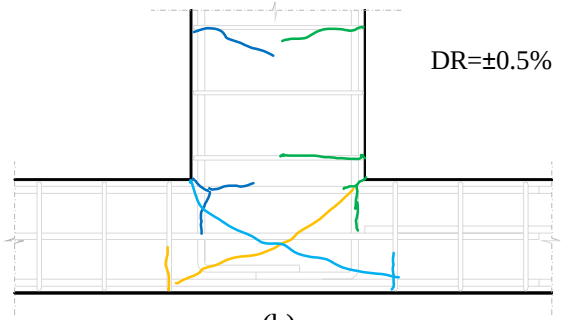

(b)

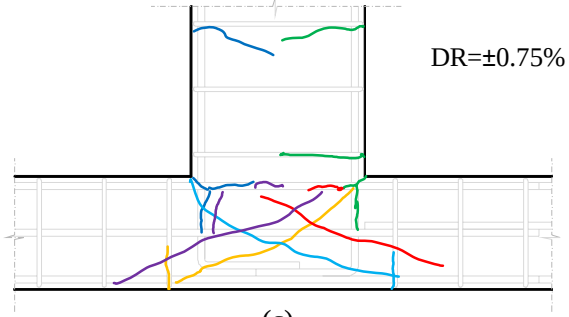

(c)

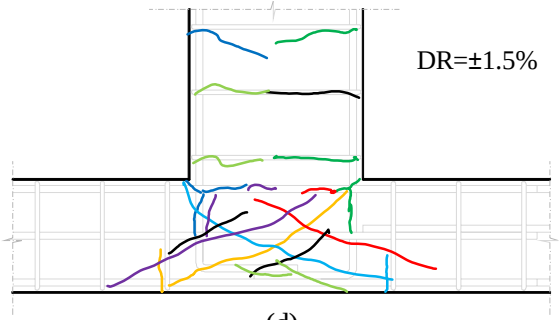

(d)

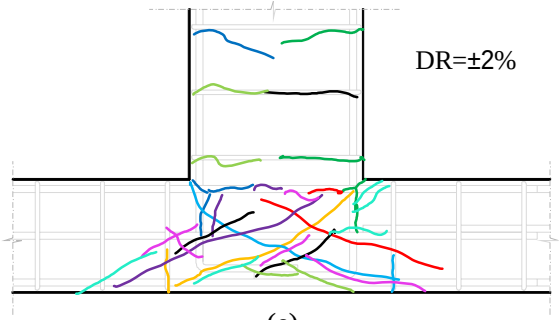

(e)

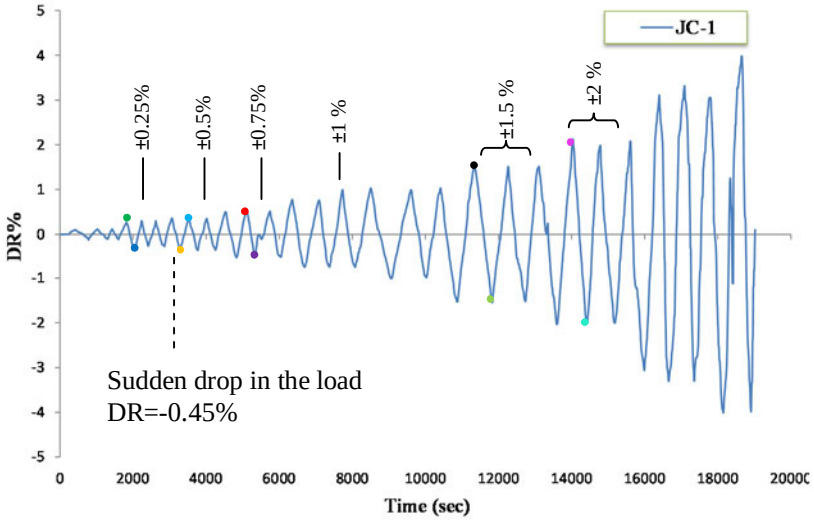

(f) Loading Regime (Displacement Control)

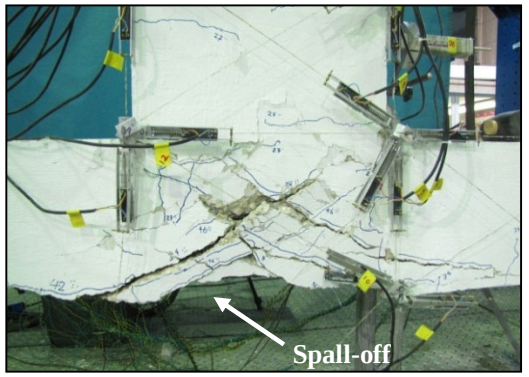

(g) Final Crack Pattern

(DR = 4%)

Figure 6-35: Cracking patterns and damage progress of test unit JC-1

The beam hysteretic load-tip drift curve of the unit is plotted in Figure 6-36. In the load step to a DR of -0.5%, a sudden drop in the load occurred coinciding with the formation of the first shear crack in the core. The response, thereafter, recovered somewhat until reaching the maximum at a DR of -1.5%. In the push direction, the maximum load was reached at DR of +2%. The maximum lateral load sustained by the assembly was +49.6 kN (DR = +2%) and -47.7 kN (DR = -1.5%). The ratio of the push to pull loads at the maximum was 1.04. Although the beam had symmetrical anchorage detailing in the core, the peaks are not perfectly symmetrical. However, it can be seen from Figure 6-36 that the loads at drifts of +1.5% and +2% were very similar (ratio of 0.97) and the same applies to the other direction (ratio of 1.01). This implies that the maximum load was sustained for two consecutive cycles similarly in both directions. In the post-peak stage, the resistance tended to degrade gradually. However, pinching of the hysteretic loops was high due to severe cracking of the core. By the end of the test, the load was found to drop to 25 kN which represents 51% of the average peak load.

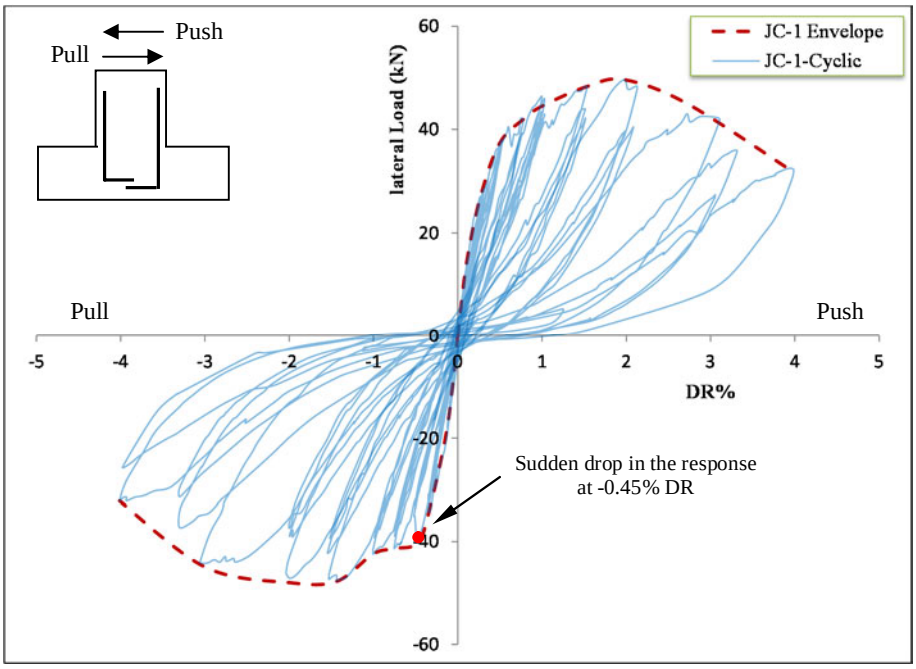

Figure 6-36: The hysteretic response of the test unit JC-1

The reduction in resistance in both loading directions is further examined by plotting the lateral loads in the pull and push directions, as shown in Figure 6-37. Also plotted in the same figure is the ratio of the push to pull lateral load (RF). As can be seen from the figure, due to similarity in the beam longitudinal reinforcement, the degradation in resistance in both loading directions was consistent and comparatively similar throughout the test. Thus, the RF, as shown in Figure 6-37(b), fluctuated around the value of 1.

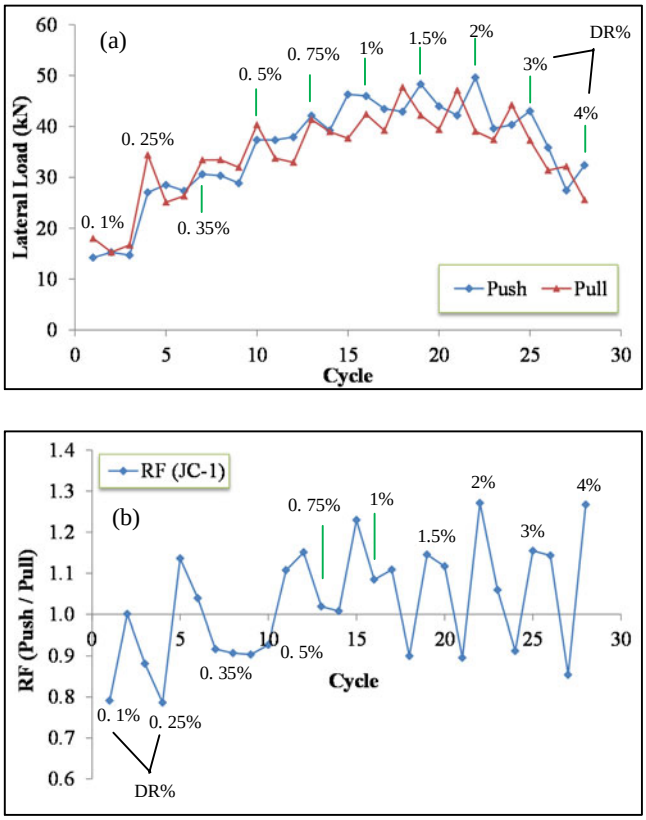

Figure 6-37: a) variation of beam tip load during cycling, b) resistance factor

Stiffness degradation of the test unit JC-1 is shown in Figure 6-38. After the first loading step, a 30% reduction in stiffness occurred due to flexural cracking. The stiffness, thereafter, degraded very gently as more flexural cracks developed. After the formation of shear cracks in the core (nominal DR of ±0.5%), a significant change in stiffness occurred which continued until the end of the test. Unlike the previous two units, the drop in stiffness due to shearing of the core was more gradual. At the conclusion of the test (DR=±4%), the joint had lost 95% of its initial stiffness.

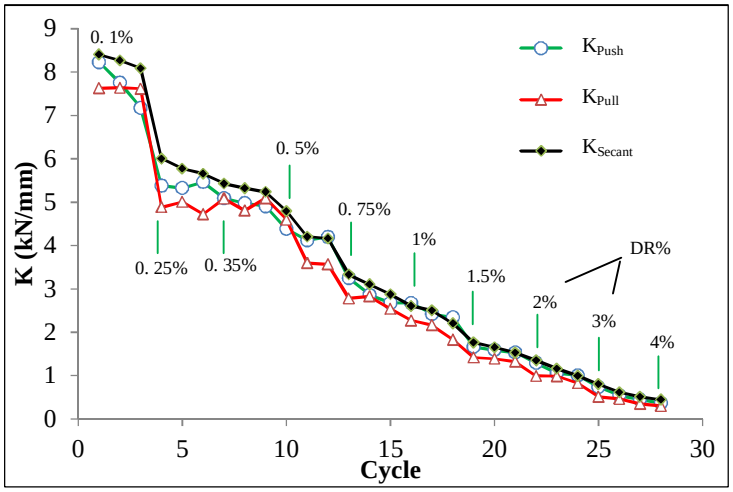

Figure 6-38: Stiffness degradation of test unit JC-1

The strains produced in the beam and column longitudinal reinforcement at the peak load are presented in Table 6-4. It can be noted that the strains generated in both hooks were very close and represented 47% of the yield strain. Also, it is clear that the top and bottom columns were more stressed than the beam. The column splices in tension had developed strains of 1982με resulting in an average bond stress of 4.43 MPa. The bond stresses at the maximum load of the bottom and top hooks were calculated at 2.20 MPa and 2.33 MPa, respectively. Figure 6-36 shows the strain history at the beam bottom reinforcement and column splices. It can be noted from the figure that the strain history is similar in nature to those of the previous units.

Table 6-4: Strains at beam and column reinforcement at maximum loading (JC-1)

Lateral Force		**δ**	**Beam**		**Top column**		**Bottom Column**	
Direction	Value		ε_s (με)		ε_s (με)		ε_s (με)	
	kN	mm	ST1	ST2	ST4	ST6	ST3	ST5
Push	49.6	33.0	1134	191	1928	-350	-1859	-352
Pull	-47.7	-24.0	76	1200	-	1075	223	-206

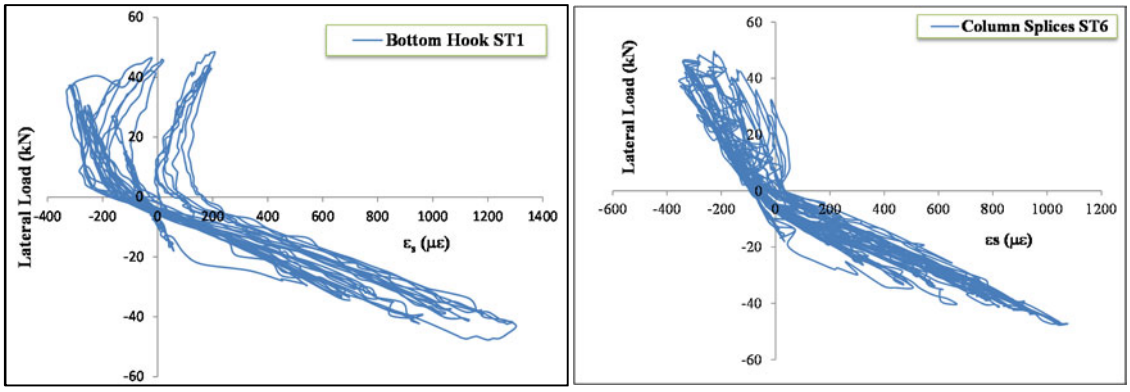

Figure 6-39: Strains at the beam bottom bars (Left) and at bottom column splices (Right)

The amounts of per-cycle energy dissipation along with the cumulative energy are plotted in Figure 6-40. Similar to the previous two tests, slow energy absorption characterised most of the pre-peak response (up to DR of ±1.5%). Increased absorption occurred in the subsequent stages of loading from step 7 (DR = ±2%) to step 10 (DR = ±4%). It is clear that the severe deterioration in load resistance within each loading step of the post peak response led to considerable drop in the energy absorption. The joint ultimately dissipated a total energy $E_{JC\text{-}1}$ of 8 kN.m during the test. It should be noted that at DR of ±1.5% and ±2%, corresponding to the peaks in the pull and push directions, the joint had dissipated 24% and 41% of the energy, respectively. At ±3% DR, the joint had dissipated 70% of the energy, and 100% of the energy was dissipated at ±4% DR.

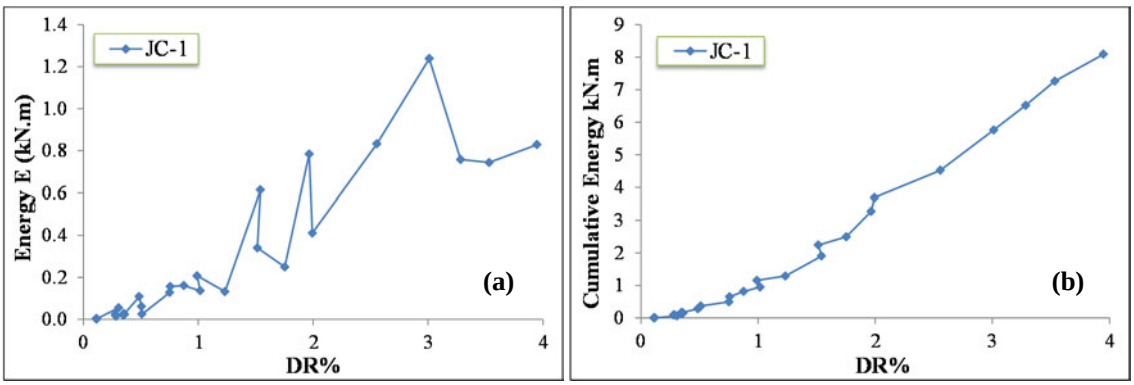

Figure 6-40: (a) Per-cycle Energy dissipated, and (b) cumulative energy of the test unit JC-1

The equivalent viscous damping of the unit is shown in Figure 6-41(a). Similarly to the previous unit, the damping increased as damage and cracking progressed during the test. Also, a decrease in damping occurred with cycling due to loss of resistance and stiffness. The increase in damping took place after a DR of 1.5% (the maximum load in the pull direction). During this stage, multiple shear and flexural cracks formed. Up to a ±1% DR, the damping averaged at 3.4%. For higher drifts, the damping had an average value of 7.3%.

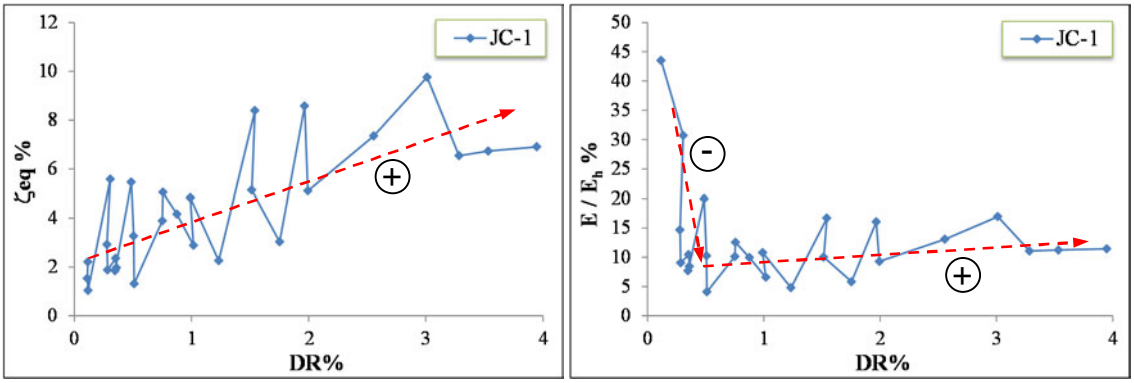

Figure 6-41: a) Equivalent viscous damping, and b) Ratio of per-cycle energy E to E_h of test unit JC-1

The ratio of per-cycle energy E to E_h is shown in Figure 6-41. As can be noted from the figure, the formation of diagonal cracks at a drift of ±0.5% had reduced the ratio significantly from 20% to 4%. After that, the ratio increased only slightly. Significant deterioration of the resistance only occurred due to cycling. On average, the ratio E/E_h was found to be 11% which is very close to the value of the previous two units.

6.3.5 Comparisons and Discussion

The performance of the four control units is compared in terms of ultimate loads and modes of failure, drift capacity, stiffness degradation and energy dissipation capacity.

6.3.1.1 Failure modes, response and load capacity

All the control units failed in a classical shear failure pattern where an X-shaped mechanism formed in the joint area after the maximum capacity was reached. The maximum capacity, limited by the core shear capacity, was reached at about 50% of the nominal yield capacity of the unit. A sudden drop in the resistance occurred in all units when the first diagonal crack formed. This drop was confined to the pull direction representing the weak loading direction (beam bottom bars in tension). At high drift ratios, a triangular cracked section formed at the bottom part of the joint area resulting in excessive loss in stiffness, along with concrete spalling. Furthermore, compressive failure of the joint diagonal struts was observed. Cracking patterns observed in the bare units are found to be similar in nature to those conducted by other researchers such as Pessiki et al. (1990), Beres et al. (1991, 1992, 1996), Ghobarah and Said (2002), Kuang and Wong (2005), among others. Figure 6-42(a) shows a typical crack pattern of deficient exterior joints observed by Beres et al. (1991). Also, the final crack pattern of a joint tested by Ghobarah and Said (2002) and Kuang and Wong (2005) is shown in Figure 6-42(b) & (C), respectively.

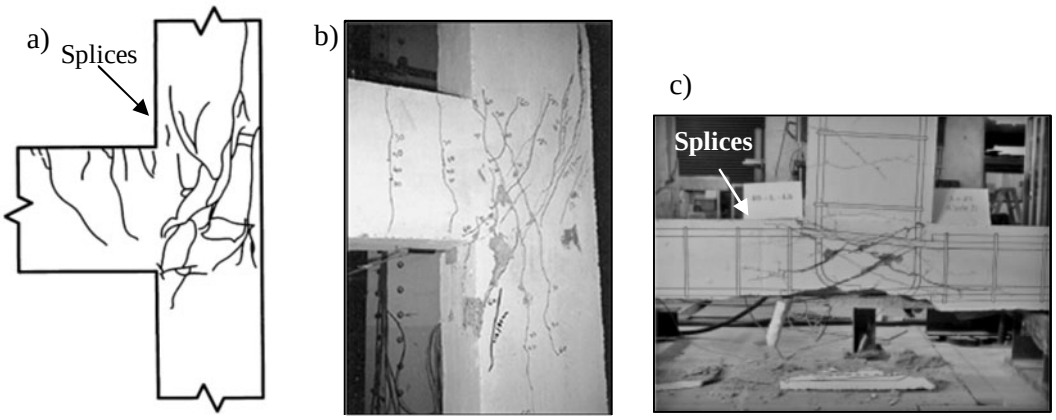

Figure 6-42: a) Typical crack pattern of substandard exterior joints observed by Beres et al. (1991), b) final crack pattern of a deficient joint tested by Ghobara and Said (2002), and c) final crack pattern for a joint with splices and L-shaped anchorages tested by Kuang and Wong (2005)

Pinching was present in all units during the post-peak stage due to severe cracking and sizable cracks within the core. Those cracks were observed to remain open at zero-displacement loading, and thus, low stiffness took place during load reversal. The pinching effect reduces the amount of energy absorbed by the unit.

Envelopes of the hysteretic responses of the test units are plotted and compared in Figure 6-43. As can be seen from the figure, Unit JA-3 showed the highest strength in both the push and pull loading directions. This unit had a deficient anchorage detailing, but it was tested under the highest compressive axial load of 250 kN. In the pull direction, it is evident that unit JC-1 showed slightly higher stiffness compared to the other units. This could be attributed to the fact

that the beam bottom bars were anchored into the core by using a 90˚ hook. In fact, the resistance factor of this unit indicated similar performance in both loading directions. On the other hand, unit JB-1 was the most deficient in the pull direction. Again, the axial load was the reason for this when compared to unit JA-3.

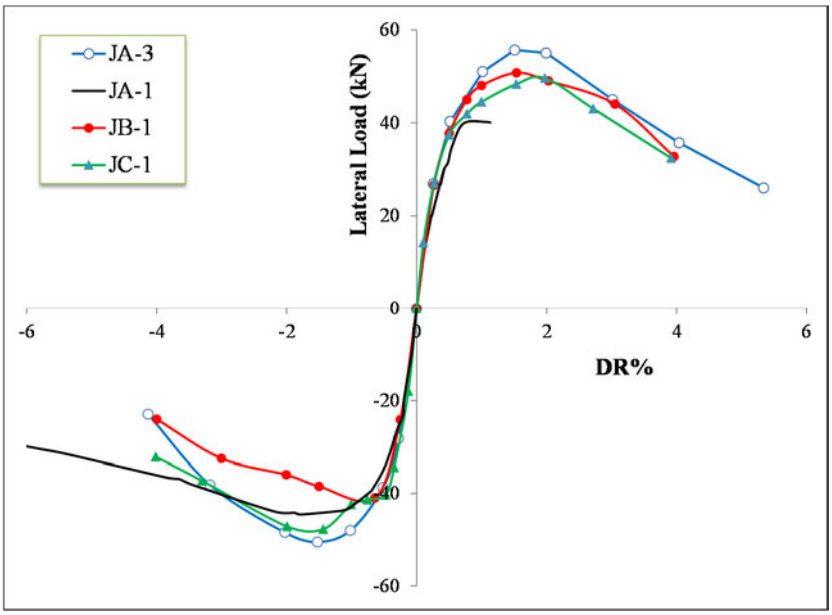

Figure 6-43: Envelopes of hysteresis loops of the control units

It is interesting to note that the sudden diagonal crack in the weak direction of all units took place at a load of -40 kN (pull direction), regardless of the different reinforcement detailing in the core and axial load applied. However, unlike the other units, the test unit JB-1 did not regain any strength in the pull direction after the main shear crack initiated. This may be attributed to the fact that the beam bars were less confined in the anchorage region as compared to that of specimen JA-3.

Table 6-5 compares load capacities and drift ratios of the four units in both loading directions at maximum loading.

Table 6-5: Load and drift capacities of the bare units at the maximum load

UNIT	**JA-1**		**JA-3**		**JB-1**		**JC-1**	
Direction	F	DR	F	DR	F	DR	F	DR
	kN	%	kN	%	kN	%	kN	%
Push (+)	40.4	1.14	55.7	1.51	50.8	1.54	49.6	1.97
Pull (-)	-45.1	-2.03	-51.9	-1.52	-41.1	-0.64	-47.7	-1.44

6.3.1.2 Energy dissipation

The amount of cumulative energy dissipation of the units is plotted against drift ratios in Figure 6-44. At load levels up to a DR of ±1%, the energy dissipation was small, slow and almost identical in all units. After the damage occurred at higher drift ratios, the energy absorption increased rapidly. The other units showed the same energy absorption capacity during the test.

In comparison to JA-3 and JB-1, the test unit JC-1 dissipated less energy at ±4% drift ratio because the last loading step comprised only one cycle.

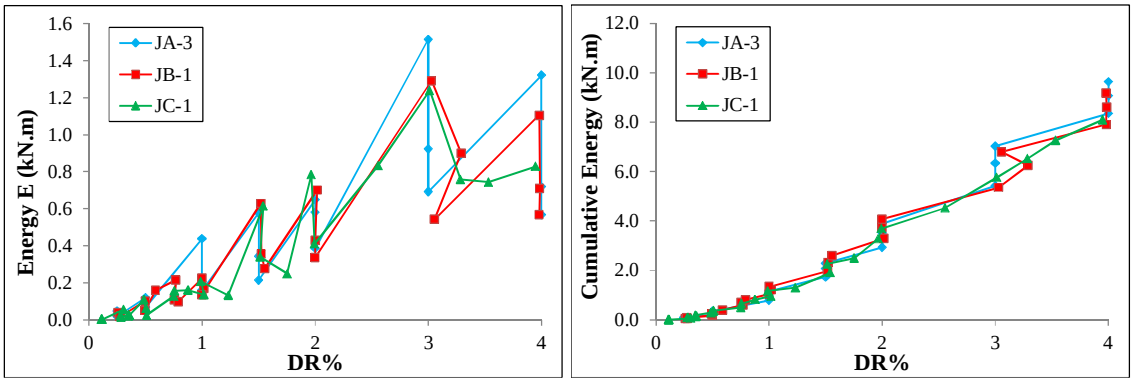

Figure 6-44: a) Per-cycle dissipated energy and b) cumulative energy of the control test units

The equivalent viscous damping of all units is plotted in Figure 6-45(a) versus drift. It is interesting to note that all units show more or less the same rate of increase in damping as the load progresses. Also, it can be noted that at drifts higher than 2%, the damping increased rapidly because of extensive cracking in the core, see Figure 6-44(a). The damping, however, decrease with cycling.

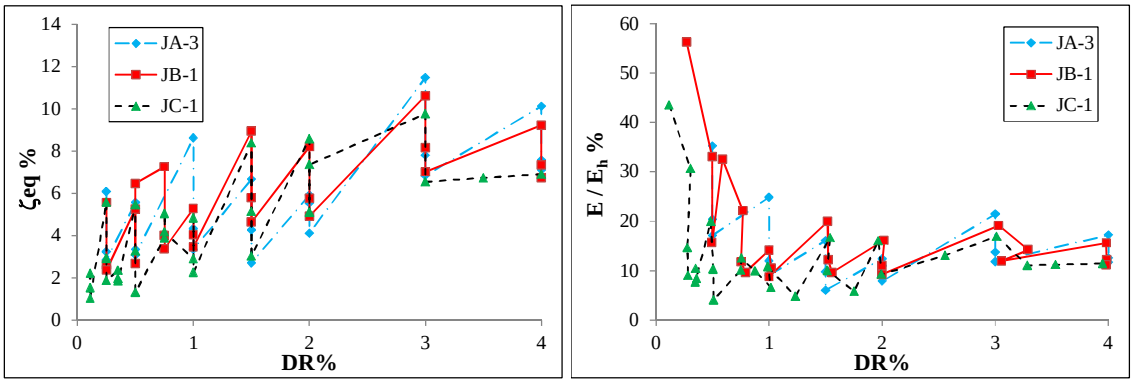

Figure 6-45: Cumulative energy dissipation of the bare deficient units

The ratio of per-cycle energy to the perfect-cycle energy (E/E_h) is shown in Figure 6-45(b) for all units. It is clear that regardless of the different reinforcement detailing and axial load applied, the pinching effect as well as the amount of plastic damage in the units is somewhat similar. The formation of diagonal cracks within the core caused somehow a significant drop in the ratio during that loading step. However, the ratio increased slightly in the following loading steps due to the formation of more cracks in the core and at the beam and column interfaces, which in turn resulted in an increase in the energy dissipated. An example of the progressive damage is shown in Figure 6-46 for test unit JA-3 when loading in the weak (pull) direction. The photos are at the end of the loading steps for drifts of -1.5%, -2%, -3% and -4%, respectively. It is clear from the figure that after the DR of -2%, the joint started to sustain considerable damage.

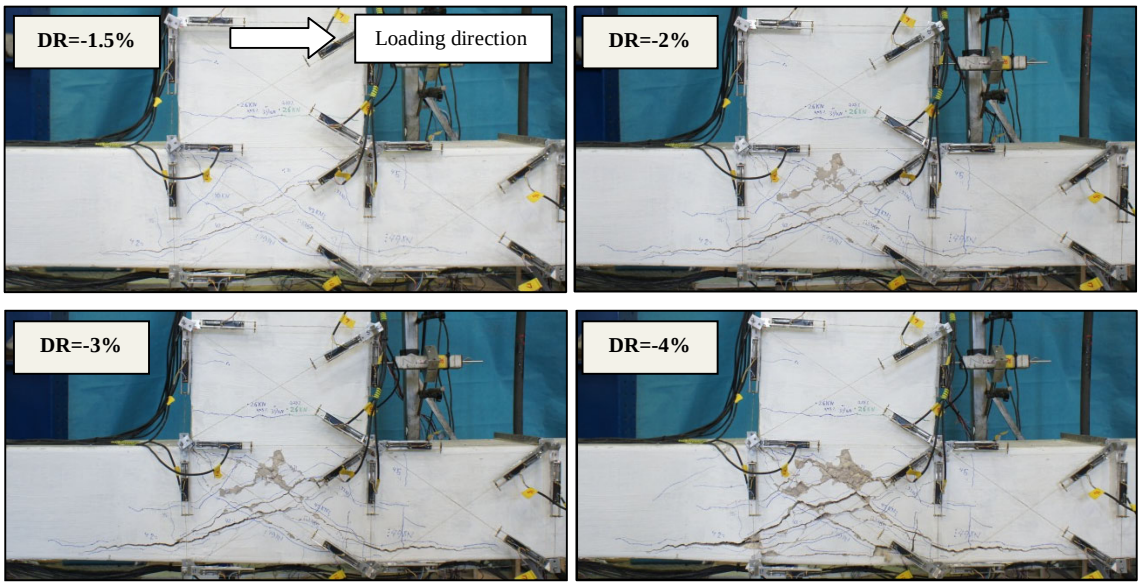

Figure 6-46: Visual damage progress of unit JA-3

6.3.1.3 Stiffness Degradation

Stiffness degradation of all units is plotted versus drift ratios DR in Figure 6-47. At small load steps of drift ratios ±0.25% to ±0.5%, all specimens showed almost identical stiffness, except for the unit JA-1 which was subjected to cycles at lower drifts that reduced slightly the stiffness before this range. With further increase in loading, stiffness degradation accelerated until the maximum capacity was reached. At high drift ratios (3% to 4%) all joints showed identical stiffness as the core was almost crashed.

At the maximum load, the reduction in the peak-to-peak stiffness was calculated at 66% for JA-3 at a DR of ±1.5%; 25% and 73% for JB-1 corresponding to drift ratios of ±0.64% and ±1.54%, respectively; and 70% and 86% for JC-1 at drift ratios of ±1.44% and ±1.97%, respectively. The unit JA-1 had a reduction in stiffness of 54% at a DR of ±1.14%. More stiffness reduction would be expected from this unit if the complete hysteretic regime was applied.

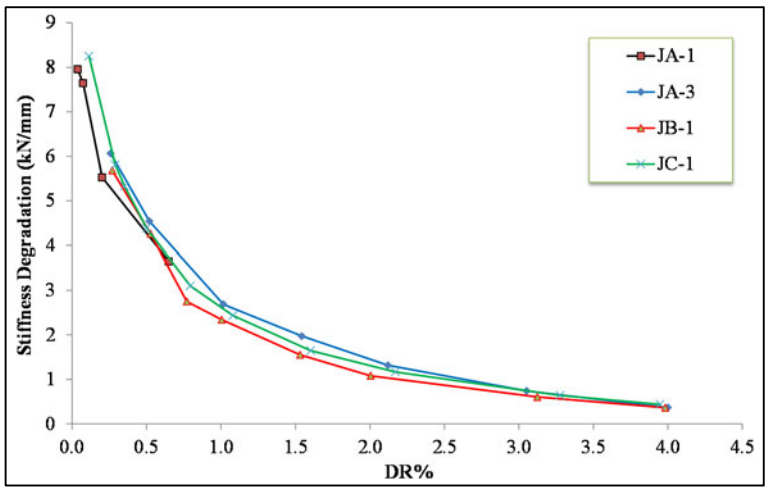

Figure 6-47: Stiffness degradation of the bare (control) units

6.3.1.4 Shear degradation

The effect of shear degradation on the response of all specimens is examined simply by plotting the load capacities at each drift for the strong directions, as shown in Figure 6-48. Based on the figure, it is interesting to note that degradation in the response of all specimens is initiated at a DR of 1.5%. It is also clear that unit JA-3 has less degradation rate after the maximum load capacity is reached. However, this difference diminishes as loading progresses. Although this enhancement could be attributed to the application of higher axial load in this test unit, this effect is not clear due to the interference of many other parameters, as explained at the beginning of this chapter. Thus, to better investigate the degradation rate, the load capacities are normalised to the maximum load capacities and the results are plotted in Figure 6-49. It is clearer now that the joints behaved more or less similarly, and the shear effect on the degradation rate is similar in all units. Further investigation on the shear problem is presented in chapter 10.

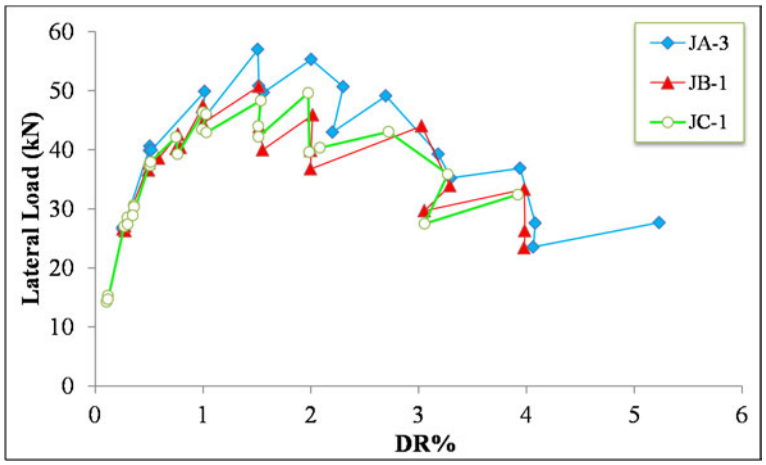

Figure 6-48: Comparisons of load capacities in the strong direction

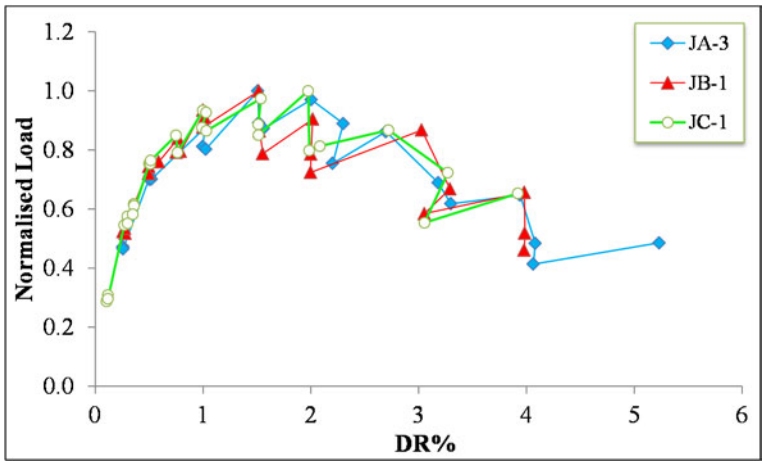

Figure 6-49: Comparisons of normalised load capacities in the strong direction

Chapter 7

REHABILITATION OF DEFICIENT BEAM-COLUMN JOINTS

7.1 INTRODUCTORY REMARKS

This chapter presents the rehabilitation strategies used to upgrade the performance of the deficient pre-damaged joints tested in the third phase of the experimental programme. Also, this chapter presents the experimental results of the strengthened joints. The performance of the test units is discussed including crack patterns and modes of failure, load-deflection response, strains on flexural and lateral reinforcement. The energy dissipation and stiffness degradation characteristics are also investigated to evaluate the performance.

7.2 REHABILITATION SCHEMES

As reported in chapter 6, failure of the bare connections in all cases was due to a shear mechanism that damaged the joint area severely. For this reason, the joint area was first

removed and replaced with a new better quality concrete. It should be noted that the concrete replacement process might be difficult or impractical in actual rehabilitation situations. The repair was done in the vertical position with the joint being inside the test rig.

Before removing the joint area, two hydraulic jacks were used to support the joint, and the beam was tied tightly to the reaction frame by means of straps as seen in Figure 7-1. In addition all instrumentation was cautiously removed.

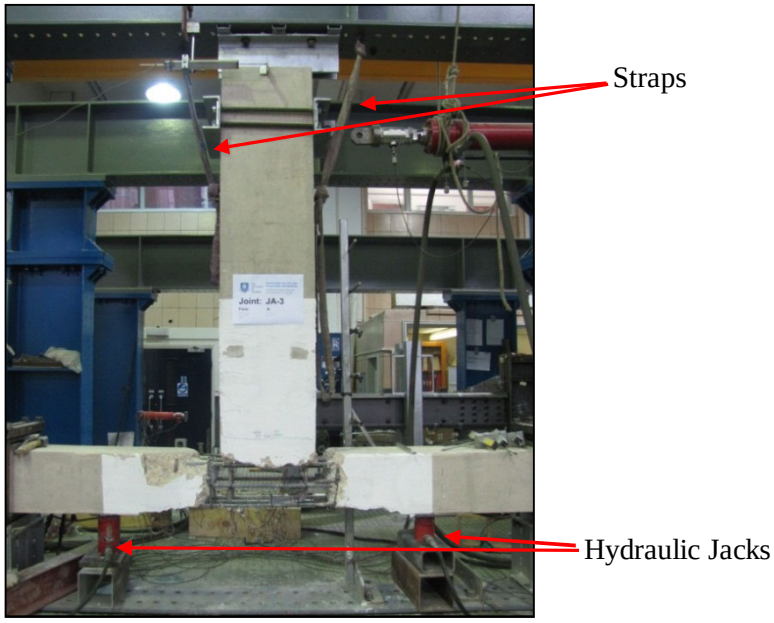

Figure 7-1: Shoring of the joint in the vertical position before the repair

An electrical hammer was used to clear the fractured concrete and expose all the bars as shown in Figure 7-2. A steel brush was used to clean the reinforcing bars and concrete surfaces. The joint area afterwards was cleaned of debris and fine particles using compressed air.

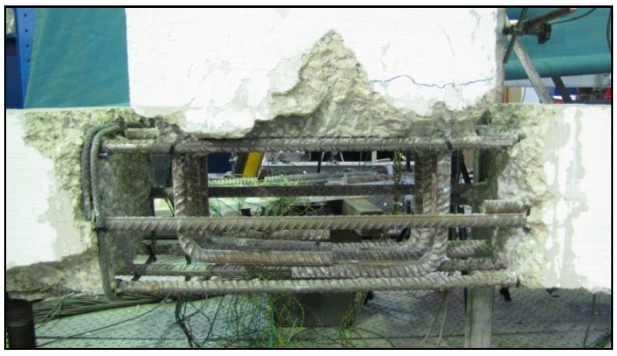

Figure 7-2: the test unit after clearing the joint area

A wooden U-shaped formwork was manufactured to cover the removed area as shown in Figure 7-3. Strain gauges in the joint area were reinstalled on the exposed bars after preparing the surfaces. The gauges were wired and protected by means of Araldite adhesive. The wires were

gathered into bundles and exited outside the formwork from the column top sides as shown in Figure 7-4.

Figure 7-3: The formwork used for the repair

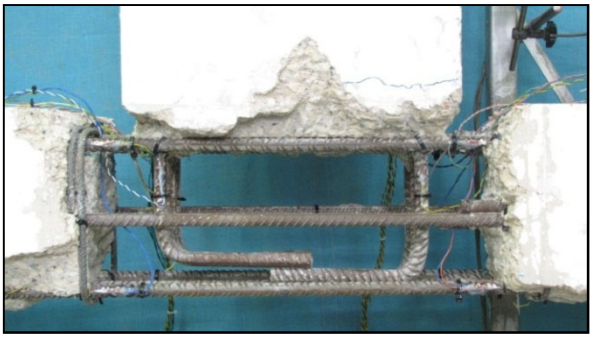

Figure 7-4: The test unit after reinstallation of strain gauges

The removed joint area included two gaps of 60*mm* to facilitate casting the joint area. The inner corners of the formwork were sealed by water-proof silicon before positioning in place. The formwork was fitted from the bottom side and supported by three jacks. Clamps were also used to restrain the formwork from expanding during casting. Figure 7-5 shows the joint with the formwork before casting.

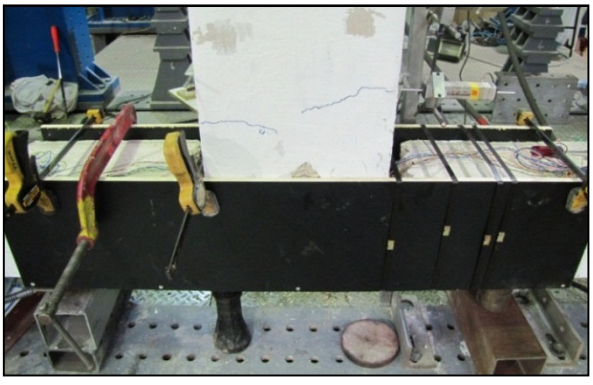

Figure 7-5: The test unit ready for casting

Fresh concrete was cast in the core with proportions as stated in Table 7-1. The concrete mix was designed to produce high compressive strength within a short period of time. The mix was prepared in the laboratory using a mixer of 175kg capacity. The concrete was poured from one side and vibrated using a small electrical poker vibrator. The casting was done in three layers

until reaching the column level from the other side. The casting process is schematically illustrated in Figure 7-6. Standard (150 *mm* diameter and 300 *mm* height) cylinders along with (100×100×100*mm*) cubes were cast to determine the concrete compressive strength at the time of testing. In addition, standard (100 *mm* diameter and 200 *mm* height) cylinders were cast to determine the concrete tensile strength. Figure 7-7 shows the core after casting.

Table 7-1: Mix proportion of the new cast concrete in the joint area

Test Unit	**JA-1 PTMS**	**(JA-3, JB-1and JC-1) PTMS**
Material	Mix: kg/m^3	Mix: kg/m^3
OPC	315	315
PFA	135	135
10 *mm* Aggregates	935	935
Sand	735	735
Water	180	180
Fibre	50	-
Plasticiser (g)	5000g	2500g

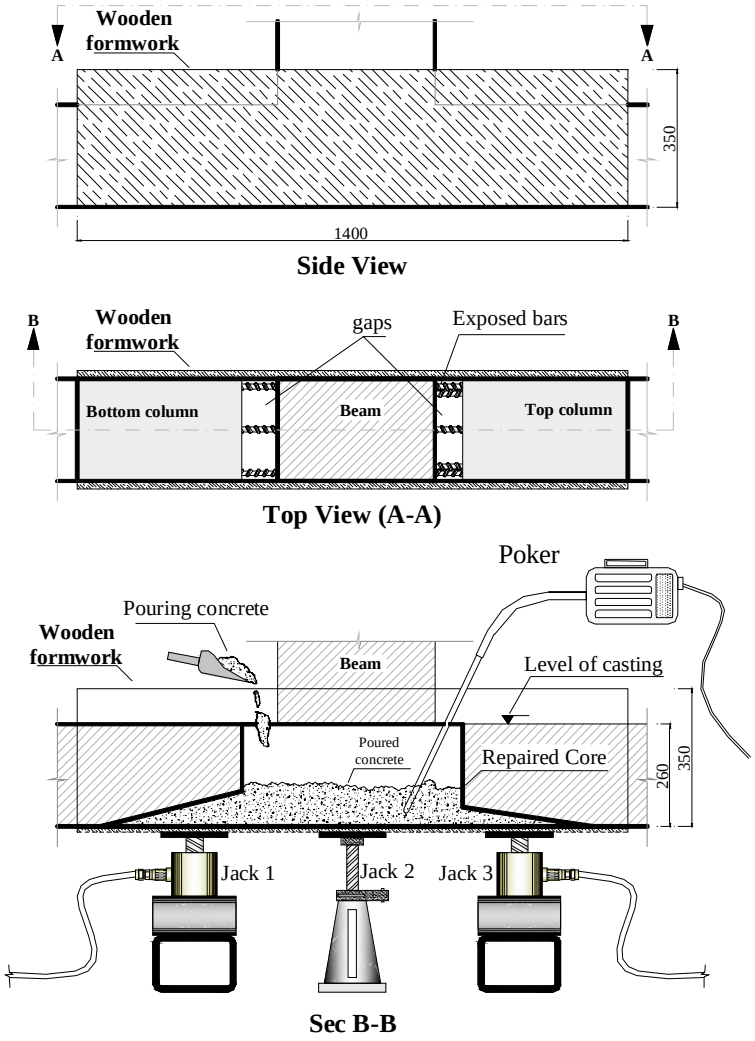

Figure 7-6: Casting process of the joint core with a new fresh concrete

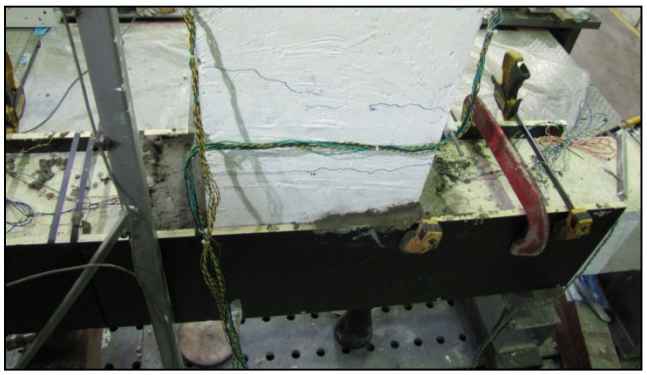

Figure 7-7: The test unit after casting of the core

After casting, the joint area was covered by plastic sheets for curing as seen in Figure 7-8. Two cubes were tested after three days to ensure the concrete strength was reached. The formwork was then removed to prepare for the strengthening.

Figure 7-8: The test unit after casting and during curing

An electrical grinder was used to round off the edges of the joint area along with the hinging areas of columns to about 20*mm* radius. The joint afterwards was cleaned from fine particles and white washed. Figure 7-9 shows the joint after the repair.

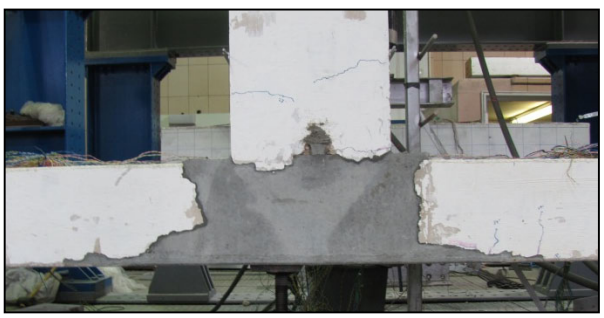

(a)

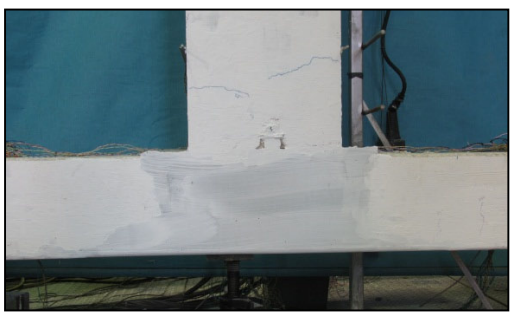

(b)

Figure 7-9: A repaired joint a) after de-moulding, b) after grinding and painting.

The joints were then upgraded using different schemes of PTMS. The following subsections describe in detail the selective upgrading schemes used and the methodology of application.

7.2.1.1 Unit I (JA-1 PTMS)

The proposed scheme included the installation of PTMS in the horizontal and vertical orientation of the joint area. The strips were extended to the beam and columns to a distance of 200 *mm* from the interfaces. Figure 7-10 shows a schematic view of the strengthening scheme.

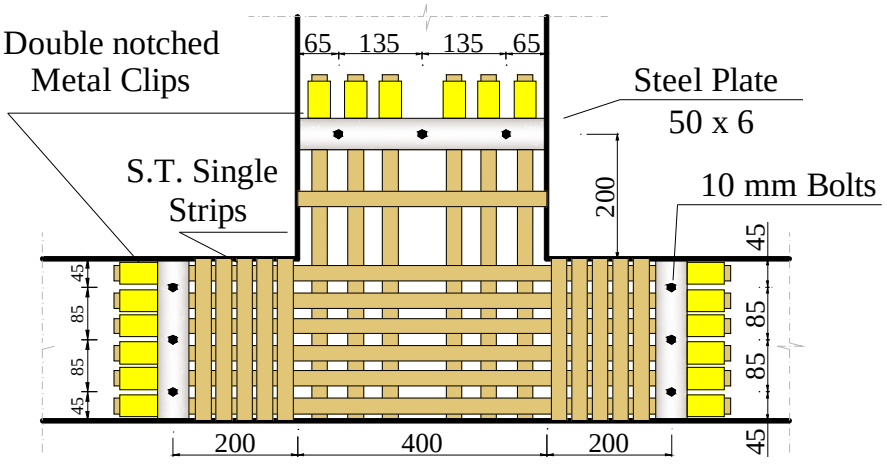

Figure 7-10: The strengthening scheme of the test unit JA-1

Standard strips (S.T.) were used to strengthen the joint. The tensioning in the strips was applied from one end with the reaction against metal plates of 50*mm* width and 6*mm* thickness. The steel plates were fixed to the connection elements by means of (10*mm* diameter and 100*mm* length) steel bolts driven through the concrete between the reinforcing bars. Before tensioning, the strips were anchored using metal clips at one side and tightened to the steel plates and then threaded underneath the other plate. After tensioning, the steel plates were tightened using washers and nuts to the bolts. The application of strips to the beam and columns aimed to enhance the flexural capacity of adjoining elements and to modify the moment strength ratio of the joint.

In this test unit, the beam flexural capacity at yielding was designed to be 144kN.m, and 52kN.m and 56kN.m for the top and bottom columns, respectively. It was evident from this design that the $M_{beam} > M_{top} + M_{bottom}$. To overcome this deficiency, the flexural capacity of both columns was enhanced. To do this, lateral strips were used over a length of 200*mm* of the columns in addition to the strength added by the horizontal strips. After strengthening, the flexural capacity of both the beam and columns, based on sectional analysis, was 166 kN.m. The shear capacity of the adjoining elements of the bare joint was designed to be sufficient to resist the new moments. In addition to the fact that the joint area capacity was upgraded using

better quality concrete and confining PTMS, the transfer of the inner tension forces acting on the joint area to the external metal strips was expected to enhance the performance.

A schematic view of the strengthened joint with acting loads and force transferring mechanism is illustrated in Figure 7-11. As can be seen from the figure, the application of PTMS in this configuration reduces the tensile forces applied to the joint area by transferring these forces externally to the PTMS. The transferred force increases the pressure applied to the joint area through the confining strips. In addition, it reduces the tension applied on the beam anchored bars in the core. Consequently, the shear mechanism should be enhanced and more ductile failure should occur.

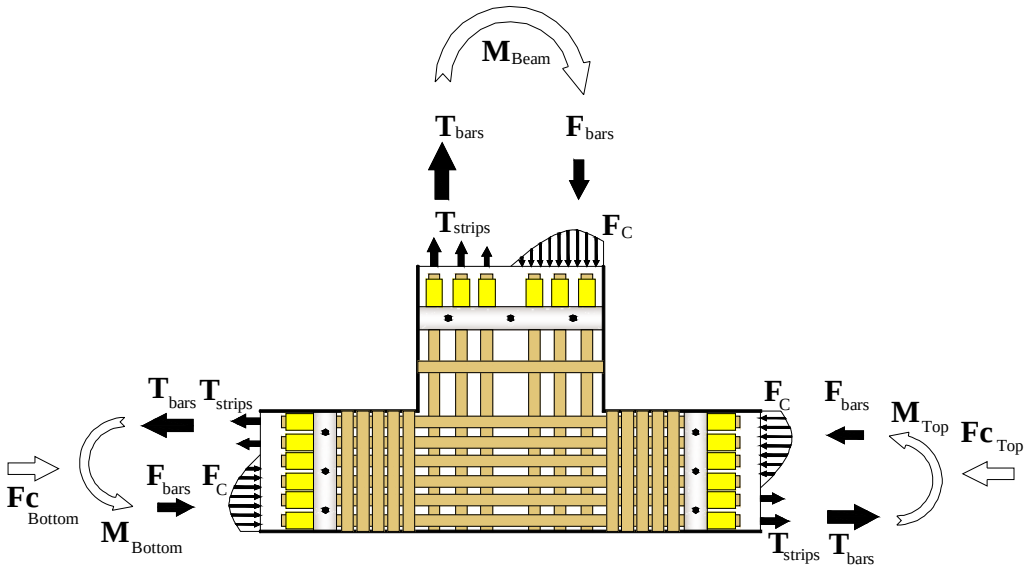

Figure 7-11: Schematic view of the acting forces on the joint and transferring mechanism

The concrete compressive strength was determined by testing two (150*mm*×300*mm*) cylinders and was found to be 85 MPa on the day of testing. The tensile strength was obtained from testing two (150*mm*×300*mm*) cylinders in indirect tension and reached 4.5 MPa. The high concrete compressive strength was used only in this joint as it was going to be rehabilitated again and tested using a CFRP strengthening scheme.

Some difficulties were encountered during the installation of PTMS since this was the first time of application on a full scale joint. One of these difficulties was due to large clearance in the holes of steel plates which resulted in some movement of the plates during tensioning.

After the application of the PTMS, the joint was instrumented in a similar way to the bare unit. Figure 7-12 presents the joint JA-1 after strengthening and with instrumentation installed.

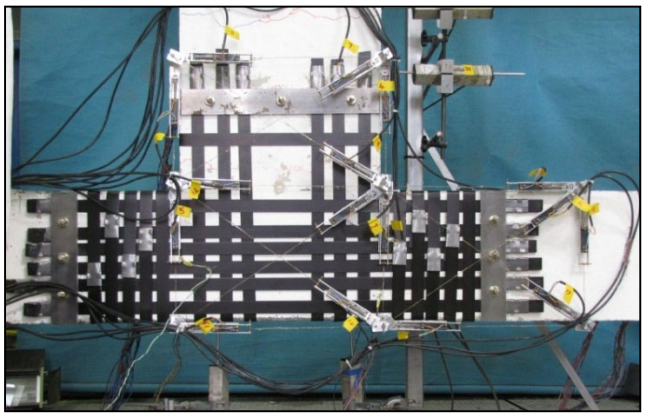

Figure 7-12: The joint JA-1PTMS after strengthening and re-instrumentation.

7.2.1.2 Unit II (JA-3 PTMS)

The reinforcement detailing of this specimen was similar to that of the previous unit but with an additional longitudinal bar in the mid column depth (see chapter 3 – Figure 3-24). The strengthening scheme was designed to avoid any damage to the concrete due to the use of steel bolts driven in the core or adjoining elements as it was the case of joint JA-1PTMS and later in JC-1PTMS. In this test unit, the strips were installed diagonally on the joint area at 33˚ to the horizontal as explained later. In addition, the columns were confined with double layers of strips over a distance of 465 *mm*. The beam was also confined with three double layers of strips over a distance of 160 *mm* from the interface with the column. Figure 7-13 shows a schematic view of the strengthening scheme. A special steel formwork was manufactured in the laboratory to provide a reaction support to the strips. The formwork was mounted on the column edges, beam sides and the external side of the joint area. The bottom part of the formwork was tightened in place using six double layers of strips wrapped around the upper part of the column. The formwork consisted of (50 *mm* width × 5 *mm* thickness) steel plates and (25×25mm^2) filled square section. The square section was cut into small pieces, at 33˚ with the vertical, and welded to the steel plates.

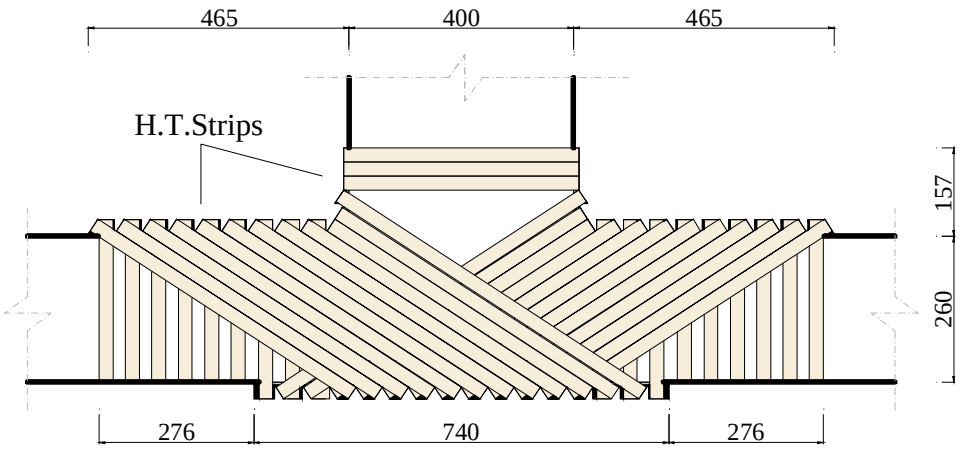

Figure 7-13: The strengthening scheme of the test unit JA-3

The shear failure of the control unit is shown in Figure 7-14. As shown in the figure, the main shear crack propagated at 25˚ with the horizontal. It was therefore desirable to install the strips at an angle of 55˚ to be perpendicular to the crack. In this strengthening scheme, however, the choice of 33˚ for the diagonal strips was made so as to provide pre-tensioning to the entire joint area. In addition, the strengthening on the joint was expected to increase the angle of the shear cracks towards the corners of the joint area, and hence, coincide more with the directions of the diagonal strips.

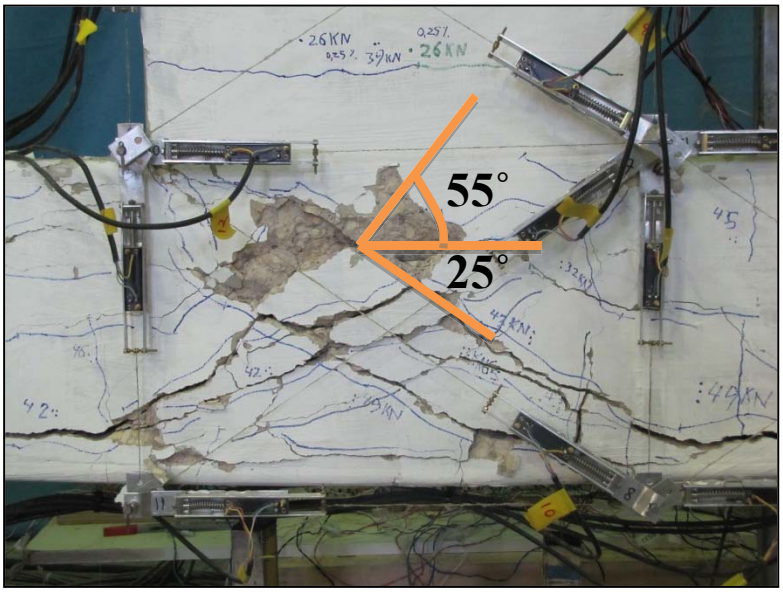

Figure 7-14: The orientation of shear cracks in the joint area of the control specimen

Normal strength concrete was used to repair the joint area. The compressive strength of the new concrete was determined by testing four (150*mm*×300*mm*) cylinders and was found to be 39 MPa on the day of testing. The tensile strength of 2.5 MPa was obtained from testing four (100*mm*×200*mm*) cylinders under indirect tension.

Some strain gauges were attached to the diagonal, vertical and horizontal strips to monitor the variation in the stress during loading.

The strengthening scheme did not allow the installation of the LVDT system on the joint area. The installation of this scheme, on the other hand, was easy regardless of the complication in design. In fact, one person was sufficient for the installation process.

The edge steel assembly used might be a drawback in this scheme due to the cutting method and welding required for assembling the plates and the square sections. However, the application was very rapid and convenient.

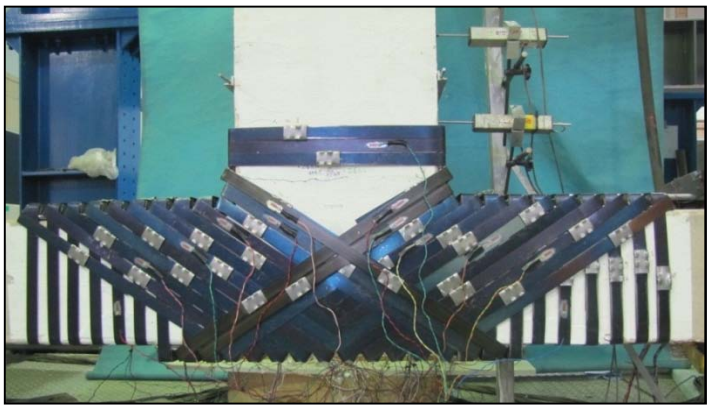

Figure 7-15: The joint JA-3PTMS after strengthening and re-instrumentation

7.2.1.3 Unit III (JB-1 PTMS)

In this unit, the bottom beam bars were also anchored into the joint area with a length of 230 *mm* (see chapter 3 – Figure 3-24). The top bars, on the other hand, were bent as a hook with a total length of 490 *mm*. The strengthening scheme used for unit JA-3PTMS was adopted with some improvement. Accordingly, diagonal strips were installed along the entire core. The vertical parts of the steel assembly were welded to the horizontal ones to form a rigid connection at the beam column interfaces. Also, the anchored bars were welded to the column longitudinal bars to delay early pullout failure. Figure 7-16 shows the welding of the beam bars.

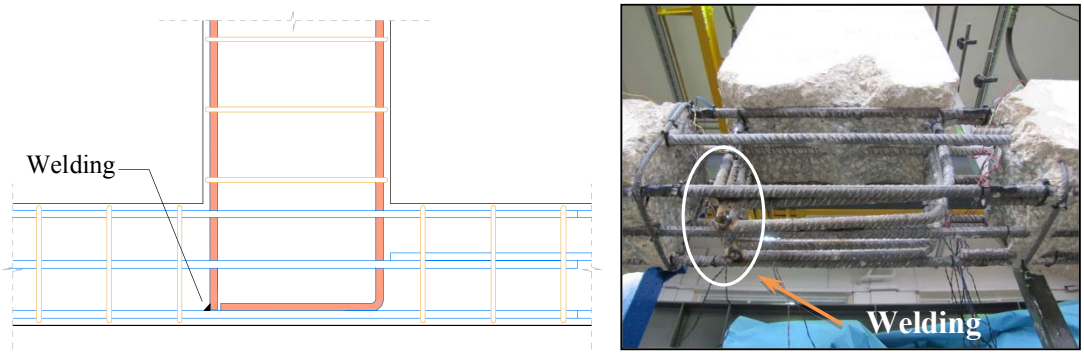

Figure 7-16: Welding of the beam bars of the unit JB-1PTMS

The concrete compressive and tensile strengths of the joint area at the day of testing were found to be 56.2 MPa and 3.4 MPa, respectively.

After strengthening, strain gauges were attached to the installed strips and all instrumentation was installed. Figure 7-17 shows the test unit after the installation of the PTMS and instrumentation.

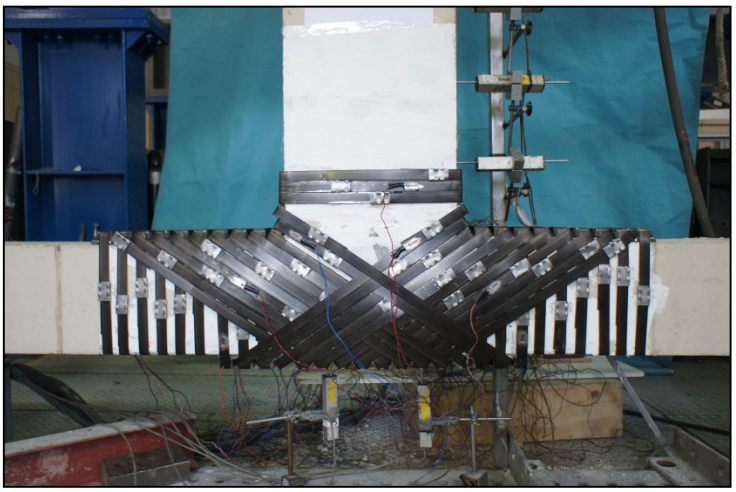

Figure 7-17: The test unit JB-1PTMS after strengthening

7.2.1.4 Unit IV (JC-1 PTMS)

The strengthening design of this test unit aimed at preventing the deformation of the joint area by restraining the movement of its interfaces. Figure 7-18 shows a schematic view of the strengthening scheme. A U-shaped steel plate assembly was manufactured and mounted on the joint area at both sides to hold the confining strips. The steel assembly comprised of (60 *mm* width × 6 *mm* thickness) welded steel plates to fit the dimensions of the joint area. The steel assembly was fixed to the joint by means of (100 *mm* length and 10 *mm* diameter) bolts driven through the concrete at the beam and column interfaces. Four bolts were used on the beam interface, while two bolts were used on each column interface. The bolts fixed on the column sides were located at the mid depth to avoid any reduction in column capacity. High ductility strips were used for strengthening in this scheme with high tensile (HT) stress of 930 MPa. The HT metal strips allowed the wrapping around the steel plates to form double layers. The extension of the confinement onto both columns was aimed to confine the repaired shear area, prevent early cracking between the old and new concrete interfaces and to enhance the bond strength of splices at the hinging area of the top column.

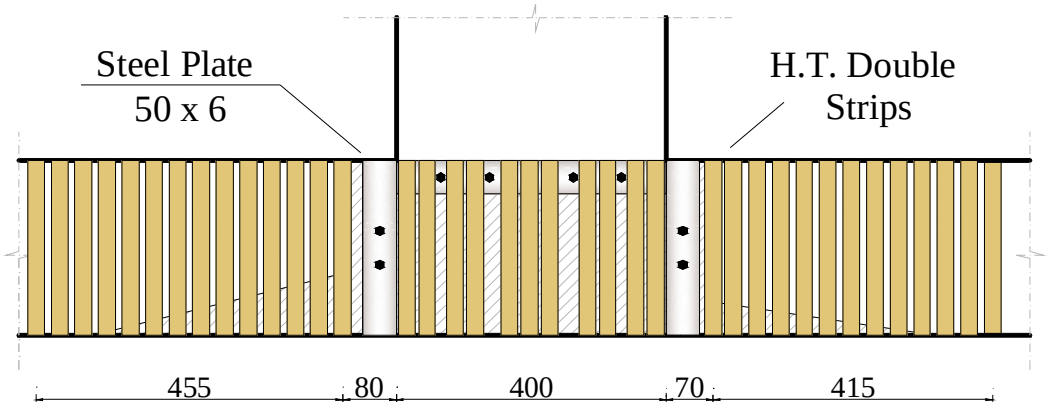

Figure 7-18 : The strengthening scheme of the test unit JC-1

In this design, the vertical strips did not extend into the beam to avoid any additional flexural enhancement that could adversely alter the moment strength ratio of the connected beam and columns. The moment strength ratio of this assembly was similar to the previous one.

The concrete compressive and tensile strengths of the new concrete at the day of testing were 57 and 3.6 MPa, respectively.

Two persons were used to install the strips at the joint area. However, in practise, when the two adjacent faces of the joint area are accessible from one side, one person will be enough to do the work.

The proposed strengthening scheme is expected to provide a lateral restraint to core movement and, therefore, add strength and ductility to the joint.

After the strengthening was done, some strain gauges were attached to the strips in the joint area and on the columns to monitor the variation in the tension force of the strips. Also, the LVDT system was mounted in the joint area and along the beam and column hinging zones. Figure 7-19 shows joint JC-1 after strengthening and instrumentation.

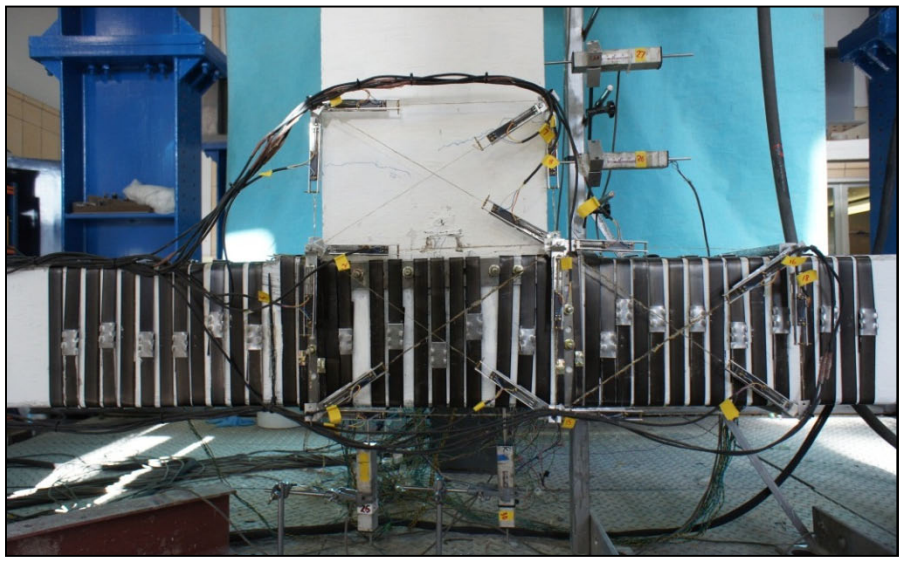

Figure 7-19 : The joint JC-1PTMS after strengthening and re-instrumentation

7.3 TEST RESULTS

7.3.1 JOINT JA-1PTMS

The actual loading regime followed in this test was analogous to that of joint JA-1 such that it comprised load and displacement control phases. The first phase comprised four loading steps at loads of ±5, ±10, ±20 and ±40 kN. The second phase, on the other hand, comprised four loading steps at drift ratios of ±1%, ±1.5%, ±2% and ±3%. The loading regime is plotted in Figure 7-20.

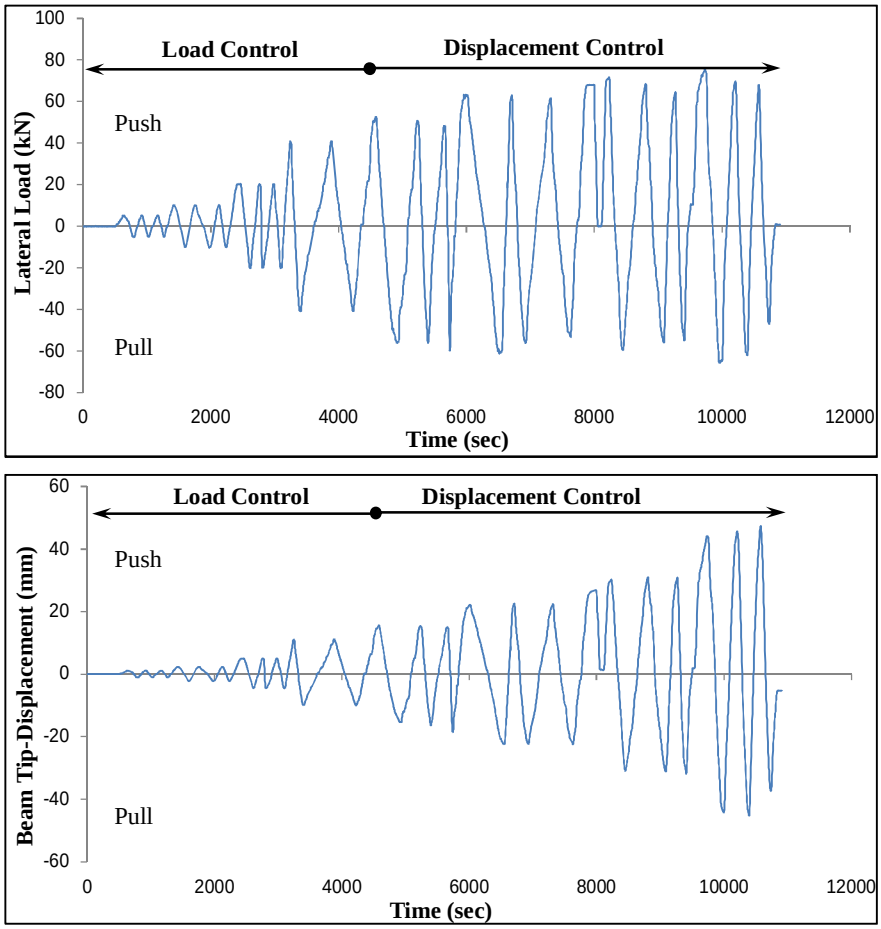

Figure 7-20: Loading regime of test unit JA-1PTMS

The axial load imposed on the column was set equal to that of the bare unit i.e. 150 kN. The fluctuation of the axial load during the test is plotted in Figure 7-21. As can be seen from the figure, the effective axial load started at 156 kN and increased with loading and reached 167 kN at a drift of -0.75%. At this point, the compression was reduced to a value of 156 kN and was kept at this level until the end of the test. The 7% average increase in the axial load which was applied to this unit is not considered important and can be ignored.

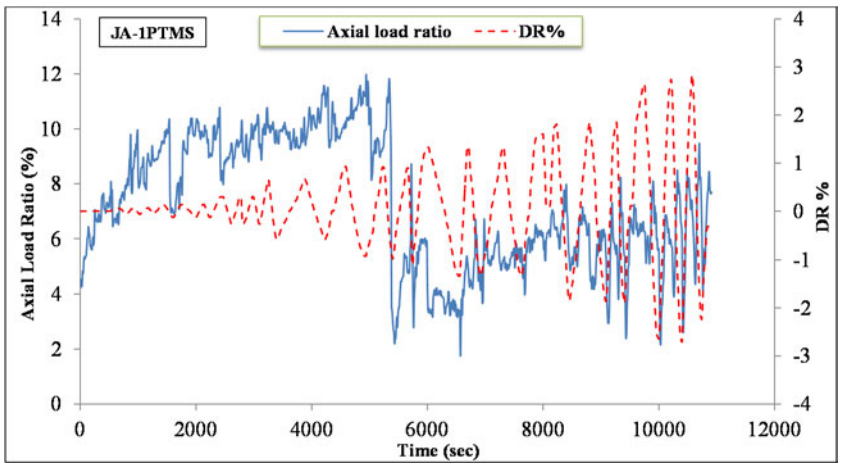

Figure 7-21: Variation of column axial load (JA-1PTMS)

At low load steps, cracking initiated in the beam where old flexural cracks reopened. Moreover, cracks between old and new concrete interfaces formed. More flexural cracks continued to appear at the beam up to a DR of 1.5%, when the first diagonal crack developed in the joint area. The crack formed in both directions due to load reversal. Because the test was terminated when the maximum capacity of the unit was believed to be reached (since this unit was to be re-strengthened later with CFRP), the cracking progress at higher drifts was not captured. Nevertheless, an X-shaped failure mechanism initiated in the joint area. Figure 7-22(a) and (b) show the final cracking pattern of the joint before and after removing the strips, respectively. Also, Figure 7-22(c) shows the cracking pattern of the bare unit JA-1 at the maximum load, for comparison reasons. As can be seen from the figures, the core of the strengthened joint had fewer shear cracks compared to the multiple cracks and cracking occurring in the bare unit. Moreover, at zero displacement, cracks of the strengthened unit were closed, whereas they remained open in the case of the bare unit.

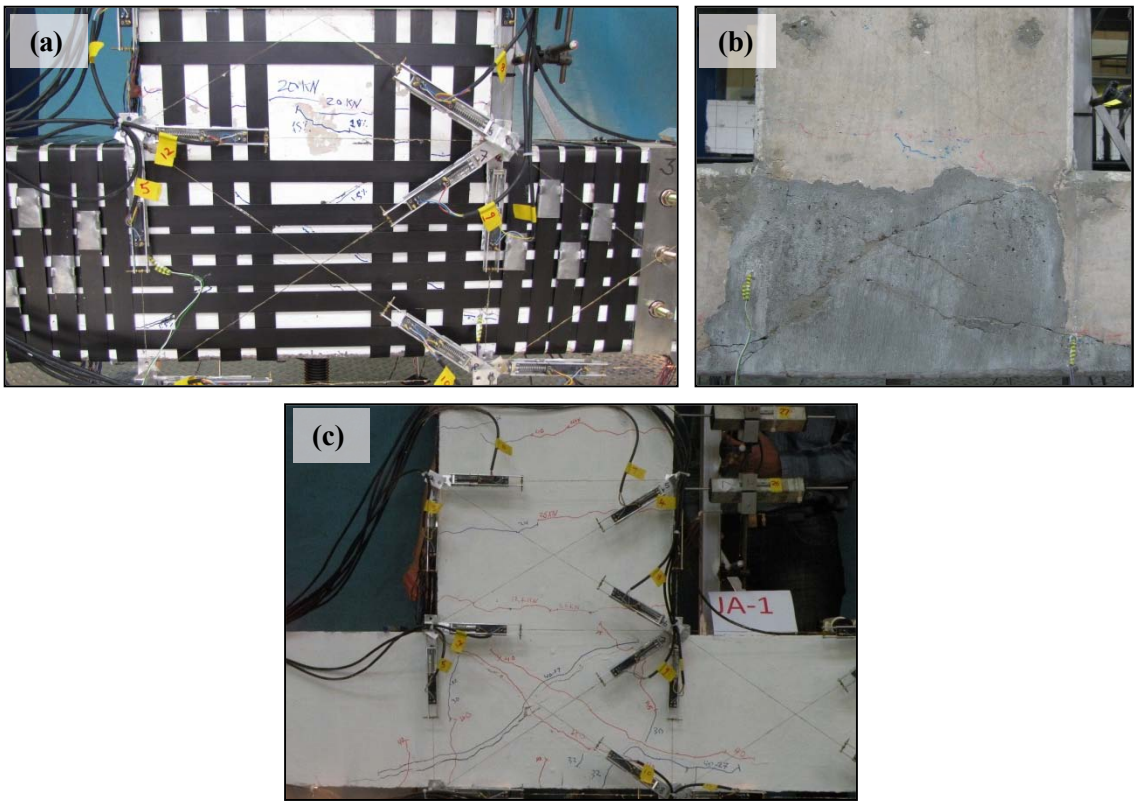

Figure 7-22: Final cracking Pattern a) with strips installed, b) after removing the strips and c) unit JA-1 at maximum

During the last loading step, the strips at the middle of the beam failed, as shown in Figure 7-23(a), which could be ascribed to the high pre-tensioning of strips. The strips used in this unit were not very ductile. The strip failure occurred at a load of 44 kN corresponding to a displacement of 24mm (DR of 1.5%). In addition, some hairline shear cracks appeared at the splice zone of the top column, as shown in Figure 7-23(b). Some cracks were also observed around the bolt locations due to the high shear transferred by those bolts.

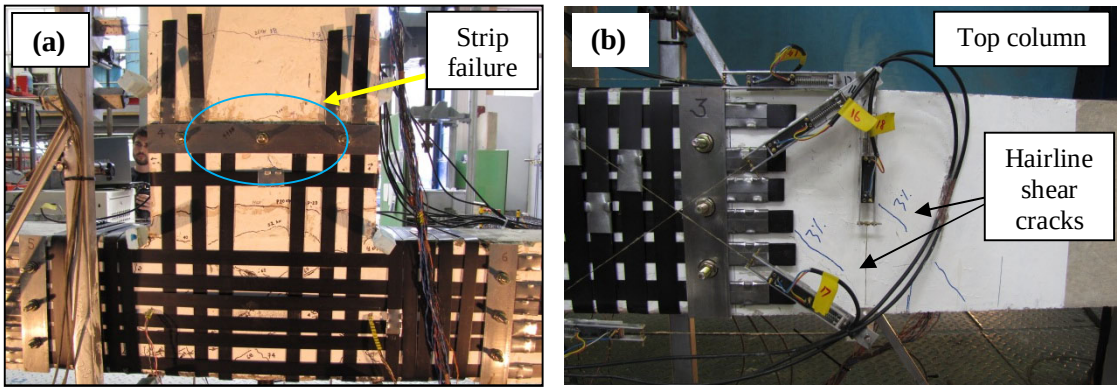

Figure 7-23: a) Strip failure from beam strengthening and b) hairline shear cracks in the top column

The hysteretic beam load-tip drift curves of unit JA-1PTMS is plotted in Figure 7-24 in comparison to that of the bare one JA-1. The envelopes of the hysteretic loops of both units are shown in Figure 7-25. The maximum load in both loading directions occurred at a drift of ±2% and had a value of +75.5 and -65.6 kN in the push and pull directions, respectively. After the first diagonal crack appeared, the stiffness as well as the capacity of the pull direction degraded for several cycles and then increased at the last loading step. The drop in the load, however, was not as severe as that observed for the bare unit. It is clear from the hysteresis response that the unit, during load reversal, had slightly reduced stiffness near the zero-displacement point. However, it can be seen that the pinching effect was more prominent in this unit than the bare joint as it was subjected to hysteretic loading whereas the bare joint was only subjected to one post-peak cycle. It should be noted also that despite the failure of strips at the mid beam section, this did not reflect on the hysteretic response as the strip contribution was low. The application of high stresses on these strips before the test is most likely responsible for their failure.

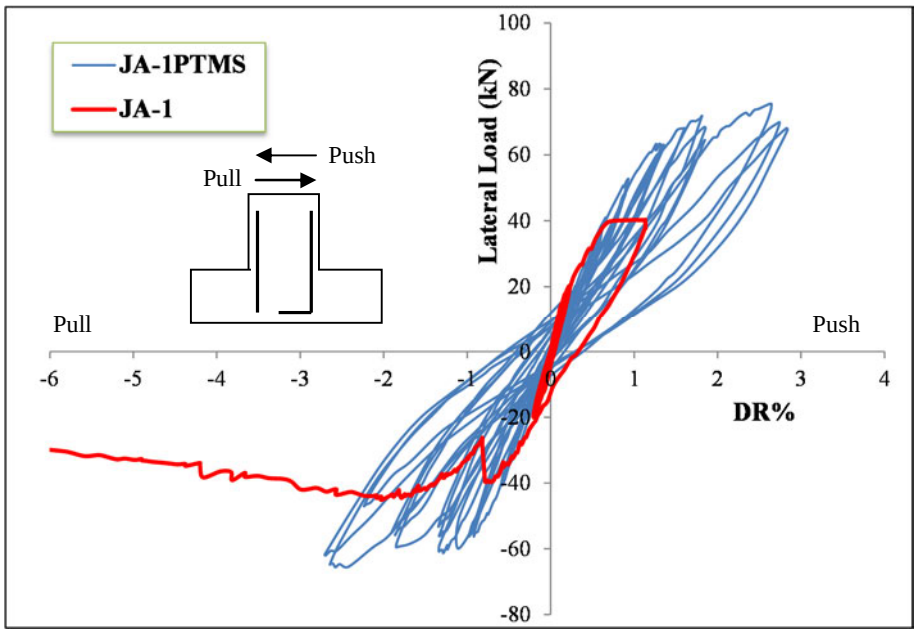

Figure 7-24: Load-drift hysteresis of the strengthened specimen JA-1PTMS and the control one JA-1

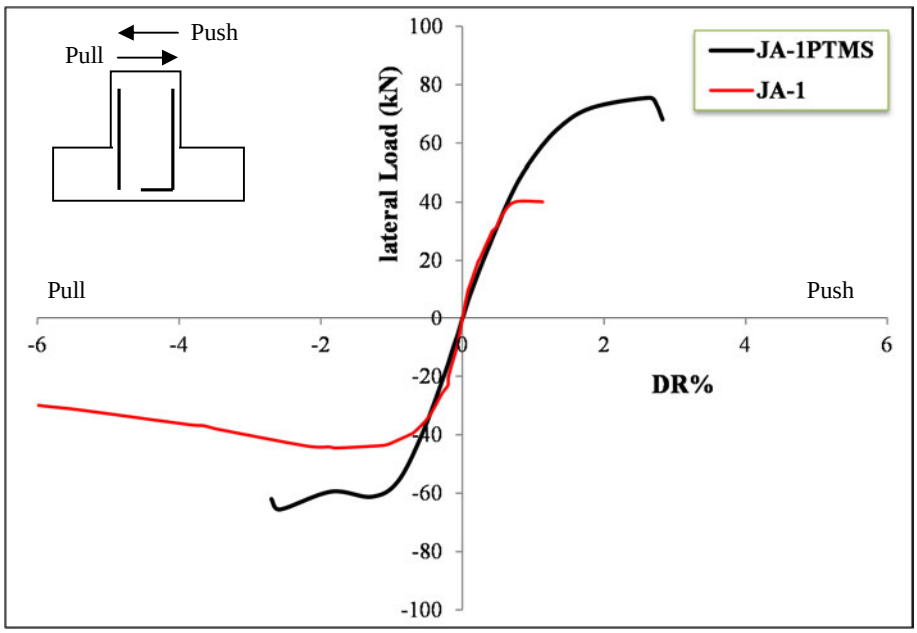

Figure 7-25: Envelopes of the bare (JA-1) and strengthened (JA-1PTMS) units

The strains developed in the beam anchorages and the top column splices at the maximum load were 2434 με, and 1366 με, respectively. The corresponding average bond stresses were calculated at 8.5 and 3.3 MPa for the anchorages and splices, respectively. The bottom column had a maximum strain of 1495 με which is very close to that of the top column. Figure 7-26 shows the strain history of anchored and spliced bars of this joint.

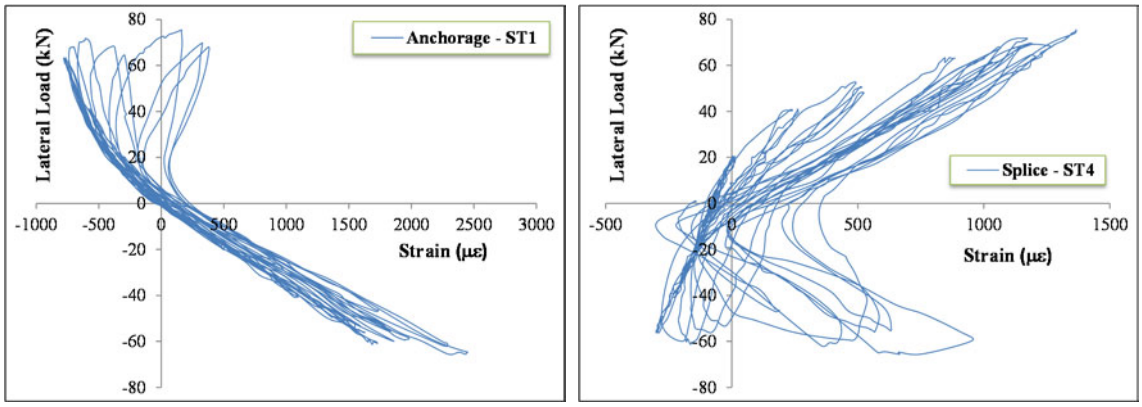

Figure 7-26: Strains at beam anchorages (left) and column splices (right)

The load resistance of the unit in the push and pull directions is plotted versus drift in Figure 7-27. In the load control phase, the pull (weak) direction had a slightly higher drift capacity than the push direction (10% increase). The reason for this may be due to the way the core was repaired where part of the concrete on the hook side was not removed. This effect continued in the displacement control phase up to a drift of about 1.5%. At this point, the capacity in the pull direction started to degrade due to bond deterioration until the end of the test.

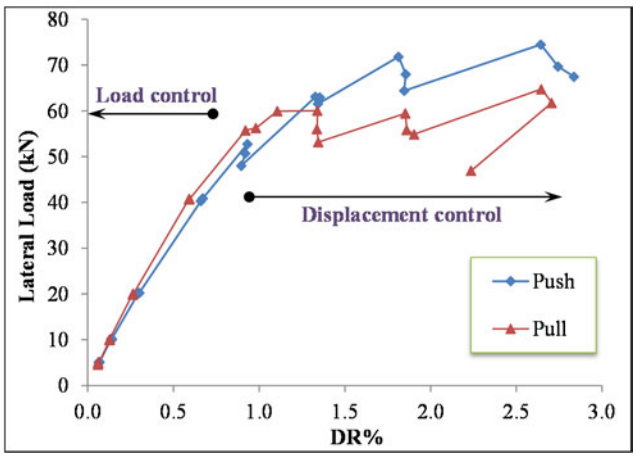

Figure 7-27: Lateral load resistance in the pull and push directions

The amount of energy dissipated per-cycle along with the cumulative energy dissipation and ζ_{eq} is plotted in Figure 7-28(a), (b) and (c), respectively. The energy was dissipated mostly because of cracking in the joint area. The dissipation rate was low at small drifts and then increased as cracking progressed. Due to the incomplete testing of the unit, the total energy dissipated does not reflect the complete performance of the joint. By the end of the test, the joint dissipated a total energy $E_{JA\text{-}1PTMS}$ of 7.5 kN.m corresponding to a DR of 2.6%. This is 3.75 times the energy dissipated by the bare unit at the same load level or 2.45 times the total energy at a drift of 4%. ζ_{eq} of this unit increased with loading (from 2% up to 6%) with drops due to cycling.

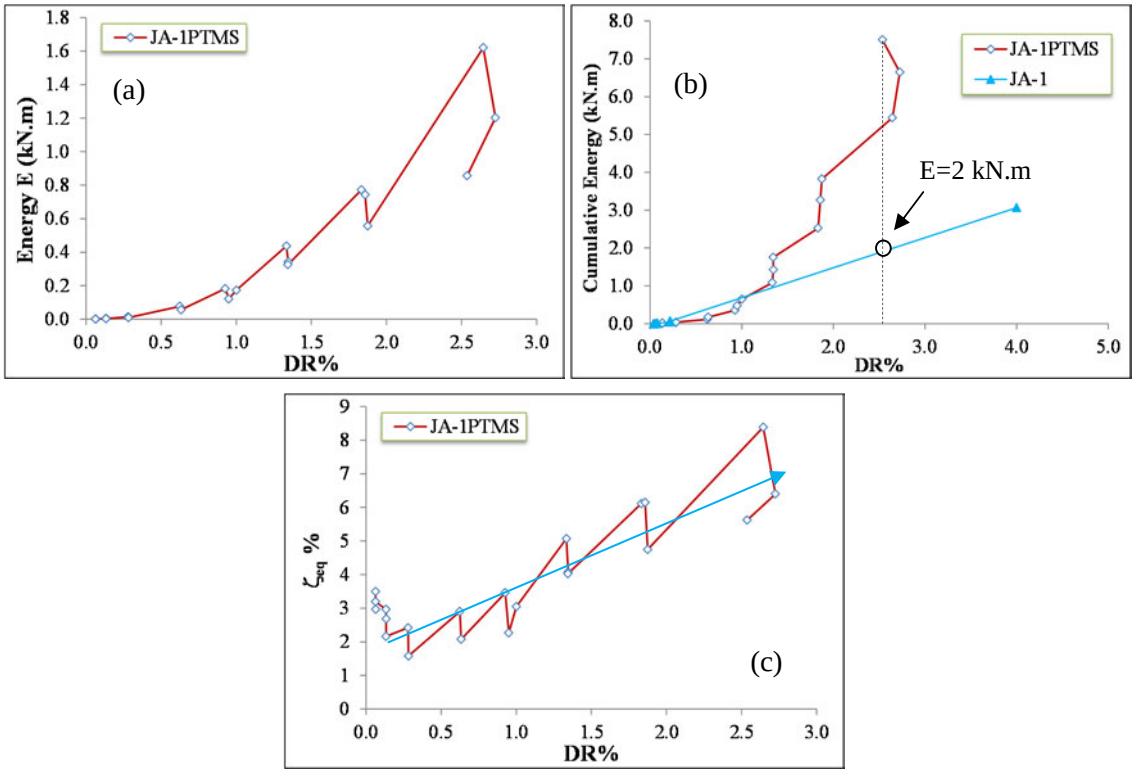

Figure 7-28: a) The amount of energy dissipation, b) Cumulative energy and c) equivalent damping

7.3.2 JOINT JA-3PTMS

In this unit, the resistance in the pull direction was deficient due to the inadequate anchorage of the beam bottom bars of only 230 mm into the joint area. The unit was tested only in displacement control according to the loading regime illustrated in Figure 7-29. Eight loading steps were applied at drift ratios of ±0.25%, ±0.5%, ±1%, ±1.5%, ±2%, ±3%, ±4% and ±6%.

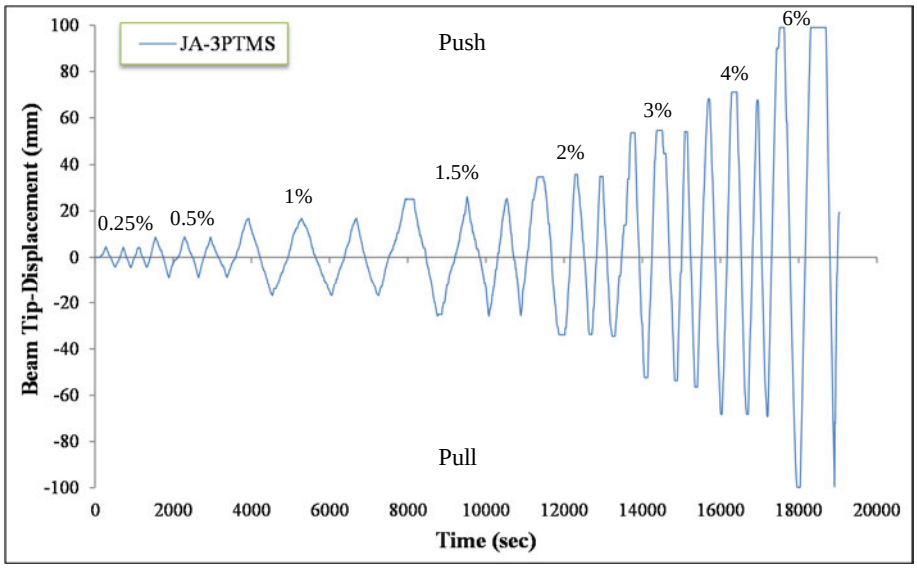

Figure 7-29: Loading regime of the test unit JA-3PTMS

The column axial load was set at 250 kN which is similar to the original specimen. Figure 7-30 shows the variation in the axial load throughout the test. As can be seen from the figure, a 6% drop in the load occurred at the end of the 1st loading step (DR = 0.25%). Consequently, the load was increased to 258 kN (+3%), which then gradually decreased during testing and levelled off at a DR of -2%. The variation in the axial load in this unit is considered insignificant for practical purposes.

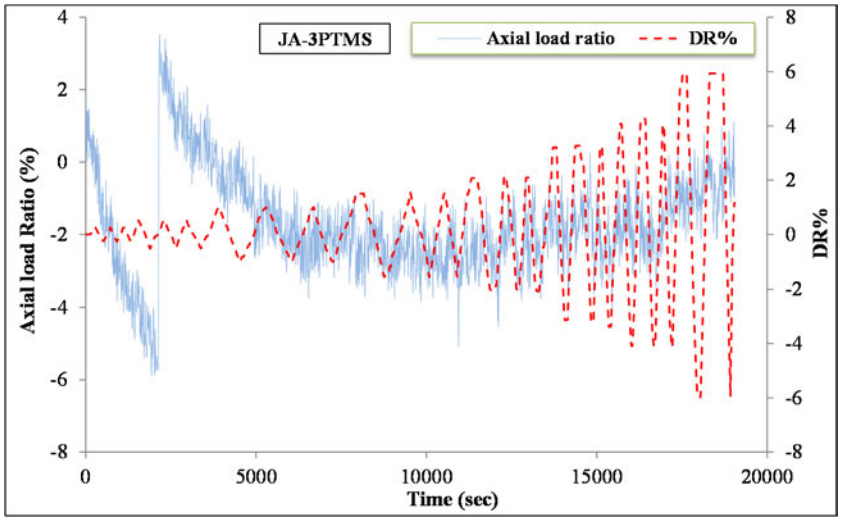

Figure 7-30: Variation of column axial load (JA-3PTMS)

At small drifts of ±0.25% and ±0.5%, existing flexural cracks in the beam hinging area opened. In addition, cracks between the old and new concrete interfaces appeared. With further increase in loading, multiple flexural cracks formed in the beam. The first diagonal crack was visually observed at a DR of 1% and appeared when loading in the weak direction. Further loading resulted in the formation of an X-shaped failure pattern in the core. The centre of this mechanism shifted towards the beam interface with the column. As loading progressed, more cracks formed in the core and beam hinging area until the joint ultimately failed in shear. Figure 7-31 shows the final crack pattern of the unit at the end of the test before and after removing the strips. As can be seen from the figure, shear cracks were confined to the core and did not propagate to the back of the column. In addition, the beam was moderately damaged at the strengthened area, where several sizable flexural cracks formed. Some hairline cracks also appeared on the column interfaces with the core. During removal of the strips, some concrete spalled-off of the beam sides and the centre of the X-pattern mechanism, as shown in Figure 7-31(b). No failure of strips occurred during the test.

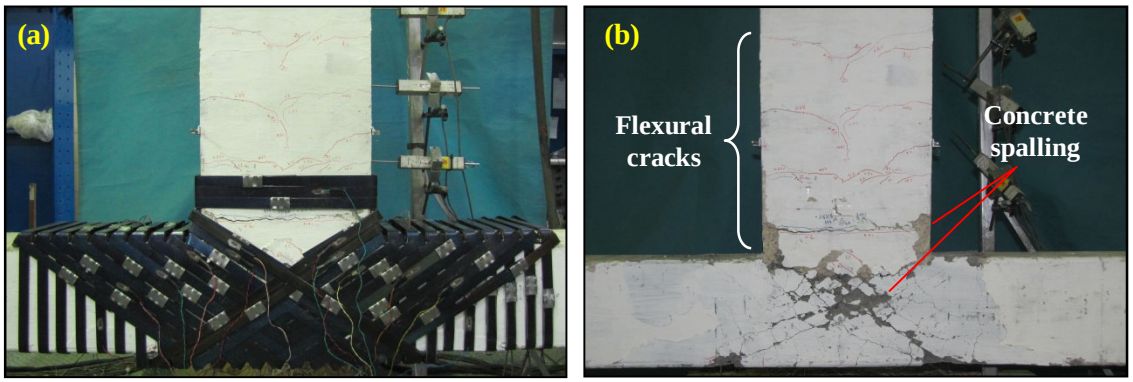

Figure 7-31: Final cracking Pattern a) with strips installed, b) after removing the strips

Figure 7-32 compares the final damage state of the bare unit JA-3 and strengthened one JA-3PTMS after removal of the strips. Although the failure pattern was similar, the strengthening was successful in preventing a) propagation of shear cracks to columns, b) widening of the shear cracks, and c) excessive cracking of the concrete at the back of the core. It was also noted that the failure triangle, which formed prominently in the bare unit, was less developed in the strengthened unit.

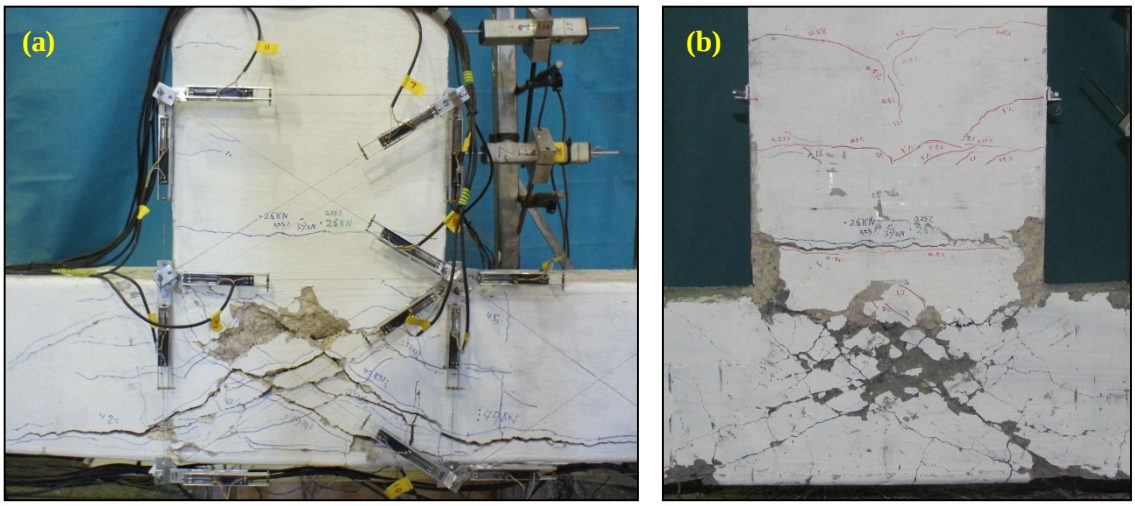

Figure 7-32: Comparison of damage states of a) JA-3, and b) JA-3PTMS

The hysteretic lateral load versus beam-tip drift curve is shown in Figure 7-33. The maximum load in the push and pull directions occurred at a DR of ±2% and had values of +75 kN and -69 kN, respectively. Hence, the ratio between the lateral load capacity in the strong and weak directions was equal to 1.09. It is interesting to note that this ratio was found to be similar to that of JA-3 but occurred at higher load levels.

In comparison with the bare unit, the strengthened unit showed higher capacity of 30% and 20% in the push and pull directions, respectively. In addition, the maximum capacities occurred at higher drifts. Moreover, the hysteretic response of specimen JA-3PTMS showed an improved ductile behaviour as compared to specimen JA-3. The joint strengthening appeared to provide a degree of confinement to the concrete and increased the joint shear strength and ductility.

By examining the hysteretic curve of the strengthened unit, it was noted that slight pinching was present in the pre-peak response. Despite the shear cracking in the core, thereafter, the post-peak loops did not completely lose their stiffness near the zero-displacement point, even at high drifts, as compared to those of the bare unit. Thus, the strengthening methodology reduced the pinching effect of this unit due to preventing excessive crack opening during the test.

Both units experienced a sudden drop in the resistance as the first diagonal crack formed. This crack tended to appear during loading in the weak direction. Due to pre-existing cracks, the initial stiffness of the strengthened joint was less compared to that of the bare joint, as shown in Figure 7-34, which represents the envelopes of the bare and strengthened units.

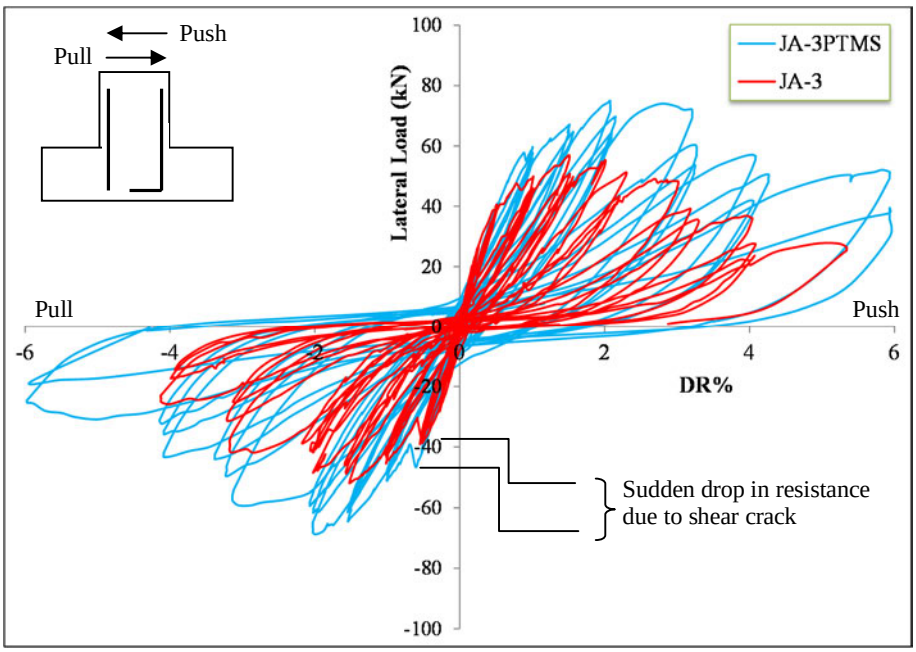

Figure 7-33: Load-drift hysteresis of the strengthened specimen JA-3PTMS and the control one JA-3

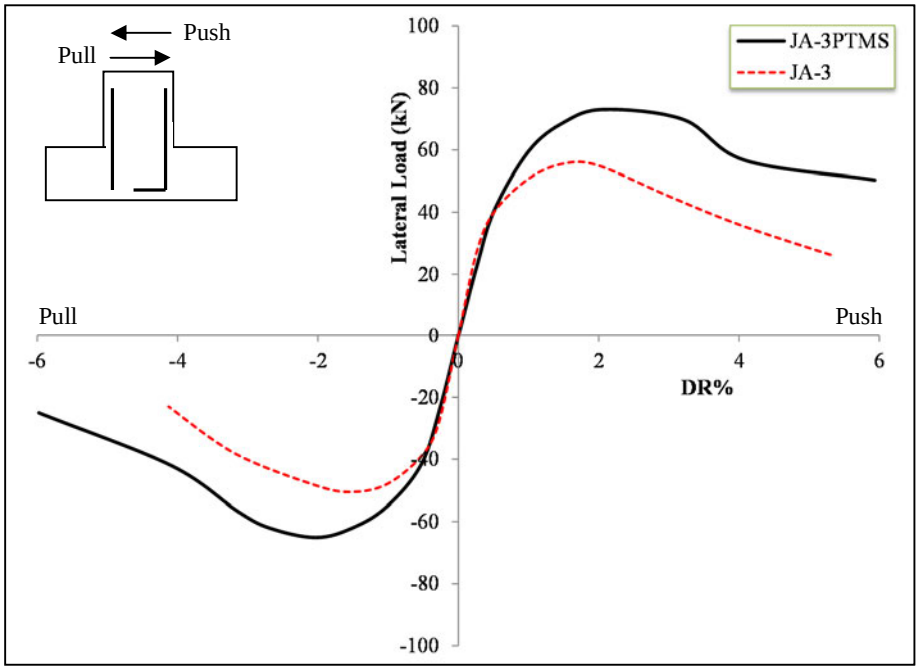

Figure 7-34: Envelopes of the bare (JA-3) and strengthened (JA-3PTMS) units

Figure 7-35 shows the stiffness degradation of the test unit in the push and pull directions along with the secant stiffness. During the first and second loading steps when only flexural cracks appeared, only a slight reduction in stiffness occurred (about 9%). Due to the formation of diagonal cracks in the core (DR=±1%), an average of 24% reduction in stiffness took place. Afterwards, the stiffness degraded gradually until the end of the test. Up to a DR of 1.5%, it can be noted that the stiffness reduction within each loading step was very small. Afterwards, more reduction occurred due to the deterioration of the hysteretic resistance. At the maximum load,

the joint lost 52% of its stiffness; and by the end of the test, the joint lost 94% of its initial stiffness.

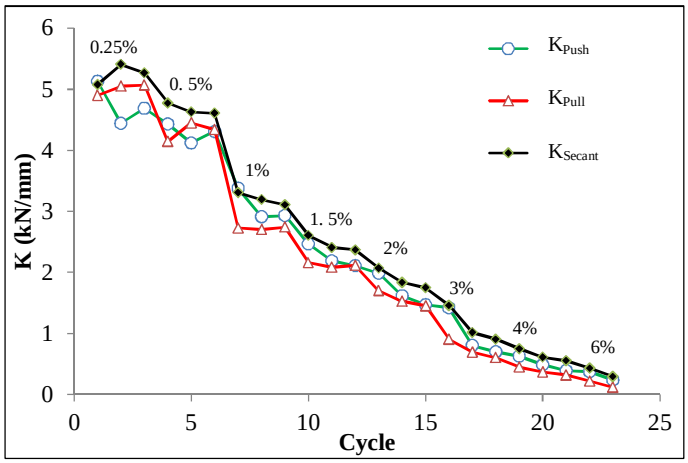

Figure 7-35: Stiffness degradation of unit JA-3PTMS

The peak-to-peak stiffness of unit JA-3PTMS is compared to that of unit JA-3 in Figure 7-36. As can be seen from the figure, prior to a DR of ±0.5% the strengthened joint had less stiffness compared to the bare one due to pre-existing crack opening. The strengthened joint, thereafter, showed higher stiffness throughout the test. Both units showed a similar rate of stiffness degradation after a DR of ±1%. The reduction in stiffness within the different loading steps was noted to be less severe in the strengthened unit. At higher drift ratios above ±2%, the strengthened joint showed almost twice the stiffness of the control unit.

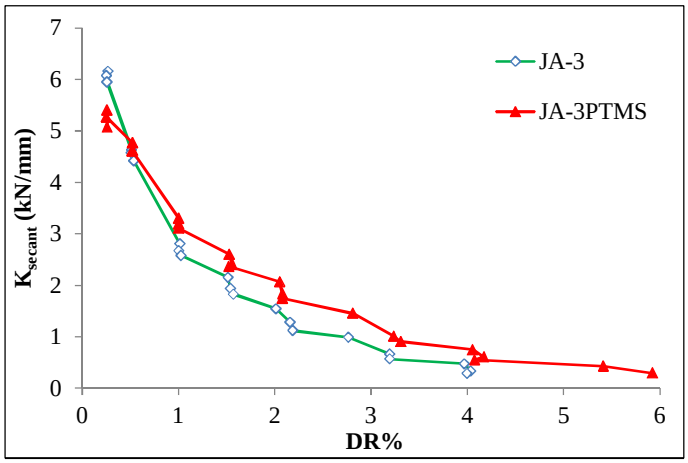

Figure 7-36: Peak-to-peak stiffness degradation of unit JA-3PTMS vs. JA-3

The effect of anchorage on load resistance was examined by plotting peak loads in the pull and push directions at each cycle, as shown in Figure 7-37. Also plotted in the same figure is the resistance factor RF of the unit. Prior to the sudden drop in resistance due to shear crack at a DR of ±1%, both loading directions behaved almost identically. At a DR of ±1%, a 20% drop in the capacity of the pull direction occurred (RF=1.2). In the next cycle (DR=±1.5%), however, the

resistance recovered, and as a result, the difference was minimised. This is attributed to strengthening since strain readings from strain gauges attached to the diagonal mid-strip showed a jump in the values, as shown in Figure 7-38. After the maximum load (DR=±2%), a prominent reduction in the pull direction capacity occurred. This reduction was calculated at 10%, 20% and 30% at drifts of ±2%, ±3% and ±4%, respectively. In comparison with the bare one, the strengthened unit did not continue to lose its resistance capacity after the sudden drop in resistance at a DR of ±1%. Permanent loss of strength occurred only after the maximum capacity was attained; while in the bare unit, the resistance in the pull direction deteriorated until the end of the test.

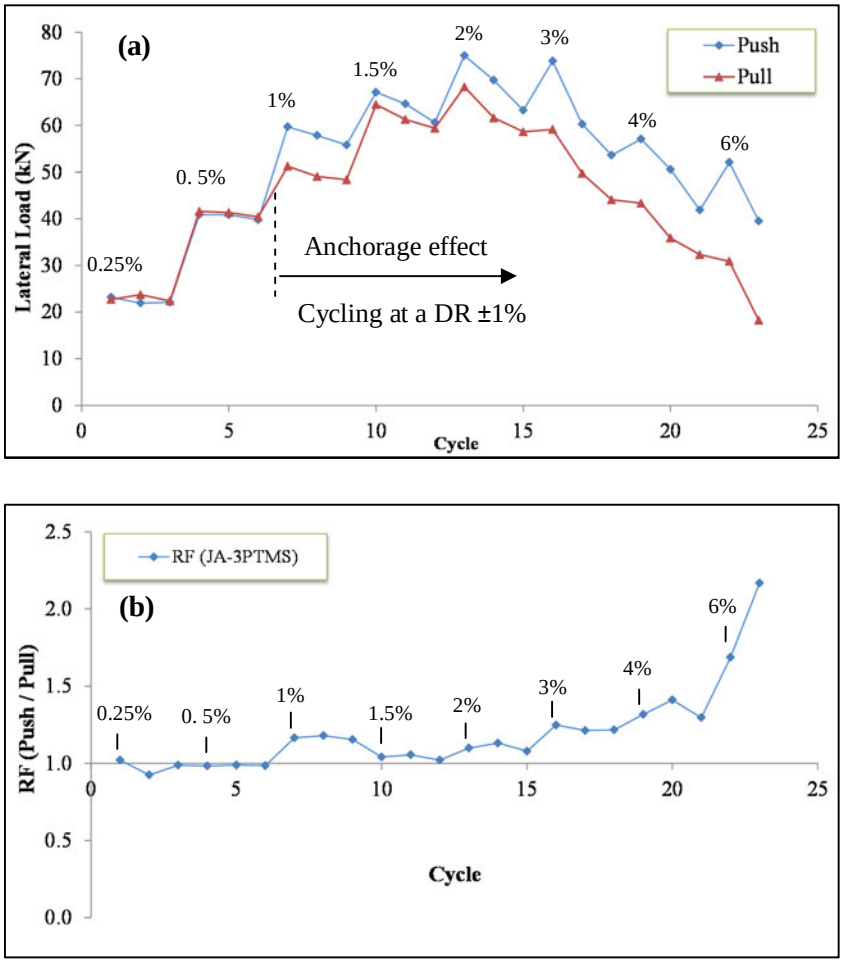

Figure 7-37: a) Lateral load capacity in the pull and push directions, and b) resistance factor of unit JA-3PTMS

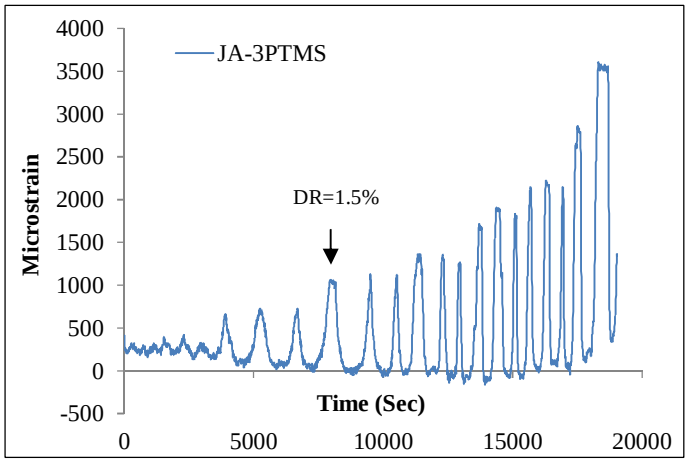

Figure 7-38: Strain gauge reading of a gauge attached to a mid-diagonal strip

Table 7-2 presents the strain results at the beam and column longitudinal bars at the maximum load state. In addition, Figure 7-39 shows the strain history of the anchored and spliced bars. It is clear that the beam was 60% more stressed than the column. Apparently, the beam bars experienced yielding during the 6th loading step at a displacement of 40 mm (DR = +2.4%). However, yielding was not clearly evident due to failure of the strain gauge ST1 (see Figure 7-39). Moreover, many of the strain gauges in the joint area failed in the post-peak stage due to excessive cracking at the core interfaces.

The resulting average bond stresses were 9.6 and 4.0 MPa for the anchored and spliced bars, respectively.

Table 7-2: Strains at beam and column reinforcement at the maximum load (JA-3PTMS)

Lateral Force		**δ**	**Beam**		**Top column**		**Bottom Column**	
Direction	Value		ε_s (με)		ε_s (με)		ε_s (με)	
	kN	*mm*	ST1	ST2	ST4	ST6	ST3	ST5
Push	75	34.7	456	1326	-290	586	1463	-
Pull	-69	-33.1	2076	206	1911	1016	913	-

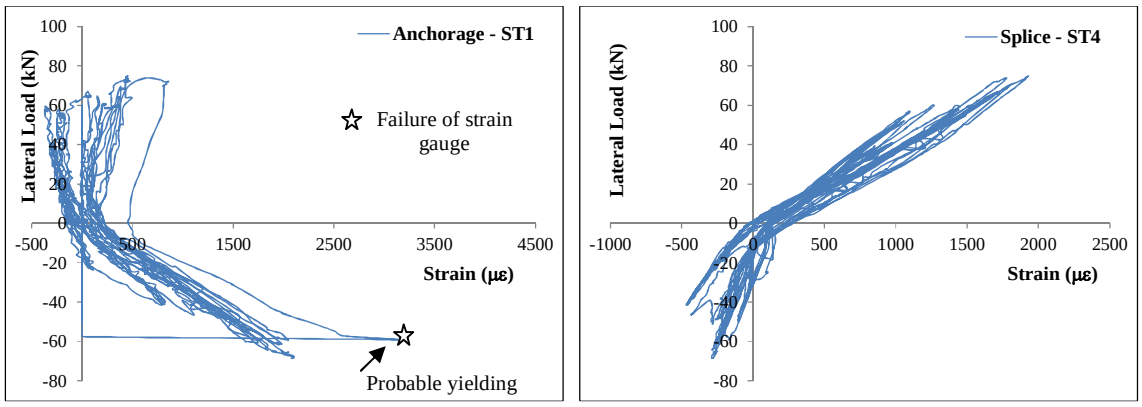

Figure 7-39: Strains at beam anchorages (left) and column splices (right)

The amount of energy dissipated per cycle and cumulative energy are shown in Figure 7-40 in comparison to those of the bare unit. Only a small amount of energy was absorbed during the first three loading steps. After the maximum capacity was reached, energy absorption kept increasing. By the end of the test, the joint dissipated a cumulative energy of 26.3kN.m. The joint dissipated 15% of the total energy at 2% DR, 50% of the energy at 3% DR, 70% of the energy at 4% DR and 100% of the energy at 6% DR.

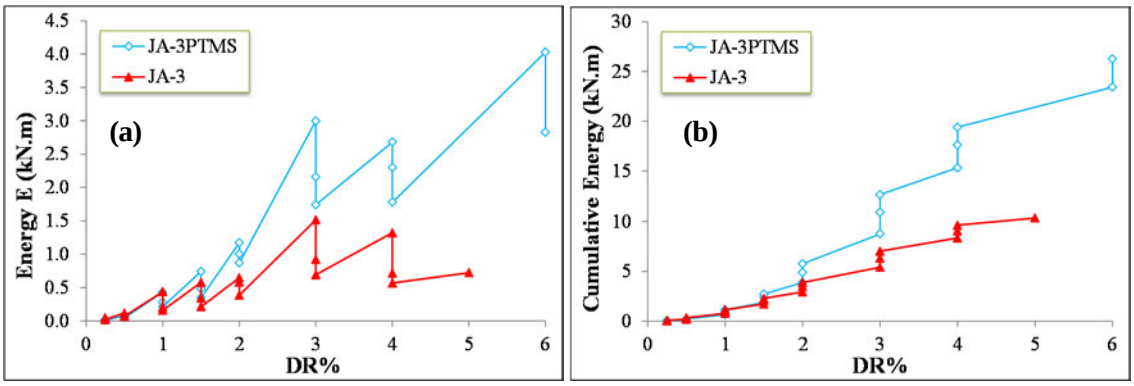

Figure 7-40: a) The amount of energy dissipation E, and b) Cumulative energy

From the previous figure, it can be noted that at small drifts up to 1.5%, both the control and strengthened units dissipated almost the same cumulative energy. The strengthened unit, thereafter, showed higher and faster energy dissipation. In comparison with the control unit, the strengthened joint dissipated twice the energy at a DR of 4%. At drifts higher than 3%, the per-cycle energy of the strengthened joint was very high compared to that of the control unit. It was also noted that the per-cycle energy of the strengthened unit was almost twice the value of the control unit throughout the test.

Figure 7-41 compares the equivalent viscous damping, as well as the normalised energy to the perfect hysteretic response of both units. The equivalent damping of both units was noted to be similar up to a DR of ±1.5% with an average of 4.5%. Due to cracking of the joint at higher drifts, the damping increased significantly in both units and averaged at 8% and 12% for the bare and strengthened units, respectively. Two noticeable drops were observed from the behaviour. The first drop occurred at a DR of ±1.5%, coinciding with the formation of 1st diagonal crack in the core. The second drop occurred at a DR of ±3%, where wide cracks developed in the core.

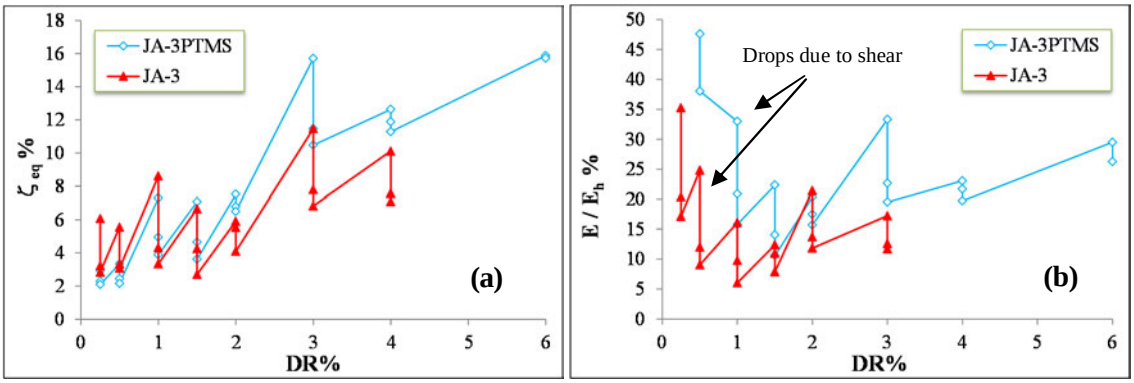

Figure 7-41: a) Equivalent viscous damping, and b) normalized energy to un-pinched hysteretic energy

As for the ratio of E/E_h, it can be seen that the strengthened unit showed better hysteretic behaviour indicating less damage and less pinching effect. It was also noted that at a DR of ±1% a severe drop of about 50% in the ratio occurred, which was attributed to joint shearing. A similar drop of about 64% also occurred in the bare joint but at a DR of ±0.5%. In the pre-peak stage, no pinching existed and the decrease in the ratio was only due to flexural and shear cracking. In the post-peak stage, on the other hand, an increase in the ratio occurred since both units showed resistance to damage. The increase, however, was more pronounced at the first cycle of each loading step. This was evident from the hysteretic response, since during these cycles more cracks appeared; but when repeating the cycles the drop in the force and stiffness along with crack opening resulted in a reduction in the amount of energy dissipated. On average, the E/E_h ratio was calculated at 15% and 26.4% for the bare and strengthened units, respectively.

7.3.3 JOINT JB-1PTMS

This unit was subjected to the loading regime in displacement control, as illustrated in Figure 7-42. The regime comprised nine loading steps at drifts of ±0.25%, ±0.5%, ±0.75%, ±1%, ±1.5%, ±2%, ±3%, ±4% and ±5%.

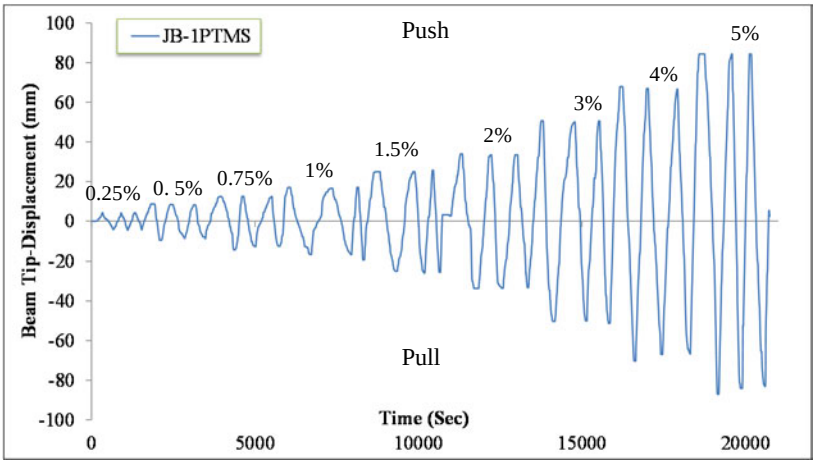

Figure 7-42: Loading regime of the test unit JB-1PTMS

The axial load applied to the column was set at 150 kN. The variation of the compressive axial load during the test is shown in Figure 7-43. With loading, the compression dropped to 125 kN (17% drop) and remained almost constant throughout the test. It should be mentioned that the drop in the axial load of unit JB-1PTMS was similar to that of unit JB-1 and both units had the same load level during the test.

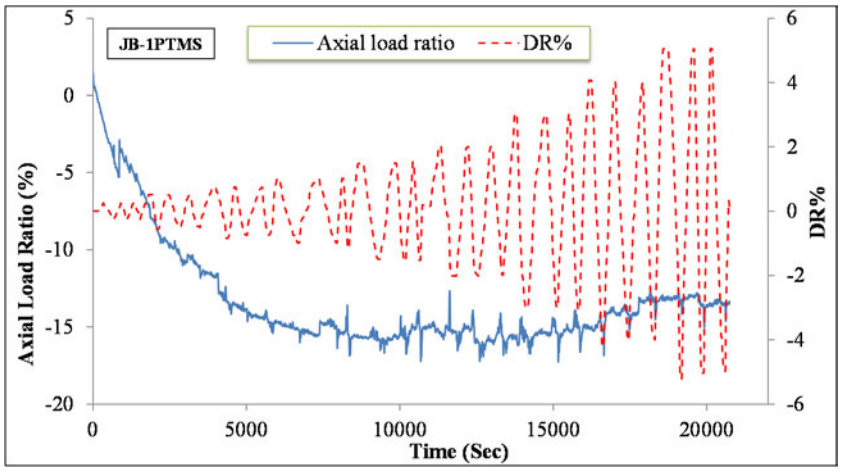

Figure 7-43: Variation of column axial load (JB-1PTMS)

The loading was initiated with a DR +0.25%. At this level, existing cracks in the beam reopened. With increase in loading to a DR of 0.5%, hairline cracks between old and new concrete appeared. These cracks were visible during the 3rd loading step or DR of ±0.75%. The first shear crack was observed when loading at a DR ±1%. At a DR of ±1.5%, multiple flexural cracks developed in the beam along with widening of the shear cracks. Loading to a DR of ±2% resulted in the formation of flexural cracks at column interfaces with the core and at the splice ends. In addition, in this step, a noise was heard when loading in the weak direction, which was attributed to the failure of some welding points. In the last three loading steps, multiple shear cracks formed in the core and sizable flexural cracks occurred along with concrete crushing within the strengthened area of the beam. In the last loading step, a slight noise was heard which could be attributed to the break of the rest welding points. The joint ultimately failed due to a shear mechanism in the core at a DR of ±5% and moderate damage in the beam strengthened area. The final cracking pattern of the unit before and after removing the strips is shown in Figure 7-44(a) & (b), respectively. Also, the final cracking pattern of the bare unit JB-1 is shown in the same figure (Figure 7-44(c)) for comparison.

As can be seen from Figure 7-44(b), the cracking and damage took place in the core, as well as the beam hinging area. An X-pattern failure mechanism formed in the joint area. In comparison to the bare unit, it was clear that the damage shifted towards the beam interface with the core and that the failure was more flexural. Also, the shear cracks were mainly limited to the core

with a slight extension of these cracks to the back of the column due to existing cracks, as shown in Figure 7-44(b).

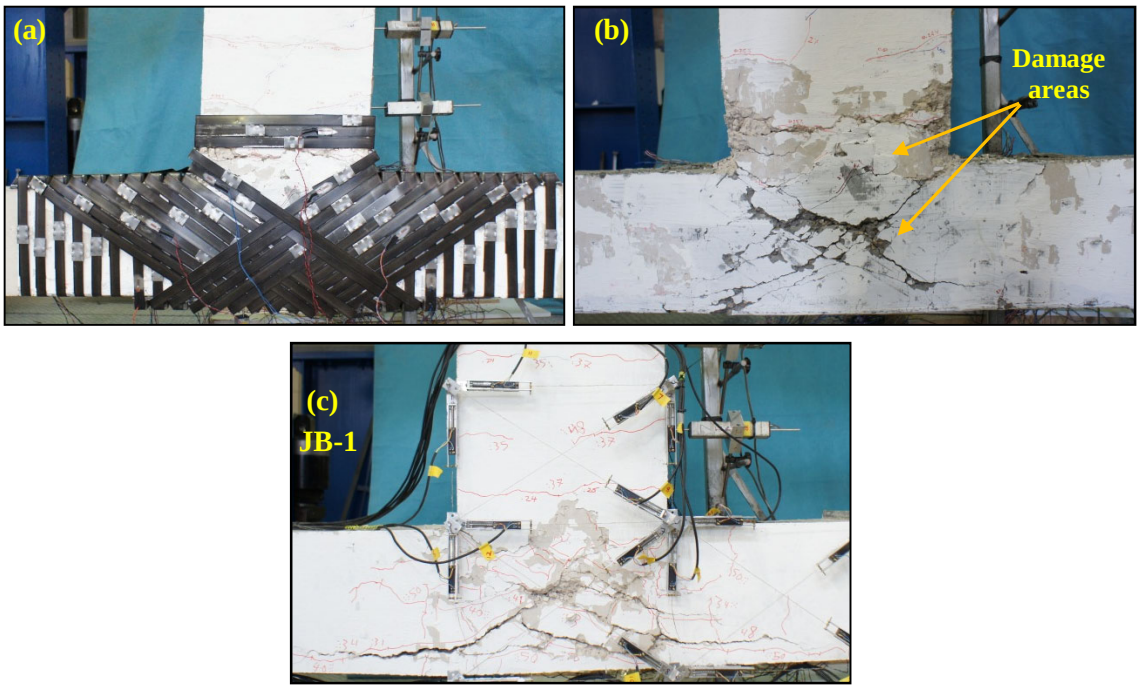

Figure 7-44: Final cracking pattern a) with strips installed, b) after removing the strips and c) unit JB-1

Figure 7-45 shows the hysteretic beam load-tip drift curve of unit JB-1PTMS compared to that of the control unit JB-1. It can be seen from the figure that the strengthened unit had better performance such that higher load and drift capacities were achieved. The maximum load in the push direction occurred at a DR of +2% and had a value of +87.4 kN; in the pull direction, the maximum load occurred at a DR of -3% and had a value of -80 kN. As a result, the ratio between the push to pull loads amounted for 1.09, which was more favourable than the 1.24 ratio obtained for test unit JB-1. The strengthened specimen was also able to sustain the maximum load for several cycles (three loading steps) in the weak direction, as shown in Figure 7-45. In the control unit, the maximum was reached once the main shear crack appeared and the resistance tended to degrade afterwards. Pinching of the hysteretic loops was observed after the 6^{th} loading step (DR of ±2%) and increased at higher drifts. The improvement in pinching behaviour was more noticeable in this unit compared to the control unit and also in comparison to the previous strengthened unit JA-3PTMS.

The lateral load at yielding was +75 kN at a lateral displacement of +28.2 mm (DR = +1.7%). Yielding took place in the beam hook bar during loading in the push direction. By the end of the test, the load dropped to +43 and -19 kN in the push and pull directions, respectively. These values represented 50% (push) and 24% (pull) of the peak loads.

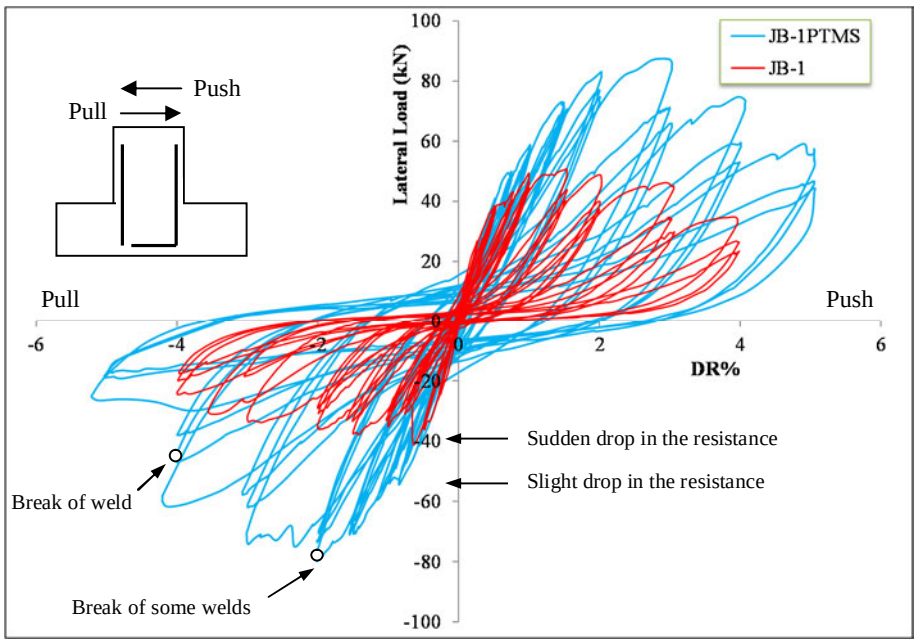

Figure 7-45: Load-drift hysteresis of the strengthened specimen JB-1PTMS and the control one JB-1

Envelopes of the beam load tip drift curves for the bare and strengthened units are shown in Figure 7-46. As can be seen from the figure, the performance of the pull (weak) direction of the strengthened unit improved considerably. Furthermore, the initial stiffness of both units was almost identical. The envelopes of both units showed similar rate of strength deterioration in the push direction, whereas strength deterioration was much faster in the strengthened unit in the pull direction. This rapid degradation in the stiffness is attributed to the complete break of weld points in the weak direction during the 8th loading step.

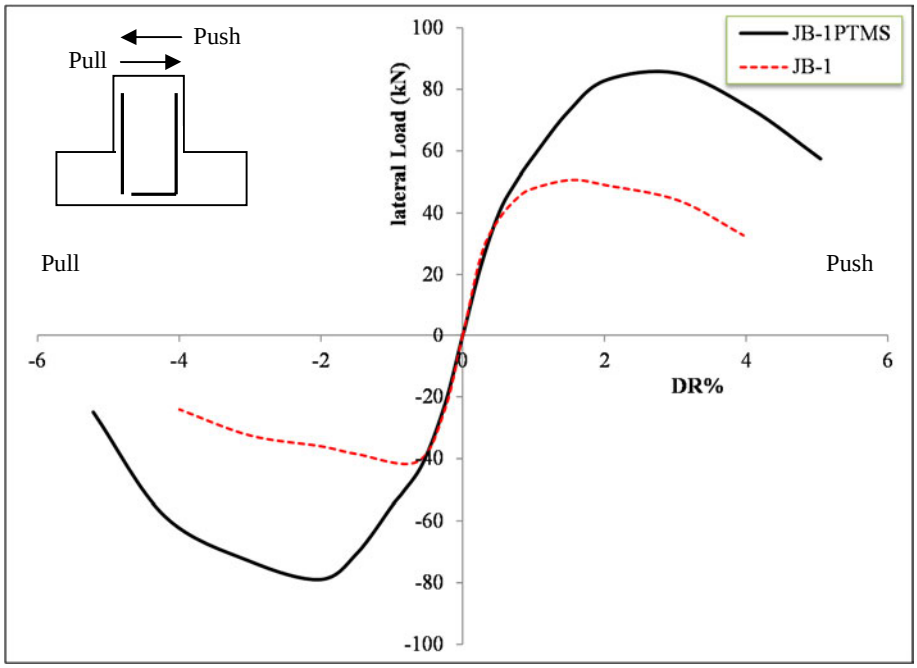

Figure 7-46: Envelopes of the bare (JB-1) and strengthened (JB-1PTMS) units

Figure 7-47 shows the calculated stiffness degradation of unit JB-1PTMS per cycle. Compared to the previous unit, no significant degradation in stiffness occurred when the first diagonal crack appeared. In fact, the degradation was consistent and gradual. Both loading directions showed comparatively similar behaviour throughout the test. It was also noted that up to a DR of ±1.5%, the stiffness during each loading step degraded gradually; whereas it was more severe thereafter due to breaks of the welds and formation of diagonal cracks.

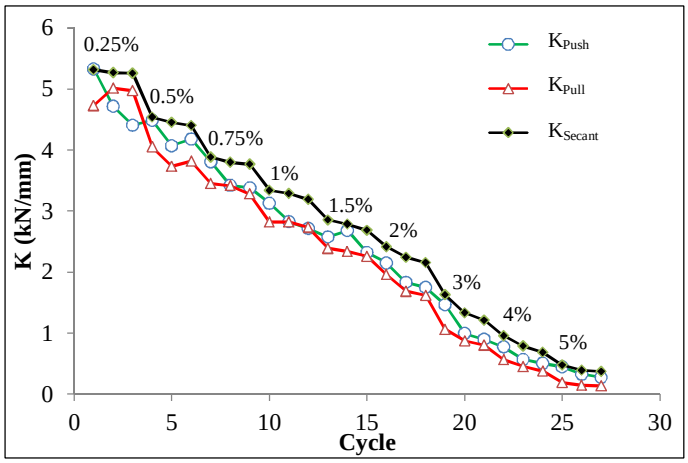

Figure 7-47: Stiffness degradation of unit JB-1PTMS

Figure 7-48 shows the peak-to-peak stiffness degradation of the strengthened unit in comparison to that of the bare unit. As can be seen from the figure, the initial stiffness of the strengthened unit was a bit lower than that of the bare unit with a ratio of 0.93. Also, it can be noted that the strengthened unit was capable of regaining its stiffness better after the first loading step. Moreover, the stiffness degradation rate was slower throughout the test. After a DR of ±1.5%, the unit JB-1PTMS was able to sustain twice the stiffness of that of unit JB-1. At a DR of ±1%, the JB-1PTMS unit lost 38% of its original stiffness, at a DR of ±2% it lost 57%, at a DR of ±3% it lost 74%, at ±4% DR it lost 85% and at ±5% DR it lost 92% of its stiffness.

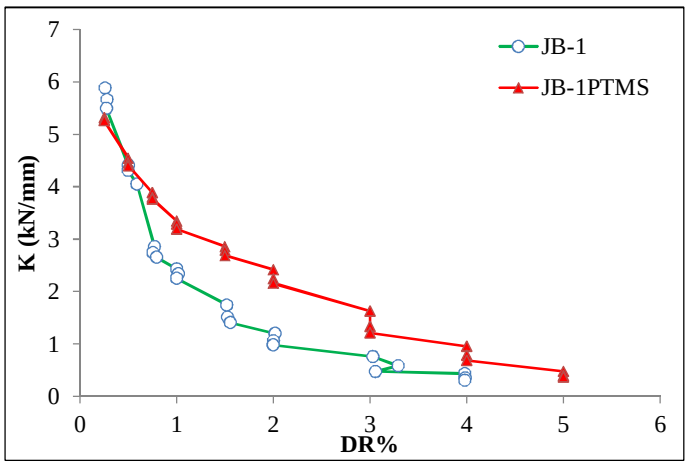

Figure 7-48: Peak-to-peak stiffness degradation

The strains developed in both the beam and column longitudinal reinforcement at the maximum load are presented in Table 7-3. Also, Figure 7-49 shows the strain histories of the top column splices and beam straight anchors throughout the test. As can be seen, the strains were more or less linear until the maximum load was reached. It can also be noted that the beam hooked bars and may be the anchored bars underwent yielding at this stage, whereas the column bars remained elastic. At the maximum peak loads, the beam anchored bars and column spliced bars developed strains of 2383 με and 1402 με in tension, respectively. This corresponded to an average bond stress of 9.65 MPa in the beam anchorage and 3.36 MPa in the column splice.

Table 7-3: Strains at beam and column reinforcement at maximum loading (JB-1PTMS)

Lateral Force		**δ**	**Beam**		**Top column**		**Bottom Column**	
Direction	Value		ε_s (με)		ε_s (με)		ε_s (με)	
	kN	*mm*	ST1	ST2	ST4	ST6	ST3	ST5
Push	87.4	48.5	354	3932	-	-376	824	1785
Pull	-80	-33.6	2383	601	-	1402	1572	378

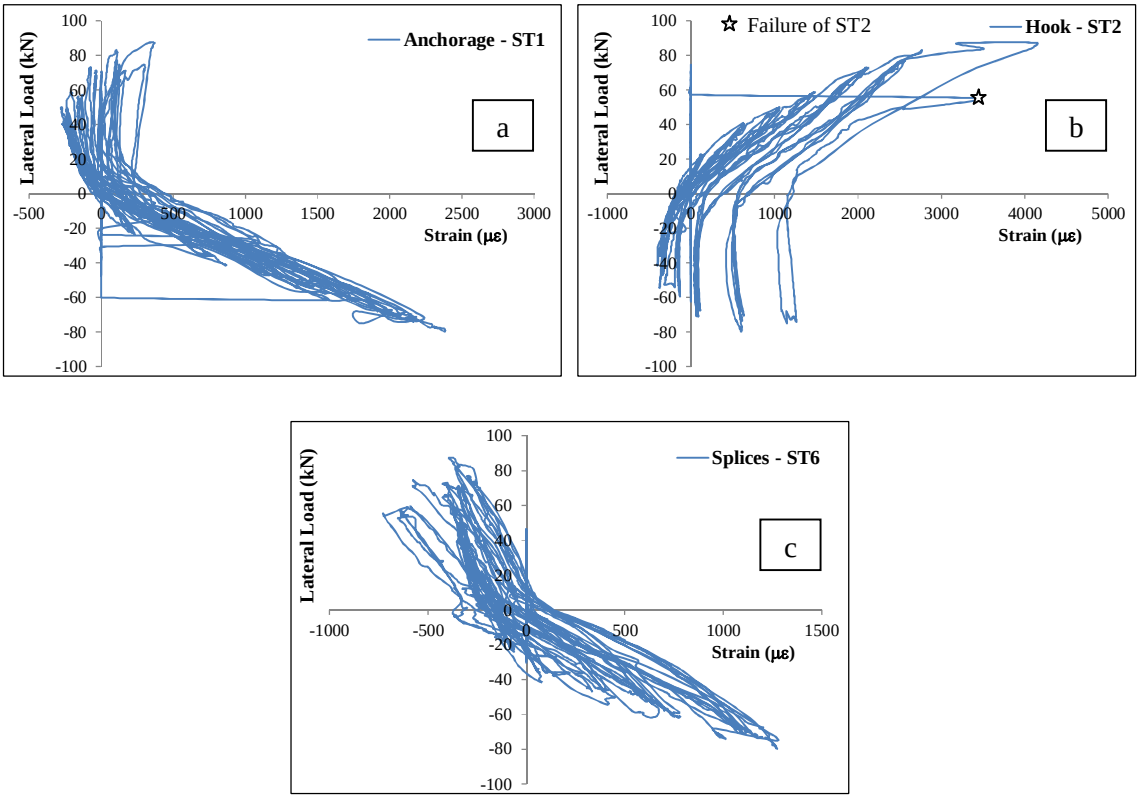

Figure 7-49: Strains at a) beam anchorages, b) hook and c) column splices

The effect of anchored bars on the joint performance was further investigated by plotting the pull load against the push load at each cycle, as shown in Figure 7-50(a). The resistance factor RF of this unit is plotted in Figure 7-50(b). Up to a DR of 1.5%, both loading directions showed identical capacity and the RF fluctuated around the value of 1. This indicated that the welding was beneficial in preventing the early bond slip of the bottom reinforcement. With loading to a

DR of ±2%, the pull capacity started to diminish and the noise heard during this loading step confirmed the fact that it was due to failure of welding points, as mentioned earlier. The decrease in the pull load was faster at the last loading step (DR of ±5%), when its RF reached 2.6.

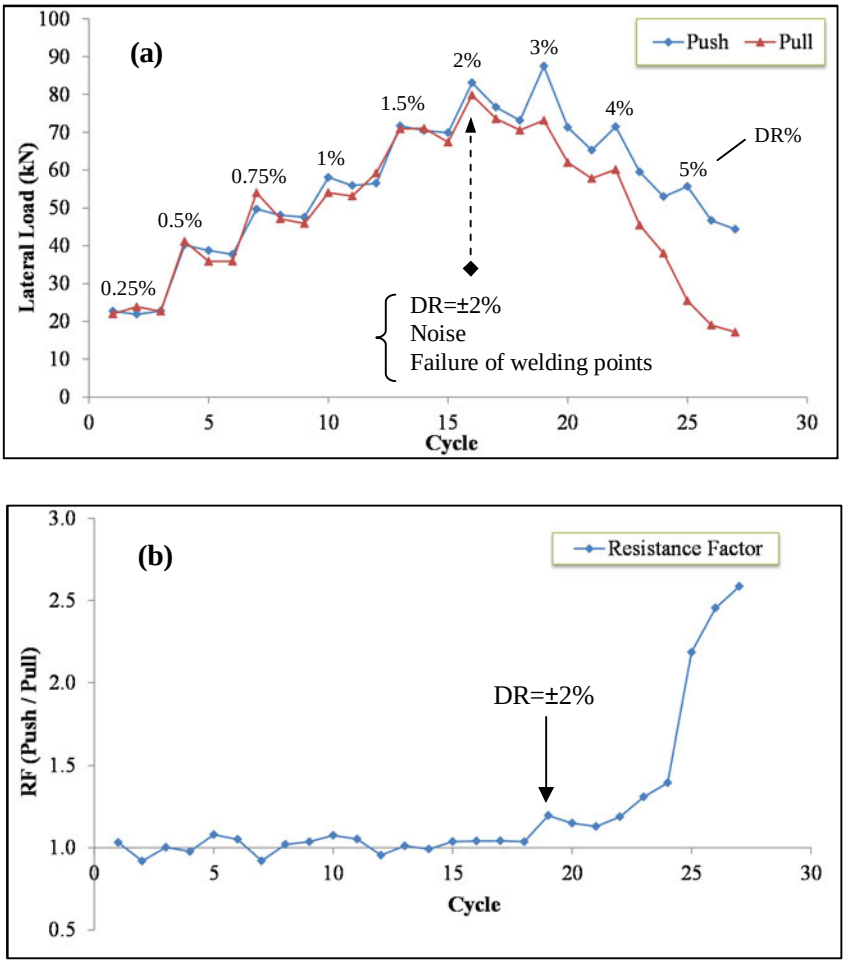

Figure 7-50: a) Lateral load capacity in the pull and push directions, and b) resistance factor of unit JB-1PTMS

The energy absorbed during the cyclic loading along with the cumulative energy of the strengthened specimen are shown in Figure 7-51. Also plotted in the same figures is the energy dissipated by the control unit JB-1. Similar to the test unit JA-1PTMS, small amount of energy was dissipated during the initial loading cycles. The last three loading steps of the test showed enhanced energy absorption starting at a DR of ±3%. The per-cycle energy E was noted to reduce with cycles within the loading step. At the end of the test, unit JB-1PTMS dissipated a total 34 kN.m of cumulative energy. The unit had dissipated 20% of the energy at ±2% DR, 44.5% at ±3% DR, 72% at ±4% DR and 100% of the energy at ±5% DR.

From Figure 7-51(b), it can be noted that the energy dissipation capability of the strengthened unit was much better than the bare unit, which dissipated a total 9.2 kN.m of energy at ±4% DR. The energy dissipation was similar in both units until a DR of ±1.5%. The strengthened unit

after that had more enhanced energy dissipation, which accounted for 2.7 times of that of the bare unit at a DR of ±4%.

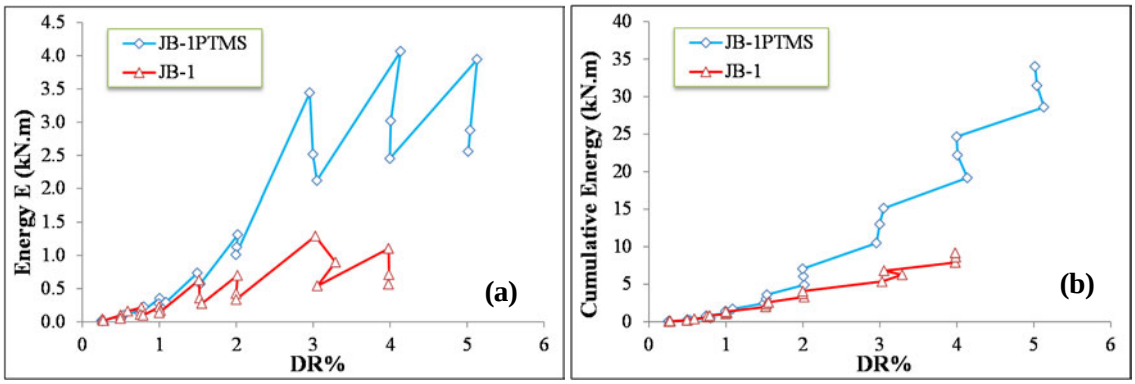

Figure 7-51: a) The amount of energy dissipation, and b) Cumulative energy

The equivalent viscous damping ζ_{eq} of this unit is shown in Figure 7-52(a) along with the results from the bare unit. As can be seen from the figure, the damping of both units increased throughout the test as damage progressed. However, unit JB-1PTMS showed higher damping after a DR of ±2%; however, when some of the welds failed the damping decreased. Up to a DR of ±2%, the average damping was found to be 5% and 4.7% for unit JB-1 and JB-1PTMS, respectively. At higher drifts, the calculated equivalent damping averaged at 8.2% and 14.2% for JB-1 and JB-1PTMS, respectively.

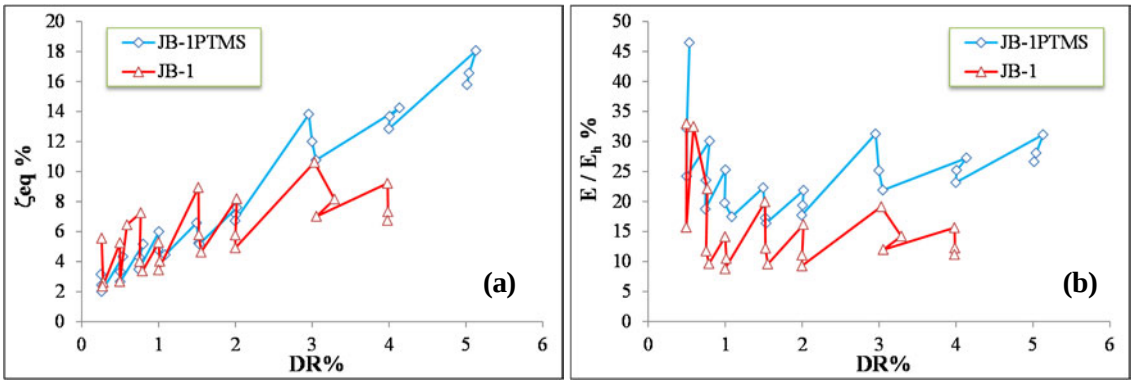

Figure 7-52: a) equivalent viscous damping, and b) normalised energy to un-pinched hysteretic energy

The ratio E/E_h for the strengthened unit is calculated and plotted versus drift in Figure 7-52(b) along with that of the bare unit. It is clear that the strengthened unit performed better and the energy released was more favourable. Moreover, up to a DR of ±2% the E/E_h ratio degraded more gradually. On average, the E/E_h ratio was calculated at 15% and 25% for the bare and strengthened units, respectively.

7.3.4 JOINT JC-1PTMS

This unit was tested according to the loading regime shown in Figure 7-53. The regime consisted of eleven loading steps at displacements corresponding to drifts of ±0.1%, ±0.25%, ±0.33%, ±0.5%, ±0.75%, ±1%, ±1.5%, (+4% to -3%), ±4%,(+4% to -5%) and one cycle at ±6%. An error occurred during the 8th loading step (±2%) that caused the actuator to continue loading until a DR of +4% was reached. Due to this error and time constraints, it was decided to perform a single cycle at each remaining loading step. Thus, single cycles were performed at (+4% to -3%), (±4%), (+4% to -5%) and (±6%).

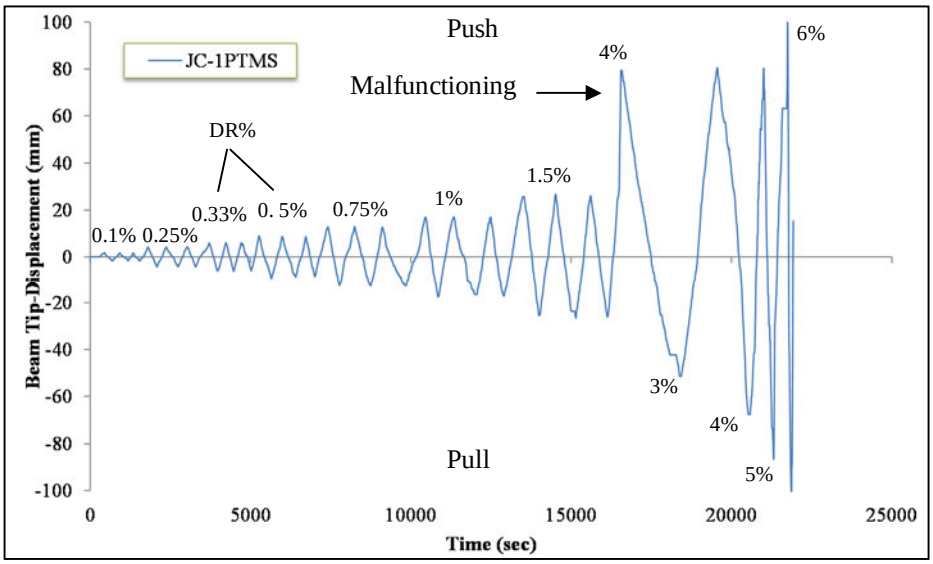

Figure 7-53: Loading regime of the test unit JC-1PTMS

The axial compressive load in the column was originally set at 150 kN corresponding to 0.1f'_c A_g. Figure 7-54 shows the variation of axial load throughout the test. The figure illustrates that the overall axial load in the column deteriorated during the test. At the conclusion of the test, the column carried 130 kN of compressive load. This is a 13% drop from the axial load that was initially applied. This drop in the axial load cannot be taken to mean that the axial capacity of the column was reduced, but rather it reflected the loss of stiffness due to progressive cracking in the joint and column at higher drift levels. It should be mentioned that the bare unit was tested under an effective compressive axial load of 144 kN with a fluctuation of ±4%.

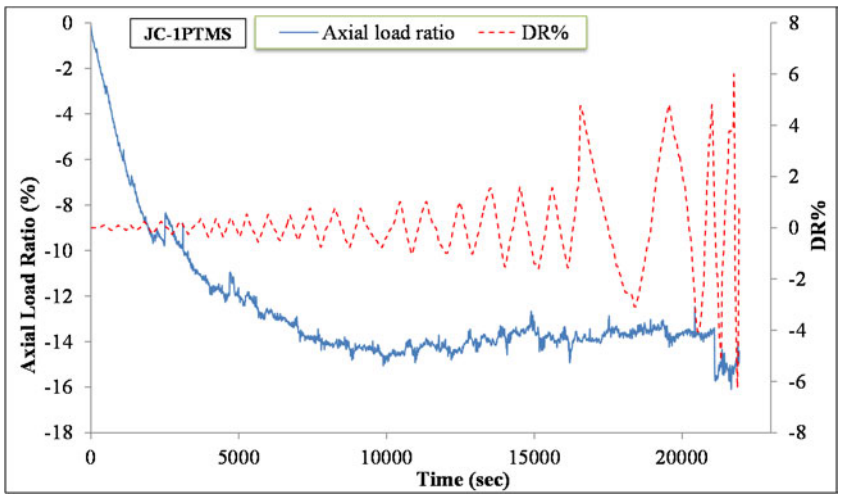

Figure 7-54: Variation of column axial load (JC-1PTMS)

Analogously to the previous tests, loading at small drifts (up to ±0.33% DR) resulted in the reopening of existing cracks in the beam hinging area along with cracking at the cast interfaces. At the end of the 3rd loading step, longitudinal cracks were observed along the beam anchored bars in the core. During the 4th loading step, multiple hairline shear cracks appeared randomly in the core, as shown in Figure 7-55(a). These cracks were visible in the next loading step, with the main diagonal cracks progressing towards the core corners. In the 5th, 6th and 7th loading steps, the X-cracking pattern developed in the core with the centre shifted towards the beam. Figure 7-55(b) shows the cracking pattern of the core at the end of the 7th loading step.

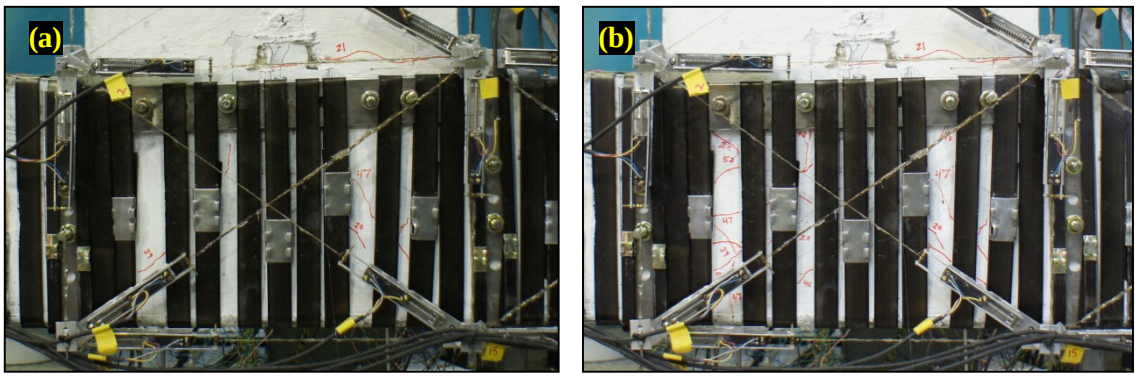

Figure 7-55: Cracking pattern of the core at the end of the a) 4th and b) 7th loading steps

During the 8th loading step, the error in loading caused accelerated growth in cracking. With further increase in loading, it was observed that the strips in the core were able to resist the large deformations of the core and the joint was able to sustain large drifts up to 6%. No failure in the strips occurred during the test. The steel plates fixed onto the core, however, were bent due to the high tension. Severe damage took place at the beam interface with the core due to the forces applied through the bolts. The test was terminated at this stage. The final crack patterns of the unit before and after removing strips from the core are shown in Figure 7-56(a) and (b), respectively. Furthermore, the crack pattern of the bare unit JC-1 is shown in Figure 7-56(c).

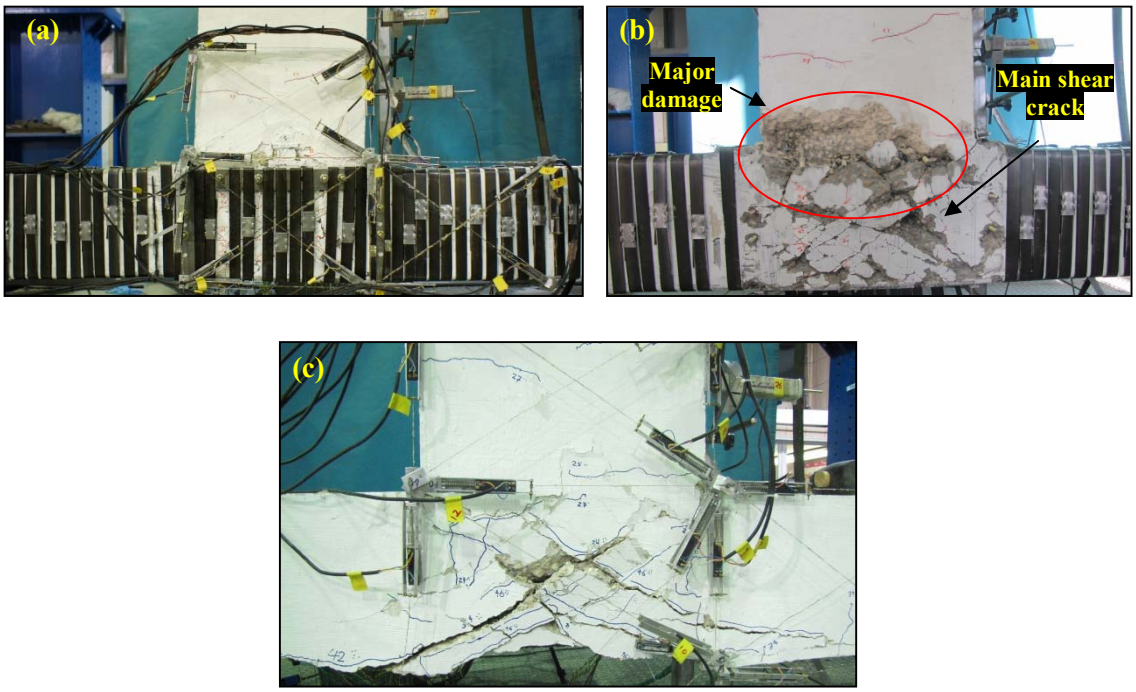

Figure 7-56: Final cracking Pattern a) with strips installed, b) after removing the strips and c) unit JC-1

After removing the strips from the core, it was observed that shear cracking was limited to the joint area. In addition, it was observed that one of the diagonal shear cracks ended in the middle of the beam, as shown in Figure 7-56(b). Moreover, it was observed from the same figure that the major damage mostly occurred in the region where the beam meets with the column. In the bare unit, on the other hand, most of the damage occurred at the back of the core resulting in spalling-off of the concrete.

The hysteretic beam load-drift curve is plotted in Figure 7-57. Also in the same figure, the performance of this unit is compared to the control one JC-1. The maximum load in the push and pull directions occurred at drifts of +4% and -3%, respectively. The load resistance of this unit was supposed to be comparatively similar in both directions. The error in loading, however, caused a difference in the resistance. Moreover, the rapid degradation in the load resistance after the peak might be attributed to the fact that the ORION data input speed was not sufficient to capture the actual degradation in the response or even the increase in resistance. The maximum capacities were +87 and -64 kN in the push and pull directions, respectively. In comparison with the bare unit, the improvement in load capacity was 75% in the push direction and 35% in the pull direction.

Up to a DR of ±1.5%, no pinching of the hysteretic loops was observed. After the damage occurred at a DR of +4%, sizable gaps at the beam interface with column opened, which were observed not to close at zero-loading. Pinching also developed in the subsequent loops.

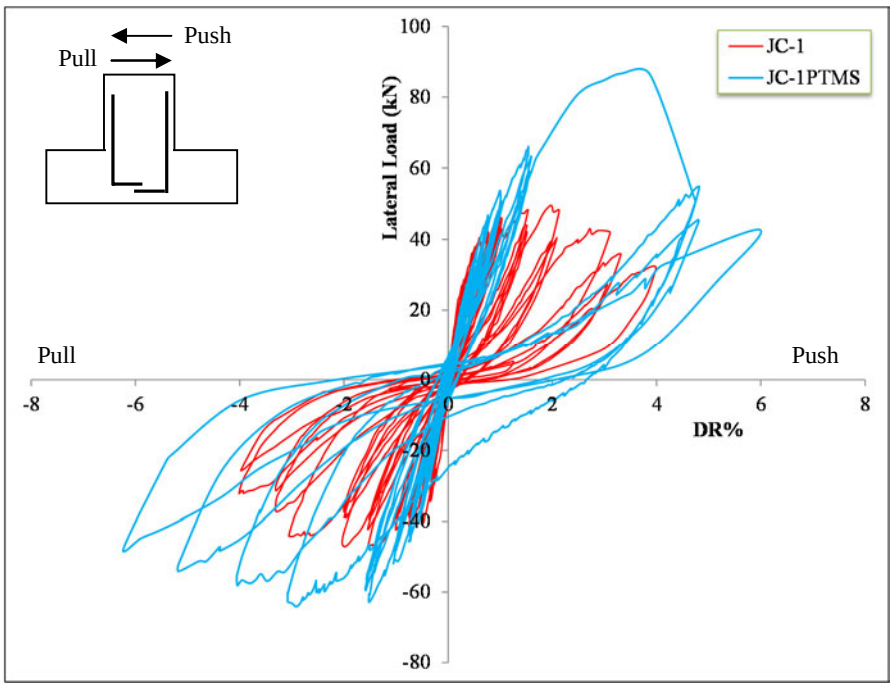

Figure 7-57: Load-drift hysteresis of the strengthened specimen JC-1PTMS and the control one JC-1

The envelopes of the hysteretic loops for the bare and strengthened units are plotted in Figure 7-58. It is clear from the figure that both curves had more or less the same characteristics. A change in the initial stiffness occurred before the maximum capacity was reached. The change occurred at a load of 40 kN, corresponding to a DR of ±0.56%. This coincided with the formation of the main shear crack in the core. In the post-peak stage, accelerated degradation in stiffness (up to a DR of +4%) occurred due to the rapid loading at this stage. The degradation rate in stiffness of the strengthened unit, in general, was higher than that of the bare unit.

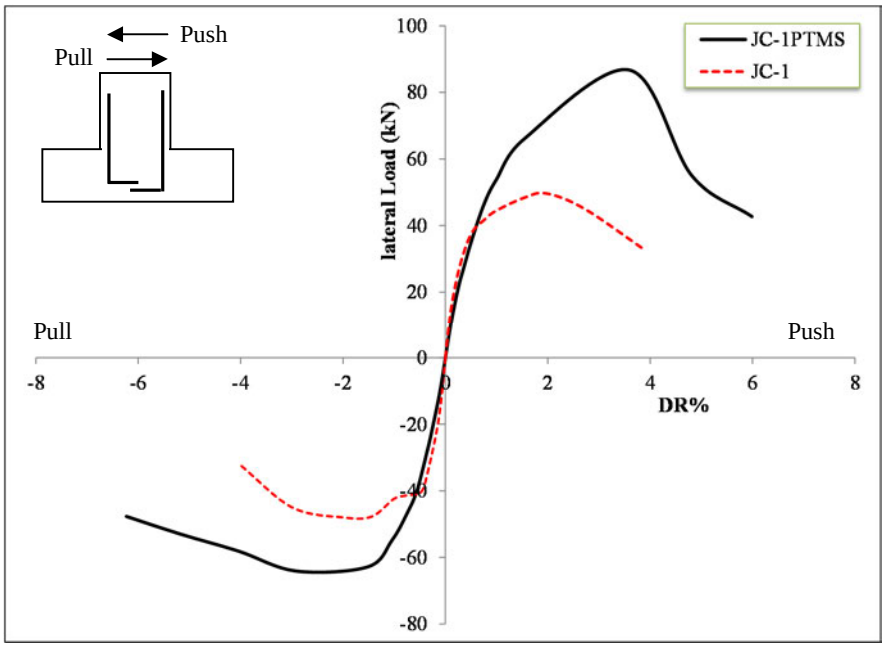

Figure 7-58: Envelopes of the bare (JC-1) and strengthened (JC-1PTMS) units

Stiffness degradation of unit JC-1PTMS is calculated and plotted in Figure 7-59 per cycle. It is clear that the stiffness degradation was gradual until the error in loading. Up to this stage, both directions showed comparatively similar behaviour. A 65% drop in the stiffness occurred, thereafter, which continued degrading until the end of the test. Stiffness degradation within each loading step was very small up to a DR of ±1%. More degradation was noted in the next loading step. On average, the joint lost 50% at the end of 6th loading step (DR=±1%); 75% of stiffness was lost at the maximum load, and 87% after the error occurred.

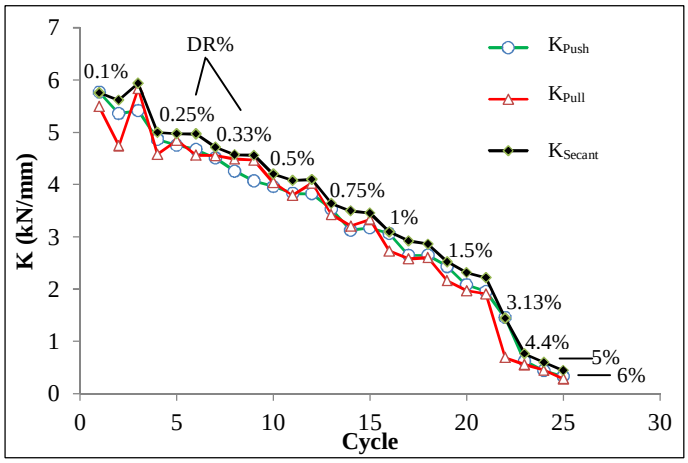

Figure 7-59: Stiffness degradation of unit JC-1PTMS

The peak-to-peak stiffness degradation is calculated and compared to that of the bare unit in Figure 7-60. The reopening of existing cracks and early cracking on the old and new concrete surfaces resulted in lower stiffness for this unit at low loading levels (< 0.5%). The unit afterwards regained higher stiffness compared to that of the bare unit. In addition, the stiffness degradation occurred at a lower rate. Despite the sudden increase in drift that deteriorated the load and stiffness, after a DR of ±2%, unit JC-1PTMS showed almost twice the stiffness of unit JC-1.

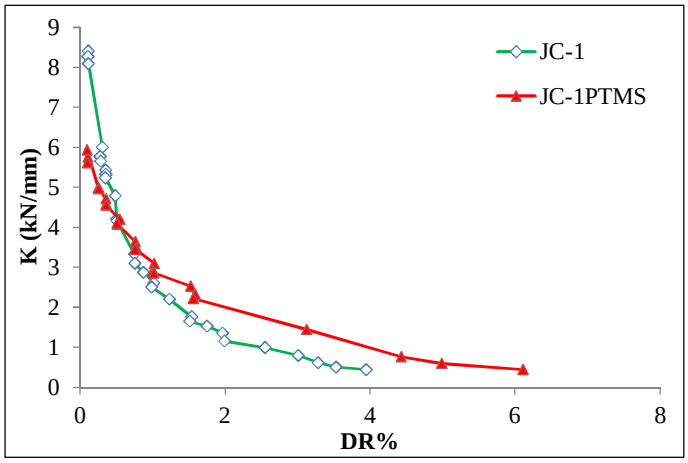

Figure 7-60: Peak-to-peak stiffness degradation

Table 7-4 presents the maximum load and corresponding deflections of the test unit. The strain values of the beam hooks and column splices, however, are obtained for the 7th loading step (DR=±1.5%). This was attributed to the error in loading that caused failure of strain gauges. The maximum strain developed in the column splices was 1442 με. This yielded an average bond stress in the splice of 2.9 MPa. Strain histories at the column splices and beam hooks are shown in Figure 7-61. Due to error in loading, plots of load-strain were unclear, and thus, for clarity the histories were presented versus drift. From Figure 7-61(a) it was noted that the bottom hook underwent yielding during the DR of 1.5%, and the strain reached 6677με. Also clear from the same figure was that the strengthened unit showed much higher strains in the beam than those of the bare unit.

Table 7-4: Strains at beam and column reinforcement at maximum loading (JC-1PTMS)

Lateral Force		**δ**	**Beam**		**Top column**		**Bottom Column**	
Direction	Value		ε_s (με)		ε_s (με)		ε_s (με)	
	kN	mm	ST1	ST2	ST4	ST6	ST3	ST5
Push	86.7	55.8	-2336	2027	980	112	-	2494
Pull	-64.1	-48.7	6677	-105	1110	1442	-	-241

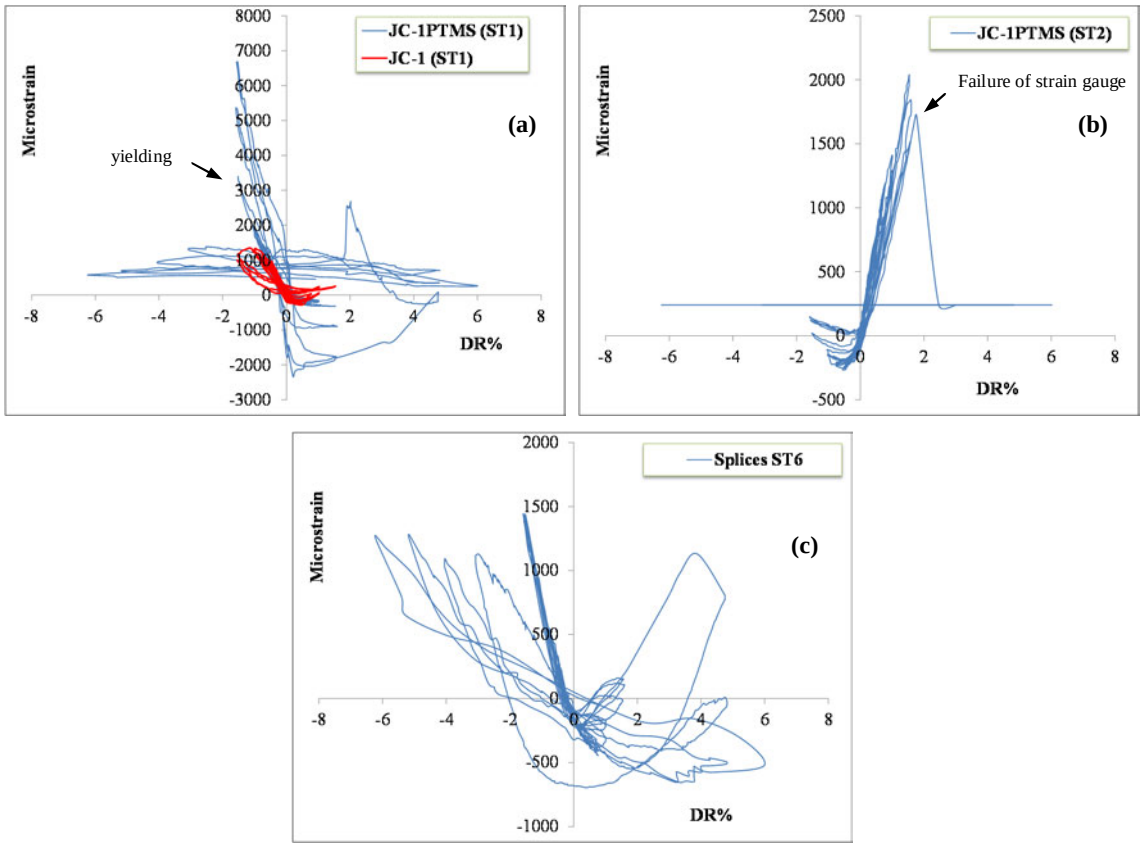

Figure 7-61: Strains at (a) beam bottom bars, (b) beam top bars, and (c) column splices

The pull and push loads of the unit are shown in Figure 7-62(a) at each cycle. Also, the resistance factor is plotted in Figure 7-62(b). This unit did not have anchorage deficiencies of the beam bottom bar, and consequently, showed almost identical load capacities in both directions throughout the test. The difference only occurred at the maximum cycle when the peak in the pull direction was missed due to the error. The resistance factor of this unit fluctuated around 1; and the peak that formed at the maximum cycle had a RF value of 1.4.

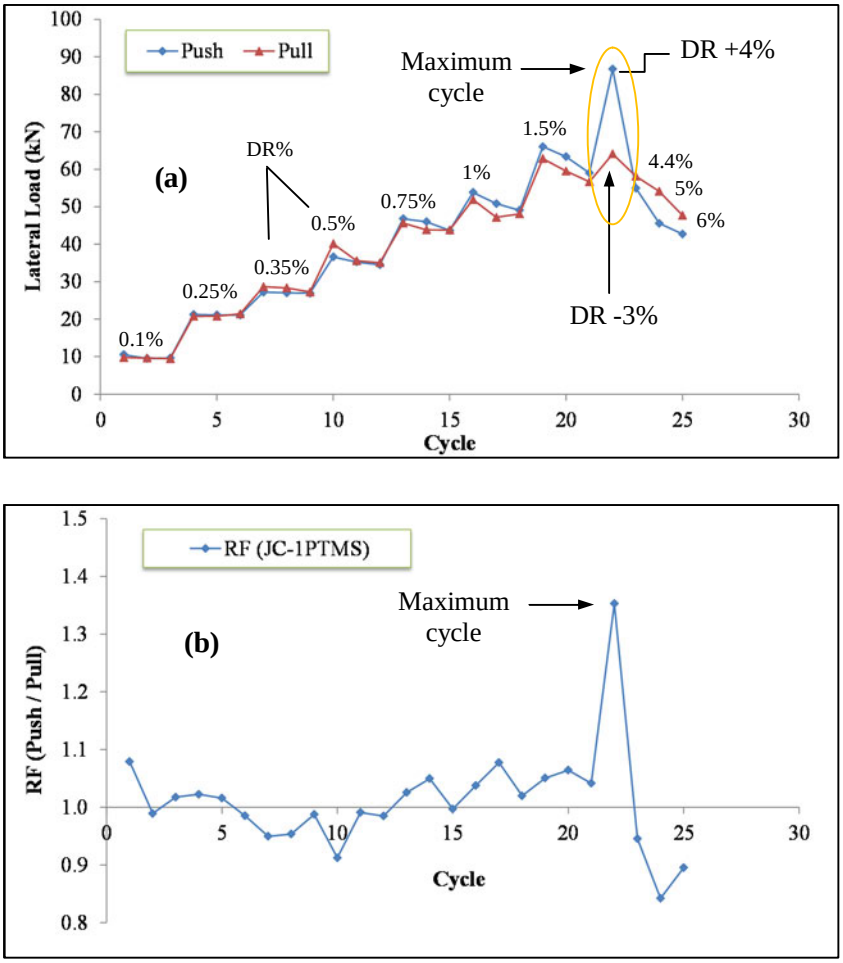

Figure 7-62: a) Lateral load capacity in the pull and push directions, and b) resistance factor of unit JC-1PTMS

The per cycle energy dissipation capacity and cumulative energy of the unit is calculated and plotted in Figure 7-63 against the energy of the bare unit. Similarly to the previous test units, the energy dissipation was small at low drifts. After the accidental damage occurred, a considerable amount of energy was dissipated, and a peak in the energy profile formed. During the maximum cycle, 6.2 kN.m of energy was dissipated. The unit dissipated almost the same amount of energy in the last three cycles.

The total energy absorbed by the unit was calculated at 16.7kN.m corresponding to a DR of ±6%. At the maximum cycle, the unit had dissipated 52% of its cumulative energy; in the subsequent cycles, the unit dissipated 69%, 83% and 100% of the total energy.

Both the bare and strengthened units showed the same energy dissipation up to a DR of 2%. The energy dissipation of the strengthened unit, afterwards, increased and by the end of the test it was almost twice the amount of energy dissipated by the control unit.

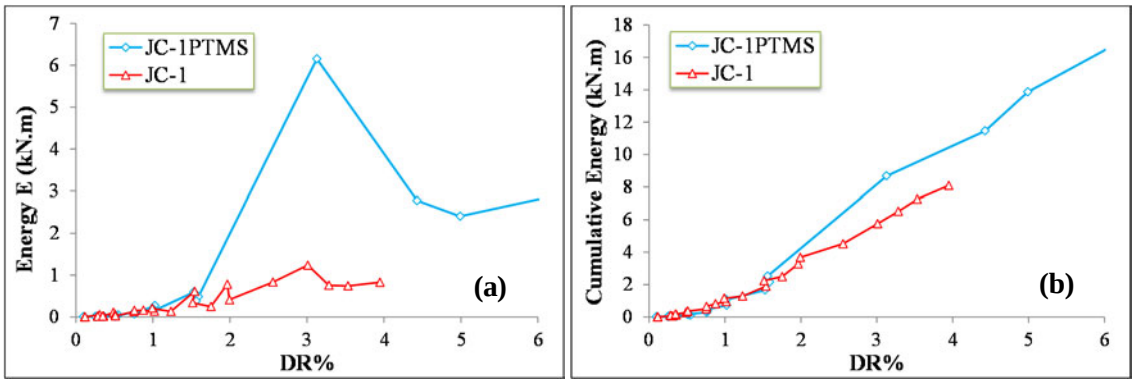

Figure 7-63: a) The amount of energy dissipation, and b) Cumulative energy

The equivalent viscous damping ζ_{eq} of both units are calculated and plotted in Figure 7-64(a) versus drift. The damping increased in both units as drift and damage progressed during loading. A jump in the curve occurred at the maximum load due to the high energy dissipated. Up to a DR of ±2%, an average damping of 3.4% and 2.8% was found for the bare and strengthened units, respectively. For higher drifts, the damping averaged at 7.3% and 13.6% for the bare and strengthened units, respectively. Before the jump in the value occurred, it was noted that small drops in the damping occurred for unit JC-1PTMS. The response of the unit at this stage was very stiff and the damage was only multiple hairline cracks in the core. Hence, the strengthened unit was resisting well the lateral cyclic load.

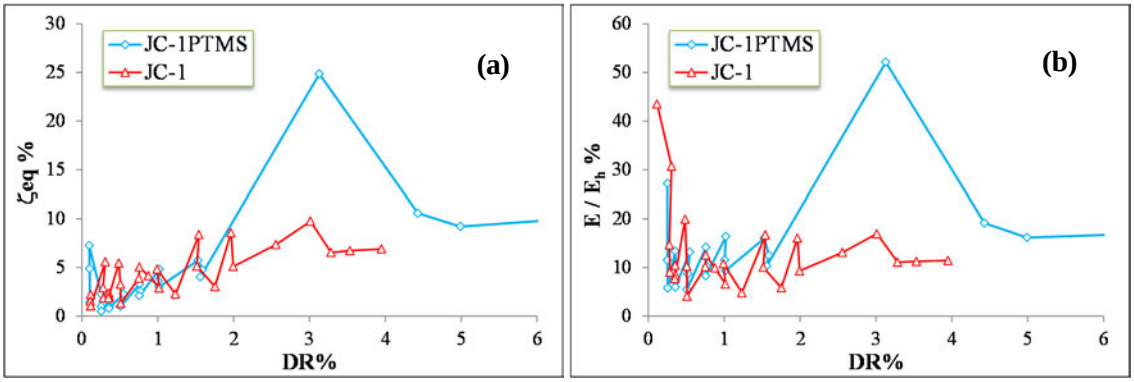

Figure 7-64: a) equivalent viscous damping, and b) normalised energy to unpinched hysteretic energy

The ratio of the energy E to E_h was calculated and plotted for both units in Figure 7-64(b). Up to a DR of ±1.5%, it can be noted that the average behaviour was more or less similar in both units. In addition, the damage was very little and no pinching of the hysteresis loops took place. At this stage, the ratio averaged around 10%. Again, the maximum loop caused the ratio of the

strengthened unit to jump to a value of 52%. For the bare unit, on the other hand, this increased only slightly. In the last three cycles, the performance of the unit levelled off with an average E/E_h value of 19%.

7.3.5 Comparisons, discussion and conclusions

An effort was made to evaluate the efficiency of various PTMS rehabilitation schemes to upgrade the performance of substandard joints with no adequate reinforcement detailing. The bare substandard units failed predominantly due to severe shear mechanism that led to a complete crashing of the core. Additional simple interventions including better concrete qualities and welding were also used in the strengthening schemes to better enhance the performance.

The strengthened beam-column joints ultimately failed due to the development of more controlled joint shear cracking along with moderate damage in the beam hinging area. The joint shear cracks were confined to the core area. Many flexural cracks developed in the beam, whereas the column remained almost intact. An X-shaped shear mechanism developed in the core with the centre shifted towards the beam. At the early loading stages, existing cracks reopened and cracks formed between the old and new concrete interfaces. That resulted in a slight reduction of the initial stiffness. With further loading, the units showed stiffer behaviour and higher load resistance.

Envelopes of the hysteretic loops for the strengthened units are shown in Figure 7-65. In terms of capacity, unit JB-1PTMS showed the best performance in both loading directions. Welding used in this unit was beneficial to prevent early bond deterioration as compared to unit JA-3PTMS. Unit JC-1PTMS performed in a similar way to JB-1PTMS in the push direction. The error in loading occurred in this unit, however, deteriorated the resistance in the pull direction. Unit JA-1PTMS and JA-3PTMS showed almost the same performance despite the difference in concrete qualities and axial load applied. A change in stiffness occurred in all units when the main shear crack appeared along the diagonals of the concrete core. However, welding used in JB-1PTMS, compared to JA-3PTMS, was efficient to reduce the severity in resistance deterioration, and consequently, stiffness degradation due to the 1st shear crack in the core.

Pinching of the hysteresis loops of all units developed in the post-peak stage. However, no complete loss of stiffness occurred near the zero-displacement point during load reversals.

Yielding of the longitudinal bars was attained almost in all units when the maximum load was nearly approached. Yielding took place in the beam, whereas the column remained elastic. However, the response of the units degraded directly after yielding.

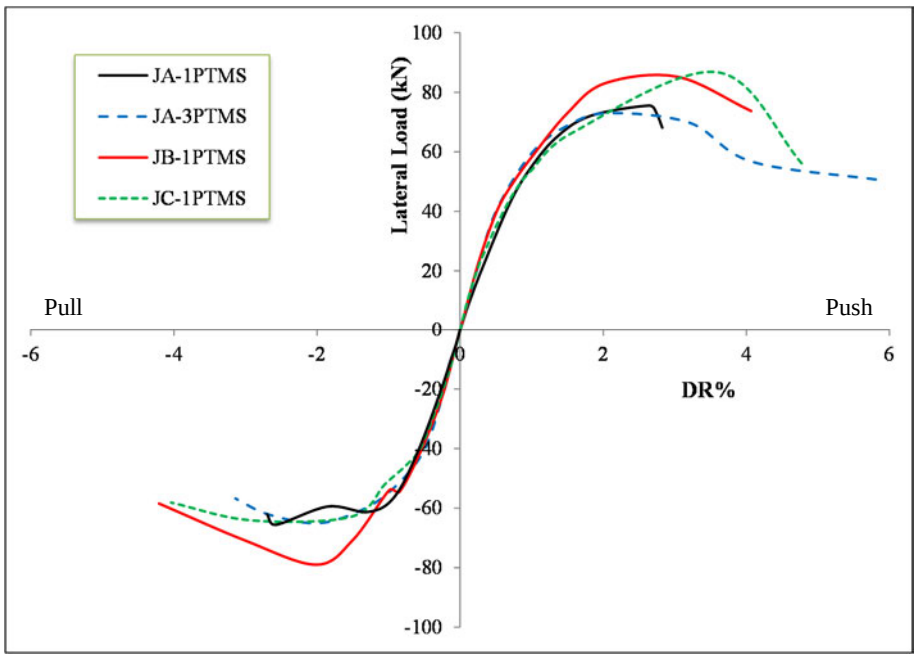

Figure 7-65: Envelopes of the hysteretic loops of the strengthened units

Table 7-5 compares load capacities and drift ratios of the four units in both loading directions at the maximum load and with respect to those of the bare units.

Table 7-5: Load and drift capacities of the strengthened units at the maximum load

UNIT	**JA-1PTMS**		**JA-3PTMS**		**JB-1PTMS**		**JC-1PTMS**	
Direction	F	DR	F	DR	F	DR	F	DR
	kN	%	kN	%	kN	%	kN	%
Push (+)	75.5	2	75	2.08	87.4	2.9	86.7	3.34
increase*	(1.87)	(1.76)	(1.35)	(1.38)	(1.72)	(1.89)	(1.75)	(1.69)
Pull (-)	-65.6	-2	-69	-2.01	-80	-2	-64.1	-2.92
increase*	(1.45)	(1)	(1.33)	(1.32)	(1.95)	(3.11)	(1.34)	(2.03)

* The increase represents the ratio of the PTMS values including load and drift capacities to those of the bare case, where 1 means equal performance.

Stiff pre-peak response and slow degradation of post-peak response are good structural properties of properly designed elements. In fact, past earthquakes revealed that in many cases, severe damage or collapse is due to loss of stiffness in the joint region at high drifts (Alsayed et al., 2010). In this study, the previous comparisons of stiffness degradation showed that the strengthened specimens had higher stiffness values as well as slower degradation rates compared to those of the bare specimens. Furthermore, at high drifts, the stiffness of the strengthened specimens was as much as twice of that of the bare specimens.

Figure 7-66 compares the peak-to-peak stiffness degradation of all strengthened units versus drift. The strengthened units, in general, had a slightly lower initial stiffness than the bare units. However, after the second loading step, the stiffness of the strengthened units was retained better and showed better characteristics than the original stiffness of bare units.

Unit JA-3PTMS and JB-1PTMS showed higher initial stiffness due to the use of higher axial load and welding, respectively. Unit JA-1PTMS showed lower stiffness at the first loading step. This was attributed to the way the unit was cast. At a DR of 0.25% (initial state), the stiffness was calculated at 4.29, 5.25, 5.28 and 5 kN/mm for units JA-1PTMS, JA-3PTMS, JB-1PTMS and JC-1PTMS, respectively. At a DR of 1.5% representing maximum capacity in most cases, stiffness was calculated at 2.88, 2.46, 2.77 and 2.35 kN/mm, respectively; and at a DR of 4%, the stiffness was calculated at 0.63kN/mm (JA-3PTMS), 0.81kN/mm (JB-1PTMS) and 0.76kN/mm (JC-1PTMS), respectively.

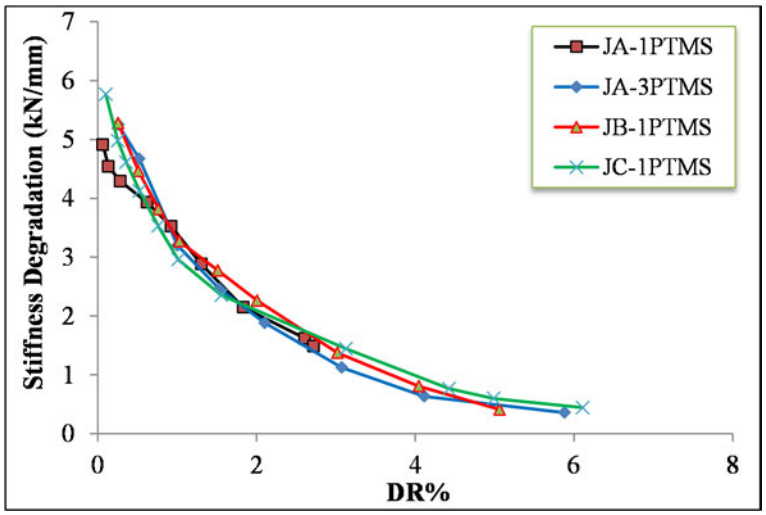

Figure 7-66: Stiffness degradation of the strengthened units

High energy capability is a very desirable characteristic of a RC member subjected to seismic loading. It is shown that all the strengthened units exhibited more than twice the energy dissipation capability of the associated bare unit. In addition, energy dissipation was higher and more stable, especially at high drifts. The analysis of the energy dissipation illustrated the effectiveness of the rehabilitation techniques tested.

The per-cycle dissipated energy and the cumulative energy of the strengthened units are plotted versus drift in Figure 7-67. As can be seen, joint JB-1PTMS showed good energy dissipation characteristics. In this unit, the shear resistance of the joint was increased the most; shear failure was delayed but ultimately, the joint failed in shear.

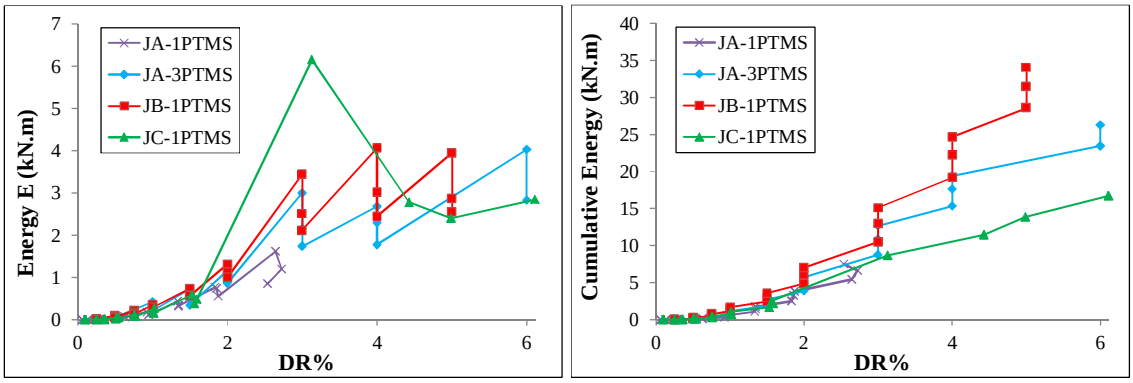

Figure 7-67: Cumulative energy dissipation of the strengthened units

The equivalent viscous damping along with the ratio E/E_h, of all units is shown in Figure 7-68. As can be seen, units JA-3PTMS and JB-1PTMS showed very similar behaviour. Joint JC-1PTMS showed very stiff hysteretic response up to a DR of 1.5%, and as a result, the damping and the E/E_h ratio were lower than those of units JA-3PTMS and JB-1PTMS. These two units appeared to sustain damage at earlier stages.

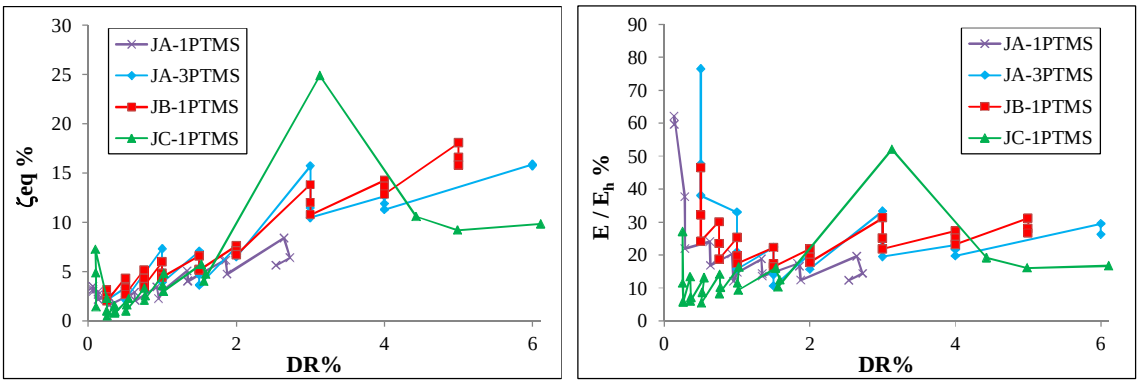

Figure 7-68: a) Equivalent viscous damping and b) E/E_h of the rehabilitated units

Finally, based on the previous findings and the experience gained by examining different strengthening methodologies, it is found that the strengthening schemes used for units JA-1PTMS and JC-1PTMS will be more suitable to repair actual beam-column connections as they are simpler and less disruptive to the function of the structure. However, some modifications in terms of material qualities and application method are necessary to increase the efficiency of the strengthening technique. Also, it is found that the use of simple additional works like welding is very effective to prevent premature bond failure.

Thus, a new strengthening scheme was designed to retrofit a full-scale deficient RC structure that had received a sizable damage due to the imposed seismic intensities. Chapter 11 gives a brief description of the results of the upgrade process and test results.

Chapter 8

ANALYTICAL STUDY: BOND

8.1 INTRODUCTION

In this chapter, the bond stress-slip results generated from the small scale (Phase I) and medium scale (Phase II) beam test series are used for analytical investigations. The test results are initially compared with predictions from state-of-the-art bond equations available in the literature, in addition to those found in codes of practice. The ability of these model equations to predict the bond strength is assessed. The experimental results then are used to investigate the influence of different parameters on the bond strength, as well as on the bond-slip response considering the different types of confinement used. Based on the trends observed, an average bond stress-slip relationship, which accounts for the effect of PTMS, is proposed. Nonlinear regression analysis is used to determine the constants of the proposed equations. The analytical predictions of the bond strength produced by the proposed bond-slip model are compared with predictions from existing bond equations. The model predictions are also used to reproduce the experimental bond stress-slip responses.

8.2 COMPARISONS WITH EXISTING STATE-OF-THE-ART BOND STRENGTH EQUATIONS

8.2.1 Existing bond strength models

A brief description of the available key equations with regard to the contribution of concrete and lateral confinement by transverse stirrups to bond strength is given. The test data are compared with the predictions of these equations in the following section.

A statically based well-known expression for evaluating the bond strength of bars embedded in confined concrete, and upon which the ACI 318-02 (ACI Committee 318, 2002) approach for calculating development/splice length of steel bars is based, is the one proposed by Orangun et al. (1975, 1977). This expression, known as "Orangun equation", is given by:

$$\frac{\tau}{fc'^{1/2}} = \frac{\tau_c+\tau_s}{fc'^{1/2}} = \left[0.1 + 0.25\frac{c_m}{d_b} + 4.15\frac{d_b}{L_d}\right] + \left[\frac{A_{tr}f_{yt}}{41.5snd_b}\right] \quad (8\text{-}1)$$

in which τ_c and τ_s represent the contribution of plain concrete and confinement to bond strength, respectively, in MPa; c_m is the smaller of minimum concrete cover or ½ the clear spacing between bars, in mm; l_d is the development or splice length, in mm; and d_b is the bar diameter, in mm; A_{tr} is the area of transverse reinforcement normal to the plane of splitting through the anchored bars, in mm^2; f_{yt} is the yield strength of the transverse reinforcement, in MPa; s is the spacing of the transverse reinforcement, in mm; and n is the number of bars developed or spliced at the same location. The second term in the expression is limited to 0.25 to safeguard against the pullout bond failure.

It can be noted from the Orangun equation that the contribution of confinement to bond strength is added linearly to that of the concrete. It is also assumed in the equation that the confining material undergoes yielding, once the maximum bond strength is attained. Orangun equation is applicable for $c_m/d_b < 2.5$ (i.e. splitting-type failure).

Using a larger data base and by performing regression analyses, Darwin et al. (1996a&b) proposed the following best-fit equation for steel bars embedded in confined concrete:

$$\frac{T=T_c+T_s}{fc'^{1/4}} = \left[[1.5l_d(c_{min} + 0.5d_b) + 51A_b]\left(0.1\frac{c_{max}}{c_{min}} + 0.9\right)\right] + \left[53.3t_r t_d \frac{NA_{tr}}{n} + 1019\right] \quad (8\text{-}2)$$

in which T is the bar force, in N; c_{min} is the minimum of c_s and c_b, where c_s is the smaller of side cover or half the clear distance between bars + 6mm, and c_b is the bottom cover; c_{max} is the maximum of c_s and c_b (c_{max} / c_{min} < 3.5); $t_d = 0.028d_b + 0.28$; $t_r = 9.6R_r + 0.28$, in mm; where R_r is

the relative rib area of the reinforcing bar (equal to the ratio of the projected rib area, normal to the bar axis, to the product of the nominal bar perimeter and centre-to-centre rib spacing).

It can be seen that a great departure from equation (8-1) to (8-2) is the exclusion of the effect of yielding in steel stirrups on bond strength when accounting for the effect of lateral steel confinement. Darwin (1996a) justifies this modification considering that the normal steel ties seldom attain yield at bond failure. Also, another observation in the Darwin equation is the use of $f'^{¼}_c$ to represent the contribution of unconfined concrete and confinement to bond strength. Darwin also found that the bar relative rib area R_r influences the bond strength by a factor quantified by t_r.

The previous work was expanded by Zuo and Darwin (1998, 2000) and Darwin et al. (2005) to include more specimens with a wider range of concrete strengths between 17 and 110 MPa. It was concluded that the normalisation of concrete strength to the power of ¼ gave better predictions to the bond strength of unconfined concrete. Moreover, it was suggested that the normalisation of concrete strength to the power of ¾ best represents the effect of concrete strength on T_s (the contribution of transverse reinforcement to bond strength). The expression proposed by Zuo and Darwin to calculate the development/splice strength is given by:

$$\frac{T}{fc'^{1/4}} = \frac{T_c+T_s}{fc'^{1/4}} = \left[[1.43l_d(c_m + 0.5d_b) + 56.2A_b]\left(0.1\frac{c_{max}}{c_m} + 0.9\right)\right] + \left[9t_r t_d \frac{NA_{tr}}{n} + 744\right] fc'^{1/2} \quad (8\text{-}3)$$

in which $t_d = 0.03d_b+0.22$; t_r is defined following equation (8-2).

The previous equation is limited to the splitting failure case by satisfying the following:

$$\frac{1}{d_b}\left[(c_m + 0.5d_b)\left(0.1\frac{c_{max}}{c_m} + 0.9\right)\right] + \left[6.26t_r t_d \frac{A_{tr}}{snd_b}\right] fc'^{1/2} \leq 4.0 \quad (8\text{-}4)$$

By including test results from a database of 635 development and splice tests of uncoated reinforcing bars in normal-weight concrete specimens, the ACI committee 408 (2003) updated equation (8-3) by making few minor changes. Therefore, the reformulated equation describing the bond strength of steel bars embedded in confined concrete is given by:

$$\frac{T}{fc'^{1/4}} = \frac{T_c+T_s}{fc'^{1/4}} = \left[[1.43l_d(c_m + 0.5d_b) + 57.4A_b]\left(0.1\frac{c_{max}}{c_m} + 0.9\right)\right] + \left[8.9t_r t_d \frac{NA_{tr}}{n} + 558\right] fc'^{1/2} \quad (8\text{-}5)$$

The same restrictions given by equation (8-4) apply to this equation.

Another important approach to calculate the bond strength of steel bars embedded in RC is the one given in CEB-FIP model code (1990). The bond strength of a steel bar embedded/spliced in confined concrete is given by the following expression:

$$\tau_s = \frac{1.64\left(\frac{f'c-2.75}{10}\right)^{\frac{2}{3}}}{\left(1.15-0.1\frac{c}{d_b}\right)\left(1-K\frac{\frac{A_{tr}L_s}{s}-\sum A_{trm}}{A_b}\right)} \quad \text{(MPa)} \quad (8\text{-}6)$$

where c (mm) is the smaller of side concrete cover of the steel bars c_s, the bottom cover c_b, or ½ the clear horizontal spacing between the bars; K=0.05 for a bar confined with a tie, and 0 for unconfined concrete; and $\Sigma A_{trm} = 0.25A_b$ for beams and 0 for slabs, where A_b is the area of the largest bar being developed/spliced, in mm^2.

Harajli (2007), using tests conducted on 70 specimens of anchorages/splices in confined concrete including beams in tension [Harajli et al. (2002), Harajli and Al-Hajj (2002), Harajli et al. (2004), Harajli and Hamad (2005), Harajli (2007)], derived a generalised local bond-slip relationship that is applicable for plain NSC and HSC concrete, steel confined concrete, concrete confined by external FRP laminates and fibre reinforced concrete. In the model, Harajli found the following equation to predict the bond strength of steel confined concrete:

$$\tau_{max} = 0.78\sqrt{f_c'}\left(\frac{c+K_c}{d_b}\right)^{2/3} \leq \tau_1 = 2.57\sqrt{f_c'} \quad \text{(MPa)} \quad (8\text{-}7)$$

The above equation takes into account the effect of confinement using ordinary transverse steel in the development/splice region as an additional concrete cover by a value of K_c equal to $7A_{tr}/sn$. It should be noted that, in this equation, Harajli used the power of 2/3 for c/d_b in comparison to a similar equation proposed by Eligehausen et al. (1979, 1983), which uses a power of ½ for the unconfined concrete.

Ahmad (2011) conducted an extensive test series on deformed bars embedded in LSC, in the University of Sheffield (UoS), University of Engineering and Technology (UET) and NED University of Engineering & Technology. Based on the test data and by using nonlinear regression analysis, Ahmad proposed the following equation for bond strength of deformed bars embedded in plain LSC:

$$\frac{\tau}{fc'^{0.62}} = \left[-0.01718 + 0.28\frac{c_m}{d_b} + 3.15\frac{d_b}{L_d}\right] \qquad R^2=0.65 \qquad \text{(MPa)} \qquad \text{(8-8)}$$

As can be seen, the above equation is based on the Orangun equation. However, large variability is noted from the equation due to the use of data from different sources. To improve the results, Ahmad used datasets reported by Darwin et al. (1992) and those by Tepfers (1973) for bars embedded in concrete with compressive strengths of 15-21 MPa and failed due to splitting. Using the additional datasets, Ahmad calibrated the previous equation, and the equation with new parameter values is given by:

$$\frac{\tau}{fc'^{0.68}} = \left[-0.048 + 0.22\frac{c_m}{d_b} + 3.22\frac{d_b}{L_d}\right] \qquad R^2=0.72 \qquad \text{(MPa)} \qquad \text{(8-9)}$$

Compared to the previous model equations, it can be noted that the contribution of concrete to bond strength, in Ahmad equation, is better represented by using f'_c with a power of 0.68.

8.2.2 Comparisons and discussions

The bar force T, calculated as ($\pi d_b l_d \tau_s$), of the specimens tested in Phases I&II were predicted using the previous equations, and plotted against the experimental data in Figure 8-1. Also, given in the same figure are the standard deviations (SD) as well as the coefficient of variations (CV) of the prediction to those from test data (all specimens are included). Specimens with PTMS confinement are treated as conventional steel stirrups considering the specified confinement ratio A_{tr}/snd_b.

From the figure, it was found that the best models predicting the test data were those by Orangun and CEB-FIP. However, the CEB-FIP model had the advantage over the Orangun model by showing reasonable underestimation of the splice strength with SD of 0.19 and CV of 0.24. The model by Harajli, on the other hand, tended to largely underestimate the test data. The models by Zuo and Darwin, as well as the ACI model showed significant overestimation of the test data.

Looking into the unconfined specimens, as shown in Figure 8-2, the models by Darwin (SD=0.16, CV=0.15), Orangun (SD=CV=0.14) as well as CEB-FIP (SD=0.17, CV=0.19) provided a very good correlation with the test data. The model by Harajli again overestimated the concrete contribution to bond strength. The test results of the unconfined specimens were further compared to the model proposed by Ahmad (2011) for low strength concrete, and better predictions were shown for specimens with $f'_c < 30$ MPa (SD=CV=0.08), whereas the model tended to largely overestimate the results of specimens with higher concrete strengths, as shown on Figure 8-2. The previous conclusion supports the suitability of Ahmad model to provide better predictions of the unconfined bond strength of bars embedded in LSC.

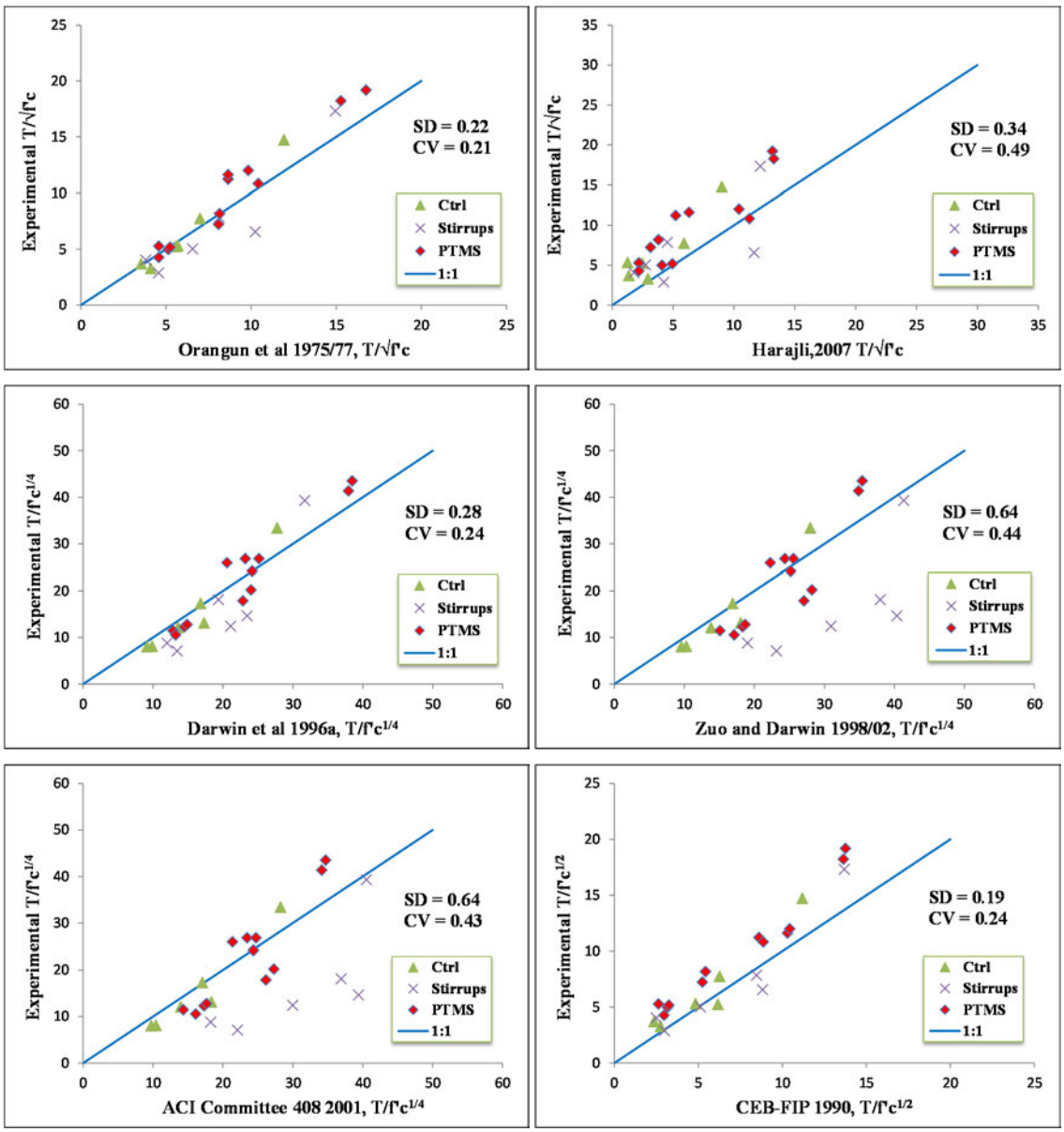

Figure 8-1: Comparison of experimental data with predictions

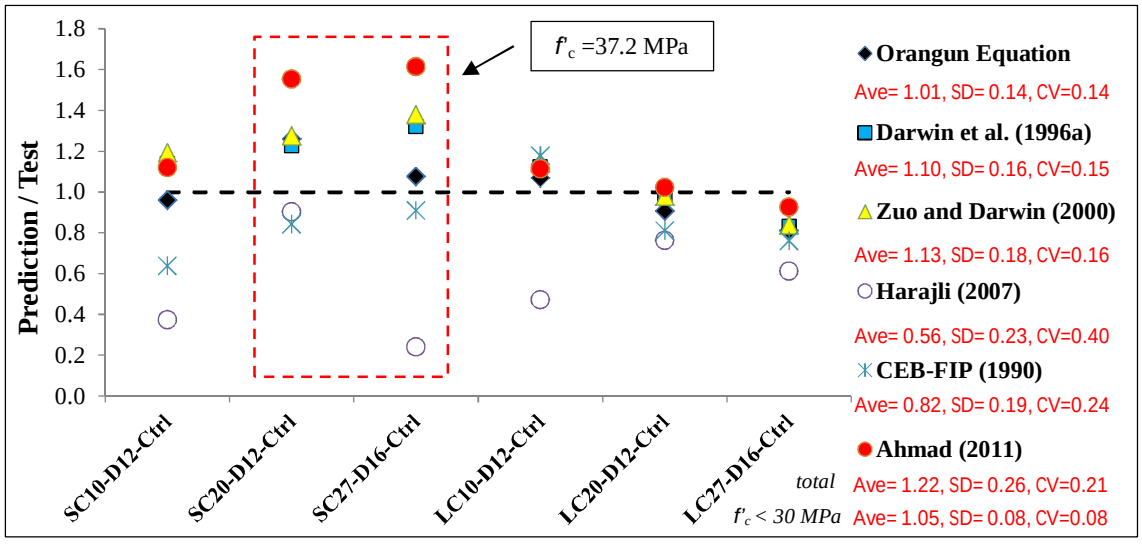

Figure 8-2: Comparison of test data of unconfined specimens with predictions

The contribution of the steel stirrups and PTMS confinement to the bond strength τ_{PTMS} was calculated by subtracting the concrete contribution of the associated unconfined specimens from the maximum bond strength ($\tau_{PTMS}=\tau_{max}-\tau_c$), and the results are presented in Table 8-1.

Table 8-1: Bond strength component of PTMS and steel stirrup specimens

Series	Specimen number	Specimen designation	Abbreviated designation*	τ_{max} MPa	τ_c MPa	τ_S MPa
PTMS Series (S)	1	SC10-D12-PTMS1	(S10-P1)	5.53	3.8	1.73
	2	SC10-D12-PTMS2	(S10-P2)	5.75	4.31	1.44
	3	SC20-D12-PTMS1	(S20-P1)	6.71	4.41	2.30
	4	SC20-D12-PTMS2	(S20-P2)	6.97	4.41	2.56
	5	SC27-D16-PTMS1	(S27-P1)	5.49	4.03	1.46
	6	SC27-D16-PTMS2	(S27-P2)	6.21	4.03	2.18
PTMS Series (L)	7	LC10-D12-PTMS1	(L10-P1)	5.31	2.47	2.83
	8	LC10-D12-PTMS2	(L10-P2)	5.45	2.47	2.97
	9	LC20-D12-PTMS1	(L20-P1)	4.26	3.43	0.83
	10	LC20-D12-PTMS2	(L20-P2)	5.31	3.43	1.88
	11	LC27-D16-PTMS1	(L27-P1)	4.91	3.71	1.21
	12	LC27-D16-PTMS2	(L27-P2)	4.67	3.71	0.96
Steel stirrups	13	SC10-D12-S	(S10-S)	4.33	3.8	0.60
	14	SC20-D12-S	(S20-S)	3.87	4.41	0.00
	15	SC27-D12-S	(S27-S)	3.82	4.03	0.00
	16	LC10-D12-S	(L10-S)	3.70	2.47	1.23
	17	LC20-D12-S	(L20-S)	2.90	3.43	0.00
	18	LC27-D12-S	(L27-S)	4.18	3.71	0.47

* An abbreviated designation of tested specimens used on figures of this chapter

Most of the internally confined specimens, especially those of Phase I, did not show noticeable improvement in bond strength, and even if it existed it was small. The steel stirrups only showed a good contribution to bond in specimen LC10-D12-Ctrl, where the concrete contribution was very small due to the large l_d/d_b and small c_{min}/d_b. Consequently, the predictions, except for the model by CEB-FIP, tended to overestimate the test results. Based on this finding, the author supports the recommendations given in the codes, such as ACI 318 (2008) and EC2 (2004), which state the permission of neglecting the contribution of steel stirrups during the design or assessment process of RC buildings.

The predictions of PTMS contribution to bond strength using the different approaches are plotted in Figure 8-3. Standard deviations (SD) as well as coefficient of variations (CV) of the ratio of predictions to test results are shown in the same figure.

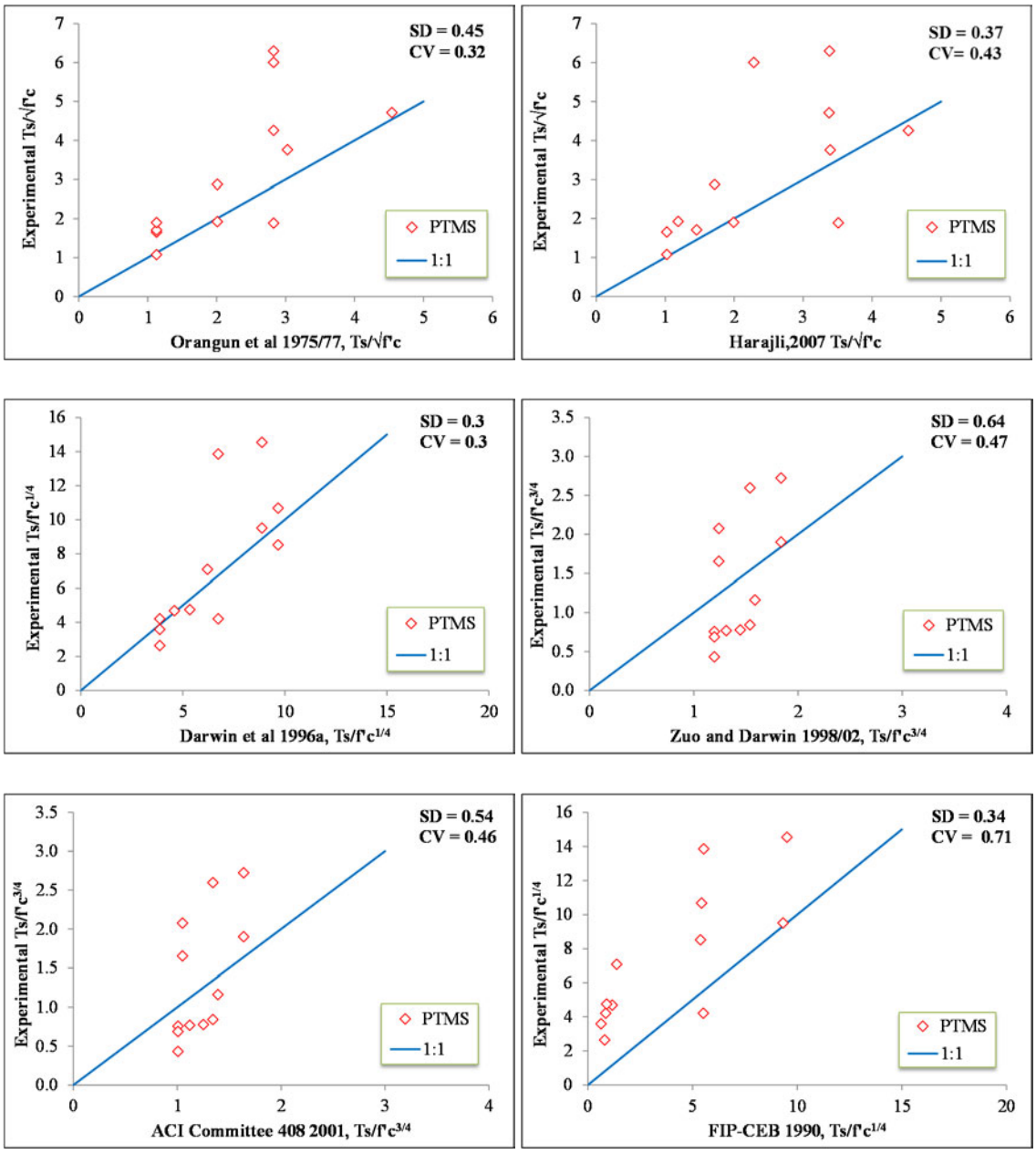

Figure 8-3: Comparison of test data of PTMS confined specimens with predictions

From the previous figure, some interesting points can be drawn. Despite the differences, the models by Orangun, Harajli and CEB-FIP largely underestimate the test results with the exception of one specimen LC20-D12-PTMS1. An additional point, to be noted in examining the figure, is that in comparison to the other model equations, the model by Darwin shows more consistency in predicting the experimental data with the least scatter (SD=CV=0.3).

Also, an important point to be considered is that all equations, with the exception of that by Orangun, are insensitive to the effect of post-tensioning “stress in the confining material” in the

strips on bond strength, which is a key feature of the PTMS technique. To further examine the model by Orangun, the normalised τ_{PTMS} is plotted against the confinement ratio A_{tr}/snd_b in Figure 8-4, and compared to the model considering different post-tensioning within strips, namely, yield stress, 600 MPa (i.e. stress level in strips of (S) series) and 300 MPa (i.e. stress level in strips of (L) series).

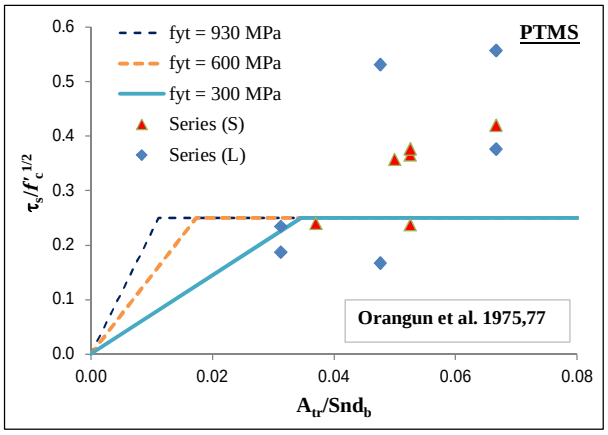

Figure 8-4: Variation of normalised bond strength by PTMS with the ratio A_{tr}/snd_b

It can be seen from the figure that the proposed upper limit of 0.25 largely underestimates the PTMS contribution to bond strength in most of the specimens, especially those of series (S). Also, it can be noted that the PTMS contribution to bond falls along the constant limitation given by Orangun equation, and therefore, the results are not affected by the change of post-tensioning in the strips. This in turn eliminates the main advantage of using this equation and modifications should be introduced.

Based on the previous comparisons and discussion, it can be concluded that although the maximum bond strength is predicted well by some models, this is not good enough as they fail to predict the PTMS contribution to bond. The overestimation of the concrete contribution in some models led to underestimation of the effect of PTMS confinement. Moreover, it is shown that no approach accounts for the effect of stress level within the confining strips to bond strength.

Consequently, an appropriate bond stress-slip model that can not only predict the PTMS confinement to bond strength, but also characterise the general behavioural response of bond is an essential requirement to provide a reliable estimation of the structural as well as deformational capacity of RC members with bond deficiencies and strengthened by PTMS.

In this regard, the following section presents a bond stress-slip model for elements with spliced bars and strengthened by PTMS.

8.3 PROPOSED BOND STRESS-SLIP MODEL

8.3.1 General

A model is developed based on the observed behaviour of bond stress-slip relationship found from Phase I & II, and only deals with the splitting-type failure. Splitting failure is noted to take place either before or after yielding of the steel bar, and thus, different behaviour is recognised. If the failure takes place before yield, a sudden but gradual drop in the response occurs immediately after the maximum bond strength is reached. On the other hand, if the splice length is long enough to enable yielding in the bar, a plateau in the response forms near the maximum strength followed by degradation in the response. The extension of the yield plateau in the latter behaviour is governed by the gradual propagation of splitting cracks towards the tail end of the bar; and this is commonly accompanied by slight increase in the bond resistance.

The observed behaviour in the current study is in agreement with that reported by other researchers such as Eligehausen et al. (1983) and Sezen (2003), among others, where the behaviour of bars failed before or after yield is differentiated. In these models, two components of slip, namely, bar movement and bar elongation due to penetration of axial strains along the tensile reinforcement inside the joint of a beam-column connection or column base are included.

In this study, a bond stress-slip model for spliced bars is proposed to account for the bar movement. The bar elongation component is considered separately. Both components are combined by a unified model equation that represents the generalised behaviour.

8.3.2 Bond stress-pure slip model

The general bond stress-pure slip response observed in the current experimental study is described using the idealisation shown in Figure 8-5.

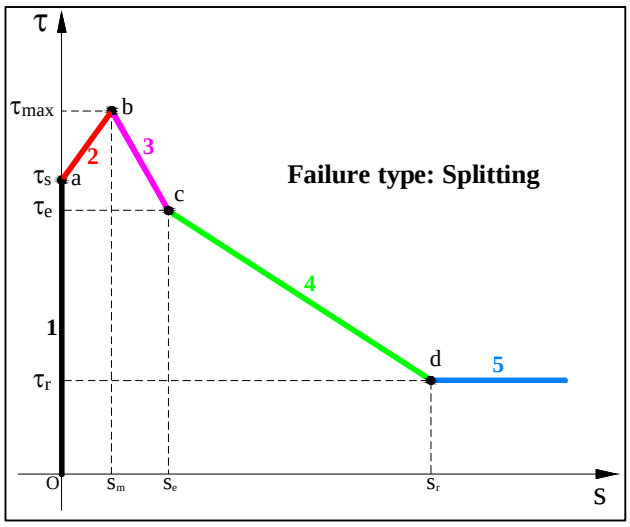

Figure 8-5: Characteristics of the proposed bond stress-pure slip model

As can be seen from the figure, the model is defined by four key points which govern its behaviour. These points are:

- Point a (τ_s, 0): corresponds to the initiation of first splitting along the splice.
- Point b (τ_{max}, s_m): corresponds to the maximum bond stress.
- Point c (τ_e, s_e): represents the end of rapid degradation following splitting.
- Point d (τ_r, s_r): represents the beginning of residual response.

In the model, the bond strength τ_{max} includes the contribution due to plain concrete τ_c as well as that by metal strips τ_{PTMS}. The following subsections quantify the previous points through model equations derived based on the trends observed.

8.3.2.1 PTMS Contribution to bond strength τ_{PTMS}

To evaluate the contribution of PTMS to bond strength τ_{PTMS}, the effects of many parameters are assessed. By examining the different parameters, it is found that f'_c, l_d/d_b, c_{min}/d_b and f_p (stress in the strip) show some influence on τ_{PTMS}, as shown in Figure 8-6.

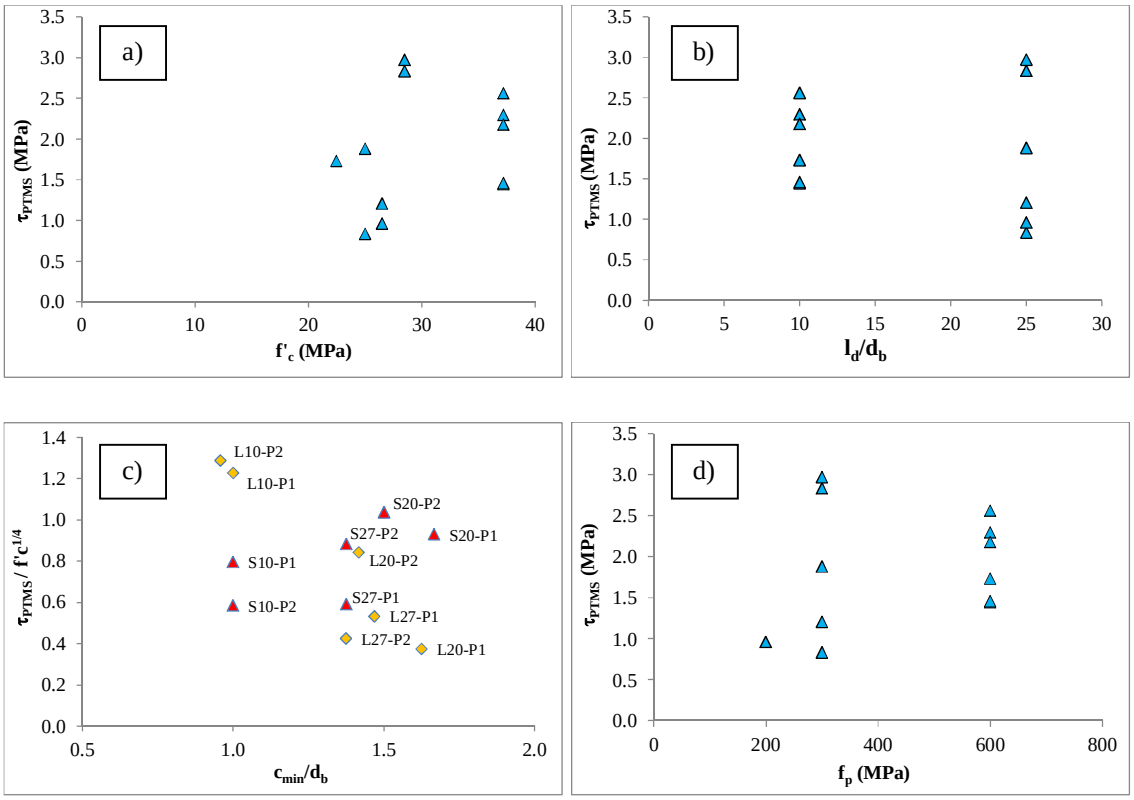

Figure 8-6: Variation of τ_{PTMS} with a) f'_c, b) l_d/d_b, c) c_{min}/d_b and d) f_p

By examining the trends from Figure 8-6, it can be noted that a relatively wide scatter in the data exists. However, from Figure 8-6(c), it can be observed that the c_{min}/d_b ratio shows a clearer trend with τ_{PTMS} if the l_d/d_b ratio is considered. In view of that, for short splices, τ_{PTMS} tends to increase as the ratio c_{min}/d_b increases. On the other hand, the long splices tend to show an

opposite relationship. Also, from the same figure, it can be noted that the increase in tensioning within strips f_p (P2 in general has higher confining stress) results in higher τ_{PTMS}.

Based on the previous observations, it can be concluded that a bond strength equation that considers the effect of c_{min}/d_b for different l_d/d_b ratios is required. The following backbone equation can be examined:

$$\frac{\tau_{PTMS}}{f_c'^{p}} = A f_p \left[1 + \left(B\frac{d_b}{l_d} - C\right)\frac{c_{min}}{d_b} + D\frac{l_d}{d_b}\right] \quad (8\text{-}10)$$

To represent the effect of concrete strength f'_c on the contribution of confinement to bond strength τ_{PTMS}, a regression analysis was conducted. Consequently, it is found that the effect of f'_c on τ_{PTMS}, see Figure 8-7, is best represented by normalising τ_{PTMS} to the concrete strength with the power of ¼ with an average $\tau_{PTMS}/f'^{1/4}_c$=0.8 giving SD=0.29 and CV=0.36.

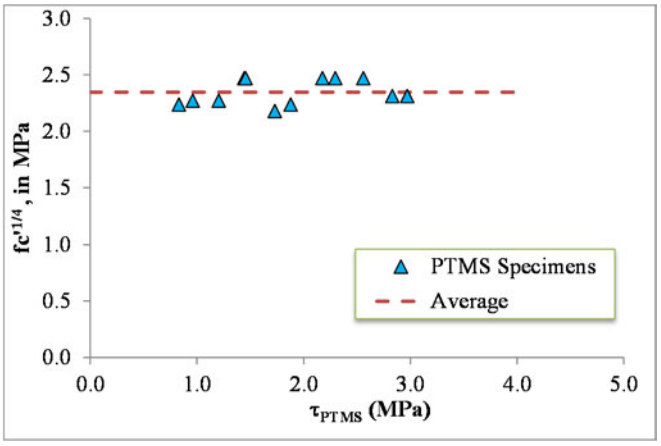

Figure 8-7: Normalisation of τ_{PTMS} to $f'^{1/4}_c$

To incorporate the amount of confinement in the previous equation, it was first attempted to modify the confinement ratios proposed by Orangun et al. (1975, 77) or that by Darwin et al. (1996a). Considering that and by performing nonlinear regression analyses, the resulting equations did not yield good results. The influence of confining strips was then further investigated by understanding the effect of confinement on the splitting plane extending along the splice length.

It was observed in the experiment that the internal bar pulls out due to formation of splitting cracks with a sectional length equal to (c_{min}) followed by the propagation of these cracks along the splice length. c_{min} denotes the minimum of a) bottom cover c_b, b) side cover c_s or c) ½ the clear distance between the internal bars c_m. Assuming the confining stress is applied to a length equal approximately to (c_{min}+d_b), as shown in Figure 8-8, and considering that splitting occurs from one side of the bar, the confining stress σ_t applied to this length will be:

$$\sigma_t = \frac{P_{strip}}{b_s(c_{min}+d_b)} = \frac{f_p \times t}{(c_{min}+d_b)} \quad (8\text{-}11)$$

in which P_{strip} is the force in the strip = $f_p \times t \times b_s$; b_s and t are the strip width and thickness, respectively.

Thus, slipping of the bar occurs in this case when the pulling force in the internal bar outbalances the friction caused by σ_t applied to a plane with an area of $(c_{min}+d_b) \times l_d$.

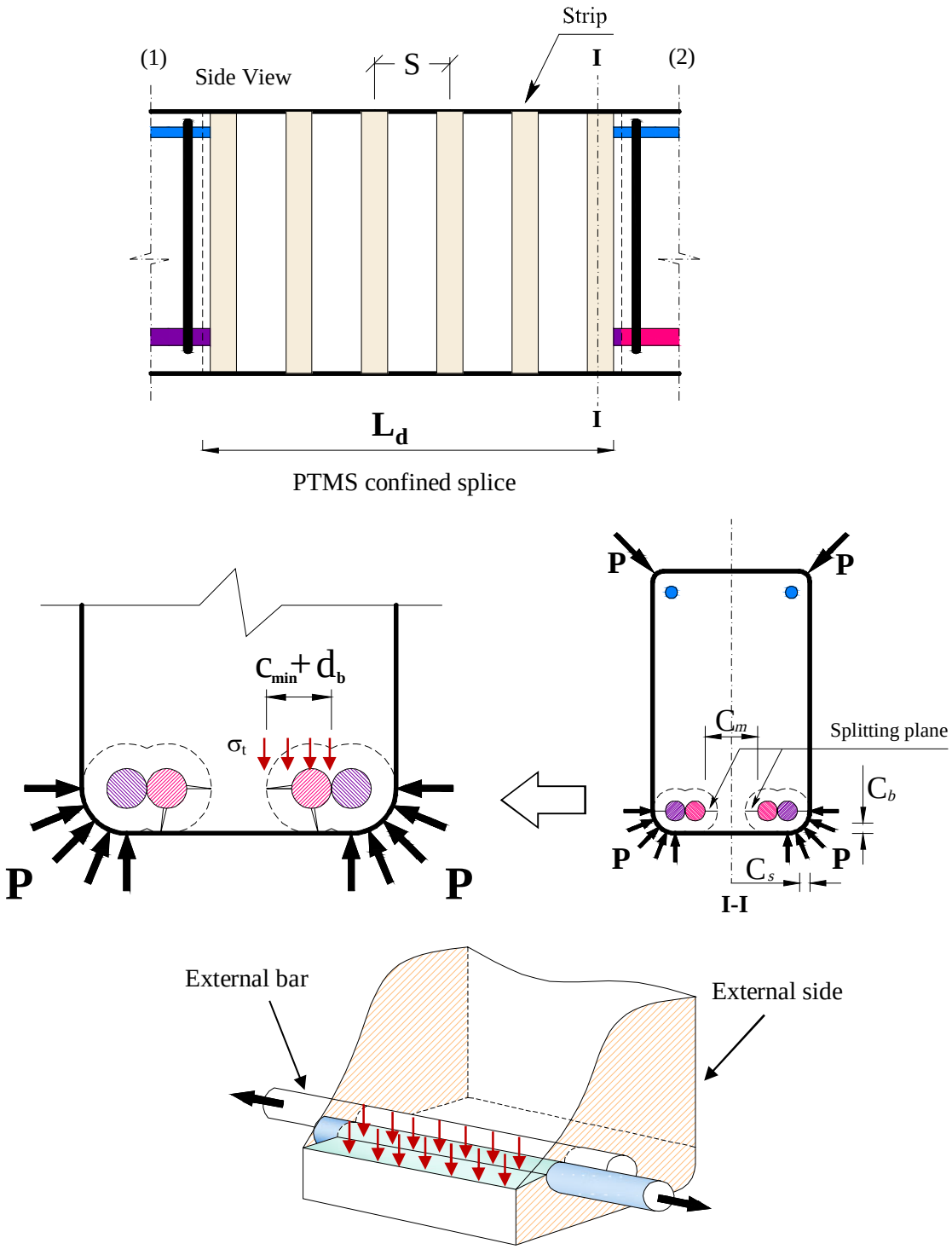

Figure 8-8: Effect of confining stresses on the splitting plane

The previous term was applied to equation (8-10) and nonlinear regression analyses were performed to determine the constants of the equation. As a result, the following equation that calculates the contribution of PTMS confinement to bond strength is found:

$$\frac{\tau_{PTMS}}{f_c'^{1/4}} = \frac{t.N}{456 n d_b\left(\frac{c_{min}}{d_b}+1\right)} f_p \left[1 + \left(150\frac{d_b}{l_d} - 12.6\right)\frac{c_{min}}{d_b} + \frac{2}{3}\frac{l_d}{d_b}\right] \quad R^2 = 0.8 \qquad (8\text{-}12)$$

where n represents the number of splices in the tension side of the cross section; n is incorporated in the equation to represent the number of cracks occurring in the tension side. Standard deviation SD and coefficient of variation CV are found to be 0.15.

To account for the enhancement in bond due to increase in the confinement along the splice length, the previous equation is multiplied by the number of strips N confining the splice.

A limitation to the previous equation should be applied. Thus, the limitation is that the maximum bond strength due to concrete and confinement τ_{max} should not exceed that due to pullout failure τ_0. The τ_0 value is evaluated to be $2.57\sqrt{f'_c}$ based on an extensive study by Harajli et al. (2004). Also, τ_{max} should not exceed the bond strength at yield.

In comparison to the previous model equations shown in Figure 8-3, the proposed equation provides more consistent predictions of the test results, as shown in Figure 8-9.

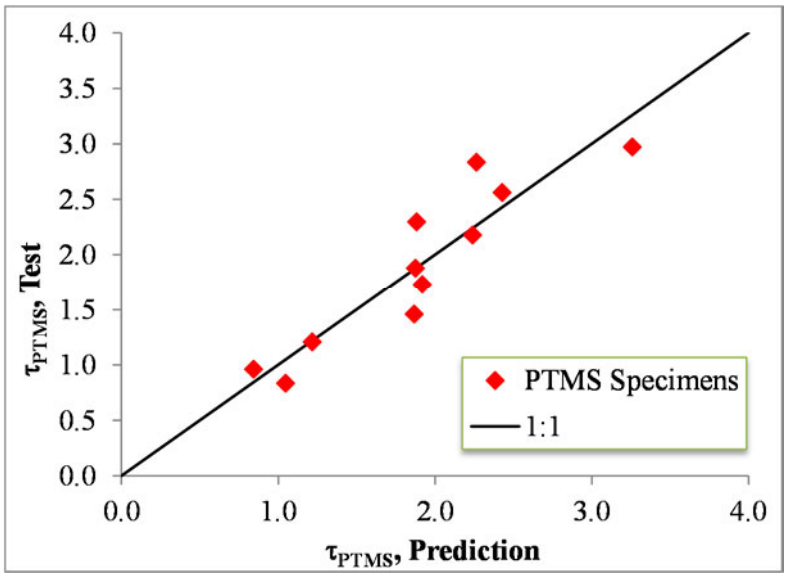

Figure 8-9: Comparison of test data of PTMS confined specimens with predictions

8.3.2.2 First splitting strength τ_s

Figure 8-10 presents the τ_s values of PTMS specimens along with those of unconfined and internally confined specimens. Variation of τ_s of the PTMS specimens was examined versus the different parameters, as shown in Figure 8-11, and no strong relationships were observed.

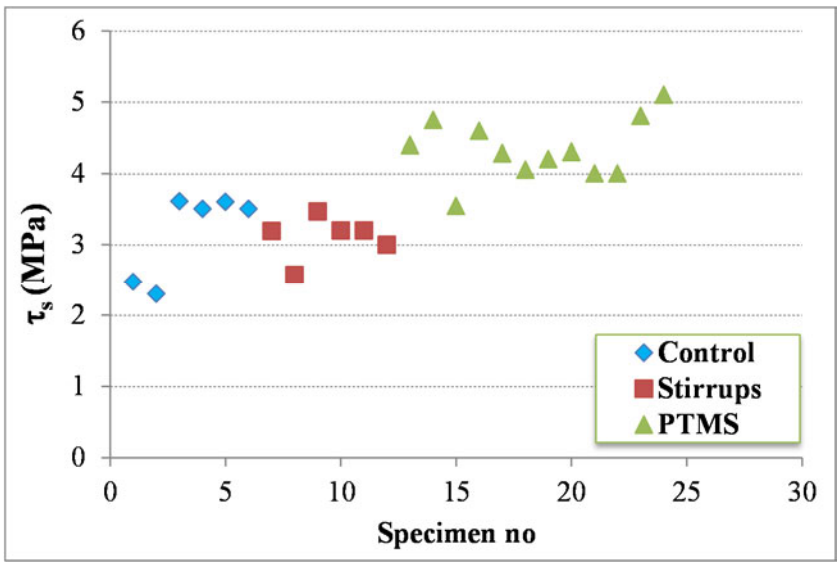

Figure 8-10: τ_s values for all test specimens of Phase I & II

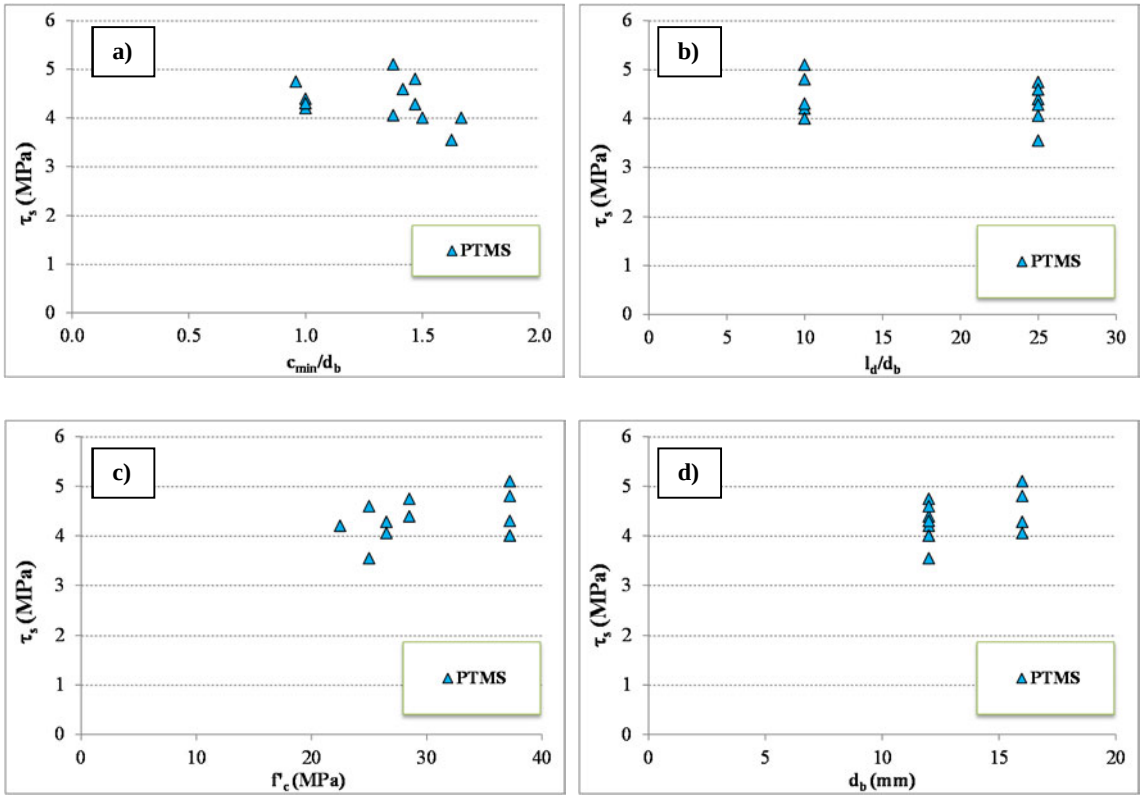

Figure 8-11: Variation of τ_s with a) c_{min}/d_b, b) l_d/d_b, c) f'_c and d) d_b

The relation of τ_s with respect to the maximum strength τ_{max} was then examined, as shown in Figure 8-12. An interesting observation was found that τ_s occurs almost at (80-90%) of the maximum strength. This was reported earlier in chapters 4&5. Nevertheless, the τ_s/τ_{max} ratio was plotted versus the different parameters and no relation was found, specifically for the confined specimens. For the unconfined specimens, however, the τ_s/τ_{max} ratio tended to approach a value of 1 as the concrete cover to bar diameter ratio c_{min}/d_b decreased, as shown in Figure 8-13.

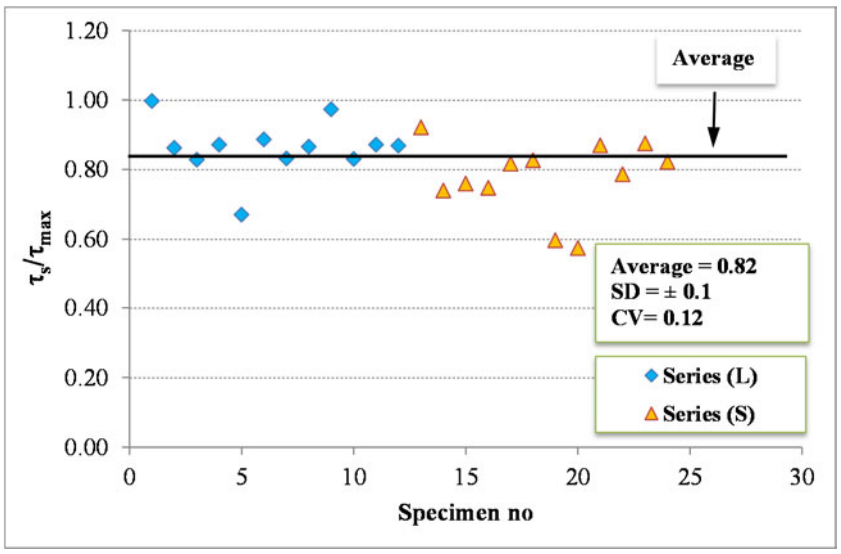

Figure 8-12: Variation of first splitting strength τ_s with respect to the maximum strength

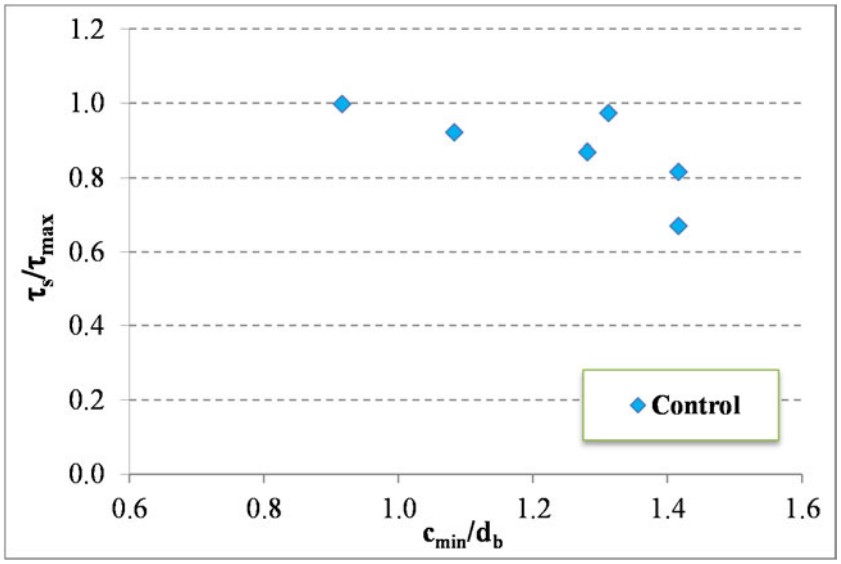

Figure 8-13: Variation of τ_s/τ_{max} ratio of the confined specimens with c_{min}/d_b

Consequently, it is decided to adopt a constant value of $\frac{\tau_s}{\tau_{max}} = 0.82$ with SD=0.1 and CV=0.12. The ratio is derived based on values from all specimens. It is reported in the literature, based on studies on different types of confinement with similar conditions including steel stirrups, CFRP and Fibre reinforced polymer (FRC), that this ratio can be taken anywhere between 0.7-0.8 (Harajli, 2009).

8.3.2.3 Post-Splitting bond τ_e

Based on a parametric study performed on τ_e/τ_{max} ratio, it is found that the concrete strength f'_c, c_{min}/d_b ratio and splice length to bar diameter ratio l_d/d_b have some influence on the post-splitting ratio. The trends of τ_e/τ_{max} with respect to these parameters are shown in Figure 8-14.

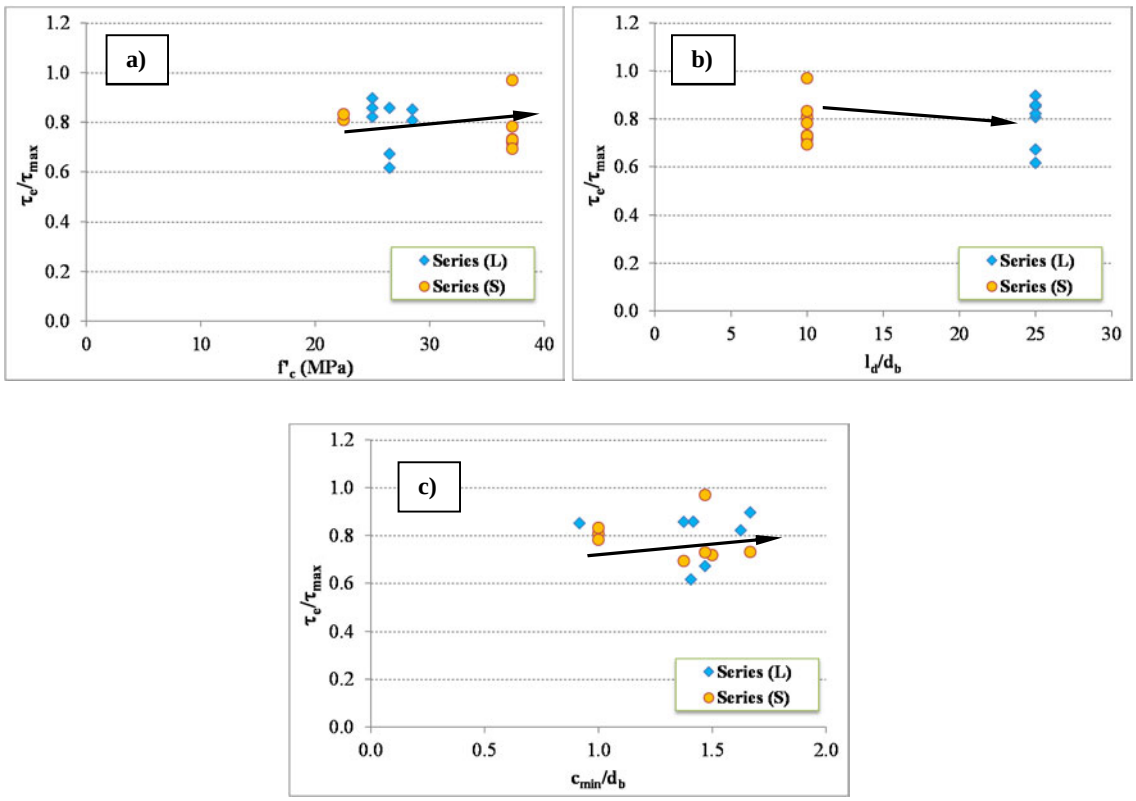

Figure 8-14: Variation of τ_e/τ_{max} ratio with a) f'_c and b) l_d/d_b and c) c_{min}/d_b

Thus, the following equation was first suggested for regression analysis:

$$\frac{\tau_e}{\tau_{max}} = \left[A\frac{l_d}{d_b} + B\frac{c_{min}}{d_b} + D\right] f_c'^{p} \tag{8-13}$$

By performing nonlinear regression analyses, the following equation is found to best represent the results:

$$\frac{\tau_e}{\tau_{max}} = 0.34 f_c'^{1/4} \leq 0.9 \qquad R^2 = 0.98,\ \text{Adj } R^2 = 0.92 \tag{8-14}$$

It is clear from the previous equation that the use of f'_c with the power of ¼ resulted in a very good correlation. It can also be indicated that the previous normalisation of the τ_e/τ_{max} ratio to the concrete strength led to insignificant influences of the c_{min}/d_b and l_d/d_b ratios. As can be seen from Figure 8-15, almost no variation in the τ_e/τ_{max} ratio can be noticed. An upper limit of 90% is set on the equation based on the test results.

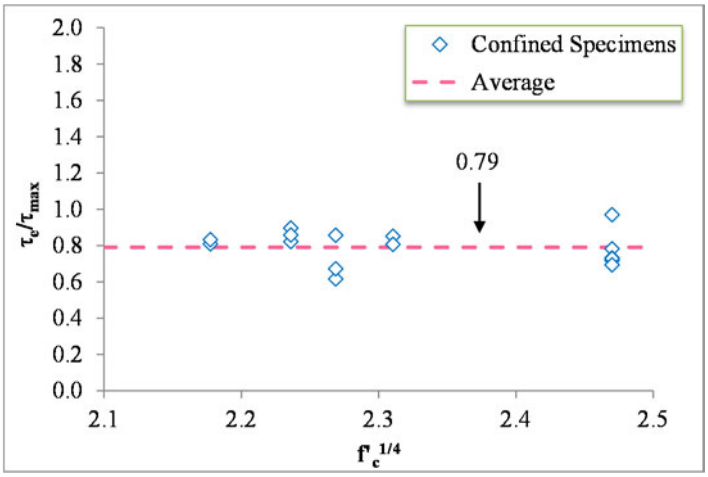

Figure 8-15: Relation of τ_e/τ_{max} to $f'_c{}^{1/4}$

For the purpose of simplicity, a mean value of the τ_e/τ_{max} ratio equal to 0.79 (SD=0.09, CV=0.11) can be adopted, as shown in Figure 8-16. This value is very close to the τ_s/τ_{max} ratio which is equal to 0.82. Thus, it is possible for simplicity and ease of design to consider an average value of 0.80 for the τ_e/τ_{max} and τ_s/τ_{max} ratios.

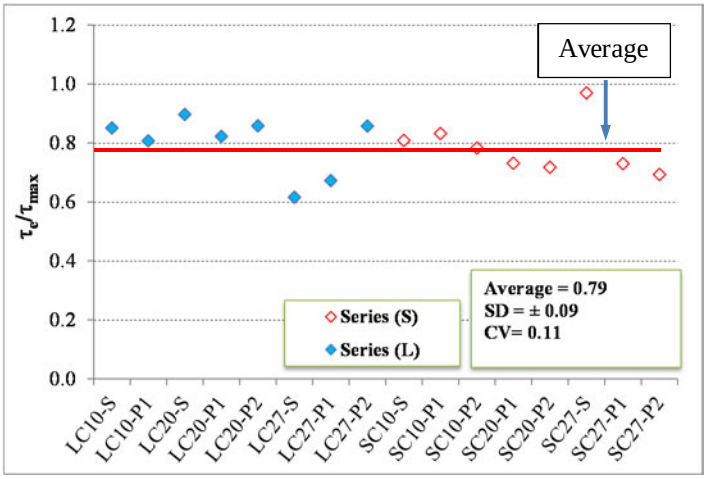

Figure 8-16: Variation of τ_e with respect to the maximum strength τ_{max}

8.3.2.4 Residual bond strength τ_r

Similarly to τ_s and τ_e, τ_r was examined with respect to the maximum strength τ_{max}. The τ_r/τ_{max} ratio is plotted in Figure 8-17 for the confined specimens. By examining the variation of the τ_r/τ_{max} ratio with the different parameters, it is found that some trends exist with l_d/d_b and c_{min}/d_b ratios and f'_c, as shown in Figure 8-18.

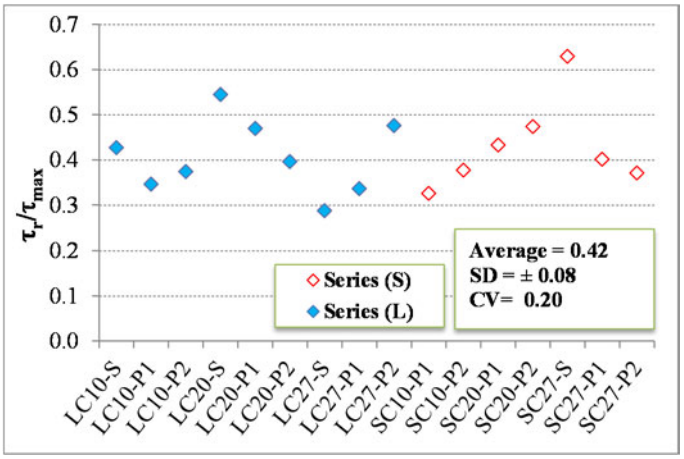

Figure 8-17: Variation of τ_r with respect to the maximum strength τ_{max}

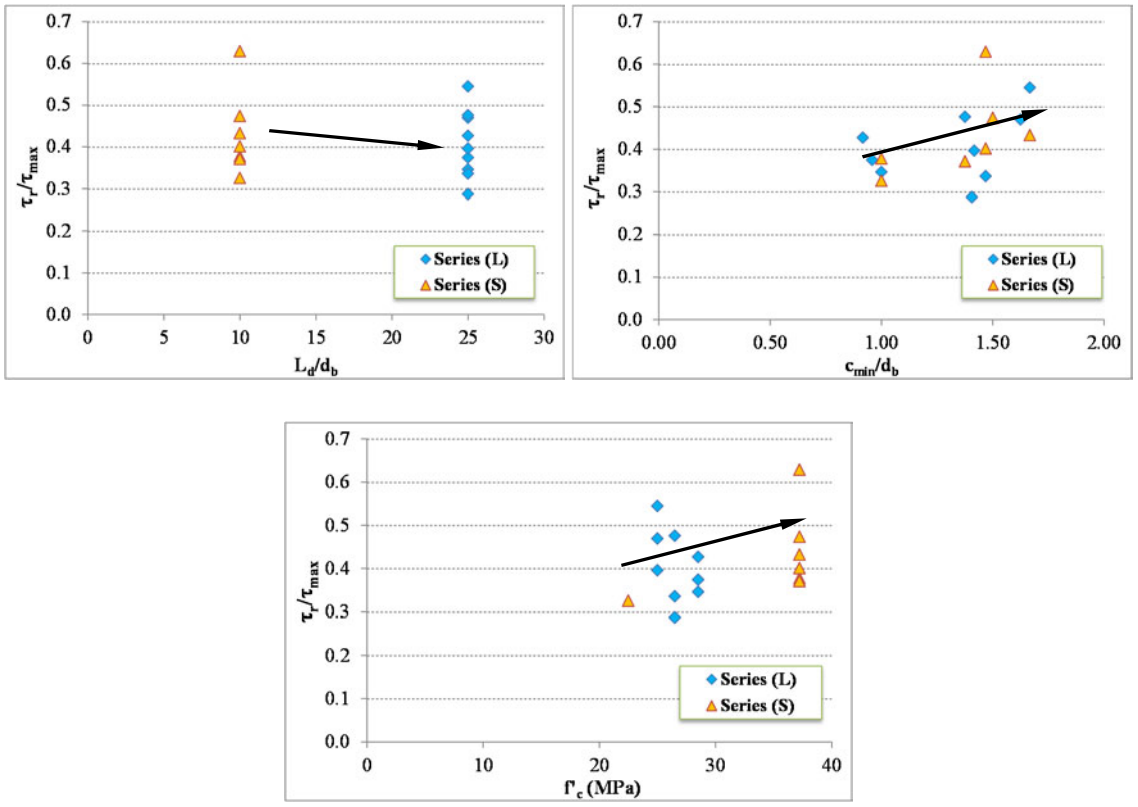

Figure 8-18: Variation of τ_r/τ_{max} ratio with a) l_d/d_b, b) c_{min}/d_b and c) f'_c

As can be noted from Figure 8-18, an increase in the c_{min}/d_b ratio and the concrete strength results in an increase in the τ_r/τ_{max} ratio. However, the residual bond ratio appears to decrease slightly for longer anchorages. Based on nonlinear regression analyses, the following expression is found to best represent the test results:

$$\frac{\tau_r}{\tau_{max}} = \left[\frac{1}{9} \times \frac{d_b}{l_d} + \frac{1}{8} \times \frac{c_{min}}{d_b}\right] \times f_c'^{1/4} \leq 0.5 \qquad R^2 = 0.96, \text{ Adj } R^2 = 0.88 \qquad (8\text{-}15)$$

As can be seen from the previous equation, the effect of concrete strength on the τ_r/τ_{max} ratio is represented by the use of $f'_c{}^{1/4}$.

For simplicity and consistency, the residual bond can be taken as $\tau_r = 0.42\ \tau_{max}$ (SD=0.08 and CV=0.20).

8.3.2.5 s_m: Slip at τ_{max}

The slip s_m at the maximum bond strength is investigated with respect to the different parameters. Figure 8-19 shows the s_m values for the tested specimens. As discussed earlier in chapter 4, the failure mechanism of specimens SC27-D16-PTMS1&2 fell in a different category, where a constant threshold in the bond-slip response occurred before degradation. As a result, s_m values of these two specimens were disregarded, as further tests are required to explain the phenomenon.

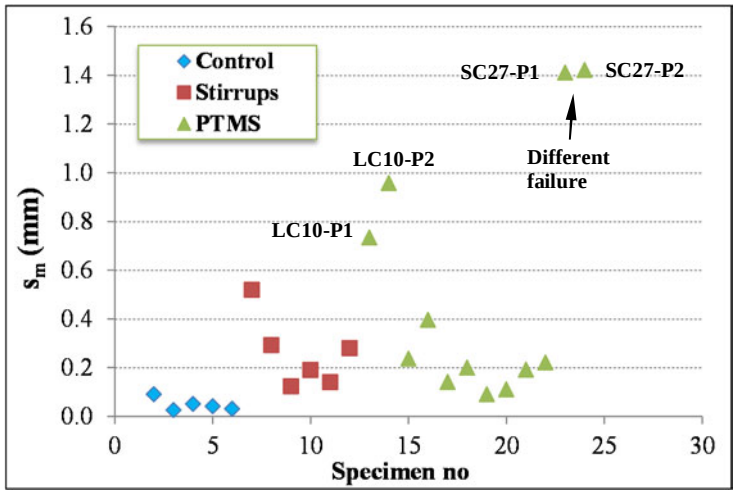

Figure 8-19: s_m values of the test specimens in Phases I&II

As can be noted from Figure 8-19, the PTMS confined specimens reach the maximum bond strength at higher slip s_m values compared to those of the associated unconfined specimens, and consequently, this can be attributed to the effect of confinement. Thus, the relation of s_m with respect to τ_{PTMS} is examined. As a result, it is found that s_m has a strong relation to the normalised $\tau_{PTMS}/f'_c{}^{1/4}$, as shown in Figure 8-20.

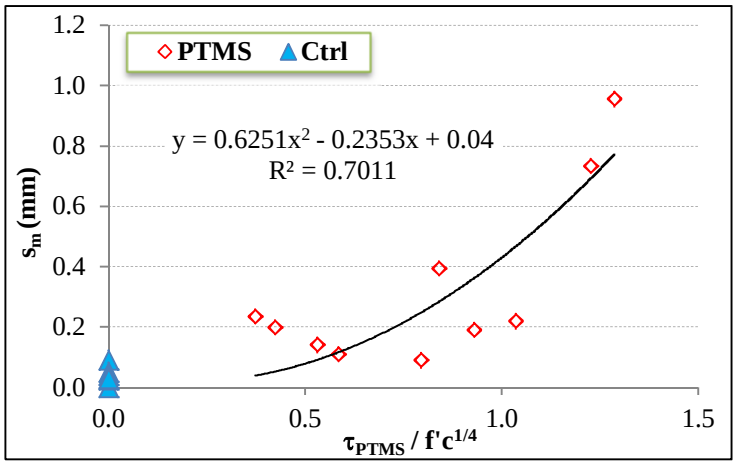

Figure 8-20: Variation of s_m with the normalised τ_{PTMS}

Based on the trend shown in Figure 8-20, the following regression equation for estimating s_m is derived:

$$s_m = 0.625\left[\frac{\tau_{PTMS}}{fc'^{1/4}}\right]^2 - 0.235\left[\frac{\tau_{PTMS}}{fc'^{\frac{1}{4}}}\right] + 0.04 \qquad R^2=0.7 \qquad (8\text{-}16)$$

The value 0.04 in the previous equation represents the mean value of slip at the maximum strength of the associated unconfined specimens with SD=0.02.

8.3.2.6 s_e: Slip at τ_e

The slip values s_e corresponding to the bond stress τ_e are plotted in Figure 8-21 for the PTMS confined specimens. The effect of different parameters on s_e was investigated. As a result, it is found that s_e shows trends with τ_{PTMS}, l_d/d_b and c_{min}/d_b, as shown in Figure 8-22.

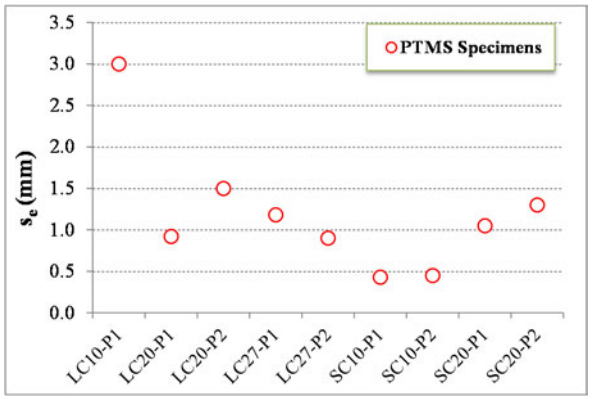

Figure 8-21: s_e values of the PTMS specimens in Phases I&II

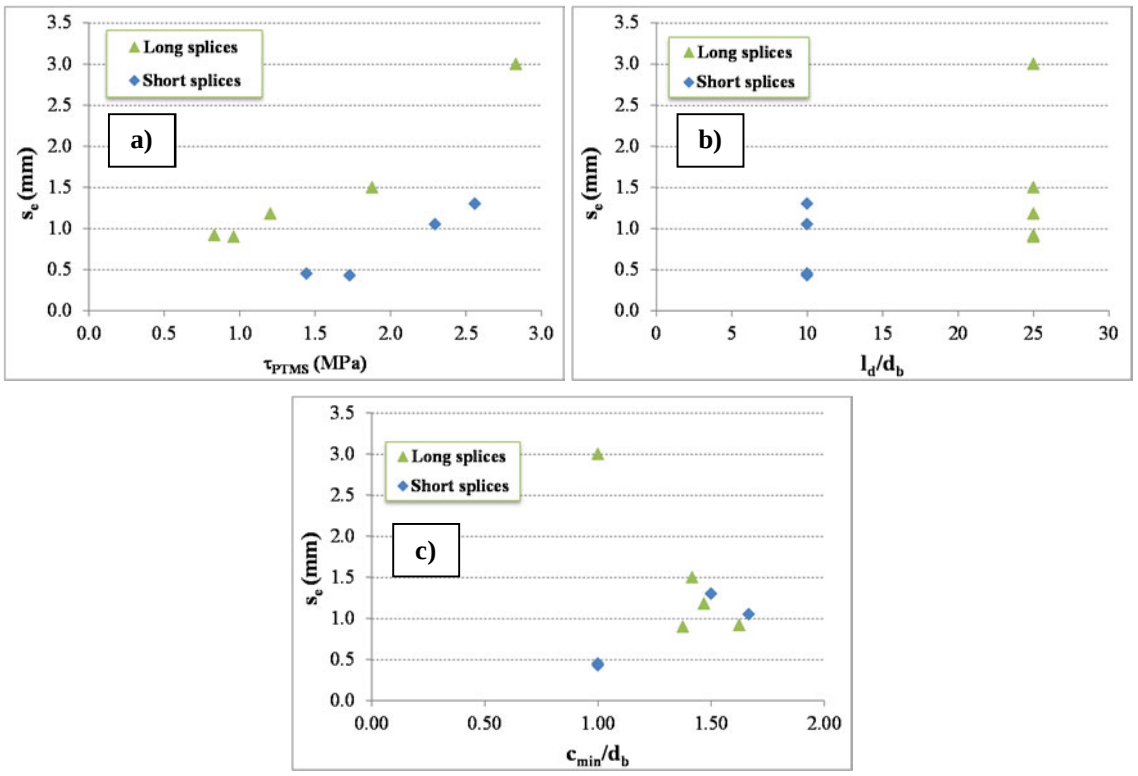

Figure 8-22: Variation of s_e with a) τ_{PTMS}, b) l_d/d_b and c) c_{min}/d_b

However, normalising s_e to the slip at the maximum s_m, as shown in Figure 8-23, was found to eliminate the effect of the previous parameters, with the exception of specimen LC27-D16-PTMS1, and a mean value of the ratio s_e/s_m of 4.6 (SD = 0.73, CV = 0.20) is considered. A limit is set on s_e in which it must not exceed the following:

$$s_e \leq s_m + (s_r - s_m) \times \frac{(\tau_m - \tau_e)}{(\tau_m - \tau_r)} \quad (8\text{-}17)$$

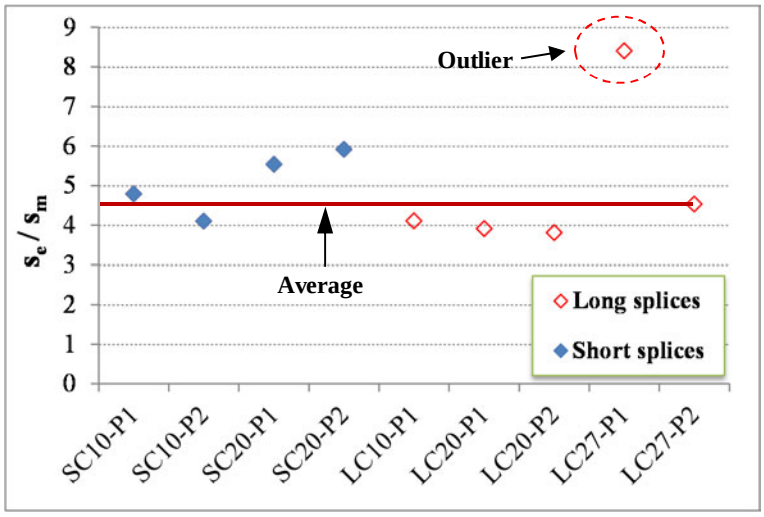

Figure 8-23: Variation of s_e in relation to s_m

8.3.2.7 s_r: Slip at residual bond t_r

The slip values s_r of the PTMS confined specimens at the residual bond τ_r are shown in Figure 8-24. As can be seen from the figure, specimens with long splices produce higher slip values s_r compared to those with short splices; however, they occur at relatively lower residual bond stresses τ_r, as previously shown in Figure 8-17.

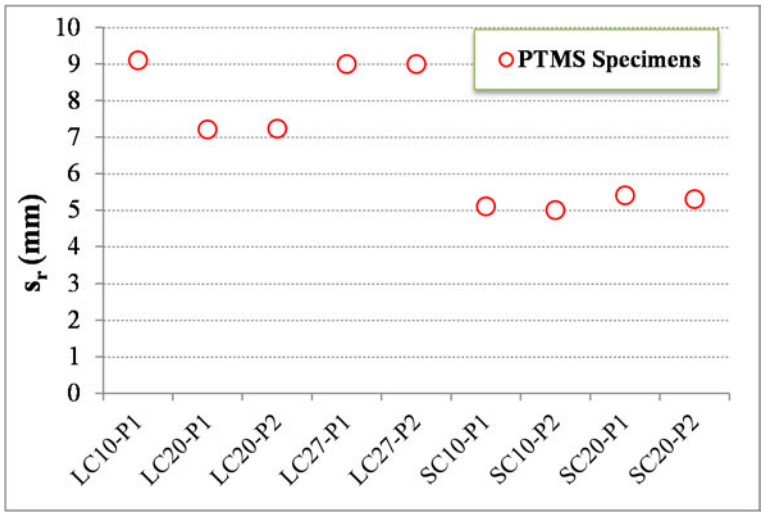

Figure 8-24: s_r values of the PTMS specimens in Phases I&II

The variation of s_r with respect to the different parameters was investigated. The only parameter that showed a clear trend was the l_d/d_b ratio, as shown in Figure 8-25(a). The increase in the

residual slip for longer anchorages could be attributed to the larger frictional surface. On the other hand, it was observed that the concrete cover to bar diameter ratio had no clear effect on the residual slip, as shown in Figure 8-25(b). Another parameter, which was believed to have an effect on s_r, was the amount of confinement represented by the PTMS contribution τ_{PTMS}. However, this parameter, as shown in Figure 8-25(c), did not show any obvious relation to the residual slip values.

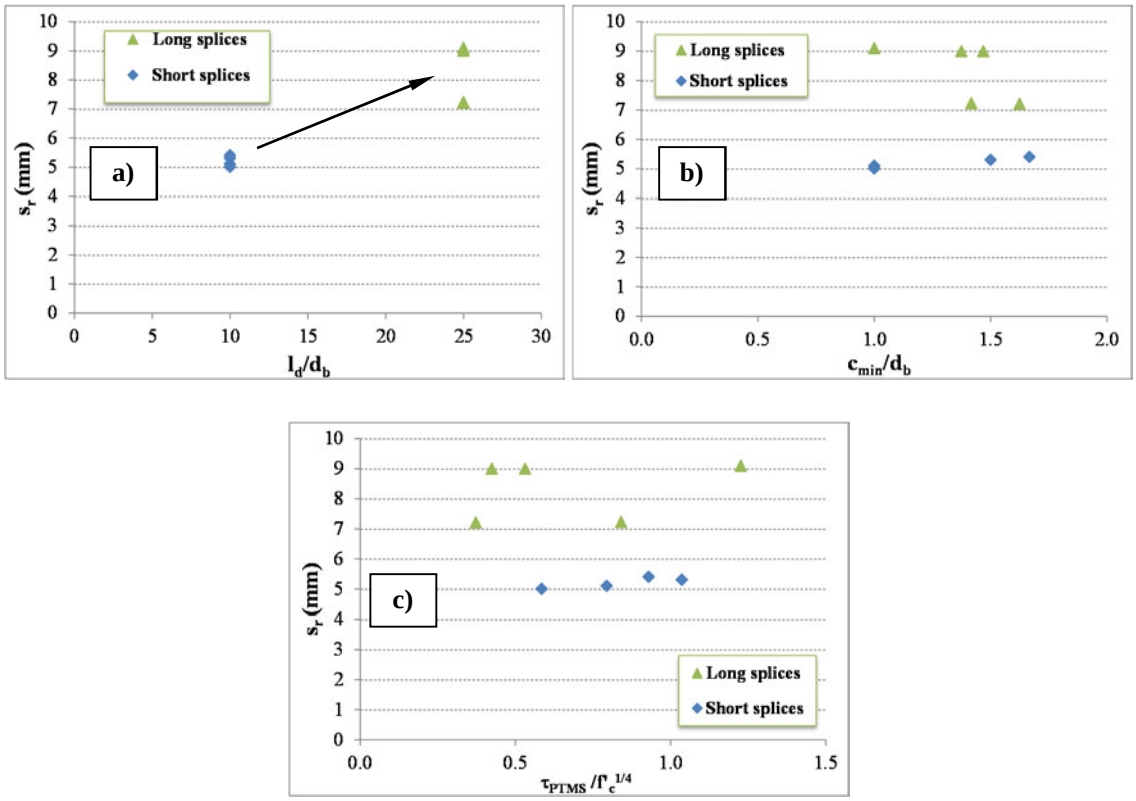

Figure 8-25: Variation of s_r with a) l_d/d_b, b) c_{min}/d_b and c) $\tau_{PTMS}/f'_c{}^{1/4}$

Regression analyses were conducted to determine the variables for a proposed equation. The following equation is best fit for the results:

$$s_r = 0.2\, l_d/d_b + 3 \leq r_d \qquad R^2=0.84,\ \text{Adj } R^2=0.81 \qquad (8\text{-}18)$$

where r_d denotes the rib spacing of the spliced bar.

8.3.3 Complete model

8.3.3.1 General

Many bond stress-slip models have been proposed based on experimental work for different bond conditions. However, these models differ largely from each other depending on the investigator and the definition of bar slippage.

Based on tests of well controlled pullout specimens conducted by Shima et al.(1987), Yamao et al. (1984) and Chou et al. (1983), Shima et al. (1987) proposed a unique bond-slip-strain

relationship that gives the slip at any location along the embedment length as the summation of slip at the free end of the bar and the bar extension. In doing this, Shima et al. (1987) established a relationship between the strain at the lead end of the bar and the slip at the free end, as shown in Figure 8-26. The bond-slip-strain relationship was shown to be applicable for elastic and post-yield cases.

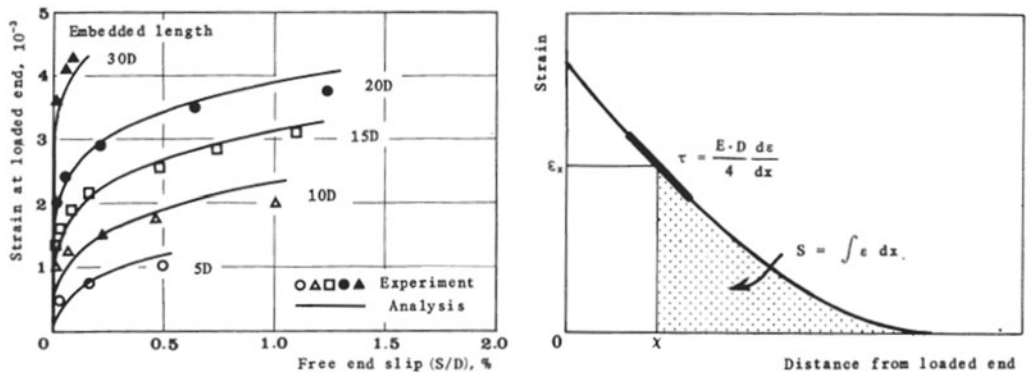

Figure 8-26: Relationship between strain at bar lead end and slip at the free end

Alsiwat and Saatcioglu (1992), from results on pullout specimens, proposed an analytical procedure to calculate the slippage of anchored bars in conditions similar to those found in interior and exterior joints. They differentiated two components of slip namely, bar movement and extension of the bar. Bar extension was calculated based on an assumed strain distribution along the bar, as shown in Figure 8-27; while bar movement was considered from the modified local bond-slip model proposed by Ciampi et al. (1982) and Eligehausen et al. (1983).

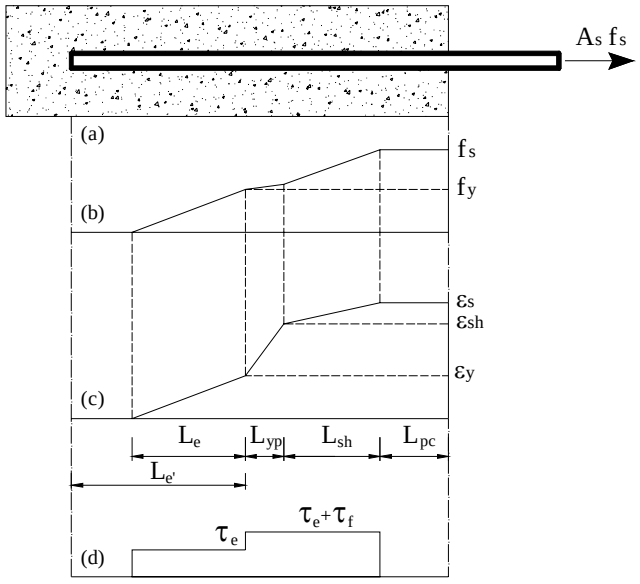

Figure 8-27: Assumed strain distribution (Alsiwat and Saatcioglu, 1992)

Other researchers such as Lehman and Moehle (2000) and Sezen (2003) measured the total slip occurring at the slip interface of bars anchored in or spliced above a column footing. Based on these slip measurements and by assuming a bilinear strain distribution along the bar, as shown

in Figure 8-28, a bond-slip relationship was developed that combined the effect of bar movement and bar extension. In their models, a reduced bond stress of about $\sqrt{f'_c}$ was calculated along the anchorage length in order to increase bar slippage to incorporate the bar movement.

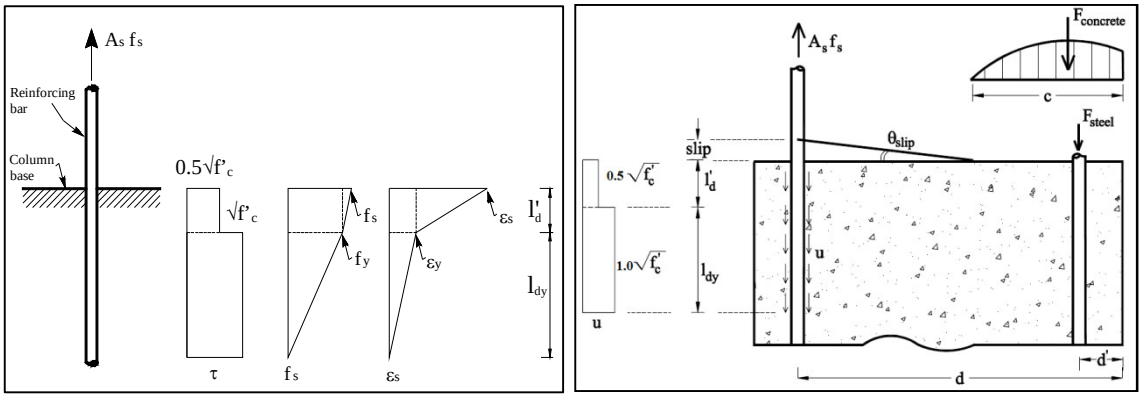

Figure 8-28: Bond, strain and stress distributions adopted by Sezen (2003)

Using results from pullout and splitting tests, Ciampi et al. (1982), Eligehausen (1983) and later by Harajli (1994, 2004) using tests on beams, among others, proposed local bond-slip relationships based on slip measurement at bar ends. The slip measurement was assumed to simulate the bar slippage of short and long anchorages/splices at the loaded end. However, this relationship, in principle, represents the bar movement. Figure 8-29 shows the local bond stress-slip relationship proposed by Eligehausen (1983) and that by Harajli (2004).

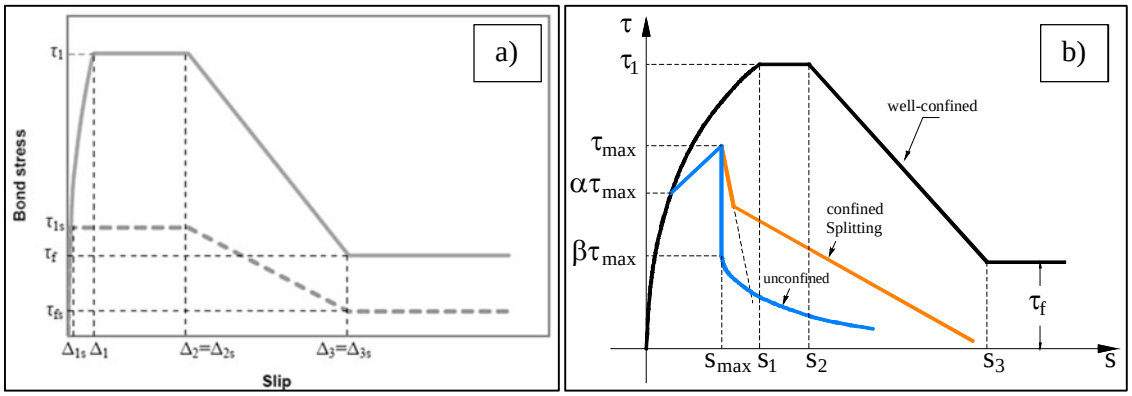

Figure 8-29: local bond-slip model by a) Eligehausen et al. (1983) and b) Harajli (2004)

Thus, it can be concluded that although slip measurement differs according to each investigator, most of the models incorporate the two slip components. In this study, elongation of the spliced bars is subtracted from the total slip with the justification that bar elongation differs largely between short and long anchorages. This conclusion is supported by many experimental works such as those by Yamao et al. (1984) and Shima et al. (1987) or numerical studies such as that by Harajli (1994, 2007). In the following section, the anchorage component for the model is addressed.

8.3.3.2 Anchorage component

As the bar anchored into the joint area of a beam-column connection is stressed, deterioration in the bond between steel and concrete may occur, especially in the case of yielding. This deterioration causes large local deformations due to crushing of concrete between bar lugs. Therefore, an additional slip (s_{Anch}) at the splice interface should be considered, as schematically shown in Figure 8-30. This component accounts for the anchorage effect due to strain penetration into the joint area, as illustrated in Figure 8-31 for the case of yielding.

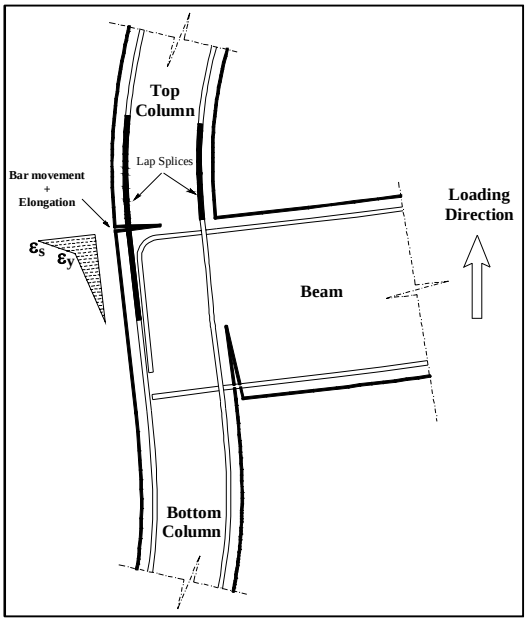

Figure 8-30: Cracks at slip interfaces of column splices and beam anchorages

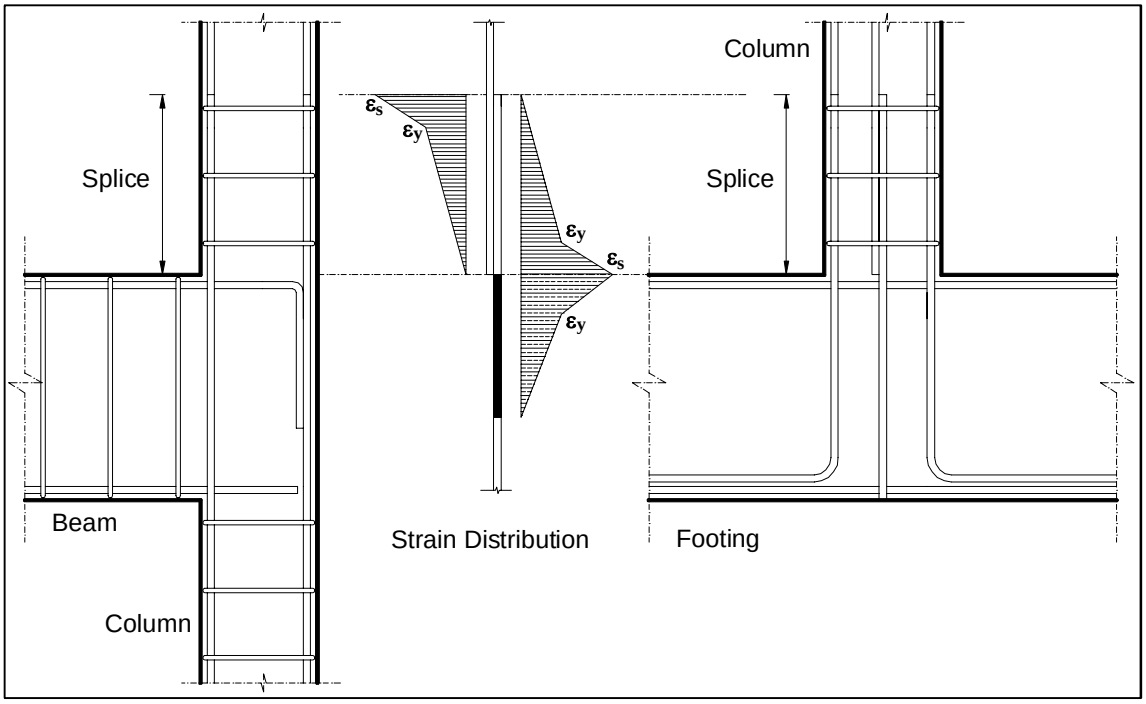

Figure 8-31: Strain distribution along the splice assembly and anchorage of beam-column joint and column footing in the case of yielding

The determination of s_{Anch} depends primarily on the strain distribution assumed along the anchorage length. Different strain distributions were assumed by different researchers such as Alsiwat and Saatcioglu (1992), Lehman and Moehle (2000), Sezen (2003), Altoontash (2004). Furthermore, in a recent study, based on results from pullout specimens, Ahmad (2011) proposed the use of a constant strain distribution along the elastic length, whereas a linear distribution was adopted for the yielded length, as shown in Figure 8-32.

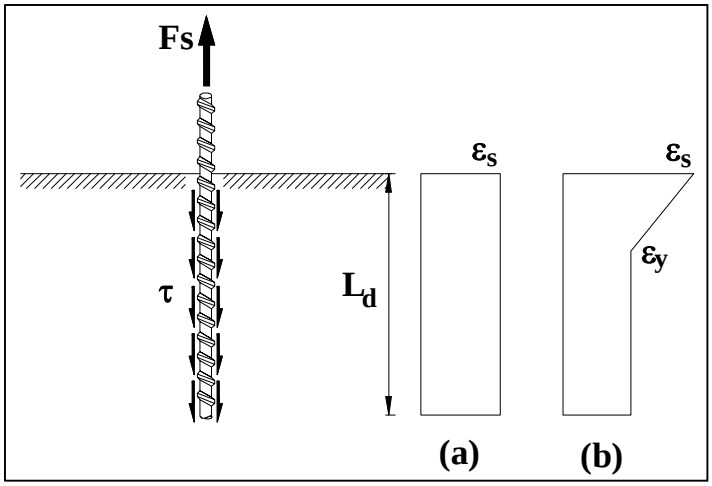

Figure 8-32: Strain distributions proposed by Ahmad (2011) for different conditions a) elastic, and b) post-yield

However, it was shown earlier in chapter 5 that strain distributions in the elastic stage near failure have approximately a linear relationship along the single bar. After yield, the strain distribution along the inelastic segment of the bar is also found that it can be approximated as a linear relationship. Consequently, the results of this study agree well with the bilinear strain distribution given by Sezen (2003).

Thus, in the model by Sezen (2003), the bar slip is calculated by integrating the strain over the elastic and inelastic lengths of the bar as follows

$$s = \int_0^{l_d + l'_d} \varepsilon(x)\,dx \tag{8-19}$$

$$s = \frac{\varepsilon_s l_d}{2} \qquad \varepsilon_s \le \varepsilon_y \tag{8-20}$$

$$s = \frac{\varepsilon_y (l_d)}{2} + \frac{(\varepsilon_s + \varepsilon_y) l'_d}{2} \qquad \varepsilon_s > \varepsilon_y \tag{8-21}$$

in which l_d is the splice length ; l'_d is the inelastic segment of the reinforcing bar.

To calculate l'_d, Sezen (2003) proposed simplifying the distribution of stresses over the inelastic length, in the bar, as the difference between the current stress and that calculated at the onset of yielding. Therefore, l'_d is calculated by:

$$l'_d = \frac{(f_s - f_y) d_b}{4 \tau'_b} \tag{8-22}$$

where τ_b' is the average value of the bond stress along the inelastic segment of the reinforcing bar, and it is equal to $0.5\tau_{max}$.

By substituting the bond values and anchorage lengths into equations (8-20) & (8-21), and considering the bi-uniform bond stress approximation in the bar, the slip due to elongation of the bar can be calculated as follows:

$$s_{Anch} = \frac{\tau_{max} \times l_d^2}{E_s d_b} \qquad \varepsilon_s \leq \varepsilon_y \qquad (8\text{-}23)$$

$$s_{Anch} = \frac{\tau_{max} \times l_d^2}{E_s d_b} + \frac{(\varepsilon_s + \varepsilon_y)(f_s - f_y) d_b}{4 \times \tau_{max}} \qquad \varepsilon_s > \varepsilon_y \qquad (8\text{-}24)$$

The strain ε_s and stress f_s in the bar are calculated based on bond stresses of the proposed model τ_{max}. In the calculation of s_{Anch}, the limit on $\tau_{max} \leq \tau_y$ should be ignored.

By adding the elongation component s_{Anch} to the pure slip, the final model will be as shown in Figure 8-33. The elongation s_{Anch} should be added as a constant value to all performance points.

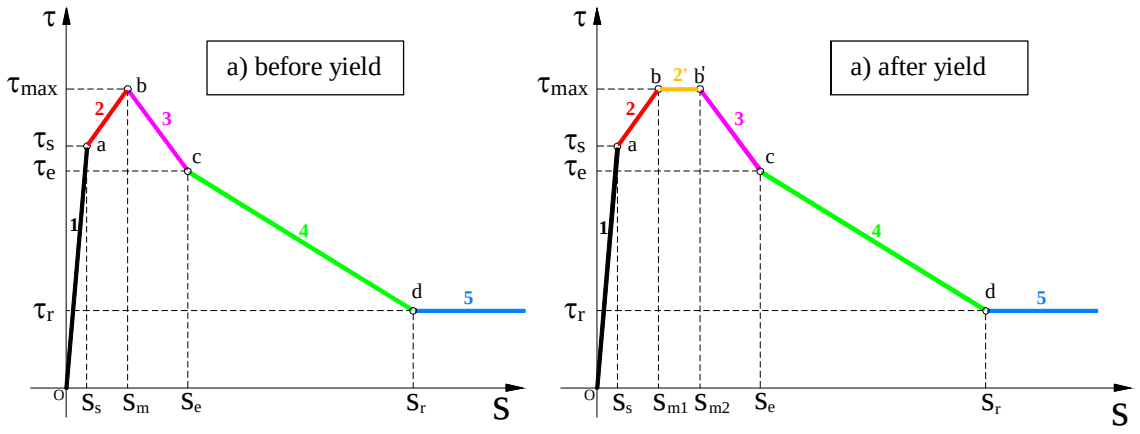

Figure 8-33: Proposed model for bond splitting failure with the addition of bar elongation

The proposed bond-slip model was used to predict the experimental results of the beams with short and long splices. Ahmad (2011) model and Orangun (1975) model for unconfined concrete were used. Table 8-2 shows the analytical predictions to those from the experimental results of all specimens. It can be noted from the table that the use of Ahmad (2011) model yields better estimation of the results, when the concrete compressive strength is less than 30MPa. For higher concrete compressive strengths, Orangun (1975) model tends to predict the concrete contribution more appropriately, and as a result, better predictions of the maximum strength. Also, Figure 8-34 shows comparisons of the model predictions to the experimental bond-slip responses of long splices, where Ahmad model is used for concrete contribution. It is clear from the figure that the pre-peak response is well represented. The predicted post-peak response, on the other hand, differs slightly from the experimental response, but the accuracy is still satisfied.

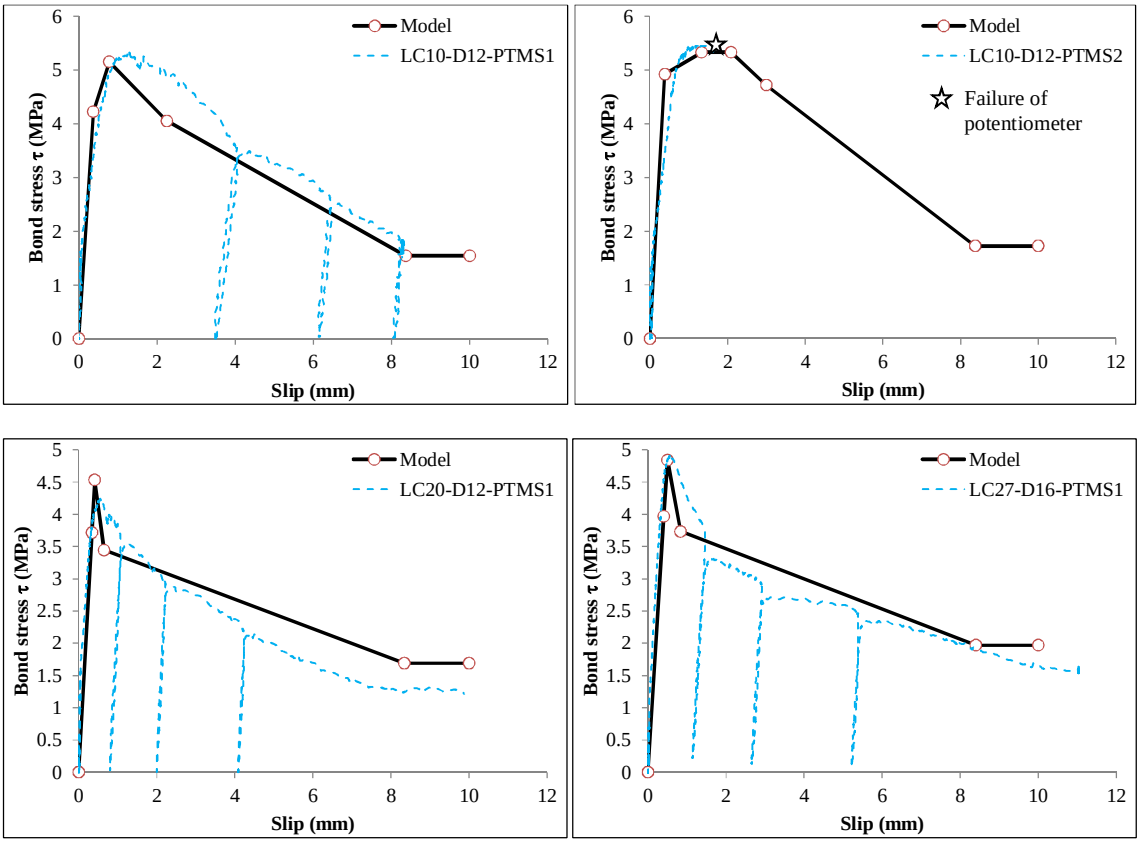

Figure 8-34: Comparison of model predictions to test results

Table 8-2: Comparison of model predictions to test results – PTMS specimens

Specimen	Test	τ_{PTMS} (Ana)	Orangun (1975)				Ahmad (2011)			
	τ_{max}	MPa	$\tau_c/\sqrt{f'_c}$	τ_c	τ_{max}	Ana / test	$\tau_c/f'^{0.68}_c$	τ_c	τ_{max}	Ana / test
SC10-P1	5.5	1.92	0.77	3.6	5.55	1.00	0.49	4.1	6.02	1.09
SC10-P2	5.8	2.18	0.77	4.7	6.84	1.19	0.49	5.8	7.96	1.38
SC20-P1	6.7	1.89	0.89	5.4	7.31	1.09	0.64	7.5	9.38	1.40
SC20-P2	7.0	2.43	0.91	5.6	7.99	1.15	0.60	7.1	9.49	1.36
SC27-P1	5.5	1.87	0.76	4.6	6.49	1.18	0.60	7.0	8.85	1.61
SC27-P2	6.2	2.24	0.77	4.7	6.91	1.11	0.58	6.7	8.98	1.45
LC10-P1	5.3	2.27	0.52	2.8	5.03	0.95	0.30	2.9	5.21	0.98
LC10-P2	5.4	3.26	0.52	2.8	5.33	0.99	0.29	2.9	5.33	0.99
LC20-P1	4.3	1.05	0.67	3.4	4.41	1.04	0.44	3.9	4.96	1.16
LC20-P2	5.3	1.88	0.62	3.1	4.98	0.94	0.39	3.5	5.38	1.01
LC27-P1	4.9	1.22	0.61	3.1	4.35	0.89	0.40	3.8	4.97	1.01
LC27-P2	4.7	0.84	0.61	3.1	3.98	0.85	0.38	3.6	4.40	0.94

8.4 CONCLUSIONS

An experimentally based model for the generalised local bond stress–slip relationship of steel bars embedded in PTMS confined concrete with splitting mode of bond failure is developed. The model is considered to be more fundamental in the sense that it accounts for the contribution of bar movement and bar elongation separately to the total slip. The relationship is

composed of four key points defined based on test observations. The developed model accounts for most of the critical parameters that influence the response, namely, the ratio of concrete cover to bar diameter, the splice length to bar diameter ratio, the concrete compressive strength and the amount of confinement (PTMS).

Additional experimental work is still needed for further validation of the model and for covering parameters other than those used in the current study, including low strength concrete LSC, low confining stress f_p, number of splices (n) and axial load.

Chapter 9

FINITE ELEMENT MODELLING: BEAMS

9.1 INTRODUCTION

This chapter discusses different aspects of modelling beam specimens with bond deficiencies and considers the use of different confinement materials.

The modelling procedure done has two objectives. The first objective is to introduce a method to predict the behaviour of deficient elements with inadequate splices using the limited number of experimental data available. The second objective is to examine the reliability of the bond-slip model to capture the beam force and deformation capacities as well as the general response. The finite element models are compared to the test data from Phases I & II. The comparisons are discussed in terms of failure mechanisms and the load-deflection response.

9.2 FINITE ELEMENT TOOL

Many FE analytical tools are available for the linear and nonlinear analysis, which can be used to simulate the problem of interest. Among those, ABAQUS 6.9 FE package (ABAQUS, 2009) is preferred due to its capability to introduce a smeared-crack concrete model into a 2-dimensional model. In addition, this package has been adopted by many researchers at the University of Sheffield for modelling RC beams with analogous behaviour, specifically anchorages. Such works were conducted by Al-Sunna (2006), Zhao (1999), Achillides (1998), Sooriyaarachchi (2005), and Imjai (2007). In these studies, RC beams with bond deficiency between reinforcing bars and the surrounding concrete are modelled using nonlinear connectors (Spring-type).

Modelling of splices introduces more complications into the model such that the slip may occur in two opposing directions. Consequently, the stability of the model due to the use of multiple nonlinear elements becomes an issue, which should be addressed.

9.3 MODELLING IN ABAQUS

A brief description of the modelling process including modelling elements (concrete, reinforcement and their connection), loading procedure and analysis method is given in Appendix G.

9.4 PHASE I: FE MODELLING OF SMALL SCALE BEAMS IN TENSION

9.4.1 General Description of the model

The elements used to model the beams in this test series are the 8-noded, plane stress, quadrilateral elements (CPS8 type). The thickness of the plane stress elements is set equal to the thickness of the tested beam specimens (150mm). The model is used for well-designed WD "continuous reinforcement" as well as deficient specimens "spliced bars at mid-span". The main purpose of modelling a beam with continuous reinforcement is to examine whether ABAQUS smeared crack model can satisfactorily simulate the flexural behaviour of the tested beam using the material characteristics determined from the experiment.

Although the specimen geometry and load arrangement are symmetrical, the whole specimen must be modelled in this case due to the splices. The model geometries used are shown in Figure 9-1 and Figure 9-2. The general model contains three layers of elements along the beam height (1 element @ concrete cover thickness, 1 element up to notch height and 3elements along the beam depth without the notch). Five meshing regions are used along the span: 1) a beam end region beyond the support @ 50 mm long element; 2) the shear span region with 90 mm long

elements; 3) the region between the load point and notch with 40 mm long element; 4) the notch region up to the splice end with two elements @50 mm; 5) the splice region with 40 mm long elements. The element mesh was selected from different meshes that converged into a stable solution and is used for deficient as well as the well-designed (WD) beams.

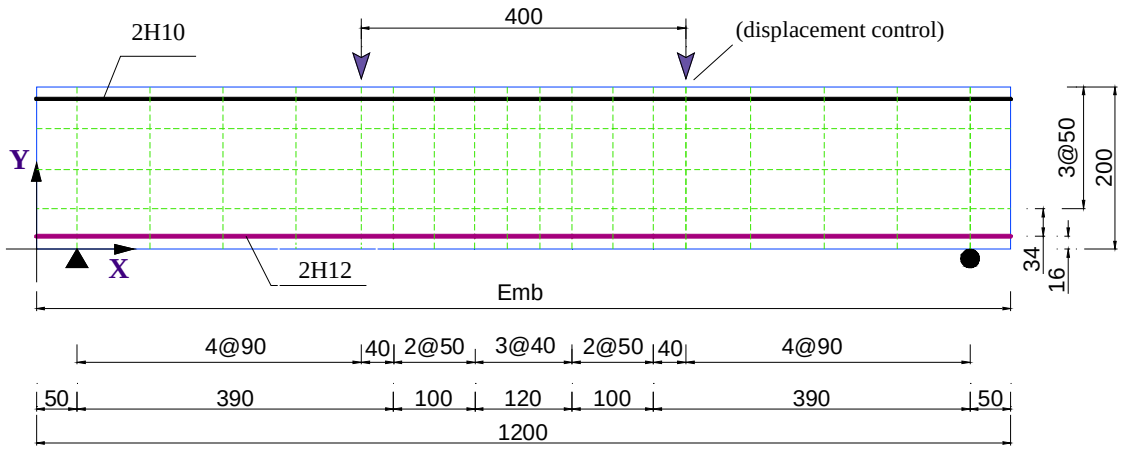

Figure 9-1: 2D FE model of a small-scale WD test specimen

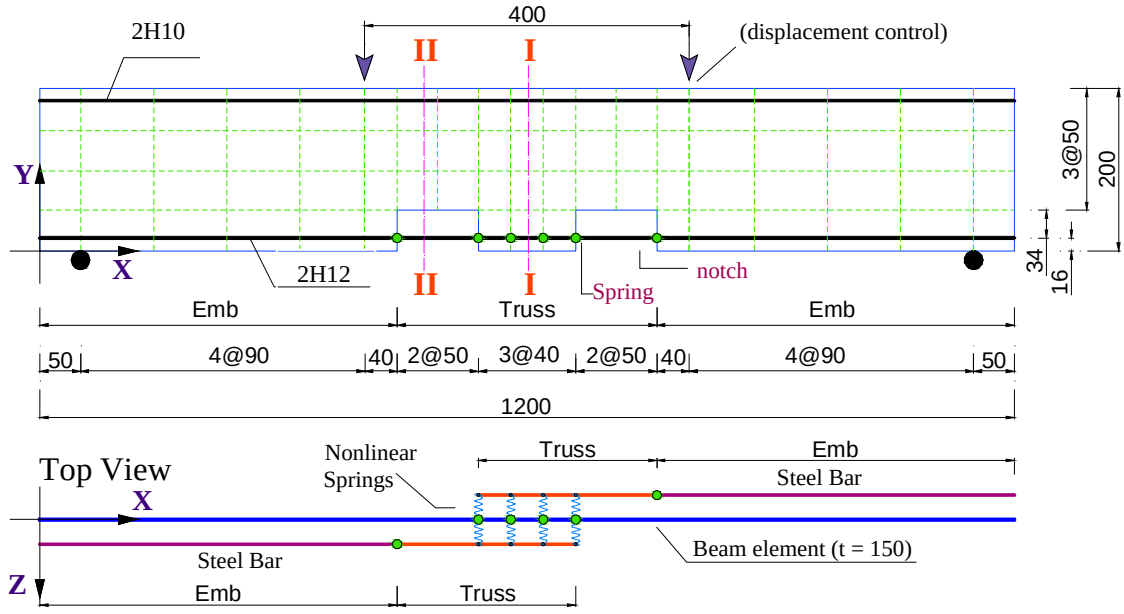

a) The geometry of tested deficient beams (units: mm)

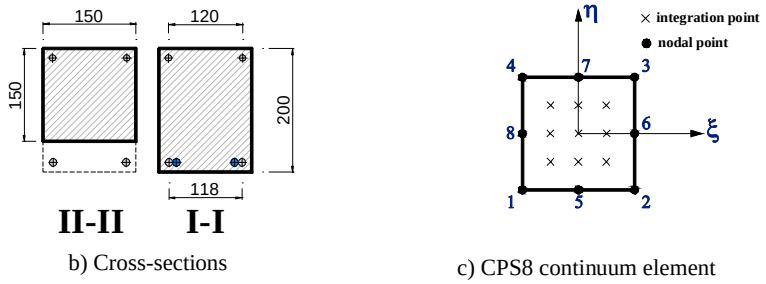

b) Cross-sections

c) CPS8 continuum element

Figure 9-2: 2D FE model of small-scale deficient test specimens

As can be seen from the previous figure, the reinforcement of the specimen is modelled with different techniques based on the location of the bars within the specimen. The main reinforcing

bars of a WD specimen with continuous flexural reinforcement are embedded in concrete elements along the entire length and no springs are used. The reinforcing bars of deficient beams, on the other hand, are modelled as follows:

- Reinforcing bars outside the splice region are modelled as embedded (Emb) rebars in the concrete element option (concrete property).
- Lap splices are modelled using two layers of one-dimensional truss elements with uniaxial stiffness only. Similar to the findings from test results, one layer of the reinforcement is assumed to slip, while the other is only allowed to elongate.
- The top reinforcing bars in compression are embedded along the entire beam length with a distance of 15 mm from the top side with an area of ($2\times78.5mm^2$).
- The shear reinforcement is modelled using embedded rebar layer in the vertical direction of the concrete elements spacing @ 70 mm and area of ($2\times28.3mm^2$).

9.4.2 Concrete compression model

Material characteristics of concrete are modelled in ABAQUS by a set of data specifying the stress in concrete and corresponding plastic strains. The concrete compressive model proposed in EC2 (2004) is used for defining the characteristics of plain as well as internally confined concrete. The externally confined concrete is modelled using the model proposed by Moghaddam et al. (2010). The concrete models are simplified into multilinear relations (4 segments) to reduce convergence problems. Figure 9-3 shows the input concrete models for a concrete compressive strength of 22.5 MPa and 37.2MPa. In the figure, plastic strains represent the concrete strain after the subtraction of the initial strain value.

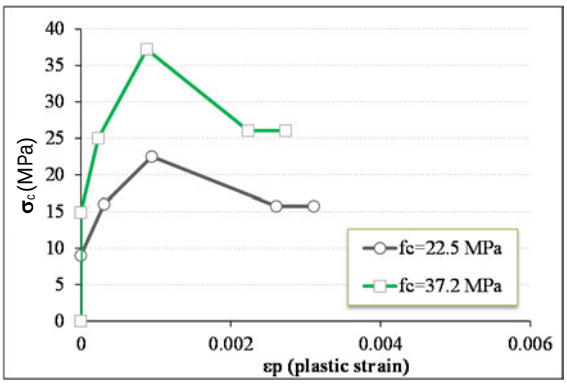

Figure 9-3: Concrete material characteristics of tested specimens

9.4.3 Failure ratios

From previous studies, it is found that the last two parameters α3 and α4 do not have a significant influence on the outcome of an analysis, specifically in terms of load-deflection response. Nevertheless, different values of α3 and α4 were examined and no effect resulted. Therefore, the default values provided by ABAQUS are adopted and used for all specimens.

To obtain a good prediction of the first cracking load, the failure ratio α2 needs to be carefully set. As a first trial, the experimental α2 values resulting from the compression and splitting tensile tests on concrete cylinders, see Table 9-1, were examined. As expected, it was found that (see Figure 9-4: specimen SC10-D12) the use of the experimental failure ratio α2=0.12 yields higher cracking load. Many trials were made to find the appropriate values and the final α2 results are presented in Table 9-1. It should be mentioned that the use of a lower concrete tensile strength through concrete specimens (concrete cylinders) can be ascribed to the variability of concrete as well as the size effect. Lower values were also used by other researchers [for example Zhao (1999); Al-Sunna (2006); El-Ghandour et al. (2003); and Guadagnini (2002)].

The resulting responses of the analyses are plotted in Figure 9-4 in comparison with the test PTMS specimens. It should be noted that, as expected, the model for the WD beams failed in flexure due to concrete crushing. The failure mechanism of the model WD beam is shown in Figure 9-4 for specimen SC10-D12.

Table 9-1: Experimental and analytical failure ratios α2

	f'_c = 22.5 MPa	f'_c = 37.2 MPa
Failure ratio (α2) – test	0.12	0.076
Failure ratio (α2) – Analysis	0.05	0.03

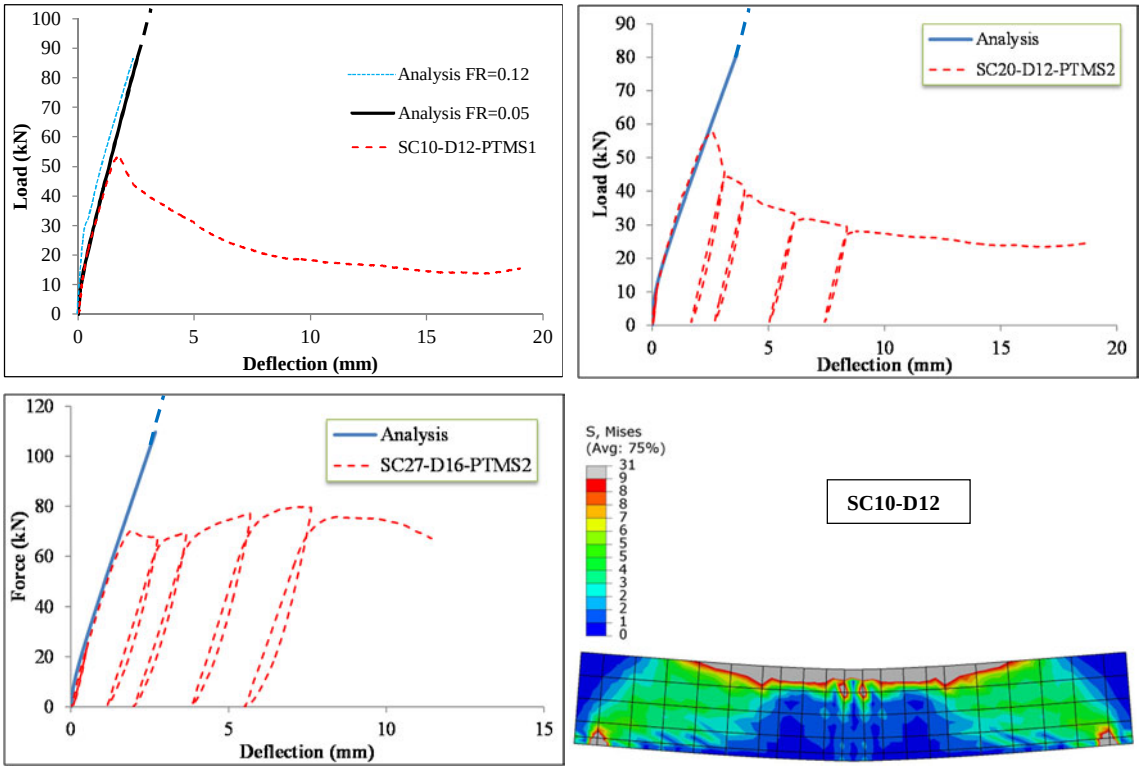

Figure 9-4: Test results versus analyses of the WD specimens

9.4.4 Input force-slip models for the deficient specimens

The steel-to-concrete connection within the splice zone is modelled using nonlinear springs allowed to stretch only in the horizontal direction. Spring behaviour is described in terms of internal force and relative displacement. The internal force is calculated based on the bond stress distribution along the distance between two springs. The relative displacement represents the slip of the bar.

To distribute the spring force, the mid springs were assigned an average force-slip relation of double that of the ends, as shown in Figure 9-5. Figure 9-6 shows the force-slip relation used for selected specimens.

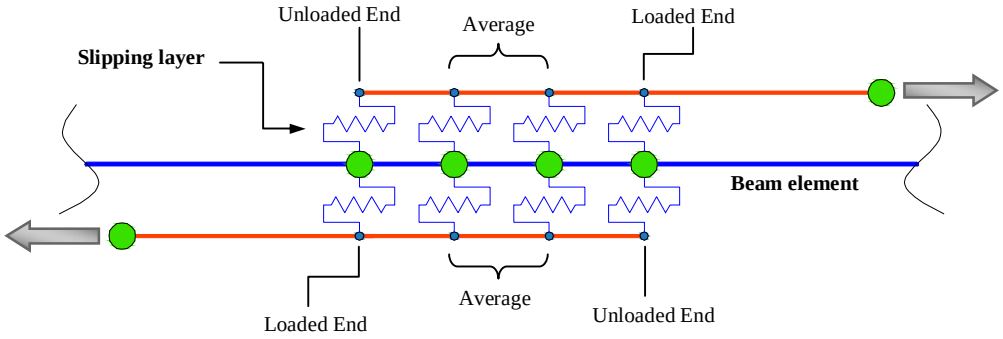

Figure 9-5: Bond-slip simplification adopted for the slipping layers

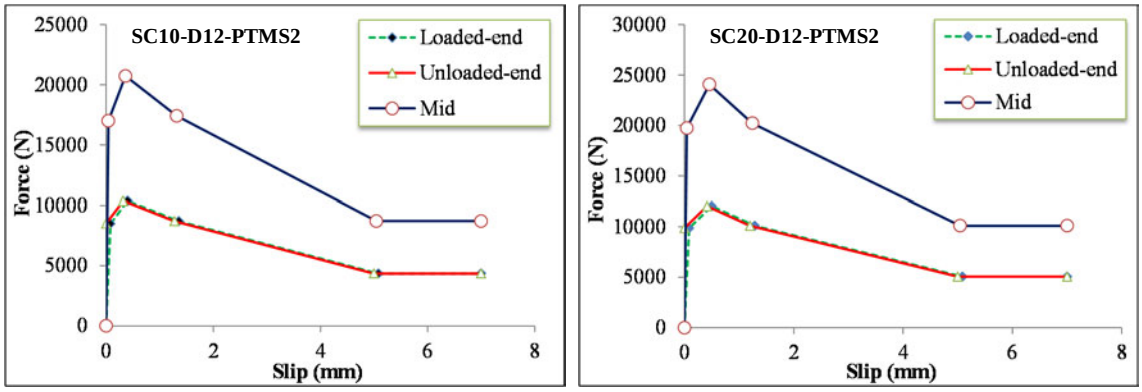

Figure 9-6: Characteristic force - slip curves introduced in the springs (four-spring layer)

The appropriate number of springs is also dictated by the capability of ABAQUS to produce reliable solutions. The use of very small embedment lengths prevents ABAQUS from converging into a solution. This is a well-known limitation in concrete FE analysis modelling, which does not produce good results for elements with dimensions less than three times the aggregate size.

A layer consisting of four (giving 3.33 of the bar diameter) and seven (giving 1.67 the bar diameter) springs were tried. Consequently, it is found that both sets produce exactly the same solution. However, more refined bond distributions are the only difference, as can be seen from Figure 9-7 for specimen SC20-D12-PTMS2; distributions are given up to the maximum load.

As the use of 7-spring solution was more difficult to converge in many cases, the 4-Spring solution was adopted.

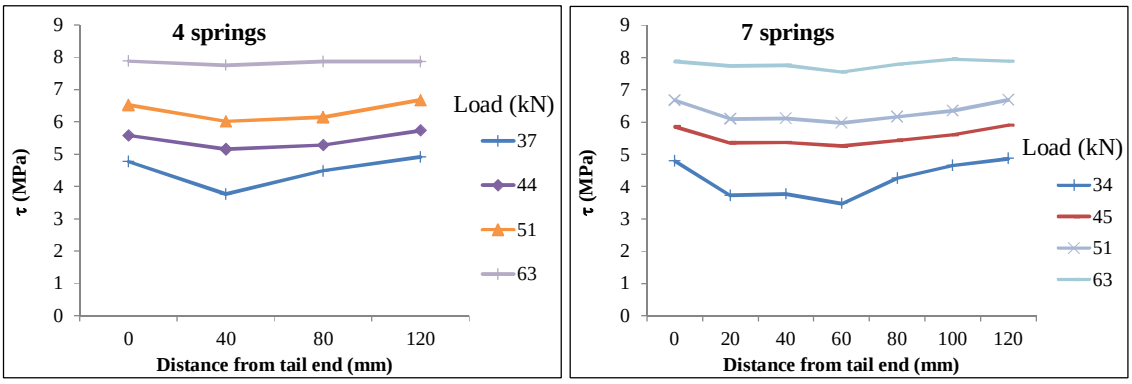

Figure 9-7: Bond distributions along the splice of specimen SC20-D12-PTMS2 using different number of springs

It should be mentioned that the test results were used as inputs for the unconfined, internally confined, and SC27-D16-P1&2 specimens. The proposed bond-slip model was used for the other PTMS specimens.

9.4.5 Results of the FE Model

As designed, all model beams failed due to bond failure mechanism within the splice zone due to pullout of one set of the spliced bars. All model beams showed the same mode of failure regardless of the type of confinement. The analytical failure mechanism of specimen SC20-D12-PTMS1 at the ultimate state is shown in Figure 9-8. As can be seen from the figure, the damage took place locally at the splice interface. The experimental mode of failure of the same specimen SC20-D12-PTMS1 is shown in Figure 9-9. It can be seen from the figure that the FE model gives a good representation of the damage state in the splice zone. However, as expected in an ideal failure case, the damage interface of the FE is always located at the slip interface. In the experiments, nonetheless, the slip interface has the tendency to shift to the end of the notch or inside the splice zone, based on the first dominant crack developing in the test. As can be seen in Figure 9-10, the slip interface of specimen SC20-D12-PTMS2 shifted to the mid splice length. The FE model is not capable of capturing this phenomenon.

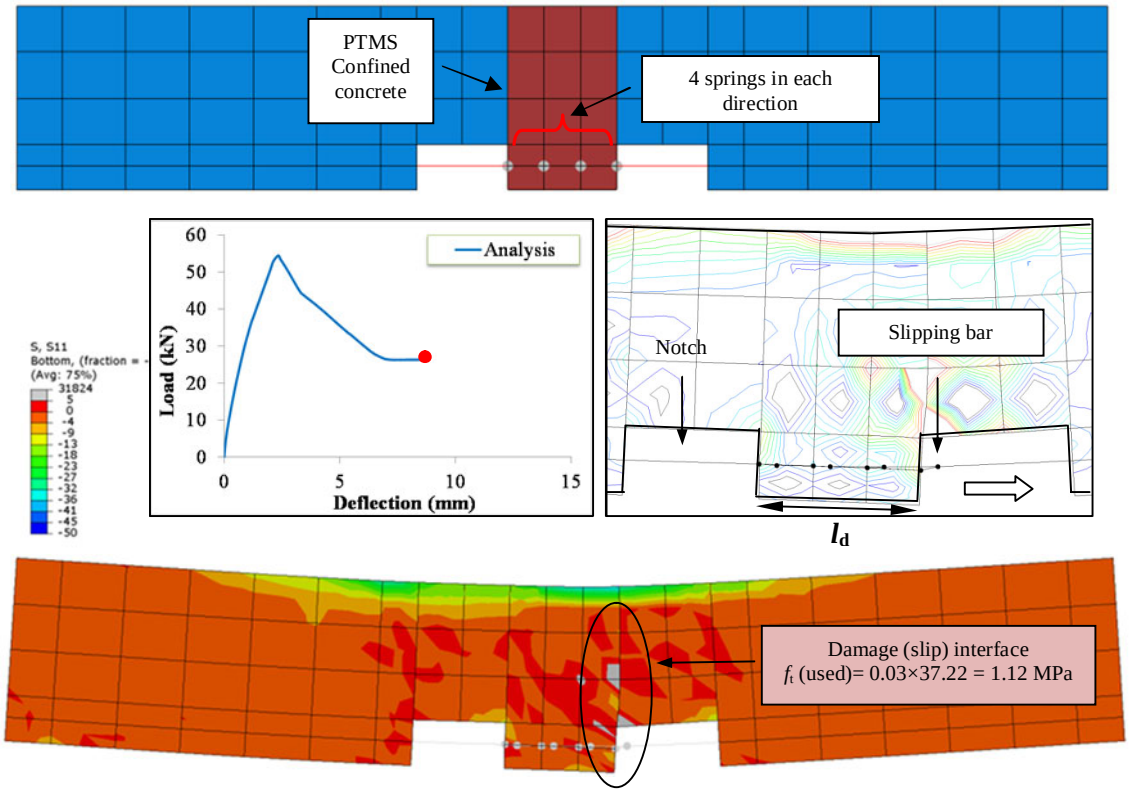

Figure 9-8: Final failure mechanism of the FE model (SC20-D12-PTMS1)

a) Failure of specimen at the end of the test b) Failure mode after removing strips

Figure 9-9: Failure mode of the test specimen SC20-D12-PTMS1

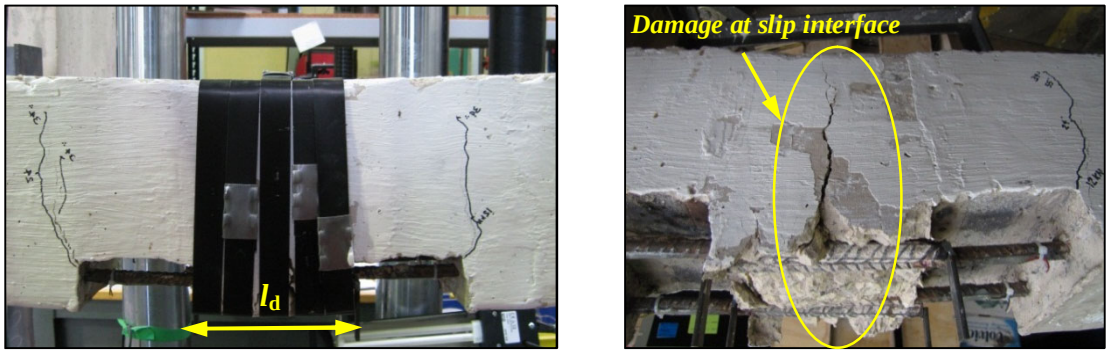

a) Failure mode at the end of the test b) Failure mode after removing strips

Figure 9-10: Failure of the test specimen SC20-D12-PTMS2

The analytical total load-midspan deflections of the beams in Group I, II and III are compared to the experimental results in Figure 9-11 through Figure 9-13, respectively.

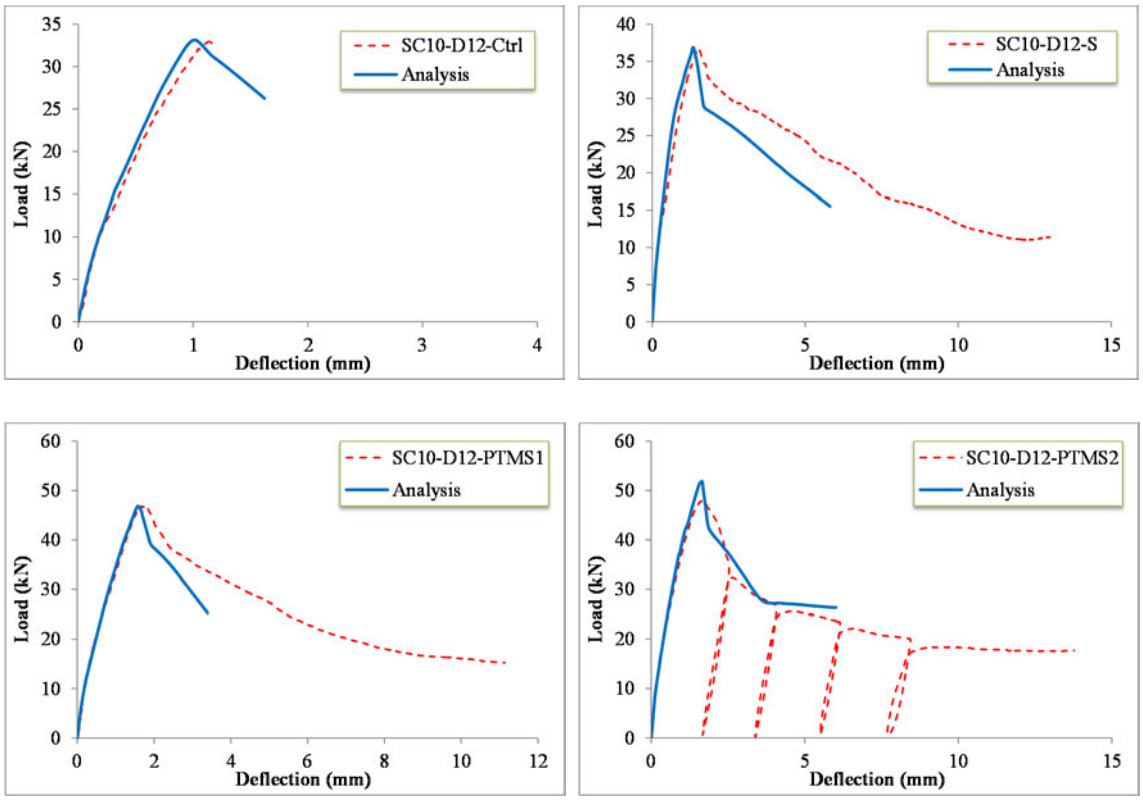

Figure 9-11: Load-midspan deflections of the tested and model beams - Group I

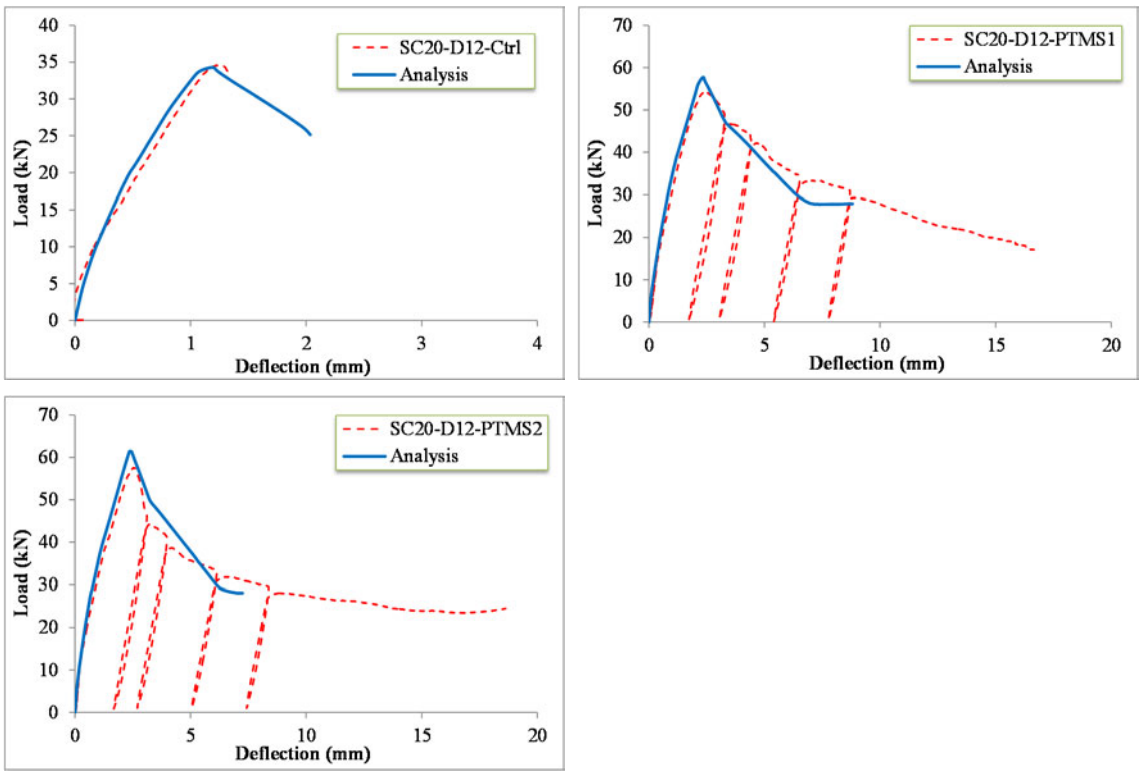

Figure 9-12: Load-midspan deflections of the tested and model beams - Group II

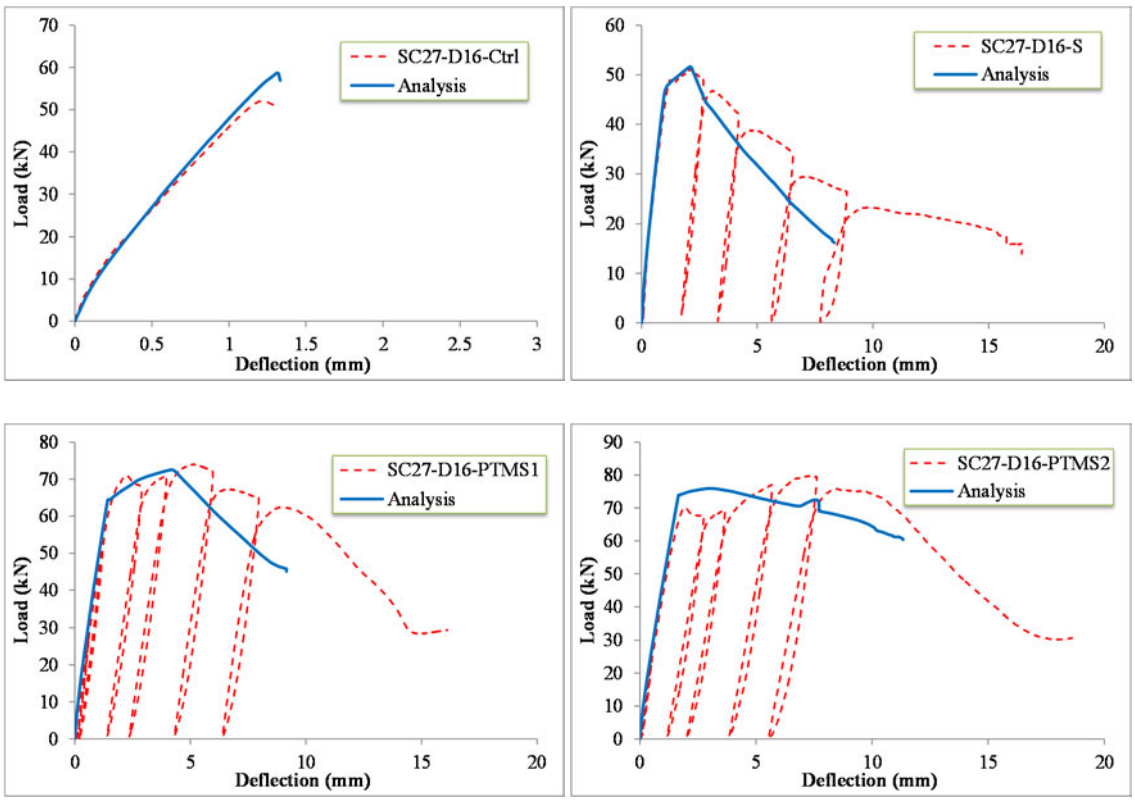

Figure 9-13: Load-midspan deflections of the tested and model beams - Group III

As can be seen from the figures, the FE model simulates the experimental response reasonably well up to the maximum load; which is the most significant part of the response. The initial stiffness is also well represented. In the post-peak stage, on the other hand, the FE model mostly results in a stiffer response than the experimental one. The use of the smeared crack approach is somewhat responsible for the inaccuracy of the post-peak response, as the behaviour is dominated by local cracking. Despite this, the FE analysis successfully captures the post-peak response of some specimens (for example SC10-D12-PTMS2 and SC20-D12-PTMS2). In these cases, however, the FE model tends to level off at slightly lower deflections than the experimental ones (i.e. stiffer response).

It should be noted that the analytical response mirrors the shape of the corresponding bond-slip model. This is due to the fact that the behaviour of the FE model is governed by the stiffness of the nonlinear springs.

The measured peak load and corresponding mid-span deflections of the tested specimens are compared to those from FE predictions in Figure 9-14. As can be seen, the load and deformation capacities are captured well in the model. For specimen SC27-D16-PTMS1&2, the FE model gives good prediction of the load, but the corresponding deflection is underestimated.

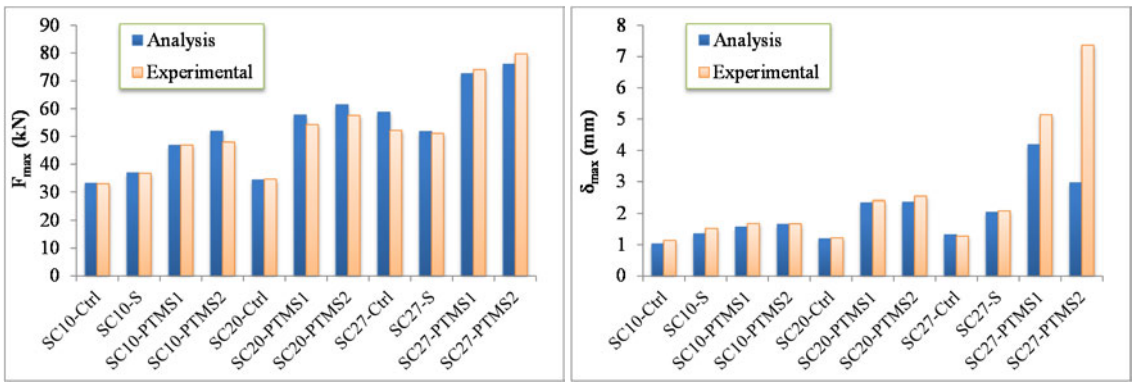

Figure 9-14: Comparison of analytical to experimental maximum loads and deflections

9.5 PHASE II: FE MODELLING OF MEDIUM SCALE BEAMS IN TENSION

9.5.1 General description of the model

9.5.1.1 Well-designed specimens

The model geometry of a specimen with continuous reinforcement is shown in Figure 9-15. Only half the specimen is modelled for simplicity. The general model comprises two layers of elements along the beam height (1 element @ concrete cover thickness and 2 elements along the beam effective depth). Three meshing regions are used along half the span: 1) a beam end region beyond the support @ 100 mm long element; 2) the shear span region with 85.22 mm long elements; 3) the region between the load point and midspan with three elements @95.75 mm. The element mesh is selected from different meshes that converged into a stable solution. The flexural reinforcement at the top and bottom is modelled as embedded rebar layers according to the specified concrete cover. The shear reinforcement is also modelled as an embedded layer of vertical rebars @ 100 mm spacing. The load is applied as increasing general steps at a distance of 383 mm from the midspan. The midspan is only allowed to move vertically. The support is modelled as a roller in the horizontal direction.

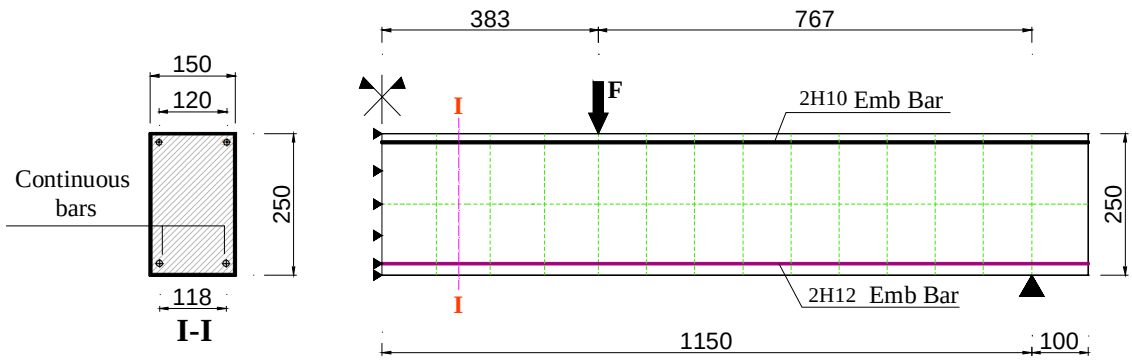

Figure 9-15: Geometry of the well-designed specimens (half beam, mm)

9.5.1.2 Deficient specimens

Similarly to the deficient specimens of Phase I, the entire specimen is modelled in this case. The model geometry of these specimens is shown in Figure 9-16. The model contains three layers of elements along the beam height (1 element @ concrete cover thickness and 2 elements @ half the effective depth of the beam). Seven meshing regions are used along the span: 1) two beam end regions beyond the supports @ 100 mm long element; 2) the shear span regions with 85 mm long elements; 3) the regions between the load point and splice end with 58.25 mm elements for splice length L_d of 300mm and with 45.75 mm for L_d of 400 mm; and 4) the splice region with 50 mm long element. The element mesh was selected from different meshes that converged into a stable solution.

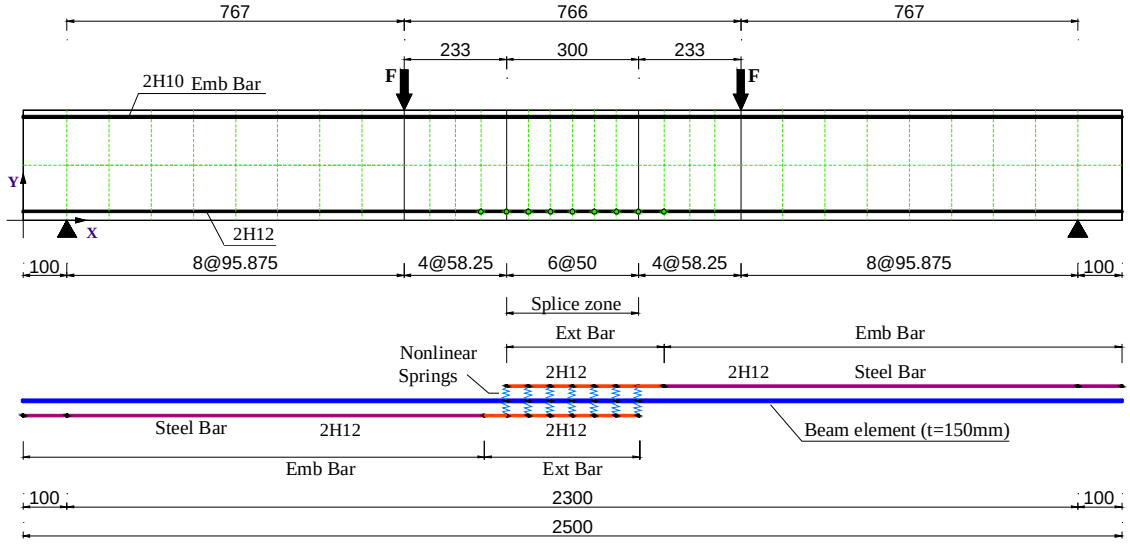

Figure 9-16: The geometry of tested deficient beams (units: mm)

As shown in the figure, the reinforcement of the specimen is modelled with different techniques based on the location of the bars within the specimen as follows:

- The reinforcing bars outside the splice region are modelled as embedded rebars in the concrete elements (concrete property).
- The lap splices are modelled using one-dimensional truss elements with uniaxial stiffness only. Two layers of truss elements are used with a distance from the bottom side equal to the concrete cover.
- The top reinforcing bars in compression are embedded along the entire beam length with a distance of 15 mm from the top side.
- The shear reinforcement within the shear span is modelled using embedded rebars in the vertical direction of the concrete elements spacing @ 100 mm.

The restraints as well as loading conditions are similar to those of the well-designed specimens.

9.5.2 Concrete compression model

The material characteristics resulting from tests on cylinders are used for the input model in ABAQUS. The characteristics of the concrete material used are shown in Figure 9-17, which presents the compressive stress- plastic strain curves of the plain concrete.

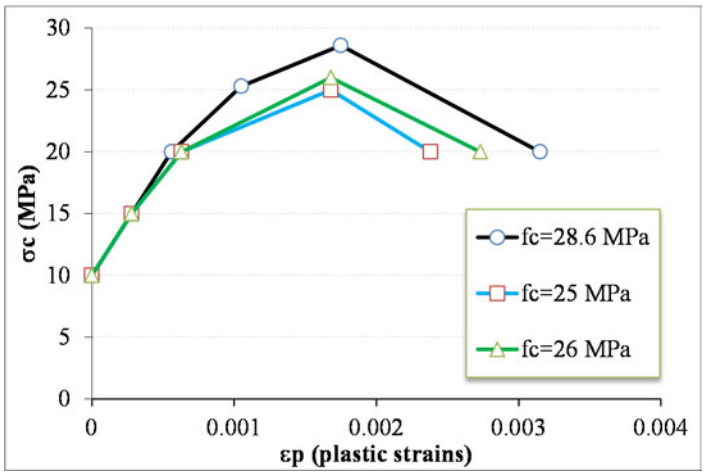

Figure 9-17: Concrete material characteristics of tested specimens

9.5.3 Failure ratios

Also in this test phase, a good prediction of the first cracking load requires a careful consideration of the failure ratio α2. From the compression and splitting tensile tests on concrete cylinders, the α2 values are calculated and presented in Table 9-2. These values are used as first trials in the FE analyses. The analytical results of specimens with continuous reinforcement in comparison with the experimental responses are shown in Figure 9-18. Similarly to Phase I, it can be seen from the figure (specimen LC20-D12) that the adoption of the experimental values resulted in a higher cracking load. The appropriate values for α2 were found by conducting many trials. The final α2 values are presented in the same table. It should be mentioned that the failure of the WD specimens was due to concrete crushing at the midspan. It can also be observed from the analyses that the WD model captured well the capacity of the beams that reached yielding.

Table 9-2: Experimental and analytical failure ratios α2

	LC10-D12-WD	**LC20-D12-WD**	**LC27-D16-WD**
Failure ratio – test	0.087	0.088	0.083
Failure ratio – Analysis	0.07	0.05	0.05

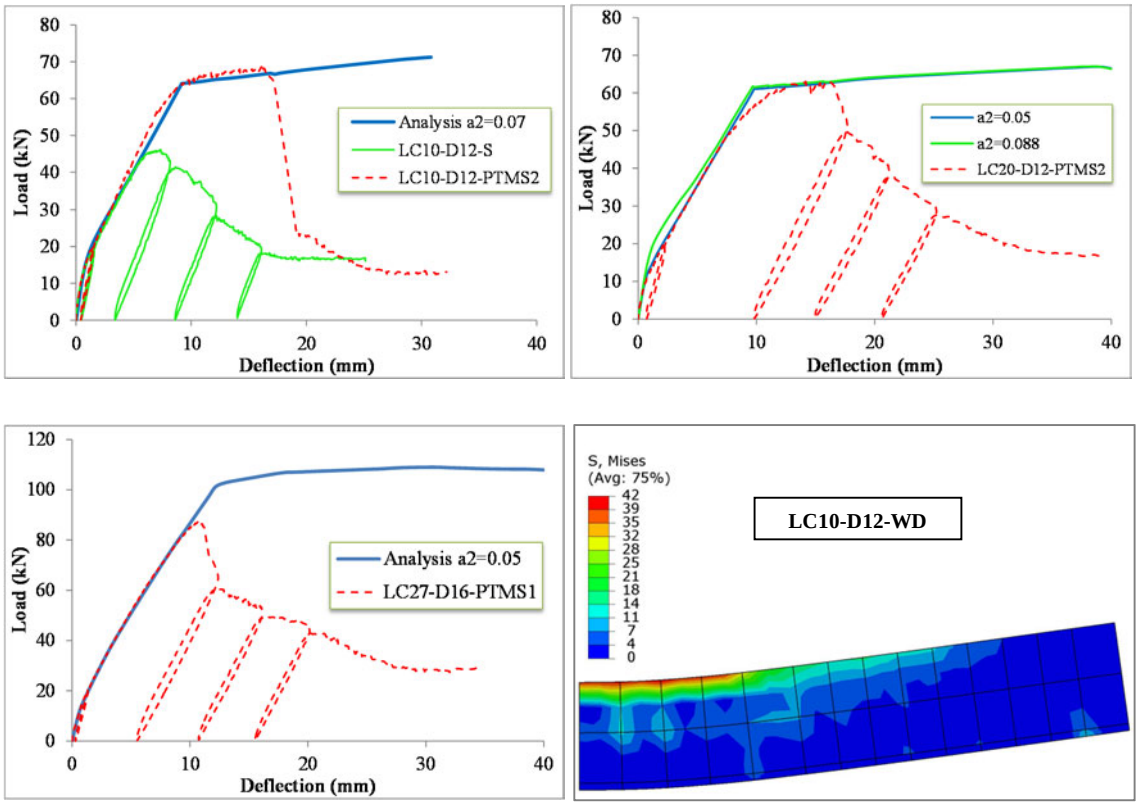

Figure 9-18: Test results versus analyses of the WD specimens

9.5.4 Input force-slip models

Similarly to Phase I, the spring characteristics are defined in terms of force-displacement. Sets of springs comprising four, seven and thirteen nonlinear springs were tried on the model with the same simplifications for force-slip inputs, as shown in Figure 9-19. From the analyses, it was observed that the use of four springs underestimated slightly the experimental results, as shown in Figure 9-20 for specimen LC27-D16. The use of seven and thirteen springs, on the other hand, produced reliable predictions of the load and deformation capacities. The use of thirteen springs, however, was difficult to converge into a solution in most of the specimens. Consequently, it was decided to use 7 springs along the spliced bar. The input force-slip models of selected specimens are shown in Figure 9-21. The end springs had half the force capacity of the mid springs. Elongation of the spliced bars was considered directly in the input models.

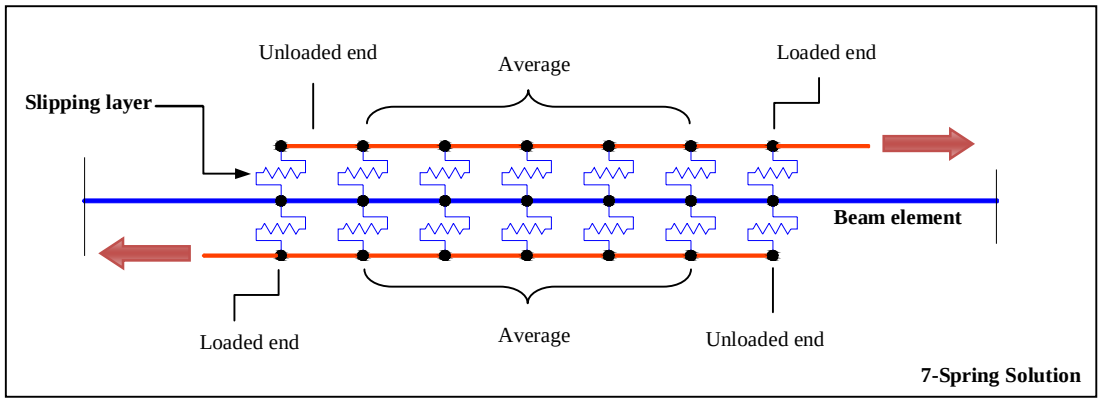

Figure 9-19: Simplification adopted for the force-slip relations

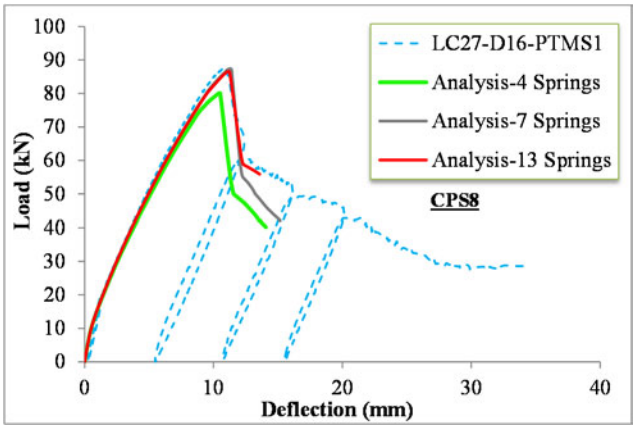

Figure 9-20: Response of specimen LC27-D16-PTMS1 using different sets of springs

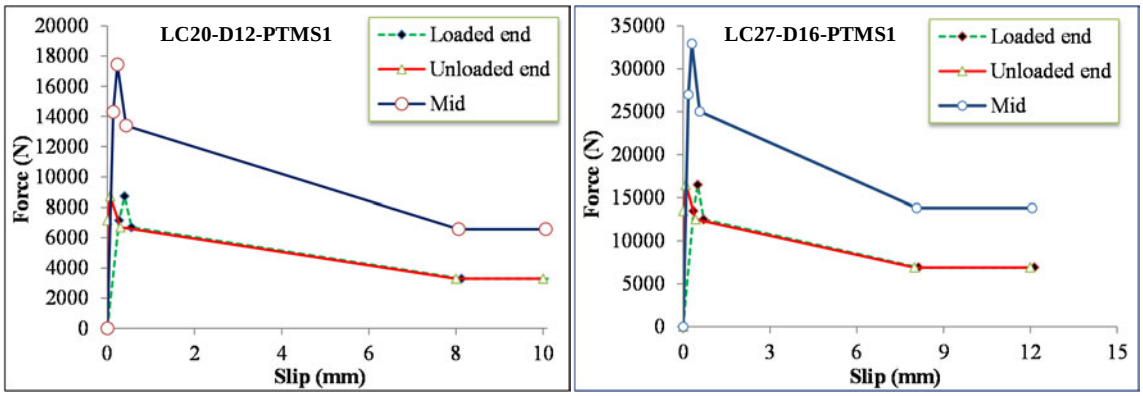

Figure 9-21: Force-slip curves used for the nonlinear springs of two selected specimens

9.5.5 FE Results

- **Failure modes**

The mode of failure of the model beams are due to bond failure within the splice zone, with a slip interface located at the end of the splice. A typical failure mode is shown in Figure 9-22 for specimen LC20-D12-PTMS1. The failure mode of the corresponding experimental specimen is shown in Figure 9-23. It can be seen that the FE model represents well the damage observed from the test. This is the case for most of the test specimens in this test series. A shift in the slip

interface is likely to occur in the test, as explained previously for specimen LC20-D12-S and LC27-D16-Ctrl.

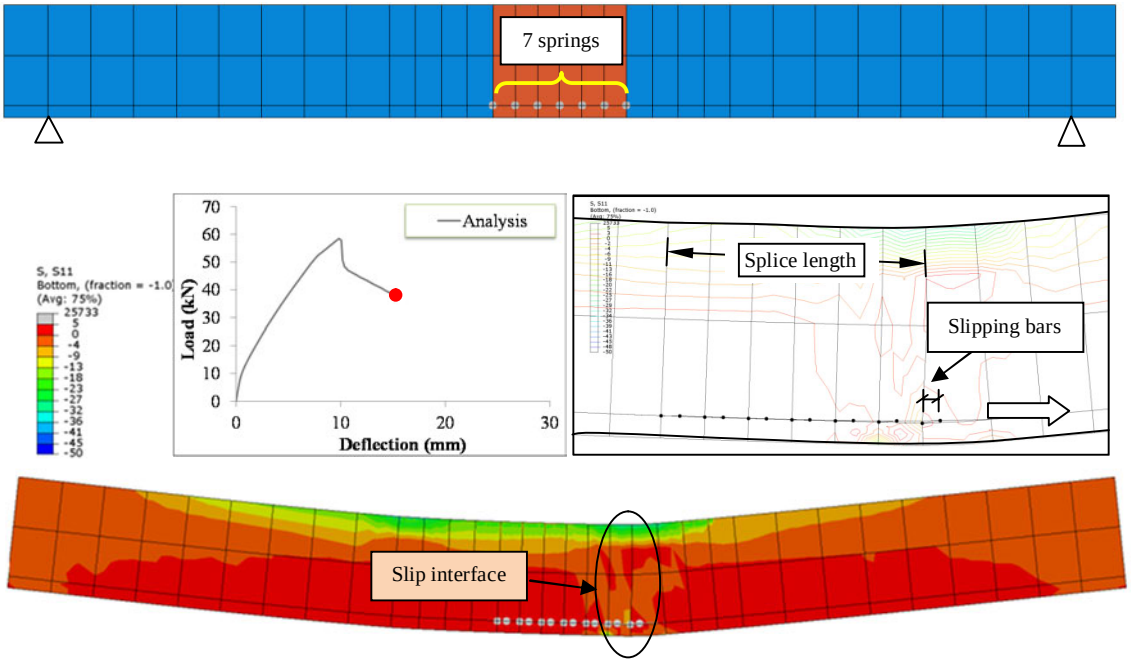

Figure 9-22: Mode of failure of the FE model of specimen LC20-D12-PTMS1

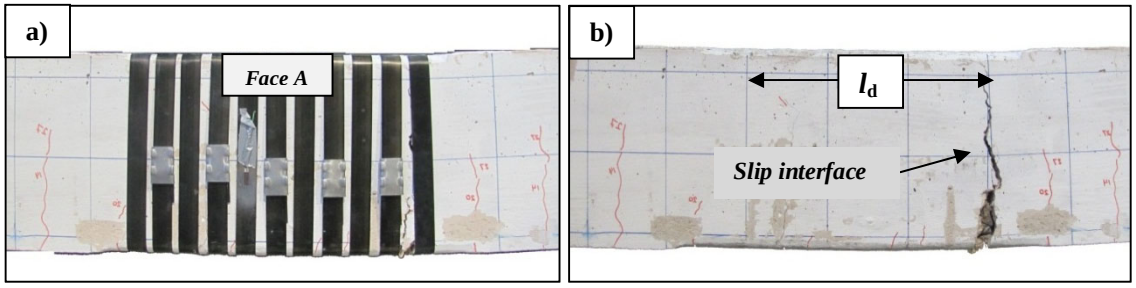

Figure 9-23: Mode of failure of the test specimen LC20-D12-PTMS1 a) before and b) after removing the confining strips of the splice zone

- **Load deflection response**

The load mid-span deflection resulting from the FE analyses are compared to the experimental results in Figure 9-24 through Figure 9-26 for Groups I, II and III, respectively. In most of the cases, the pre-peak response was predicted well in the model. The use of modelling element CPS8R improved slightly the response of specimen LC10-D12-PTMS2. Due to divergence issues in the FE model, the entire post-peak response was difficult to capture in all specimens for the reasons mentioned earlier in Phase I. However, it seems that the model simulates well the response in most of the PTMS specimens. The use of 7 springs in specimen LC27-D16-PTMS1 tends to underestimate the post-peak response after the rapid drop in the response. The use of 13 springs in the specimen shows a better representation of the response. The measured peak load and associated mid-span deflections are compared to those from the model in Figure 9-27. As can be seen, a good estimation of the test data is found.

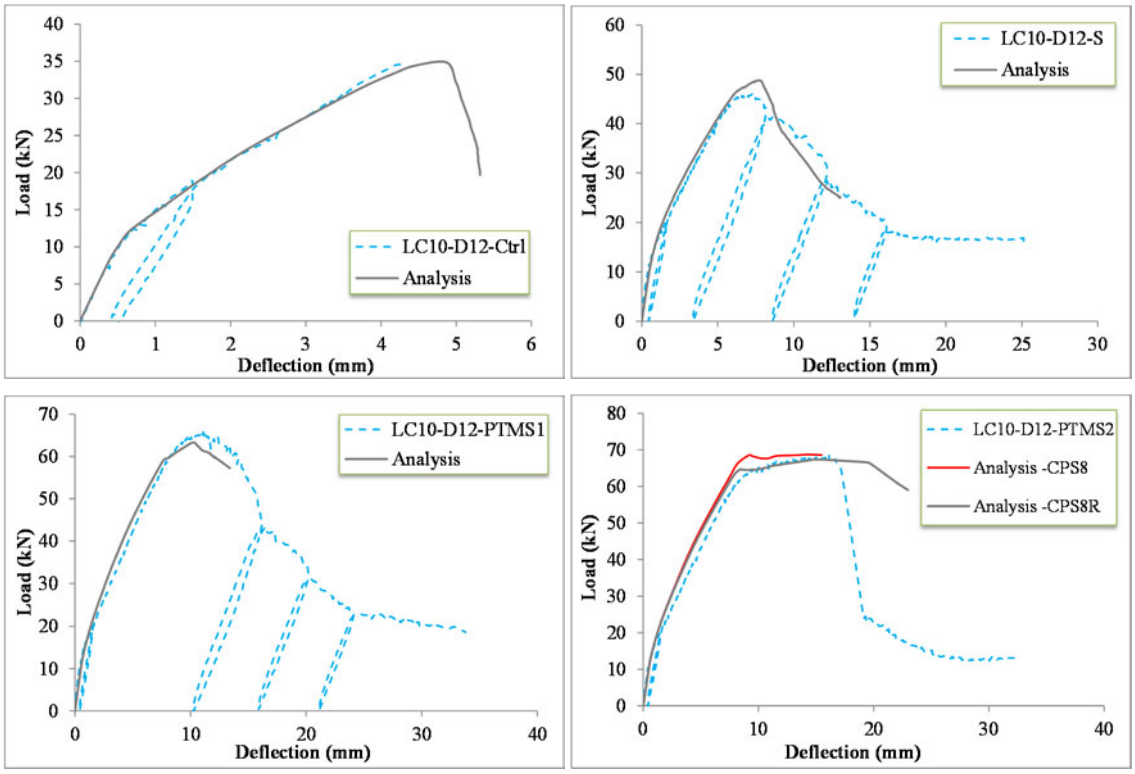

Figure 9-24: Load-midspan deflections of the tested and model beams - Group I

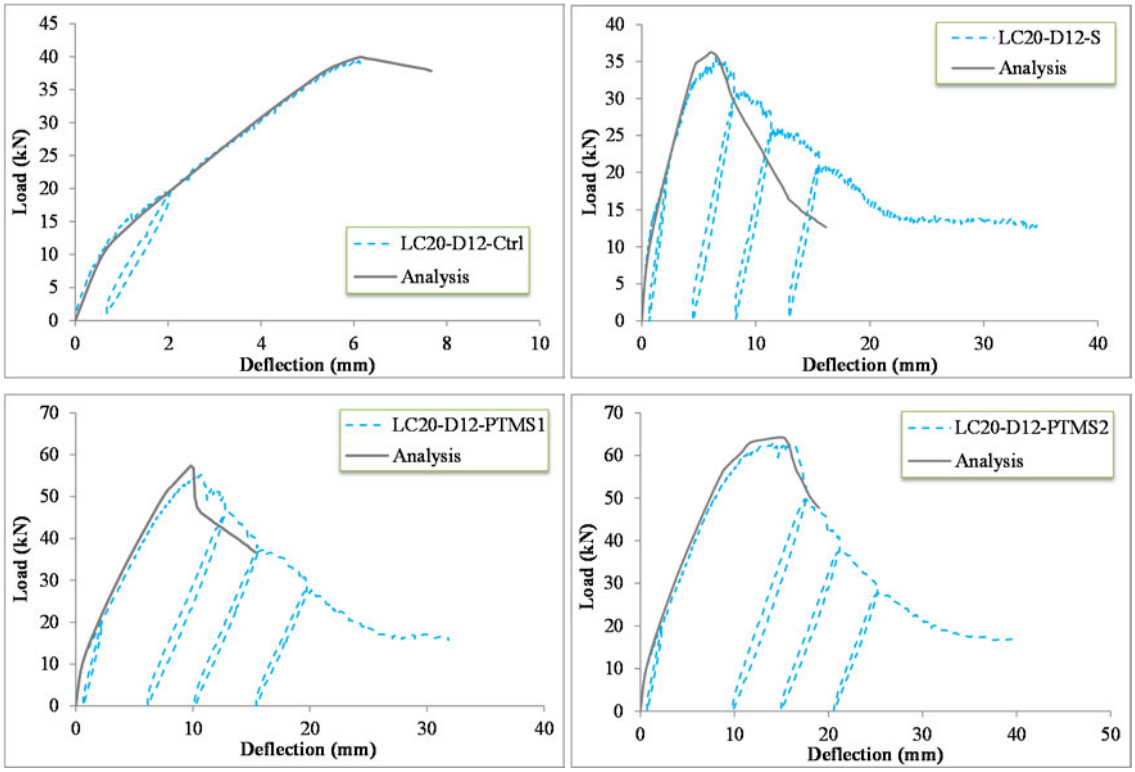

Figure 9-25: Load-midspan deflections of the tested and model beams - Group II

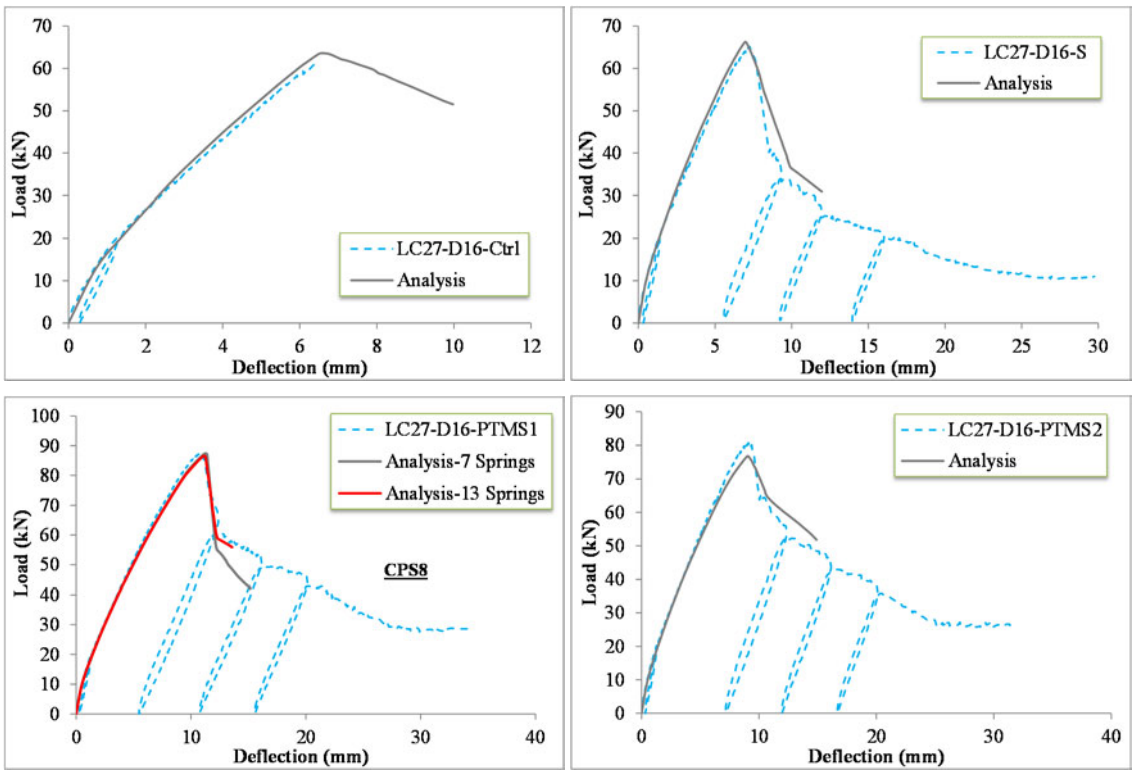

Figure 9-26: Load-midspan deflections of the tested and model beams - Group III

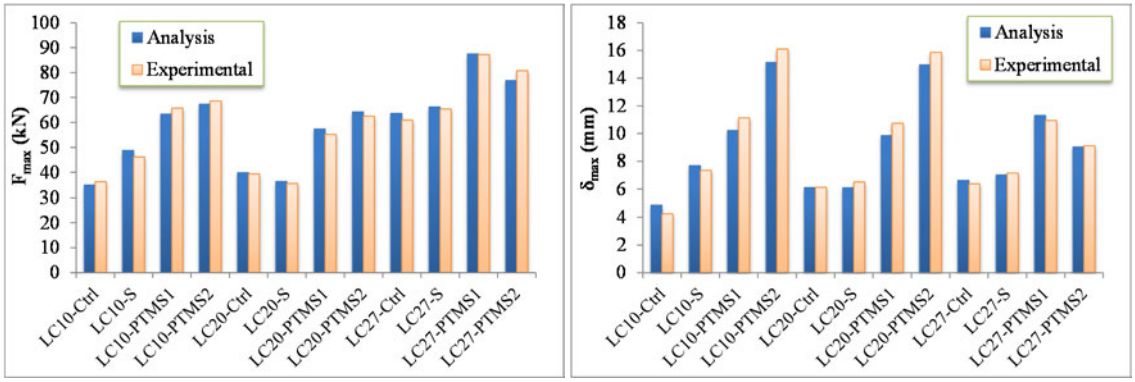

Figure 9-27: Comparison of analytical to experimental maximum loads and deflections

9.6 CONCLUSIONS

In this chapter, an attempt has been made to use FE analysis to simulate the behaviour of concrete beams with bond deficiency in the mid flexural region in order to verify the ability of this method to capture the deficient response and failure mechanisms in the RC beams. ABAQUS 6.9, a commercially available finite element code, is employed in the analyses. The results of the numerical study are compared to the experimental data obtained during the first (I) and second (II) phases of the experimental work. Although the numerical analysis yielded satisfactory results in terms of load-deflection response up to the maximum load, some problems occurred in the post-peak stage. This is expected when dealing with beams having local damage (crack concentration). In the model, after the maximum capacity is reached, damage and cracks are localised within the splice zone (at slip interface), which in turn prevents

the formation of uniform cracks along the model. In such cases, the assumptions of the smeared crack model are somewhat difficult to satisfy. It is reported that in cases when the failure is dominated by development of a single crack, the adoption of a smeared crack model is hard to capture the phenomenon [Ayoub and Filippou (1998), Ayoub and Filippou (2001)]. Despite this fact, the FE simulations performed in this study were successful, in many cases, to provide stable solutions with an acceptable level of accuracy, especially for test specimens in Phase I.

Chapter 10

MODELLING OF BEAM-COLUMN JOINTS

10.1 INTRODUCTION

This chapter presents the modelling of RC beam-column connections subjected to cyclic lateral loads. The modelling process explicitly incorporates joint shear behaviour, as well as other appropriate inelastic behaviour occurring at the connection interfaces, namely, flexure and bond. A simplified joint shear stress-strain model is proposed to simulate shear deformations of the panel zone. The model is also suitable for predicting the nonlinear behaviour of PTMS confined exterior joints.

A simplified multi-spring scissors model is used for simulating deformational components of the panel zone. The model was incorporated in nonlinear static as well as cyclic analyses of the test specimens. Finally, results of the static and cyclic analyses are compared with the test results.

10.2 JOINT SHEAR DEFORMATIONS

Shear deformations of the core can be calculated from the LVDT system mounted on the joint region (9, 10), as shown in Figure 10-1.

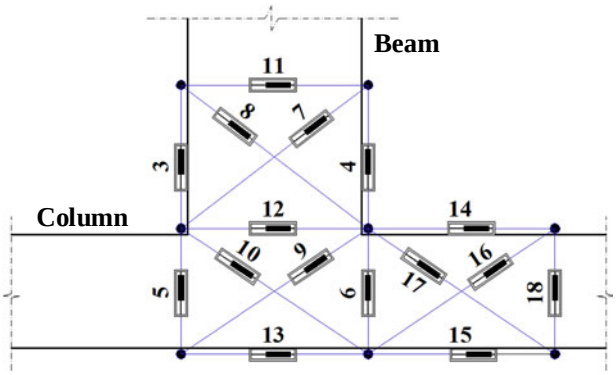

Figure 10-1: LVDT system mounted on the joint region

When only shear forces act on the joint panel, shear deformations can be derived from geometry, as illustrated in Figure 10-2, as follows:

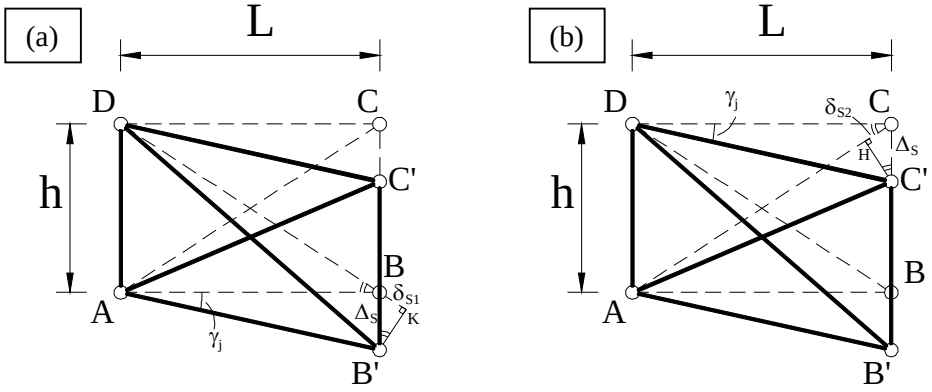

Figure 10-2: Shear deformations of the joint region (Guadagnini, 2002)

From Figure 10-2(a), and by utilising the similarity between the triangles Δ(BKB′) and Δ(DAB), the relationship between shear deformations (Δ_s) and diagonal deformations (δs_1 - lengthening) can be obtained from the following:

$$\Delta_s = (\delta_{s1})\frac{d}{h} \tag{10-1}$$

where d represents the length of the diagonal (DB).

Also, from Figure 10-2(b), and by considering similarity between the triangles Δ(CC′H) and Δ(CDA), the relationship between shear deformations Δ_s and diagonal deformation (δs_2 - shortening) can be given by the following:

$$\Delta_s = -(\delta_{s2})\frac{d}{h} \tag{10-2}$$

By adding both deformations from the previous equations and rearranging in terms of the shear deformations, Δ_s, the following equation is obtained:

$$\Delta_s = (\delta_{s1} - \delta_{s2}) \frac{d}{2h} \tag{10-3}$$

10.3 RESULTS OF THE UNCONFINED JOINTS

The test results of the unconfined joints were calculated and compared with the ASCE 41-06 (2006) modelling parameters for RC beam-column joints. Specifically, the shear deformation angle parameters at the end of the peak strength, a, and at the collapse level, b, and the residual strength ratio, c, as defined in Figure 10-3, are compared to Tables 6-9 and 6-10 of ASCE 41-06 (2006) for nonconforming reinforcement (NC) of exterior joints. A joint is considered nonconforming if hoops are spaced at s > 1/3 of the column effective width within the joint, otherwise, the component is considered as conforming. The comparisons are shown in Table 10-1 and Figure 10-4.

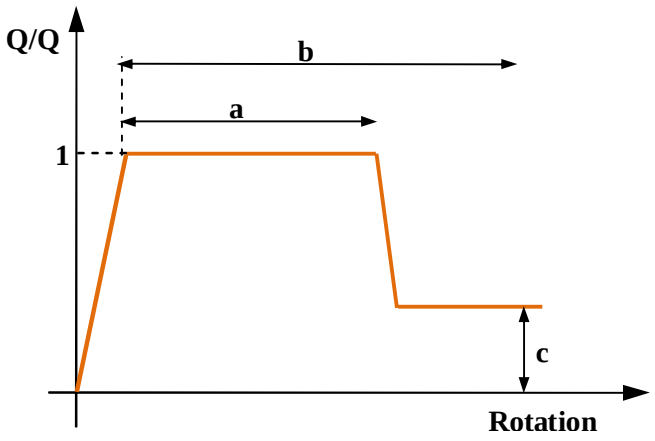

Figure 10-3: Modelling parameters definition in ASCE 41-06 (2006)

Table 10-1: Modelling parameters for specimens in comparison with ASCE 41-06

	V/V_n	$P/A_g f'_c$	a	b	c	$\pm\tau_j/\sqrt{f'_c}$
ASCE 41-06 (NC-Ext)	All	< 0.4	0.005	0.01	0.2	0.5
JA-1	2	0.091	0.0027	-	-	0.48
			-0.0057	-0.02	-0.33	-0.53
JA-3	1.58	0.114	0.0051	0.025	0.23	0.58
			-0.0056	-0.023	-0.257	-0.53
JB-1	1.77	0.072	0.00588	0.026	0.24	0.53
			-0.00097	-0.017	-0.26	-0.43
JC-1	1.81	0.082	0.00944	0.02	0.3	0.55
			-0.00447	-0.013	-0.4	-0.53

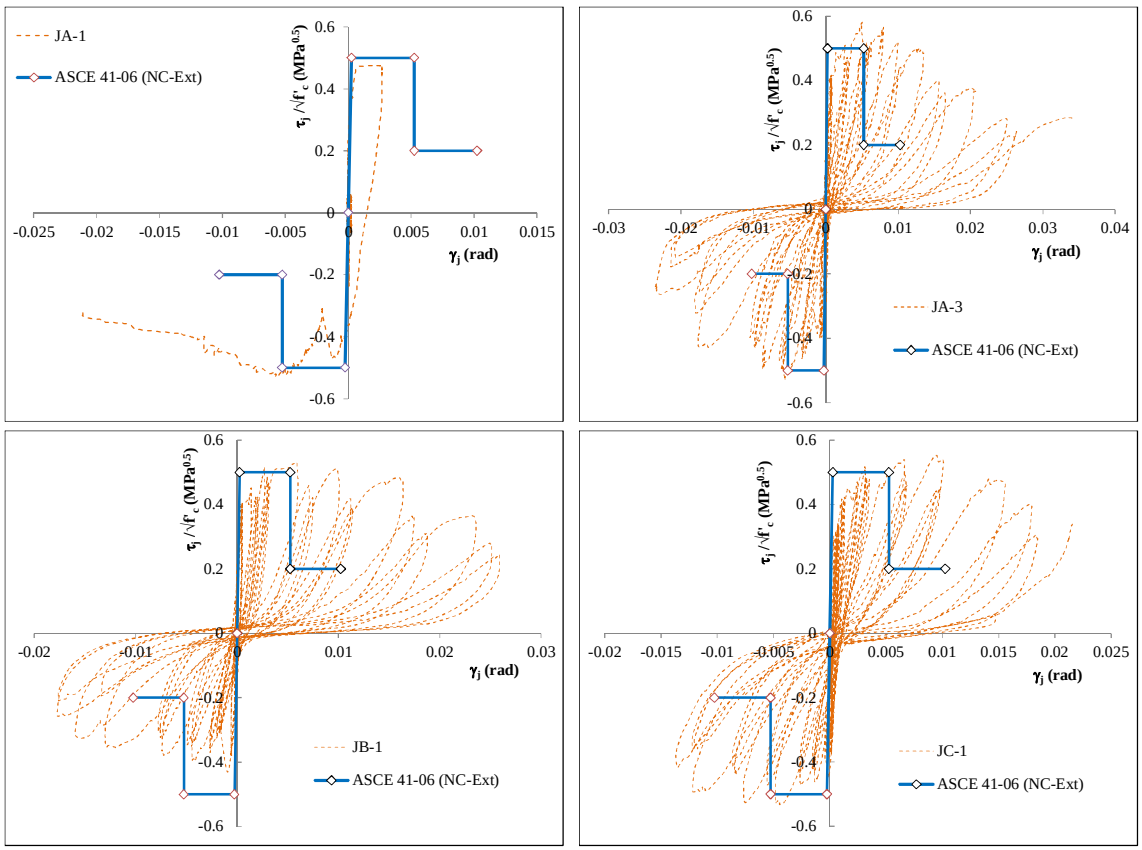

Figure 10-4: Shear stress-strain of the unconfined joints in comparison with ASCE 41-06 recommendations of exterior joints (Ext)

It is clear that the ASCE 41-06 provides good predictions of the peak shear stress for all unconfined joints. It is also clear that the shear strain at the peak stress is well predicted. However, the shear strain at failure (b) is massively underestimated. Moreover, it can be noted that the ASCE model considers a sharp drop in the response at the end of the peak stage which is very conservative in comparison with the actual response. The ASCE conservativeness, however, can be justified as it may represent poorer test conditions than the current tests. The residual stresses of the test results are also underestimated by about 25%.

Despite the fact that the ASCE 41-06 predicts the shear strength of the bare joints well, this cannot be taken as a general basis. To further investigate this point, a test data reported by Hassan (2011) on J-type joints under low and high axial load levels is used, as shown in Figure 10-5. The test data along with the results of the current study is compared to the ASCE 41-06 recommendations. It is clear from the figure that the normalised joint shear stress is influenced by the joint aspect ratio (h_b/h_c), where it decreases as the ratio increases. In addition, it is clear that the ASCE recommendations constitute a lower bound of the test results, which is also justified for safe assessment of such poor elements. In this study, the use of a high joint aspect ratio is a main reason for the low joint shear strength.

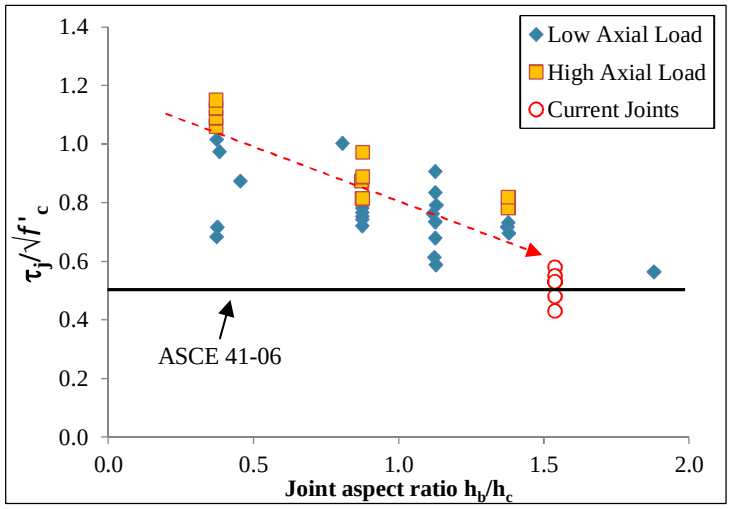

Figure 10-5: Comparison of joint tests with ASCE 41-06 recommendations

The maximum shear strength of the unconfined specimens is also compared to the results of the modified ACI strut-and-tie model by Hassan (2011). The comparison is made for the J-failure case. The results are presented in Table 10-2. In addition, Figure 10-6 presents comparisons of the predictions by Hassan (2011) model to those of a dataset on exterior joints reported by Hassan, along with the current dataset.

Table 10-2: Comparison of test results with the strut and tie models

	ACI-based Strut-and-tie model Hassan (2011)	**test** $+\tau_j/\sqrt{f'_c}$	**test** $-\tau_j/\sqrt{f'_c}$
JA-1	0.64	0.48	-0.53
JA-3	0.71	0.58	-0.53
JB-1	0.67	0.53	-0.43
JC-1	0.66	0.55	-0.53

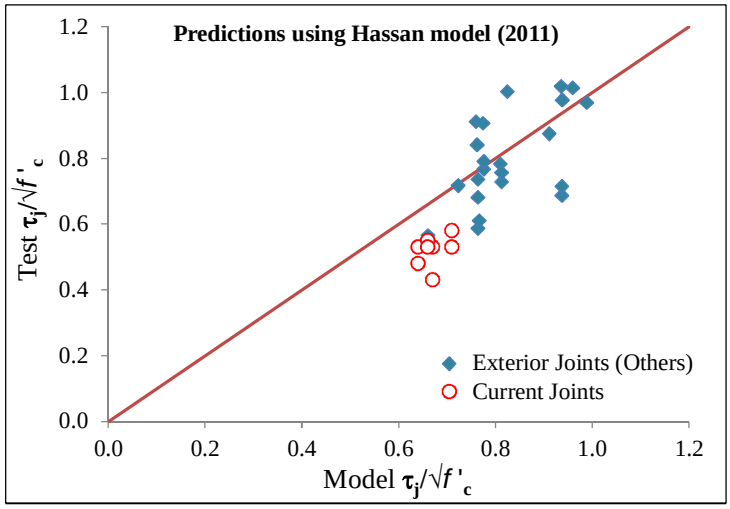

Figure 10-6: Comparison of joint test results with predictions using Hassan (2011) model

It is clear from the table and the figure that the predictions by the modified ACI model proposed by Hassan (2011) overestimate the test results by a ratio of (25%).

10.4 RESULTS OF THE STRENGTHENED JOINTS

By using the previous procedure, the experimental shear rotations of the test units JA-1PTMS and JC-1PTMS were also calculated. The normalised shear stress-strain curves of these two joints are presented in Figure 10-7 in comparison with the recommendations by ASCE/SEI 41 (2006) for conforming (C) and nonconforming (NC) transverse reinforcement of exterior joints. Table 10-3 also compares the modelling parameters a, b, c and τ_j of ASCE model and those from the tests. For test units JA-3PTMS and JB-1PTMS, only shear stresses are presented as no LVDT system was possible to be installed on the joint area.

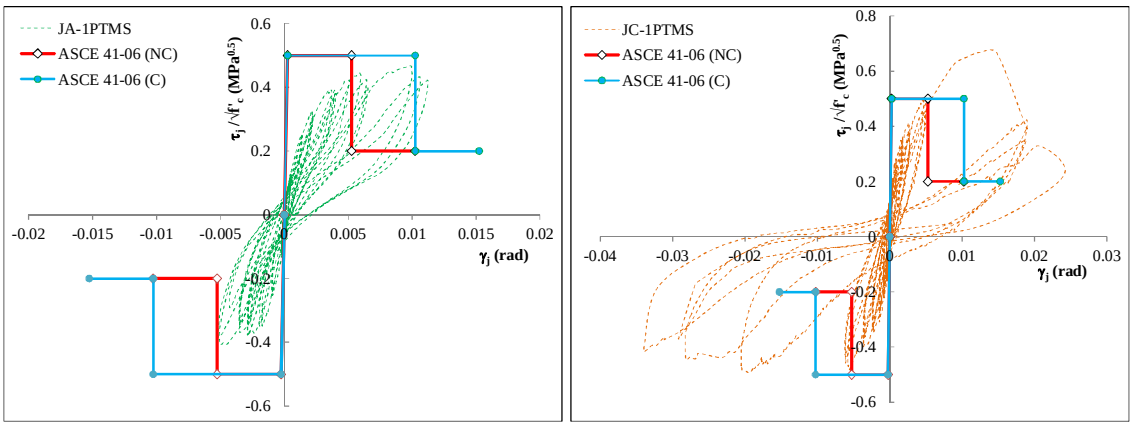

Figure 10-7: Principal tensile stress vs. shear rotation of the panel zone

Table 10-3: Modelling parameters for PTMS specimens in comparison with ASCE 41-06

	V/V_n	$P/A_g f'_c$	a	b	c	$\pm\tau_j/\sqrt{f'_c}$
ASCE 41-06 (NC-Ext)	All	< 0.1	0.005	0.01	0.2	0.5
ASCE 41-06 (C-Ext)			0.01	0.015	0.2	0.5
JA-1PTMS	1.32	0.091	0.01	-	-	0.47
			-0.0059	-0.02	-	-0.40
JA-3PTMS	1.27	0.114	-	-	0.36	0.70
			-	-	-0.26	-0.64
JB-1PTMS	1.06	0.072	-	-	0.34	0.68
			-	-	-0.20	-0.62
JC-1PTMS	1.05	0.082	0.014	0.025	0.26	0.67
			-0.01	-0.035	-0.26	-0.50

It is clear from the previous table and figure that the ASCE/SEI 41 model overestimates slightly the shear strength of the test unit JA-1PTMS but it is very conservative in predicting the shear

strength of the other specimens with a ratio of about 25%. It should be mentioned that the error in loading which occurred in the JC-1PTMS unit is responsible for the low shear strength and strain values in the pull direction. Also, it is worth mentioning that the unit JA-1PTMS was not tested to its maximum capacity which could explain why the ASCE model over-predicted the results. The shear strains at the peak stress for units JA-1PTMS and JC-1PTMS are very close to those by the ASCE model for conforming reinforcement. The shear strains at failure, on the other hand, appear to be largely underestimated by the ASCE (C) model. The initial stiffness of the test results is less than the predicted elastic stiffness. This could be attributed to the cracking at the cast interfaces within the joint area. More data is still required to verify the previous conclusions with relation to strains.

The shear strengths of the tested units are further compared to the strut and tie model, as seen in Table 10-4. As yielding was observed in some specimens, the results are compared with the BJ failure case considering yielding of the beam flexural reinforcement.

Table 10-4: Comparison of test results with the strut and tie models

	Strut-and-tie model Hassan (2011)	**BJ Failure (yielding case)**	**Test** $+\tau_j/\sqrt{f'_c}$	**Test** $-\tau_j/\sqrt{f'_c}$
JA-1PTMS	0.55	0.6	0.47	-0.40
JA-3PTMS	071	0.9	0.70	-0.64
JB-1PTMS	0.66	0.74	0.68	-0.62
JC-1PTMS	0.66	0.74	0.67	-0.50

From the table, it is interesting to note that the modified ACI model predicts well the results in the push (strong) direction. However, in the pull direction, the shear strength is overestimated slightly. The use of the BJ failure assumption leads to a slight overestimation of the results. This is expected as the joints failed shortly after yielding; in addition, yielding occurred slightly earlier than the expected nominal value.

10.5 SIMPLIFIED SHEAR STRESS-STRAIN MODEL

In the development of a shear stress-strain model for the confined case, the backbone curves of the joints were first established, as shown in Figure 10-8 through Figure 10-11. As nearly complete data is available from only two PTMS strengthened specimens, the data from the unconfined joints were used as guidance for more appropriate modelling.

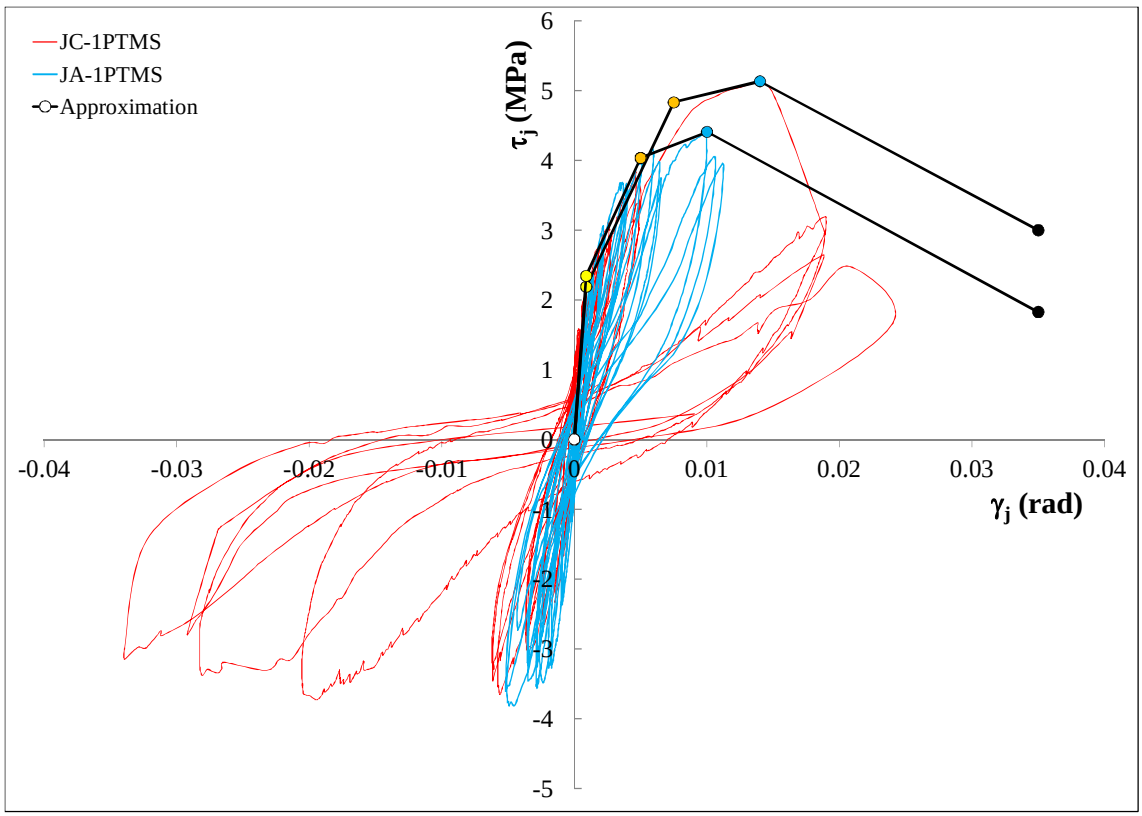

Figure 10-8: Shear stress-strain responses of the PTMS confined units

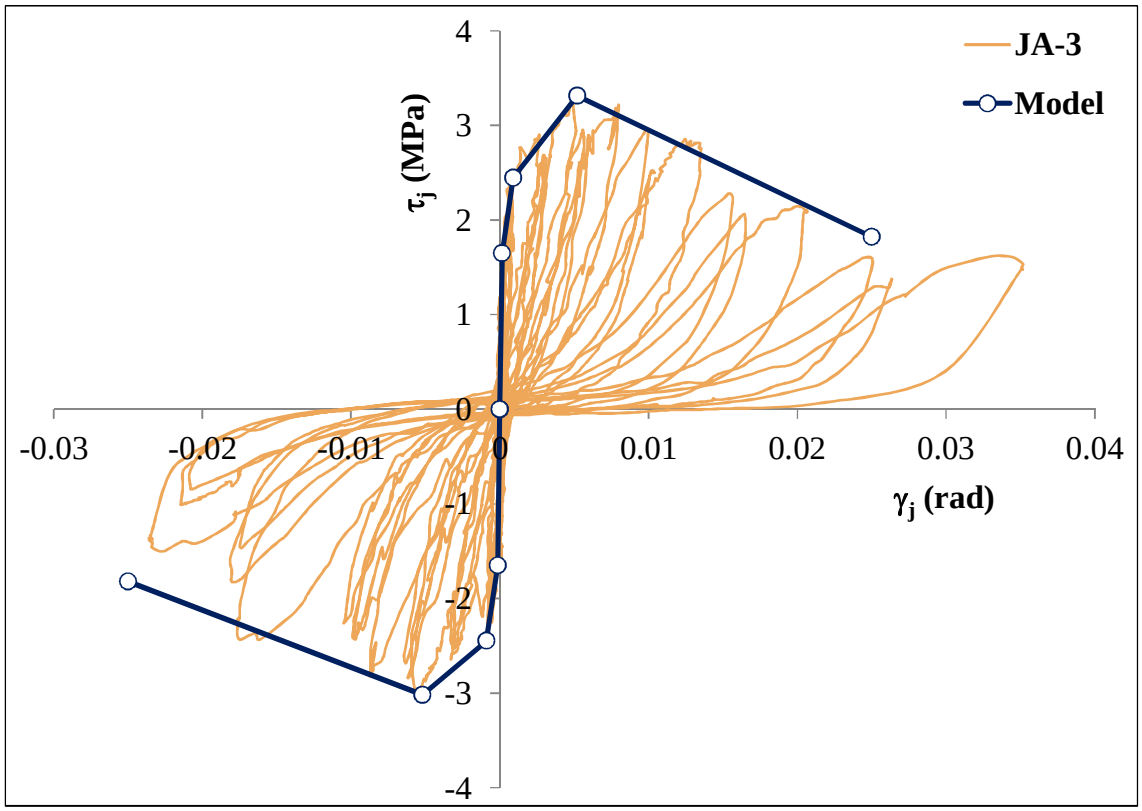

Figure 10-9: Shear stress-strain response of test unit JA-3 and model characteristics

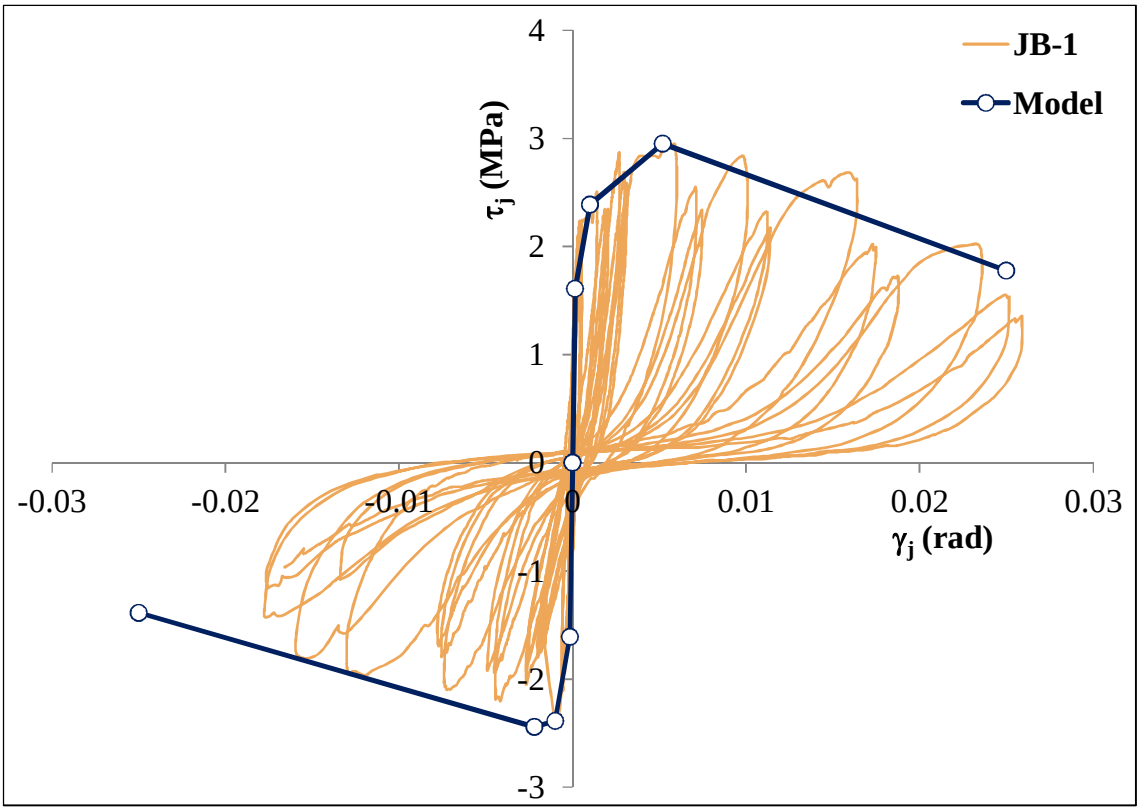

Figure 10-10: Shear stress-strain response of test unit JB-1 and model characteristics

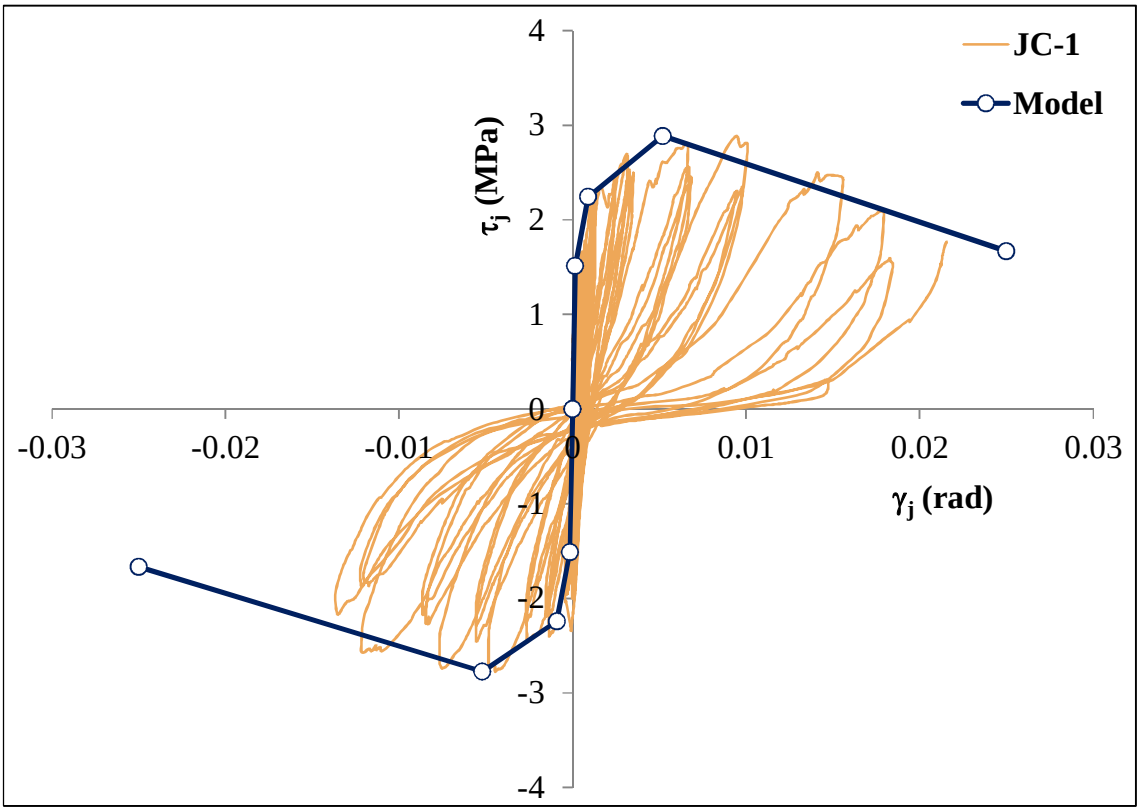

Figure 10-11: Shear stress-strain response of test unit JC-1 and model characteristics

Based on the test observations, the shear stress-strain response of the unconfined and PTMS confined units are divided into four distinct stages of behaviour. These stages are shown schematically in Figure 10-12 and are described below:

- (O-A): Initial elastic stiff response accompanied by initial cracking at the core corners and along the cast surfaces for the confined case. In addition, in this stage, hairline diagonal shear cracks form randomly within the core.
- (A-B): In this stage, major shear cracks develop along the diagonals of the core.
- (B-C): A shear mechanism develops within the core due to the formation of the X-cracking pattern.
- (C-D): Gradual degradation in the response associated with widening of shear cracks and formation of multiple major shear cracks along the compressive strut of the core.

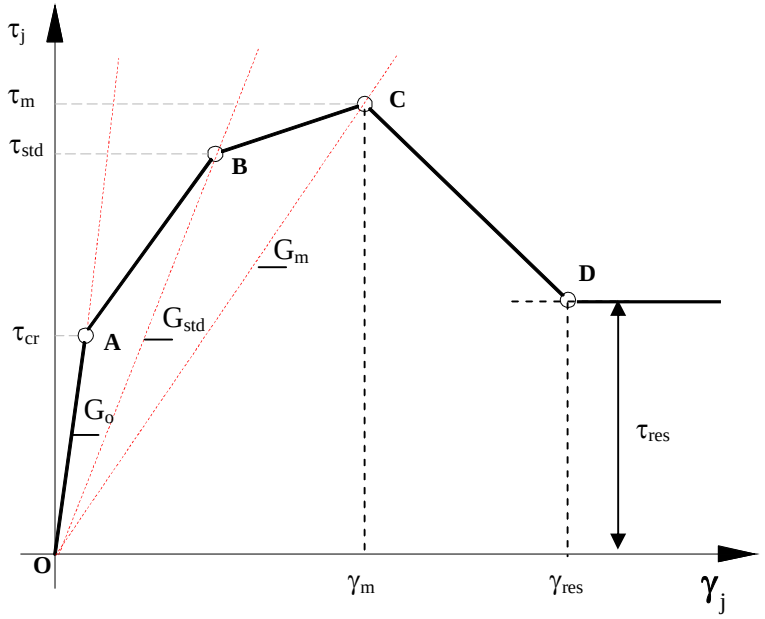

Figure 10-12: Idealised shear stress-strain of the PTMS confined joints

The modelling strategy is built based on the modified ACI model developed by Hassan (2011). However, a different joint failure mechanism is proposed by utilising failure criteria of nodal zones within a beam-column joint region. The proposed failure mechanism takes into consideration the use of variable anchorage lengths for the beam bars as well as the contribution of PTMS to joint strength. The following subsections quantify the performance points of the proposed model:

10.5.1 Cracking point (Point A)

- *Shear stress*

It is well established that the initial shear cracking strain of unconfined and confined concrete is different (Hassan, 2001). Nevertheless, as the PTMS applied to the joint area is not bonded to

the surface, the shear cracking stress is not expected to be restored. In fact, it is noted that the shear cracking stress occurs at the same level as that of the unconfined joints.

Sharma et al. (2011) assumed that the first cracking point (A) of the unconfined joints occurs at a principal stress of $0.29\sqrt{f'_c}$. However, this value is found to be very high compared to the test results in this study ($0.13\sqrt{f'_c}$ and $0.15\sqrt{f'_c}$ for unconfined and confined specimens, respectively). Pampanin et al. (2002), on the other hand, defined the first cracking to occur at a principal stress of $0.2\sqrt{f'_c}$ for exterior joints which is still 25% higher than the test results. Shin and Lafave (2004) observed that the joint shear stress at initial cracking varies largely with concrete strength and axial load. However, due to lack of consistency, stress values were not reported. Hassan (2011), on the other hand, suggested the use of equation (10-4), which was used by Uzumeri (1977) for unconfined joints. The equation was adopted from ACI 318-71 (1971), and considers the effect of the axial load as well as the concrete strength.

$$\frac{\tau_{cr}}{\sqrt{f'_c}} = 0.29\sqrt{1 + 0.29\frac{P}{A_j}} \qquad \leq 0.6\frac{\tau_m}{\sqrt{f'_c}} \qquad MPa^{0.5} \tag{10-4}$$

where P is the column axial load, in N; and A_j is the effective joint area, in mm^2.

Based on a parametric study conducted by Hassan (2011), it was found that the axial load affected the joint shear strength only at high load levels ($> 0.2f'_cA_g$), as shown in Figure 10-13. However, a limit of 60% the maximum shear stress was set on the previous equation by Hassan (2011) based on comparisons with databases of unconfined joints.

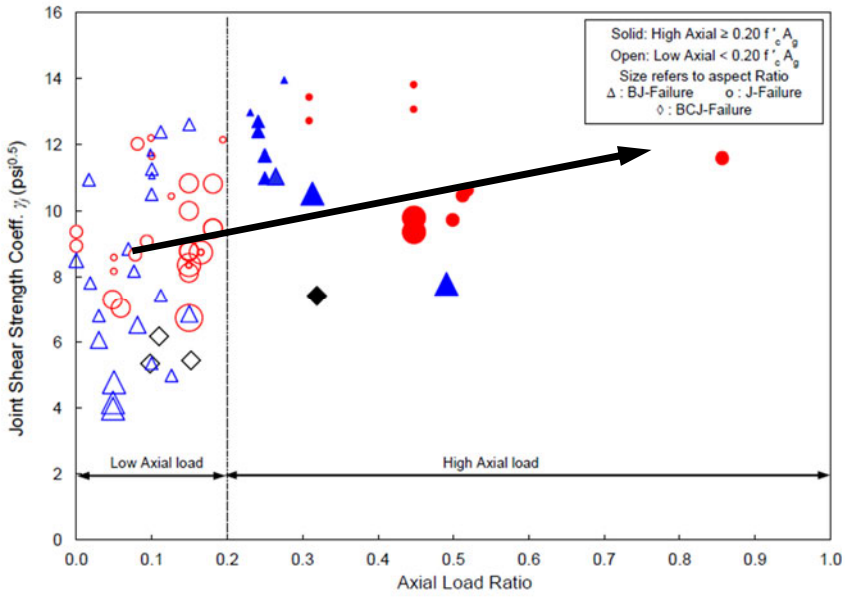

Figure 10-13: Effect of axial load on the shear strength of joints (Hassan, 2011)

In the tests of this study, the axial load was less than $0.2f'_cA_g$, and thus, no significant stress enhancement was noted on the cracking point. Specifically, the cracking point was found to be $0.29\sqrt{f'_c}$, which represented the lower bound of the previous equation (P=0).

Consequently, it can be suggested that for joints with low axial load levels (< 20% $f'_c A_g$), a cracking stress of about $0.29\sqrt{f'_c}$ can be used. For higher load levels, the previous equation can be used, considering the limit set by Hassan (2011).

- *Initial slope G_o*

The shear modulus G_o of the cracking point can be taken as G_c and $0.25G_c$ for the unconfined and PTMS-strengthened joints, respectively, where G_c is the shear modulus of concrete and is calculated by:

$$G_c = \frac{E_c}{2(1+\nu)} \tag{10-5}$$

where E_c and ν are the modulus of elasticity and Poisson ratio of concrete

The use of low initial shear modulus was reported by Hassan (2011) and Anderson et al. (2008), where it was taken as $0.5G_c$ for plain unconfined concrete. Hassan as well as Anderson et al. attributed this reduction to micro-cracking of concrete. However, the current study shows that the full elastic modulus G_c can be used for unconfined joints, as suggested by most researchers and codes of practice such as Sharma (2011), ASCE/SEI 41 (2006), ACI 318-08 (2008), and Pantelides et al. (2002), among others.

The use of lower initial stiffness for the pre-damaged strengthened joints can be attributed to the reopening of existing cracks between the old and new concrete.

10.5.2 Diagonal cracking of the core (Point B)

- *Shear stress*

Based on the test results, the shear stress τ_{std} at which the main diagonal shear cracks develop can be taken as $0.85\tau_m$ for the unconfined joints and $0.9\tau_m$ for the confined joints.

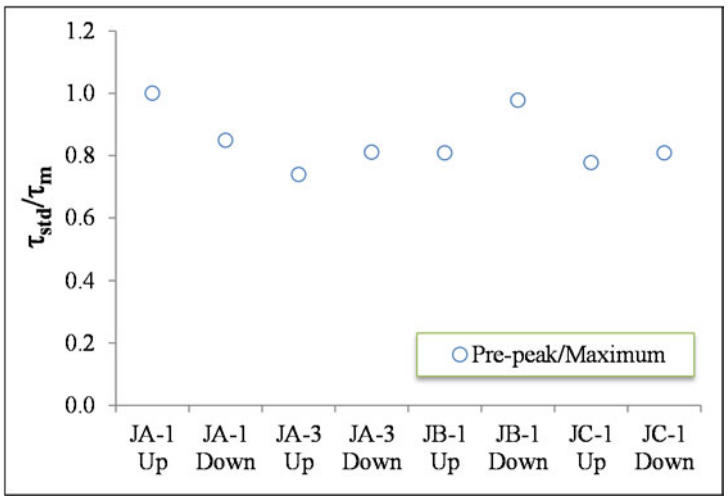

Figure 10-14: Ratio of the pre-peak to the maximum shear stress of the unconfined joints

Shin and Lafave (2004) reported that the shear stress for the pre-peak point before the joint strength is reached represents 90% of the maximum joint stress. Hassan (2011) also proposed a lower limit on the pre-peak point at 90% of the maximum joint shear stress. However, he gave different values based on the type of joint failure and the level of axial load. For example, in joints with J-type failure, the shear stress is taken as $0.0002G_c$ and $0.00025G_c$ for the downward (top bottom bars in tension = push) and upward (bottom beam bars in tension = pull) loading directions, respectively. While in a BJ-type failure with high axial load, the pre-peak shear stress in the downward direction was taken as 90% of the maximum joint stress.

- *Secant slope G_{std}*

Based on the test results, the secant slope G_{std} can be taken as $0.23G_c$ for unconfined joints and $0.04G_c$ for strengthened (pre-damaged) joints. In fact, the values were found to be well consistent for all units. Hassan (2011) used a secant slope value of $0.1G_c$ from his test results.

10.5.3 Peak strength (ACI 318-08 based model) (Point C)

- *Shear stress (General Case)*

The ACI-based approach developed by Hassan (2011) is adopted as a basis for determining the joint shear strength, as it offers a simple strut-and-tie model which considers different softening coefficients and can accommodate various confinement conditions. In addition, the model predictions are found to be close to the test results. The ACI-based model, however, does not appear to consider the effect of different beam anchorage cases; this is addressed in the proposed model. A single diagonal strut is assumed to transfer the shear forces in the joint region. The strut is pinned on two nodal zones within the joint region, as shown in Figure 10-15.

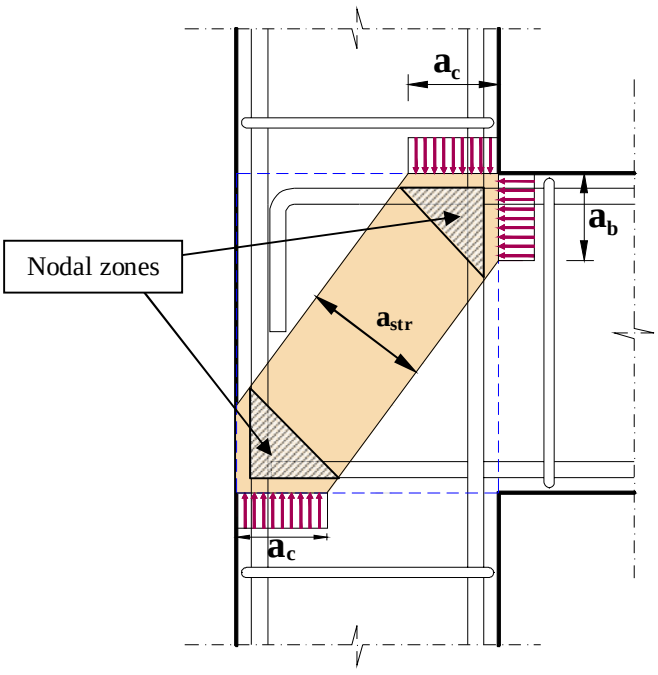

Figure 10-15: Nodal zones of a diagonal strut in the joint area

According to ACI, the nodal zone by definition is "*the volume of concrete around a node that is assumed to transfer strut-and-tie forces through the node*". Three forces at least are required to satisfy the equilibrium of a nodal zone, as shown in Figure 10-16. The presence of ties or confinement within the joint area results in an extension of the nodal zone, as shown in the same figure.

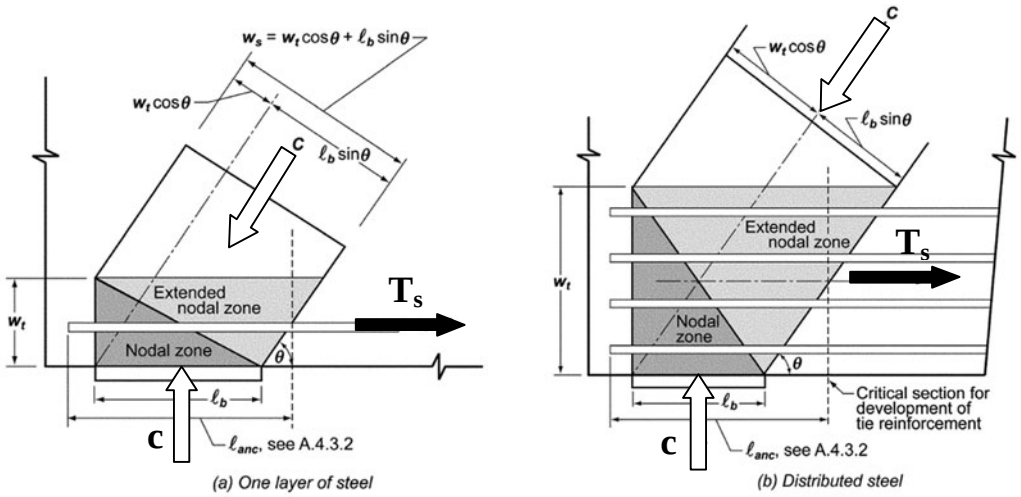

Figure 10-16: Nodal zones (ACI 318-08, 2008)

Instability of the nodal zone is considered as a failure criterion of the strut and corresponds to the joint maximum strength.

The nominal compressive strength of a strut without longitudinal reinforcement can be calculated as follows:

$$D = A_{str} f_{ce} \tag{10-6}$$

where A_{str} and f_{ce} are the minimum strut area and effective strut compressive stress, respectively, and can be calculated by:

$$f_{ce} = 0.85\beta_s f_c' \tag{10-7}$$

$$A_{strut} = a_{str} b_j \tag{10-8}$$

where β_s is a concrete softening coefficient taken equal to 0.6 for unconfined joints; a_{str} is the strut width; b_j is the effective joint width defined by ACI 352R-02.

The ACI-based approach considers that the failure always occurs due to crushing of a well stabilised strut. Thus, the strut width is calculated considering the compressive depths of beam and column sections. This is true in the case of interior joints. In the case of exterior joints, however, failure most probably takes place at the external side of the strut due to instability of forces at the nodal zone. Even if a proper hook exists, it was observed from the current tests that the strut might exert a force on the reinforcement at the outer corner of the core, which in turn

might rotate causing spalling of concrete at the back of the joint. This phenomenon is also in agreement with the findings by Hakuto et al. (2000) and Wong and Kuang (2008).

Thus, the minimum strut width in an exterior joint is assumed to occur at the external side of the core and is affected by the anchorage detail, as shown in Figure 10-17(a) & (b).

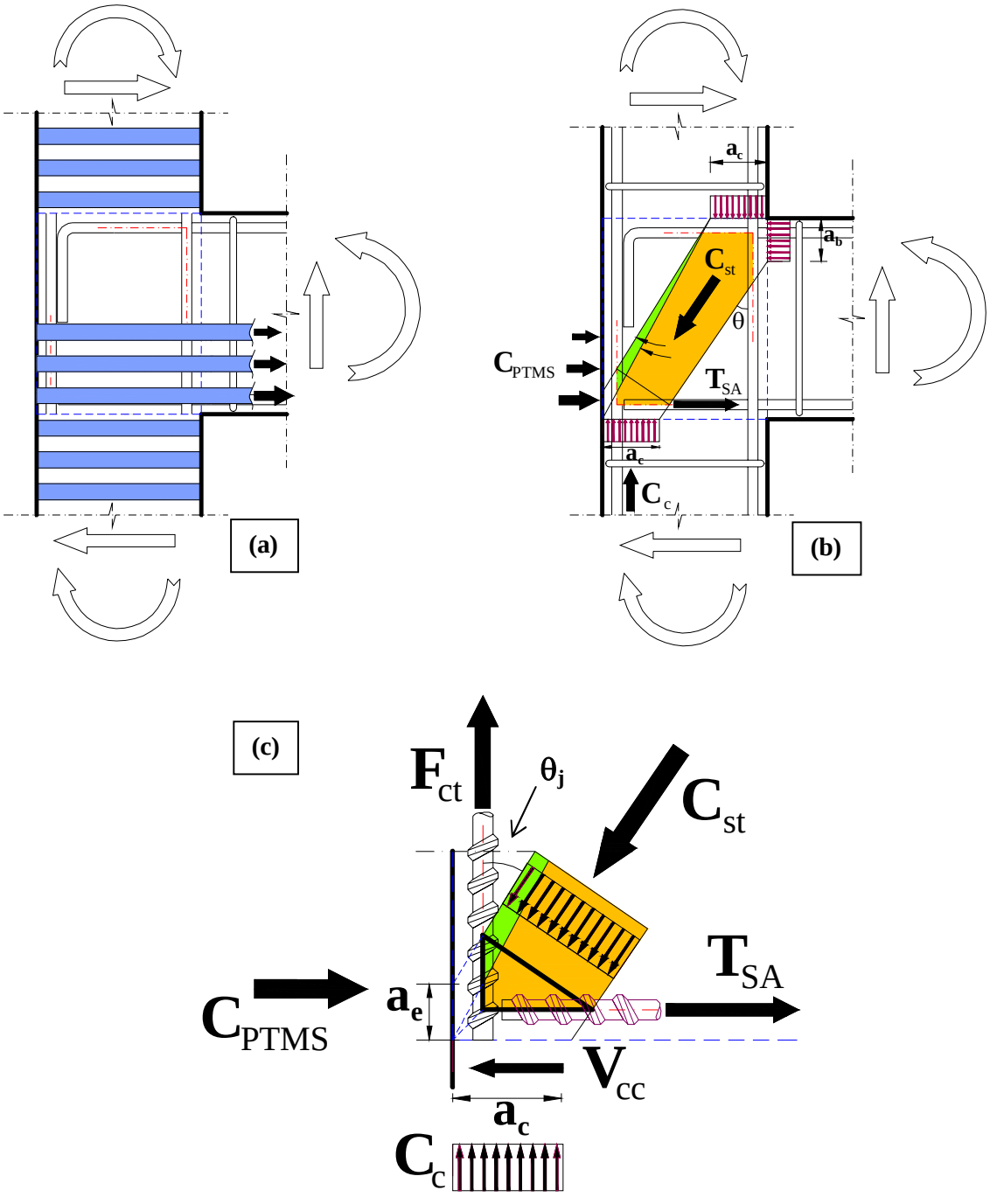

Figure 10-17: Analysis of forces on a nodal zone

The strut width at the internal corner is defined by the following equation:

$$a_{str} = \sqrt{a_b^2 + a_c^2} \tag{10-9}$$

where a_c and a_b are the compressive zone depths of the beam and columns, given by the following expressions:

$$a_c = \left[0.25 + 0.85\frac{P}{f'_c A_g}\right] h_c \qquad \leq 0.4h_c \tag{10-10}$$

$$a_b = kd_b \tag{10-11}$$

$$k = \left[(\rho + \rho')^2 n^2 + 2\left(\rho + \rho'\frac{d'_{sb}}{d_{sb}}\right)n\right]^{0.5} - (\rho + \rho')n \tag{10-12}$$

$$n = E_s/E_c \tag{10-13}$$

in which a_b and a_c are the compression beam and column zone depths, respectively; The quantity a_c is estimated using the equation by Paulay and Priestley (1992); d_{sb} and d'_{sb} are depths from the extreme compression fibre to centroids of beam longitudinal reinforcement in tension and compression, respectively; n is the modular ratio; E_c and E_s are the modulus of elasticity of concrete and steel, respectively; ρ and ρ' are reinforcement ratios of the beam longitudinal reinforcement in tension and in compression, respectively; P is the column axial load and A_g is the column gross sectional area.

The previous expressions are adopted from the model by Hassan (2011). Equation (10-10) is derived from an equivalent rectangular stress block for concrete in compression of a column section under axial load P. On the other hand, equation (10-12) is derived considering the first moment area of a transformed elastic cross-section.

The strut width at the external side of the joint area, on the other hand, is determined by equilibrium of forces acting at the nodal zone, as shown in Figure 10-17(c).

Thus, the effective contributing width a_e is determined based on the contribution of the PTMS, the anchorage length and the shear force using the following expression:

$$a_e = \frac{C_{PTMS} + T_{SA} - V_{cc}}{0.85 f'_c b_j} \tag{10-14}$$

where C_{PTMS} is the axial compressive force applied by the PTMS on a length equal to a_b, in which the maximum strip capacity is considered; T_{SA} is the tension force of any beam reinforcement acting on the nodal zone. V_{cc} is the shear force applied along the compression part of the nodal zone and can be calculated from force equilibrium on the beam-column joint, as given by equation (10-15). Thus, the shear force along the nodal zone side can be calculated using equation (10-16):

$$V_c = \frac{M_b}{L_b} \times \left[\frac{L_b + h_c/2}{H}\right] \tag{10-15}$$

$$V_{cc} = \frac{(j\pi n_s d_b l_d d_{sb} \tau_{max}) \times a_c}{h_c}\left[\frac{L_b + h_c/2}{HL_b}\right] \tag{10-16}$$

in which d_b is the bar diameter of beam anchorages, l_d is the beam anchorage length ($\leq l_y$ at yield), n_s is the number of beam bars in tension, τ_{max} is the bond strength and defined later in this section, L_b is the beam length from the contraflexure point up to the column interface; h_c is the column width; H is the column height; d_{sb} is the effective depth of the beam section; and j is the effective beam lever arm ratio = 0.875 for J-type failure and 0.9 for BJ-type failure.

To determine the anchorage length l_{st} participating in the tension force T_{SA}, the idealised strut enclosed by the beam and column compression areas is considered, as schematically shown in Figure 10-18. Accordingly, l_{st} is calculated from the strut top side until the end of l_d or l_y, whichever is smaller. Thus, l_{st} can be calculated as $l_{st} = l_d - (d'_c - a_c)$, where d'_c is the distance from the column tension side up to compression reinforcement.

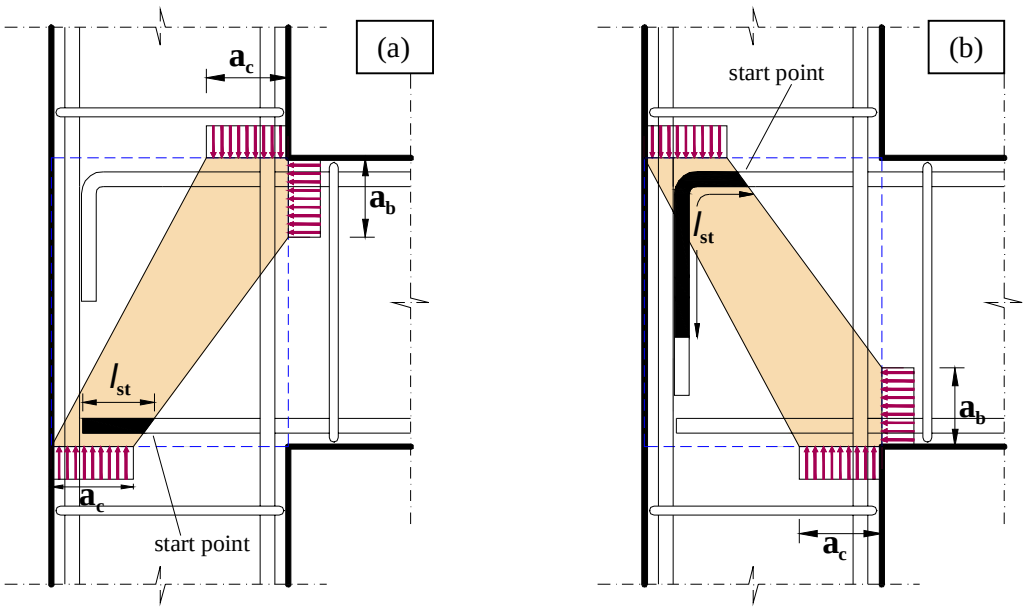

Figure 10-18: Participating anchorage length at a nodal zone – Case: a) anchorage, and b) hook

The bond stress along the length l_{st} can be calculated using the model proposed by Hassan (2011) accounting for the effect of axial load on the bond strength, and given by the following equation:

$$\frac{\tau_{max}}{\sqrt{f'_c}} = 1.1\left(\frac{P}{f'_c A_g}\right)^{1/4} \beta_d \gamma_b \left(\frac{c}{d_b}\right) \qquad MPa^{0.5} \qquad (10\text{-}17)$$

where P is the column axial load; β_d is a bar diameter factor equal to 1 for bar diameters $\geq$ 19 mm and 1.25 otherwise; γ_b is a factor accounting for confinement by transverse beams and is equal to 1 for isolated exterior joints, 1.12 for one-sided transverse beam, and 1.2 in the case of transverse beams on both sides. c/d_b is the minimum concrete cover to bar diameter ratio $\leq$ 2.5, where c is measured to the bar centroid.

Therefore, the strut width a_{str} at the exterior side can be calculated based on force equilibrium as follows:

$$a_{str} = \sqrt{a_e^2 + \left(a_c + \frac{nA'_{sc}}{b_c}\right)^2} \quad (10\text{-}18)$$

where n is the modular ratio, A'_{sc} is the area of column reinforcement in compression, and b_c is the column depth.

The horizontal shear force in the joint area is calculated by projecting the strut force on the horizontal axes as follows:

$$V_{jh} = D \times \sin(\theta_j) = a_{str} b_j f_{ce} \sin(\theta_j) \quad (10\text{-}19)$$

where θ_j is the modified strut angle, as shown in Figure 10-17(c), and determined by the following expression:

$$\theta_j = tan^{-1}\left(\frac{d_c - a_c}{d_{sb} - a_e}\right) \quad (10\text{-}20)$$

where d_c and d_{sb} are the distances of tension reinforcement in the column and beam cross-sections measured from the outermost fibre in compression.

Thus, the maximum normalised horizontal shear stress is given by the following equation:

$$\frac{\tau_m}{\sqrt{f'_c}} = \frac{V_{jh}}{h_c b_j} \quad (10\text{-}21)$$

- *Maximum slope G_m*

Based on the test results, it is found that the equation proposed by Hassan (2011) for secant shear modulus overestimates the results of the confined specimens on average by 60%; whereas it overestimates the results of the unconfined specimens by 25%. Thus, for simplicity and consistency, the following equations are found to be suitable for determining the secant shear modulus at the maximum point:

For unconfined joints

$$G_m = (0.2 - 0.095\alpha_j) G_c \quad (10\text{-}22)$$

For confined specimens

$$G_m = (0.07 - 0.03\alpha_j) G_c \quad (10\text{-}23)$$

Figure 10-19 compares the results of equations (10-22) & (10-23) and those from tests results. In general, the modified equation provides good estimations of the test results with the exception of the joint JB-1, which failed at a lower strain in the weak (pull) direction.

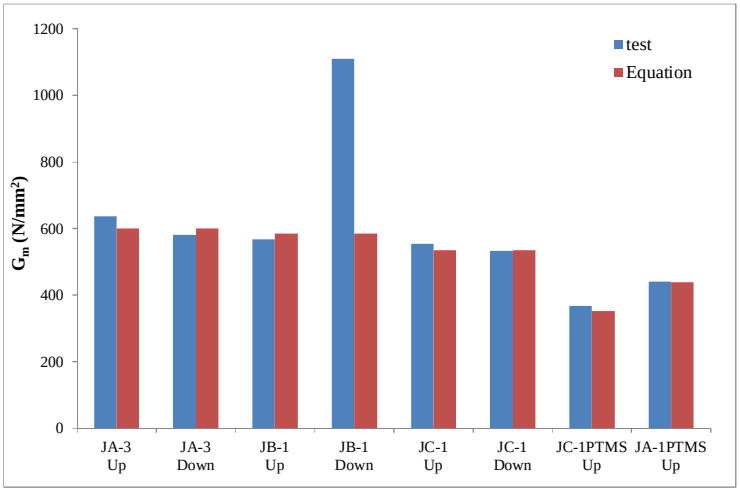

Figure 10-19: Comparison of test results to predictions of G_m

10.5.4 Residual strength (Point D)

Despite the small differences, it is observed from comparisons in chapter 6 that the joint response, specifically in terms of stiffness degradation, is similar in nature. Thus, it is decided to define a degrading curve with a slope of -10 (considering $\tau/\sqrt{f'_c}$ - γ curve) and levels off at a normalised shear stress of $0.3\sqrt{f'_c}$. Consequently, the shear strain at the residual point is given by the following expression:

$$\gamma_{res} = \gamma_m + \frac{1}{10}\left(\frac{\tau_m}{\sqrt{f'_c}} - 0.3\right) \tag{10-24}$$

in which γ_m is the shear strain at the peak point and equal to τ_m/G_m.

In the calculation of the moment-rotation relationship, the following conventional equation can be used to determine the moment M_j of the shear spring:

$$M_j = \tau_j A_j \frac{L}{\frac{L - 0.5h_c}{jd_{sb}} - \frac{L}{H}} \tag{10-25}$$

where τ_j is the shear stress; A_j is the effective joint area; L is the beam length from the contraflexure point up to the column centroid; h_c is the column width; H is the column height; d_{sb} is the effective depth of the beam; and j is a the effective beam lever arm ratio = 0.875 for J-type failure.

10.6 COMPARISON OF MODIFIED STRUT-AND-TIE MODEL WITH TEST RESULTS

The modified ACI-based model was used to predict the test results of the unconfined and strengthened beam-column joints conducted in the current study. The comparisons are presented in Table 10-5 and Table 10-6 in terms of the maximum shear stress in the push and pull loading

directions. The contribution of PTMS is neglected when the model is used to predict the shear strength of the unconfined joints.

In general, the proposed model predicted the test results reasonably well with an average of 107% for the unconfined joints and 120% for the confined joints. Again, the overestimation in predicting the test results of unit JA-1PTMS was due to the fact that it was not tested up to the maximum capacity. In addition, the model overestimated the shear strength of unit JC-1PTMS in the pull direction due to error in loading that led to a lower value.

Table 10-5: Comparison of model predictions with test results of unconfined joints

Test Unit	Direction	Model $\tau_j/\sqrt{f'_c}$	Test $\tau_j/\sqrt{f'_c}$	Model / test
JA-1	Push	0.55	0.48	1.15
	Pull	0.49	0.53	0.92
JA-3	Push	0.63	0.58	1.09
	Pull	0.57	0.53	1.08
JB-1	Push	0.56	0.53	1.06
	Pull	0.51	0.43	1.19
JC-1	Push	0.55	0.55	1.00
	Pull	0.55	0.53	1.04

Table 10-6: Comparison of model predictions with test results of confined joints

Test Unit	Direction	Model $\tau_j/\sqrt{f'_c}$	Test $\tau_j/\sqrt{f'_c}$	Model / test
JA-1PTMS	Push	0.75	0.47*	1.6
	Pull	0.72	0.4*	1.8
JA-3PTMS	Push	0.68	0.7	0.97
	Pull	0.62	0.64	0.97
JB-1PTMS	Push	0.67	0.68	0.99
	Pull	0.63	0.62	1.02
JC-1PTMS	Push	0.67	0.67	1.00
	Pull	0.67	0.5#	1.34

* Not tested to capacity; # error in loading

The model was also used to predict the joint shear strength of some beam-column joints found in the literature (J-type failure). The data included tests on unconfined isolated exterior beam-column joints conducted by Kuang and Wong (2005), Pantelides et al. (2002), and Clyde et al. (2000). Table 10-7 presents comparisons of the joint shear strength predictions to those from experiments. Details of the test units including geometries, reinforcement detailing, and material qualities are given in Appendix H.

Table 10-7: Comparison of model predictions to beam-column joint tests

Specimen	Direction	Model $\tau_j/\sqrt{f'_c}$	Test $\tau_j/\sqrt{f'_c}$	Model / test
BS-L[1]	Hook – Top[#]	0.720	0.630	1.14
	Hook – Bottom[##]	0.670	0.560	1.20
BS-U[1]	Hook – both*	0.720	0.680	1.06
BS-L-LS[1]	Hook – Top	0.720	0.680	1.06
	Hook – Bottom	0.670	0.540	1.24
03[2]	Anchorage	0.874	0.870	1.01
	Hook – Top	0.947	0.870	1.09
04[2]	Anchorage	0.965	0.940	1.03
	Hook – Top	1.016	0.992	1.02
05[2]	Hook – Top	0.942	0. 825	1.14
	Hook – Bottom	0.942	0.940	1.00
06[2]	Hook – Top	1.016	0.933	1.09
	Hook – Bottom	1.016	0.946	1.07
2[3]	Hook – both	1.011	1.010	1.00
6[3]	Hook – both	0.995	1.060	0.94
4[3]	Hook – both	1.110	1.010	1.10
5[3]	Hook – both	1.064	1.060	1.00

1 Kuang and Wong (2005); 2 Pantelides et al. (2002); 3 Clyde et al. (2000); *both sides are hooks; [#] beam top bars; [##] beam bottom bars.

From the table, it can be noted that the proposed strut-and-tie model provides good predictions in most cases, with an average of 107%. This indicates that the use of the softened concrete model for the unconfined panel zones, given in the ACI 318-08, is appropriate for predicting the strut strength.

10.7 CONTRIBUTION OF STRENGTHENING COMPONENTS

To calculate the contribution of each strengthening component (PTMS, concrete and welding) to the joint capacity, Equation (10-25) was utilised by subtracting the shear capacity of the bare joint considering the use of τ_j / f'_c of the unconfined condition (see Table 10-1 last column). Figure 10-20 through Figure 10-22 presents plots of the unit responses with detailed contributions of the strengthening components. Also Table 10-8 presents the contributions in a tabular form. It should be mentioned that the unit JA-1PTMS was not tested to capacity, and thus, the contribution of the PTMS was not clear.

From the figures, it can be noted that the PTMS contributions ranged between 17-22% of the total capacity. The highest contribution by PTMS was in unit JB-1PTMS due to the use of

welding works on the external steel formwork. In the tested joints, the PTMS contribution was not as good as expected, and better PTMS systems are necessary. This issue is solved by providing an improved rehabilitation measure as presented in chapter 11.

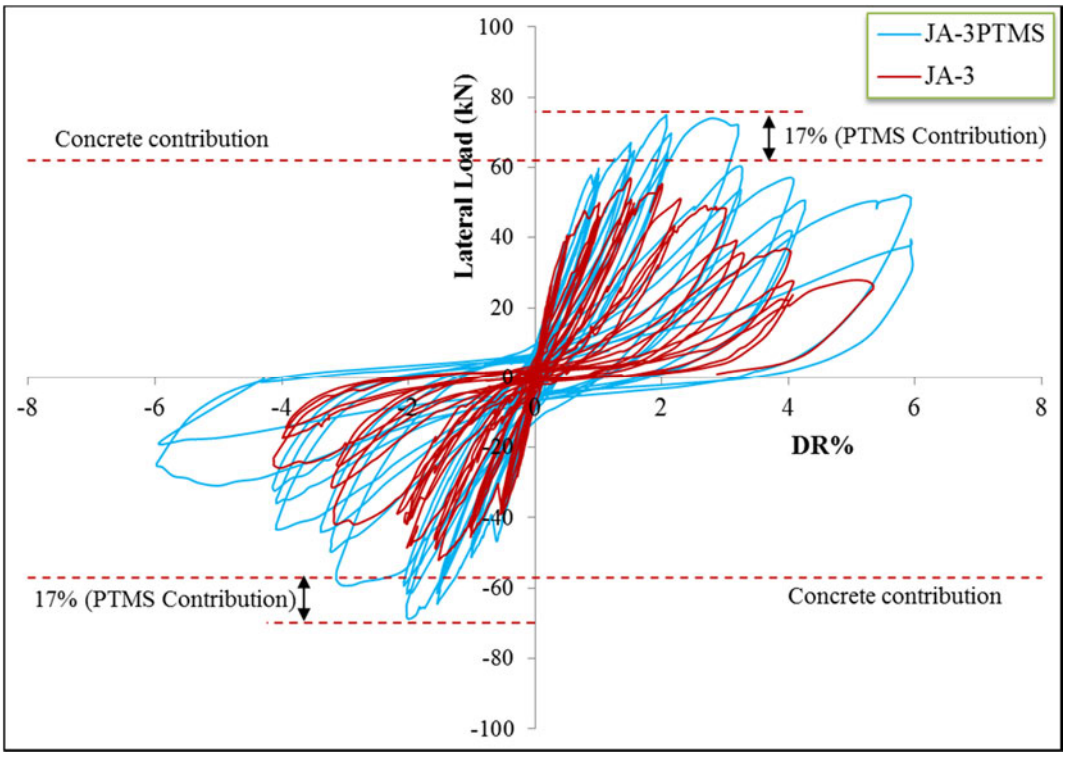

Figure 10-20: Contribution of strengthening components to capacity of joint JA-3PTMS

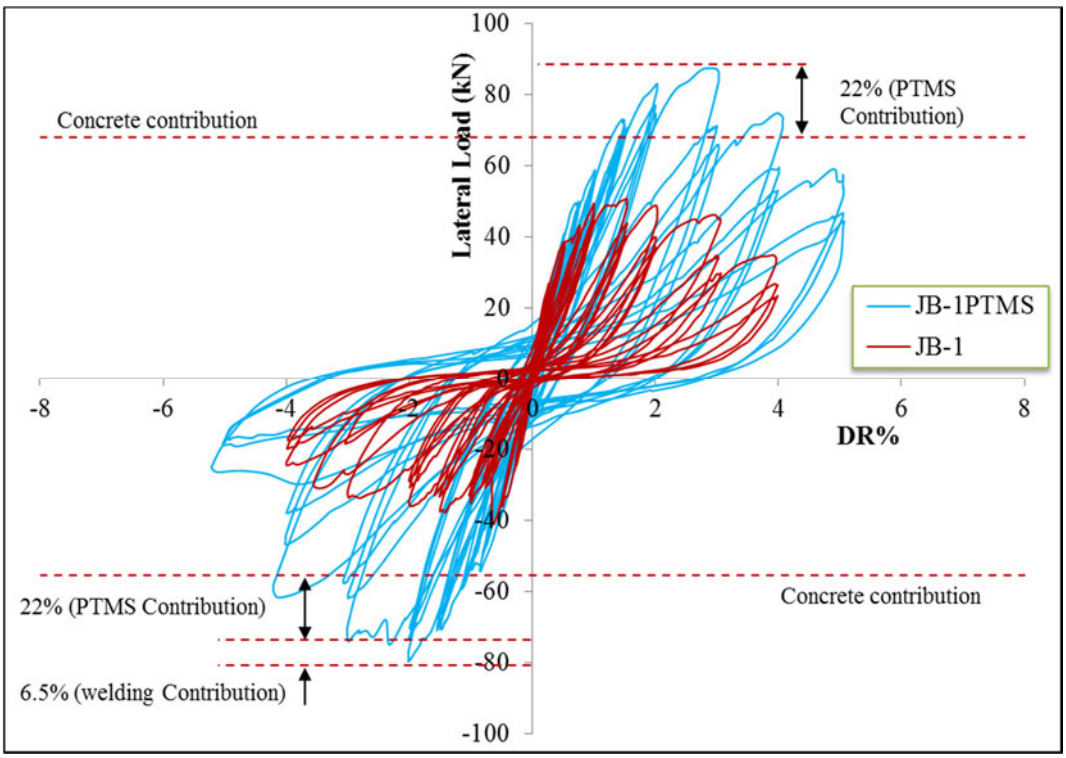

Figure 10-21: Contribution of strengthening components to capacity of joint JB-1PTMS

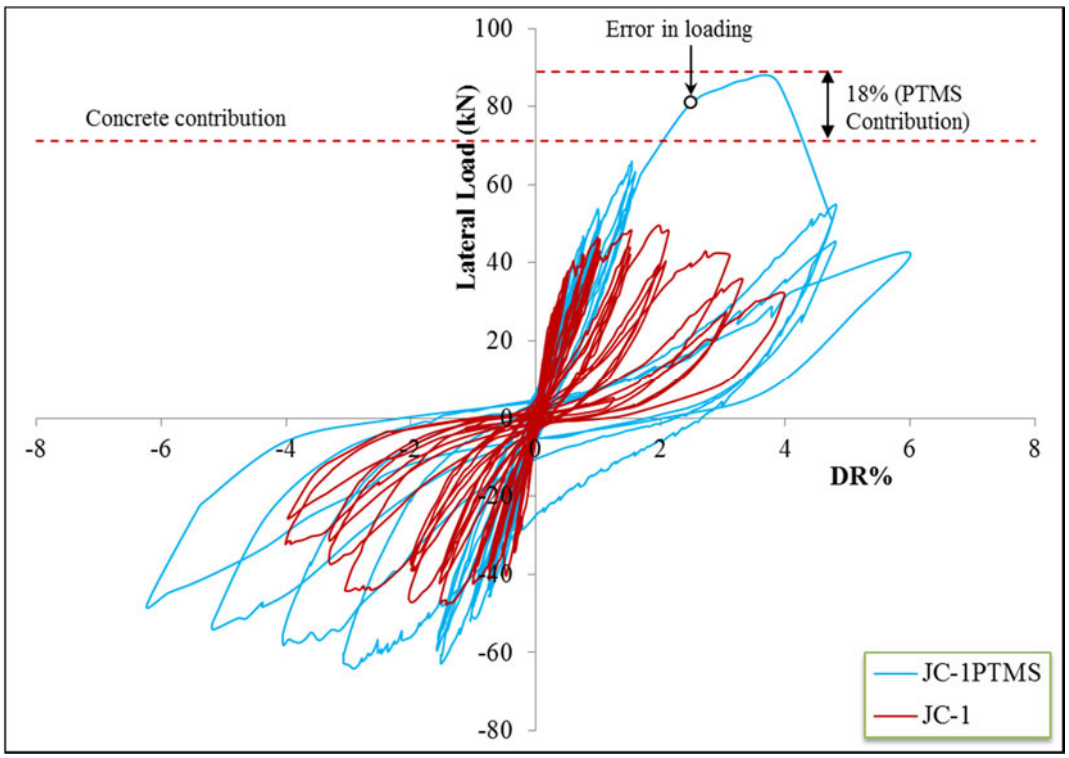

Figure 10-22: Contribution of strengthening components to capacity of joint JC-1PTMS

Table 10-8: Contribution of strengthening components to the total load capacity

Unit	$\frac{PTMS\ load\ capacity}{bare\ load\ capacity}$		Concrete contribution %		PTMS contribution %		Welding contribution %	
	Strong	Weak	Strong	Weak	Strong	Weak	Strong	Weak
JA-1PTMS	1.87	1.45	100%	100%	-	-	-	-
JA-3PTMS	1.35	1.33	33%	31%	67%	69%	-	-
JB-1PTMS	1.72	1.95	47%	37%	53%	45%	-	18%
JC-1PTMS	1.75	1.34	37%	-	63%	-	-	-

* It should be noted that the contributions mentioned in the table represent the percentage of the pure increase in the load capacity due to PTMS. The sum of contributions is supposed to be 100% in each direction.

10.8 MODELLING AND ANALYSIS OF BEAM-COLUMN JOINTS

10.8.1 Modelling strategy

In order to provide an accurate modelling strategy, the different deformational components of the joint must be calculated properly. Thus, joint deformations are assumed to be due to:

- Flexural behaviour (extension of beams and columns)
- Shear deformations of joint area
- Beam anchorages
- Column splices

The determination of the different components is related to the modelling methodology, which in turn is dependent on the analytical tool.

10.8.2 Selection of the analytical tool

Modelling the different deformational components requires a sophisticated analytical tool capable of simulating the existent deficiencies. General-purpose FE packages for seismic analysis such as OpenSees and DRAIN, developed mainly for research, fulfil the requirements. In this study, it is decided to use DRAIN-2D frame analysis FE software (Prakash et al., 1993), as it offers comprehensive modelling elements with degradation characteristics, and complex material models with nonlinear behaviour (Powell, 1993). In addition, many researchers such as [Deng (2000), Rubiano (2001), Shin (2004), Karayannis (2005), Kyriakides (2007), Ahmad (2011), Shin and Lafave (2004), etc.] utilised this software for performing linear or nonlinear static and dynamic analyses.

10.8.3 Contribution of joint panel zone deformations

The contribution of the joint panel zone shear deformations to the total deformations in a RC frame is shown in Figure 10-23 (Tsonos, 2007). Accordingly, the beam experiences a rotation of γ_j resulting in a beam tip displacement of $\gamma_j L_b$, where L_b is the length of the beam from the contraflexure point to the beam/joint interface. This rotation is additional to any rotation in the beam that occurs due to external bending moment. On the other hand, the column experiences a relative horizontal shear displacement of $\gamma_j h_b$, in which h_b is the beam depth. The column relative displacement is divided between the top and bottom column as $\gamma_j h_b/2$ for each. This displacement is also added to the column shear deformations due to the external shear forces on the column. Thus, a joint model should be selected such that it simulates the additional beam and column deformations due to the joint rotation.

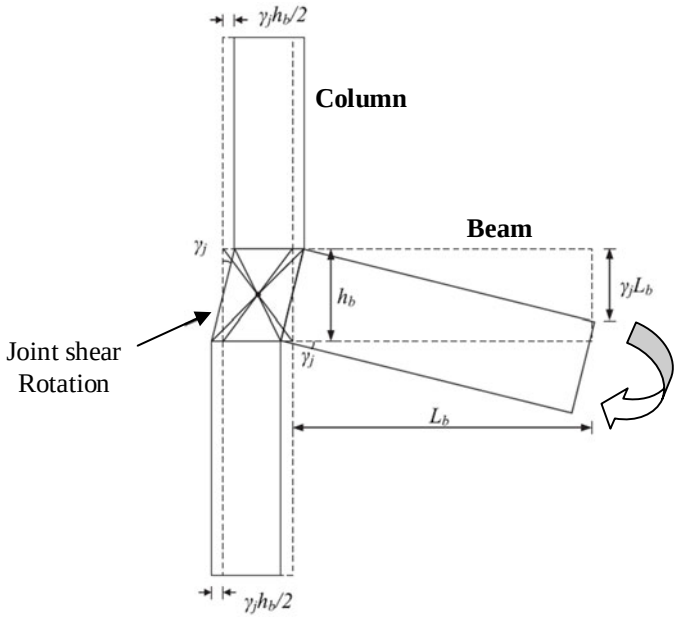

Figure 10-23: Assumed shear deformations of beam-column joints in a RC frame (Tsonos, 2007)

10.8.4 Joint model with a rotational spring and rigid links

As discussed earlier in chapter 2 (Part II), many numerical (computer-based) joint models have been developed to simulate joint behaviour. Some are inappropriate for FE modelling, as they are too complicated to implement. On the other hand, some are relatively easy to implement. One of these models that may be suitable is the scissors model (Figure 10-24), which is composed of a rotational spring with rigid links extending along the joint dimensions. The scissors model was first suggested by Alath and Kunnath (1995). The model was used by Theiss (2005), Celik and Ellingwood (2008), Favatta et al. (2008), Hassan (2011), Sharma (2011), Pampanin et al. (2003), and Birely et al. (2012) for interior, exterior and corner unconfined beam-column joints under the effect of cyclic and dynamic loading, and by Burak (2010) for confined beam-column joints under cyclic loading.

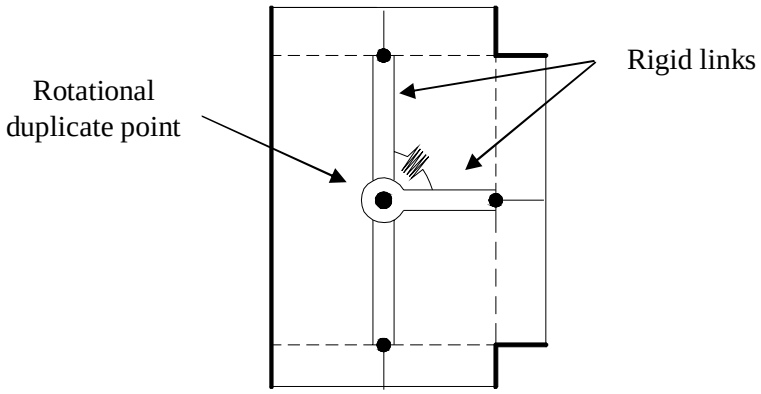

Figure 10-24: Scissors panel-zone joint model

Figure 10-25 & Figure 10-26 illustrate a DRAIN-2DX computer model for a typical exterior RC beam-column connection subjected to lateral loading. As can be seen, the joint is represented by two rigid link elements spanning along the joint dimensions and one nonlinear rotational spring embedded in the connecting node of the rigid elements. Also, two translational nonlinear springs were embedded in the column/joint interfaces. Physically, the springs should have characteristics as a moment in the beam (M_b) vs. shear deformation of joint (γ_j) for the rotational spring, and joint horizontal shear force (V_j) vs. shear deformations in the column portion of the joint ($\Delta_c = \gamma_j h_b/2$). For the rigid joint elements, Element 02 (E02) was used with very stiff characteristics.

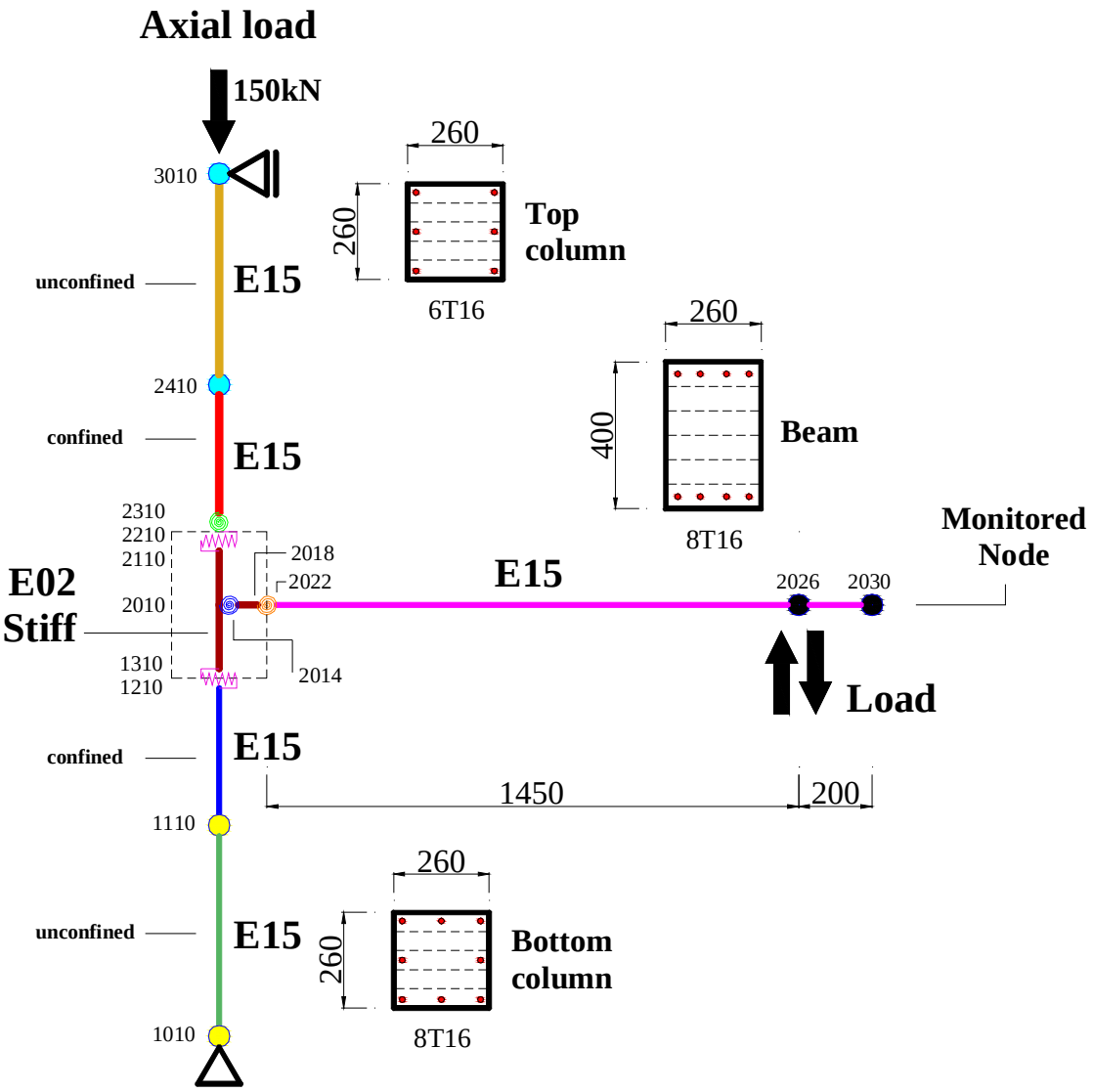

Figure 10-25: Beam-column joint model used in DRAIN-2D

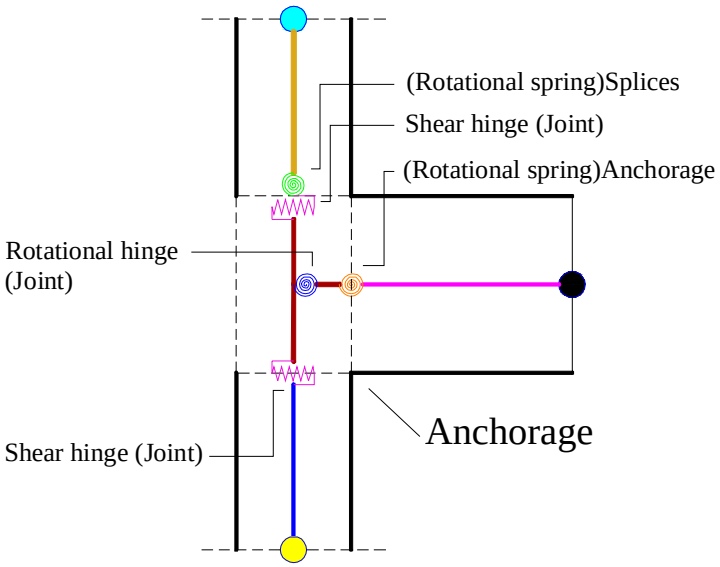

Figure 10-26: Philosophy of joint core modelling in a frame analysis

DRAIN-2DX Element 10 (E10), which was developed by Foutch and Shi (1997), is used for the nonlinear rotational and translational springs at the joint. The element is capable also of incorporating typical hysteretic properties such as stiffness degradation, strength degradation, and pinching (Figure 10-27). The necessary input parameters for Element 10 are initial stiffness (k1), strain-hardening ratio (k2/k1), positive and negative yield moments (My^+ and My^-), strength degradation factor, and positive and negative pinching moments (Mg+ and Mg-), as illustrated in Figure 10-27. The hysteretic rule of the element curve, however, is questionable, specifically in the case when a negative stiffness k2/k1 is given (J-type failure), as will be shown later. As this study deals only with the backbone of the shear stress-rotation relationship, and the fact that the hysteretic rules are not pursued, only some comments and recommendations are given, when dealing with E10 for dynamic analyses.

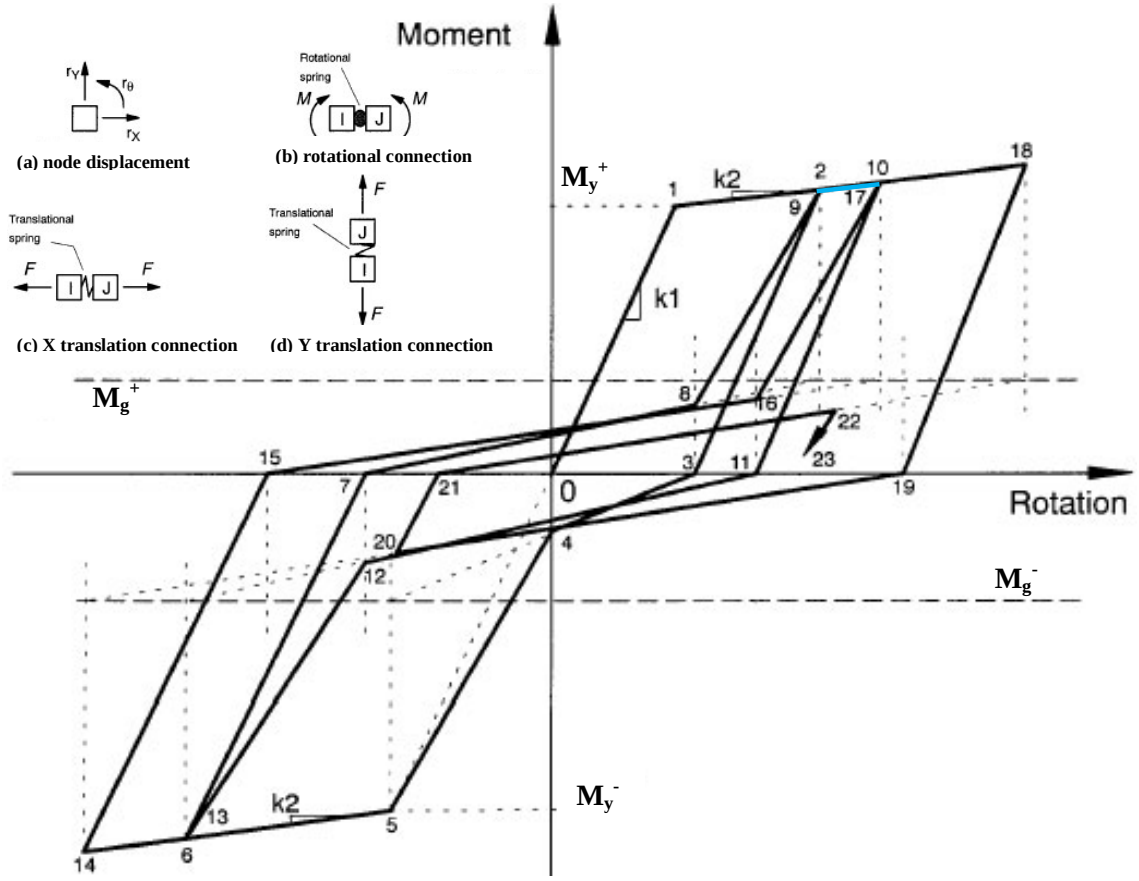

Figure 10-27: Element 10 - concrete connection hysteresis model, Foutch and Shi (1997)

As can be seen from Figure 10-27, Element 10 can only simulate a single bi-linear moment/force vs. rotational/translational relationship as a primary curve. Input parameters for the joint rotational/translational springs, however, may be determined from multi-linear envelope curves (M_b vs. γ_j) & (V_c vs. $\gamma_j h_c/2$), as schematically shown in Figure 10-28. To overcome this problem, the multi-linear curves are decomposed into multiple bilinear springs connected in parallel, as illustrated in the same figure. Thus, the springs are implemented

between the same connecting points. The strain hardening ratio k2/k1 value can be set to have positive or negative values.

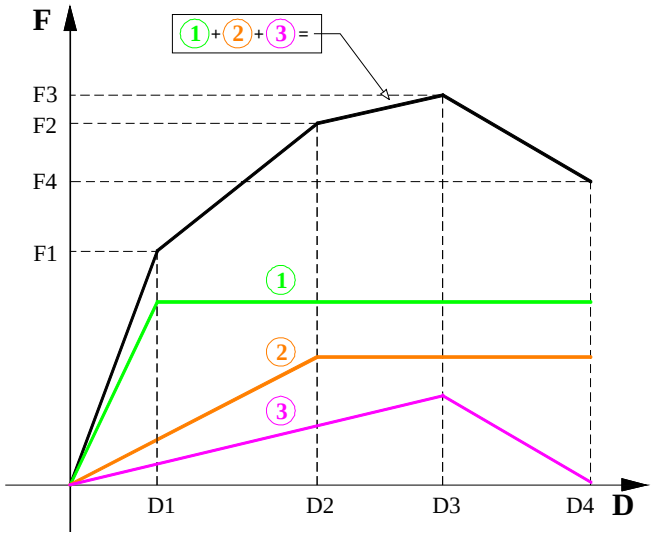

Figure 10-28: Decomposition of a quad-linear deformational curve into bilinear curves

Outside of the joint panel zone, beam and column elements are modelled using DRAIN-2DX Element 15 (E15), which is a section analysis element and has the provision to model concrete and steel as fibres. This element has distributed plasticity accounting for the spread of the inelastic behaviour both over the cross section and along the member length (Powell, 1993). The interaction between axial force and bending in columns (P-M interaction) is also considered automatically. The response of each fibre is concentrated at its centre of gravity. As a result, the strength and stiffness of the section depend on the location and number of fibres. Accuracy in the flexural capacity predicted by the section analysis routine of Drain-2DX can be increased by using a dense rectangular grid discretization, but this is computationally more intensive.

The actual test boundary conditions were modelled in DRAIN-2D platform as follows:

- A pinned support was provided at the bottom column to restrain vertical and horizontal movements
- Axial column shortening was permitted through a top vertical roller.

Figure 10-25 shows the boundary conditions used in the simulation.

Static as well as cyclic analyses are performed to produce the load–displacement curves of the joints and these are compared with the hysteretic curves obtained from the experiments. For each test unit, two types of analysis are performed, one without considering nonlinearities in the joint panel zone (no joint model or rigid connections) and one considering the joint springs as per the joint model. The load protocol used for the cyclic analyses is shown in Figure 10-29.

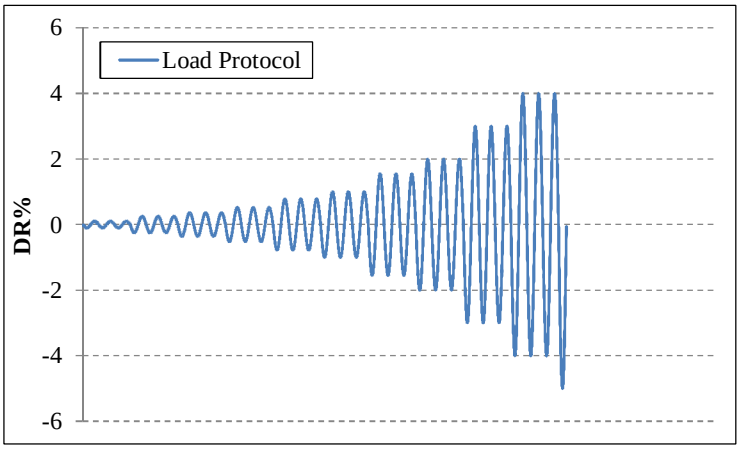

Figure 10-29: Load protocol used for cyclic analysis

The beam moment M_b-γ relation and column shear force V_c-$\gamma_j h_c/2$ relation are calculated for all units using equation (10-25) and the equilibrium of external forces. The quad-linear curves are decomposed into multiple bilinear curves and fed as inputs for DRAIN-2DX platform.

10.8.5 Anchorage component

Modelling the slip component in the beam-column joints can be achieved by different techniques. A common way of modelling slip rotations is by introducing an explicit spring at the beam/joint interface for anchorages and an additional spring at the column/joint interface for splices. Another approach is by combining the anchorage and shear spring in a single spring introduced at the joint centroid. An alternative way to model the slip is by reducing the element stiffness's, so higher drifts are produced, as recommended by ASCE/SEI 41 supplement 1 (2006). In this study, the first approach is considered, as it has a simple and straightforward application method.

To calculate the slip component due to beam anchorages, a bond-slip model should be utilised. In this regard, the bond-slip model by Sezen (2003) is used. The model has been used widely in numerous investigations, and moreover, it agrees with the findings from this study. Figure 10-30 shows the strain and bond distributions of Sezen model.

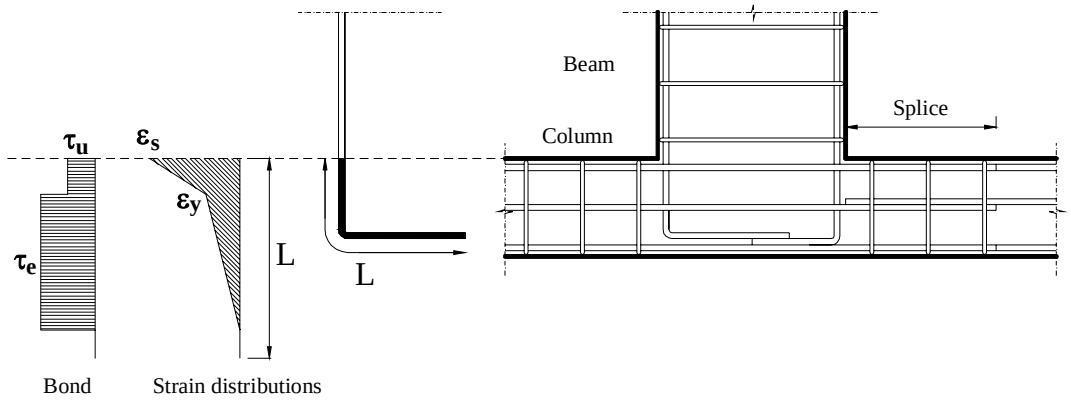

Figure 10-30: Bond-slip models adopted for beam anchorages

Slip deformations are fed to DRAIN-2DX platform as moment rotations. Thus, slip deformations should be transformed into rotations at the beam/joint interface. In doing so, the assumption made by Sezen (2003) is adopted, in which the cross-section rotation due to slip is assumed to occur about the neutral axis, as shown in Figure 10-31. Accordingly, the slip rotation is calculated as the bar slip divided by the distance between the neutral axis and the slipping bar i.e. the width of the open crack.

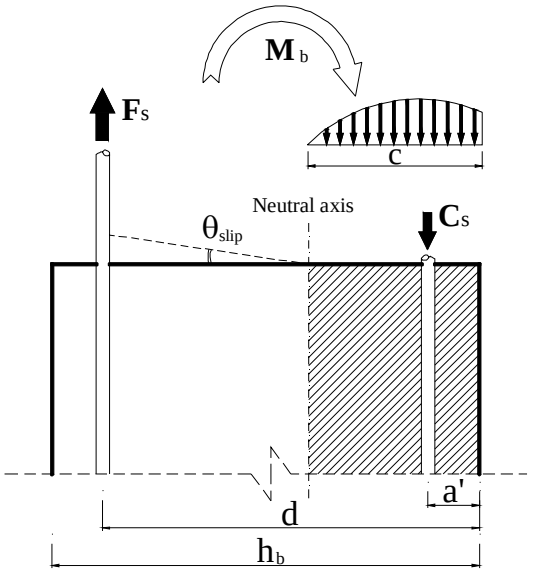

Figure 10-31: Calculations of rotation due to slip of anchored bars

$$\theta_s = \frac{slip}{d - c} \tag{10-26}$$

By performing sectional analyses on the beam section, the moment-rotation relationships of both joints are produced and fed to the rotational spring at the beam/joint interface.

10.8.6 Splice component

For the unconfined joints, the rotation at the splice interface is also calculated using the model by Sezen (2003). For the PTMS confined specimens, the moment-slip rotations are calculated based on the proposed bond-slip model in this study.

10.9 RESULTS AND COMPARISONS

The produced shear and bond deformational curves were fed as the hinge characteristics in the structural model and then static pushover and cyclic analyses were performed to obtain the load-displacement curves. The results were then compared with the measured hysteretic curves. DRAIN-2DX codes for static as well as cyclic analyses are presented in Appendix I for specimen JC-1PTMS.

10.9.1 No joint model

The analytical results of no joint model within the joint region (conventional centreline rigid joint assumption) are shown in Figure 10-32 and Figure 10-33 for the unconfined and PTMS confined joints, respectively. It is clear from the figures that the model with rigid connections led to quite unacceptably un-conservative results. The well-designed units had considerably higher strength and stiffness capacities compared to the test units; in addition, the failure was dominated by beam flexural capacity, whereas the experimental failure was due to joint (J) failure for the unconfined specimens and due to (beam/joint) BJ-Failure mode for the PTMS confined specimens.

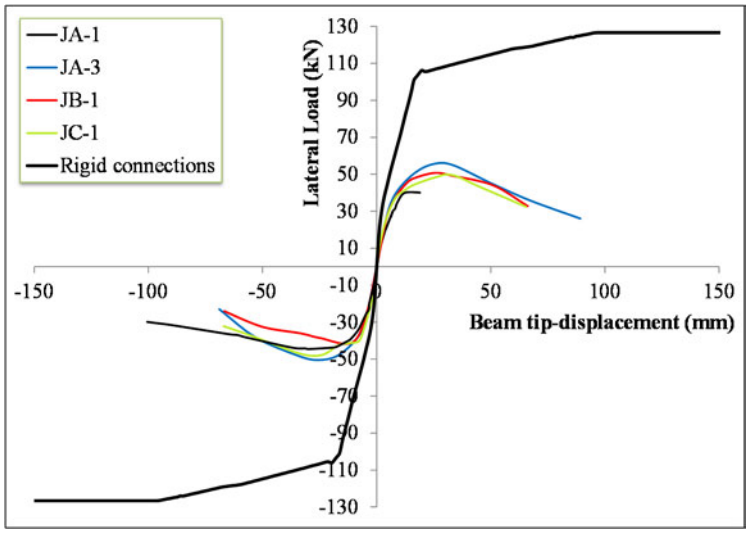

Figure 10-32: Comparison of rigid connection joint model with measured responses of unconfined joints

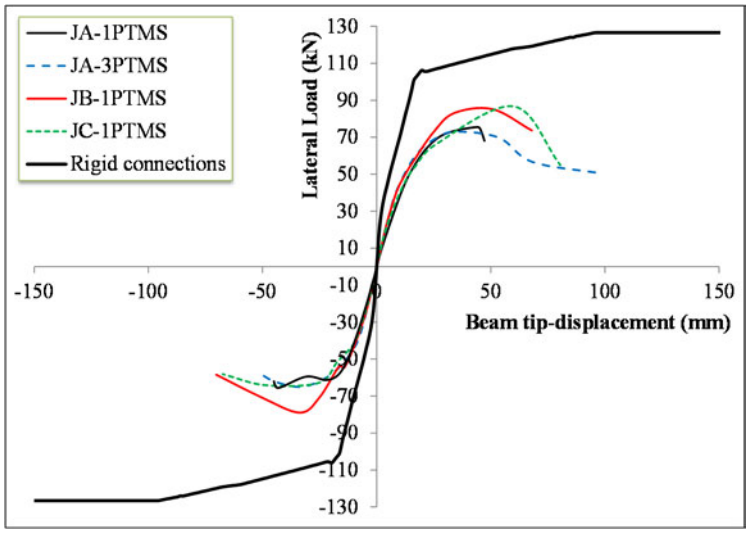

Figure 10-33: Comparison of rigid connection joint model with measured responses of PTMS confined joints

10.9.2 Scissors model – static analysis

Simulation results of the bare joints considering the ASCE 41-06 model are shown in Figure 10-34. As can be seen from the figure, the model response was dominated by reaching peak joint strength before beam yielding. It can be noticed also that the ASCE model produced good predictions of the initial stiffness as well as the maximum capacity. However, it is clear that the ASCE 41-06 nonlinear modelling parameters resulted in unacceptably inaccurate simulations of the post-peak response. However, it should be noted that the simulation results using ASCE recommendations are expected to provide a certain safety level for such elements. It should be mentioned also that the sudden drop in the ASCE model after the peak plateau was given a negative gradient to assist the analysis stability.

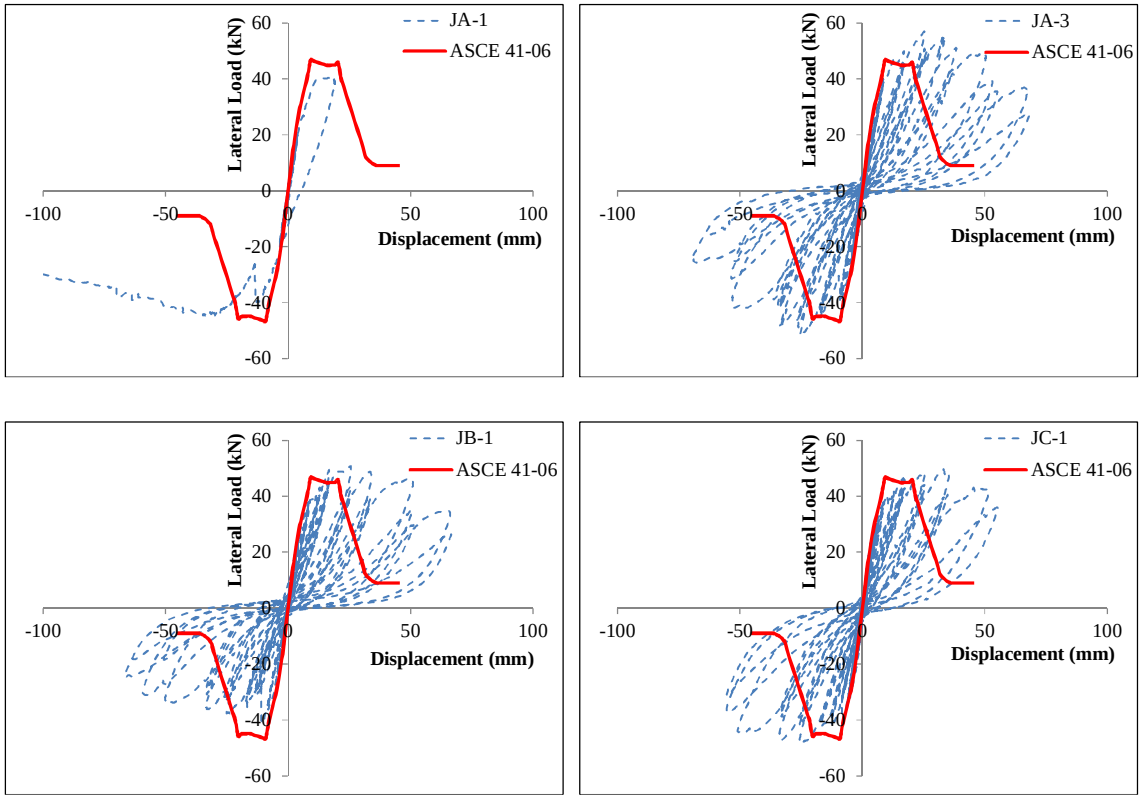

Figure 10-34: Comparison of ASCE 41-06 model results and measured response

Figure 10-35 through Figure 10-37 present the analytical results of the bare joints considering the proposed model in comparison with the measured responses. It is clear that the model was able to predict the test response with reasonable accuracy much better than the ASCE model, specifically in terms of the post peak response. As the modified strut-and-tie model underestimated the peak shear strength on the envelope curve of some specimens, a slight underestimation of the response envelope of those specimens occurred. It can be also noted that the model provided different degrading responses in the post peak stage.

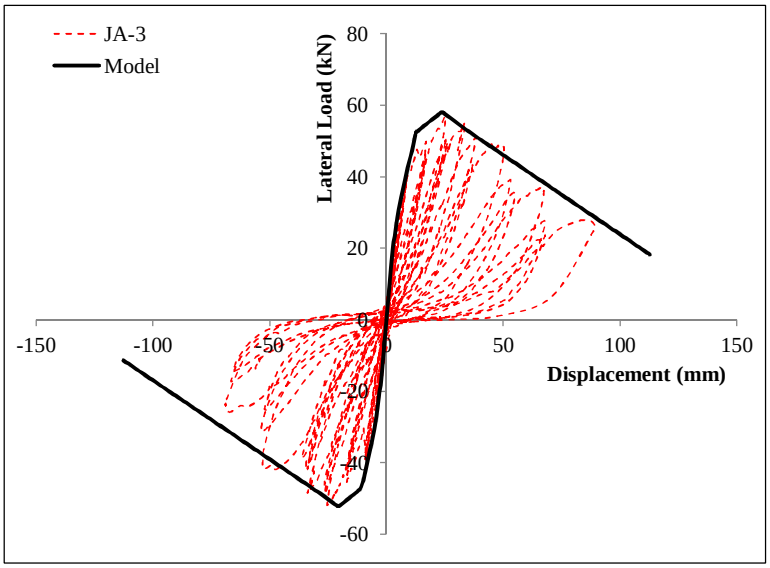

Figure 10-35: Simulation of joint JA-3– Case: static analysis

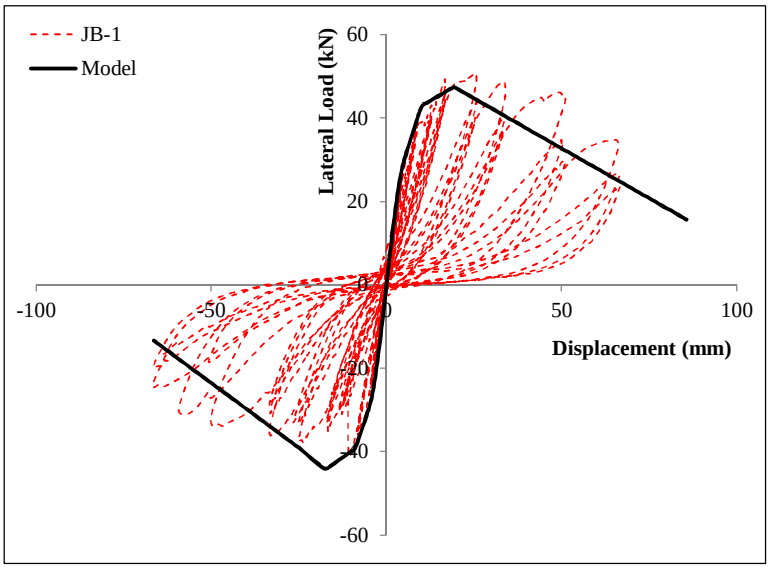

Figure 10-36: Simulation of joint JB-1– Case: static analysis

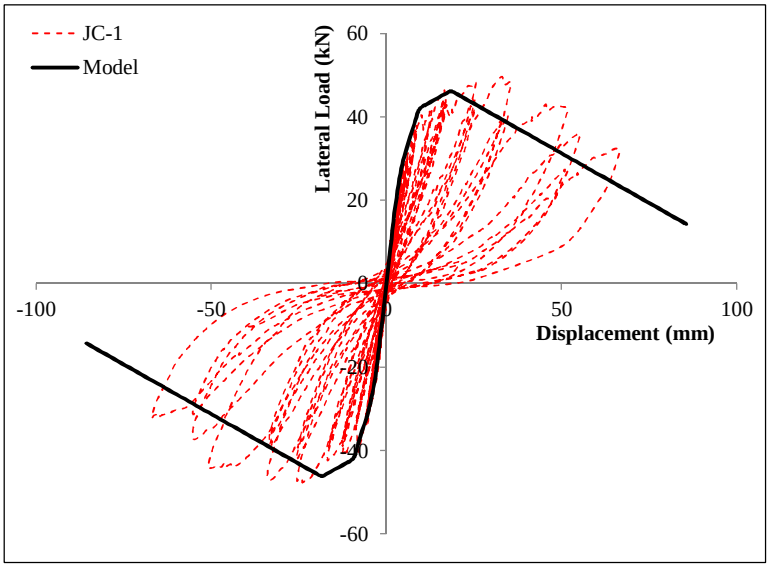

Figure 10-37: Simulation of joint JC-1– Case: static analysis

Figure 10-38 through Figure 10-40 show comparisons between the test and simulation responses of specimens JA-3PTMS, JB-1PTMS and JC-1PTMS using the proposed model. As can be seen from the figure, the model was able to predict the test responses with reasonable accuracy; specifically, the first cracking, initial stiffness, peak strength and post-peak degradation. However, the model overestimated the second stiffness slightly in specimens JA-3PTMS and JB-1PTMS. The model provided symmetrical response for the test unit JC-1PTMS, which failed in unsymmetrical way due to error in loading. Although, yielding was observed in the beam longitudinal reinforcement at the maximum capacity, the proposed model led to a failure of specimens before reaching the nominal flexural capacity of the beam.

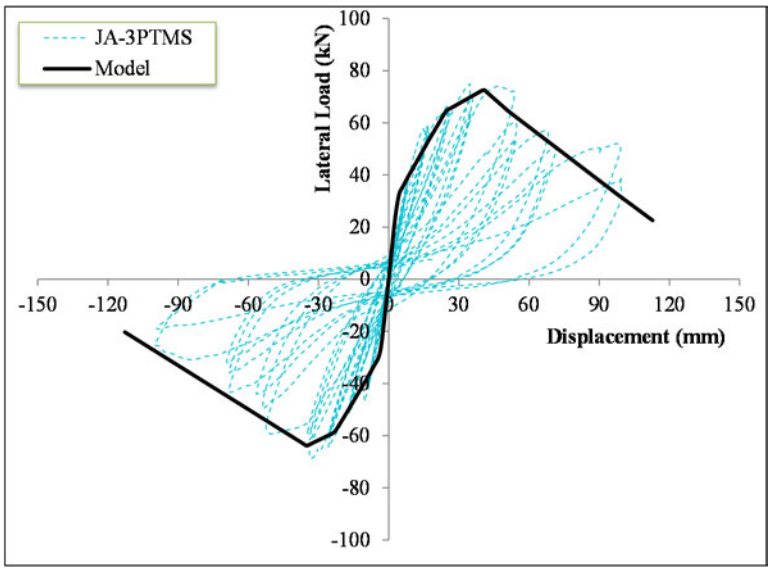

Figure 10-38: Simulation results of joint JA-3PTMS– Case: Static analysis

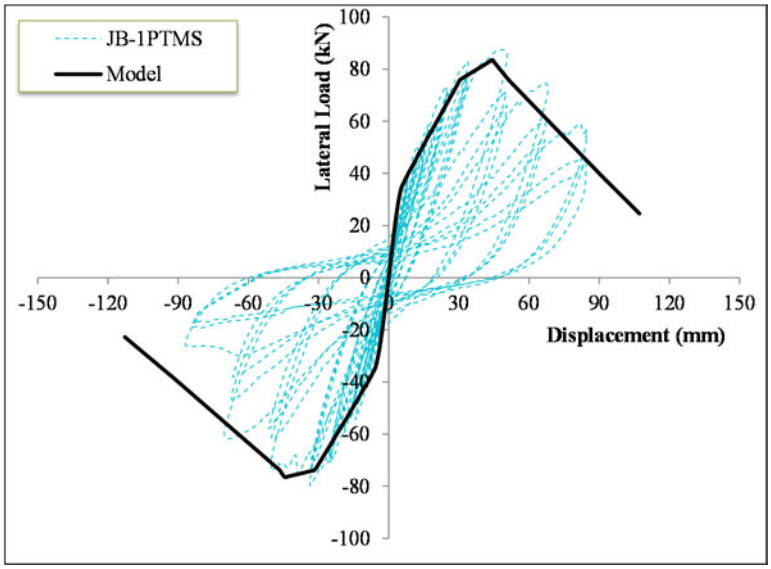

Figure 10-39: Simulation results of joint JB-1PTMS– Case: Static analysis

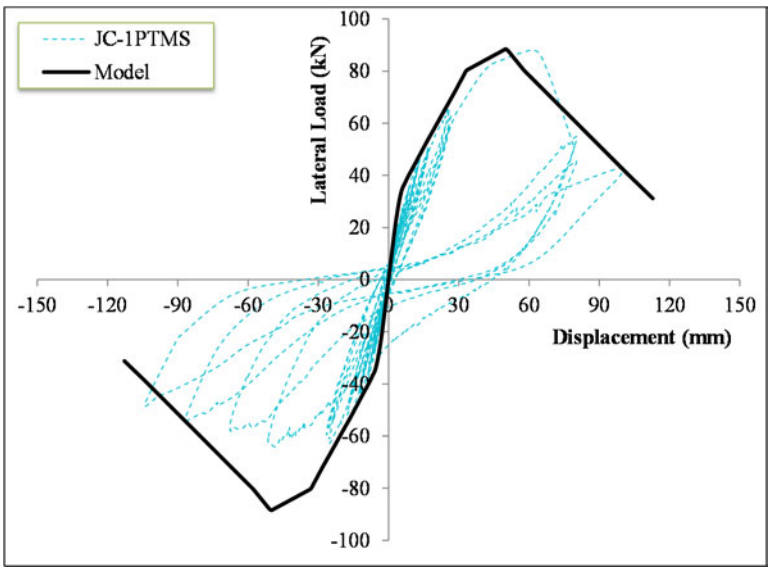

Figure 10-40: Simulation results of joint JC-1PTMS– Case: Static analysis

Figure 10-41 through Figure 10-47 show the simulation results of some joints tested by Pantalides et al. (2002), Clyde et al. (2000) and Kuang and Wong (2005). It can be observed from the figures that the proposed model captures reasonably well the initial stiffness as well as the cracking point in most cases. The pre-peak stiffness, on the other hand, is slightly underestimated resulting in stiffer responses (such as units 02 and BS-L). The model also shows good estimations of the peak point with some deviation based on the results of the proposed strut-and-tie model (see Table 10-7). The post peak degradation is well simulated in most cases. However, in some cases, such as unit 03, the post-peak degradation rate is somewhat stiffer than that of the test results.

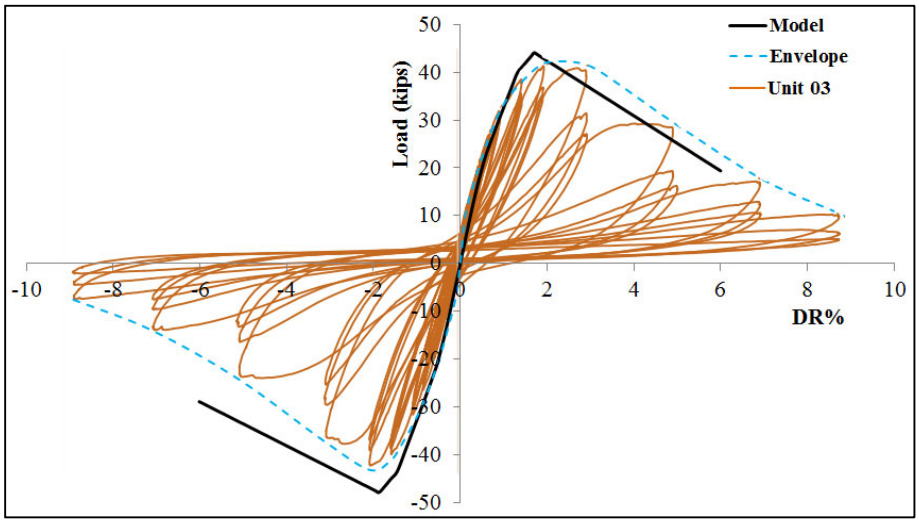

Figure 10-41: Simulation results of unit 03 tested by Pantelides et al. (2002)

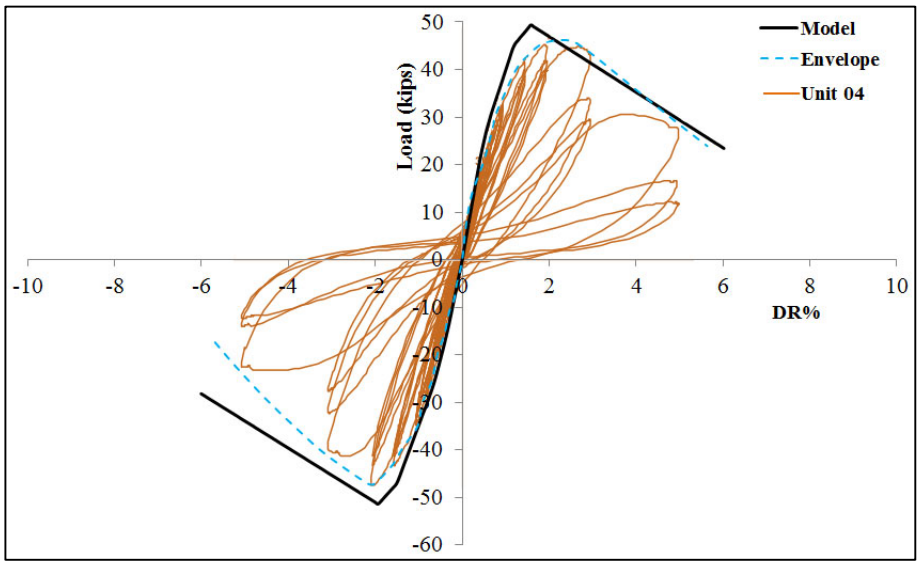

Figure 10-42: Simulation results of unit 04 tested by Pantelides et al. (2002)

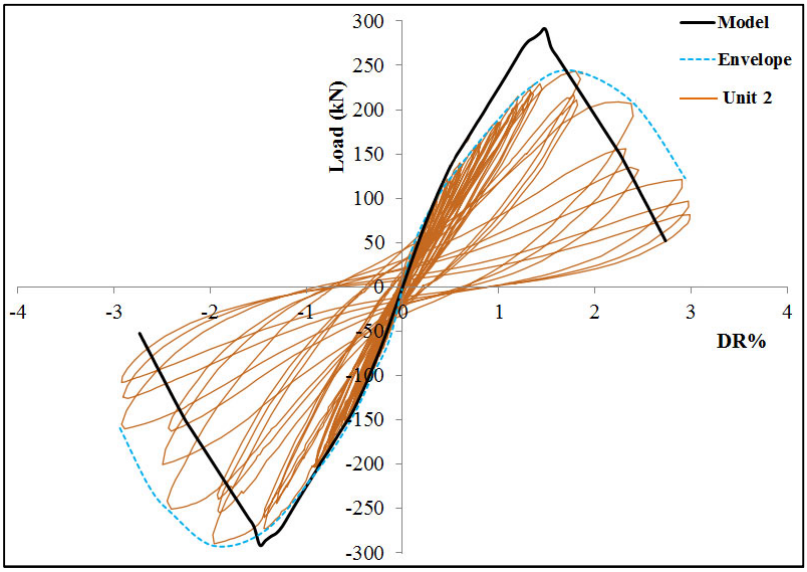

Figure 10-43: Simulation results of unit 2 tested by Clyde et al. (2000)

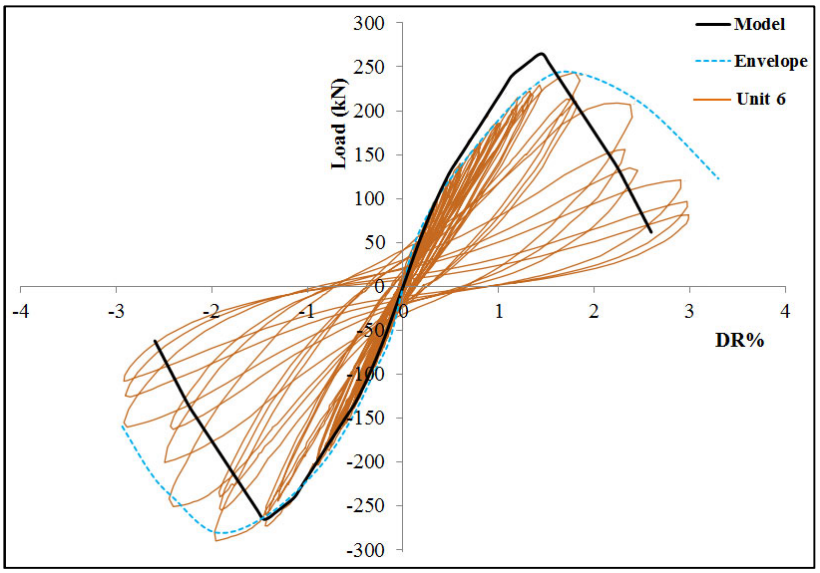

Figure 10-44: Simulation results of unit 2 tested by Clyde et al. (2000)

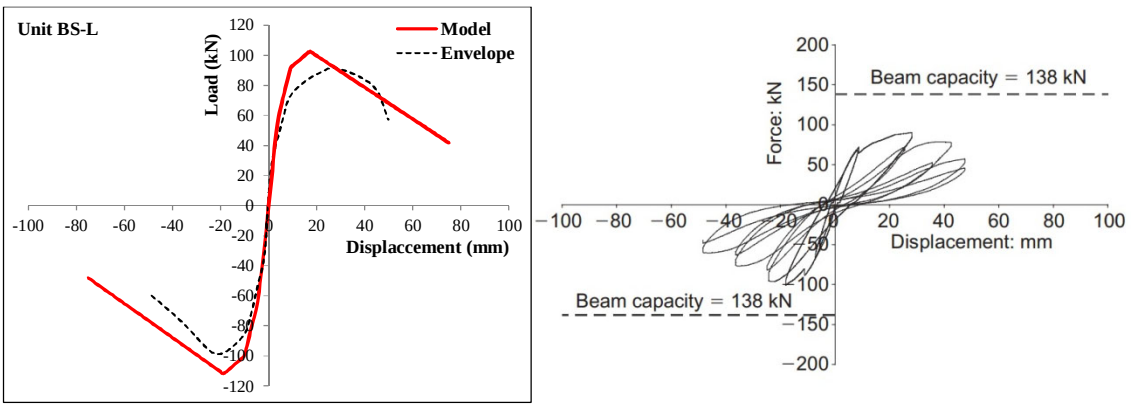

Figure 10-45: Simulation results of unit BS-L tested by Kuang and Wong (2005)

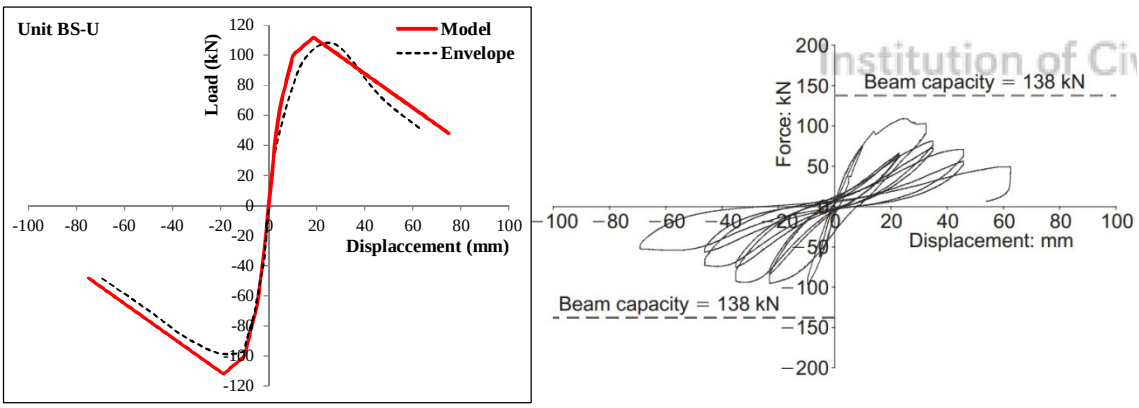

Figure 10-46: Simulation results of unit BS-U tested by Kuang and Wong (2005)

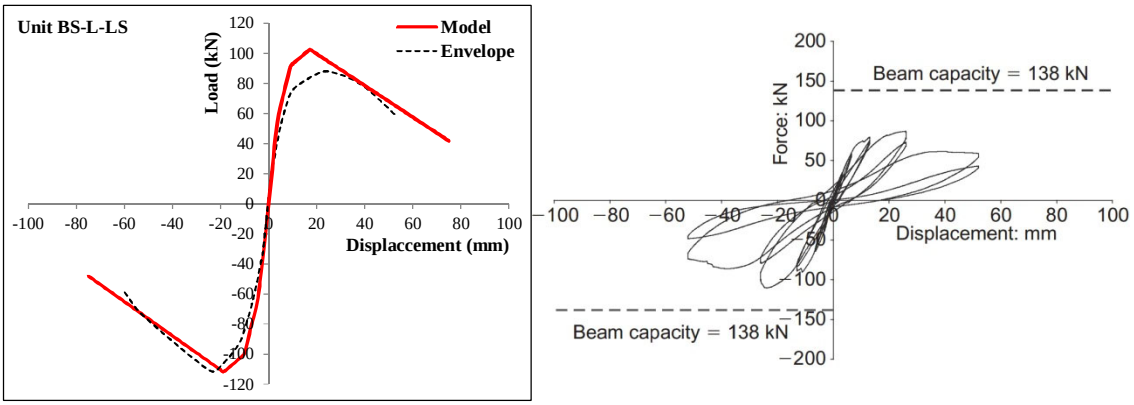

Figure 10-47: Simulation results of unit BS-L-LS tested by Kuang and Wong (2005)

10.9.3 Joint model – cyclic analysis

Results of the cyclic analyses of the PTMS confined specimens, in comparison with the measured responses are shown in Figure 10-48 through Figure 10-50. In general, the suggested joint model was able to represent well the enclosing load-displacement response and to capture the contributions from the beam, columns, and joint region to the overall story drift. Slight overestimation of the stiffness after the first cracking was noted in the test units JA-3PTMS and JB-1PTMS. Also, it was observed that, up to the maximum capacity, the hysteretic characteristics of the model represented well those from the measured response. In the post-peak

stage, however, some disturbance occurred in the hysteretic rules due to the use of negative stiffness in Element 10. This caused a slight overestimation of the energy dissipated using the analytical model, as shown in Figure 10-51. In the figure, the per-cycle energy dissipated by the analytical models at the post-peak loading steps was calculated and compared to the experimental results. The overestimation was calculated at 22% for units JA-3PTMS and JB-1PTMS. Thus, the use of the hysteretic rules of E10 must be dealt cautiously so as to avoid unacceptably high damping systems.

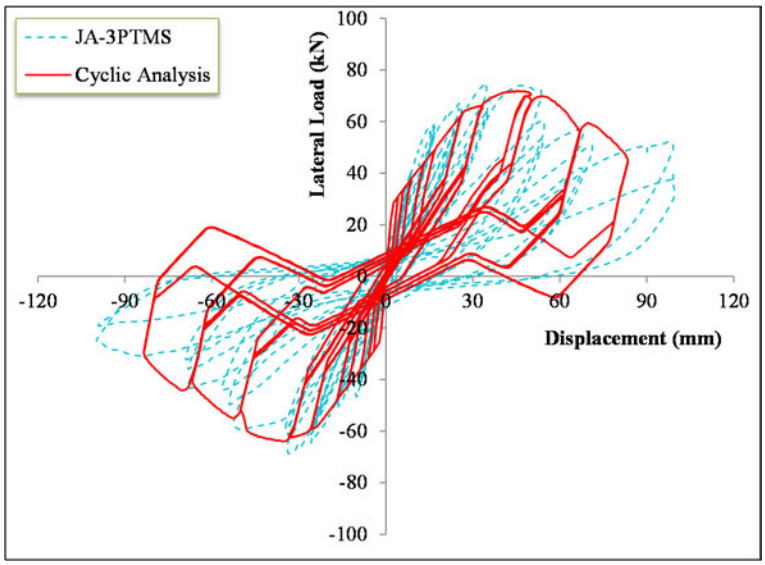

Figure 10-48: Simulation results of joint JA-3PTMS– Case: cyclic analysis

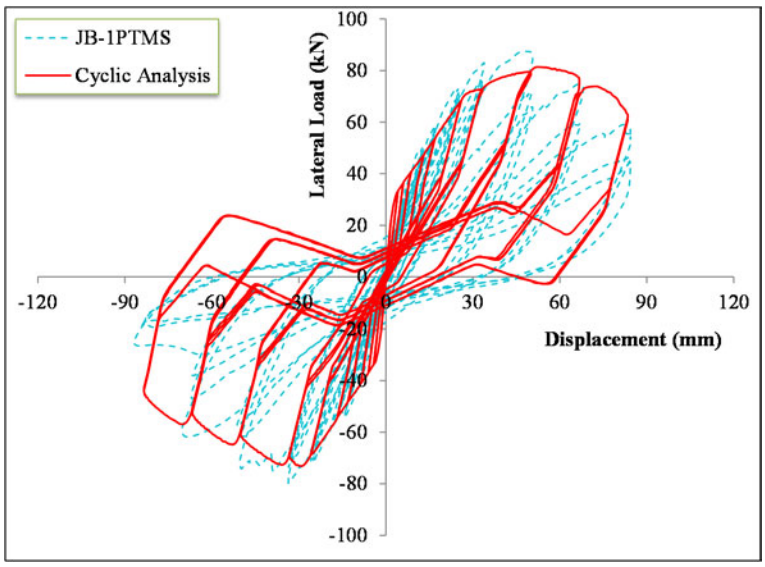

Figure 10-49: Simulation results of joint JB-1PTMS– Case: cyclic analysis

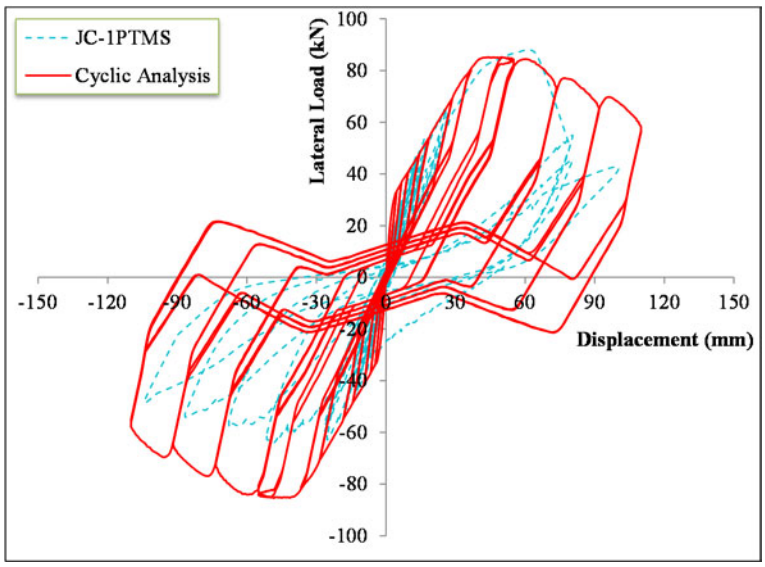

Figure 10-50: Simulation results of joint JC-1PTMS– Case: cyclic analysis

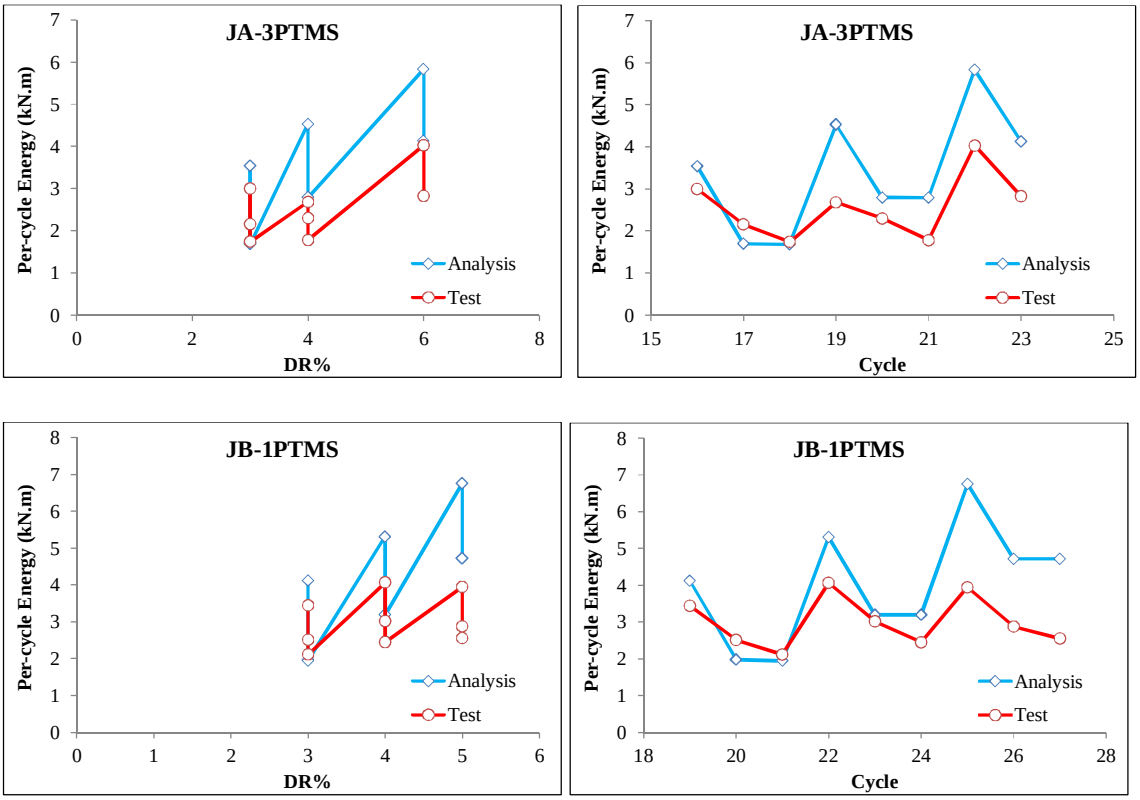

Figure 10-51: Analytical versus experimental post-peak per-cycle energy

10.10 CONCLUSIONS

A shear stress-strain joint model is proposed based on the available test results to predict the shear behaviour of the deficient exterior joints strengthened by PTMS technique. The model is built based on the modified strut-and-tie ACI-based model developed by Hassan (2011), and it considers various beam anchorage detailing as well as the contribution of PTMS confinement. The developed model is shown to predict reasonably well the joint shear strength in both loading directions of the unconfined and confined joints.

Also in this chapter, an analytical method using the scissors panel zone model is proposed for predicting the joint behaviour of RC beam-column connections, including deformational components by flexure, slip and shear. The modelling is performed using DRAIN-2DX software package. The joint model resulted in good analytical predictions of the measured responses. The use of ASCE model for joint modelling was found to be suitable for simulating the pre-peak response of the deficient beam-column joints. However, in the post-peak stage, unacceptable brittle behaviour occurred. Cyclic analyses were also performed on the strengthened joints, which showed good simulation of the behaviour. However, an increase of 22% in the energy dissipation capacity was obtained. The scissors model was found to be simple, rational and straightforward in implementation for simulating the behaviour of RC joints.

Chapter 11

REHABILITATION OF A FULL-SCALE RC FRAMED STRUCTURE

11.1 INTRODUCTION

In this chapter, shake table tests on a full-scale structure strengthened with PTMS are presented. The preliminary results include damage states and cracking patterns.

11.2 BANDIT PROJECT

The Earthquake Engineering (EEG) research group at the University of Sheffield (UoS), as the proposing team led by Professor Kypros Pilakoutas, had received the support of the SEISMIC ENGINEERING RESEARCH INFRASTRUCTURES FOR EUROPEAN SYNERGIES (SERIES, EU IFP7 project), to perform seismic shaking table tests on a full scale building so as to investigate the reliability of the PTMS strengthening methodology. The main partners included: The University of East London (UK); Istanbul Technical University – ITU (Turkey);

Technical University of Iasi (Romania); University of Girona – UdG (Spain); University of Nevada – Reno (US); and Cyprus University of Technology (Cyprus). Other partners included: University of Michoacan (Mexico); Sharif University of Technology (Iran); Damascus University (Syria); NUST (Pakistan); Malaysia Sarawak (Malaysia); Bung Hatta University (Indonesia); National University of Singapore (Singapore). The project aimed to validate work by the members of the consortium on structural elements as well as previous work carried out under the Ecoleader project. The tests were carried out in the same laboratory as for the Saclay building.

In the research project, a deficient full-scale two-story RC framed building was tested under unidirectional and XYZ shaking table excitations to assess the potential and limitations of new rehabilitation strategies using PTMS and CFRP. The RC frames were designed to be typical of substandard construction in Mediterranean and developing countries and to suffer from low strength concrete (f'_c= 10-20 MPa) and poor detailing in joints and columns. The seismic performance of the deficient building was evaluated by imposing initial damage to the bare frame in unidirectional shaking table tests. The building was then repaired by using the PTMS strengthening technique to assess its efficiency and performance for rehabilitation purposes.

The second test series on the building was done on a strengthened frame using strengthening configurations of PTMS and CFRP laminates. The retrofitted building was subjected to seismic intensities in Y-direction and followed by tests in XYZ directions.

The building was designed with different beam geometries and detailing of reinforcement in the X and Y directions to obtain maximum benefit from the frames. A summary of the building design and details are given in Appendix J.

11.3 SHAKE TABLE TESTS

The artificial acceleration signal used as input on the shaking table, was generated by CEA stuff in Saclay facility using the EC8 elastic response spectrum corresponding to a medium soil category (type C), which simulates the magnitude of the input on a structure located on medium dense sand. The excitation acceleration signal, shown in Figure 11-1, had duration of 30 seconds and was calculated with damping ζ of 5%. The input record was scaled, as shown in Figure 11-2, to obtain increasing levels of PGA according to the test sequence listed in Table 11-1.

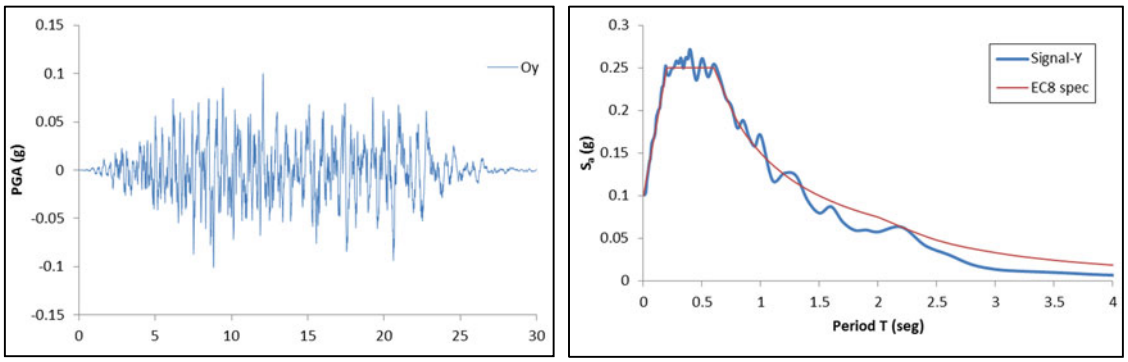

Figure 11-1: Input record and match with EC8 design spectrum, EC8 (2004)

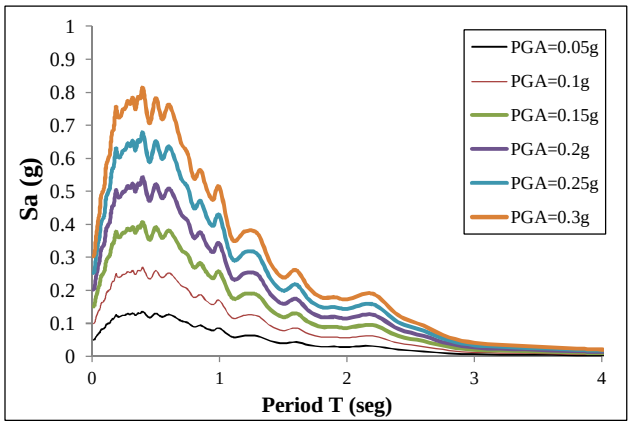

Figure 11-2: Scaled response spectrum used in the test

Table 11-1: Tests and acceleration levels

Direction	Condition of the test	PGA level (g)
X-direction	- Bare frame	0.05, 0.10 and 0.15g
	- Frame strengthened by PTMS	0.05, 0.10, 0.15, 0.20, 0.30 and 0.35g
Y-direction	- Frame strengthened by PTMS	0.05, 0.10, 0.15, 0.20 and 0.30g
Y-direction	- Frame strengthened by PTMS & CFRP	0.05, 0.20, 0.30 and 0.35g
XYZ test	PTMS & CFRP	0.10, 0.20, 0.30, 0.35, 0.4, 0.5 and 0.6g

As can be seen from the table, during the tests on the bare frame in the X-direction, three uniaxial seismic tests with artificial acceleration records and increasing peak ground acceleration (PGA) levels from 0.05g to 0.15g were applied to the building. The natural frequencies of the frame were measured before and after each test by white noise tests. The first natural frequency of the frame before testing was measured at 2.1Hz. The PTMS strengthened structure in X-direction was subjected to increasing peak ground accelerations up to 0.35g. The same PTMS structure was subjected to PGAs in Y-direction up to 0.3g. After retrofitting with PTMS and CFRP laminates, the test included seismic intensities in Y-direction up to 0.35g. In the last test phase, the structure was subjected to a 3D seismic test with intensities up to 0.6g.

11.4 PTMS STRENGTHENING SCHEME

Before strengthening, the damaged concrete debris was removed and replaced with repair mortar, as shown in Figure 11-3(a) and (b). In addition, the main cracks within the joint regions were injected with epoxy resin; see Figure 11-4(a). Moreover, welding works were also done by welding two of the beam bottom anchorages to the column longitudinal reinforcement at the top story, as shown in Figure 11-4(b).

Figure 11-3(a): Concrete debris removal (left) and joint shoring after casting with new repair mortar (right)

Figure 11-3(b): Joints after repair with new mortar

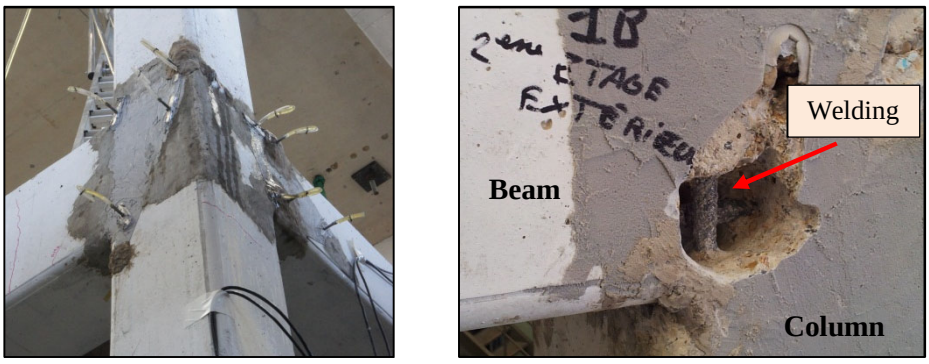

Figure 11-4: a) Injection of resins, and b) welding of beam bottom bars to column bars

Using the experience from tests on beam-column joints with the PTMS technique conducted in this study, a new strengthening scheme was developed to upgrade the structure capacity. Figure 11-5 shows a schematic view of the PTMS configuration used in the first storey joint. The strengthening scheme included providing lateral and longitudinal post tensioned metal strips along the beam and column hinge zones. Double strips were used for the strengthening. Lateral strips spaced at 25 mm were first used to confine the column and beam sections up to a length of 500mm. Narrow holes were made along the beam hinge zone at the connection with the slab to facilitate full confinement of the cross-sections. The holes were formed during the construction of the building. The cross-section corners of columns and beams at the hinge zones were rounded with a radius of 20 mm to provide better placement of strips and, consequently, better confinement. To apply the longitudinal strips, steel plates were fixed onto the column and beam surfaces by means of 12mm diameter and 120mm length steel bolts driven through the concrete between reinforcing bars (Figure 11-6). Before tensioning, the strips were threaded underneath the steel plates. After that, the strips were tensioned from one side and sealed by double-notched metal clips. Few lateral strips were applied above the longitudinal strips to prevent out-of-plane movements or sliding of strips away from the steel plates. Figure 11-7 shows views of the strengthened joints at the first floor from inside and outside and also view of 2nd floor joint. In addition, Figure 11-8 shows a full view of the strengthened building before testing in X-direction.

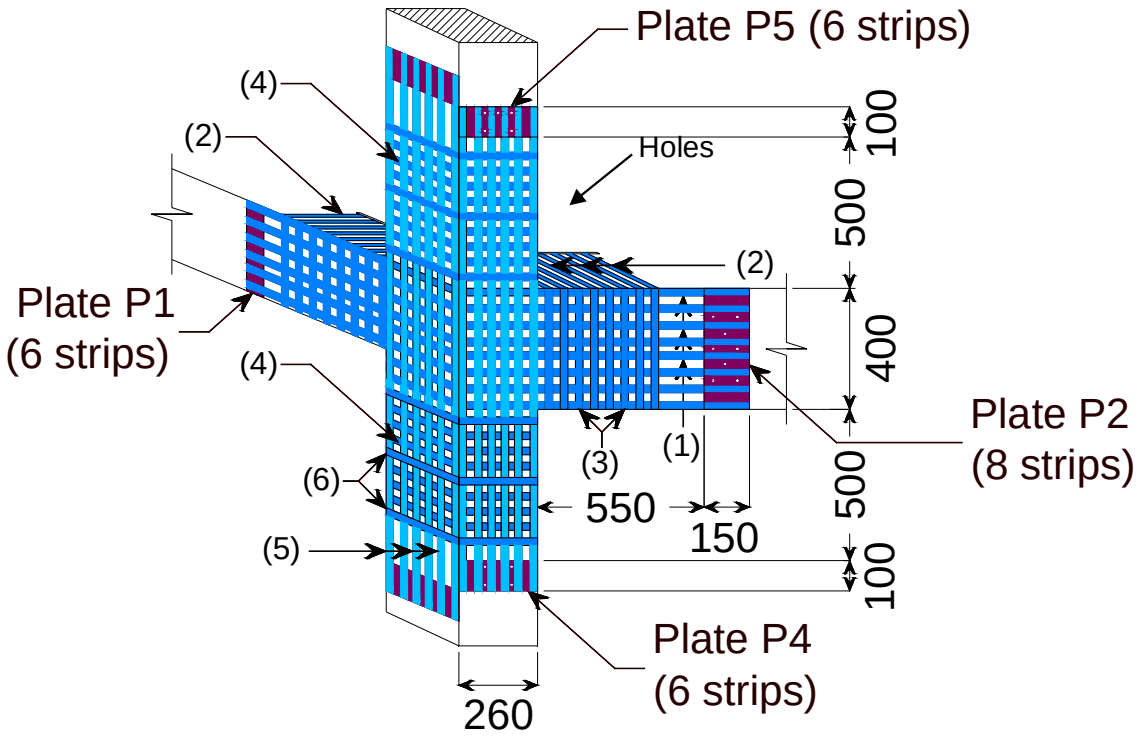

Figure 11-5: Proposed PTMS strengthening methodology

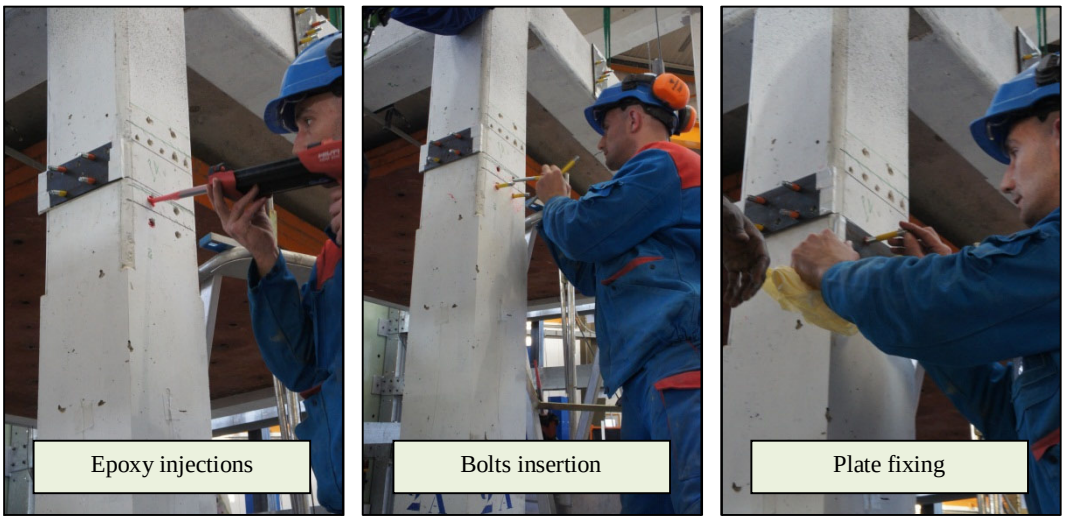

Figure 11-6: Stages of fixing the steel plates on a column side

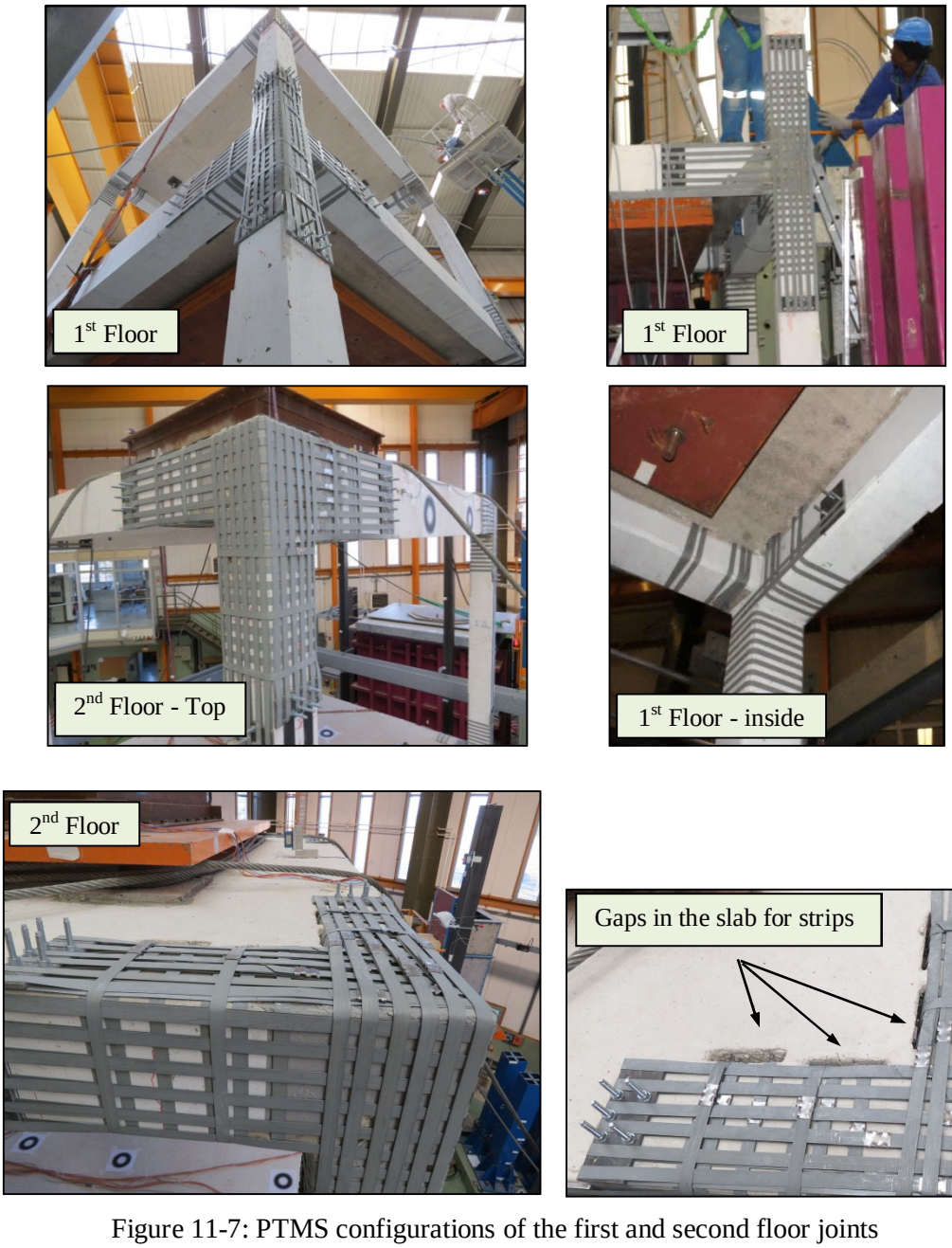

Figure 11-7: PTMS configurations of the first and second floor joints

Figure 11-8: View of the strengthened structure tested in X-direction

11.5 PRELIMINARY TEST RESULTS

The full test results of shake table tests including damage states at each loading stage, strain gauge readings, and channel sequence are not yet available, and thus, only preliminary conclusions are made.

11.5.1 Test results of the bare building

11.5.1.1 Observed Damage

The test started at a low seismic intensity of 0.05g. From damage observations, it was noted that most cracks developed close to the joints and very few in the beams.

Cracking of the joints was visually observed after the first seismic test (0.1g). During the 0.15g PGA test, diagonal cracks appeared on the 1st floor joints along with horizontal cracking at the top column/joint interface (splice ends). In addition, cracking was observed along the splice regions in some joints. The 2nd floor joints had received extensive damage due to high drifts and large flexibility of the top story. The high flexibility of the second floor may be attributed to the large rotations at splice ends. At this stage a severe drop in frequency was noted (Table 11-2), and consequently, the test was halted. Figure 11-9 through Figure 11-12 show the damaged areas after 0.15g PGA seismic test.

Table 11-2: Frequencies before and after the shaking table tests

Intensity	**0.05g**		**0.10g**	**0.15g**
	Before	after	after	after
	Hz	Hz	Hz	Hz
1st Mode	2.1	1.6	1.34	1.08

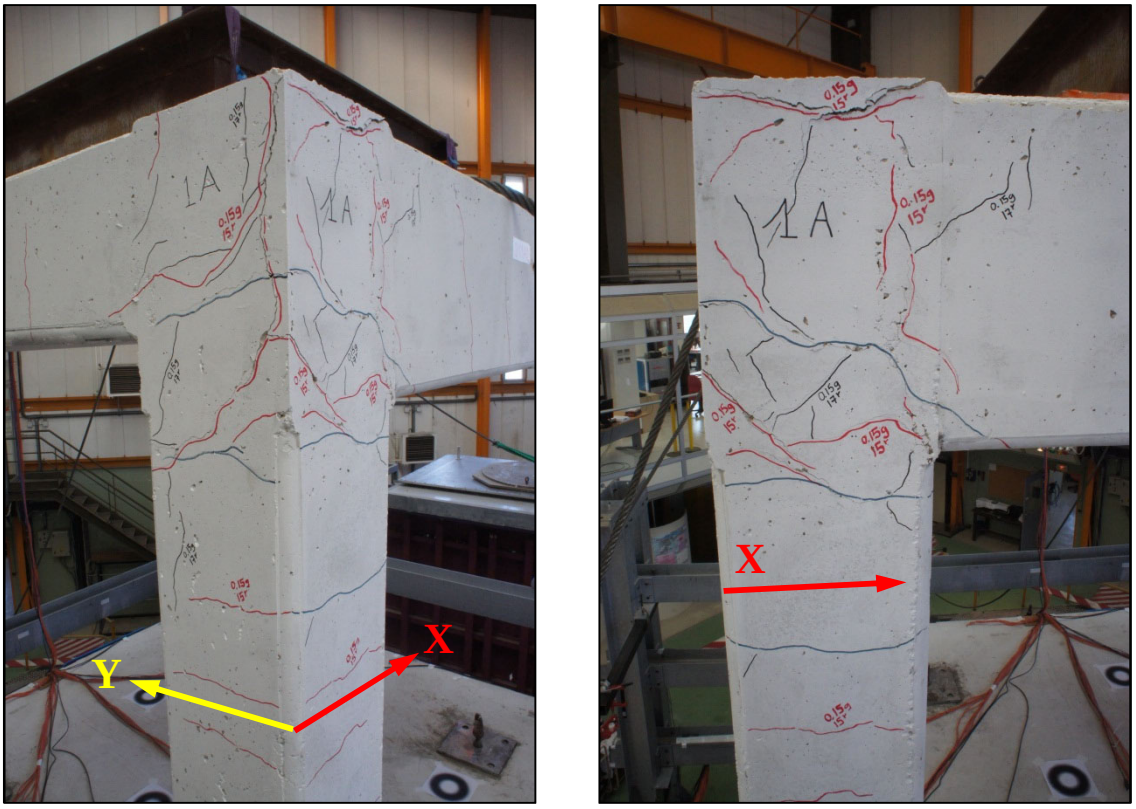

Figure 11-9: Damage of joint J1A-2nd at 0.15g – bare structure

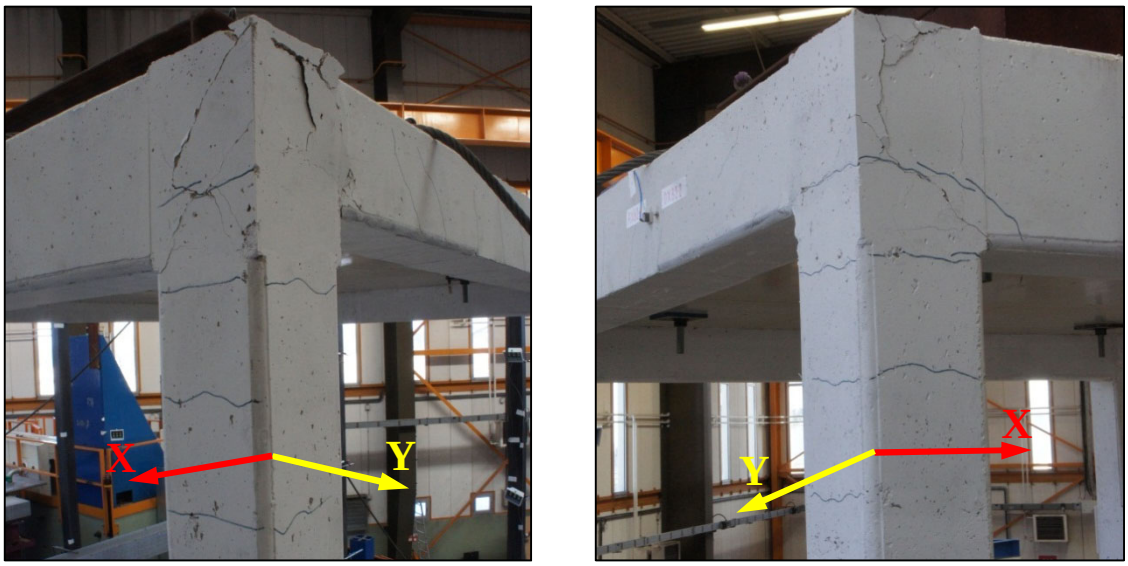

Figure 11-10: Damage of joint J2A-2nd (left) and J2B-2nd (right) at 0.15g – bare structure

Figure 11-11: Damage of joints J2A-1st (left) and J2B-1st (right) at 0.15g – bare structure

Figure 11-12: Damage of joint J1A-1st at 0.15g – bare structure

It is clear from the previous figures that most of the cracks were localised at the joint regions and did not spread in the columns. Sizable shear cracks developed in the top story joints along with spalling of concrete cover. Also, multiple smaller shear cracks formed diagonally within the joint region. As the column capacity of the top story was less than that of the beam, cracking also occurred at the bottom column/joint interface. At the joints of the first story, diagonal cracks initiated from the bottom beam anchorages towards the back of the top column. Some flexural cracks were also observed along the beam span.

The bare structure was noted to behave as expected from an initial analytical model built with DRAIN-2DX. Comparisons are presented in Figure 11-13 through Figure 11-15. The model used element 15 to represent the bond-slip and shear deformations in the core. The bond-slip model by Sezen (2003) was used to simulate the bond component. The ASCE 41-06 model for shear was used with considerations for transverse beams and knee joints. Details of the model are given in Appendix K. Further enhancement to the work is still required using more sophisticated FE software; specifically for damping issues as it was highlighted in the previous chapter.

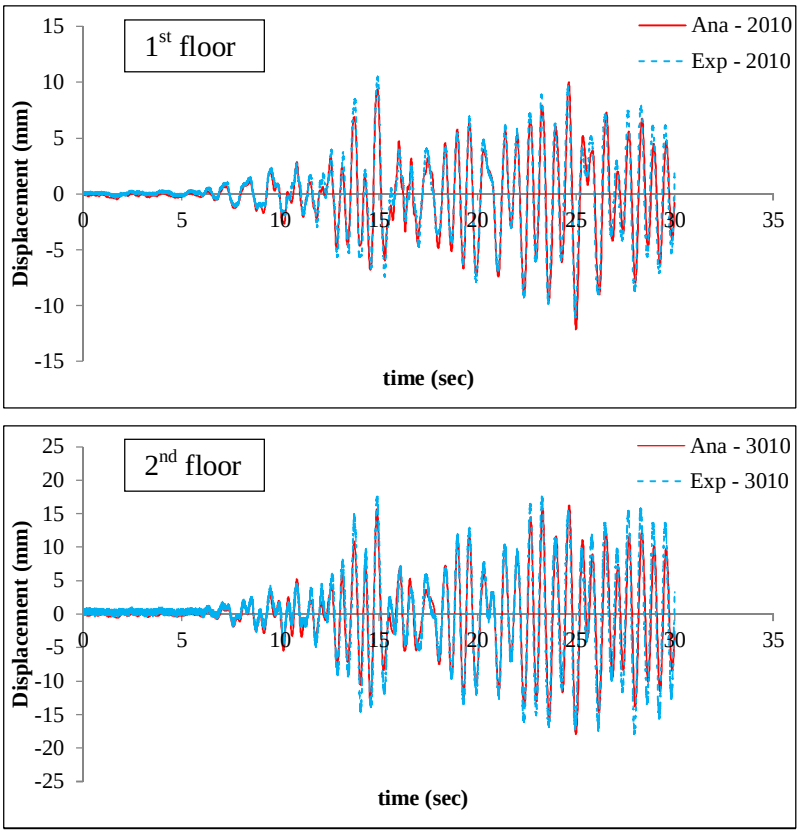

Figure 11-13: Comparison of analytical and measured responses – 0.05g

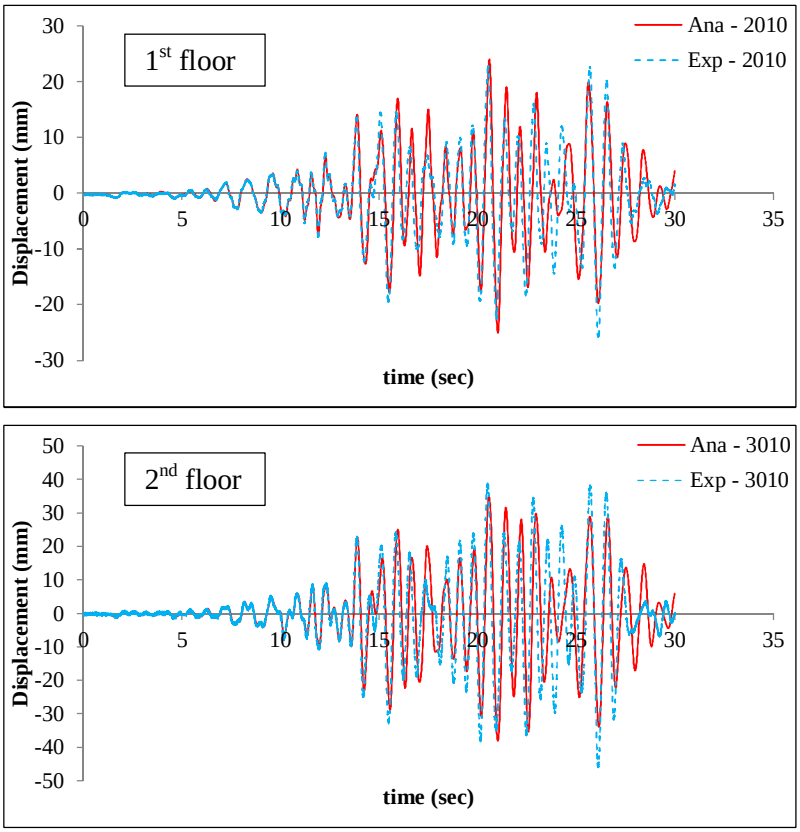

Figure 11-14: Comparison of analytical and measured responses – 0.10g

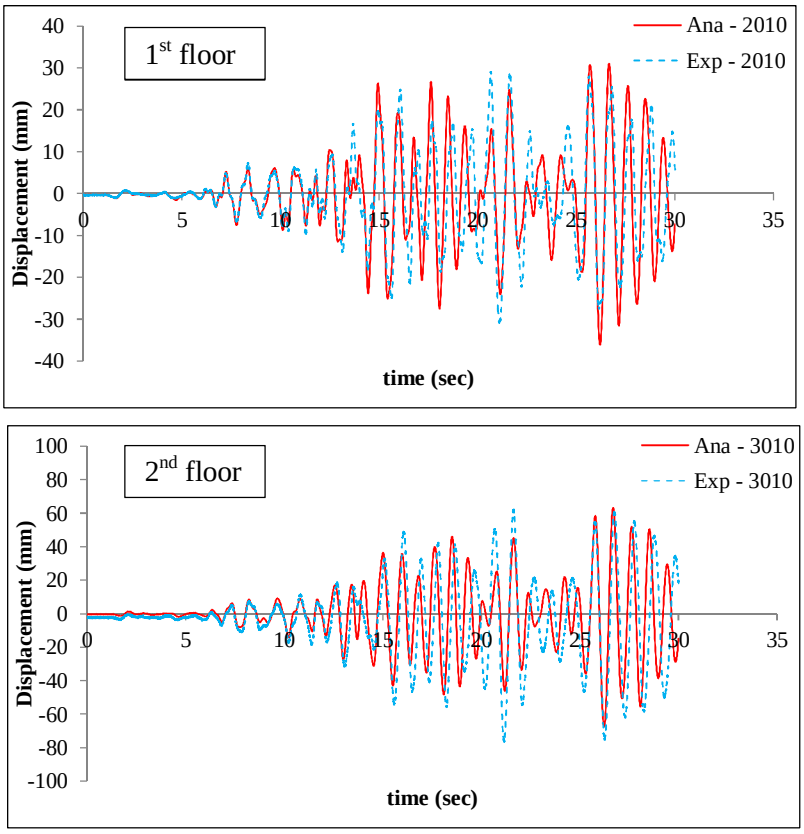

Figure 11-15: Comparison of analytical and measured responses – 0.15g

11.5.2 Test results of the strengthened building: Stage II PTMS (X-direction)

11.5.2.1 Observed damage

Description of the damage in this test phase is after the test in X-direction up to a seismic intensity of 0.35g and in Y-direction up to intensity of 0.3g. The strips were kept during the test in Y-direction and removed thereafter. Figure 11-16 through Figure 11-23 show the damage observed in the beam-column connections after the test.

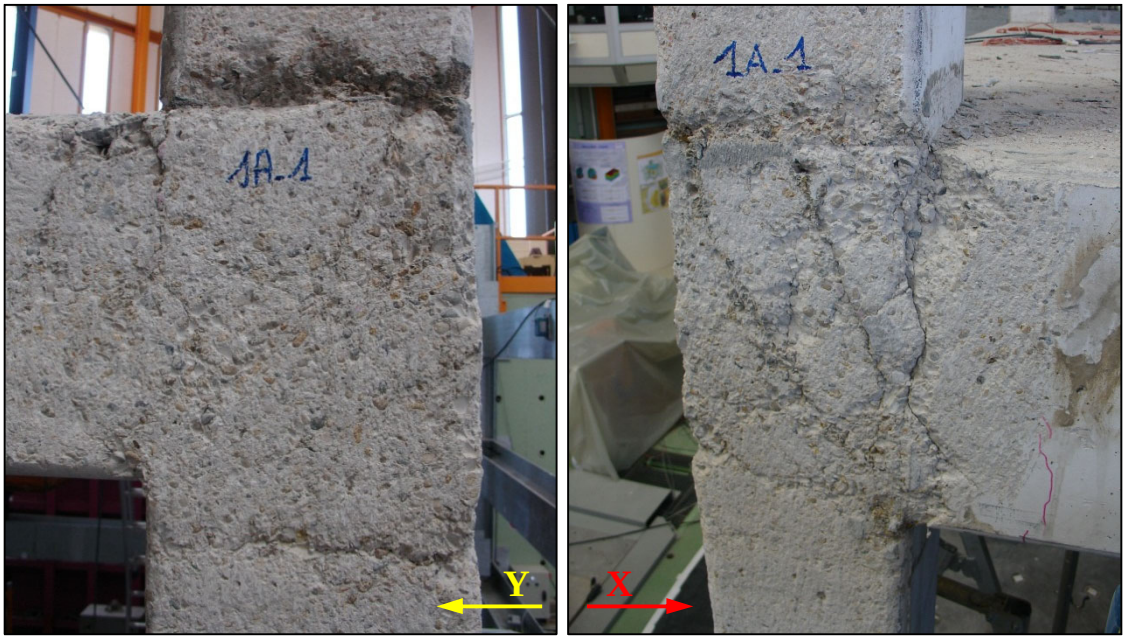

Figure 11-16: Damage of joint J1A-1st at 0.15g – second series

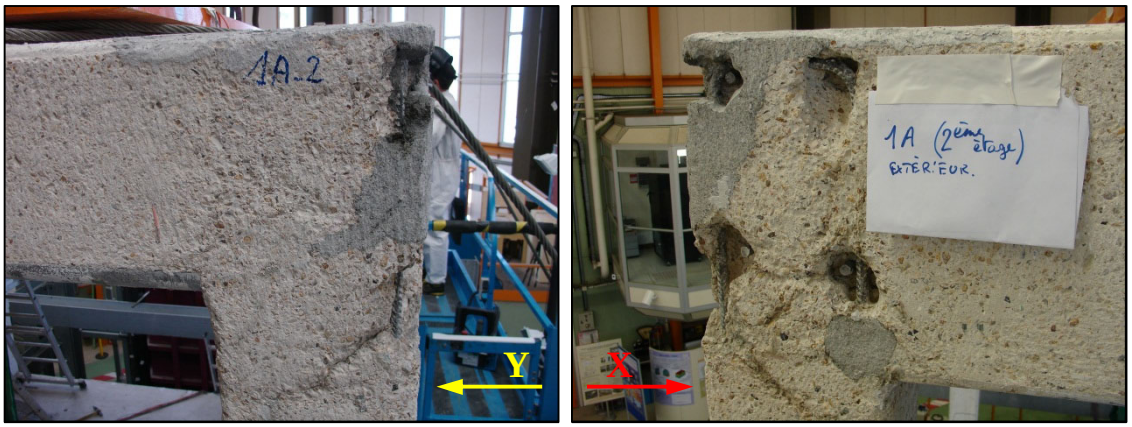

Figure 11-17: Damage of joint J1A-2nd at 0.15g – second series

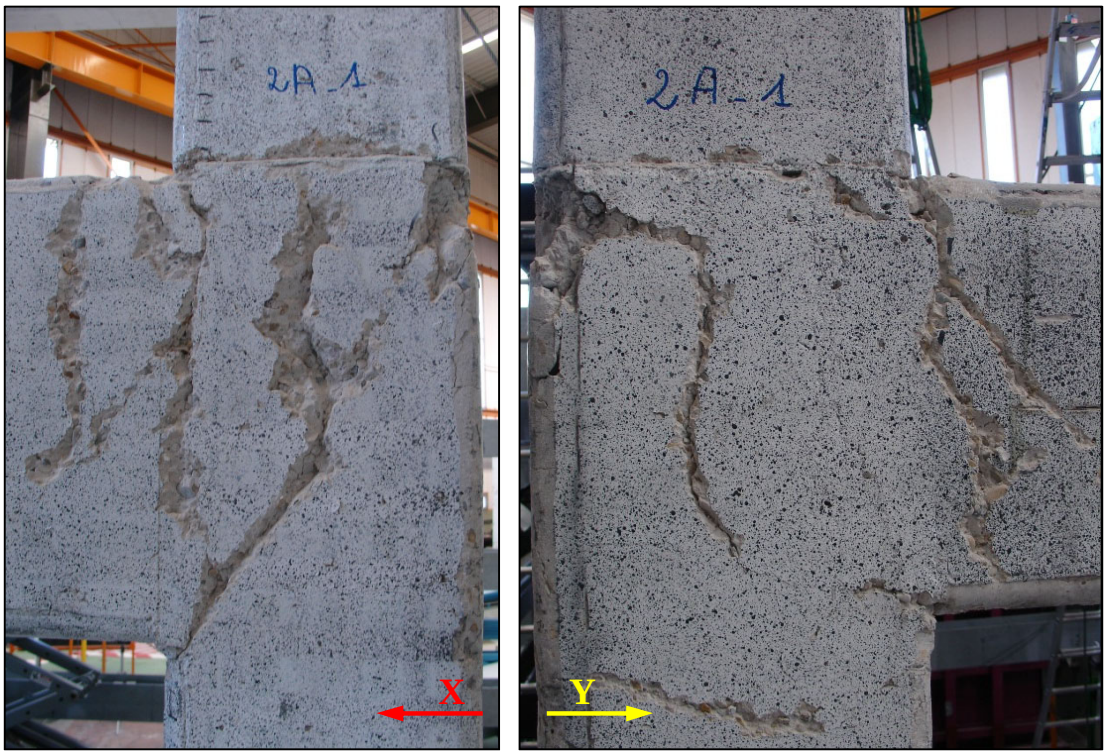

Figure 11-18: Damage of joint J2A-1st at 0.15g – second series

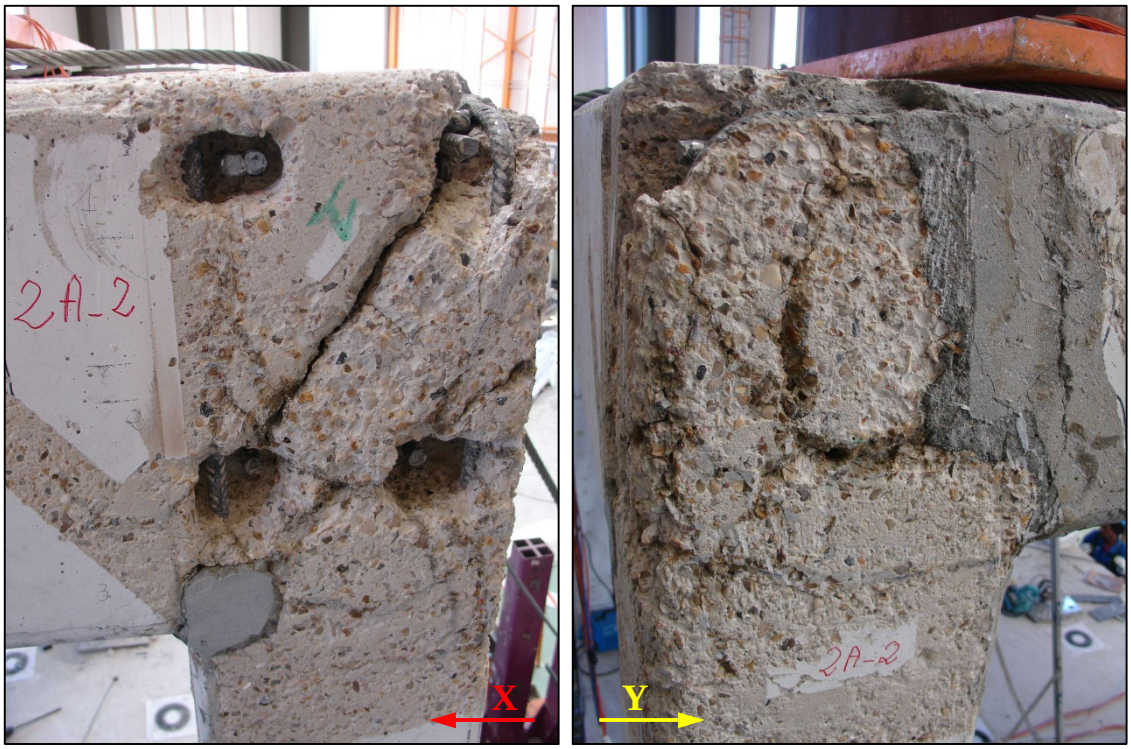

Figure 11-19: Damage of joint J2A-2nd at 0.15g – second series

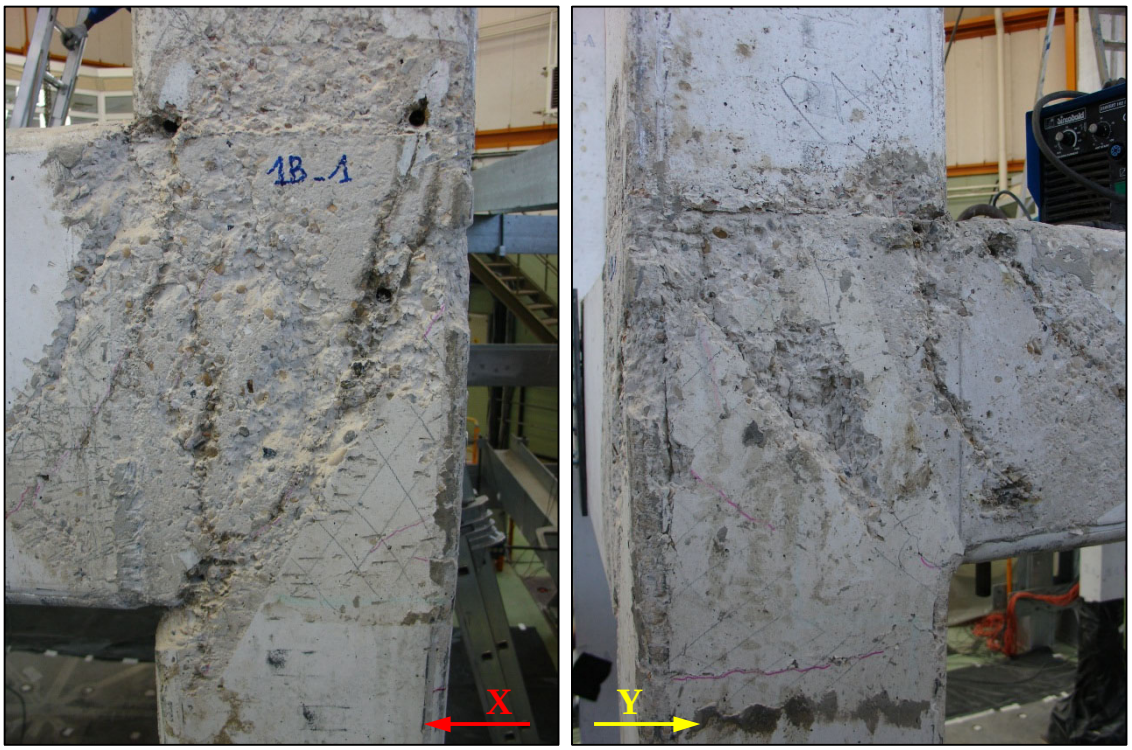

Figure 11-20: Damage of joint J1B-1st at 0.15g – second series

Figure 11-21: Damage of joint J1B-2nd at 0.15g – second series

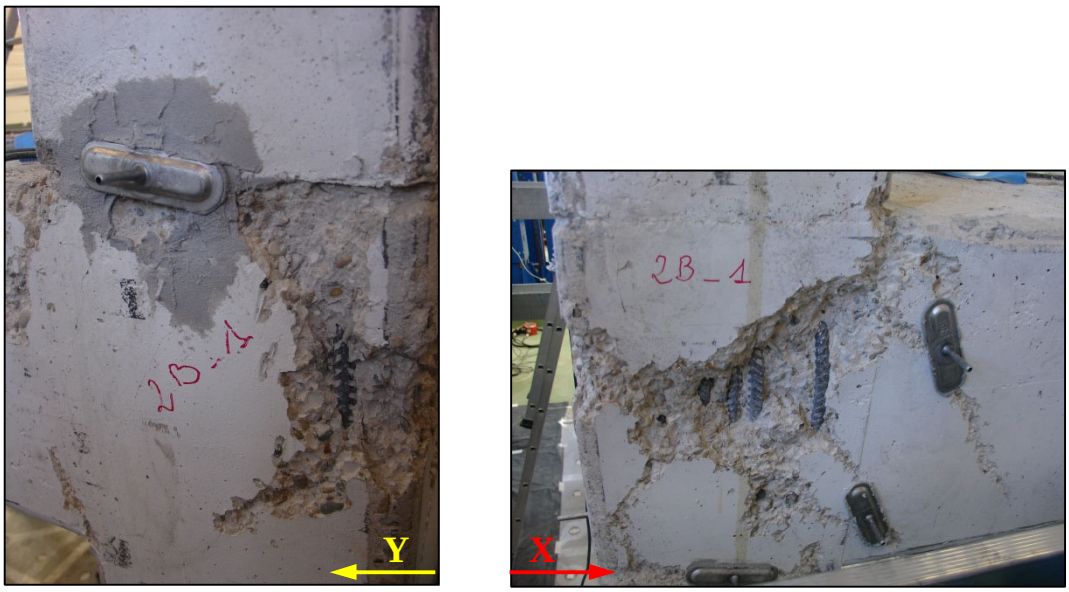

Figure 11-22: Damage of joint J2B-1st at 0.15g – second series

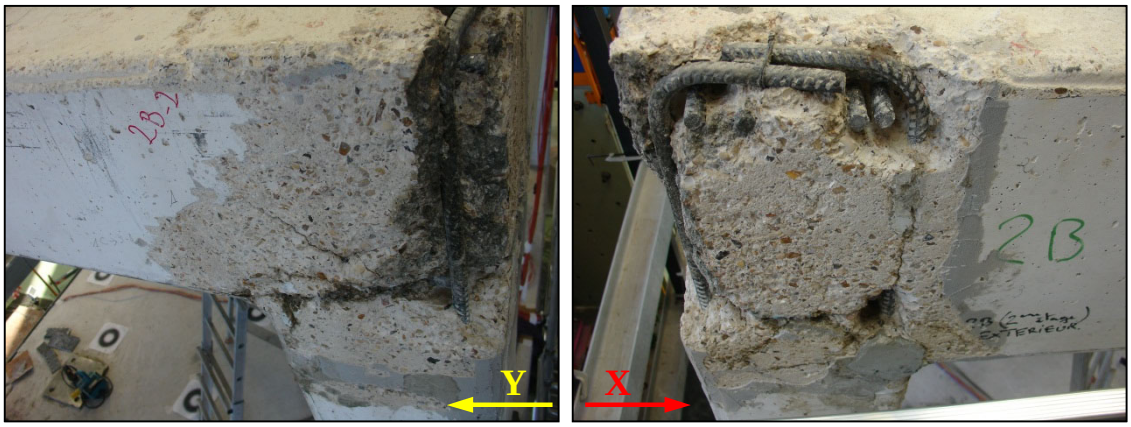

Figure 11-23: Damage of joint J2B-2nd at 0.15g – second series

As can be seen from previous figures, almost all first story joints experienced diagonal cracks in the joint region initiating from the anchorage zone of beam bottom bars and extending towards the top column interface or splices. Most of these cracks were observed in the test of the bare structure. Also, it is clear that cracks formed at the beam and column interfaces with the core indicating bond deterioration of anchorages and splices. In addition, few cracks formed at hinge zones of the beams and columns.

11.6 DISCUSSION AND INITIAL CONCLUSIONS

The structure was designed in such a way to study a multiple number of parameters including shear and bond demands in the beam-column joints, buckling of column reinforcement, plastic hinge lengths and most importantly the effectiveness of Pre-Tensioned Metal Straps (PTMS) and Carbon Fibre laminates (CFRP) strengthening techniques. From the tests, the following preliminary conclusions were drawn:

1. Substandard buildings typical of those found in Mediterranean countries may sustain considerable damage under minor earthquakes. In the case of this tested structure, the joints on the top floor sustained severe damage at 0.15g.
2. The bare deficient structure had experienced considerable damage within the joint regions.
3. The PTMS strengthened structure showed remarkably improved behaviour in comparison with the bare structure. In the first tests on the PTMS case, the strengthened structure sustained a seismic intensity of 0.35g with little damage compared to 0.15g of the bare structure.
4. At the final test stage, in which one frame of the building was strengthened by PTMS and the other frame strengthened by CFRP, the building withstood a 0.6g earthquake in the XYZ direction with some damage.
5. In terms of the application of PTMS strengthening technique, the proper installation of metal plates on element sides was found to be essential for a safe transfer of tensioning forces to the strengthened elements, and thus, the success of the strengthening technique.
6. Overall, the PTMS technique was found to be easy to install and very efficient in addressing the problems of this substandard structure.

Chapter 12

CONCLUSIONS AND RECOMMENDATIONS FOR FUTURE WORK

12.1 INTRODUCTION

This research focuses on assessing the behaviour of strengthened low strength RC exterior beam-column joints with substandard details typical of those in developing countries. Emphasis is given to bond and shear issues. A new method to upgrade the strength of the deficient joints using external pre-tensioned metal strips is examined.

The research aims to contribute towards providing a reliable and efficient joint model that can be used by structural engineers for the seismic assessment and strengthening of existing buildings. The research involved i) a literature review, ii) an experimental programme on beams

and full-scale exterior RC joints under cyclic loads, iii) development of a new bond stress-slip relationship for premature bond failures and short splices taking into account the effects of external strengthening, iv) development of a model to predict the shear strength of PTMS confined joints.

This chapter presents a summary of the conclusions from the different tasks and finishes with recommendations for further enhancement of this work.

12.2 SUMMARY OF CONCLUSIONS

From the background study of this topic it was concluded that:

- Many RC buildings in developing countries are badly designed, and thus, they are highly vulnerable to earthquake actions. Many catastrophic collapses occurred in such buildings in the last four decades under moderate seismic intensities.
- When gravity loaded designed (GLD) RC frames are subjected to lateral actions, they experience severe cracking and damage in the joint region, and many ultimately suffer joint shear failure before development of plastic hinges in the adjoining members.
- Deficient details in substandard RC beam-column connections in existing non-seismic buildings have been studied before; however, most studies examine isolated connections disregarding slabs or transverse beams. Moreover, most tests on deficient structures were performed on scaled models, which may not appropriately simulate the actual effect of critical details.
- Exterior joints are highly vulnerable to severe damage due to discontinuity of geometry and inappropriate curtailment of anchored bars in addition to the poor detailing.
- The absence of sufficient amount of lateral confinement in joints could lead to flexural strength degradation, shear failure, significant loss in stiffness and large instability of the structural system due to bar buckling and/or bond failures.
- During seismic actions, the joint region in GLD RC frames undergoes much larger shear distress and deformations than expected from well designed structures. Therefore, it is recommended that joint shear deformation, which is commonly disregarded in the analysis of well-designed frames, be properly taken into consideration in the analysis of GLD RC frames.

From the review on substandard column splices and bond behaviour it can be concluded that:

- Column splices typical of those found in older RC framed buildings are deficient as they are short and lightly confined by transverse reinforcement. This, in turn, may cause severe degradation in the performance and collapses.

- Two main types of bond failure exist in RC elements, namely, pullout and splitting. A third type of bond failure referred to as "*pullout failure induced by splitting cracks*" may also occur. This failure is a result of splitting cracks along with pullout nature due to shearing of concrete keys between bar lugs.
- Splitting-type of bond failure is commonly encountered in elements with small concrete cover and small amount of lateral confinement. Such failure mode is typically characterised by an abrupt and brittle nature; however, it becomes more ductile as the amount of confinement increases.
- Concrete cover, concrete compressive strength, bar diameter, and anchorage length are the most important parameters affecting the concrete contribution to bond strength.
- The presence of transverse pressure along the anchorage length leads to an increase in the peak bond strength and a reduction in the associated slip.
- The bond strength of a given anchored length of a reinforcing bar experiencing yielding before failure was found to differ slightly compared to that of a bar failing in bond during the elastic stage. The difference was evaluated to be only 2% less for unconfined concrete and 10% higher for confined concrete.

From the review on computer-based panel zone models, it is found that:

- Many panel zone models have been proposed to simulate the behaviour of beam-column joints in RC frames.
- Most of the panel zone models are developed for unconfined joints. The addition of strengthening may require some modifications.
- Few of the joint models are suitable for numerical simulations, as they are complicated to implement in a FE model, and many input data is required.
- The scissors joint model is used in many investigations as it is simple to use and time efficient.

From the review on strengthening existing beam-column connections it can be concluded that:

- Many repair and strengthening methodologies were developed using different materials and construction applicability. Few, however, provide economic solutions for GLD buildings in Mediterranean countries.
- Most strengthening techniques have limited applicability due to practical issues such as dealing with floors and transverse beams.
- Developing of new simple and cost-effective methods is still yet open and more real test conditions should be considered such as bidirectional loading or even 3D tests.
- There is a big shortcoming and less effort on developing analytical methods to accurately and safely evaluate the performance of strengthened structures. In addition,

evaluation guidelines are still yet to be established for different strengthening methodologies.

From the review of recent development on PTMS technique it can be concluded that:

- The PTMS technique is suitable to confine small and medium scale RC elements in compression and/or in tension. The confined elements show considerable enhancement in strength as well as ductility.
- The use of EC8 confinement model provides reasonably conservative predictions of additional enhancement in compressive strength due to PTMS.
- The strapping technique is effective in upgrading the strength of over-reinforced beams in flexure and beams with shear or bond problems.
- A confined concrete model is proposed by Moghaddam et al. (2010), which accounts for passive and active PTMS confinement.

From the test series on beams with short splices, the following conclusions were drawn:

- All beam specimens, confined or unconfined, in which the flexural reinforcement is spliced with a deficient length of 10 times the bar diameter and loaded in tension, failed in the elastic stage due to development of splitting cracks along the spliced bars. Splitting failure led to stiffness and strength degradation and considerable concrete damage within splice zone.
- The absence of confinement within the splice region resulted in a sudden and brutal failure within the splice zone such that the cover concrete spalled off abruptly leading to complete loss of concrete bond with the reinforcing bars. In such cases, few or nil flexural cracks tended to develop along the splice.
- Reinforcing the splice zone with internal confinement using steel stirrups only improved ductility. Lateral confinement allowed for multiple flexural and splitting cracks to develop after the maximum strength was reached. Large ultimate deflections were achieved along with a gently degraded post-peak response. In comparison to the unconfined specimens, the internally confined specimens resulted in insignificant enhancement in bond strength.
- Providing post-tensioned external confinement had a considerable impact on the behaviour. Sizable enhancement in strength and ductility were achieved regardless of the concrete strength, bar diameter, c_{min}/d_b ratio and the amount of PTMS confinement in the section. The PTMS specimens experienced both controlled splitting and flexural cracking within the splice zone; a reason for the improvement in ductility.
- Reducing the strip spacing resulted in better behaviour in which higher bond strengths were obtained.

- The increase in concrete cover also led to beneficial effects on externally confined specimens where bond strength increased for larger concrete covers.
- Cracked section analysis gave accurate predictions of the bar force and maximum bond strength. This implied that the assumption of linear strain profiles or uniform bond distributions along the splice is suitable for predicting the bond capacity.
- The bond stress-slip characteristics of confined specimens are defined by a simplified model with five stages of behaviour.

From the test series on beams with long splices, the following conclusions were drawn:

- Similarly to Phase I, all specimens failed due to splitting-type of bond failure within the splice zone.
- Unconfined and internally confined specimens behaved in a similar manner to those of Phase I.
- The use of an amount of PTMS confinement equivalent to that of the associated internally confined specimens allowed the spliced bars to develop post-yield strains and the beams to acquire considerably larger loads and large deformations and, as a consequence, high energy dissipation capacities.
- Although yielding was attained in the PTMS confined specimens, spread of splitting cracks prevented the strengthened specimen from mobilising its full flexural strength.
- The improved behaviour of PTMS specimens led to a pullout-like failure type, where the bars pulled out of the concrete matrix along with shearing off the concrete keys between bar lugs.
- Strain profiles resulting from strain gauge readings along the spliced bars showed that, at the maximum loading, the distributions are approximately linear.
- In contrast to specimens of Phase I, a decrease in concrete cover had positive influence on bond strength of long splices. This is attributed to the concrete contribution to bond which decreases as the splice length increases.

From the test series on deficient exterior beam-column joints it was found that:

- All units failed in a classical manner due to shearing of the connection region when the maximum capacity was reached. Cracks initiated at the embedment region and then merged with the joint shear cracks. Failure was accompanied by spalling of concrete at the back of the joint due to spread of shear cracks along the longitudinal bars at the back of the column.
- Failure occurred during the elastic stage before reaching the nominal flexural capacity of the assembly.
- On average, at a DR of 1.5%, which represents the maximum capacity, the bare specimens lost 76% of the initial stiffness.

- Before failure, energy dissipation was small and slow. Higher amount of energy was dissipated during the post-peak stage due to the formation of multiple cracks.
- At the maximum load, the bare joints dissipated 28% of their total cumulative energy. 72% of the energy was dissipated in the post-peak stage.
- The average equivalent damping of the bare units was found to be 5.7% which lies within code recommendations.
- Despite the moderately poor performance of the joints due to shear cracking of the core along with bond deterioration, no complete loss in strength occurred (at 4% drift where the test was halted). In addition, the energy dissipation capacity was maintained. However, the specimens suffered severe stiffness degradation.

From the strengthening of the deficient joints, it was found that:

- The strengthened units failed due to the development of a more controlled shear mechanism in the core along with moderate damage at the beam hinging region, specifically up to the second shear link of the beam.
- All units reached their yield capacity, but there was no evidence of extensive yielding.
- The initial response of the PTMS units was slightly softer than that of the bare units due to opening of old cracks. However, as load increased, the PTMS units showed higher stiffness, especially at higher drifts.
- On average, the strengthened units had lost 59% of the initial stiffness at the drift of 2% at which the maximum load was reached.
- Improvement in ductility of the PTMS units was evident by the high drifts reached and the lower rate of post-peak stiffness degradation.
- Welding of the beam bottom bars to the column longitudinal bars was found to be beneficial and led to improved behaviour. However, the joint ultimately failed in shear.
- The anchorage deficiency of the beam bottom bars eventually led to deterioration in load resistance.
- Average damping of the strengthened units was calculated at 6.6%. Although this value is close to that of the bare units, the post-peak stage showed a noticeable increase in damping which averaged at (13.3%) compared to (7.8%) in the bare units.
- At the maximum load (DR~2%), the strengthened units had dissipated 32% of the cumulative energy; and thus, most of the energy was dissipated during the post-peak stage.
- Despite the fact that the beam-column joint specimens repaired with PTMS schemes discussed in this study exhibited good enhancement in performance compared to that of the baseline substandard specimens, they did not achieve the standard performance level of a well-designed joint, which underlines the limitations in what can be achieved with the strengthening technique.

From the analytical study on bond, the following is concluded:

- Although the existing state-of-the-art model equations available in the literature and codes of practice for bond strength were able to reasonably predict portion of the experimental data, they cannot take into accounts the post-tensioning of strips.
- A unique bond stress-slip model is proposed to account for the enhancement due to PTMS on bond strength. The model consists of four points which govern the response, namely, first splitting, maximum strength, post-splitting bond strength, and residual strength.
- The parameters most affecting the contribution of PTMS to maximum bond strength are identified to be the concrete cover to bar diameter ratio, splice length, and stress in the strip. The effect of concrete compressive strength f'_c on τ_{PTMS} was best represented by a power of ¼.
- First splitting strength is found to be proportional to the maximum strength regardless of the type of confinement provided along the splice length. The first splitting strength is evaluated to be 82% of the maximum strength.
- Slip at the peak bond S_m is found to be related mainly to the PTMS contribution to bond, τ_{PTMS}.
- An additional slip component should be added to the bar movement to account for additional deformations of the bar extending into the connection region or column base. A modification is proposed on the model by Sezen (2003) to simplify the calculation of bar extension in the elastic and plastic stages.

From the FE modelling of beams and validation, it is shown that:

- Splices in reinforced concrete can be modelled, using ABAQUS 6.9 FE package, by means of steel bars connected to the concrete through nonlinear spring-type elements. Two layers of reinforcement are required to simulate slippage of the spliced bars.
- The smeared crack approach is adequate to simulate the behaviour of the beam specimens up to the maximum point. The maximum load and corresponding deflections are captured well.
- The FE model captures well the mode of failure in the test specimens (i.e. failure due to slippage one set of the spliced bars).
- The FE model can reasonably simulate the post-peak response of the test specimens; however, divergence problems may occur.

From the modelling and analysis of joints, the following conclusions are made:

- The ASCE 41-06 modelling parameters of unconfined exterior joints are only found to be suitable for predicting the peak shear strength and corresponding shear rotation of the unconfined specimens in this study.
- The modified strut-and-tie model by Hassan (2011) over-predicts the results of the unconfined joints.
- A quad-linear shear stress-strain model is proposed to simulate the behaviour of PTMS confined joints failing predominantly due to shear.
- An ACI-based strut-and-tie model is enhanced to predict the shear strength of PTMS confined specimens. The model can account for different beam bar anchorages within the joint area. A state of force equilibrium at predefined joint nodal zones is used to calculate the strut dimensions. The same model can be used to predict the capacity of the unconfined deficient joints.
- The enhanced strut-and-tie model gives good predictions for the tested joints. The model also shows reasonable predictions of the shear strength of unconfined beam-column joints tested by others.
- A joint core can be modelled by separating the framing beams and columns, and by assigning hinges in the core region to consider the shear deformations of the joint.
- The scissors model is a simple modelling technique that can be used to simulate the nonlinear behaviour of deficient RC beam-column joints. The scissors model is utilised in this study with a special focus on the shear resisting mechanism and the corresponding deformational behaviour of the joint including splices and anchorages.
- The analytical results of the scissors model with rigid connections deviates unacceptably from the measured responses, especially in terms of stiffness. This highlights the need for a more detailed model that can account for any joint deformations.
- The use of ASCE 41-06 model in numerical joint simulations is only suitable for the pre-peak behaviour of the unconfined beam-column joints of this study. The simulation results of the post-peak stage, however, deviate largely from the actual response.
- The implementation of the proposed quad-linear shear stress-strain model in FE analyses of specimens in this study results in good simulations of the measured responses. The degrading curve is reasonably captured.

From the rehabilitation of full-scale deficient RC structure, the following conclusions were drawn:

- Deficient joints led to premature behaviour of the structure.

- Preliminary analyses of the bare structure correlated reasonably well with the measured responses.
- The use of the PTMS technique along with minor works of welding and epoxy injections was successful to enhance the general performance significantly. Specifically, in the second test series, the PTMS upgraded building endured a seismic intensity of 0.35g. The structure with strengthening of PTMS and CFRP withstood an earthquake of 0.6g.

In summary, the current thesis has contributed towards the understanding of the effect of external confinement by means of PTMS to bond deficient regions as well as to poorly detailed beam-column connections with shear and bond deficiencies. That was done through identifying the various parameters influencing bond development and modes of failure, by understanding the influence of those parameters on confinement, by introducing new equations towards the formulation of design codes of practice, by introducing different strengthening schemes to upgrade the capacity of deficient joints, and by quantifying the confined joint behaviour through suitable joint model and modelling.

12.3 RECOMMENDATIONS FOR FUTURE WORK

- Development of a complete hysteretic bond-slip model of column splices confined by PTMS is still necessary to provide better evaluation of the behaviour under seismic loading.
- A detailed investigation on the effect of strips on bond in compression elements such as columns is still required. Unlike elements in tension, the axial force could mobilise higher confinement effect due to increase in stresses within strips, and therefore, better improvement in bond strength.
- The less than expected enhancement in bond strength due to double strips should be further investigated, especially in compression elements.
- The failure case with pullout-like failure type encountered in specimens SC27-D16-P1&2 should be examined further by conducting more tests on short splices and larger bar diameters.
- Additional tests on beams with various splice lengths are still needed to verify the reliability of the proposed bond-slip model for the PTMS case. The model was only utilised in FE simulations of the current beam tests.
- Additional tests on longer splices (> 25 the bar diameter) are still needed to further validate the limitations set on the maximum bond strength of the proposed bond-slip model.
- The enhanced strut-and-tie joint model in this study can be improved by providing modifications to account for nodal zone shifting, as well as cases with beam anchorages

bent outside the joint panel. Also, the model can be enhanced by providing more suitable bond equation for beam anchorages that considers different anchorage lengths in addition to the axial load and concrete cover.

- Results from well-instrumented PTMS confined joints are still required to validate and improve the findings from the current study; specifically, joint shear deformations and strut-and-tie model.
- Hysteretic rules for the proposed shear stress-strain model must be developed. Cyclic analyses using appropriate modelling elements are required to investigate the behaviour, especially in terms of stiffness and energy dissipation capacity.
- Comprehensive dynamic as well as static analyses of the bare and PTMS structure is necessary to validate the findings of the current study with regard to the upgraded shear capacity, additional shear deformations, and bond enhancement. More sophisticated FE nonlinear software such as OpenSees (2010) is suggested for modelling.
- The use of the PTMS technique in combination with composites may lead to more effective rehabilitation measures giving reasonable costs. Composites could be used to provide confinement to a joint core while strips could be used to provide flexural, shear and bond confinement to adjoining elements.
- Bar buckling is also a critical detailing in columns of older designed RC frames, and thus, it should be addressed. This deficiency could jeopardise the structure integrity especially in external bottom columns of a building. A strengthening by PTMS could be very efficient, practical, and fast way for upgrading such elements.

REFERENCES

ABAQUS version 6.9. (2009). "Analysis User's Manual." ABAQUS Inc.

ABAQUS version 6.9. (2009). "Theory Manual." ABAQUS Inc.

Aboutaha, R., Engelhardt, M.D., Jirsa, J.O., Kreger, M.E., (1996). "Retrofit of Concrete Columns with Inadequate Lap Splices by the Use of Rectangular Steel Jackets", Earthquake Spectra, Vol.12, No.4, November, pp. 693-714.

Achillides, Z., (1998). "Bond behaviour of FRP bars in concrete", PhD Thesis, The University of Sheffield, UK.

ACI 318-71, (1971). "Building Code Requirements for Reinforced Concrete", American Concrete Institute, Detroit, Michigan.

ACI-ASCE Committee 352 (1976). "Recommendations for Design of Beam-Column Joints in Monolithic Reinforced Concrete Structures", American Concrete Institute.

American Concrete Institute Committee ACI 318-89 (1989). "Building Code Requirements for Reinforced Concrete (ACI 318-89)", American Concrete Institute, Detroit, 351 pp.

ACI Committee 352, (1991). Recommendations for design of beam-column joints in monolithic reinforced concrete structures (ACI 352R-91). Farmington Hills, Mich.: American Concrete Institute.

ACI Committee 318, (1995). "Building Code Requirements for Structural Concrete (ACI 318-95) and Commentary," American Concrete Institute, Farmington Hills, Mich., 369 pp.

ACI Committee 224, (1998). "Causes, Evaluation, and Repair of Cracks in Concrete Structures (ACI 224.1R-93 [Reapproved 1998])," American Concrete Institute, Farmington Hills, Mich., 1993, 22 pp.

American Concrete Institute Committee ACI318-02. "Building Code Requirements for Reinforced Concrete (ACI 318-02)", ACI 318-95, 99, 02, Detroit, Michigan, 1995, 1999, 2002

ACI Committee 408, (2003). "Bond and Development of Straight Reinforcing Bars in Tension (Reapproved 2012)", Technical Documents, American Concrete Institute, Farmington Hills, Mich.

ACI 318M-08 (2008). "Building Code Requirements for Reinforced Concrete", American Concrete Institute, Detroit, Michigan.

ACI 369R-11, (2011). "Guide for Seismic Rehabilitation of Existing Concrete Frame Buildings and Commentary", American Concrete Institute, Farmington Hills, Michigan.

Adin, M. A., Yankelevsky, D. Z., and Farhey, D. N., (1993). "Cyclic Behavior of Epoxy-Repaired Reinforced Concrete Beam-Column Joints", ACI Structural Journal, V. 90, No. 2, Mar.-Apr., pp. 170-179.

Ahmad, S. (2007). "Assessment of Damages Caused to Structures due to October 8th, 2005 Kashmir Earthquake, Pakistan", The University of Sheffield, Sheffield, UK.

Ahmad, S., (2011). "Seismic Vulnerability of Non-Ductile Reinforced Concrete Structures in Developing Countries", PhD thesis, the University of Sheffield, Sheffield, UK.

Alath, S., and Kunnath, S.K., (1995). "Modeling Inelastic Shear Deformation in RC Beam-Column Joints", Engineering Mechanics Proceedings of Tenth Conference, University of Colorado at Boulder, ASCE, Vol.2, pp 822-825.

Alcocer, S. M. and Jirsa, J. O., (1993). "Strength of Reinforced Concrete Frame Connections Rehabili-tated by Jacketing", ACI Structural Journal 90(3), 249–261.

Almusallam, T. H., and Salloum, Y. A., (2007). "Seismic response of interior RC beam-column joints upgraded with FRP sheets—Part II: analysis and parametric study." J. Compos. Constr., 11(6), 590–600.

Alsiwat, J. M., and Saatcioglu, M., (1992). "Reinforcement Anchorage Slip under Monotonic Loading", Journal of Structural Engineering, ASCE, V. 118, No. 9, Sept., pp. 2421-2438.

Al-Sunna, R. (2006). "Deflection Behaviour of FRP Reinforced Concrete Flexural Members", PhD Thesis, The University of Sheffield, Sheffield, 318 pp.

Alsayed S. H., Al-Salloum Y. A., Almusallam T. H., and Siddiqui N.A. (2010). "Seismic response of FRP-upgraded exterior RC Beam-column joints", Journal of Composites for Construction Volume 14, Issue 2, Pages 195-208

Altoontash, A., (2004). "Simulation and damage models for performance assessment of reinforced concrete beam- column joints", PhD Dissertation, Department of Civil and Environmental Engineering, Stanford University, Stanford, California.

Amoury, T., and Ghobarah, A., (2002). "Seismic rehabilitation of beam column joints using GFRP sheets", Eng. Struct., 24, 1397–1407.

Anderson, M., Lehman, D., and Stanton, J., (2008). "A Cyclic Shear Stress-Strain Model for Joints without Transverse Reinforcement", Engineering Structures, No. 30, pp. 941-954.

Antonopoulos, C. P., and Triantafillou, T. C., (2002). "Analysis of FRP-Strengthened RC Beam-Column Joints", Journal of Composites for Construction, ASCE, V. 6, No. 1, Feb., pp. 41-51.

Antonopoulos, C. P., and Triantafillou, T. C., (2003). "Experimental investigation of FRP-strengthened RC beam-column joints." J. Compos. Constr., 7(1), 39–49.

ASCE/SEI 41-06 (2006). "Seismic Rehabilitation of Existing Buildings", American Society of Civil Engineers, Reston, Virginia.

Ayoub, A., and Filippou, F. C., (1998). "Nonlinear Finite-element Analysis of RC Shear Panels and Walls", Journal of Structural Engineering, 124(3), 298-308.

Ayoub, A., and Filippou, F. C., (2001). "Nonlinear Finite-element Analysis of RC Shear Panels and Walls - Discussion", Journal ofStructural Engineering, 127(3), 721-722.

Aycardi, L. E., Mander, J. B., and Reinhorn, A. M., (1994). "Seismic Resistance of Reinforced Concrete Frame Structures Designed Only for Gravity Loads: Experimental Performance of Subassemblages", ACI Structural Journal, V. 91, No. 5, Sept.-Oct., pp. 552-563.

Barnes, M., and Jigoral, S., (2008). "Exterior Non-Ductile Beam Column Joints", PEER/NEESREU Research Report, University of California, Berkeley, August.

Bedirhanoglu, I. (2009). "The behavior of reinforced concrete members with low strength concrete under earthquake loads: an investigation and improvement." PhD thesis, Istanbul Technical University, Istanbul, Turkey.

Bedirhanoglu, I., Ilki, A., Pujol, S., and Kumbasar, N., (2010). "Seismic behavior of joints built with plain bars and low-strength concrete", ACI Structural Journal, Vol. 7, No.3, pp. 1-11. (SCI Journal), May-June.

Belarbi, A. & Hsu, T.C., (1995). "Constitutive laws of softened concrete in biaxial tension-compression", ACI Structural Journal, 92(S54), p.562–573.

Beres, A.; Pessiki, S. P.; White, R. N.; and Gergely, P., (1991). "Seismic Performance of Existing Reinforced Concrete Frames Designed Primarily for Gravity Loads", Sixth Canadian Conference on Earthquake Engineering, Toronto, Ontario, Canada, pp. 655-662.

Beres, A.; White, R. N.; Gergely, P.; Pessiki, S. P.; and El-Attar, A., (1992). "Behavior of Existing Non-Seismically Detailed Reinforced Concrete Frames" Proceedings of the Tenth World Conference on Earthquake Engineering, Balkema, Rotterdam, pp. 3359-3363.

Beres, A., El-Borgi, S., White, R. N. and Gergely, P., (1992). "Experimental Results of Repaired and Retrofitted Beam-Column Joint Tests in Lightly RC Frame Buildings', Technical Report NCEER-92-0025, National Centre for Earthquake Engineering Research, State University of New York at Buffalo.

Beres, A.; Pessiki, S. P.; White, R. N.; and Gergely, P., (1996). "Implications of Experiments on the Seismic Behavior of Gravity Load Designed RC Beam-to-Column Connections", Earthquake Spectra, V. 12, No. 2, May, pp. 185-198.

Biddah, A., Ghobarah, A., and Aziz, T. S., (1997). "Upgrading of Nonductile Reinforced Concrete Frame Connections", Journal of Structural Engineering, ASCE, V. 123, No. 8, Aug., pp. 1001-1009.

Biddah, A., (1997). "Seismic Behaviour of Existing and Rehabilitated Reinforced Concrete Frame Connections", PhD Thesis, McMaster University, Hamilton, Ontario, Canada, 326 p.

Biddah, A., and Ghobarah, A., (1999). "Modeling of Shear Deformation and Bond Slip in Reinforced Concrete Joints", Structural Engineering and Mechanics, V.7, No. 4, pp. 413–432.

Birely, A. C.; Lowes, L. N.; and Lehman, D. E., (2012). “A Model for Practical Nonlinear Analysis of Reinforced Concrete Frames Including Joint Flexibility,” Engineering Structures, V. 34, Jan., pp. 455-465.

Blondet, J. M., Clough, R.W. (1980). "Evaluation of a Shaking Table Test Program on Response Behavior of a Two Story Reinforced Concrete Frame", Report No. UCB/EERC-80/42.

Bousselham, A., (2010). “State of Research on Seismic Retrofit of RC Beam-Column Joints with Externally Bonded FRP”, Jour composites for construction ASCE January-February 2010, 49-61.

Bracci, J. M., Reinhorn, A. M., and Mander, J. B., (1992). “Seismic Resistance of Reinforced Concrete Frame Structures Designed only for Gravity Loads: Part I-Design and Properties of a One-third Scale Model Structure”, Technical Report NCEER-92-0027, State University of New York at Buffalo, 152pp.

Bracci, J. M., Reinhorn, A. M., and Mander, J. B., (1992). “Seismic Resistance of Reinforced Concrete Frame Structures Designed only for Gravity Loads: Part III-Experimental Perfrmance and Analytical study of Structural Model”, Technical Report NCEER-92-0029, State University of New York at Buffalo, 138pp.

Bracci, J. M., Reinhorn, A. M., and Mander, J. B., (1995). “Seismic Retrofit of Reinforced Concrete Buildings Designed for Gravity Loads: Performance of Structural Model”, ACI Structural Journal, V. 92, No. 6, Nov.-Dec., pp. 711-723

Bracci, J. M., Reinhorn, A. M., and Mander, J. B., (1995). “Seismic Resistance of Reinforced Concrete Frame Structures Designed for Gravity Loads: Performance of Structural System”, ACI Structural Journal, V. 92, No. 5, Sept.-Oct., pp. 597-609.

Brena, S.F., and Schlick, B.M., (2007). "Hysteretic behavior of bridge columns with FRP-jacketed lap splices designed for moderate ductility enhancement", Journal of Composite for Construction, ASCE 11(6): 565–574.

BS 8110, (1985). Structural use of concrete- code of practice for design and construction. London: British Standards Institution.

BRITISH STANDARDS INSTITUTION. BS 8110 Structural Use of Concrete. Part 1: Code of Practice for Design and Construction. BSI, London, 1997.

Burak, B. (2010). “Analytical Verification of a Simplified Reinforced Concrete Joint Model”, Proceedings of the 9th U.S. National and 10th Canadian Conference on Earthquake Engineering, Toronto, Ontario, Canada, July 25-29.

Castellani, A., Negro, P., Colombo, A., Grandi, A., Ghisalberti, G., and Castellani, M. (1999). “Carbon fiber reinforced polymers (CFRP) for strengthening and repairing under seismic actions”, Special Publication No. 1.99.41, European Laboratory for Structural Assessment, Joint Research Center, Ispra, Italy.

Caughey, T.K., (1962). "Vibration of Dynamic Systems with Linear Hysteretic Damping, Linear Theory", Proceedings of the Fourth US National Congress of Applied Mechanics, pp 87-97.

CEB-FIP (Mc90) (1993). “CEB-FIP Model Code 1990: Design code. Comite Euro-International Du Beton(Ceb)”.

Celik, O.C., and Ellingwood, B.R., (2008). “Modelling beam-column joints in fragility assessment of gravity load designed reinforced concrete frames”, Journal of Earthquake Engineering, Vol.12, No. 3, pp. 357-381.

CEN Technical Committee 250/SC8 (1998). "Eurocode 8: earthquake resistant design of structures—part 1: general rules and rules for buildings". ENV 1998-1-1/2/3. Berlin (Germany): CEN

Chai, Yuk; Priestley, M.; and Seible, Frieder (1991). "Seismic Retrofit of Circular Bridge Columns for Enhanced Flexural Performance", ACI Structural Journal, V88, No.5, September-October, pp. 572-584.

Chaudat T., Garnier C., and Poupin S. (2005). “Ecoleader project No.2-Seismic tests on an RC frame with FRP retrofitting-Tests report”. SEMT/EMSI/RT/05-006/A.

Chopra, A.K., (2006). “Dynamics of Structures: Theory and Applications to Earthquake Engineering, 3rd Edition”, Prentice-Hall, Upper Saddle River, New Jersey.

Chou, L., Niwa, J., and Okamura, H., (1983). "Bond Model for Deformed Bars Embedded in Massive Concrete", Proc. of 2nd JCI Colloquium on Shear Analysis of RC Structures, JCI, 45-52 (1983).

Choudhuri, D., Mander, J. B., and Reinhorn, A. M., (1992). "Evaluation of Seismic Retrofit of Reinforced Concrete Frame Structures: Part I—Experimental Performance of Retrofitted Subassemblages", Technical ReportNCEER-92-0030, SUNY/Buffalo.

Ciampi, V., Eligehausen, R., Betero, V.V., and Popov, E.V., (1982). "Analytical model for deformed bar bond under generalized ex-citations", Rep. No., UCB/EERC-82/23, Univ. of Calif., Berkeley, Calif.

Clyde, C., Pantelides, C.P., and Reaveley, L.D. (2000). Performance-based evaluation of exterior reinforced concrete building joints for seismic excitation. Pacific Earthquake Engineering Research Center, PEER Report 2000/05, University of California, Berkeley, CA.

Clyde, C., and Pantelides, C. P. (2002). "Seismic Evaluation and Rehabilitation of R/C Exterior Building Joints," Proceedings of the Seventh U.S. National Conference on Earthquake Engineering, Boston, July.

Coffman, H.L., Marsh, M.L., Brown, C.B., (1993). "Seismic Durability of Retrofitted Reinforced-Concrete Columns", ASCE Journal of Structural Engineering, Vol. 119, No.5, 1643-1661.

Collins, M.P., Mitchell, D., Adebar, P., and Vecchio, F.J., (1996). "General Shear Design Method", ACI Structural Journal, V. 93, No. 1, Jan.-Feb, pp. 36-45.

Corazao, M. and Durrani, A. J., (1989). "Repair and Strengthening of Beam-to-Column Connections Subjected to Earthquake Loading", NCEER Technical Report No. 89-0013, National Center for Earthquake Engineering Research, State University of New York at Buffalo, NY, 93 p.

Darwin, D.; McCabe, S. L.; Idun, E. K.; and Schoenekase, S. P., (1992). "Development Length Criteria: Bars Not Confined by Transverse Reinforcement", ACI Structural Journal, V. 89, No. 6, Nov.-Dec., pp. 709-720.

Darwin D., Tholen M.L., Idun E.K., and Zuo J., (1996a). "Splice Strength of High Relative Rib Area Reinforcing Bars", ACI Journal, V. 93, No. 1, Jan.-Feb., pp. 95-107.

Darwin, D., Idun, E. K., Zuo, J., and Tholen, M. L., (1998). "Reliability-Based Strength Reduction Factor for Bond", ACI Structural Journal, V. 95, No. 4, July-Aug., pp. 434-443.

Deng C., Oreste B., and Zandonini R. (2000) A hysteretic connection element and its applications, Computers and Structures, 78, (1), 93-110.

Dogan, E., Hill, H., and Krstulovic-Opara, N., (2000). "Suggested Design Guidelines for Seismic Retrofit with SIMCON and SIFCON", High-Performance Fiber-Reinforced Concrete in Infrastructural Repair and Retrofit, SP-185, N. Krstulovic-Opara and Z. Bayasi, eds., American Concrete Institute, Farmington Hills, Mich., pp. 207-248.

Durrani, A.J., and Wight, J.K., (1985). "Behavior of interior beam-to-column connections under earthquake-type loading", ACI J. Proc., 82(3), 343-349

Dhakal, R.P., Pan, T.C., Irawan, P., Tsai, K.C., Lin, K.C. and Chen, C.H. (2005). "Experimental study on the dynamic response of gravity-designed reinforced concrete connections", Engineering Structures, 27(1), 75-87.

Dutta, A., and Mander, B., (2001). "Energy based methodology for ductile design of concrete columns", J. of Structural Engineering, ASCE, 127(12), 1374-1381.

Dymiotis C. (1999). "Probabilistic seismic assessment of reinforced concrete buildings with and without masonry infill walls". Department of Civil and Environmental Engineering. Imperial College of Science, Technology and Medicine, PhD Thesis.

Earthquake Engineering Research Institute (1999a). "EERI Special Earthquake Report September 1999, the Tehuacan, Mexico, Earthquake of June 15", http://www.eeri.org

Earthquake Engineering Research Institute (1999b). "EERI Special Earthquake Report November 1999, the Athens, Greece Earthquake of September 7", http://www.eeri.org

Earthquake Engineering Research Institute (1999c). "EERI Special Earthquake Report December 1999. The Chi-Chi, Taiwan Earthquake of September 21, 1999", http://www.eeri.org

Earthquake Engineering Research Institute (2012). “EERI Special Earthquake Report, March the 20th, 2012, M_w7.4 Ometepec, Mexico, Earthquake”, May. http://www.eeri.org

Earthquake Engineering Research Institute (2012). “EERI Special Earthquake Report, the M_w7.1 Erciş-Van, Turkey Earthquake of October 23, 2011”, April. http://www.eeri.org

EC2 (2000). "Design of concrete structures-Part 1 General rules and rules for buildings", (DD ENV-1992-1-1:1992).

EC8 (2004). "Design of structures for earthquake resistance-Part 1 General rules, seismic actions and rules for buildings", (BS EN 1998-1:2004).

Ehsani, M.R. and Wight, J.K., (1985). "Exterior Reinforced Concrete Beam to Column Connections Subjected to Earthquake Type Loading", J. of the American Concrete Institute (ACI), 82(4), 492-499.

El-Attar, A., White, R.N., and Gergely, P., (1991). "Shake Table Test of a 1/6 Scale Two-Story Lightly Reinforced Concrete Building", Technical Report NCEER-91-0017, National Center for Earthquake Engineering Research, University at Buffalo, February 30.

El-Ghandour, A.W., Pilakoutas, K., and Waldron, P., (2003), “Punching Shear Behavior of Fiber Reinforced Polymers Reinforced Concrete Flat Slabs: Experimental Study”, ASCE Journal of Composites for Construction, 7(3), 258-265 pp.

El-Gawady, M. A., Lestuzzi, P., and Badoux, M.,(2005). “In-plane seismic response of URM walls upgraded with FRP”, J. Compos. Constr., 9(6), 524–535.

Eligehausen, R., (1979). “Bond in Tensile Lapped Splices of Ribbed bars with Straight Anchorages”, Publication 301, German Institute for Reinforced Concrete, Berlin, 118 pp. (in German).

Eligehausen, R.,(1979). “Lapped splices of tensioned deformed bars with straight ends”, Schriftenreihe des Deutschen Ausschusses fur Stahlbe-ton, Wilhelm Ernst & Sohn, Berlin (in German).

Eligehausen R., Bertero V. V., Popov E. P., (1983). “Local bond stress-slip relationships of deformed bars under generalised excitations: tests and analytical model”, Technical Report UCB/EERC-83, Earthquake Engineering Research Center, University of California, Berkeley.

Endeshaw, Mesay A. (2008). “Retrofit of Rectangular Bridge Columns Using CFRP Wrapping”, M.S. Thesis, Department of Civil and Environmental Engineering, Washington State University.

Engindeniz M., Kahn L.F., and Zureick A., (2005). "Repair and Strengthening of Reinforced Concrete Beam-Column Joints: State of the Art”, ACI Structural Journal, V. 102, No. 2, March-April, pp 1-14.

Engindeniz, M., (2008). "Repair and Strengthening of Pre-1970 Reinforced Concrete Corner Beam-Column Joints Using CFRP Composites”, PhD Thesis, Civil and Environmental Engineering Department, Georgia Institute of Technology, August.

Erol, G., Demir, C., Ilki, A., Yuksel, E., Karadogan, F., (2006). “Effective Strengthening of RC Frames with and without Lap Splice Problems”, 8th National Conference on Earthquake Engineering, San Francisco.

Estrada, J. I., (1990). “Use of Steel Elements to Strengthen a Reinforced Concrete Building”, MSc Thesis, University of Texas at Austin, TX, USA, 66 p.

Favatta M., Izzuddin B.A., Karayannis, C.G., (2008). “Modelling Exterior Beam-Column Joints for Seismic Analysis of RC Frame Structures”, Earthquake Engineering and Structural Dynamics, 37:1527-1548.

Fédération Internationale du Béton FIB, (2001). “Externally bonded FRP reinforcement for RC structures”, FIB: Bulletin 14, Fédération Internationale du Béton, Lausanne, Switzerland.

FEMA 356 (2000). "Pre-standard and Commentary for the Seismic Rehabilitation of Buildings", Federal Emergency Management Agency, Washington D.C.

FEMA 273 (1997). "NEHRP Guidelines for the seismic rehabilitation of buildings", Federal Emergency Management Agency, Washington DC.

Filiatrault, A., and Lebrun, I., (1996). “Seismic Rehabilitation of Reinforced Concrete Joints by Epoxy Pressure Injection Technique”, Seismic Rehabilitation of Concrete Structures, SP-160, G. M. Sabnis, A. C. Shroff, and L. F. Kahn, eds., American Concrete Institute, Farmington Hills, Mich., pp. 73-92.

FIP, “Bond of reinforcement in concrete: state-of-art report”, Fip Bulletin No. 10, CEB-FIP, Lausanne, Switzerland, 2000.

Forell, N. F., and Nicoletti, J. P., (1980). "Mexico Earthquakes, Oaxaca- November 29, 1978, and Guerrero - March 14, 1979," Earthquake Engineering Research Institute, El Cerrito, California, October, 89 pp.

Foutch DA, Shi S., (1997). "Connection element (type 10) for DRAIN-2DX", Internal Report, University of Illinois, Urbana, Illinois.

Frangou, M., (1992). "Repair/strengthening of concreteby lateral post-tensioning", MPhil Thesis, Sheffield University, December.

Frangou, M., Pilakoutas, K. and Dritsos, S., (1993). "Repair/strengthening of columns by a simple localised strengthening technique", Proceedings of the 5th International Conference on

Frangou, M. and Pilakoutas, K., (1994a). "Strengthening of RC columns by lateral tensioning", Proceedings of the Second International Conference on Earthquake Resistant Construction and Design, Berlin, Germany, 15-17 June, pp 841-848

Frangou M., and Pilakoutas K., (1994b). "Novel technique for the repair and strengthening of RC columns", Proceedings of the Fifth U.S. National Conference on Earthquake Engineering, Vol III, Chicago, pp 637-646.

Frangou, M., Pilakoutas, K. and Dritsos, S., (1995). "Structural repair/strengthening of RC columns", Construction and Building Materials Journal, Vol.9, No.5, pp 259-266

Frangou, M., (1996). "Strengthening of concrete by lateral confinement", PhD Thesis, Sheffield University, Sheffield, UK.

French, C. W., Thorp, G. A., and Tsai, W. J., (1990). “Epoxy Repair Techniques for Moderate Earthquake Damage”, ACI Structural Journal, V. 87, No. 4, July-Aug, pp. 416-424.

Genesio, G., Eligehausen, R., Sharma, A., and Pampanin, S., (2010). "Experimental and numerical study towards a deformation-based seismic assessment of substandard exterior RC beam–column joints", In: Int. conf. on fracture mechanics of concrete and concrete structures.

Gergely, I., Pantelides, C. P., Nuismer, R. J., and Reaveley, L. D., (1998). “Bridge Pier Retrofit Using Fiber-Reinforced Plastic Composites”, Journal of Composites for Construction, ASCE, V. 2, No. 4, Nov., pp. 165-174.

Gergely, J., Pantalides, C. P., and Reaveley, L. D., (2000). “Shear strengthening of RC T-joints using CFRP composites”, J. Compos. Constr., 4(2), 56–64.

Ghobarah, A., Aziz, T. S., and Biddah, A., (1997). “Rehabilitation of Reinforced Concrete Frame Connections Using Corrugated Steel Jacketing”, ACI Structural Journal, V. 4, No. 3, May-June, pp. 283-294.

Ghobarah, A., and Said, A., (2001). “Seismic rehabilitation of beam-column joints using FRP laminates”, J. Earthquake Eng., 5(1), 113–129.

Guadagnini, M., (2002). "Shear Behaviour and Design of FRP RC Beams", The University of Sheffield, Sheffield, 348 pp.

Gunja, G.Y., 2005. “Seismic Strengthening of Reinforced Concrete Structures”, MSc dissertation, University of Sheffield, Sheffield, UK.

Hakuto, S., Park, R. and Tanaka, H. (2000). “Seismic load tests on interior and exterior beam-column joints with substandard reinforcing details”. ACI Structural Journal, Vol. 97, No.1, 11-25.

Harajli, M.H., (1994). "Development/Splice Strength of Reinforcing Bars Embedded in Plain and Fiber Reinforced Concrete," ACI Structural Journal, Vol. 91, No.5, September-October, pp.551-520.

Harajli M. H. and Mabsout M. E., (2002). "Evaluation of Bond Strength of Steel Reinforcing Bars in Plain and Fiber-Reinforced Concrete", ACI Structural Journal, V. 99, No. 4, July-August 2002, pp.509-517.

Harajli, M.H., Hamad, B., and Karam, K.,(2002). “Bond-slip response of reinforcing bars embedded in plain and fiber concrete”, J. Mater. Civ. Eng.,14(6), 503–511.

Harajli, M.H., and Al-Hajj, J., (2002). “Bond-slip response of reinforcing bars embedded in high-strength concrete”, Proc. Int. Symp. On Bond in Concrete—From Research to Standards, Budapest, Hungary.

Harajli, M.H., (2004).“Comparison of Bond Strength of Reinforcing Bars in Normal and High-Strength Concrete,” Journal of Materials in Civil Engineering, ASCE, Vol. 16, No. 4, August.

Harajli, M.H., Hamad, B. S., and Rteil, A.,(2004). “Effect of confinement on bond strength between steel bars and concrete”, ACI Struct. J., 101(5), 595–603.

Harajli, M.H., and Hamad, B.,(2005). “Local bond stress–slip response of steel bars embedded in FRP-confined concrete”, Proc. Mindess Symp. on Construction Materials, N. Banthia, T. Domoto, A. Bentur, and S.P. Shah, eds., Univ. of British Columbia, Vancouver, B.C., Canada.

Harajli, M.H., (2006). “Effect of Confinement using Steel, FRC, or FRP on the Bond Stress-Slip Response of Steel Bars under Cyclic Loading,” Journal of Materials and Structures, RILEM, Vol. 39, 2006, pp. 621-634.

Harajli, M.H., (2007). "Numerical Bond Analysis Using Experimentally Derived Local Bond Laws: A Powerful Method for Evaluating the Bond Strength of Steel Bars", Journal of Structural Engineering (ASCE), 133 No. 5.

Harajli, M. H. and Dagher, F. (2008). “Seismic Strengthening of Bond-Critical Regions in Rectangular Reinforced Concrete Columns Using Fiber-Reinforced Polymer Wraps”, ACI Structural Journal, Vol. 105, No. 1, 68-77.

Harajli, M.H., (2009). "Bond stress–slip model for steel bars in unconfined or steel, FRC, or FRP confined concrete under cyclic loading", J Struct Eng; 135(5):509–18.

Harries, K.A., Ricles, J.R., Pessiki, S., and Sause R., (2006). “Seismic Retrofit of Lap Splices in Nonductile Square Columns Using Carbon Fiber-Reinforced Jackets”, ACI Structural Journal, V.103, No.6, Nov.-Dec.,pp. 874-884.

Hassan, W. M., (2009). “Seismic Performance of Exterior and Corner Substandard Beam-Column Joints in Gravity Load Designed Reinforced Concrete Buildings”, CE 299 Research Report, University of California, Berkeley, August.

Hassan, E.M., (2011). “Analytical and Experimental Assessment of Seismic Vulnerability of Beam-Column Joints without Transverse Reinforcement in Concrete Buildings”, PhD thesis, University of California, Berkeley, CA.

Hoffschild, T. E., Prion, H. G. L., and Cherry, S., (1995). “Seismic Retrofit of Beam-to-Column Joints with Grouted Steel Tubes”, Recent Developments in Lateral Force Transfer in Buildings: Thomas Paulay Symposium, SP-157, N. Priestley, M. P. Collins, and F. Seible, eds., American Concrete Institute, Farmington Hills, Mich., pp. 397-425.

Hwang, S., and Lee, H., (1999). "Analytical Model for Predicting Shear Strengths of Exterior Reinforced Concrete Beam-Column Joints for Seismic Resistance". ACI Structural Journal, Vol. 96, No. 5, 846-858.

Ilki, A., Bedirhanoglu, I., and Kumbasar, N. (2008). “Seismic retrofit of beam-column joints with FRP sheets”, Proc., 5th Int. Conf. on Advanced Composite Materials in Bridges and Structures (ACMBS-V), Sep. 22–24, Winnipeg, Manitoba, Canada.

Ilki, A., Bedirhanoglu, I., Kumbasar, N. (2011). “Behavior of FRP-Retrofitted Joints Built With Plain Bars and Low-Strength Concrete”, ASCE Journal of Composites for Construction, Vol. 15, No.3, pp.1-13.

Imjai, T., (2007). "DESIGN AND ANALYSIS OF CURVED FRP COMPOSITES AS SHEAR REINFORCEMENT FOR CONCRETE STRUCTURES", PhD Thesis, The University of Sheffield, Sheffield, UK.

Karayannis, C. G., Chalioris, C. E., and Sideris, K. K., (1998). “Effectiveness of RC Beam-Column Connection Repair Using Epoxy Resin Injections”, Journal of Earthquake Engineering, V. 2, No. 2, pp. 217-240.

Karayannis, C. G., and Sirkelis, G. M., (2002). “Effectiveness of RC Beam-Column Connections Strengthening Using Carbon-FRP Jackets”, Proceedings of the Twelfth European Conference on Earthquake Engineering, London, Sept., PR 549.

Karayannis CG, Sirkelis GS, Chalioris CE, (2006). “Seismic performance of RC beam–columns joints retrofitted using light RC jacket: experimental study”. First European Conference on Earthquake Engineering and Seismology, Geneva, Switzerland, 3-8 September; Paper 136.

Karayannis, C. G., Chalioris, C. E., and Sirkelis, G. M., (2008). “Local retrofit of exterior RC beam-column joints using thin RC jackets: An experimental study.”Earthquake Eng. Struct. Dyn., 37, 727–746.

Karayannis, C. G., and Sirkellis, G. M., (2008). “Strengthening and rehabilitation of RC beam-column joints using carbon-FRP jacketing and epoxy resin injection. ”Earthquake Eng. Struct. Dyn., 37, 769–790.

Kim, J and LaFave, J. M., (2009). “Joint Shear Behavior of Reinforced Concrete Beam-Column Connections subjected to Seismic Lateral Loading”. Department of Civil and Environmental Engineering University of NSEL Report Series Report No. NSEL-020 November.

Koru, B. Z., (2002). “Seismic vulnerability assessment of low-rise reinforced concrete buildings”, PhD thesis, Purdue Univ., West Lafayette, IN.

Kuang, J. S., and Wong, H. F. (2005). “Effects of beam bar anchorage on beam-column behavior”, Struct. Des. Tall Special Build., 159(2), 115–124.

Kyriakides N., (2007). “Vulnerability of RC Buildings and Risk Assessment for Cyprus”. PhD Thesis, Sheffield University, Sheffield, UK.

Lee, D. L. N., Wight, J. K., and Hanson, R. D., (1977). “Repair of Damaged Reinforced Concrete Frame Structures”, Proceedings of the Sixth World Conference on Earthquake Engineering, V. 3, New Delhi, India, Jan., pp. 2486-2491.

Lehman D.E., and Moehle J.P., (2000). "Seismic Performance of Well-confined Concrete Bridge Columns", PEER-1998/01. Pacific Earthquake Engineering Research Center, University of California, Berkeley. 316 pages.

Lehman, D., ed., (2002). “Performance Characterization of Non-Ductile Reinforced Concrete Frame Components”, Unpublished Technical Report PEER 2002, Pacific Earthquake Engineering Research Center (PEER), University of California, Berkeley, CA. (Credits to Hassan 2011)

Lin J. and Nagasaka T. (2005). “Loading capacity and deformability of rc beams with extremely low strength concrete”. Tokai University, Vol.44, No. 2, pp. 25-30.

Lowes, L.N., and Altoontash, A., (2003). "Modeling Reinforced-Concrete Beam-Column Joints Subjected to Cyclic Loading”, ASCE Journal of Structural Engineering, V. 129, No. 12, pp. 1686-1697.

Lynn, A.C., Moehle, J.P., Mahin, S.A., Holmes W.T., (1996). “Seismic Evaluation of Existing Reinforced Concrete Building Columns”, Earthquake Spectra, Vol.12, No.4, November, pp. 715-739.

Melek, M., Wallace, J.W., and Conte, J.P., (2003). “Experimental Assessment of Columns with Short Lap Splices Subjected to Cyclic Loads”, Report No. PEER 2003/2004, University of California-Berkeley, Berkeley, CA, 179 pp.

Migliacci, A., Antonucci, R., Maio, N. A., Napoli, P., Ferretti, A. S. and Via, G., (1983). “Repair Techniques of Reinforced Concrete Beam-Column Joints”, in Final Report of IABSE Symposium on Strengthening of Building Structures – Diagnosis and Therapy, Venice, pp. 355-362.

Mohamad, A. Z., and Clark, L. A., (1992). "Bond behaviour of low-strength concrete", Mangzine of concrete research, 44 No.160, 195-203.

Moehle, J.P. and Mahin, S.A., (1991). “Observationson the behavior of reinforced concrete buildings during earthquakes”, Earthquake-Resistant Concrete Structures Inelastic Response and Design SP-127, American Concrete Institute, ed. S.K. Ghosh, Detroit.

Moghaddam H, Samadi M, Mohebbi S, Pilakoutas K., (2008). “Lateral Post-Tensioned Metal Strips for Strength and Ductility Enhancement of Concrete Columns: Investigation of Size and Shape Effects”, 14th World Conference on Earthquake Engineering (14WCEE), Beijing, China.

Moghaddam, H., Samadi, M., Pilakoutas, K., (2008). "Behavior and modeling of high-strength concrete columns confined by external post-tensioned strips", In: Proceedings of ASCE/SEI structural engineering congress, Vancouver, Canada.

Moghaddam, H., Samadi, M., Pilakoutas, K., and Mohebbi, S., (2010). "Axial compressive behavior of concrete actively confined by metal strips; part A: experimental study", Materials and Structures, 15 January.

Moghaddam, H., Samadi, M., and Pilakoutas, K., (2010). "Compressive behavior of concrete actively confined by metal strips, part B: analysis", Materials and Structures, 15 January.

Mosallam, A. S., (2000). “Strength and ductility of RC frame connections strengthened with quasi-isotropic laminates”, Composites, Part B, 31(6–7), 481–497.

Mosier, W.G. (2000). “Seismic Assessment of Reinforced Concrete Beam-Column Joints”, Master’s Thesis, Department of Civil Engineering, University of Washington.

Mukherjee, A., and Joshi, M. (2005). “FRPC reinforced concrete beam-column joints under cyclic excitation.” Compos. Struct., 70(2), 185–199.

Murty C.V.R., Rai D., Bajpai K.K., Jain S.K., (2003). "Effectiveness of reinforcement details in exterior reinforced concrete beam–column joints for earthquake resistance", ACI Struct J; 100(2):149–56.

Naseer, A., Khan, A.N., Hussain, Z., Ali, Q., (2010). "Observed Seismic Behavior of Buildings in Northern Pakistan during Kashmir Earthquake", Journal of Earthquake Spectra Vol:26 No.2 pp:425-449.

NZS 3101 (1995). “The Design of Concrete Structures“, Standards New Zealand, Wellington.

OpenSees 2.2.2, (2010). "Open System for Earthquake Simulation", McKenna, F. and Fenves G. PEER, University of California, Berkeley. http://opensees.berkeley.edu.

Orangun, C.O., Jirsa, J.O., and Breen, J.E., (1975). “Strength of Anchored Bars: A Reevaluation of Test Data on Development Length and Splices”, Research Report No. 154-3F, Center for Highway Research, University of Texas at Austin, Austin, Tex., 78 pp.

Orangun, C.O., Jirsa, J.O., and Breen, J.E., (1977). “Reevaluation of Test Data on Development Length and Splices”. ACI JOURNAL, Proceedings V. 74, No. 3, Mar., pp. 114-122.

Pampanin, S., Calvi G.M., and Moratti M., (2002). “Seismic Behaviour of R.C. Beam Column Joints Designed for Gravity Loads”, 12th European Conference on Earthquake Engineering, London, Paper No.726.

Pampanin, S., Magenes, G., Carr, A., (2003). ”Modelling of Shear Hinge Mechanism in Poorly Detailed R.C. Beam-Column Joints”, fib Athens, Paper no. 171.

Pampanin, S., Christopoulos, C., and Priestley,M.J.N., (2003). “Performance-based seismic response of frame structures including residual deformations. Part II: Multi-degree of freedom systems”, J. of Earthquake Engineering, 7(1), 119-147.

Pantelides, C. P., Gergely, I., Reaveley, L. D., and Nuismer, R. J. (1997). “Rehabilitation of cap beam-column joints with carbon fiber jackets”, Proc., 3rd Int. Symp. on Non-Metallic (FRP) Reinforcement for Concrete Structures, 1, Japan Concrete Institute, Sapporo, Japan, 587–595.

Pantelides, C. P., Gergely, I., Reaveley, L. D., and Volnyy, V. (1999). “Retrofit of RC bridge pier with CFRP advanced composites”, J. Struct. Eng., 125(10), 1094–1099.

Pantelides, C. P., Gergely, J., Reaveley, L. D., and Volnyy, V. A., (1999). “Retrofit of Reinforced Concrete Bridges with Carbon Fiber Reinforced Polymer Composites”, Fourth International Symposium for Fiber Reinforced Polymer Reinforcement for Reinforced Concrete Structures, SP-188, C. W. Dolan, S. H. Rizkalla, and A. Nanni, eds., American Concrete Institute, Farmington Hills, Mich., pp. 441-453.

Pantelides, C., Hansen, J., Nadauld, J., and Reaveley, L.D., (2002). “Assessment of Reinforced Concrete Building Exterior Joints With Substandard Details”, Technical Report PEER 2002-18, Pacific Earthquake Engineering Research Center (PEER), University of California, Berkeley, CA, May.

Pantelides, C. P., and Gergely, J., (2002). “Carbon-Fiber-Reinforced Polymer Seismic Retrofit of RC Bridge Bent: Design and In-Situ Validation”, Journal of Composites for Construction, ASCE, V. 6, No. 1, Feb., pp. 52-60.

Pantelides, C. P., Okahashi, Y., and Reaveley, L. D., (2008). “Seismic rehabilitation of reinforced concrete frame interior beam-column joints with FRP composites”, J. Compos. Constr., 12(4), 435–445.

Pantazopoulou, S., and Bonacci, J., (1992). “Consideration of Questions about beam-column joints”, ACI Structural Journal, V. 89, No. 1, pp. 27-37.

Park, R., and Paulay, T., (1975). “Reinforced Concrete Structures”, John Wiley and Sons, New York, 769 pp.

Park, R.; Priestley, M. J. N.; and Gill, W. D., (1982). “Ductility of Square-Confined Concrete Column”, Journal of Structural Division, ASCE, V. 108, No. ST4, pp. 929-950.

Park, S., and Mosalam, K.M., (2009). “Shear Strength Models of Exterior Beam-Column Joints without Transverse Reinforcement”, PEER Report 2009/106, University of California, Berkeley.

Park, S., and Mosalam, K.M., (2012). “Parameters for Shear Strength Prediction of Exterior Beam-Column Joints without Transverse Reinforcement”, Engineering Structures, Vol. 36, No. 3, pp. 198-209.

Paulay T, Park R., (1984). "Joints in reinforced concrete frames designed for earthquake resistance", Research report 84-9. Christchurch: Department of Civil Engineering. University of Canterbury.

Paulay, T., Park, R., and Priestley, M.J.N., (1987). "Reinforced Concrete Beam-Column Joints under Seismic Actions", ACI Journal, Vol. 75, No. 60, pp. 585-593.

Paulay, T., and Priestley, M. J. N., (1992). “Seismic Design of Reinforced Concrete and Masonry Buildings”, John Wiley and Sons, New York, 767 pp.

Pessiki, S.P., Conley, C., Gergely, P., and White, R.N., (1990). “Seismic Behavior of Lightly Reinforced Concrete Column and Beam Column Joint Details”, NCEER-90-0014, National Center for Earthquake Engineering Research, State University of New York at Buffalo.

Powell, G. (1993). “Drain-2DX element description and user guide for element type 01, 04, 05, 08, 09, and 15”, version 1.10. Report No. UCB/SEMM-93/18. Department of Civil Engineering, University of California, Berkeley.

Prakash V, Powell GH, Campbell S. (1993). “DRAIN-2DX base program description and user guide”, University of California, Berkeley, California.

Priestley, M. J. N., and Park, R., (1987). “Strength and Ductility of Concrete Bridge Columns under Seismic Loading”, ACI Structural Journal, V. 84, No. 1, Jan.-Feb., pp. 61-76.

Priestley, M.J.N., and Hart, G., (1994). “Royal Palm Resort, Guam, Seismic Behavior of As-Built and As-Designed Corner Joints”, SEQAD Consulting Engineers, Solana Beach, CA.

Priestley, M.J.N. and Hart, G., (1994). “Royal Palm Resort, Guam, Seismic Behavior of As-Built and As-Designed Corner Joints”, SEQAD Consulting Engineers, Solana Beach, CA.

Priestley, M. N. J., & Calvi, G. M., (1991). "Towards a capacity — Design assessment procedure for reinforced concrete frames", Earthquake Spectra 7(3), 413-437.

Prion, H. G. L. and Baraka, M., (1995). “Grouted Steel Tubes as Seismic Retrofit for Beam to Column Joints”, in Proceedings 7th Canadian Conference on Earthquake Engineering, Montreal, pp. 871–878.

Prota, A., Nanni, A., Manfredi, G., and Cosenza, E., (2001). “Selective Upgrade of Beam-Column Joints with Composites”, Proceedings of the International Conference on FRP Composites in Civil Engineering, Hong Kong, Dec.

Prota, A., Manfredi, G., Nanni, A., and Cosenza, E., (2002). “Selective Seismic Strengthening of RC Frames with Composites”, Proceedings of the Seventh U.S. National Conference on Earthquake Engineering, Boston, July.

Prota, A., Nanni, A., Manfredi, G., and Cosenza, E., (2003). “Capacity assessment of RC subassemblages upgraded with CFRP.” J. Reinf. Plast. Compos., 22(14), 1287–1304.

Rubiano N. (2001) A comparison of nonlinear models for RC frames, Advances in Earthquake Engineering, Earhquake Resistance Engineering Structures III, 9, 327-336.

Rubiano N., (2001). "A comparison of nonlinear models for RC frames", Advances in Earthquake Engineering, Earthquake Resistance Engineering Structures III, 9, 327-336.

Ruitong, D. and Park, R., (1987). "A comparison of the behaviour of reinforced concrete beam-column joints designed for ductility and limited ductility", Christchurch, N.Z. : University of Canterbury, Dept. of Civil Engineering, Research report / University of Canterbury, Dept. of Civil Engineering, 0110-3326, vi,65p.

Saatcioglu, M., (2003). “Research on seismic retrofit and rehabilitation of reinforced concrete structures”, Proc., 31st Annual Conf. of the Cana-dian Society for Civil Engineering, CSCE, M. Massiéra and G. Poi-tras, eds., Vol. GCU-542, Canadian Society for Civil Engineering, Moncton, Canada, 10.

Saatcioglu, M.,(2006). “Seismic risk mitigation through retrofitting non-ductile concrete frame systems”, Advances in earthquake eng. for urban risk reduction, S. T. Wasti and G. Ozcebe, eds., Springer, The Netherlands, 179–194.

Said, A., and Nehdi, M., (2004). “Use of FRP for RC in seismic zones, Part I: Evaluation of FRP rehabilitation techniques for beam-column joints”, Journal of Applied Composite Materials, Vol. 11, No. 4, pp. 205-226.

Said, A., and Nehdi, M., (2004). “Use of FRP for RC in seismic zones, Part II: Behaviour of steel-free GFRP reinforced concrete frames under reversed cyclic loading”, Journal of Applied Composite Materials, Vol. 11, No. 4, pp. 227-245.

Salloum, Y. A., and Almusallam, T. H., (2007). “Seismic response of interior RC beam-column joints upgraded with FRP sheets—Part I: Experimental study.” J. Compos. Constr., 11(6), 575–589.

Sasmal, S., (2009). "Performance Evaluation and Strengthening of Deficient Beam-Column Sub-assemblages under Cyclic Loading", PhD Thesis, Universitaet Stuttgart, Institut für Leichtbau Entwerfen und Konstruieren.

Sasmal S., Ramanjaneyulu K., Novak B., Srinivas V., Saravana Kumar K., Korkowski C., Roehm C., Lakshmanan, N., Iyer N.R., (2011). "Seismic retrofitting of nonductile beam-column sub-assemblage using FRP wrapping and steel plate jacketing", Construction and Building Materials, 25 (1), pp. 175-182.

Schofield, H.A., Ingham, J.M., and Pampanin, S.,(2006). “Critical earthquake risk detailing in New Zealand’s multi-storey building stock: Understanding and improving the current perception”, New Zealand Society for Earthquake Engineering (NZSEE) Conference-2006, Paper Number 39.

Sezen, H., (2003). “Seismic Behaviour and Modelling of Reinforced Concrete Building Columns” Ph.D. Dissertation. University of California, Berkeley.

Sezen, H., Elwood, K.J., Whittaker, A.S., Mosalam, K. M., Wallace, J.W., and Stanton, J.F., (2000). “Structural engineering reconnaissance of the August 17, 1999 earthquake: Kocaeli (Izmit), Turkey”, PEER-2000/09, Berkeley: Pacific Earthquake Engineering Research Center, University of California, Dec.

Shannag, M. J., Barakat, S., and Abdul-Kareem, M., (2002). “Cyclic Behavior of HPFRC-Repaired Reinforced Concrete Interior Beam-Column Joints”, Materials and Structures, V. 35, pp. 348-356.

Sharma, A., Eligehausen, R., Reddy, G.R., (2011). "A new model to simulate joint shear behavior of poorly detailed beam–column connections in RC structures under seismic loads, Part I: Exterior joints", Engineering Structures 33(3), pp 1034–1051, Jan.

Shima, H., Chou, L. and Okamura, H. (1987). "Bond stress-slip-strain relationship of deformed bars embedded in massive concrete", Concrete Library International, No.10, Japan Society of Civil Engineers, Dec. 1987, pp.79-94

Shima H., Choo L., and Okamura H. (1987). "Bond characteristics in post-yield range of deformed bars", Concrete Library of JSCE, 10, 113-124.

Shin, M., and LaFave, J.M., (2004). "TESTING AND MODELING FOR CYCLIC JOINT SHEAR DEFORMATIONS IN RC BEAM-COLUMN CONNECTIONS", 13th World Conference on Earthquake Engineering (13WCEE), Canada, August, Paper No.0301.

Shin, M., and LaFave J.M., (2004). “Seismic performance of reinforced concrete eccentric beam-column connections with floor slabs,” ACI Structural Journal, 2004, 101, in press.

Shin, M., and LaFave, J. M., (2004). "Modeling Of Cyclic Joint Shear Deformation Contributions In RC Beam-Column Connections To Overall Frame Behavior", Structural Engineering and Mechanics, 18(5), pp. 645-669.

Shrestha, R., and Smith, S. T., (2007). “An experimental investigation on the strengthening of RC beam-column connections with FRP composites.” Proc., First Asia-Pacific Conference on FRP in Structures, APFIS 2007, Hong Kong.

Shrestha, R., (2009). “Behaviour of RC beam-column connections retrofitted with FRP strips.” PhD thesis, Univ. of Technology, Sydney, Australia.

Smith, S. T., and Shrestha, R., (2006). “A review of FRP-strengthened RC beam column joints.” Proc., Third Int. Conf. on FRP Composites in Civil Engineering, CICE2006, Miami.

Sooriyaarachchi, H., Pilakoutas, K., and Byars, E., (2005). "Tension Stiffening Behaviour of GRP-Reinforced Concrete", Proceedings of 7th International Symposium for Fibre-

Reinforced Polymer (FRP) Reinforcement for Concrete Structures, FRPRCS7, American Concrete Institute SP-230, 975-989 pp.

Stevens, N.J., Uzumeri, S.M. & Collins, M.P., (1991a). "Reinforced concrete subjected to reversed cyclic shear-experiments and constitutive model", ACI Structural Journal, 88(2), p.135–146.

Stratta, J. L., et. al., (1981). "Earthquake in Campania-Basilicata, Italy, November 23, 1980," National Research Council and Earthquake Engineering Research Institute, El Cerrito, California, 100 pp.

Tepfers R., (1973). "A theory of bond applied to overlapped tensile reinforcement splices for deformed bars", Publication 73:2, Division of Concrete Structures, Chalmers University of Technology, Goteborg, Sweden.

Theiss, A.G., (2005) "Modeling the Earthquake Response of Older Reinforced Concrete Beam-Column Building Joints", M.Sc. Thesis, University of Washington.

The Design of Concrete Structures, NZS 3101:1995, Standards New Zealand, Wellington, 1995.

Tsonos, A. G., and Stylianidis, K. A., (1999). "Pre-seismic and post-seismic strengthening of reinforced concrete structural subassemblages using composite materials (FRP)", Proc., 13th Hellenic Concrete Conf., 1, Rethymno, Greece, 455–466.

Tsonos, A. G., (2001). "Seismic Rehabilitation of Reinforced Concrete Joints by the Removal and Replacement Technique", European Earthquake Engineering, No. 3, pp. 29-43.

Tsonos, A. G., and Stylianidis, K., (2002). "Seismic Retrofit of Beam-to-Column Joints with High-Strength Fiber Jackets", European Earthquake Engineering, V. 16, No.2, pp. 56-72.

Tsonos A, and Papanikolaou K. (2003). "Post-earthquake repair and strengthening of reinforced concrete beam–column connections (theoretical and experimental investigation)". Bulletin of the New Zealand Society for Earthquake Engineering; 36:73–93.

Tsonos A.G., (2007). "Cyclic load behaviour of reinforced concrete beam–column subassemblages of modern structures", ACI Struct J; 104(4):468–78.

Uang, C-M., et al. (1999). "Ji-Ji Taiwan Earthquake of Sep.21, 1999: A Brief Reconnaissance Report", Department of Structural Engineering, University of California, San Diego.

University of Sheffield "Repair and Reinforcement of Load Bearing Members". International Patent Application No. PCT/EP94/01222, Publication No. WO 94/24391, 27 October 1994

UNDP/UNIDO PROJECT RER/79/015, UNIDO (1983). "Repair and Strengthening of Reinforced Concrete, Stone and Brick-Masonry Buildings", Building Construction Under Seismic Conditions in the Balkan Regions, V. 5, Vienna, 231 pp.

Uzumeri, S. M., (1977). "Strength and Ductility of Cast-in-Place Beam Column Joints", Reinforced Concrete Structures in Seismic Zones, SP-53, Hawkins, N. M., ed., American Concrete Institute, Detriot, Michigan., pp. 293-350.

Valluvan, R., Kreger, M.E., Jirsa, J.O., (1993). "Strengthening of Column Splices for Seismic Retrofit of Nonductile Reinforced Concrete Frames", ACI Structural Journal, V. 90, No. 4, July-Aug, pp. 432-440.

Vecchio, F.J., and Collins, M.P., (1993). "Compression Response of Cracked Reinforced Concrete", Journal of Structural Engineering, ASCE, V. 119, No. 12, Dec, pp. 3590-3610.

Vollum, R.L., (1998) "Design and Analysis of Exterior Beam Column Connections", PhD Dissertation, Imperial College of Science Technology and Medicine-University of London, 1998.

Walker, S. G.; Yeargin, C. M.; Lehman, D. E.; and Stanton, J. F., (2002). "Performance-Based Seismic Evaluation of Existing Joints," Proceedings of the Seventh U.S. National Conference on Earthquake Engineering, Boston, July.

Wong, H.F., and Kuang, J.S., (2008). "Effect of beam-column depth ratio on seismic behaviour of exterior beam-column joints", Structures and Buildings, ICE, 161(2): 91-101.

Wong, H.F. (2005). "Shear Strength and Seismic Performance of Non-Seismically Designed Reinforced Concrete Beam-Column Joints", PhD Dissertation, Department of Civil Engineering, The Hong Kong University of Science and Technology, August.

XTRACT (2004). "Cross-Section Analysis Structural Software", http://www.imbsen.com/xtract.htm

Yamao, H., L. Chou, L., Niwa, J., (1984). “Experimental study on bond stress slip relationship”, Proceedings of Japan Society of Civil Engineers, vol. 343, pp. 219–228.

Youssef, M., and Ghobarah, A., (2001). "Modeling of RC Beam-Column Joints and Structural Walls", Journal of Earthquake Engineering, 5(1), pp93-111

Zhang, L.X.B., and Hsu, T.T.C., (1998). “Behavior and Analysis of 100 MPa Concrete Membrane Elements”, Journal of Structural Engineering, ASCE, V. 124, No. 1, Jan, pp. 24-34.

Zhao, W. (1999). "Crack and Deformation Behaviour of FRP Reinforced Concrete Structures", PhD Thesis, The University of Sheffield, Department of Civil & Structural Engineering.

Zuo, J., and Darwin, D., (1998). “Bond Strength of High Relative Rib Area Reinforcing Bars”, SM ReportNo. 46, University of Kansas Center for Research, Lawrence, Kans., 350 pp.

Zuo, J., and Darwin, D., (2000). “Splice Strength of Conventional and High Relative Rib Area Bars in Normal and High-Strength Concrete,” ACI Structural Journal, V. 97, No. 4, July-Aug., pp. 630-641.

APPENDICES

Appendix A

BOND BEHAVIOUR

This appendix reviews briefly the state of knowledge on bond behaviour of reinforcing bars embedded in reinforced concrete. The key parameters, most relevant to the current work, are also briefly discussed.

A.1 GENERAL

Transfer of forces between steel bars and concrete, through bond, is regarded as one of the most significant characteristics influencing the structural performance of RC members (Hyatt, 1877). Most structural problems such as cracking, deflections, structural strength, hinge formation and energy dissipation during seismic excitations are aspects connected directly or indirectly to bond. Research on the bond interaction between concrete and steel bars has probably occupied the majority of analytical and experimental work conducted on RC for well over 100 years. Consequently, several numerical models have been proposed and many experimentally based relationships have been derived to describe the bond characteristics of steel bars. Moreover, the main factors influencing the bond behaviour have been identified. The studies, in general, cover different loading conditions, pullout and splitting bond type failures, anchorages and splices in compression or tension, unconfined concrete, internally or externally confined concrete using

different materials. The first report issued on the bond subject was that by ACI Committee 408 (1966). The report was then followed up by Committee 408 (1979) with updated design requirements for anchorages, splices, and hooks. A state-of-the-art report on bond under cyclic loads was issued (ACI 408.2R-92) after that in 1992. In 2001 new design provisions were issued for splices and anchorages of steel bars having high relative rib area (ACI 408.3-01). The last state-of-the-art report emphasising bond behaviour and design of anchored/spliced steel bars in tension is that by ACI Committee 408 (2003) and upon which most of the work in this study is based or compared to.

A.2 STEEL BAR-TO-CONCRETE INTERACTION

It is well established that transfer of forces between steel bars and concrete results from a combination of three components, namely, adhesion (V_a), the bearing resistance of lugs (V_b) and a frictional action (V_f), as shown in Figure A-1. The first component results from the chemical adhesion on the concrete-to-steel interface and breaks down at low pullout forces or even due to shrinkage. In this stage, the bond resistance is rather small and no slip exists. As the pullout force increases, bar lugs induce large bearing stresses in the surrounding concrete and as a consequence transverse microcracks, known as Goto (1971) cracks, form at the tips of the lugs allowing for the bar to start slipping. Slippage of the bar, however, is small due to the wedging action of the lugs. With further increase in the bar force, the concrete stuck to the front of the lugs crushes and longitudinal cracks spread radially forming a conical failure surface. The pullout force in this case is balanced by rings "hoops" of tensile stresses originating due to the bearing resistance of lugs (Figure A-2 by Tepfers (1979) and Eligehausen (1983)). This mechanism of force equilibrium is explained by Tepfers (1979) and referred to as "the concrete ring theory". Once the conical ring approaches its capacity, splitting cracks propagate towards the surface of concrete cover.

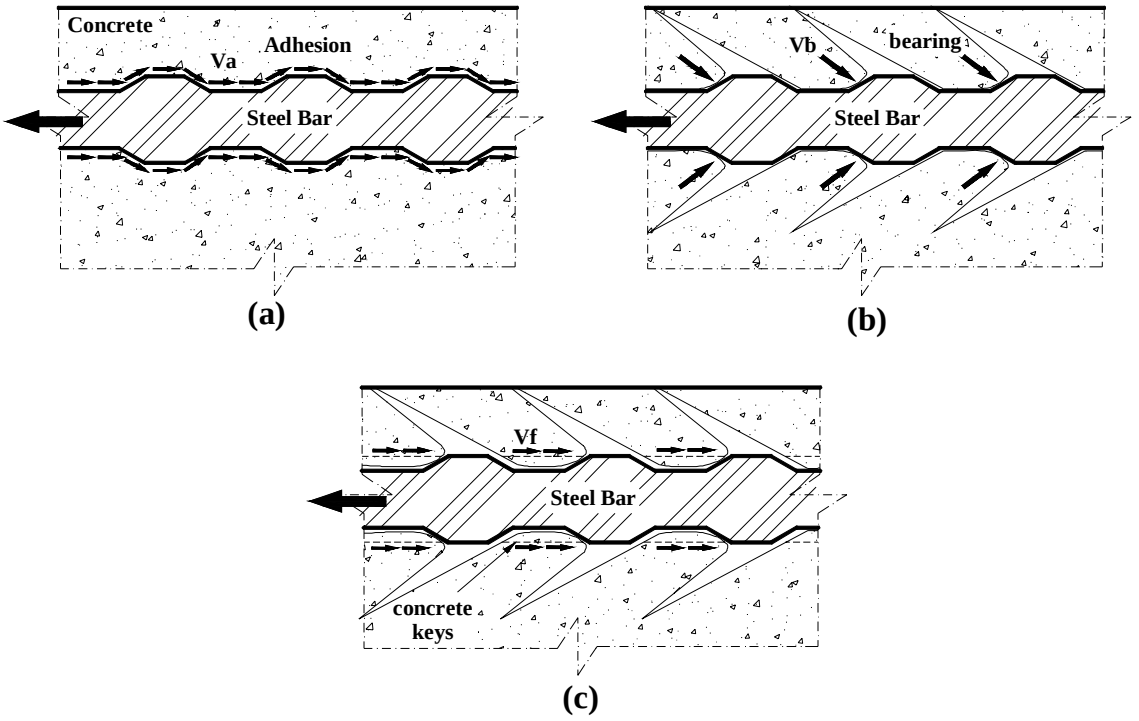

Figure A-1: Forces between deformed bar and concrete a) adhesion, b) mechanical bearing and c) friction, based on CEB Bulletin 151 (1982)

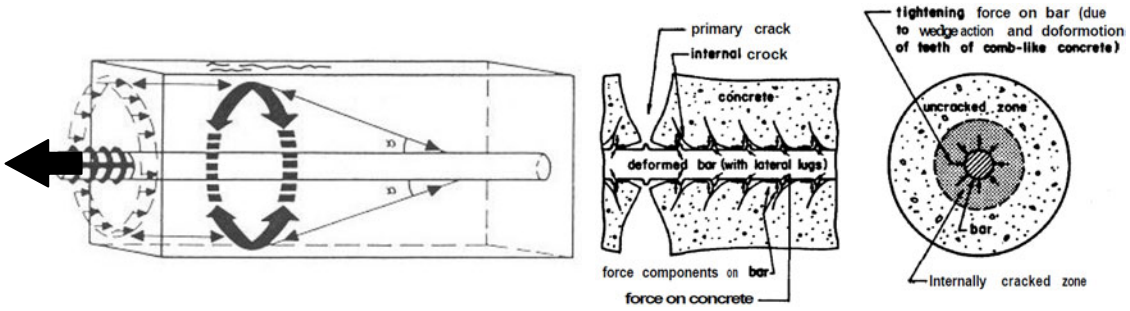

Figure A-2: Tensile stresses in the bar and surrounding concrete [Tepfers (1979), and Eligehausen (1983)]

Two distinct types of bond failure can be expected based on the concrete cover and the confinement provided. If the concrete cover is small or the lateral confinement is light, splitting cracks develop along the bar and reach to the concrete surface resulting in severe damage to concrete cover and probably to concrete spall-off. This type of failure is known as splitting failure and is characterised by a brittle nature. On the other hand, if a large concrete cover exists or relatively intense amount of lateral confinement is provided, the load resistance increases until the concrete keys between the bar lugs are crushed or sheared-off. This mode of bond failure is referred to as pullout failure, and it is mostly encountered in elements with well detailed reinforcement. Splitting failure is reported to be more common in existing buildings [Clark (1950); Menzel (1952); Chinn et al. (1955); Ferguson and Thompson (1962); Losberg and Olsson (1979); Soretz and Holzenbein (1979); Johnston and Zia (1982); Treece and Jirsa (1989); Choi et al. (1991); and Eligehausen (1983)]. A pullout failure induced by splitting

cracks due to limited concrete cover or moderate confinement ratio is also a common type of failure where concrete keys between bar lugs shear-off.

After the bond strength reaches a peak, it degrades with increasing slip values. Although high slip values may be reached, the post-peak bond strength remains significant, as reported by Gambarova et al. (1989) and Gambarova and Rosati (1997), among others.

In the case of pullout failure, mechanical bearing changes into friction after the peak. The post-peak behaviour in the case of splitting failure, however, depends largely on the confinement efficiency which in turn depends on concrete cover and bar spacing [Ferguson (1965), Morita and Kaku (1979), Harajli (2010), ACI 318-08 (2008), EC2 (2004), Orangun et al. (1975, 1977)], on transverse reinforcement [Ferguson (1966), Chinn et al. (1955), Orangun et al. (1975,1977), Losberg and Olsson (1979), Fujii and Morita (1981), Darwin et al. (1992,1996a), Zuo and Darwin (2000), Harajli (2009, 2010)], on lateral pressure [Dorr (1978), Robins and Standish (1982), Gambarova et al. (1994), Malvar (1992), Modena (1992)], and crack cohesion [Reinhardt and van der Veen (1990), Rosati and Schumm (1992), Gambarova et al. (1994)].

Bond force-slip or bond stress-slip can be used to explain the concrete-to-steel bond phenomenon. Slip can be measured at the loaded or unloaded end of the bar. The difference is the extension of the bar between the two ends (ACI Committee 408, 2003).The local change in the bar force or bond stress along the length of the bar can be obtained by installing strain gauges along the bar. Much experimental and analytical work is done in this regard and many models have been proposed by adopting a bond stress distribution function along the anchorage length of the reinforcing bars[for example: Bertero and Bresler (1968), Bertero and Popov (1977), Bertero et al. (1978), Guiriani (1981), Shah and Somayayi (1981), Filippou (1986), Alsiwat and Saatcioglu (1992), Lehman and Moehle (2000), Sezen (2003), and Ahmad (2011)].

It should be mentioned also that other methods were used to solve the bond problem. One method is by solving differential equations of bond [for example Vos and Reinhart (1982) and Filippou (1986), among others]. Also, fracture mechanics were used to develop models for bond [for example Gerstle et al. (1982) and Gylltoft et al. (1982), among others].

A.3 FACTORS INFLUENCING BOND STRENGTH

Many parameters are reported to influence the bond behaviour between concrete and reinforcing bars. It is important to understand these parameters and their relations especially those related to confinement. The following sections discuss the key parameters most relevant to the current research.

A.3.1 Concrete compressive strength, f'_c

As splitting or pullout bond failures are a consequence of tensile cracks, it is believed that they are influenced by the tensile strength of concrete which in turn is related to compressive strength [Tepfers (1979), Carino and Lew (1982)]. Thus, the concrete compressive strength f'_c is considered a key factor influencing the bond behaviour.

Early studies on bond strength such as those by [Tepfers (1973); Orangun et al. (1975, 1977); Darwin et al. (1992); Esfahani and Rangan (1998a&b)] and design equations found in codes of practice (ACI 318; CEB-FIP) considered that the normalisation of average bond strength τ_u at failure to $\sqrt{f'_c}$ best represents the effect of concrete properties on bond strength, as long as the concrete strength is less than 55 MPa. Studies on higher concrete compressive strengths, for example those by [Azizinamini et al. (1993); Azizinamini et al. (1995); Zuo and Darwin (1998, 2000); Hamad and Itani (1998); and Darwin et al. (2005)] showed that the normalised τ_u to $\sqrt{f'_c}$ decreases as f'_c increases. This phenomenon was reported to be more pronounced for longer splices (Azizinamini et al., 1993, 1995).

The normalisation to $\sqrt{f'_c}$, however, has not been adopted universally. Zsutty (1985) found better predictions of the experimental data when the $f'_c{}^{1/3}$ is used. Darwin et al. (1996a) using a larger test database showed that an average bond strength normalised to $f'_c{}^{1/4}$ better predicts the data. Zuo and Darwin (1998, 2000) continued the work by Darwin including a large number of tests with high-strength concrete and observed that the use of $f'_c{}^{1/4}$ provides the best representation for the effect of compressive strength on the concrete contribution to bond strength. A recent study conducted by Ahmad (2011) using a large database including specimens with $f'_c < 30$ MPa showed that $f'_c{}^{0.68}$ provides a good representation of concrete properties on the average bond strength.

For bars confined by transverse reinforcement, Darwin et al. (1996) found that the effect of concrete compressive strength on the additional bond strength due to confinement T_s is best represented using $f'_c{}^{1/4}$. Zuo and Darwin (1998, 2000), however, found that $f'_c{}^{1/4}$ significantly underestimates the effect of f'_c on T_s. Instead, they found that $f'_c{}^{3/4}$ better represents the effect of compressive strength on the additional bond strength T_s. The last finding is supported by Darwin et al. (2005).

A.3.2 Bar spacing and concrete cover

Laboratory tests on deformed steel bars show that the bond behaviour and, as a consequence, type of failure depend largely on the configuration of reinforcement within the member cross-section [Tepfers (1973), Orangun et al. (1977), Eligehausen (1979)]. If the arrangement of reinforcement results in a small concrete cover, early splitting cracks originate around the reinforcing bar and break through to the cover concrete resulting in a splitting-type failure. On the other hand, if the concrete cover is large, the concrete keys between bar lugs shears off and

as a result the bar pulls out. Earthquake loading, because of its cyclic nature, is expected to accelerate the crack formation and crack propagation, particularly at small concrete covers. All seismic codes of practice for example (ACI, EC2) reflect the importance of this factor by providing specific detailing on the configuration of reinforcement within the element cross-section.

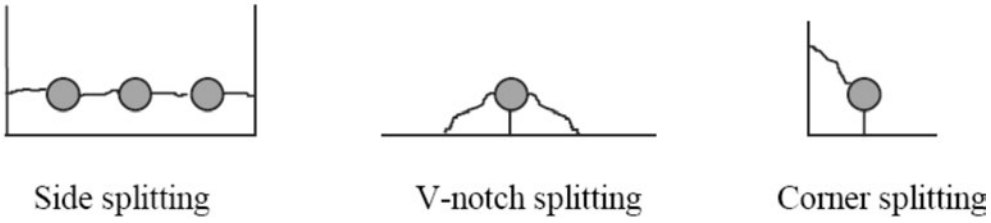

Figure A-3: Formation of splitting cracks, adopted from Nagamoto and Kaku (1992)

All model equations proposed to account for the concrete contribution to bond strength consider the concrete cover and bar spacing a key factor [Ahmad (2011), Hassan (2011), Orangun et al. (1977), and others].

A.3.3 Bar size

Studies on bond such as those by Soretz (1979), Kimura and Jirsa (1992), De Larrard (1993), Rehm and Eligehausen (1979), and Soroushian and Choi (1989) showed that the bar diameter influences the ultimate bond strength as well as the bond stress-slip relationship (an example is shown in Figure A-4). It is observed that, for a certain bonded length, less bond stress is obtained for bars with larger bar areas. It is also true that the amount of force that requires transfer increases as the bar size increases. Therefore, it is preferable, for a certain amount of transferred force, to use multiple bars with smaller diameter rather than the use of less bars with bigger diameters; this is actually true as long as bar spacing does not affect the bond strength.

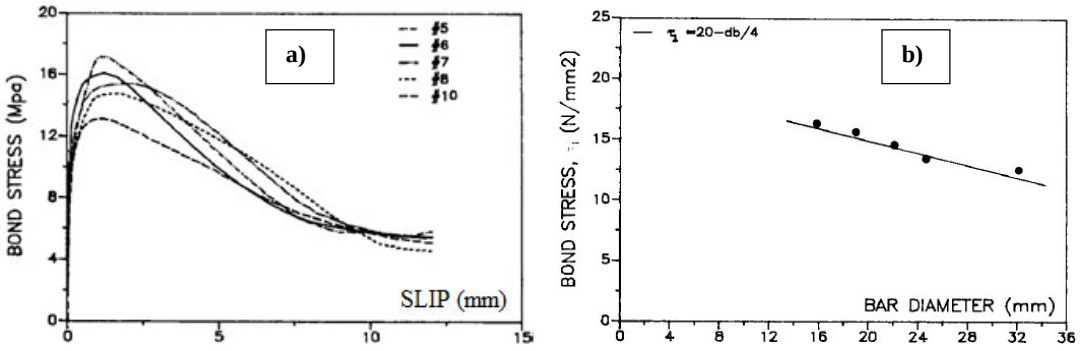

Figure A-4: Bar diameter effect on a) the average bond stress-slip relationship b) the ultimate bond stress (Soroushian and Choi, 1989)

The bar size also has a significant influence on the contribution of confinement to bond strength. The slip of bars with larger areas induces higher stresses in the confining transverse reinforcement resulting in better confinement. As a consequence, the contribution of

confinement to the bond strength enhances. This conclusion is supported by the findings of this study (see chapter 4).

A.3.4 Steel stress and yield strength

It is a concern that yielding of a bar before bond failure would result in considerably lower average bond stresses compared to those that did not yield (Orangun et al., 1975). However, the bond strength of a given anchored length of a bar that yielded before bond failure was estimated to be only 2% less for unconfined concrete and 10% higher for confined concrete [Darwin et al. (1996a); Zuo and Darwin (1998, 2000)].

A.3.5 Anchorage/splice length

It is known that longer anchorages/splices produce higher bond capacity. However, the increase in bond capacity is not proportional to the increase in the embedded length due to the nature of bond failure. In anchorages, splitting cracks as well as failure initiates at the lead end (loaded end) of the bar or at a transverse flexural crack located along the anchored length; with loading splitting cracks propagate towards the bar end. In splices, on the other hand, failure starts at the lead end due to splitting cracks and propagate towards the mid length. As a result, in both cases, the tail end (unloaded end) is less effective in transferring the force. This, in turn, explains the non-proportional increase in bond strength when the bonded length increases. Despite this fact, the relation of bond strength to the bonded strength is approximated by a linear relationship (ACI Committee 408, 2003).

In cases where the bonded length is long enough to induce yielding in the bar, the nature of bond failure as well as bond capacity will not be the same compared to those failed in the elastic stage, as shown in Figure A-5, (Setzler and Sezen, 2008).

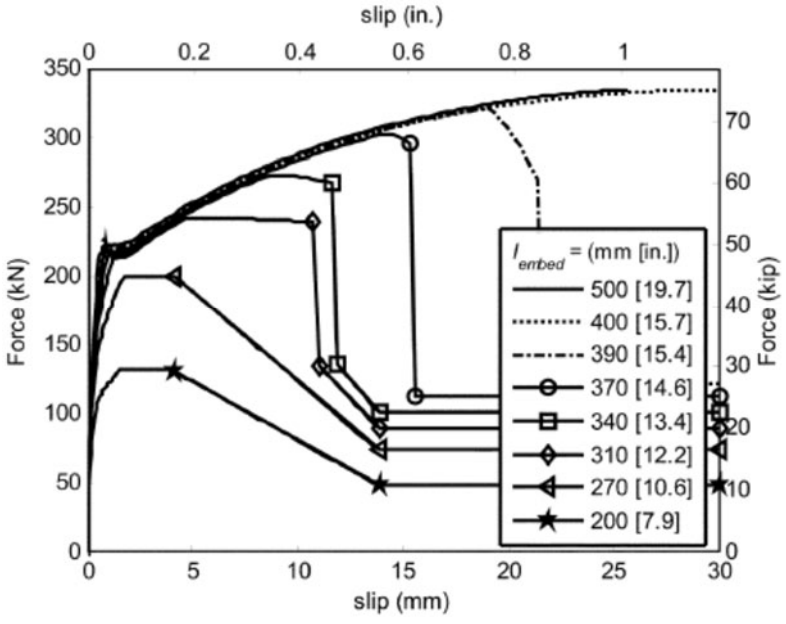

Figure A-5: The effect of embedment length on force-slip relation (Setzler and Sezen, 2008)

A.3.6 Confinement

Research on the effect of steel confinement on bond behaviour shows that the type of bond failure is strongly related to the amount of confinement provided along the bonded length. Lateral confinement is found to restrict the growth of splitting cracks and improve the failure mechanism [Tepfers (1973, 1979), Orangun et al. (1977), Eligehausen (1979), Darwin and Graham (1993a&b)]. However, it is reported that an upper limit beyond which the bond capacity can be improved due to additional confinement may exist [Eligehausen et al. (1983), Giurianni et al. (1991), Plizzari et al. (1996)].

Results from investigations on anchorages in tension indicate that confining reinforce concrete enhances the ultimate average bond strength limitedly; however, it leads to a significant enhancement in the ductility of splitting bond failure [Hamad et al. (2001, 2004, 2011); Harajli et al. (2004, 2009), Harajli (2006)].

Confinement is also found to improve the concrete contribution to bond as it reduces the effective crack length between the bars (Zuo and Darwin, 1998, 2000). The increase is reported to be small; however it is measurable, (ACI Committee 408, 2003).

The contribution of confinement to bond strength is traditionally measured by the additional increase in bar force or bond stress with respect to the unconfined case. Much work is done in this regard and many expressions were proposed (See for example ACI Committee 408 (2003)).

A.3.7 Transverse pressure

According to CEB Bulletin 151 (1982), reinforcing bars anchored in supports or joints may be subjected to transverse compression leading to improved bond behaviour. Transverse compression delays the onset of splitting failure in a plane perpendicular to the direction of compressive stresses and also increases the frictional force applied to the concrete-to-steel failure surface. The presence of transverse pressure leads to an increase in the peak bond strength and a reduction in the associated slip. The peak bond stress is reported to have approximately a linear relationship with the transverse pressure, whose efficiency increases with the increase in the side and bottom concrete cover [Gambarova and Rosati (1997), Gambarova et al. (1994), Malvar (1992), Modena (1992)]. However, cases where excessive concrete covers exist negate the effect of transverse pressure (fib Bulletin 10, 2000). Moreover, transverse pressure is only beneficial as long as bond failure in governed by concrete splitting.

A test series of cylindrical concrete specimens was conducted by Malvar (1992) where different levels of lateral pressure were applied. The test results showed that increasing the confining pressure leads to a considerable improvement in the maximum bond stress. In fact, increasing the confining pressure from 3.5 to 31 MPa increased the maximum bond almost threefold. A

local bond stress-slip relationship was proposed by Malvar (1992) accounting for various degrees of confining pressure.

As for the codes of practice, only EC2 (2004) takes into consideration the effect of transverse pressure on the potential splitting plane. In the code, the design anchorage length is increased by a factor α_5 ($0.7 < \alpha_5 = 1 - 0.02p < 1.0$) depending on the transvers pressure p applied to the splitting plane.

A.4 SPLICES

Much research has been conducted to investigate bond behaviour of spliced reinforcing bars under different loading conditions (ACI Committee 408, 1992). Splitting type-failure is mostly dominant in elements with spliced bars. Such failure mode, as previously mentioned, has an abrupt and brittle nature; however, it becomes more ductile as the amount of confinement increases. Splitting cracks of splices are characterised by different patterns leading in most cases to early cover spalling, as schematically shown in Figure A-6. Development of a specific crack pattern depends largely on the configuration of reinforcement within the element cross-section and along the splice length. For example, closely spaced splices with small side and bottom covers produce face and side split, whereas widely spaced splices positioned away from corners show V-type split.

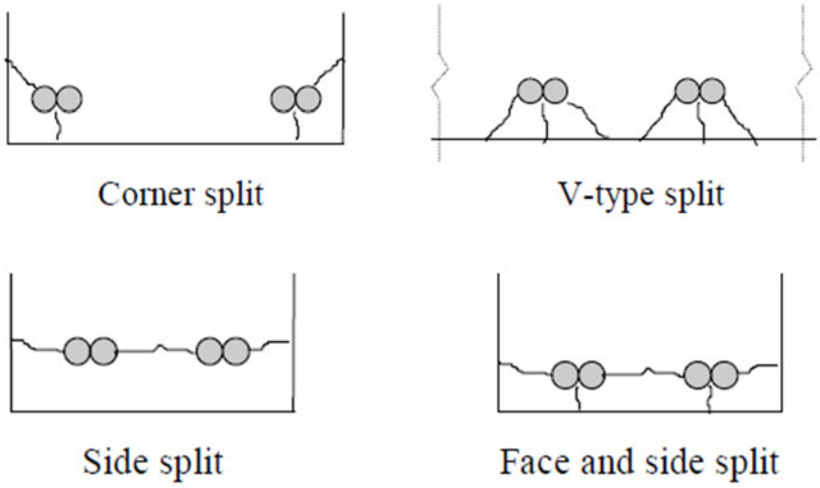

Figure A-6: Splitting crack patterns of splices, adopted from CEB Bulletin 151(1982)

The distribution of radial pressure around lap splices was extensively explored by many researchers. Accordingly, different stress distribution patterns were proposed, such as those shown in Figure A-7. Stress distributions depend on and at the same time are proportional to bond stresses developing along the splice length. A well-known pattern is that proposed by Tepfers (1973) considering that splices induce pressure similar to that by a single bar, Figure A-7 (a&b). Tepfers (1973), however, pointed out that the slip between bars of splices could be double the value generated by a single bar. Consequently, he proposed splitting pressure around

splices to be twice the value produced by a single bar, as shown in Figure A-7 (c). As it turned out, based on the experimental investigations conducted by Reynold (1982), that the distributions suggested by Tepfers (1973) were found inappropriate. The test results showed that the bond strength of spliced and single bars is the same, which agrees with the conclusion drawn by Orangun et al. (1977). In light of the previous finding, Reynold (1982) proposed a uniform distribution of splitting stresses around the splice, as shown in Figure A-7 (d). The previous conclusion together with Reynold's distribution was also verified due to experimental work on FRP bars carried out by Achillides (1998). Cairns and Jones (1996) observed in their tests that splitting stresses in the normal orientation of the splice plane were 30% higher than those in a single bar. As a result, they proposed a distribution pattern as shown in Figure A-7 (e).

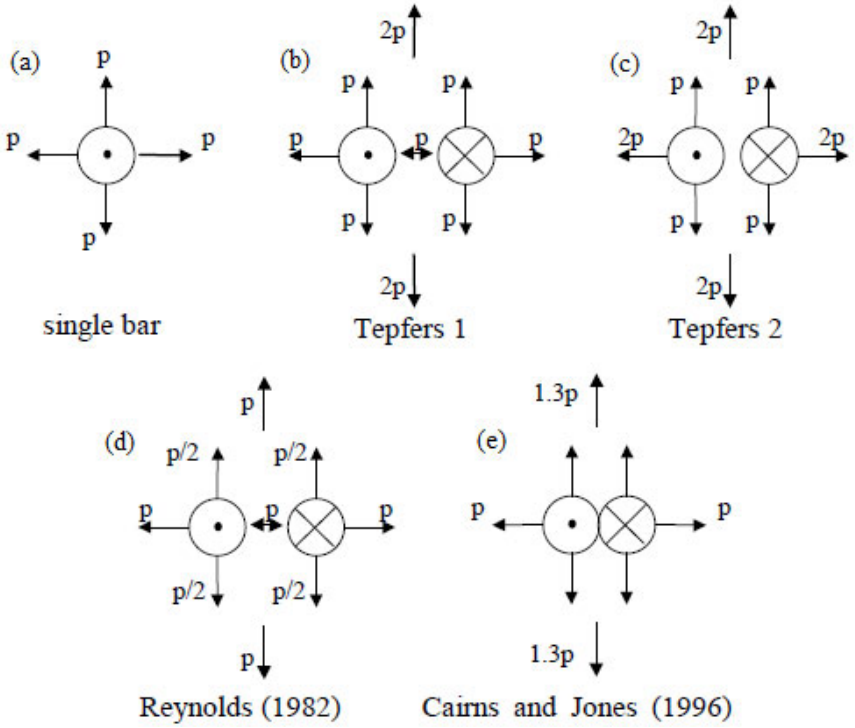

Figure A-7: Stress distributions of radial stresses in single and spliced bars

Many studies were conducted to measure the behaviour of spliced zones under cyclic loading rather than under monotonic loading conditions. Most of studies imply that a minimum amount of reinforcement should be provided in the lap length, and point out that this amount increases for loading of repetitive nature (ACI Committee 408, 1992). Although some studies indicate that confining splices at the two ends mostly improve their performance, many studies including seismic codes recommend using a uniform distribution of transverse reinforcement along the lap length. Moreover, it is found that cycling above yield stresses, for elements with spliced bars, has noticeable effect on the cumulative concrete deterioration and the energy absorption characteristics and therefore on the displacement capacity (ACI Committee 408, 1992).

Appendix B

STRENGTHENING OF BEAM-COLUMN JOINTS

In the following sections, a brief of the state-of-the-art on strengthening of deficient beam-column joints is given. It should be mentioned that the description is partly a summary of the work by [Engenidiz et al., (2005) and Bousselham (2010)] with some explanations and detailing when necessary based on reviews of the original works. Also, updates from recent experimental works were added.

B.1 EPOXY REPAIR

French et al. (1990) used the vacuum impregnation method to repair two moderately damaged interior joints, as seen in Figure B-1. Beres et al. (1992) used also the vacuum impregnation method to repair a deficient joint ruptured due to anchorage failure along with severe cracking in the core. Filiatrault and Lebrun (1996) used epoxy pressure injections to repair two damaged exterior joints including one with and one without ductile detailing for reinforcement.

Karayannis et al. (1998) used pressure epoxy injections to repair eleven exterior joints with different joint reinforcement configurations. The test results of the different epoxy repair measures indicated that the technique is able to restore partially the original characteristics of the specimens (~80% in average). Moreover, bond characteristic could not be recovered completely which was evident from the lower stiffness and pinching of the hysteresis response obtained.

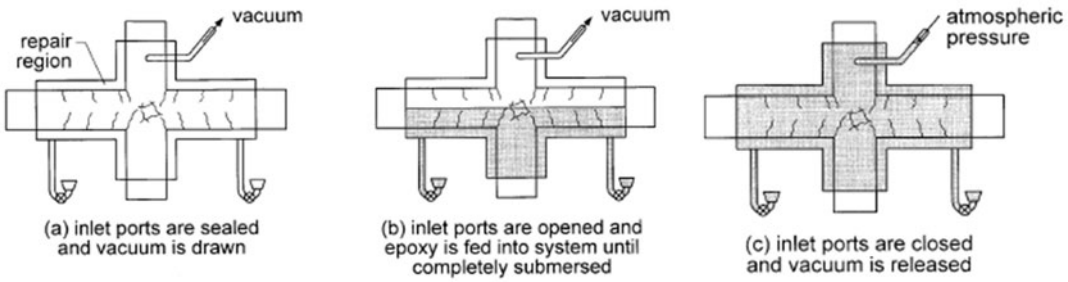

Figure B-1: Epoxy repair using vacuum impregnation (French et al., 1990)

B.2 CONCRETE RENEWAL

Karayannis et al. (1998) presented the test results of six substandard exterior beam-column connections which failed due to severe damage and spalling of concrete in the joint area. The damage was ascribed to no joint hoops in two of the specimens and to low reinforcement ratios in the rest. Repair of the joints was achieved by removal of spalled-off concrete and the replacement by using high strength-low shrinkage cement paste with a compressive strength of 83 MPa. In addition, epoxy injections were used to repair remaining cracks. The test results showed that specimens with no or one joint hoop exhibited the same failure mode of the original specimens. Enhancement in performance, however, was 39% to 71% in peak load, 15% to 39% in stiffness, and 19% to 34% in energy dissipation capacity. On the other hand, specimens with more joint hoops exhibited beam flexural hinging and no joint rapture occurred. Enhancement in performance was 42% in peak load and 170% in energy dissipation, whereas partial recover of stiffness could be obtained which accounted for 80% of the original specimen.

Two half-scale exterior joints were repaired by Tsonos (2001) using high strength concrete of 70MPa. The new concrete was provided for the entire joint area and parts of the column. In addition, two steel ties were placed into the joint area of one specimen. From the test results, better behaviour was observed in the repaired joints with higher strength and stiffness, and improved energy dissipation capability. However, the mode of failure of the repaired joints was similar to the original specimens.

Finally, it should be mentioned that the use of the concrete removal and replacement repair depends on other factors such as accessibility of the damaged connection and cost of shoring. Exterior and corner joints are usually readily accessible compared to interior joints. It is also

reported that, in some cases where only beams are the accessible elements, their sole repair may shift damage to the column or joint (Lee et al., 1977).

B.3 RC JACKETING

Corazao and Durrani (1989) used the RC jacketing technique to upgrade the strength of six beam-column connections including three single and two 2-bay exterior joints and two single interior joints. Slabs were provided in some of the specimens. Strengthening was applied to columns, joint regions and in some cases parts of the beams. Dowels with end hooks were used for joint reinforcement due to difficulties with bending cross-tie hooks. In addition, some welding was done for spliced bars. Reinforcement detailing used in one of the joints is shown in Figure B-2. The test results showed that higher strength, stiffness and energy dissipation capability were obtained for three single specimens, two of which with damage being moved out of the joint area. The two bay specimens, on the other hand, did not reach high performance levels. Consequently, it was reported that safe load transfer mechanisms must be ensured when this technique is used.

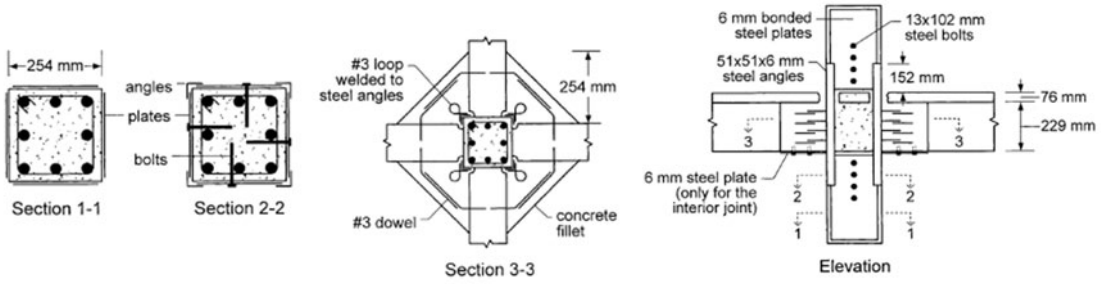

Figure B-2: Reinforcement detailing used in the RC jacketing, Corazao and Durrani (1989)

Alcocer and Jirsa (1993) strengthened four 3D beam-column connections in the pre- and post-earthquake conditions. Steel angles and longitudinal flat steel bars were used to provide confinement to the joint, the column, and in some cases beams. Another factor examined was the use of bundles or distributed vertical reinforcement within the strengthened area. Figure B-3 shows the RC jacketing technique studied by Alcocer and Jirsa (1993). The test results showed that the reinforcement provided was able to sustain large confining pressures up to high drifts of 4% where extensive damage occurred. This indicated considerable improvement in the performance. It was also indicated that the use of distributed reinforcement within the strengthened area was more effective than bundles.

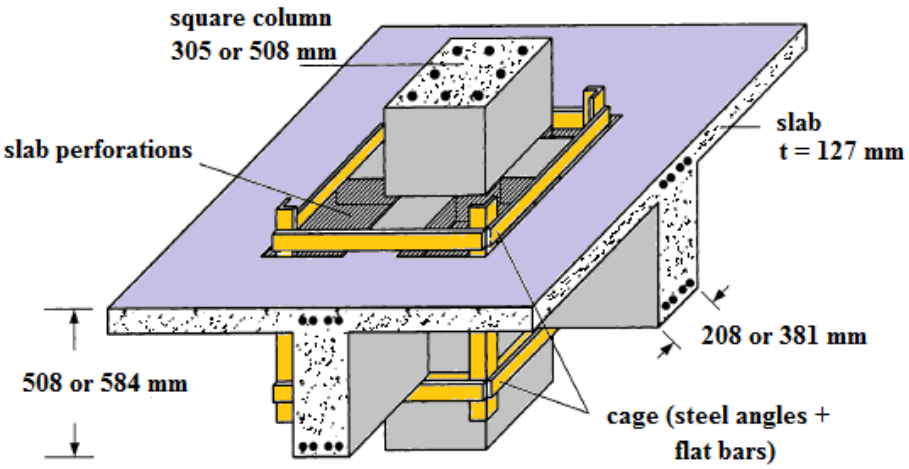

Figure B-3: RC jacketing technique investigated by Alcocer and Jirsa (1993)

Choudhuri (1992) explored a new RC jacketing technique that involves post-tensioning of additionally placed column reinforcement along with using new high strength concrete and concrete fillets around the connection, as seen in Figure B-4. One-third scale interior beam-column connections tested in the bare condition by Aycardi et al. (1994) were used for the strengthening. Bracci et al. (1995) also by adopting the same previous joint geometries investigated the technique on a 1/3 scale frame structure. The test results showed that the failure occurred due to beam flexural hinging with no damage to columns or joints; and as a result, soft story failure mechanism was avoided.

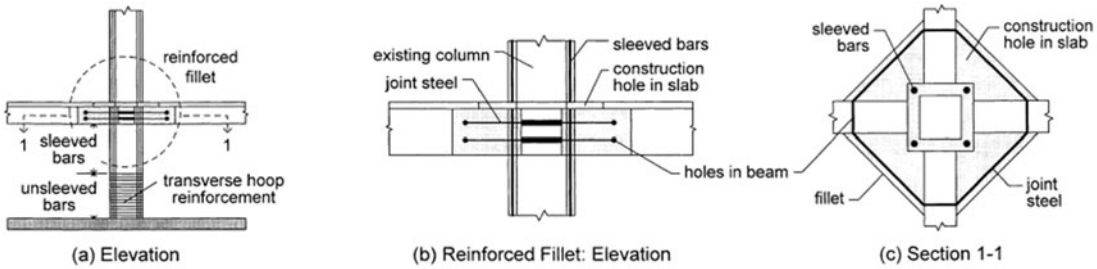

Figure B-4: Prestressed RC jacketing technique studied by Bracci et al (1995)

In the tests conducted by Hakuto (2000), one pre-damaged and two undamaged interior joints were strengthened using RC jacketing. Steel cages were used for additional reinforcement. Joint hoops of the pre-damaged unit consisted of plain U-shaped ties inserted in the joint region through holes and then welded. The other two units were not provided with any additional joint reinforcement, and furthermore one of which did not have beam cages. Figure B-5 shows the test units with reinforcement cages. With the exception of the single column-cage unit which suffered an early shear failure at beam hinging zones, the other two units showed very ductile behaviour along with formation of plastic hinges at beams ends.

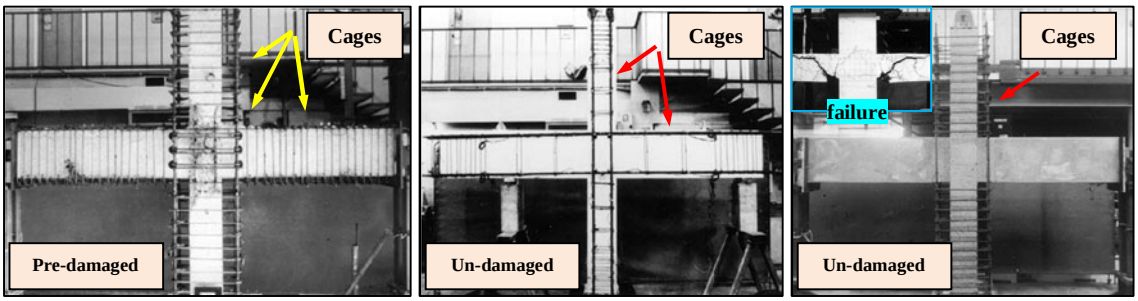

Figure B-5: Reinforcement cages used for the RC jacketing repair (Hakuto et al., 2000)

Tsonos (2001, 2002) also used RC jacketing to repair exterior beam-column connections with insufficient or no transverse reinforcement in the joint region. Tests on the bare units resulted in severe damage in the core and at column ends. For the strengthening process, the specimens were assumed inaccessible to simulate practical situations. Additional ties were placed in the joint area and additional anchorages were provided to beams to enhance bond conditions. Two-sided and three-sided jacketing schemes were used. Test results of the strengthened units indicated better failure modes including beam hinging and buckling of beam bars. In addition, considerable improvement in performance characteristics was observed.

B.4 STEEL JACKETING

Two beam-column connections including one exterior and one interior with beam anchorage deficiency were tested by Beres et al. (1992). Steel formworks for the interior unit included the use of steel channels bolted to the bottom beam surface and steel-tie bars for connection with columns. Test results indicated that the damage had shifted away from the anchorage zone. In addition, enhancement in strength and stiffness were observed; however, no improvement in energy dissipation occurred. For the exterior joint, steel plates were bolted to column faces so as to force the hinge to develop at the beam end and to provide a degree of confinement to the joint area. The test results showed that failure occurred due to hinging within the joint area along with anchorage failure of beam bottom bars. However, cracks were inhibited from extending to column splices. An increase in performance characteristics was also obtained. Figure B-6(a) & (b) show the steel jacketing schemes used for interior and exterior joints, respectively.

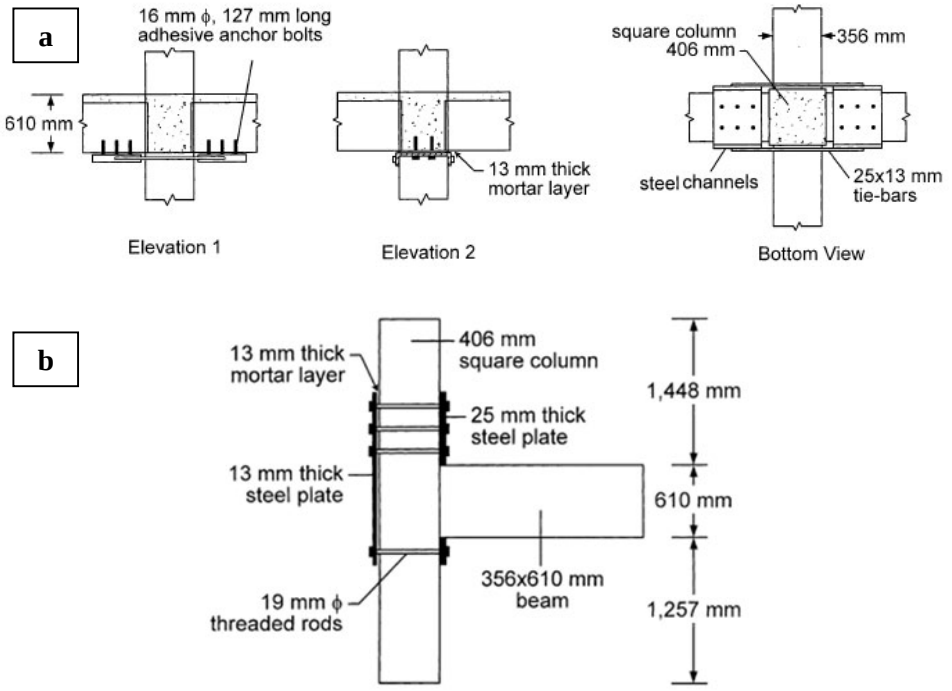

Figure B-6: Steel jacketing of a) interior and b) exterior joints (Engindeniz et al., 2005)

A strengthening system involving the use of external corrugated steel elements was developed by Ghobarah et al. (1997) and Biddah et al. (1997). Welding along with steel angles and anchors were used to assemble and fix the system on the tested specimens. The system was designed to upgrade the shear capacity of the connection and adjoining elements and to boost the initial performance. The test results showed that the strengthening system was effective in moving the damage away from the joint area to the beam hinging zone. However, it failed to prevented pullout failures in specimens with inadequate anchorages. Nevertheless, the system had improved the performance including strength and energy dissipation.

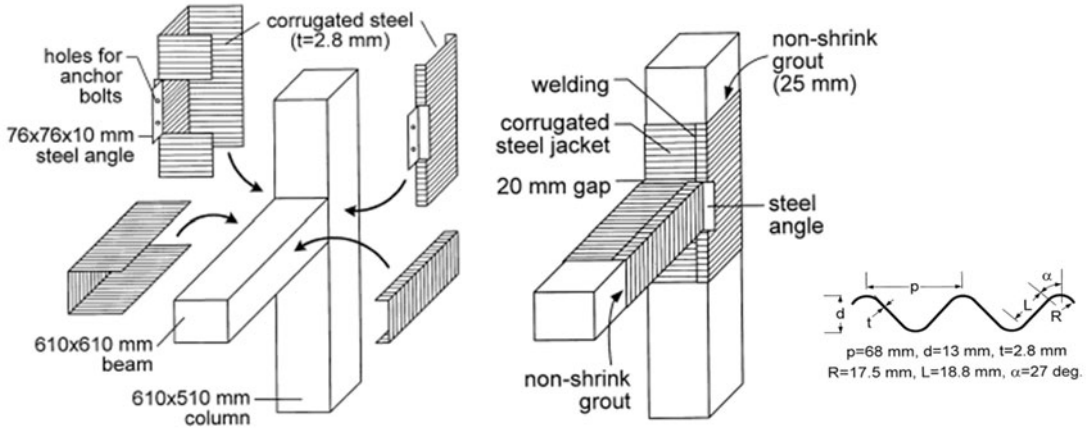

Figure B-7: corrugated steel system developed by Ghobarah et al. (1997) and Biddah et al. (1997)

Genesio et al. (2010) introduced a method to strengthen deficient joints using haunch type elements connected with post-installed anchors “Haunch Retrofit Solution”. The technique was

first proposed by Pampanin et al. (2006), see Figure B-8(c), and then development was followed by [Genesio and Akgüzel (2009), and Genesio and Sharma (2010)] using post-installed anchors, see Figure B-8(d). The development aimed to shift the brittle joint failure into plastic hinging in the beam.

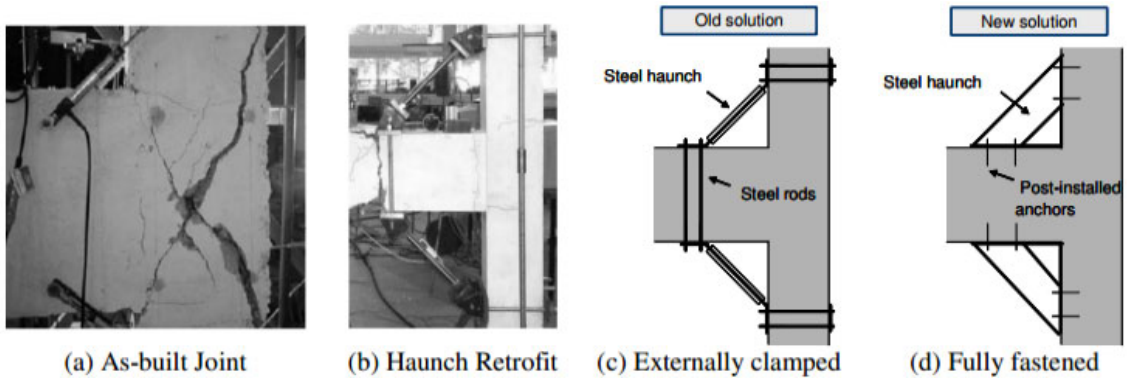

Figure B-8: Haunch Retrofit Solution of deficient joints (Genesio et al., 2010)

The results of one of the tests carried out by Genesio and Sharma (2010) are shown in Figure B-9. The technique was noted to enhance the flexural hinging of the beam with limited damage in the core. Also, an improvement in stiffness was observed. However, in some cases, the partial failure of the anchorage of the haunch limited the performance.

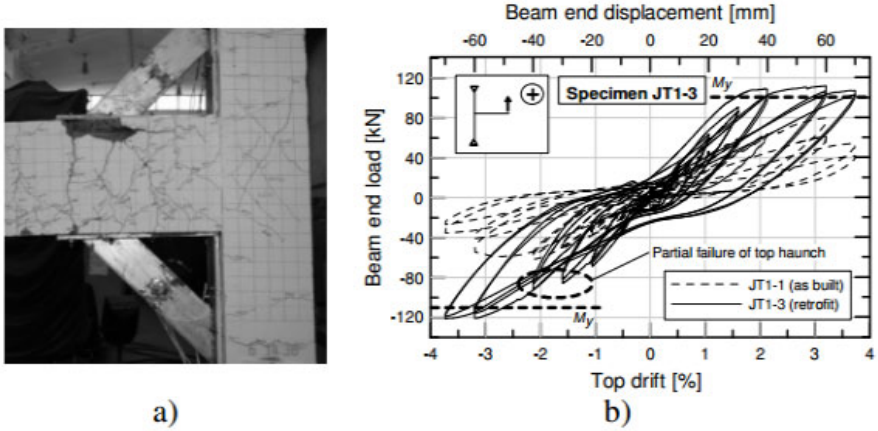

Figure B-9: a) Failure of a retrofitted specimen, and b) comparison of unconfined and strengthened joint. (Genesio and Sharma, 2010)

Sharma et al. (2010) indicated that the Haunch retrofit solution is an easy and practical solution with cheap cost. However, the solution needs some development to be suitable for strengthening damaged joints and to strengthen weak column-strong beam configurations.

Finally, as reported by Sharma et al. (2010), the Haunch Retrofit Solution is planned to be tested on a one-bay two-story frame.

B.5 FRP COMPOSITE APPLICATIONS

A test series including four full-scale and fifteen ¼ scale beam-column joints was carried out by Geng et al. (1998) to investigate the efficiency of CFRP sheets to upgrade the bond strength and ductility of the specimens. Two and four layers of CFRP sheets were used. For specimens with deficient anchorages, steel angles and rods were placed at joint corners to enhance bonding of the CFRP sheets to concrete. The test results demonstrated that strengthened specimens had obtained a substantial increase in ductility which accounted for 3 times that from the bare specimens. The increase in the moment capacity was found to be (24-35%) and 17% for the full and ¼ scale specimens, respectively. However, as can be seen from Figure B-10, the specimens tested by Geng et al. do not represent actual joints and thus different behaviour may be obtained.

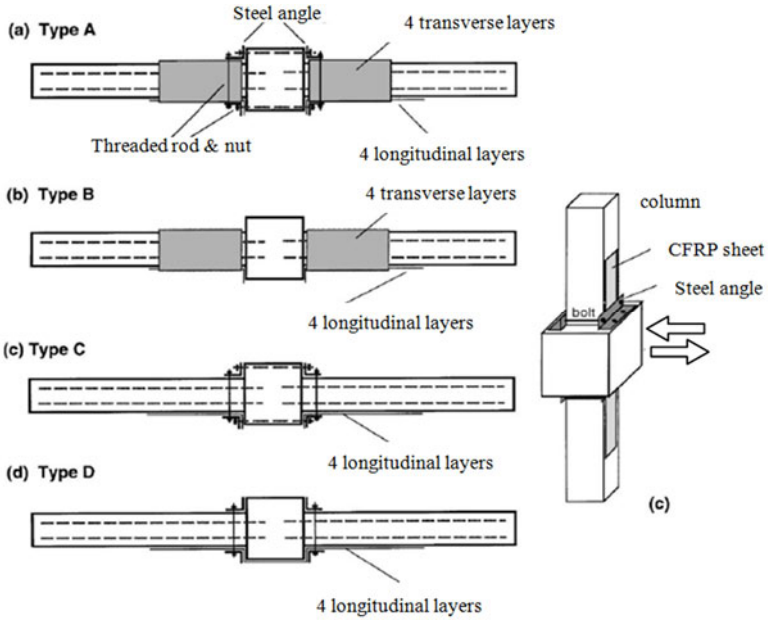

Figure B-10: CFRP retrofitted full-scale specimens tested by Geng et al. (1998)

Mosallam (2000) conducted six cycling testes on four ½ scale interior joints simulating those of a typical RC structure. Two of the joints were first tested until failure then repaired by means of epoxy injections and CFRP or GFRP laminates. The other two joints were upgraded by GFRP and CFRP laminated in the undamaged state. On the basis of the test results, a considerable enhancement in stiffness, strength and ductility was observed. In terms of ductility and strength, the enhancement was reached 42% and 53%, respectively. It was also indicated that CFRP specimens performed better than GFRP specimens in terms of strength. However, the use of GFRP was recommended when ductility is of concern. Figure B-11 shows an example of the final failure mode of a specimen repaired by GFRP.

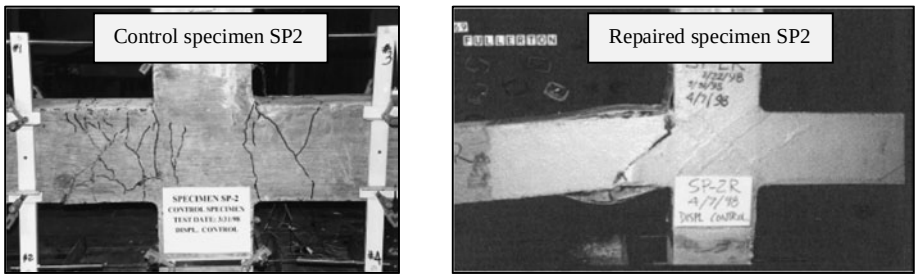

Figure B-11: Final failure mode of repaired specimen tested by Mosallam (2000)

Ghobarah and Said (2002) tested four weak column-strong beam exterior joints with no joint hoops. Two of the specimens were pre-damaged then repaired. Unidirectional and bidirectional GFRP sheets were used for strengthening. The GFRP applications on joints included unanchored or anchored U-shape sheets, diagonal sheets, and anchored U-shape sheets with column wrapping, as seen in Figure B-12(a). Steel plates and threaded bolts were used for the anchored sheets. The test results indicated that control specimens failed in joint shear mechanism. From the ductility point of view, the strengthened specimens showed considerable enhancement compared to the bare specimens. Specimen with unanchored sheets T4 failed prematurely due to joint failure and dissipated the least energy. The other specimens showed more ductile behaviour with beam hinging and superior energy dissipation. Figure B-12(b) shows final failure modes of a control specimens and one repaired and one strengthened specimens.

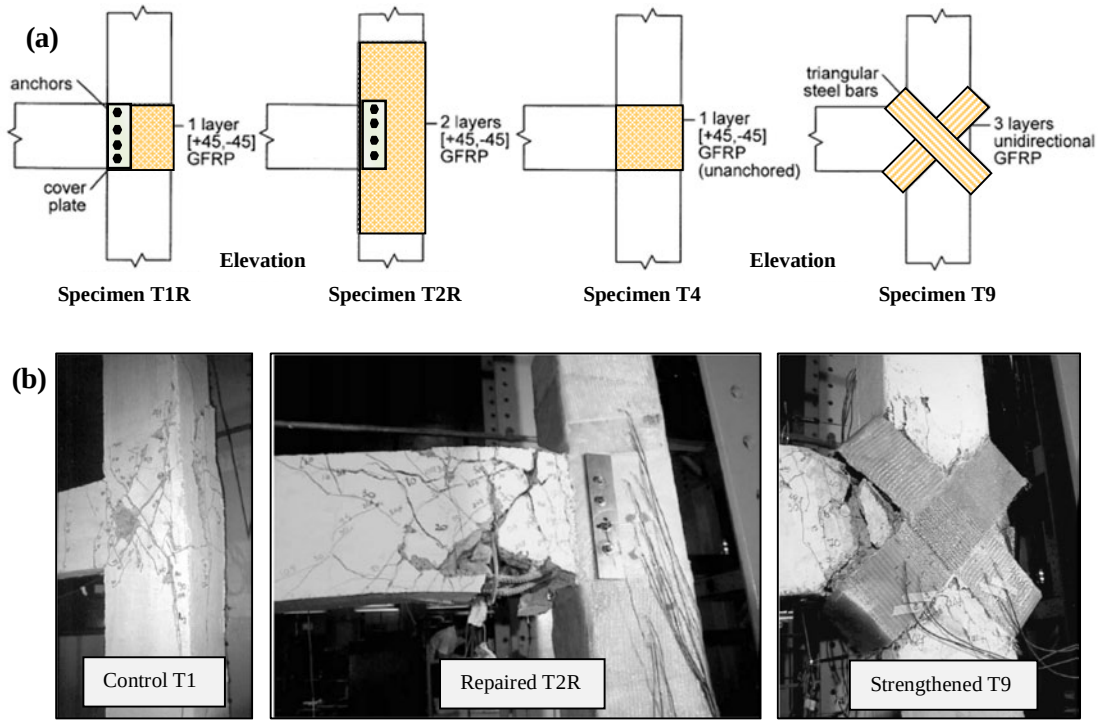

Figure B-12: a) Specimens tested (reproduced from Engindeniz et al. (2005)), and b) Final modes of failure (Ghobarah and Said, 2002)

An extensive test programme including 18 2/3-scaled exterior joints with no joint confinement was carried out by Antonopoulos and Triantafillou (2003). The efficiency of different FRP applications was investigated and various parameters were examined such as: a) the presence of reinforcement in the joint area, b) FRP ratio, c) anchorage conditions of FRP, d) strips versus sheets, e) GFRP and CFRP, f) axial load level, and g) the presence of transverse beams. Based on the test results, shear failure was prominent in all specimens and was accompanied by partial or complete debonding of FRP at mechanical anchor areas or near corners. It was concluded from the tests that: i) the use of FRP increases the strength and energy dissipation but this is not proportional to the increase in the number of FRP layers, ii) the presence of transverse reinforcement in the joint area reduces the efficiency of FRP, iii) the use of mechanical anchors enhances the performance by delaying debonding of FRP and it is a more effective system than just using anchors of lateral FRP strips, and iv) the axial load increases the effectiveness of FRP.

D'Ayala et al. (2003) conducted 16 cyclic tests on 12 interior joints with two geometrical configurations depending on whether the strong beam-weak column design is satisfied or not. CFRP laminates were used for repair and strengthening of the joints including orthogonal or diagonal configurations of FRP. Damage of the control specimens took place in the joint region and interfaces. In general, the strengthening/repair was found to be effective and the damage was shifted to the beam hinging zone for the strong beam-weak column specimens.

Prota et al. (2004) tested eleven under-designed interior joints having no transverse reinforcement in the joint, and designed in accordance with the weak column-strong beam concept. Different innovative combinations of FRP sheets and external FRP bars were used to upgrade the joints. Parameters investigated were the axial load level, and the type and amount of FRP reinforcement. As expected, control specimens failed due to concrete crushing of the column. The strengthening systems used had improved the strength and ductility. However, undesirable modes of failure including column failure and joint shearing could not be eliminated. Moreover, beam hinging was not achieved as intended.

Ghobarah and El-Amoury (2005) tested six substandard exterior joints. Three of the specimens had inadequate beam bottom bar anchorages; two of them were strengthened using CFRP laminates. The other three specimens had no transverse reinforcement within the joint panel and inadequate beam bottom bar anchorages; two of the specimens were strengthened using jackets of GFRP laminates and anchorage systems of steel rods or plates. From the test results it was shown that CFRP specimens with only anchorage deficiency failed either due to FRP debonding or beam hinging. FRP debonding occurred due to the absence of an appropriate anchoring system. The GFRP specimens, on the other hand, failed due to shear of the rehabilitated section or fracture of rehabilitating rods. Despite the undesirable failure of rehabilitating systems in specimens, joint shear failure was avoided and beam hinging was achieved.

Mukherjee and Joshi (2005) carried out two test series on 13 substandard interior joints. The first series had inadequate anchorages of beam bars into the joint panel, while the other series had proper anchorage detailing. No transverse reinforcement was provided into the joint panel. The parameters investigated covered i) different anchorages, ii) type and amount of FRP, and iii) different FRP strengthening schemes. The test results showed that failure modes occurred in a desirable manner due to flexural beam hinging and with the damage being concentrated at the beam interface with the column. In addition, all FRP upgrading systems were proven to be effective, and a considerable increase in the performance including higher yield loads, stiffness and energy dissipation capacities.

Al-Salloum and Almusallam (2007) performed six cyclic tests on four substandard interior joints. Two of the specimens were tested in the bare condition then repaired by epoxy injections and then rehabilitated. No joint hoops were provided in the test specimens to simulate pre-seismic code design or old construction practice. Two shear retrofitting schemes of CFRP were applied, some of which with and some without mechanical anchorages. The test results indicated that specimens without mechanical anchorages failed due to debonding of FRP followed by joint shear mechanism. On the other hand, in specimens with anchorages, flexural beam hinging was the predominant failure mode. Although shear failure occurred in some specimens, it is indicated that the failure was delayed substantially enough in order to achieve good performance in terms of shear resistance or ductility.

In the study performed by Tsonos (2008), six cyclic tests were carried out on four exterior joints having a slab and transverse stub beams. To simulate conditions similar to those of older GLD structures, no shear reinforcement was provided in the joint area. In addition, the amounts of lateral and longitudinal reinforcement in columns were less than seismic code recommendations. Two retrofit methods including CFRP or RC jacketing were investigated for pre-earthquake and post-earthquake cases. The test results showed that a) failure of the control specimens was due to premature shear mechanism in the joint area at early loading stages, b) the proposed upgrading schemes exhibited more ductile behaviour along with flexural hinging in the beam, and c) RC jacketing was more effective in the post-earthquake “rehabilitation” case whereas both the CFRP and RC jacketing performed equally in the pre-earthquake “strengthening” case.

Karayannis and Sirkelis (2008) presented results of an experimental investigation involving cyclic tests on 12 exterior joints. Some of the specimens were provided with transverse reinforcement in the joint area whereas some were not. The test specimens were either repaired and/or strengthened using combinations of epoxy resin injections and CFRP jacketing. With the exception of the control specimens that failed due to joint shearing, all repaired and strengthened specimens failed due to beam flexural hinging. Furthermore, in comparison to the

control specimens, the repaired/strengthened specimens exhibited higher load capacities, higher drifts and higher energy dissipation capabilities, less bond deterioration, and lower damage factors.

Pantelides et al. (2008) carried out an experimental programme including eight interior joints with pre 1970s detailing including beam anchorage deficiencies and no shear reinforcement in the joint area. Two types, I & II, of beam-column joints were tested depending on whether the strong beam-weak column concept is met or not, where type I had deeper beams. In addition, columns were designed with widely spaced ties and splices in accordance with old codes such as ACI Building Code Requirements for Reinforced Concrete 318-63 ACI (1963). Three types of CFRP composites were used to strengthen the tested specimens. On the basis of the experimental results, the main conclusions were: a) all control specimens ruptured due to diagonal shear mechanism in the core along with partial or complete anchorage failure of beam bottom bars, and failure occurred at a drift of 3%; b) in comparison to the control specimens, all strengthened specimens reached higher shear capacities (1.5 for type I&II), higher storey drifts (2.2 type I, 2.7 type II), higher elastic stiffness (1.3 type I, 1.6 type II), higher beam plastic rotations (1.5 type I, 1.1 type II), and higher energy dissipations (2.3 type I, 1.2 type II)

Sasmal (2009) tested six exterior joints designed according to either EC2 (2004), EC8 (EN 1998-1:2004) or IS 456 (2000). All joints had the same general and cross-sectional dimensions. The specimen design included two GLD specimens, two specimens with moderate seismic detailing, and two specimens with ductile seismic detailing. Tests of the control GLD and moderately ductile joints showed that brittle failure modes in the form of joint shear failure and anchorage failure of the beam bottom longitudinal bars are the expected failure modes for deficient joints. The tests also showed that joint shear reinforcement is needed not only to avoid joint shear failure but also to maintain concrete integrity in the anchorage zone and to avoid concrete wedging failure, so that the strength of the joint can be fully developed. The ductile specimens, on the other hand, were observed to fail with a ductile manner but the joint area had experienced severe damage. Two of the control specimens were repaired with replacement of crashed concrete, injections of resin epoxy and then the use of a steel plate in the core and FRP laminates for the column. The retrofitting strategies were found to be effective and able to restore the seismic performance to the original level. In the study, three specimens were also strengthened but with the aim to achieve highly ductile behaviour. Longitudinal and lateral CFRP and GFRP sheets were used to wrap the column, beam and joint area. In addition, a steel plate was fixed at the joint area using steel bolts. CFRP plate was also used in one of the specimens. The test results showed that the upgraded specimens obtained superior performance compared to the original specimens and their performance was comparable to the joints with high ductile detailing. Moreover, the damage of the upgraded specimens occurred outside the joint area. An example of a retrofitted specimens is given in Figure B-13.

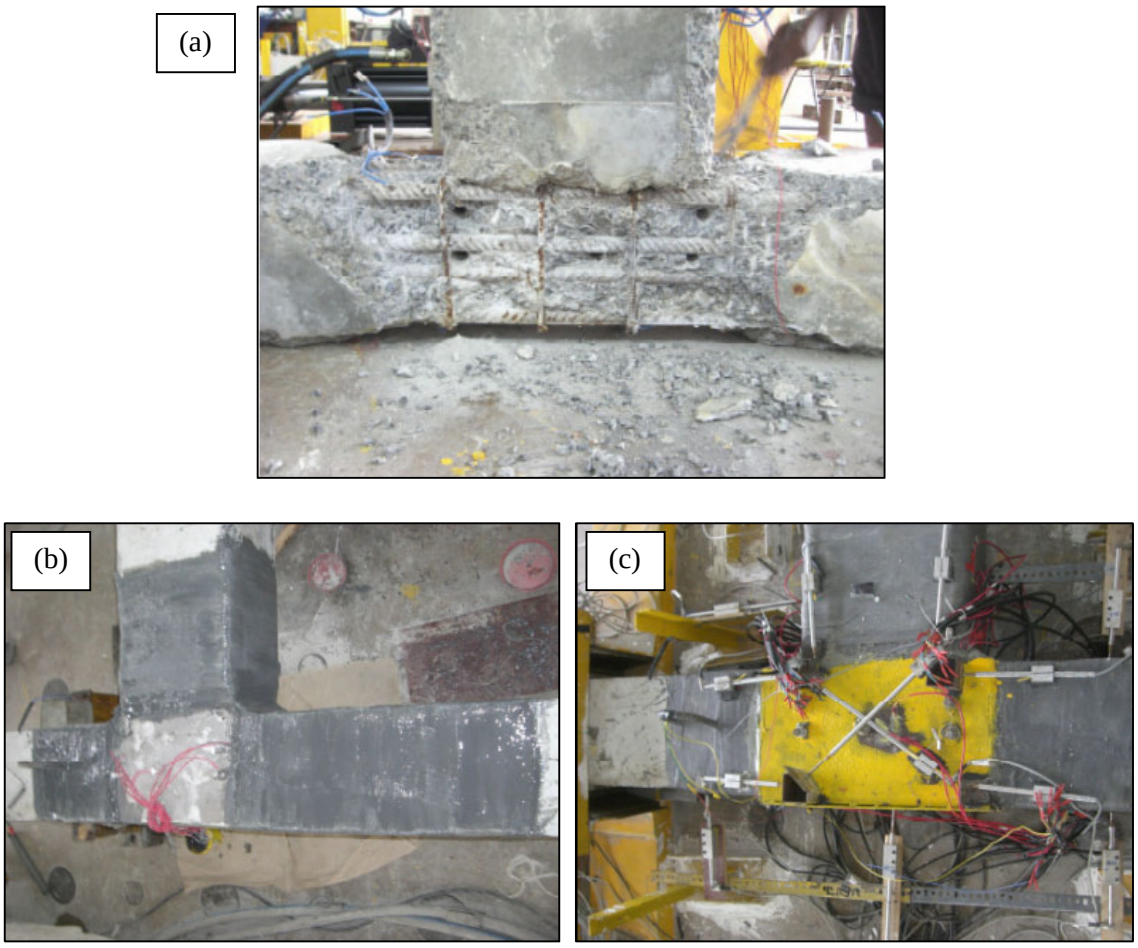

Figure B-13: a) Removal of damaged concrete and drilling for through bolts in SP-3R; b) Application of FRP on repaired surface, and c) application of steel plate on joint (Sasmal, 2009)

Ilki et al. (2011) retrofitted eight full-scale exterior beam-column joints constructed with low material qualities and plain bars. The specimens had no transverse reinforcement within the joint area. Six of the specimens were provided by segments of slabs and a lateral beam. The retrofitting schemes included using welding and repair mortar (1 specimen), FRP composites (1 specimen), and welding and repair mortar and FRP (4 specimens). Application details and strengthening schemes are shown in Figure B-14. Based on the test results, the following conclusions were made: a) the presence of welding along with the FRP was essential for the assemblies to reach their nominal strength; b) specimens retrofitted with welding only had reached their nominal strength and were able to sustain the maximum strength up to a drift of 4% where severely degraded response occurred; c) applying FRP to specimens with welding measures had postponed largely the degradation in the response until very high drifts were reached (about 9 to 10%).

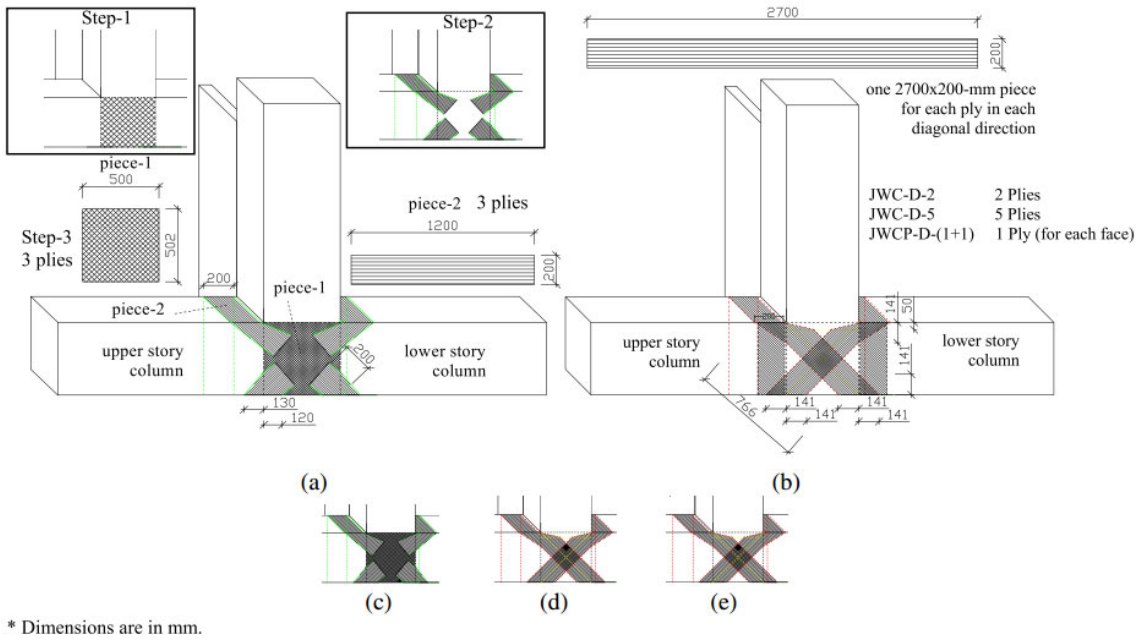

Figure B-14: (a) FRP application details of specimens JC-F-3 and JWC-F-3; (b) FRP application details of specimens JWC-D-2, JWC-D-5, and JWCP-D-(1+1); (c) specimens JC-F-3 and JWC-F-3; (d) specimens JWC-D-2 and JWC-D-5; (e) specimen JWC-D-P-(1+1) (Ilki et al., 2011)

Li and Pan (2011) used CFRP and GFRP laminates to rehabilitate four pre-damaged interior beam wide-column joints. Two innovative schemes were applied along with utilising FRP anchors to improve bonding of FRP sheets. The test results showed that general improvement in behaviour was obtained. However, the final failure was due to delaminating of FRP at anchor locations.

Appendix C

DEVELOPMENTS RELATING TO PTMS

In the following sections, developments relating to the PTMS technique are presented.

C.1 FRANGOU (1992, 1996)

The PTMS technique and its suitability as an effective strengthening methodology were first explored by [Frangou (1992), Frangou et al. (1993), Frangou and Pilakoutas (1994a)]. In this regard, an experimental work was carried out aiming mainly to assess the capacity and ductility of concrete members when they are confined externally by post-tensioned metal strips. A total of eighteen (100 *mm* diameter and 200 *mm* height) cylinders together with twenty-eight (100x100 mm^2 cross-section and 200 *mm* height) prisms were tested under increasing axial loads. Consequently, it was concluded that the use of design equations of EC8 (1988 as draft, later1993) for strength and strain enhancement due to confinement can lead to conservative predictions. The semi-empirical equation investigated is given by the following

$$f_{cc} = f_{co}(1 + 2.5\alpha\omega_w) \qquad \alpha\omega_W \leq 0.1 \qquad \text{(C-1)}$$

$$f_{cc} = f_{co}(1.125 + 1.25\alpha\omega_w) \qquad \alpha\omega_W > 0.1 \qquad \text{(C-2)}$$

where f_{co} is the unconfined concrete compressive strength, in MPa; f_{cc} is the increased compressive strength, in MPa; α is a reduction factor accounting for the effectiveness of confinement in plan and elevation; ω_w is the volumetric mechanical ratio of confinement reinforcement and can be given by the following expression

$$\omega_w = \frac{volume of\ stirrups}{volume of\ concrete\ surrounded\ by\ stirrups} \frac{f_{yh}(yield\ stress of\ stirrups)}{f_{co}} \quad \text{(C-3)}$$

Frangou (1996) thereafter extended the work on the technique with two main objectives. The first objective was to verify that the technique can be successfully applicable for larger scale RC members, whereas the second objective was to provide a suitable analytical tool and modelling capable of predicting the effects of intervention due to the technique. In light of the above, a total of 66 cylinders of 100 *mm* diameter and 200 *mm* height, and 18 prisms of 100 x 100 cross sectional area and 200 *mm* height were tested by Frangou (1996). Three different types of strips and clips were used in the confinement. The reliability of EC8 (1993) equations to predict enhancement in the concrete strength and strain were further examined in this work. The test results were additionally compared to three well-known concrete models, namely, Mander et al. (1988a&b), Ahmad and Shah (1982) and Fafitis and Shah (1985). As a result, it was found that the effect of confinement due to PTMS is better represented by EC8 equations with a reasonable margin.

Furthermore, based on the test results, two observations were made with regarding to the calculation of the ratio $\alpha\omega_\omega$. First, the calculation of the volumetric ratio $\alpha\omega_\omega$ should be based on the centre-to-centre spacing between strips instead of the total length, as illustrated in Figure C-1. Second, the yield stress in strips at failure may not be attained because of potential slip failure at the clip. Hence, suitable clips should be used.

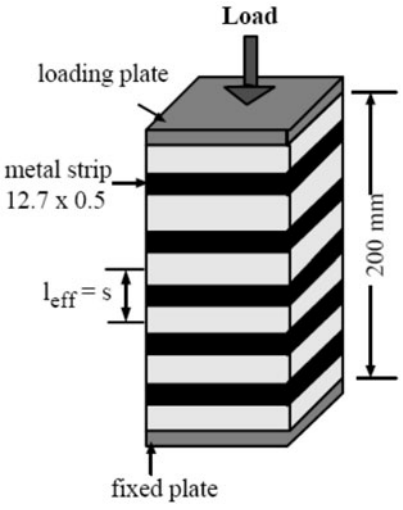

Figure C-1: The effective length and total length approaches used to calculate the $\alpha\omega_\omega$ ratio

The PTMS technique was also investigated in terms of the effect of creep on the metal joint. Three cylinders of 100 mm diameter and 200 mm height were externally confined by PTMS and maintained under a constant axial pressure for two years, (Frangou, 1992, 1996). Based on the test results, it was demonstrated that there was no reduction in the pre-tensioning stress applied initially on specimens.

Ten over-reinforced medium RC beams (see Figure C-2) confined by PTMS technique and tested in bending were carried out, in the Light Structures Laboratory of Sheffield University, by Frangou (1996). The main objective was to examine the potential enhancement in the load carrying capacity and ductility in the beams. In comparison to the associated unconfined specimens, it was demonstrated that a considerable improvement in the maximum load capacity and the corresponding deflections was obtained in all cases. Moreover, it was noted that most of the confined specimens reached yielding in the reinforcement, while it was absent in the unconfined state. Comparison of the experimental results to analytical predictions from section analysis programme and by adopting the EC8 concrete confined model showed that a good correlation can be obtained with maximum difference of about 16%.

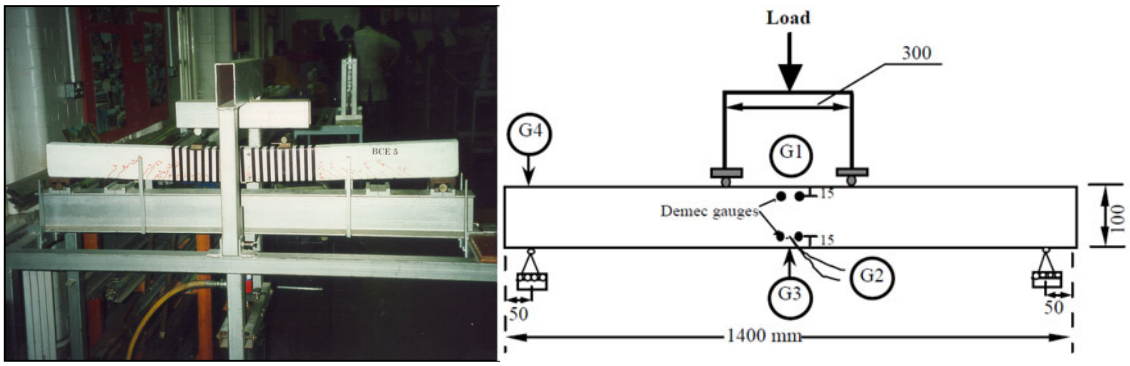

Figure C-2: Medium scale beam (Frangou, 1996)

Further work was conducted by Frangou (1996) including a total of seventeen (250 x 150 *mm* rectangular cross-section) medium scale beams in bending. The objective of this part of the work was to explore the efficiency of using the technique on larger scale beams reinforced by different materials and failed due to undesirable types of failure i.e. shear and debonding. Based on the test results, the use of the technique was successful to eliminate the premature failures and high ductility levels were achieved. Some successful applications using the PTMS technique on medium scale beams are given in the following paragraphs:

- **CASE 1**: the PTMS technique was used to rehabilitae a RC beam failed abruptly due to peeling of the concrete cover at one of the ends of the CFRP plate. The spalled-off conrete was replaced with a better quality mortar and the FRP plate was reglued to the bottom surface of the beam. In addition, two steel angles were mounted on the bottom corners of the repaired side of the beam. After that, post tensioed metal strips spacing at 50.8 mm were

applied along the angles and confining the cross-section (see Figure C-3). After the test, the beam load resistance of the strengthened beam increased by 20%, whereas the deflection capacity increased by 30% compared to the unstrengthened case.

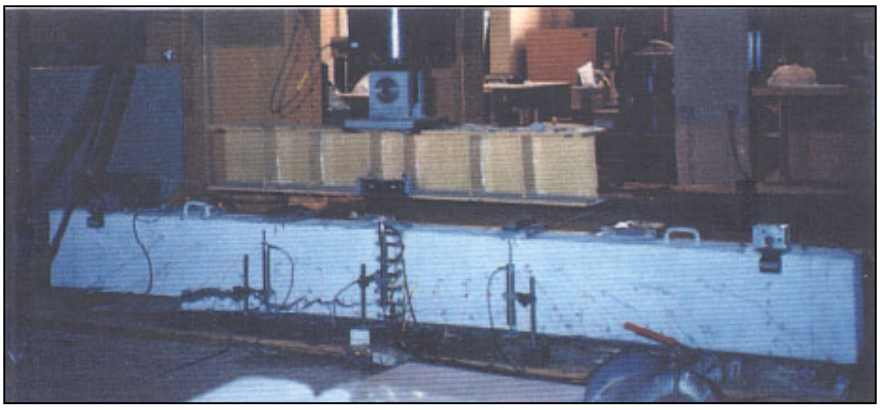

Before repairing

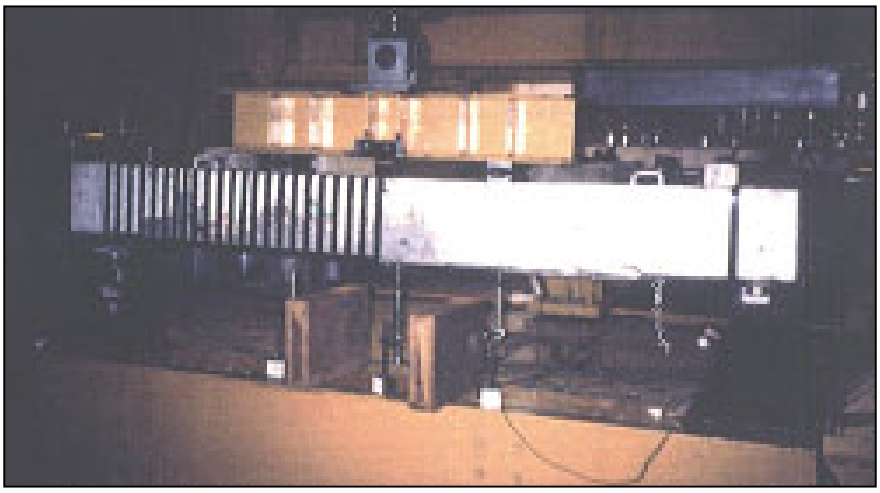

After repairing

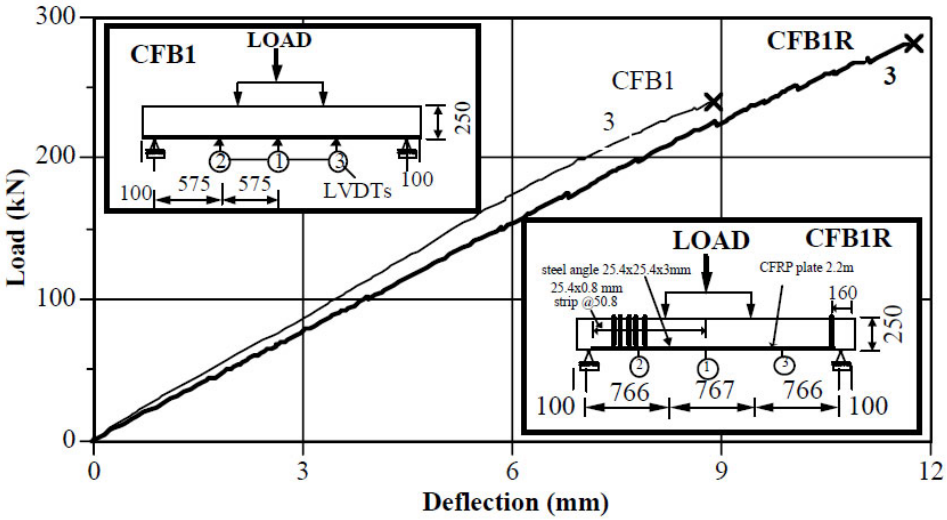

Figure C-3: Rehabilitation of a RC beam failed due to debonding of FRP plate (Frangou, 1996)

- **CASE 2:** the PTMS was used to stregthen a concrete beam reinforced by two GFRP bars as a flexural reinforcement. The beam failed in a brittle explosive manner due to concrete cruching at the middle region. In the rehabilitation process, the damaged concrete was replaced by a strong mortar. Two steel plates were bolted along the mid depth on each side of the beam. High elongation strips were tensioned between the plates and secured by means of double-notch clips reacting against the metal plates. Metal strips spacing at 100 mm were also provided along the shear span of the beam. After the test, the load capacity increased by 35%. The failure was due to rapture of GFRP bars before any significant crashing of the concrete. The behaviour was noted to be more ductile in comparison to the original beam.

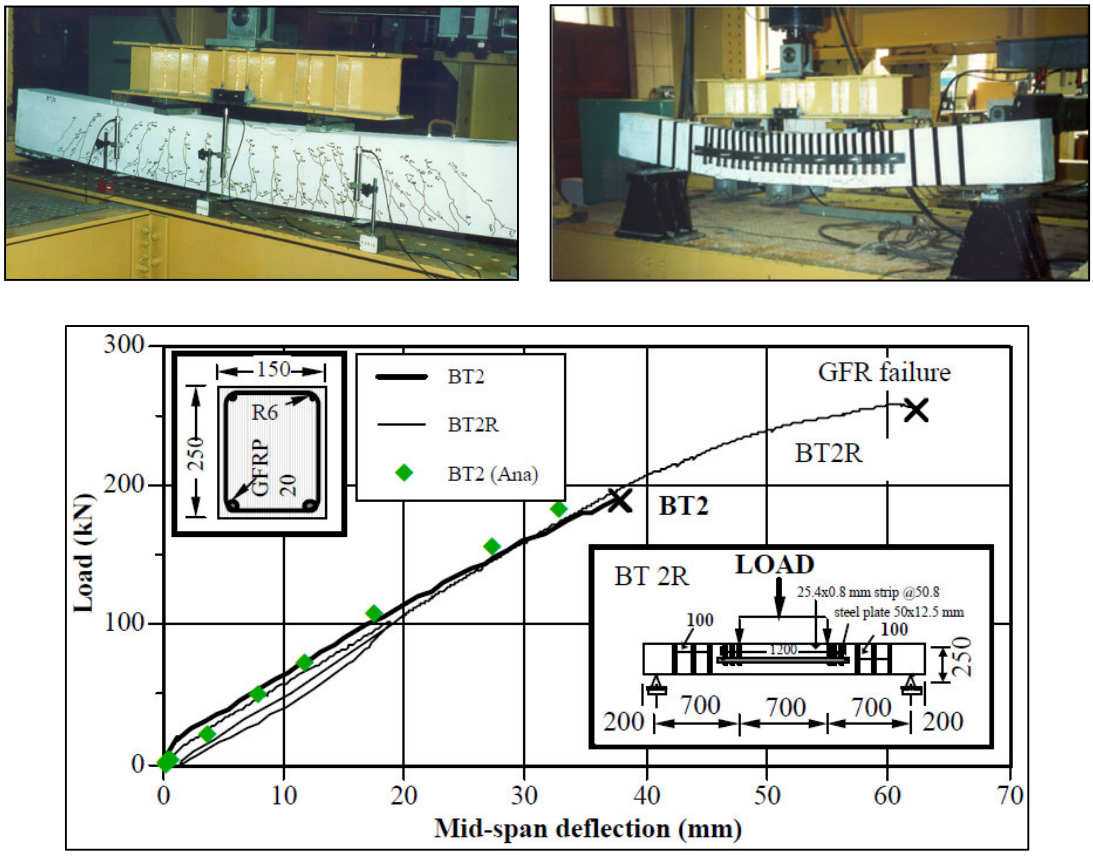

Figure C-4: Rehabilitation of a RC beam failed due to concrete crushing (Frangou, 1996)

- **CASE 3:** The PTMS technique was used to strengthen a RC beam reinforced by two 20mm GFRP bars. The original beam failed due to concrete crushing at the mid-span in a very brittle manner. The beam was rehabilitated twice using post tensioned metal strips along the flexural region. Before strengthening, the crushed concrete was removed and a new fresh concrete was cast (see Figure C-5). The first strengthening method included using PTMS directly on the repaired beam section. While in the second method, two steel angles were fixed on the compression side of the beam and the PTMS were tensioned around them. The test results showed that load capacity improved by 20% and the failure was more ductile. The second method resulted in failure of the GFRP bars due to the presense of the steel

angles in the compression zone. Figure C-6 presents the rsults of the overreinforced specimen, the rehabilition process and the two strengthening methodologies.

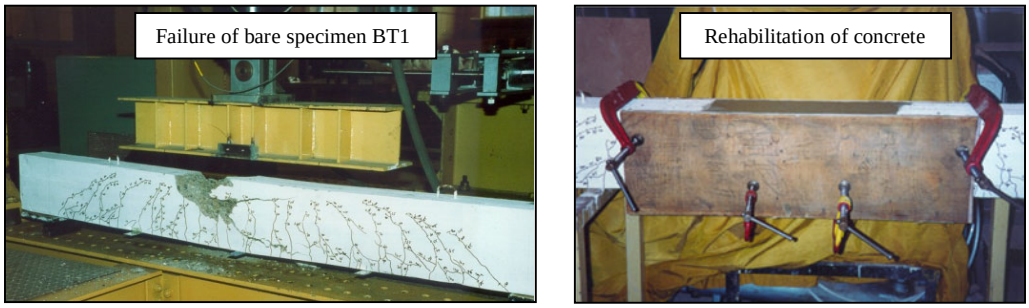

Figure C-5: Failure of specimen BT1 (left) and repair method (right), (Frangou, 1996)

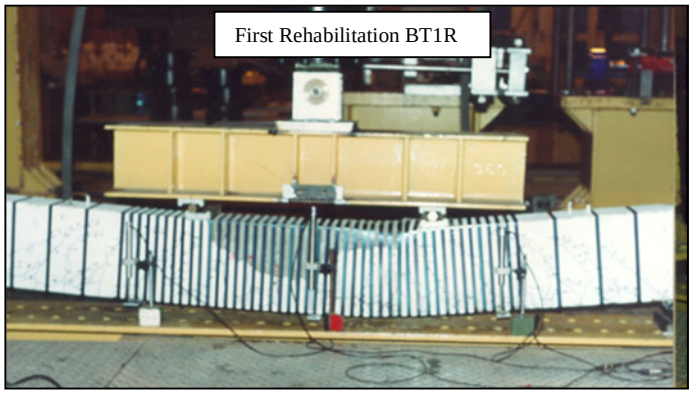

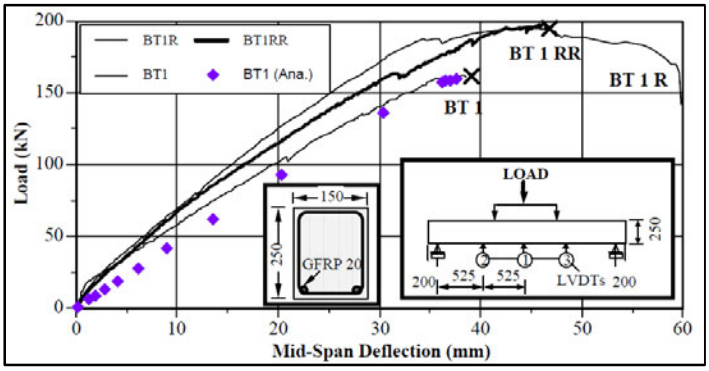

Figure C-6: Using of PTMS to strengthen the over reinforced beam BT1 (Frangou, 1996)

C.2 GUNJA (2005)

In an effort to carry on with the work done by Frangou (1996), a total of twelve 100 *mm* diameter and 200 *mm* height cylindrical specimens were tested by Gunja (2005). Eight of the tested specimens were subjected to monotonic loading, while cyclic loading was applied to the rest. Despite the premature failure experienced in test results due to brittleness of the strip material used, good enhancement in concrete compressive strength and ductility was achieved in comparison with those of unconfined specimens. Furthermore, the increase in peak strength of some specimens, confined with full PTMS jacket, accounted for 2.15 times the unconfined value. The test results were compared to predictions of the models used by Frangou (1996). As a result, it was concluded that the CEB-FIP Model (1990) (same as old EC8) yields a safe prediction to the increase in compressive strength for the specimens externally confined by PTMS.

C.3 MOGHADDAM ET AL. (2007-2010)

A comprehensive experimental programme was conducted by Moghaddam et al. (2007). Seventy two cylinders and prisms (see Figure C-7) were tested under increasing monotonic loading until failure. The novelty of the work was the effort made to quantify the measured increase in concrete strength and corresponding ductility due to the intervention by PTMS technique. Several parameters were examined including concrete strength (10-50MPa), number of layers (single and double), spacing, volumetric ratio, sectional shape of specimens and strip ductility. Another important parameter examined in the study was the application of PTMS in passive and active state to the specimens. In doing so, some of the tested specimens were strengthened by single and double layers of PTMS stressed up to 5% of the yield stress, while it reached 31% in the strips of the actively confined specimens.

Figure C-7: Cylinders and prisms (Moghaddam et al., 2007)

The test results showed that better improvement in strength and ductility is achieved for cylindrical specimens compared to the prismatic ones. Active confinement increased the

strength of confined concrete by up to 25% higher than that due to passive confinement. Furthermore, the onset of degradation in the passive state tended to start earlier. Specimens with double layers of metal strips in general resulted in higher enhancement in concrete strength and ductility than those with a single layer. A strong relationship is found between the effective mechanical volumetric ratio $\alpha\omega_\omega$ of confining strips and the strength as well as ductility of confined specimens. Prismatic specimens with rounded corners were more effectively confined in comparison to specimens with chamfered corners or sharp edges. Specimens with higher strength concrete showed poorer post-peak behaviour.

Moghaddam et al. (2010) proposed an experimentally-based model to predict the enhancement in concrete compressive stress and corresponding strain. Figure C-8 shows a schematic of the stress-strain curves for the passive and active confinement states. The proposed model accounts for different parameters including shape of cross section, strength of plain unconfined concrete, volumetric ratio, yield strength and ultimate strain of confining strips. The model is characterised by three key points, namely, the critical point, yield point and ultimate point. The critical point represents the stiff response until major cracks in the concrete initiate. The yield point represents the start of significant irreversible dilation in concrete (due to the combined effect of cracks and plasticity) which is believed to be the reason for the activation of external confinement. After this stage, the response is represented by a linear relationship with a slope strongly dependant on the confinement level. The end of this line is defined as the ultimate point. The expressions which define the three points of the proposed model are given below

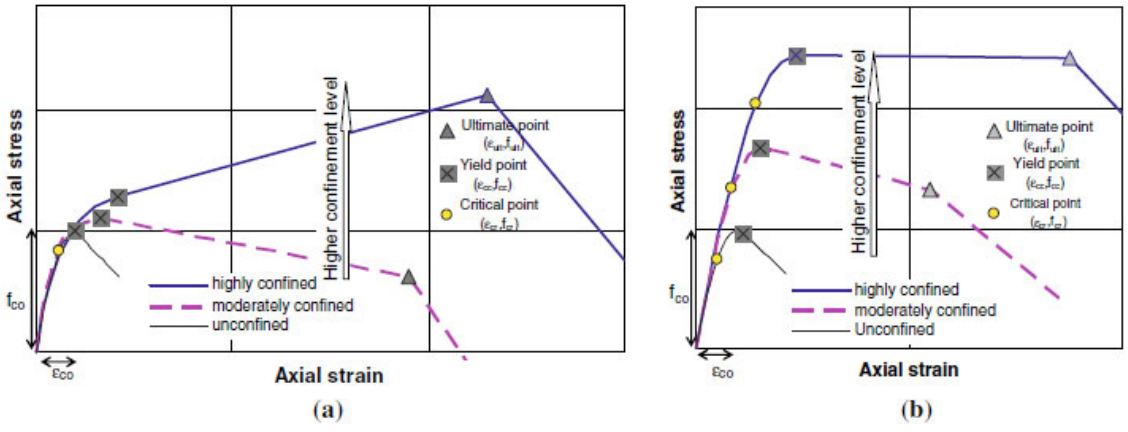

Figure C-8: Idealised stress–strain curves of concrete specimens with a) passive and b) active PTMS confinement (Moghaddam et al., 2010)

Key points of the curve are:

- Critical point

$$f_{cr} = 0.85 f_{cc} \quad \text{(C-4)}$$

$$\varepsilon_{cr} = 3.1 \times 10^{-4} \frac{f_{cr}}{\sqrt{f_{co}}} \quad \text{(C-5)}$$

- Yield point

$$\frac{f_{cc}}{f_{co}} = 1 + 8\frac{f_{1e}}{f_{co}} - 4\left(\frac{f_{1e}}{f_{co}}\right)^{1.2} \quad \text{(C-6)}$$

$$\varepsilon_{cc} = \varepsilon_{co}\left(\frac{f_{cc}}{f_{co}}\right)^{1.1} \quad \text{(C-7)}$$

- Ultimate point

$$\varepsilon_{ult} = 0.003e^{\left(160\frac{f_{1e}}{f_{co}}\varepsilon*_{ult}\right)} + 1.3\frac{f_{1e}}{f_{co}}\varepsilon^*_{ult} \quad \text{(C-8)}$$

$$\alpha = -62300\left(\frac{f_{1e}}{f_{co}}\right)^2 + 31150\frac{f_{1e}}{f_{co}} - 3900 \quad \text{(C-9)}$$

where f_{cc} and f_{co} are the strengths of confined and plain concrete, respectively; f_{le} is the confinement induced effective lateral pressure at the point of peak stress of confined concrete; ε_{cc} is the enhanced compressive strain at the yield point; ε^*_{ult} is the strip ultimate tensile strain; α is the post yield slope.

The pre-yield branch of the curve can be reasonably approximated by a second order polynomial given by the following expression

$$\sigma_c = \frac{f_{cc} - f_{cr}\frac{\varepsilon_{cc}}{\varepsilon_{cr}}}{\varepsilon_{cc}^2 - \varepsilon_{cc}.\varepsilon_{cr}}\varepsilon_c^2 + \frac{1}{\varepsilon_{cr}} \times \left[f_{cr} - \left(\frac{\varepsilon_{cr}}{\varepsilon_{cc}}\right)^2 \frac{f_{cc} - f_{cr}\frac{\varepsilon_{cc}}{\varepsilon_{cr}}}{1 - \frac{\varepsilon_{cr}}{\varepsilon_{cc}}}\right]\varepsilon_c \quad \text{(C-10)}$$

in which σ_c and ε_c are the stress and corresponding strain of the curve.

The model was compared to some of the available confinement models and showed good capability in predicting the compressive stress–strain curve of tested strapped concrete specimens. The proposed σ-ε model was also implemented in a nonlinear FE plasticity model of prismatic and cylindrical specimens with different levels of confinement. The FE results showed that the model is capable of capturing the experimental response reasonably well.

Appendix D

MATERIAL TESTING

D.1 COMPRESSION TESTS - CONCRETE

D.1.1 Beams: SC10-D12-WD, Ctrl, S, and PTMS1, in addition to the joint JA-1

Table D-1: Results of the compression tests on concrete cubes 100×100×100

Specimen	Weight (kg)	Load at failure (kN)	Compressive strength (MPa)
1	2.22	327.2	32.7
2	2.23	291.6	29.2
3	2.26	322	32.2
4	2.23	322.7	32.3
5	2.22	317	31.7
6	2.24	316.8	31.7
7	2.25	325.3	32.5
8	2.2	303.9	30.4
9	2.23	291.2	29.1
10	2.23	303	30.3
11	2.22	305.5	30.6
12	2.19	314.8	31.5
	Average		31.2
	Standard Deviation		**1.2**

Table D-2: Results of the compression tests on concrete cylinders (100 diameter×300 height)

Specimen	diameter	height	weight	Load	f'_c
	mm	*mm*	kg	kN	MPa
1	150	300	12.15	440	24.9
2	150	300	12.14	358	20.3
3	150	300	12.09	401	22.7
4	150	300	12.04	389	22.0
		Average			**22.5**
		Standard Deviation			**1.67**

D.1.2 Beam SC10-D12-PTMS2 in addition to beams of Group I and II

Table D-3: Results of the compression tests on concrete cylinders (100 diameter×300 height)

Specimen	diameter	height	weight	Load	f'_c
	mm	*mm*	kg	kN	MPa
1	152	300	12.254	656.6	37.2
2	150	297	11.848	665.8	37.7
3	152	300	12.292	686.5	38.9
4	150	300		621.5	35.2
5	150	300		667.1	37.7
6	150	300		672.2	38.0
7	150	300		682	39.0
8	150	300		659.6	37.3
9	150	300		672.8	38.1
10	150	300		646.5	36.6
11	150	300		657.9	37.2
12	150	300		649.4	36.7
13	150	300		610.7	34.6
14	150	300		684.3	38.7
15	150	300		628.5	35.6
		Average			**37.2**
		Standard Deviation			1.28

D.1.3 Medium scale beams

D.1.3.1 Group I: LC10-D12 and Joints JB-1, JB-2 and JC-1

Table D-4: Results of the compression tests on concrete cylinders

Specimen	diameter	height	weight	Load	f'_c
	mm	*mm*	g	kN	MPa
1	152	305	12371	507.4	28.71
2	153	305	12375	483	27.33
3	153	304	12451	502	28.46
4	150	296	11786	489.5	27.70
5	152	301	12276	519.8	29.41
6	151	302	12352	533.3	30.18
		Average			**28.6**
		Standard Deviation			0.97

D.1.3.2 Group II: LC20-D12

Table D-5: Results of the compression tests on concrete cylinders

Specimen	diameter	height	weight	Load	f'_c
	mm	*mm*	g	kN	MPa
1	150	300	12153	470	26.6
2	152	300	12135	426.8	24.15
3	152	302	12087	448.2	25.36
4	151	298	12040	448.0	25.35
5	150	300	12142	428.6	24.25
6	149	294	11.537	421.1	23.83
		Average			**25**
		Standard Deviation			0.95

D.1.3.3 Group III: LC27-D16 & Joints JB-1, JB-2, JC-1

Table D-6: Results of the compression tests on concrete cylinders

Specimen	diameter	height	weight	Load	f'_c
	mm	*mm*	g	kN	MPa
1	152	300	12125	453.3	25.65
2	153	300	12145	490	28.18
3	153	300	12229	487.2	27.57
4	150	291	11416	451.3	25.50
5	152	294	12896	455.7	25.79
6	152	298	12039	461.6	26.12
		Average			**26.5**
		Standard Deviation			1.03

D.1.4 Joint JA-2, JA-3 and JC-2

Table D-7: Results of the compression tests on concrete cylinders

Specimen	diameter	height	weight	Load	f'_c
	mm	*mm*	g	kN	MPa
1	152	295	12312	566.1	32.04
2	151	298	12317	561.4	31.77
3	151	298	12286	496.6	28.10
4	150	296	12340	581.2	32.89
5	152	301	12341	596.7	32.88
6	151	302	11684	574.4	32.08
7	152	301	12385	569.1	31.36
8	152	302	12386	556.6	30.67
9	150	295	11849	548.9	31.06
		Average			**31.4**
		Standard Deviation			1.37

D.1.5 Joint JA-3PTMS (The core)

Table D-8: Results of the compression tests on concrete cylinders

Specimen	diameter	height	weight	Load	f'_c
	mm	*mm*	g	kN	MPa
1	150	301	12822	718.5	40.7
2	150	302	12917	729.8	41.3
3	150	301	12407	620.9	35.1
4	151	300	12959	710.8	40.2
		Average			**39.3**
		Standard Deviation			2.45

D.1.6 Joint JB-1PTMS (The core)

Table D-9: Results of the compression tests on concrete cylinders

Specimen	diameter	Height	Load	f'_c
	mm	*mm*	kN	MPa
1	150 × 300		991.2	56.1
2			982.3	55.6
3			1003.5	56.8
		Average		**56.2**
		Standard Deviation		0.49

Table D-10: Results of the compression tests on concrete cubes

Specimen	Section	Height	Load	f'_c
	mm	*mm*	kN	MPa
1	100 × 100 × 100		577.7	57.77
2			587.1	58.71
3			568.2	56.82
	Average			**57.8**
	Standard Deviation			0.77

D.1.7 JC-1PTMS (The core)

Table D-11: Results of the compression tests on concrete cylinders

Specimen	diameter	height	weight	Load	f'_c
	mm	*mm*	g	kN	MPa
1	150	303	12809	1023.3	57.9
2	150	303	12818	1008	57.09
3	150	298	12234	992.1	56.14
	Average				**57.0**
	Standard Deviation				0.72

Table D-12: Results of the compression tests on concrete cubes – age = 3days

Specimen	Cross Section	height	weight	Load	f'_c
	mm × *mm*	*mm*	g	kN	MPa
1	100 × 100	100	2305	402.8	40.28
2	100 × 100	100	2317	414.5	41.44
	Average				**41**
	Standard Deviation				0.58

D.2 SPLITTING TESTS - CONCRETE

D.2.1 Beams: SC-D12-WD, Ctrl, S, and PTMS1, in addition to the joint JA-1

Table D-13: Results of the splitting tests on concrete cylinders

Specimen	diameter	height	Load	f_t
	mm	*mm*	kN	MPa
1	150	300	202.6	2.87
2	150	300	185.5	2.62
3	150	300	182.3	2.58
4	150	300	171.9	2.43
	Average			**2.63**
	Standard Deviation			0.16

D.2.2 I.2.2 Beam SC-D12-PTMS2 in addition to beams of group I and II

Table D-14: Results of the splitting tests on concrete cylinders

Specimen	diameter	height	Load	f_t
	mm	*mm*	kN	MPa
1	100	200	96	3.06
2	100	200	92.8	2.95
3	100	200	81.2	2.58
4	100	200	77	2.45
5	100	200	92.9	2.96
6	100	200	88.3	2.81
7	100	200	89.9	2.86
	Average			**2.81**
	Standard Deviation			0.20

D.2.3 Medium scale beams

D.2.3.1 Group I: LC10-D12 and Joints JB-1, JB-2 and JC-1

Table D-15: Results of the splitting tests on concrete cylinders

Specimen	diameter	height	Load	f_t
	mm	*mm*	kN	MPa
1	101	204	80	2.47
2	100	201	79.7	2.52
3	100	202	76.3	2.40
4	100	200	69.7	2.22
5	100	200	69.1	2.20
6	100	200	90	2.86
	Average			**2.45**
	Standard Deviation			0.22

D.2.3.2 Group II: LC20-D12

Table D-16: Results of the splitting tests on concrete cylinders

Specimen	diameter	height	Load	f_t
	mm	*mm*	kN	MPa
1	101	203	64	1.99
2	102	203	73.9	2.27
3	101	202	67	2.09
4	102	203	75.7	2.33
5	100	200	70.2	2.23
6	100	200	71.8	2.29
	Average			**2.20**
	Standard Deviation			0.12

D.2.3.3 Group III: LC27-D16 & Joints JB-1, JB-2, JC-1

Table D-17: Results of the splitting tests on concrete cylinders

Specimen	**diameter**	**height**	**Load**	f_t
	mm	*mm*	kN	MPa
1	100	202	75.2	2.37
2	100	200	42.5	1.35
3	101	204	73.9	2.28
4	101	201	80.1	2.51
5	102	202	70	2.16
6	100	201	81.9	2.59
	Average			**2.21**
	Standard Deviation			0.41

D.2.4 Joints JA-2, JA-3 and JC-2

Table D-18: Results of the splitting tests on concrete cylinders

Specimen	**diameter**	**height**	**Load**	f_t
	mm	*mm*	kN	MPa
1	100	200	80.2	2.55
2	100	200	74	2.36
3	100	200	72.2	2.30
	Average			2.40
	Standard Deviation			**0.11**

D.2.5 Joint JA-3PTMS (The core)

Table D-19: Results of the splitting tests on concrete cylinders

Specimen	**diameter**	**height**	**weight**	**Load**	f_t
	mm	*mm*	g	kN	MPa
1	100	200	3836	135.5	4.31
2	100	200	3680	117.9	3.75
3	100	200	3673	105.7	3.36
4	100	200	3642	116.9	3.72
	Average				**3.8**
	Standard Deviation				0.34

D.2.6 Joint JB-1PTMS (The core)

Table D-20: Results of the splitting tests on concrete cylinders

Specimen	diameter	Height	Load	f_t
	mm	*mm*	kN	MPa
1	100	200	109.8	3.50
2	100	200	120.8	3.85
3	100	200	103.9	3.31
4	100	200	92	2.93
		Average		**3.4**
		Standard Deviation		0.33

D.2.7 Joint JC-1PTMS (The core)

Table D-21: Results of the splitting tests on concrete cylinders

Specimen	diameter	height	f_t	Load	f_t
	mm	*mm*	Exp	kN	MPa
1	100	200	5.52	110.3	3.51
2	100	200	6.24	124.8	3.97
3	100	200	5.28	105.7	3.36
			Average		**3.6**
			Standard Deviation		0.26

D.3 FLEXURAL TESTS ON CONCRETE BEAMS

D.3.1 Beam SC-D12-PTMS2 in addition to beams of group I (SC20-D12) and II (SC27-D16)

Table D-22: Results of the flexural tests on concrete prisms

Specimen	b x b	Length	Load P	f_t
	mm	*mm*	kN	MPa
1	100	300	16	4.80
2	100	300	16.9	5.07
3	100	300	16	4.80
4	100	300	16.9	5.07
5	100	300	15.4	4.62
6	100	300	15.4	4.62
	Average			**4.83**
	Standard Deviation			0.18

D.3.2 Medium scale beams

D.3.2.1 Group I: LC10-D12 and joints JB-1, JB-2 and JC-1

Table D-23: Results of the flexural tests on concrete prisms

Specimen	b x b	Length	Load P	f_t
	mm	*mm*	kN	MPa
1	100	300	11.2	3.36
2	100	300	11.6	3.48
3	100	300	12.3	3.69
	Average			**3.51**
	Standard Deviation			0.14

D.3.2.2 Group II: LC20-D12

Table D-24: Results of the flexural tests on concrete prisms

Specimen	b x b	Length	Load P	f_t
	mm	*mm*	kN	MPa
1	100	300	11.6	3.48
2	100	300	11.9	3.57
3	100	300	11.9	3.57
	Average			**3.54**
	Standard Deviation			0.04

D.3.2.3 Group III: LC27-D16

Table D-25: Results of the flexural tests on concrete prisms

Specimen	b x b	Length	Load P	f_t
	mm	*mm*	kN	MPa
1	100	300	12.3	3.69
2	100	300	11.7	3.51
3	100	300	12	3.60
	Average			**3.60**
	Standard Deviation			0.07

D.3.3 Joints JA-2, JA-3 and JC-2

Table D-26: Results of the flexural tests on concrete prisms

Specimen	b x b	Length	Load P	f_t
	mm	*mm*	kN	MPa
1	100	500	11.1	5.55
2	100	500	12.1	6.05
3	100	500	11.6	5.80
	Average			**5.80**
	Standard Deviation			0.20

The specifications of the mix were: 10 mm maximum aggregate size, cement type CIIIA with an average slump of 50mm and a water cement ratio of 0.8.

D.4 STEEL MATERIAL – MEDIUM SCALE BEAMS AND JOINTS

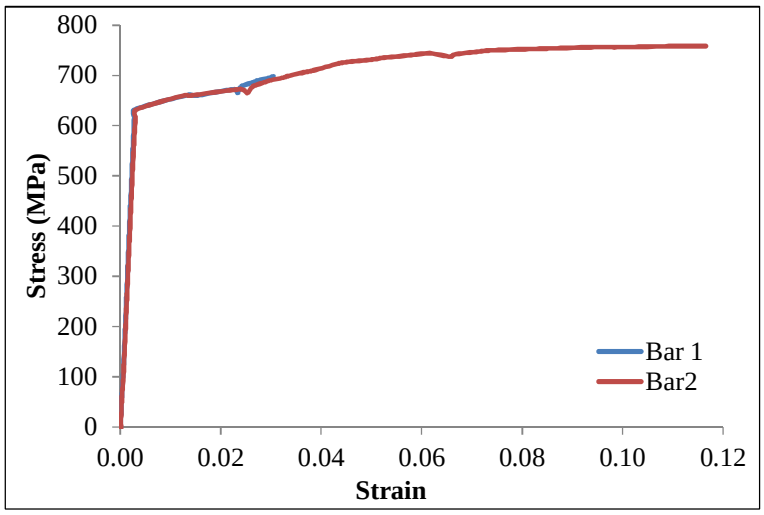

Figure D-1: Stress-strain curve of bar diameters 8 *mm*

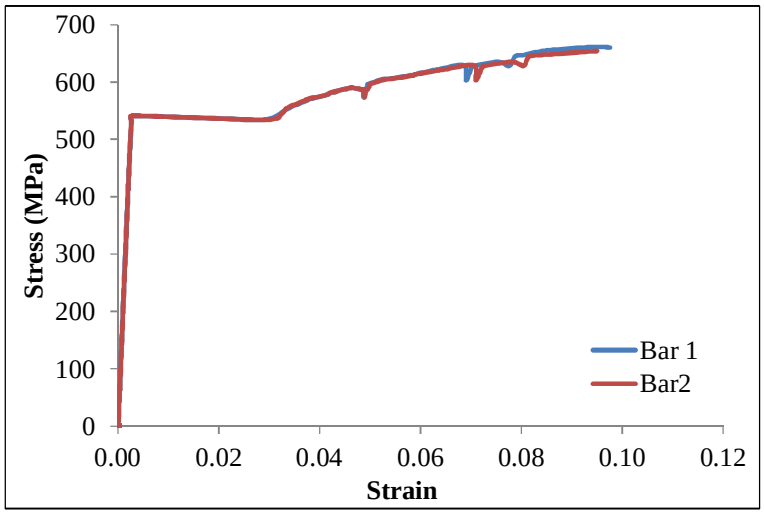

Figure D-2: Stress-strain curve of bar diameters 10 *mm*

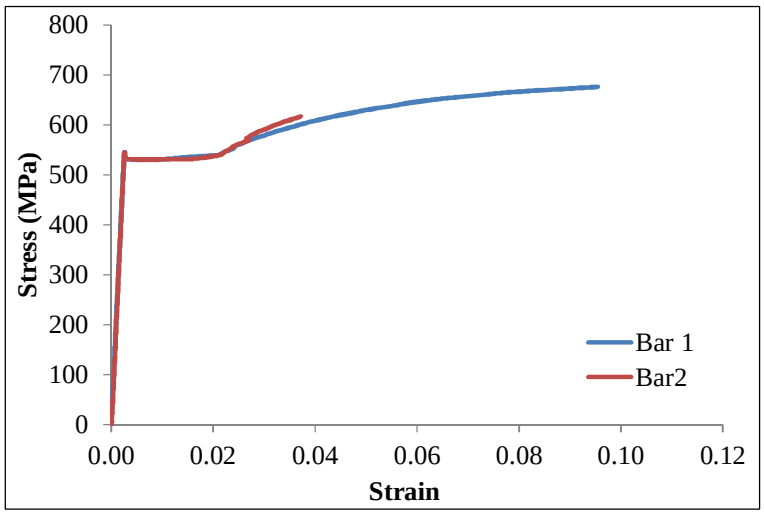

Figure D-3: Stress-strain curve of bar diameters 12 *mm*

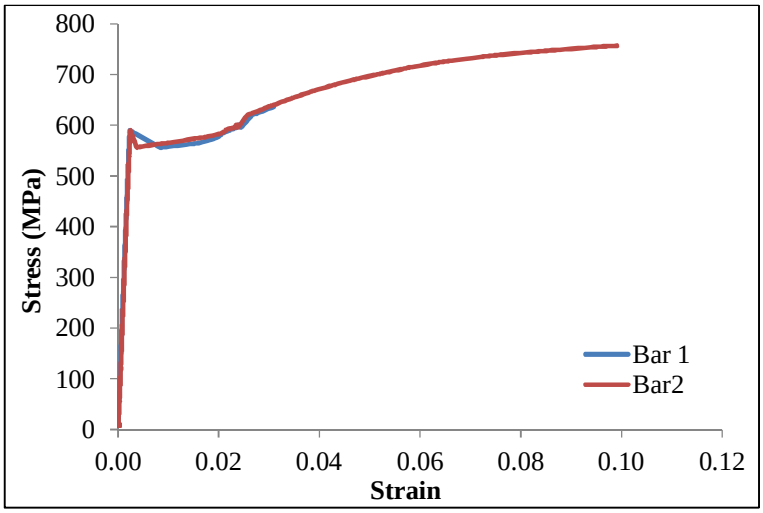

Figure D-4: Stress-strain curve of bar diameters 16 *mm*

Appendix E

TEST RESULTS – PHASE I

E.1 STRAIN GAUGE READINGS

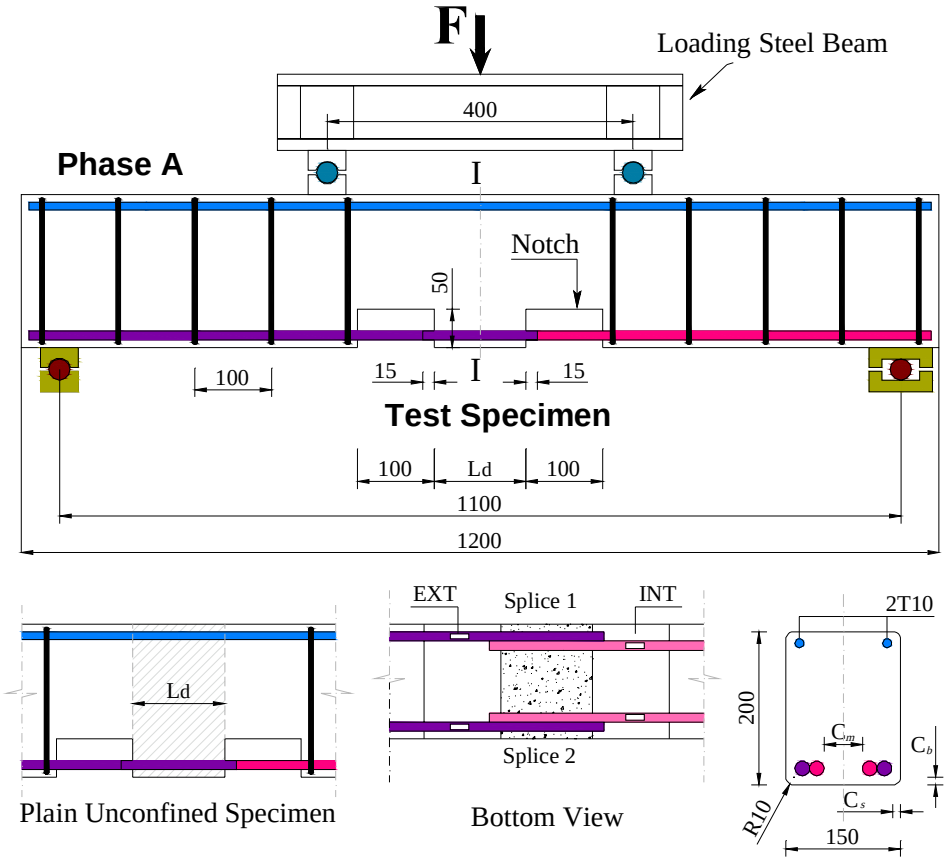

Figure E-1: Schematic view of the test specimen and strain gauge locations

E.1.1 Specimen SC10-D12-PTMS1

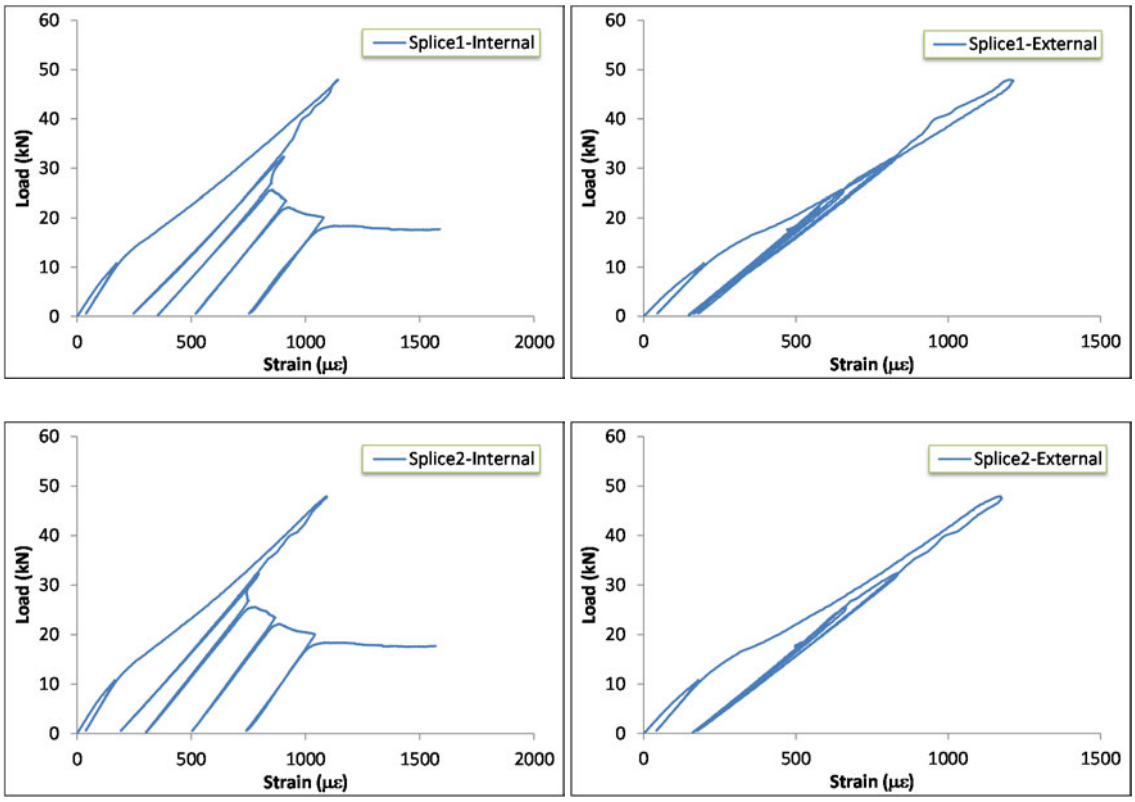

Figure E-2: Strain gauge readings of specimen SC10-D12-PTMS2

E.1.2 Specimen SC20-D12-Ctrl

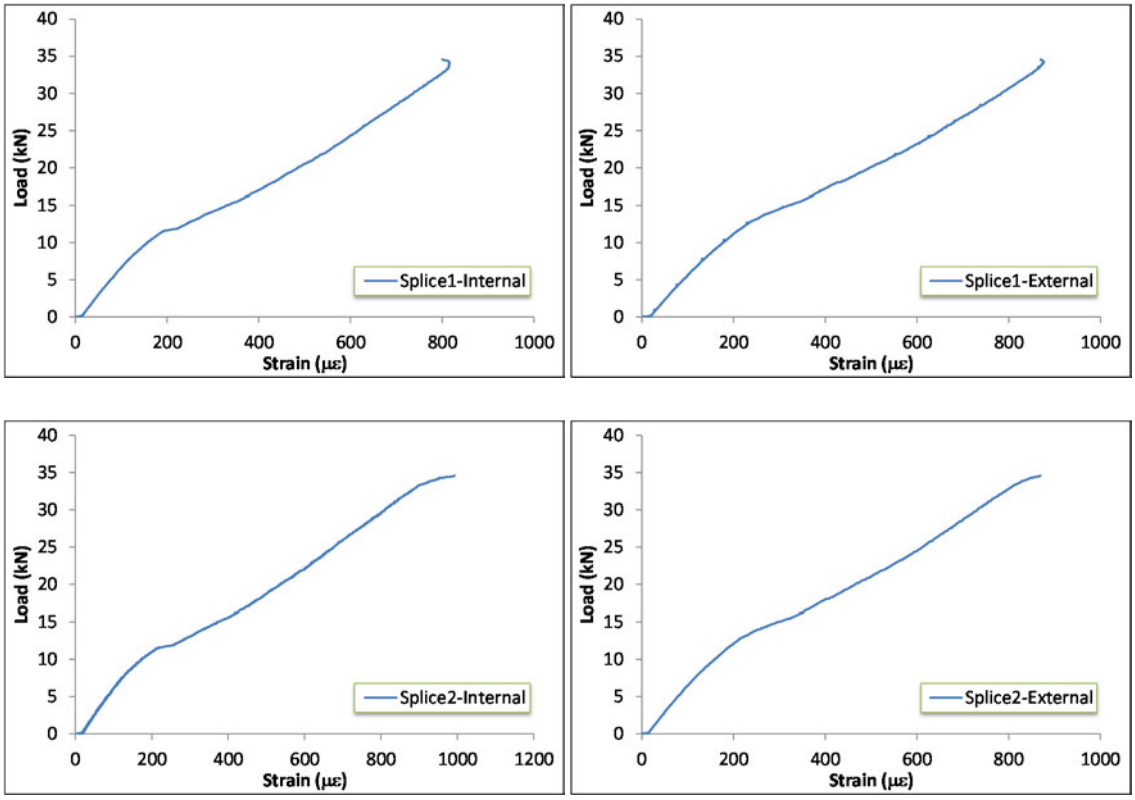

Figure E-3: Strain gauge readings of specimen SC20-D12-Ctrl

E.1.3 Specimen SC20-D12-S

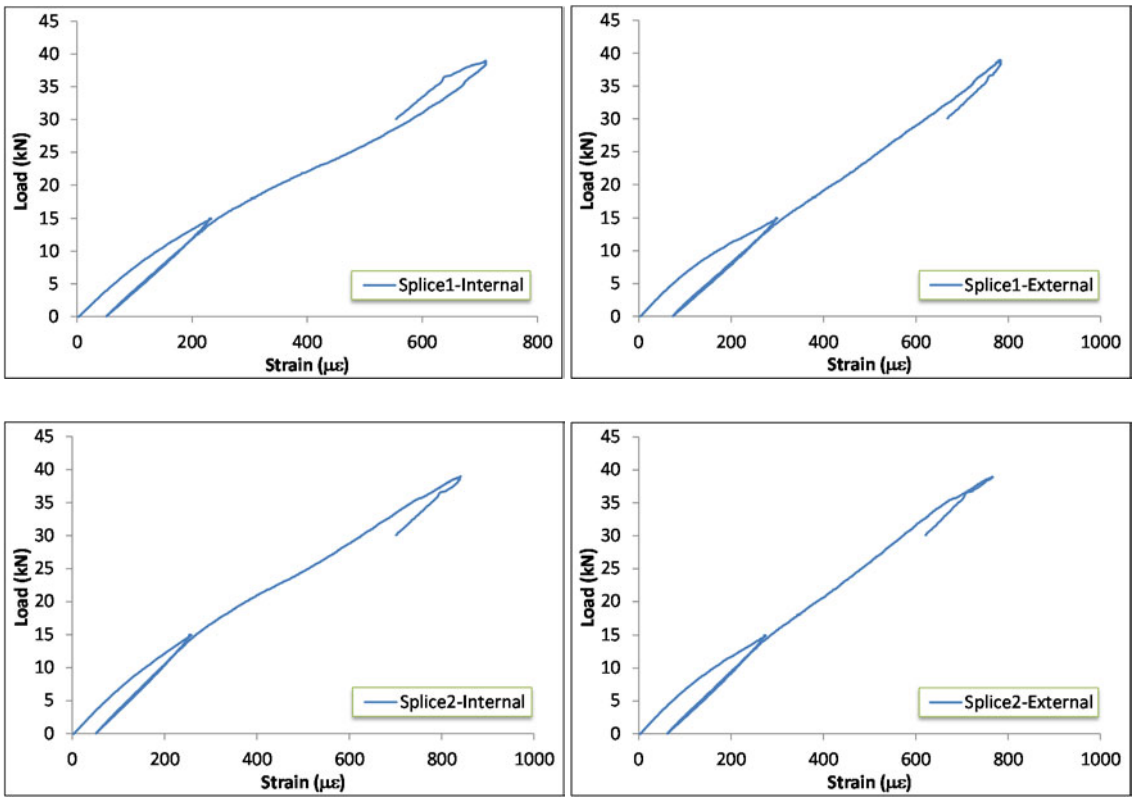

Figure E-4: Strain gauge readings of specimen SC20-D12-S

E.1.4 Specimen SC20-D12-PTMS1

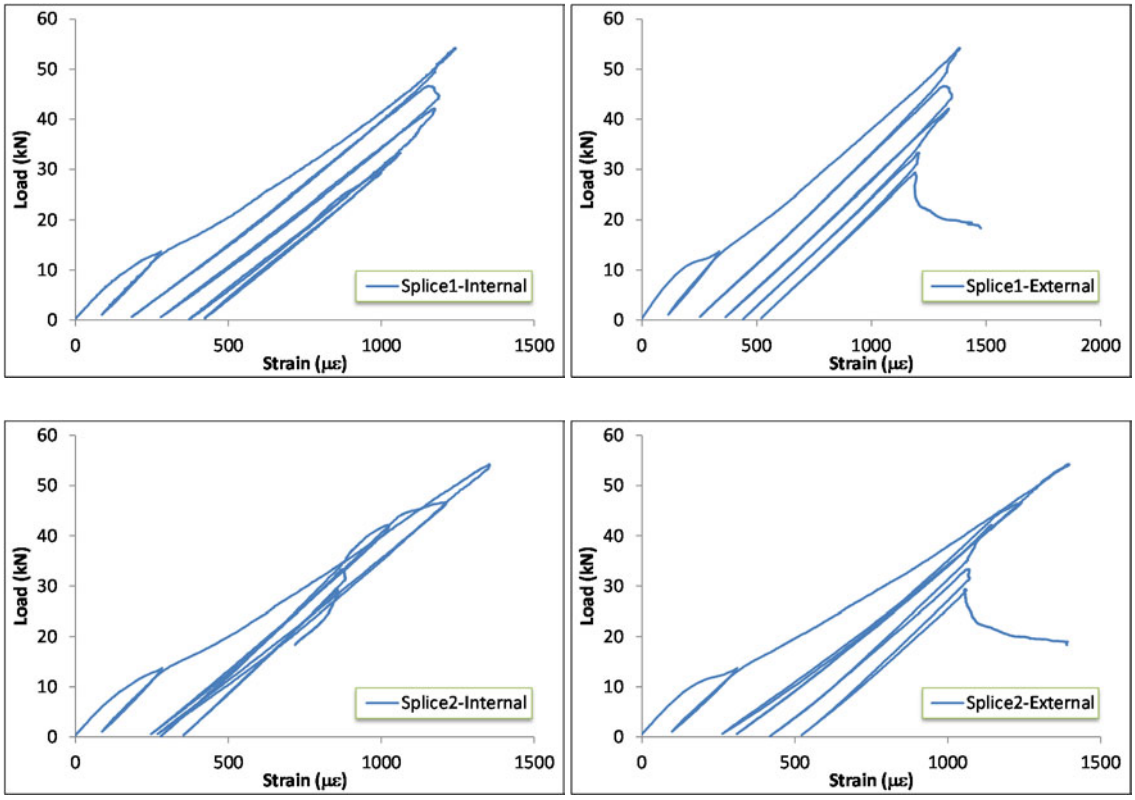

Figure E-5: Strain gauge readings of specimen SC20-D12-PTMS1

E.1.5 Specimen SC20-D12-PTMS2

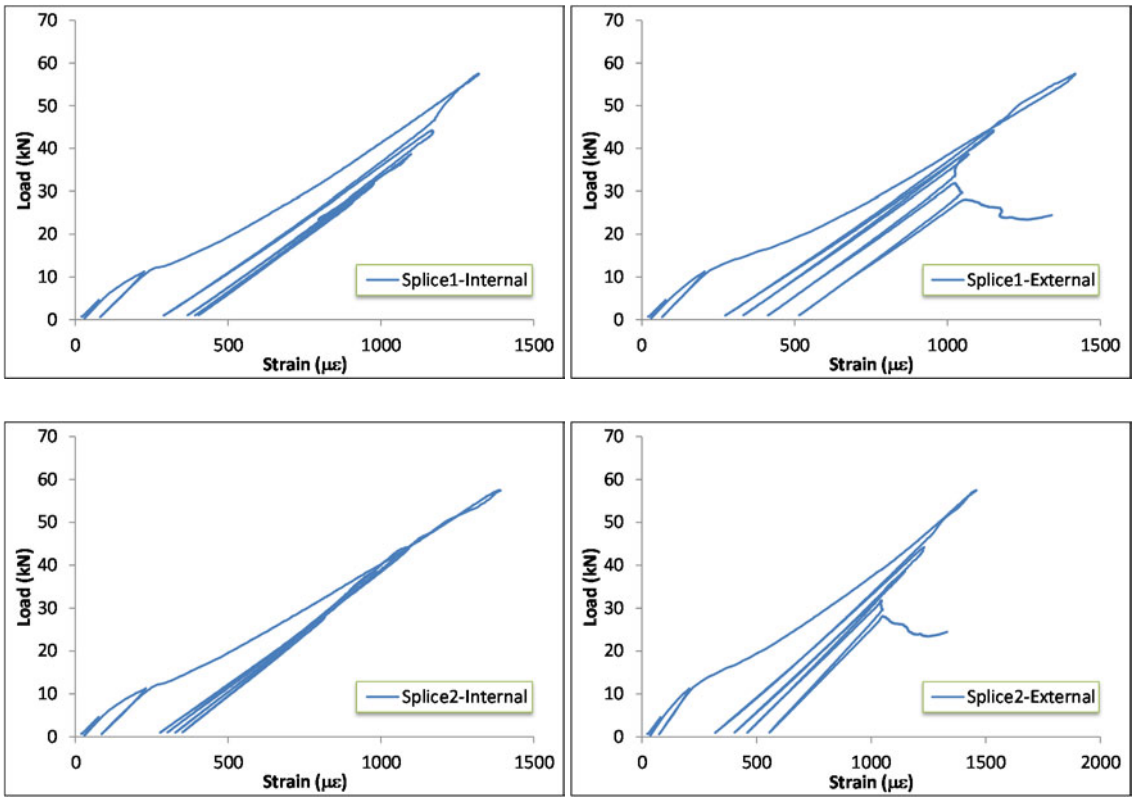

Figure E-6: Strain gauge readings of specimen SC20-D12-PTMS2

E.1.6 Specimen SC27-D16-Ctrl

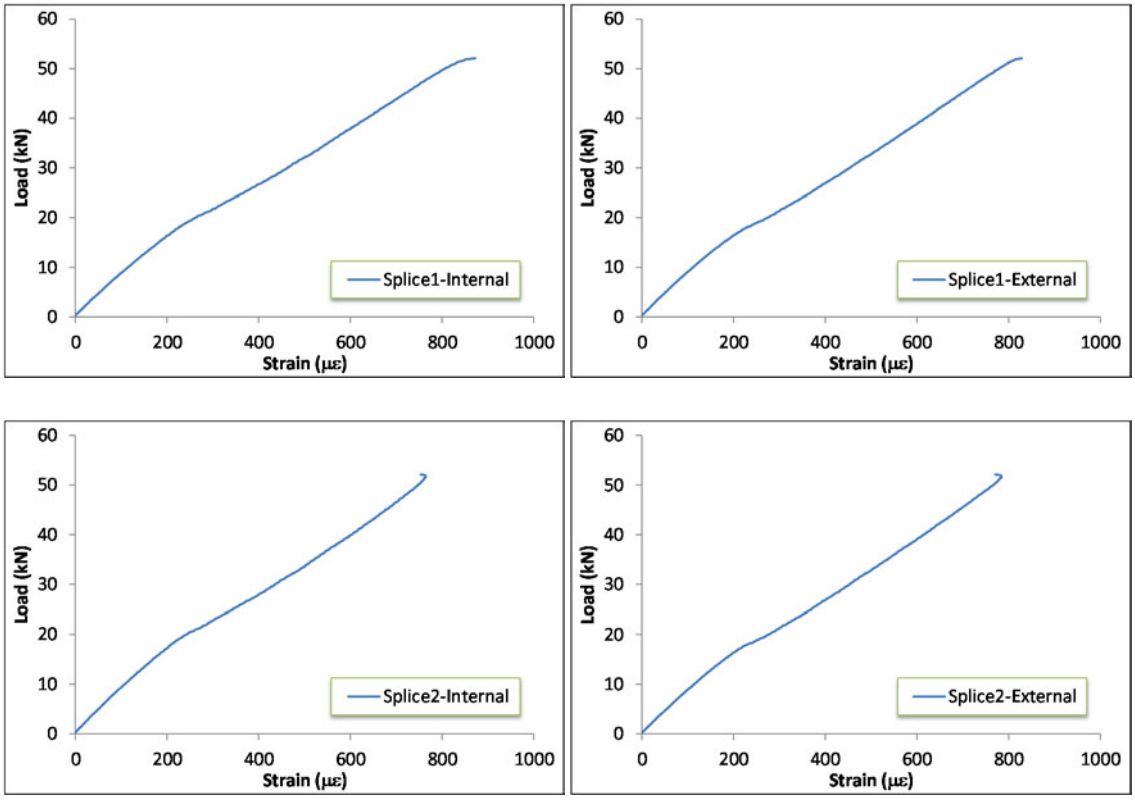

Figure E-7: Strain gauge readings of specimen SC27-D16-Ctrl

E.1.7 Specimen SC27-D16-S

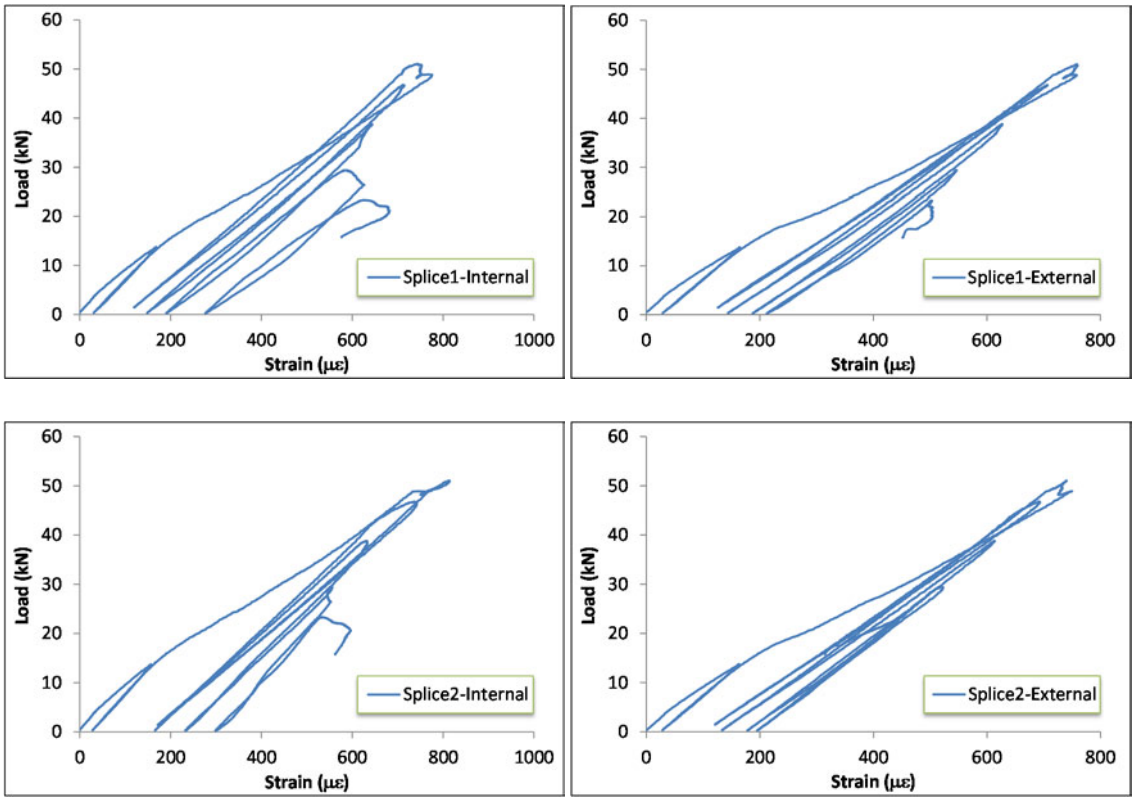

Figure E-8: Strain gauge readings of specimen SC27-D16-S

E.1.8 Specimen SC27-D16-PTMS1

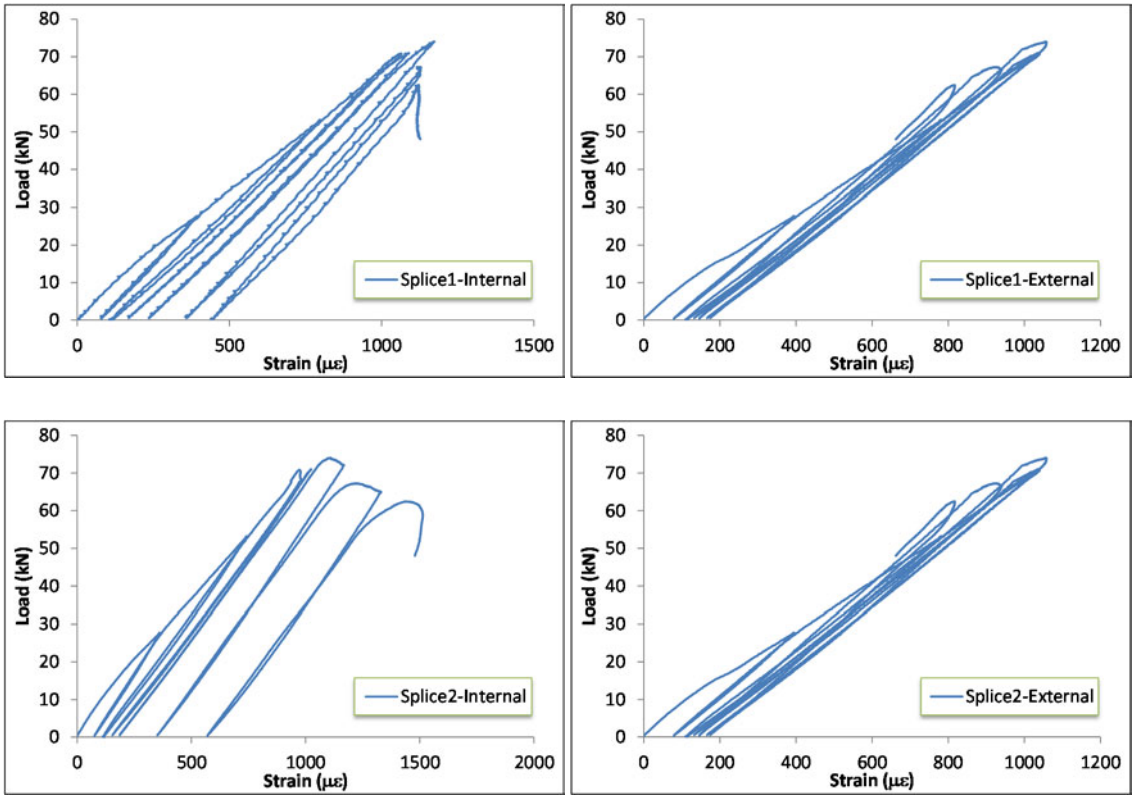

Figure E-9: Strain gauge readings of specimen SC27-D16-PTMS1

E.1.9 Specimen SC27-D16-PTMS2

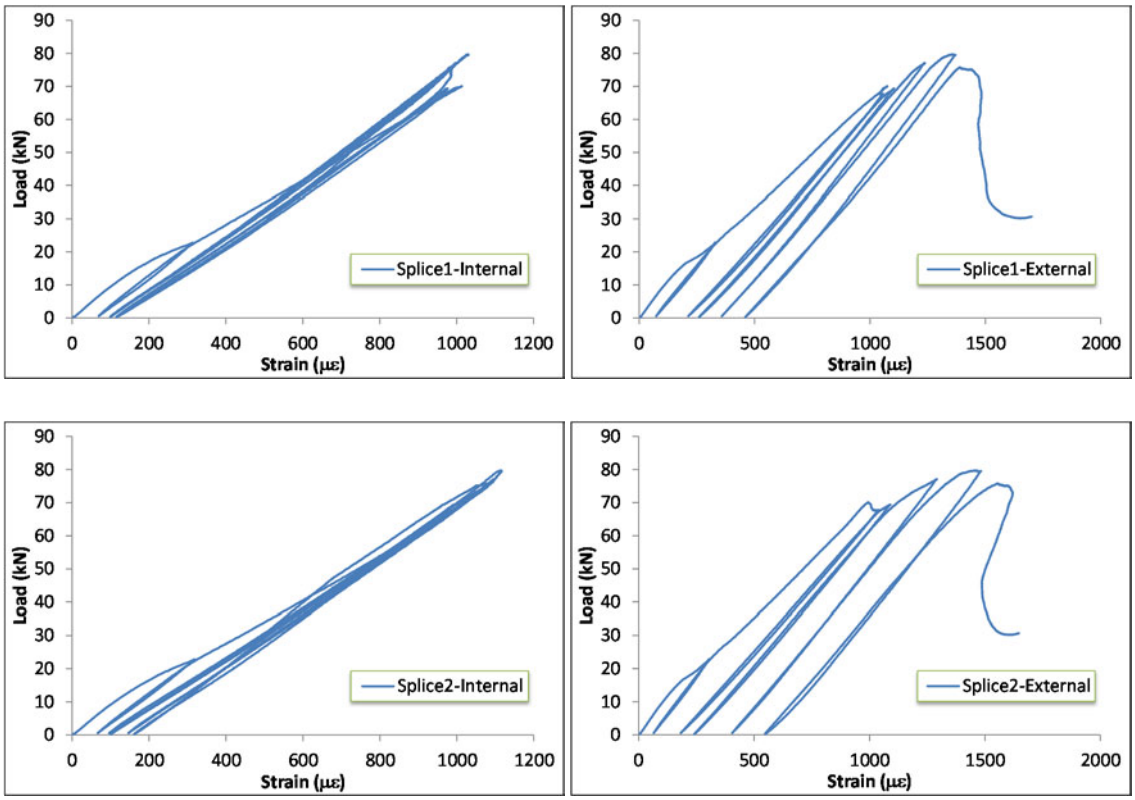

Figure E-10: Strain gauge readings of specimen SC27-D16-PTMS2

E.2 ACTUAL LOAD-DEFLECTION RESPONSE

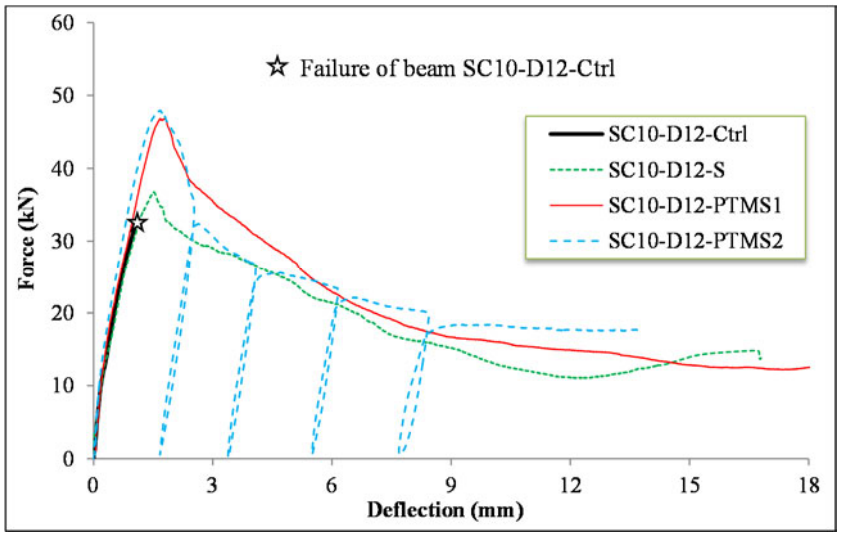

Figure E-11: Load-deflection response of test beams (Group I, Phase I)

Appendix F

TEST RESULTS – PHASE II

F.1 STRAIN GAUGE READINGS

The strain gauge readings are presented to the point where the strain gauge is believed working.

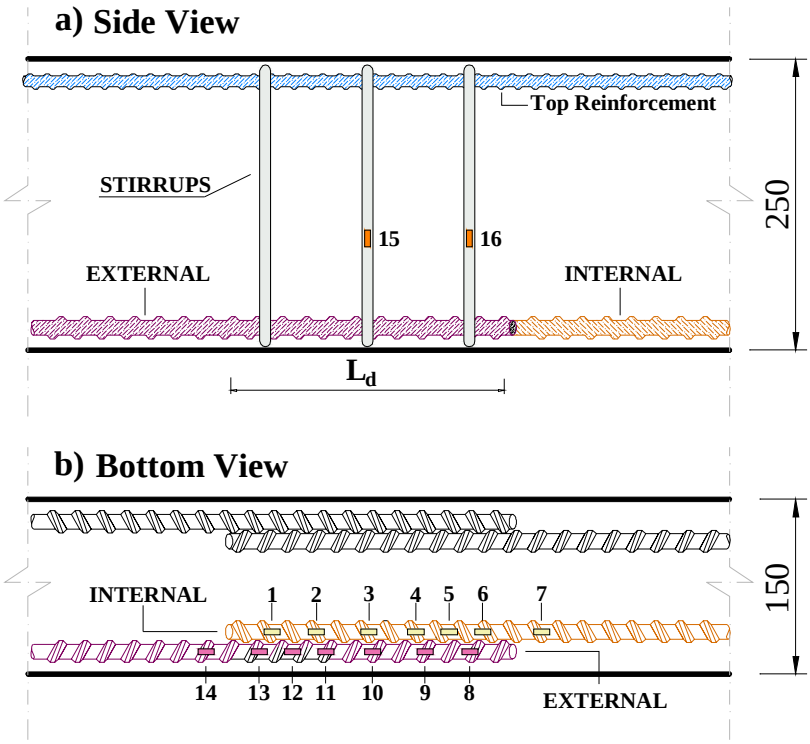

Figure F-1: Spliced bar arrangement & strain gauge numbers

F.1.1 BEAM LC10-D12-Ctrl

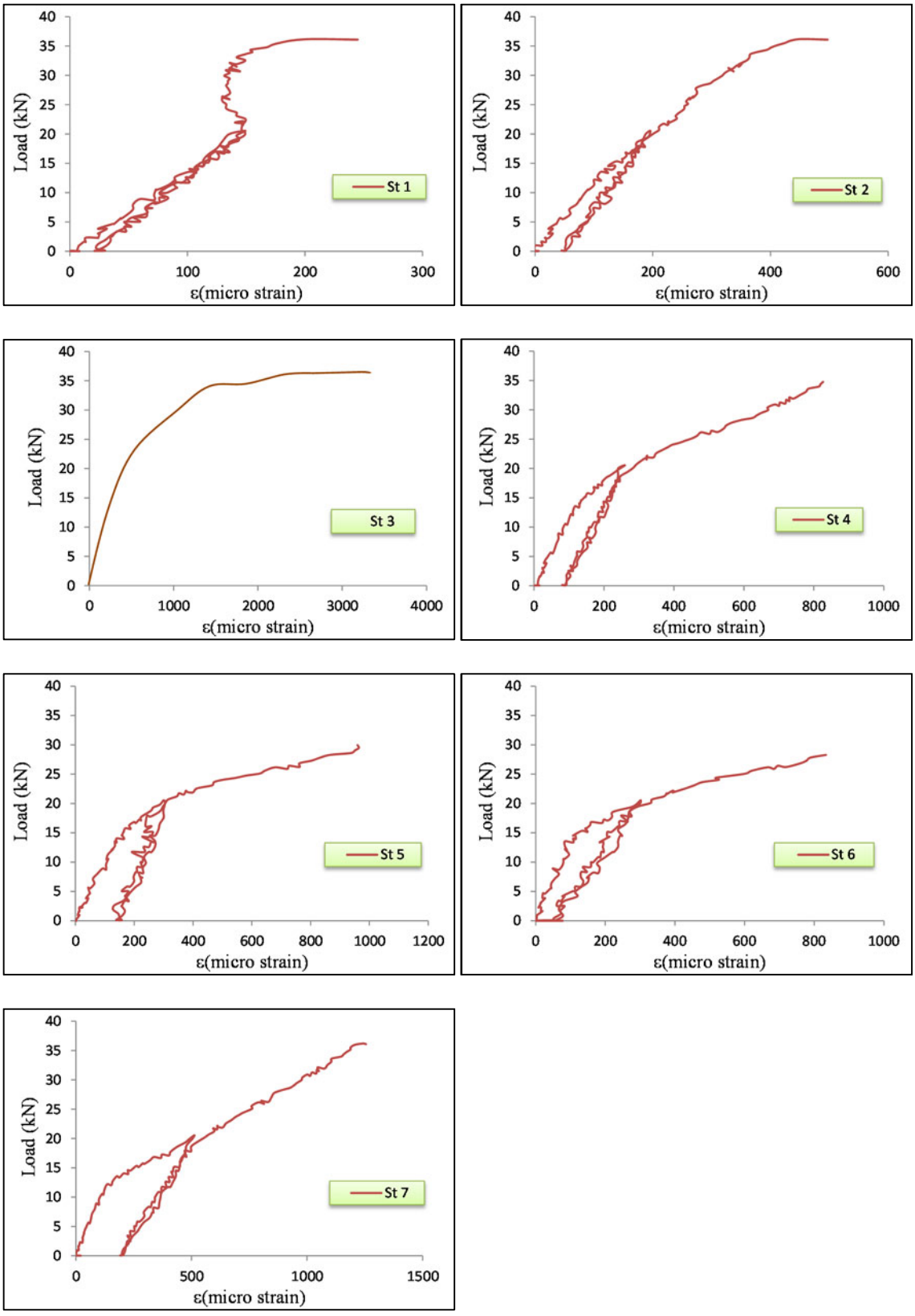

Figure F-2: Strain gauge readings of internal spliced bar – LC10-D12-Ctrl

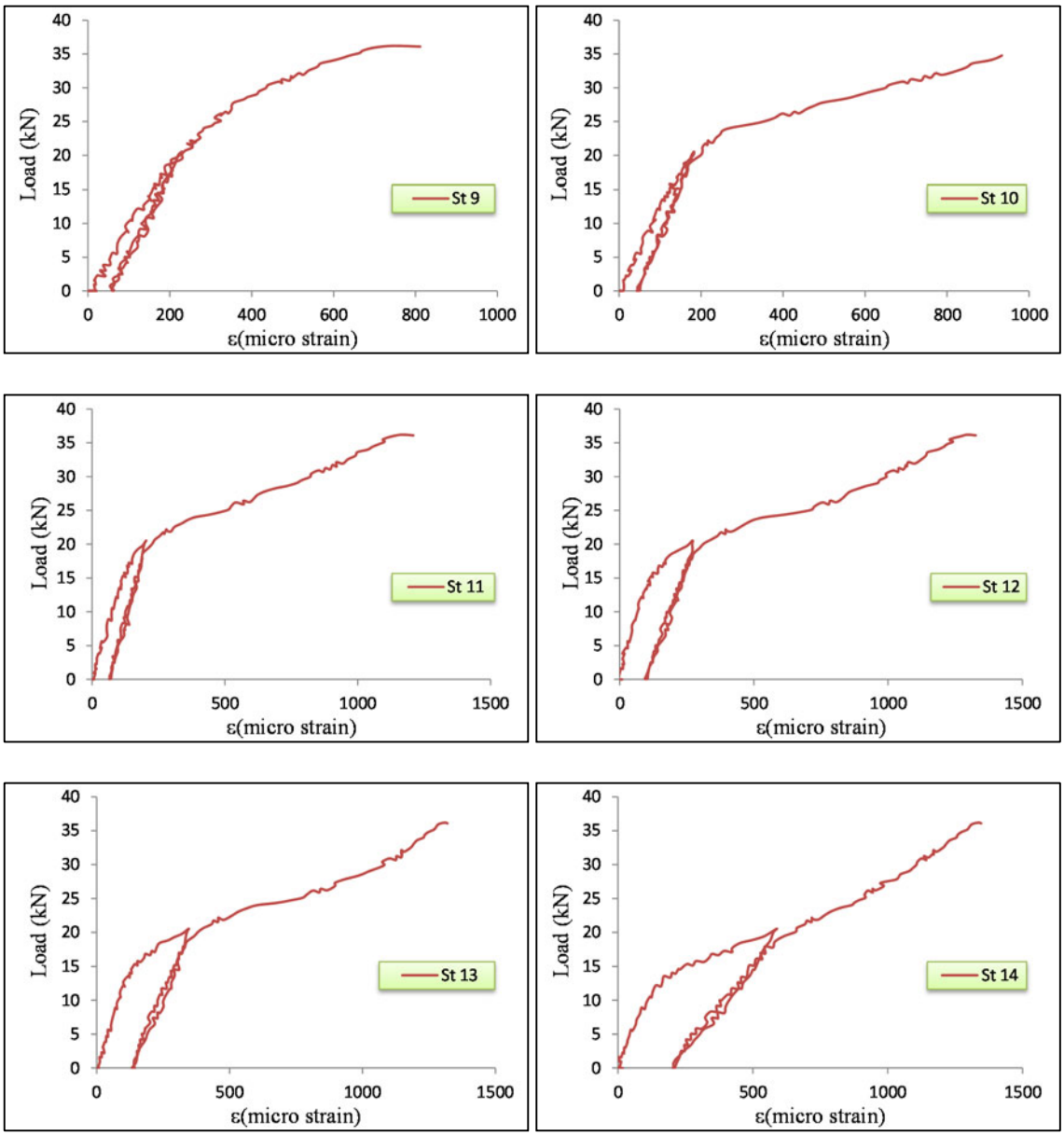

Figure F-3: Strain gauge readings of external spliced bar – LC10-D12-Ctrl

F.1.2 BEAM LC10-D12-S

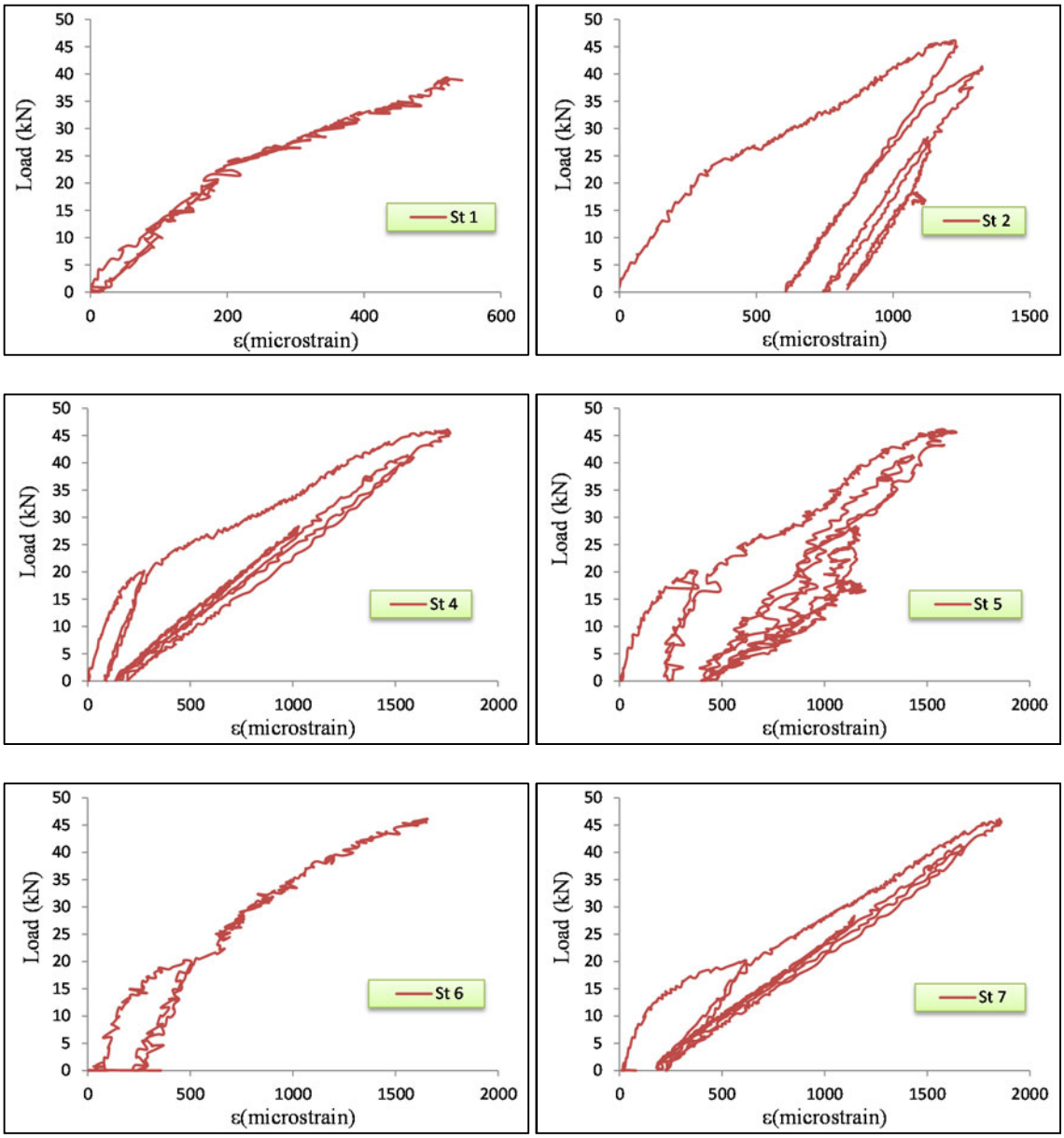

Figure F-4: Strain gauge readings of internal spliced bar – LC10-D12-S

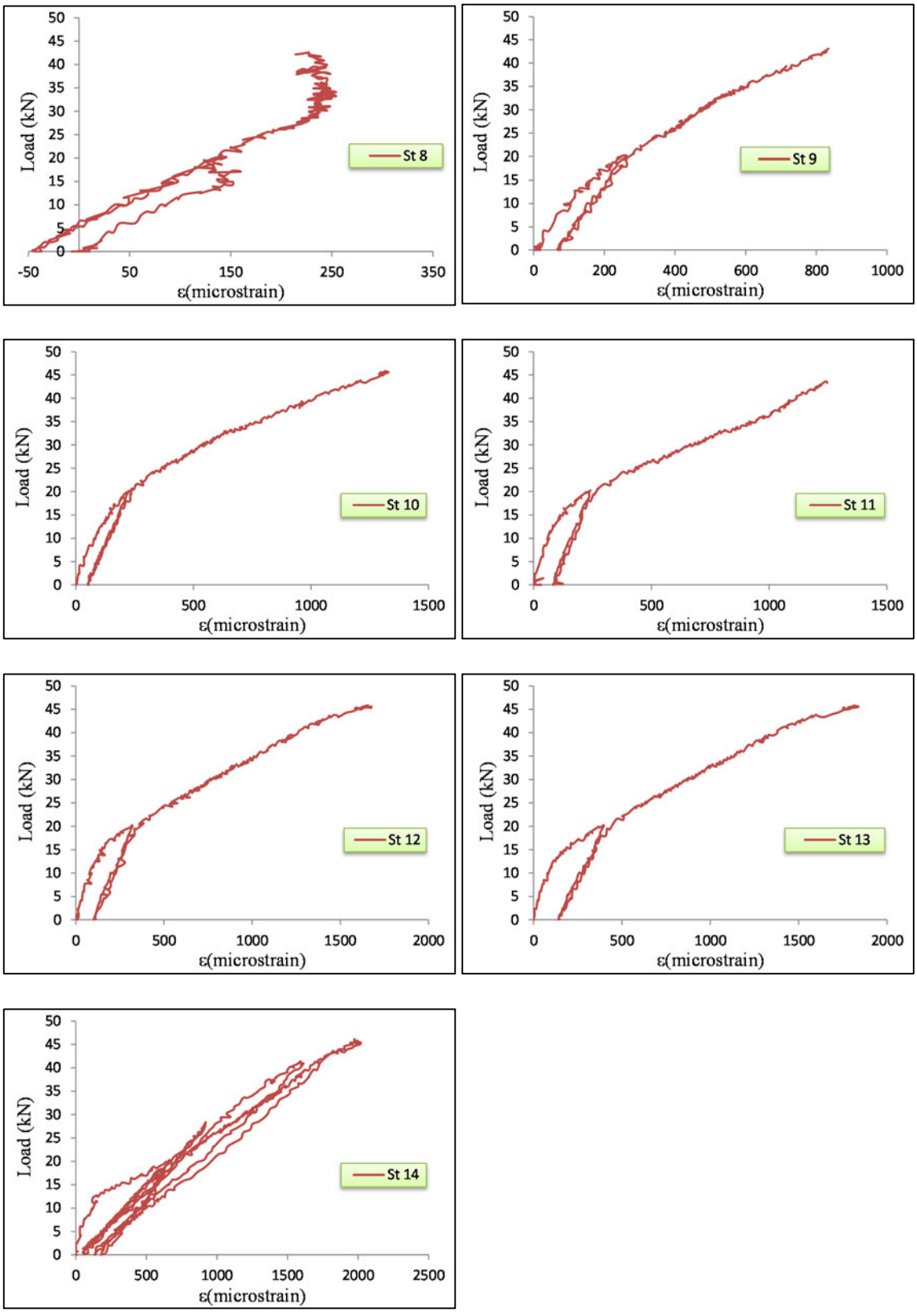

Figure F-5: Strain gauge readings of external spliced bar – LC10-D12-S

F.1.3 BEAM LC10-D12-PTMS1

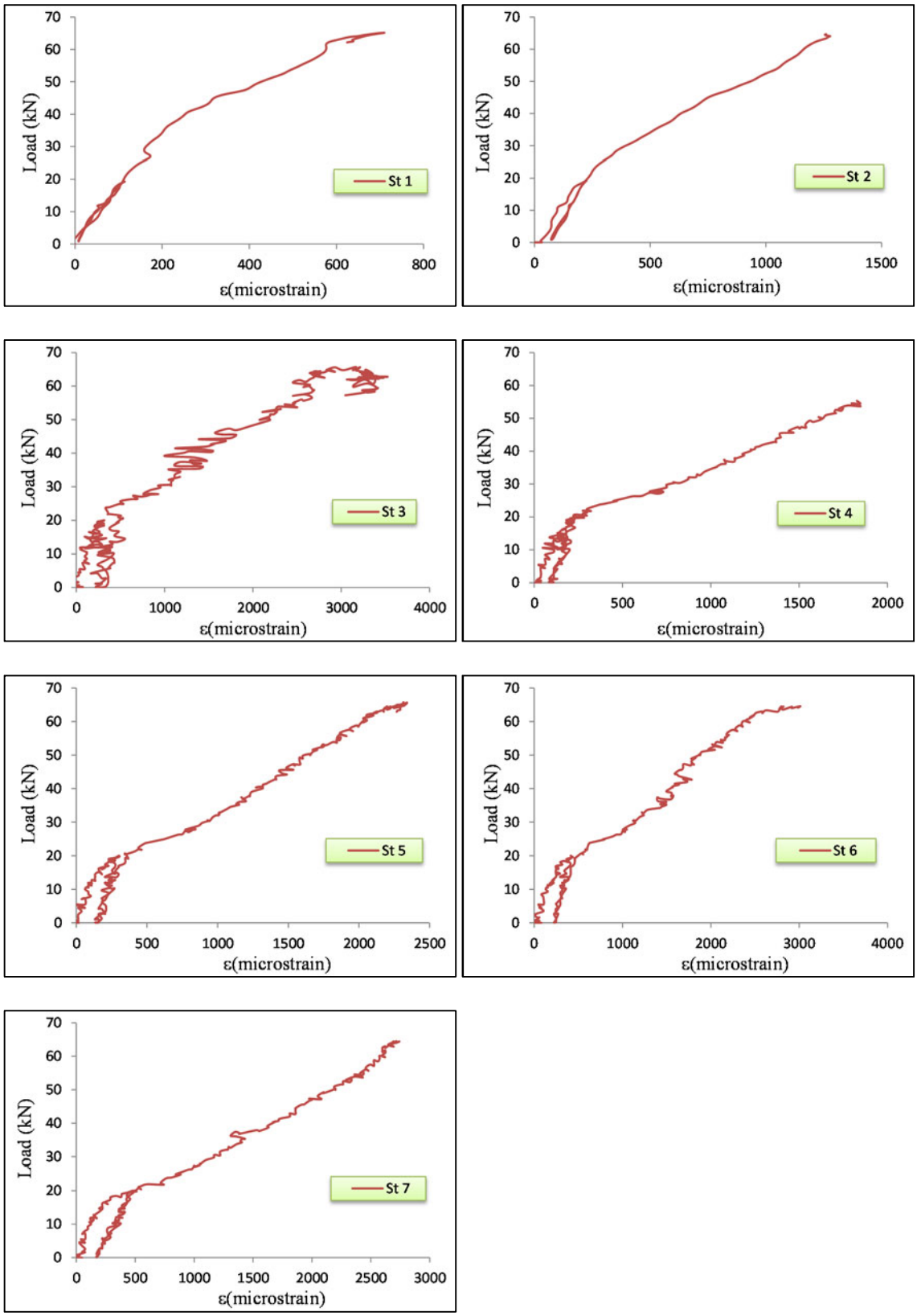

Figure F-6: Strain gauge readings of internal spliced bar – LC10-D12-PTMS1

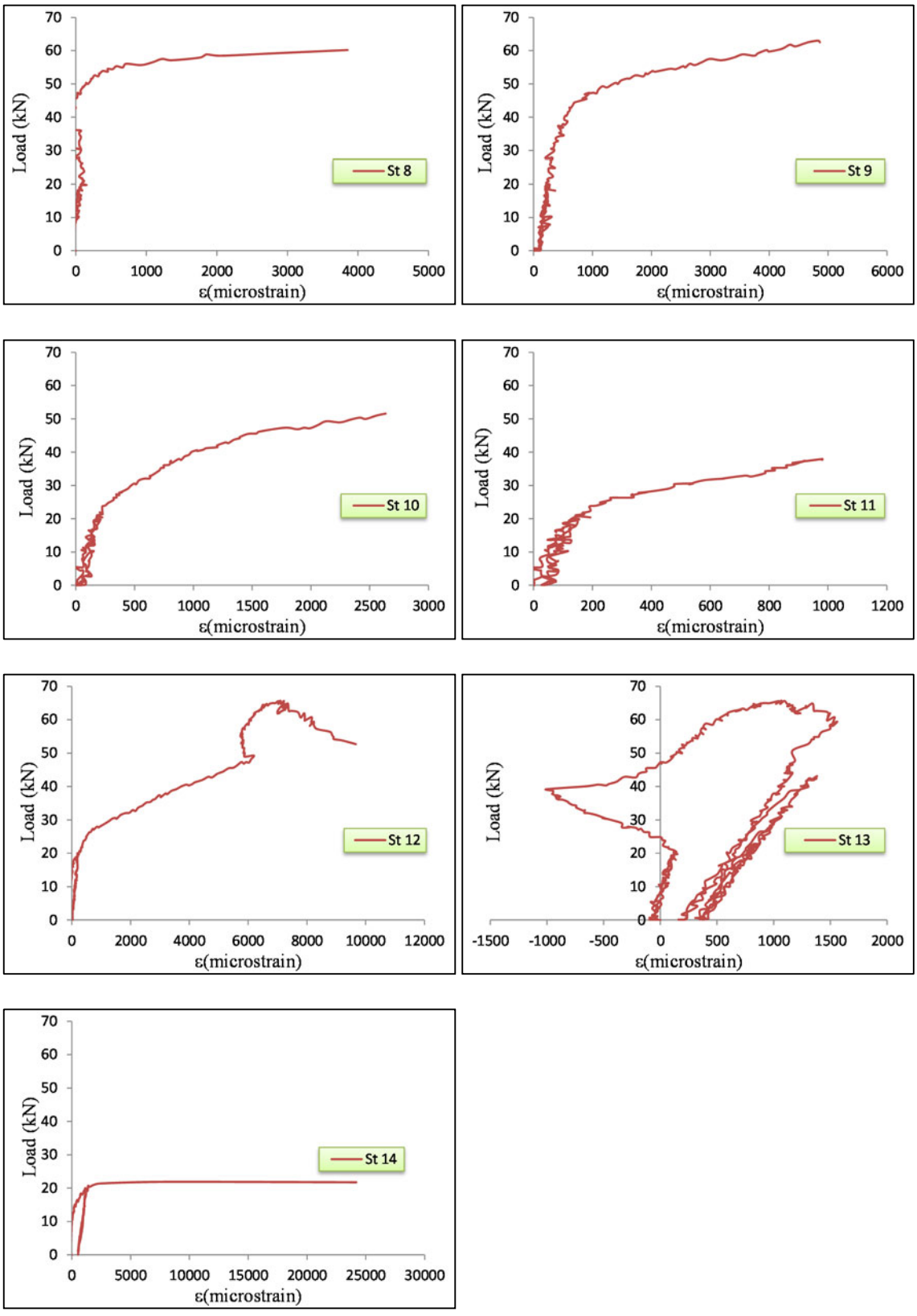

Figure F-7: Strain gauge readings of external spliced bar – LC10-D12-PTMS1

F.1.4 BEAM LC10-D12-PTMS2

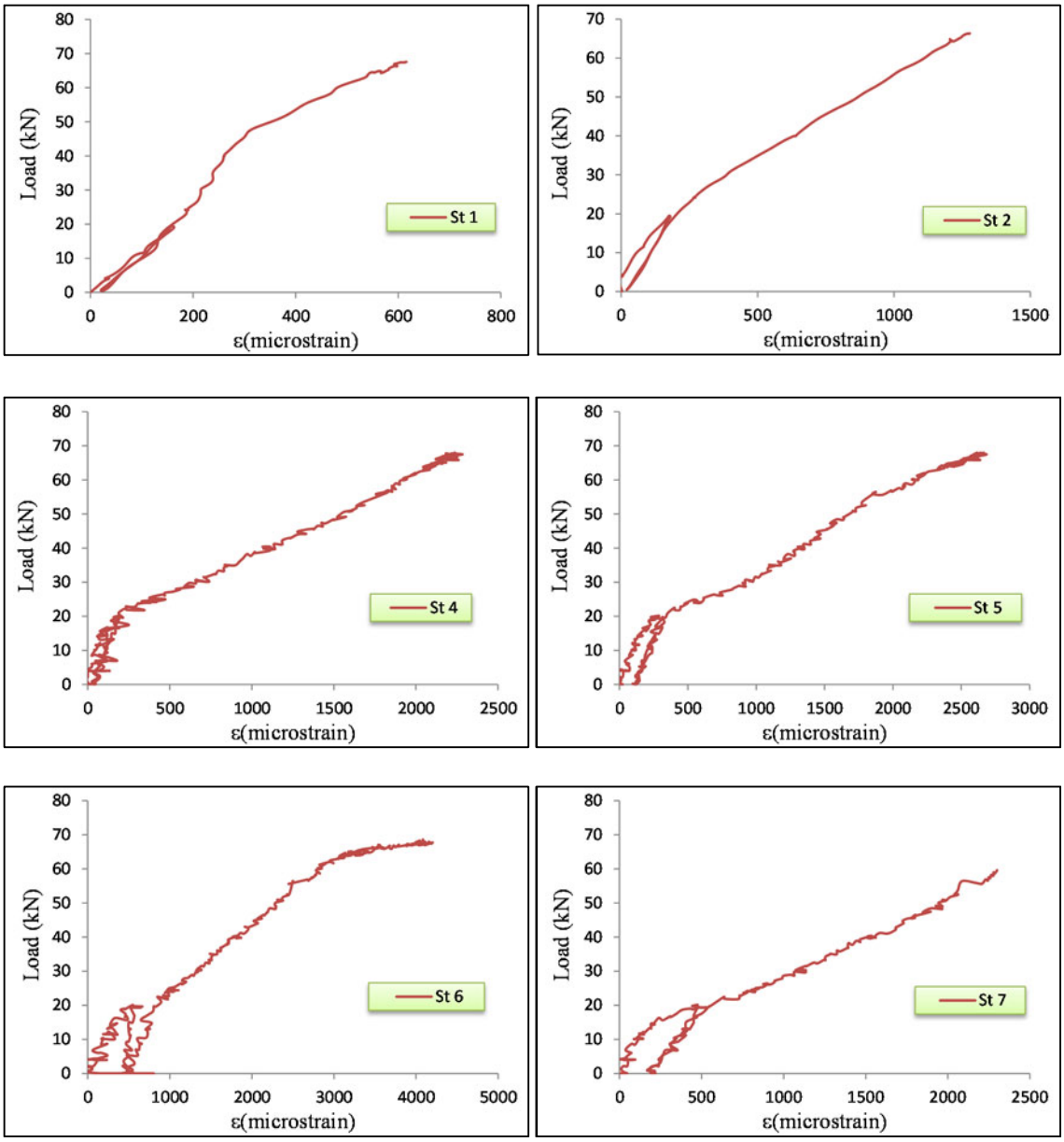

Figure F-8: Strain gauge readings of internal spliced bar – LC10-D12-PTMS2

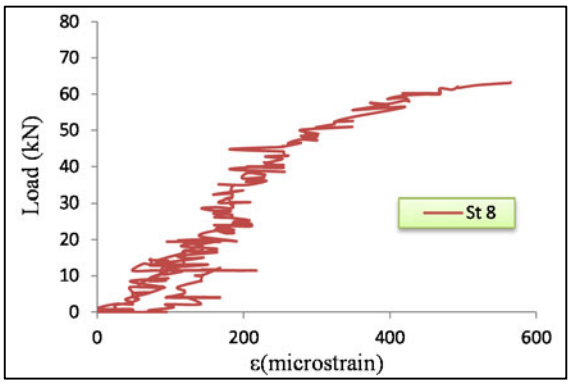

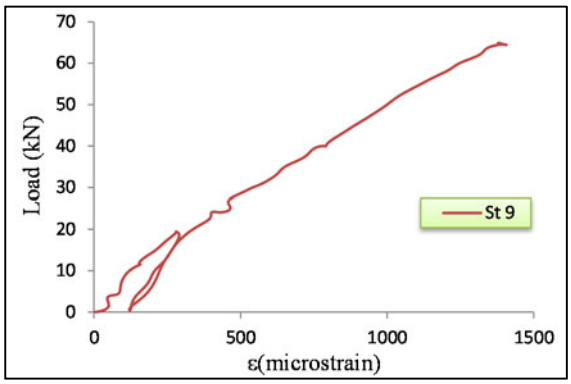

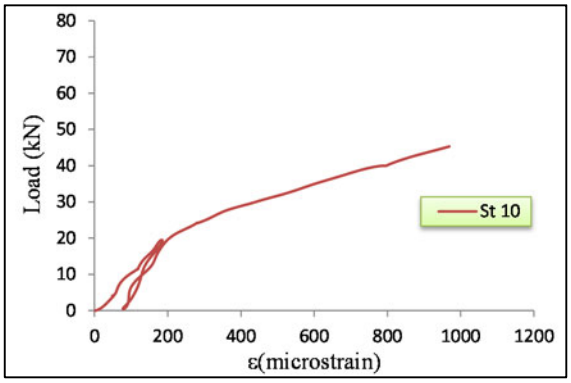

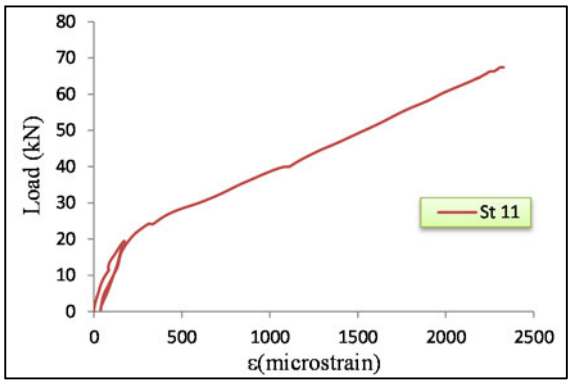

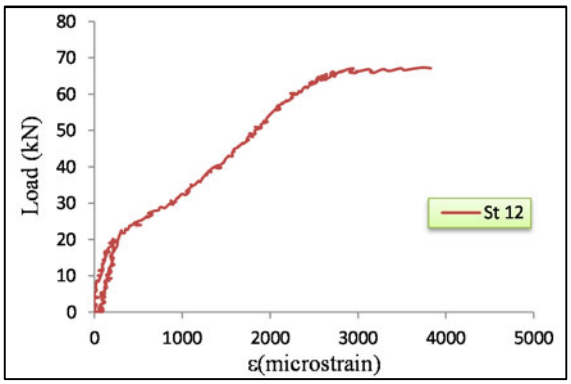

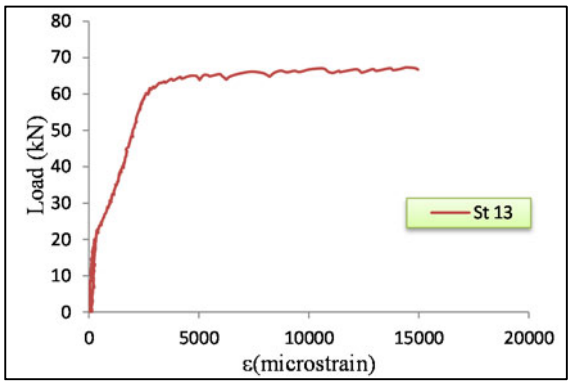

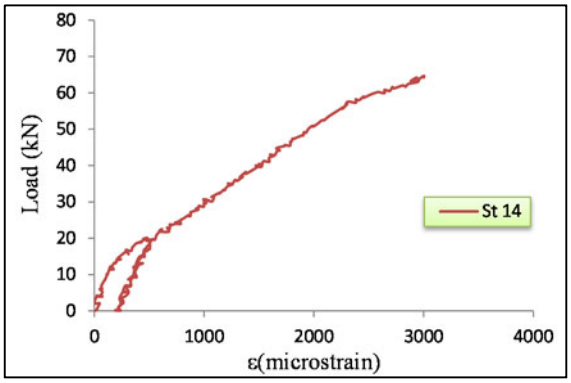

Figure F-9: Strain gauge readings of external spliced bar – LC10-D12-PTMS2

F.1.5 BEAM LC20-D12-Ctrl

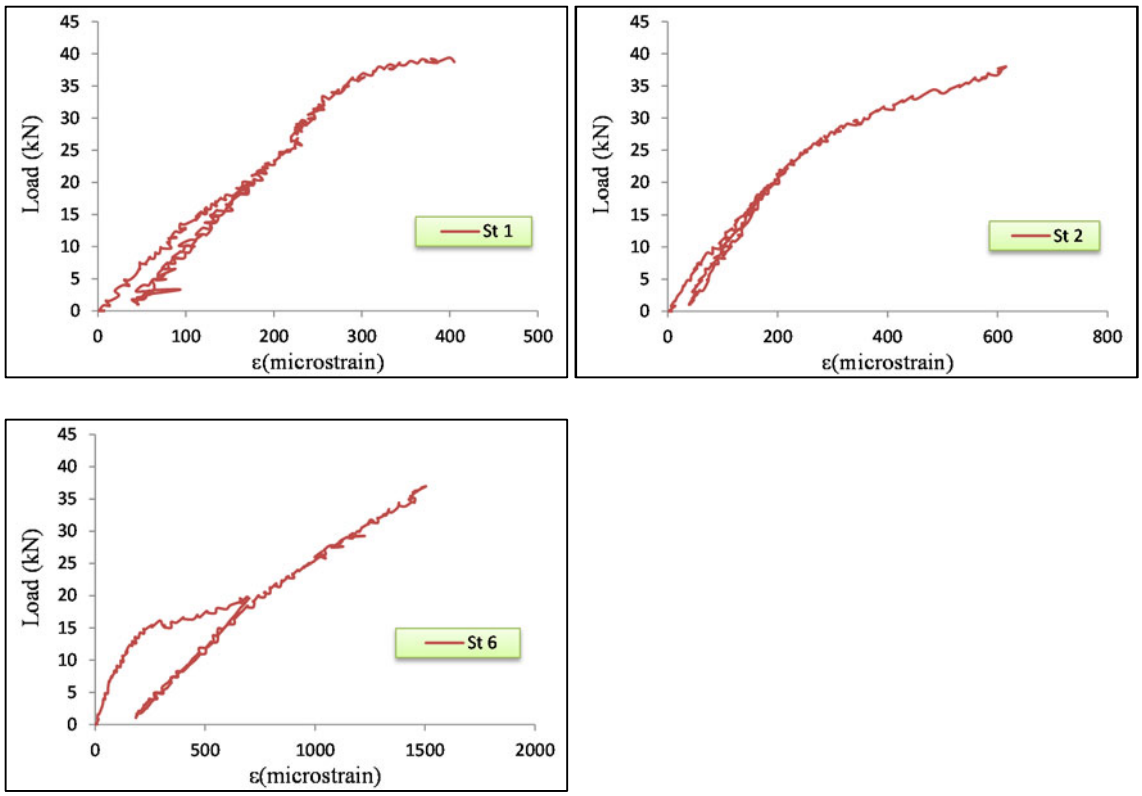

Figure F-10: Strain gauge readings of internal spliced bar – LC20-D12-Ctrl

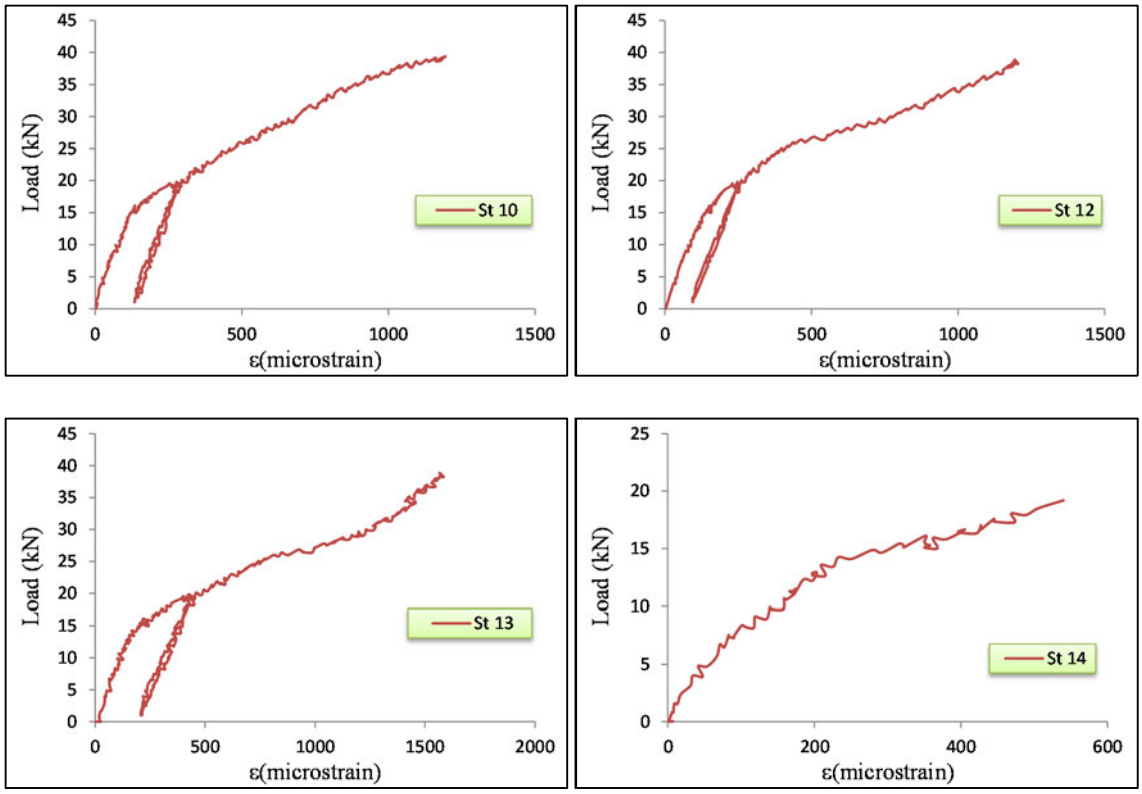

Figure F-11: Strain gauge readings of external spliced bar – LC20-D12-Ctrl

F.1.6 BEAM LC20-D12-S

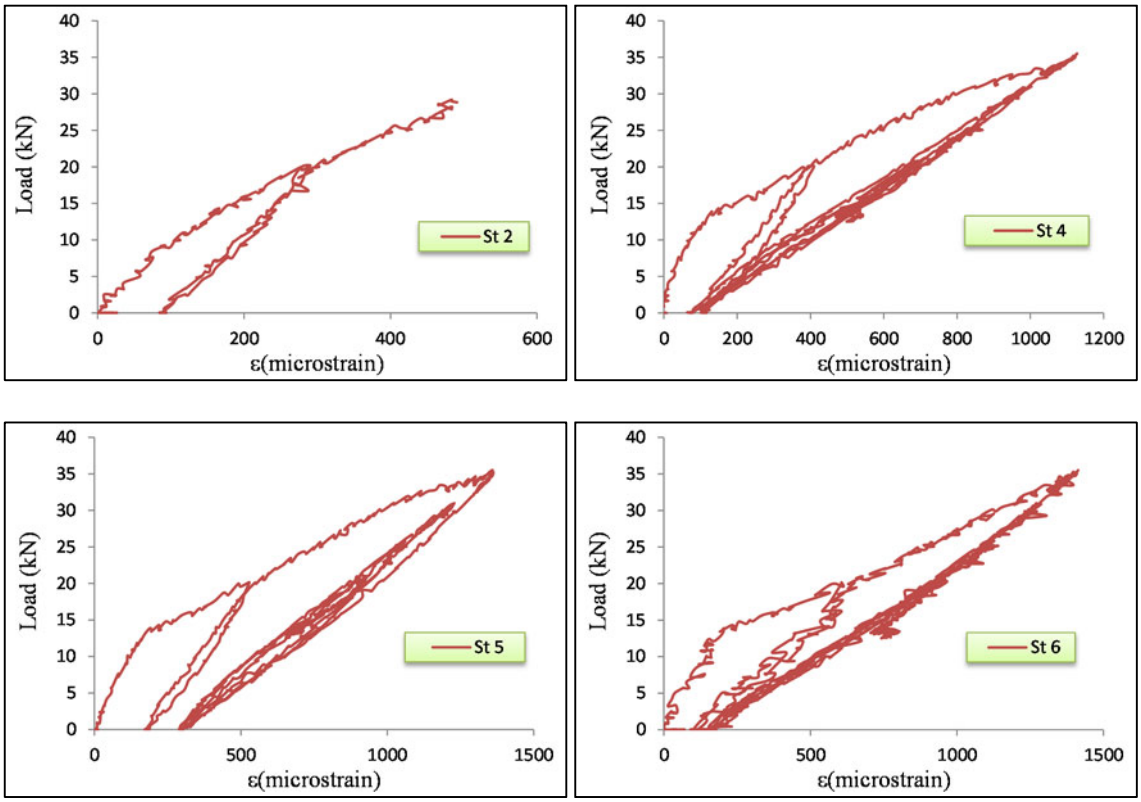

Figure F-12: Strain gauge readings of internal spliced bar – LC20-D12-S

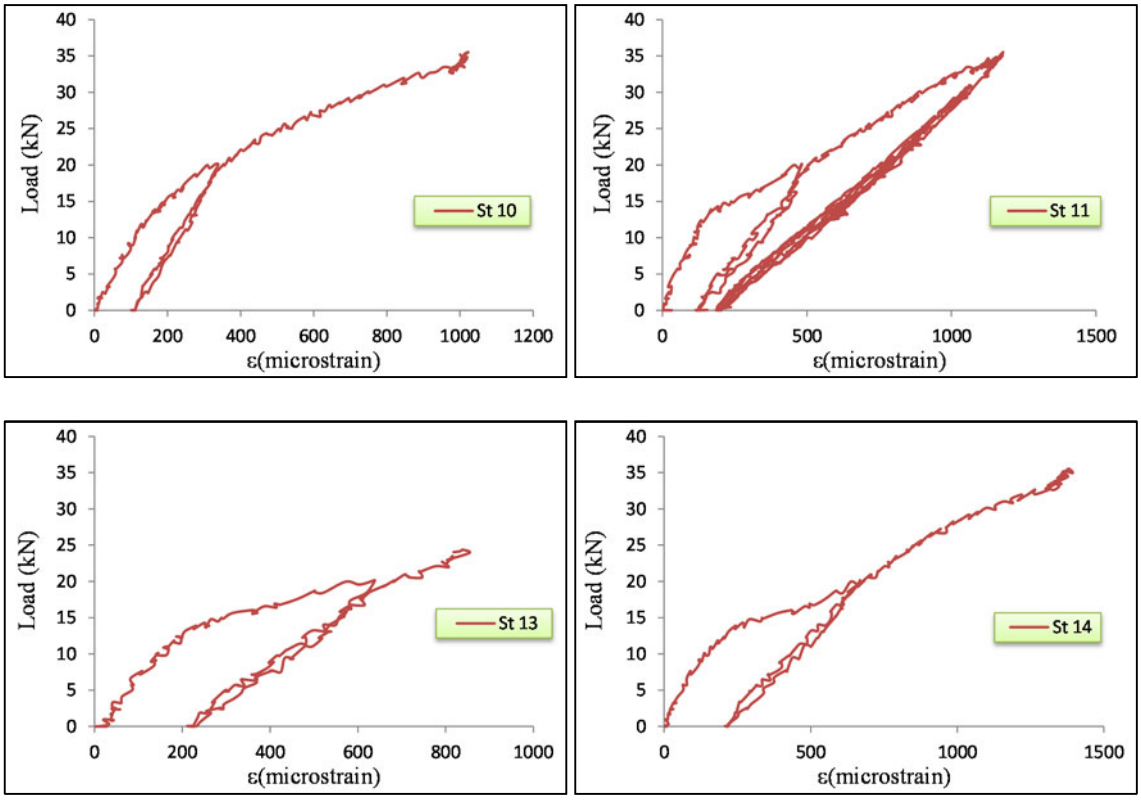

Figure F-13: Strain gauge readings of external spliced bar – LC20-D12-S

F.1.7 BEAM LC20-D12-PTMS1

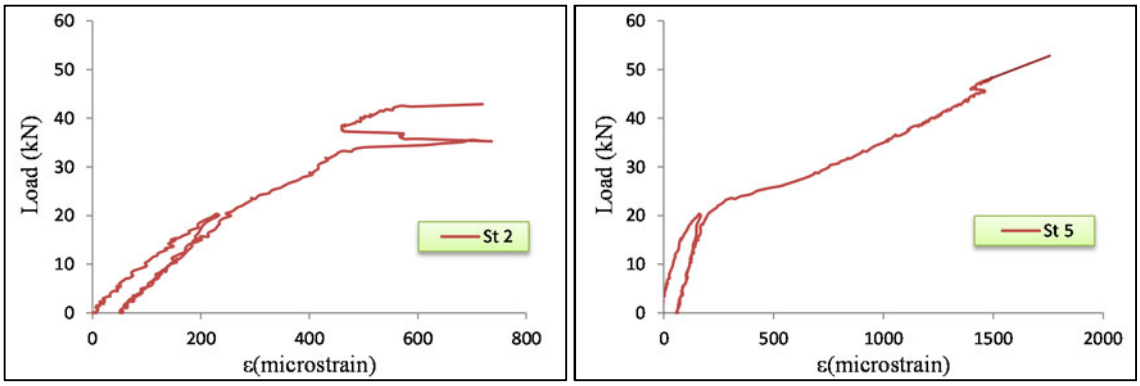

Figure F-14: Strain gauge readings of internal spliced bar – LC20-D12-PTMS1

F.1.8 BEAM LC20-D12-PTMS2

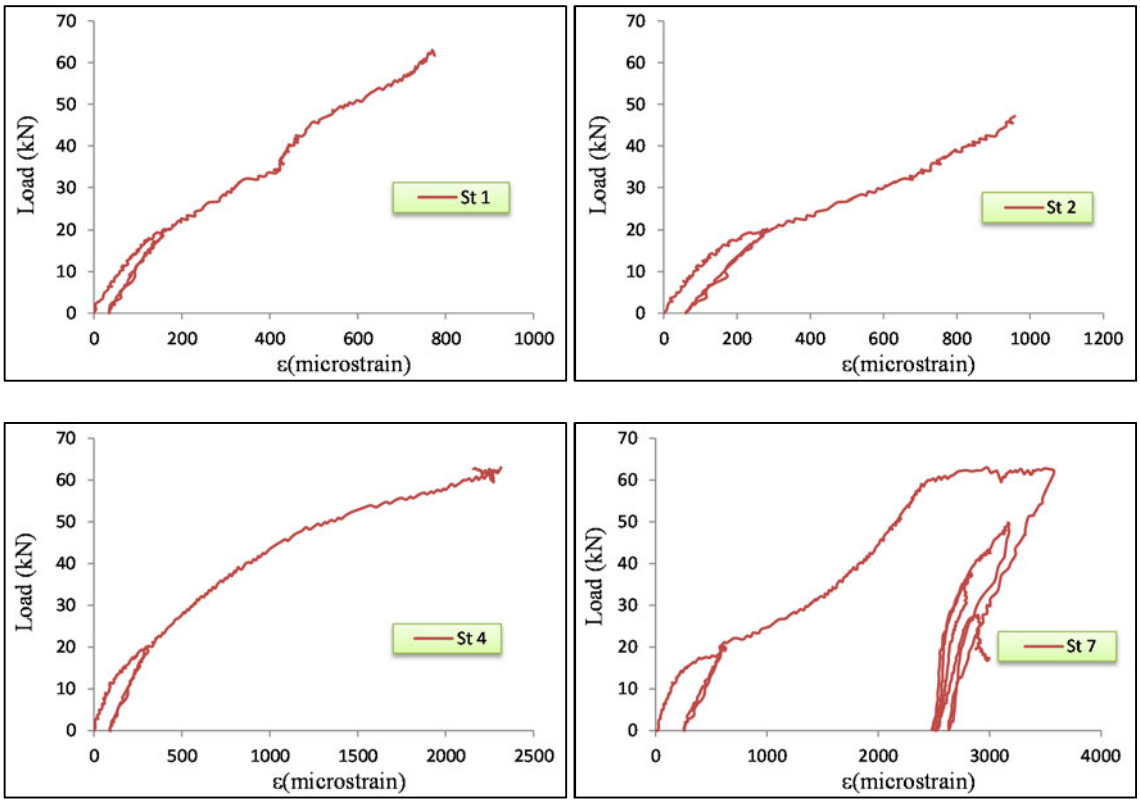

Figure F-15: Strain gauge readings of internal spliced bar – LC20-D12-PTMS2

F.1.9 BEAM LC27-D12-Ctrl

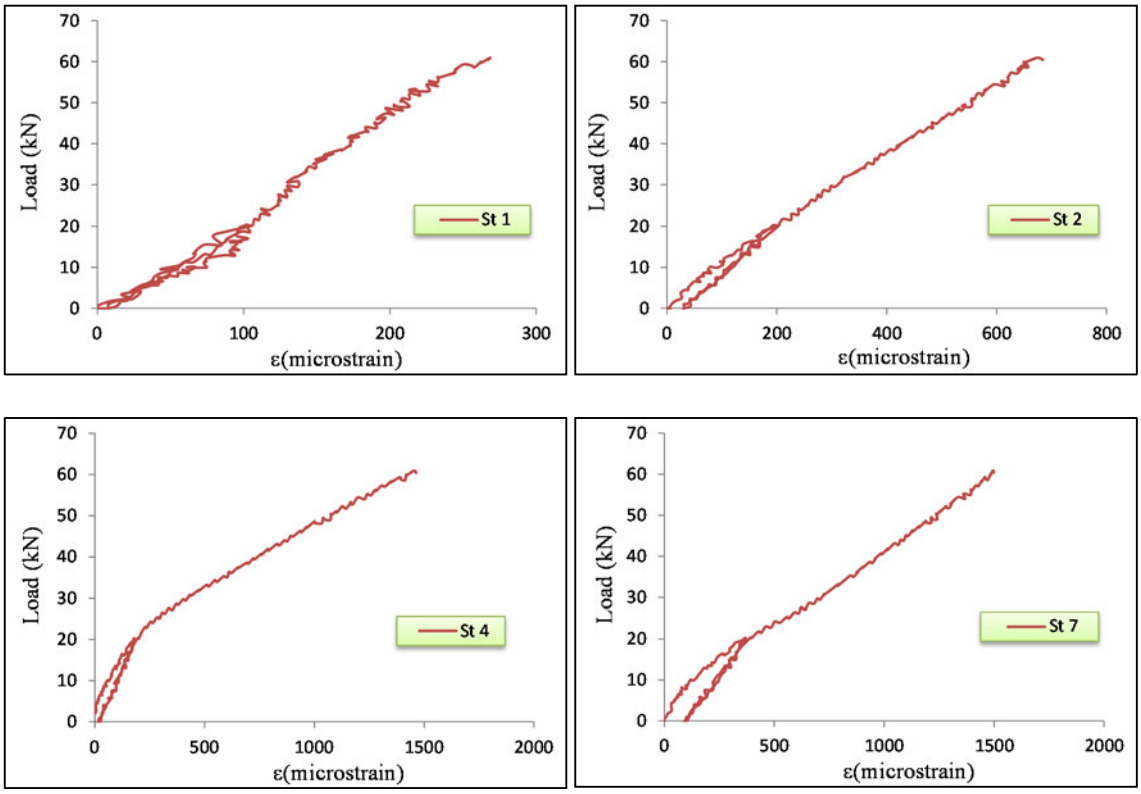

Figure F-16: Strain gauge readings of internal spliced bar – LC27-D16-Ctrl

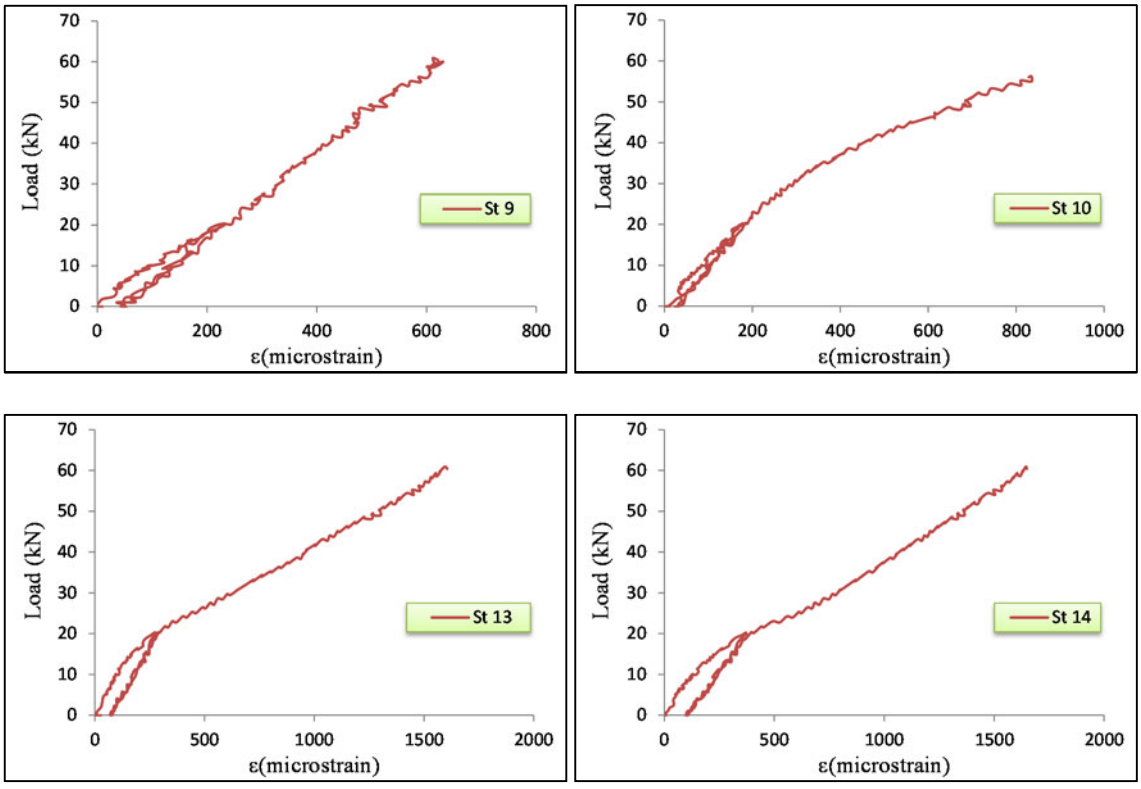

Figure F-17: Strain gauge readings of external spliced bar – LC27-D16-Ctrl

F.1.10 BEAM LC27-D12-S

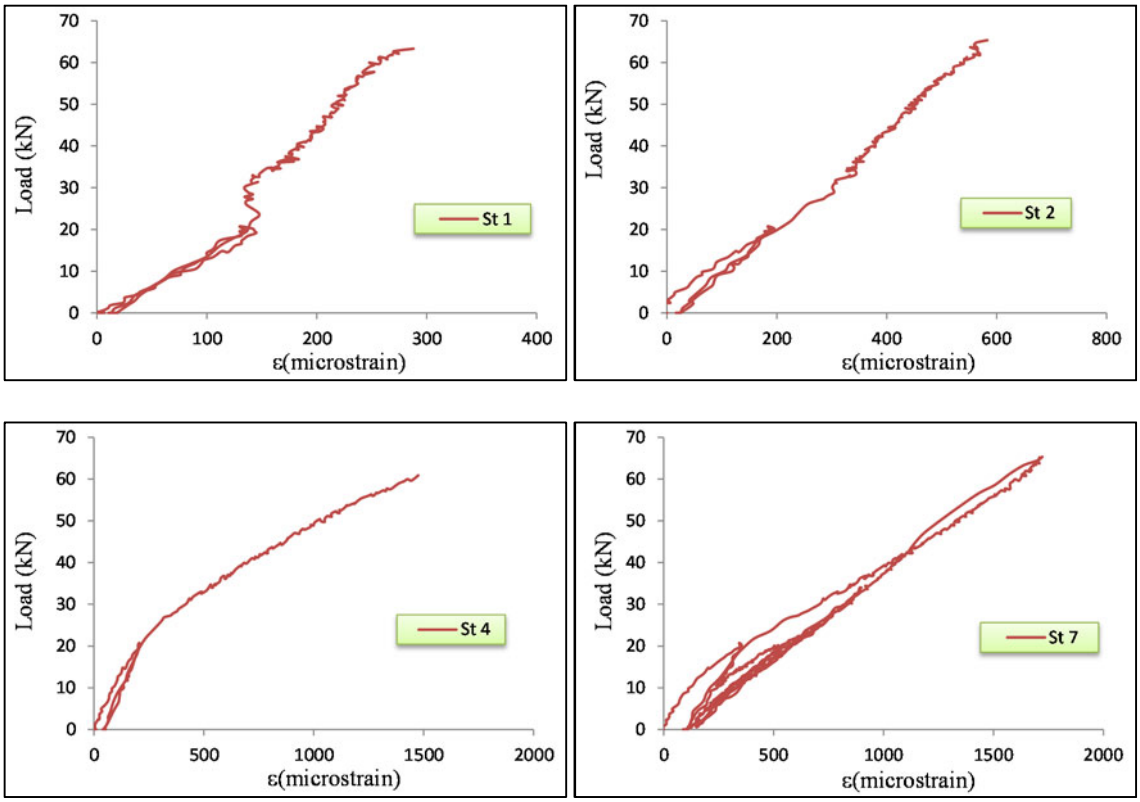

Figure F-18: Strain gauge readings of internal spliced bar – LC27-D16-S

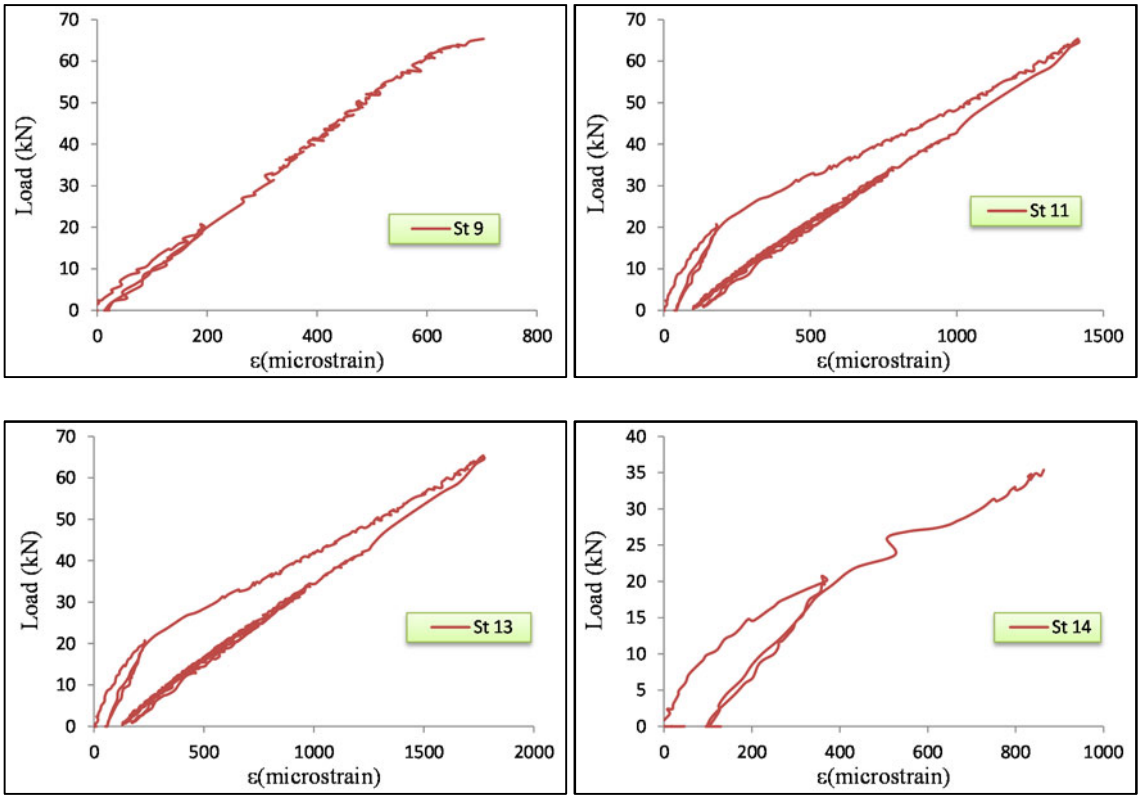

Figure F-19: Strain gauge readings of external spliced bar – LC27-D16-S

F.1.11 BEAM LC27-D12-PTMS1

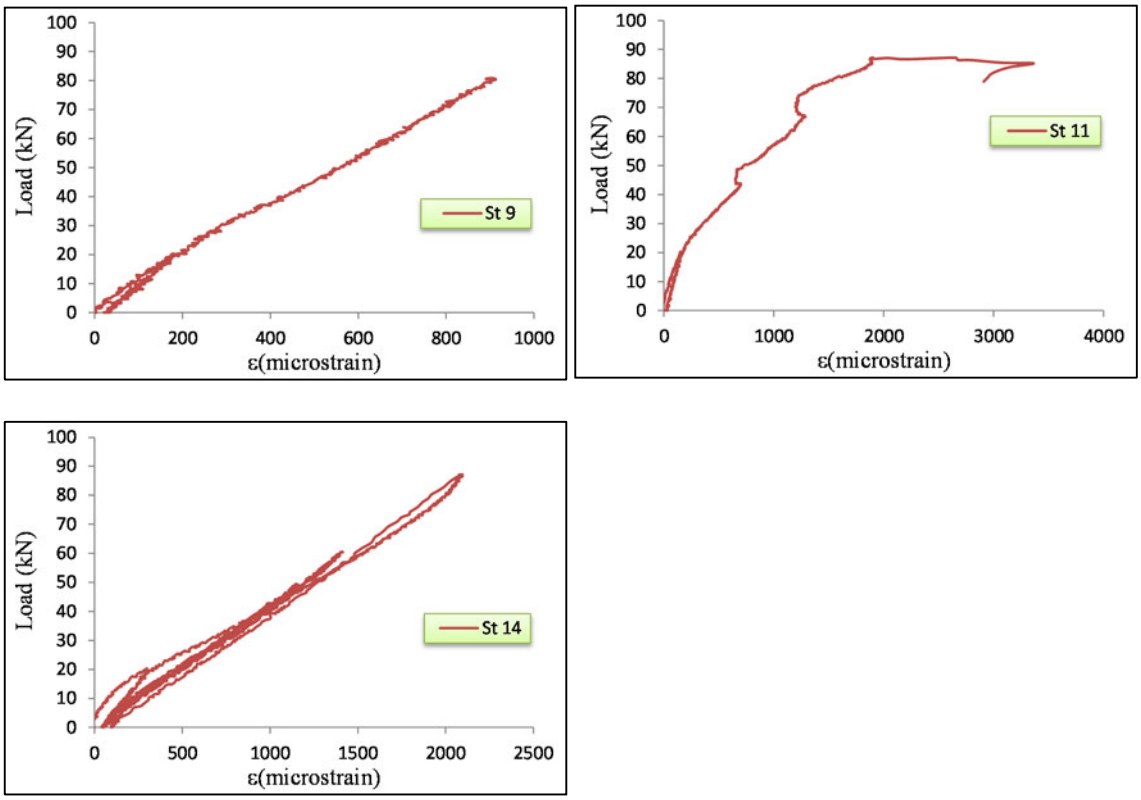

Figure F-20: Strain gauge readings of external spliced bar – LC27-D16-PTMS1

F.1.12 BEAM LC27-D12-PTMS2

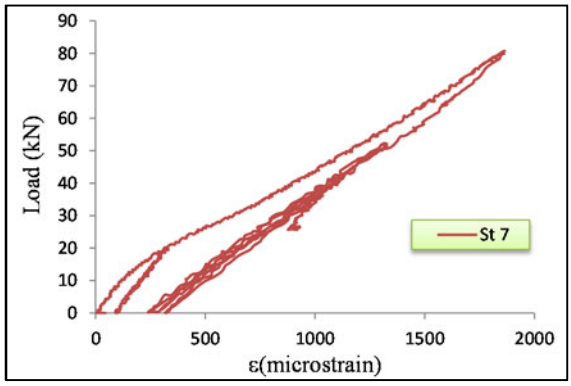

Figure F-21: Strain gauge readings of internal spliced bar – LC27-D16-PTMS2

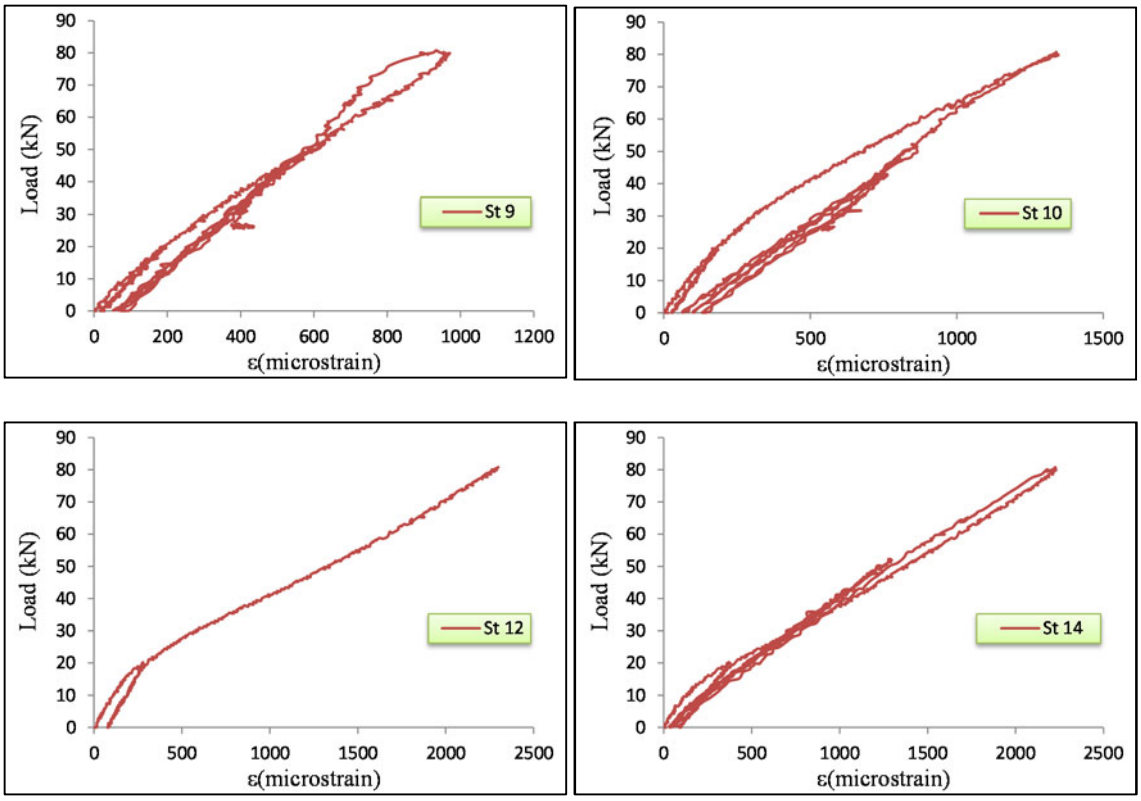

Figure F-22: Strain gauge readings of external spliced bar – LC27-D16-PTMS2

F.2 MEASURED LOAD-TOTAL SLIP CURVES

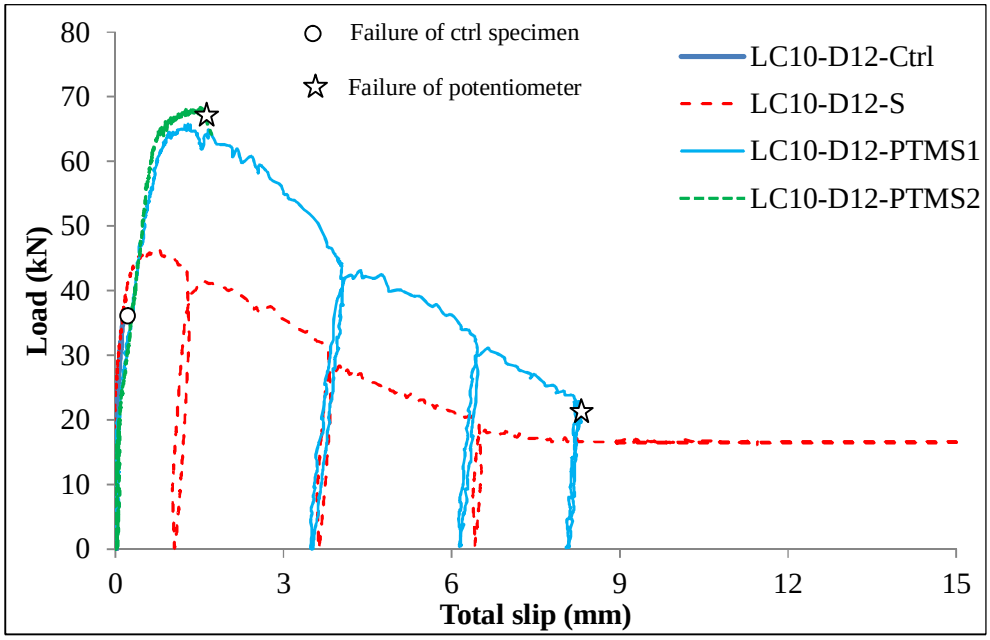

Figure F-23: Load-total slip curves of specimens in Group I

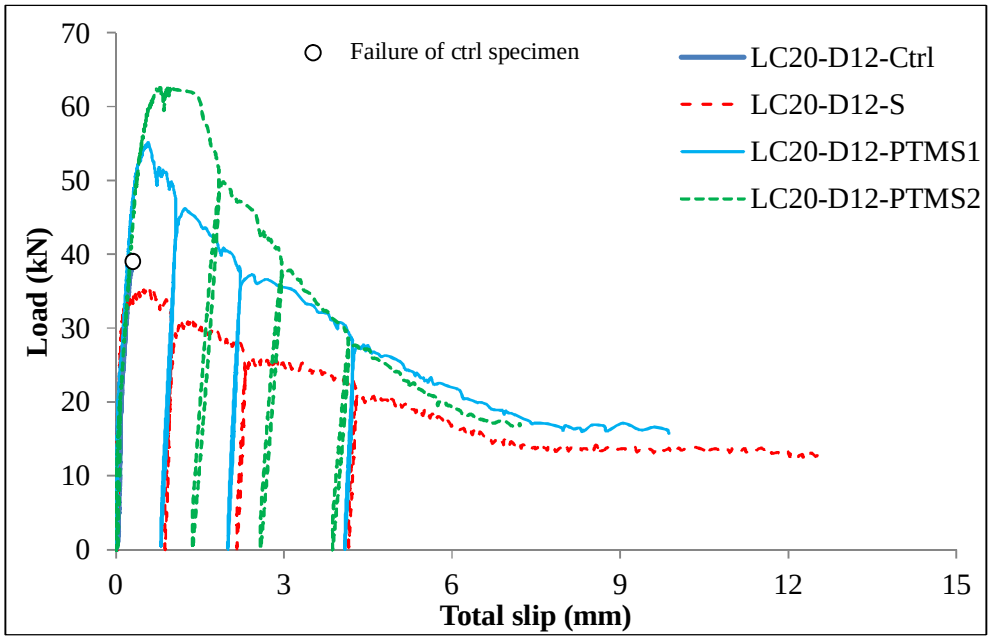

Figure F-24: Load-total slip curves of specimens in Group II

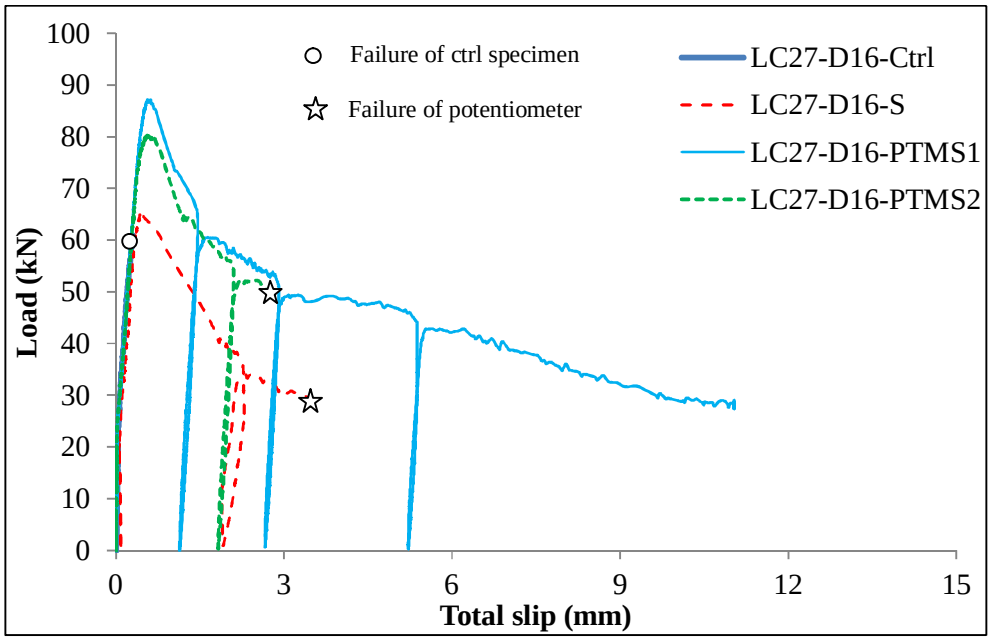

Figure F-25: Load-total slip curves of specimens in Group III

F.3 ACTUAL BOND STRESS - PURE SLIP RELATIONSHIPS

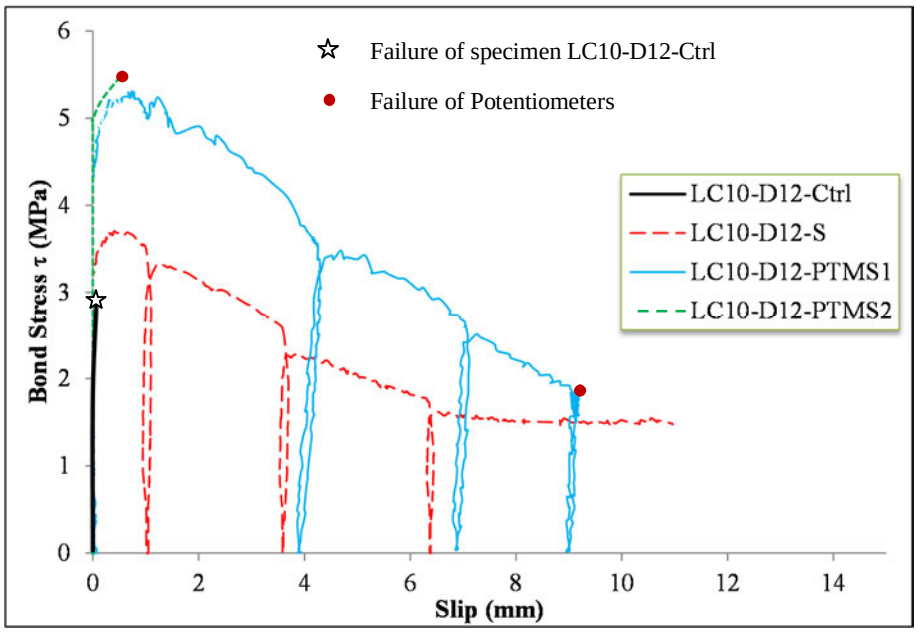

Figure F-26: Average bond stress-slip response of specimens in Group I

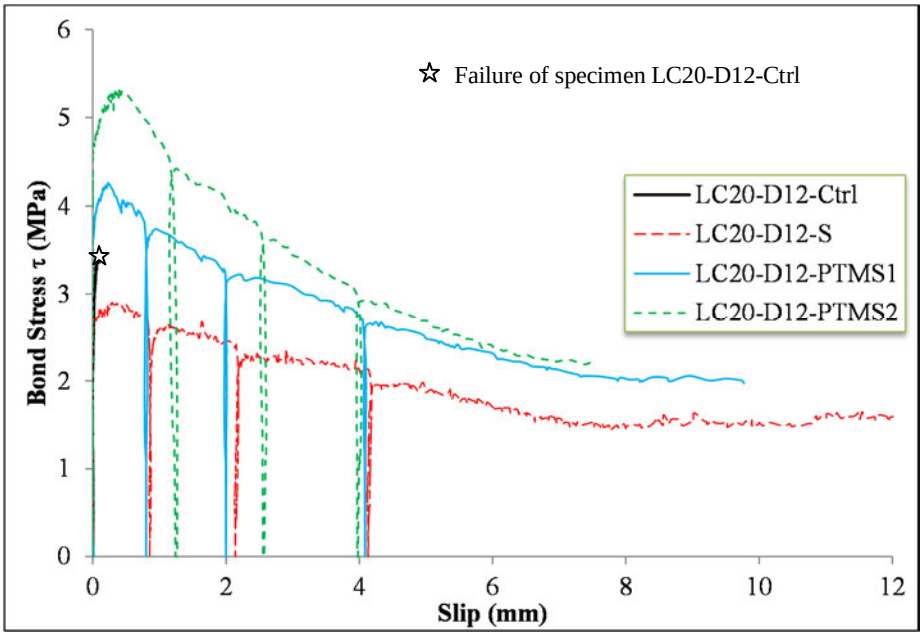

Figure F-27: Average bond stress-slip response of specimens in Group II

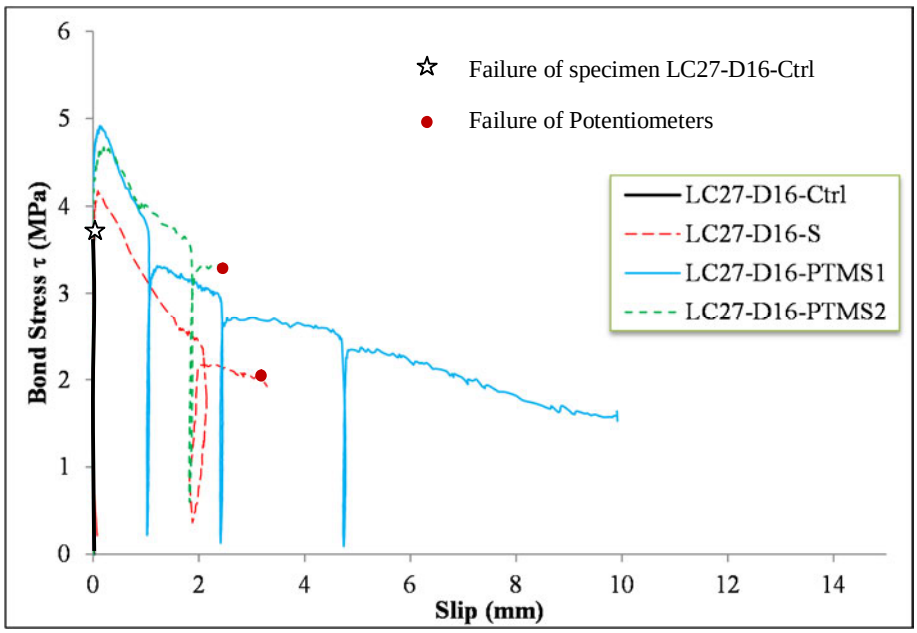

Figure F-28: Average bond stress-slip response of specimens in Group III

Appendix G

ABAQUS MODELLING

G.1 MESHING ELEMENTS

Different elements are available in ABAQUS which can be used for modelling. Continuum elements are the most comprehensive as they can be used in nonlinear stress-displacement analyses and can take almost any shape. Moreover, these elements are available in two- and three-dimensional (2D & 3D) forms. In this study, the 2D quadrilateral continuum model elements are adequate for the modelling purpose, and as a result, they are used. The 2D elements are available in plane-strain or plane-stress elements. As the out-of plane dimension of the elements is somewhat small relative to the in-plane dimensions, the plane-stress theory is chosen; where out-of-plane normal and shear stresses are assumed zero.

The 2D quadrilateral continuum elements can be either four or eight circumferential nodded elements. The 4-node element can be used; however, the use of the element has to be treated carefully as in bending, it tends to suffer shear rather than bending deformations resulting in a stiffer response. This phenomenon is referred to as shear locking. To overcome this problem, ABAQUS has the option to use 4-node quadrilateral reduced integration elements such that the integration points along these elements are reduced to one mid-point. However, the use of very fine mesh is required to avoid numerical problems, referred to as hourglassing, where a zero-energy mode is created in the element along with unrealistic deformations under bending. Therefore, the 4-node quadrilateral elements are disregarded.

On the other hand, the 8-node quadrilateral elements, also known as quadratic or second order elements, normally obtain displacements away from the nodes using quadratic interpolation and as a result the shear locking effect is eliminated. These elements are also available in either full or reduced integration forms referred to as CPS8 and CPS8R, respectively, see Figure G-1. The CPS8 has an advantage over the CPS8R in which it has more integration points which improves the accuracy of the results. The shear locking problem with the 8-node element is typically not an issue to start with and does not appear unless very coarse meshes are used. In line with the previous studies and based on the results of the FE analyses, it is found that the CPS8 element is a suitable element for the modelling and as a result it is adopted. In few cases, however, the use of CPS8 caused divergence problems. This issue is solved by using the CPS8R element. The specimens where the CPS8R element is used are clearly stated during modelling.

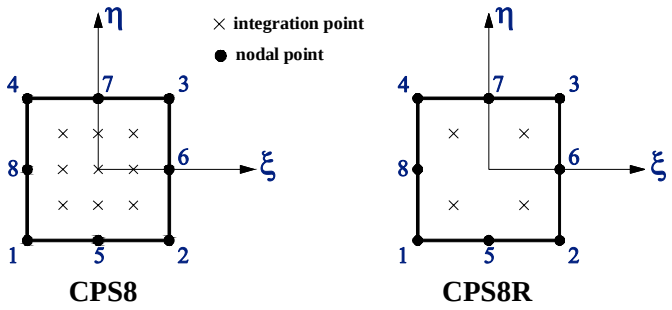

Figure G-1: CPS8 and CPS8R quadrilateral continuum elements

G.2 REINFORCEMENT

Reinforcement in ABAQUS can be defined by two methods in continuum 2D plane-stress elements. In the first method, truss elements can be used as external reinforcement. Those elements are typically hosted in the continuum elements with predefined translation degrees of freedom at the connected nodes. Alternatively, reinforcement can be provided by means of rebars, which are one-dimensional strain theory elements defined as embedded elements in oriented surfaces. Rebars can be defined singly or as layers. A reinforcement layer is treated as a smeared layer within the volume of the element, with a constant thickness equal to the area of each rebar divided by the rebar spacing. Rebars are typically used with metal plasticity models to describe the behaviour of the rebar material and are superposed on a mesh of standard element types used to model the concrete. With this modelling approach, the concrete behaviour is considered independently of the rebar. Effects associated with the rebar/concrete interface, such as bond slip and dowel action, are modelled approximately by introducing some “tension stiffening” into the concrete modelling to simulate load transfer across cracks through the rebar. Details regarding tension stiffening are provided below.

Defining the rebar can be tedious in complex problems, but it is important that this is done accurately since it may cause the analysis to fail due to lack of reinforcement in key regions of a

model (ABAQUS, inc 2004). It should be noted that both approaches are adopted in the modelling process of this study as will be explained later.

G.3 CONCRETE

The smeared crack concrete model in ABAQUS provides a general capability of modelling concrete in all types of structures. Also, it can be used to model plain as well as reinforced concrete subjected to essentially monotonic straining at low confining pressures, Kupfer and Gerstle (1973). The reduction in stiffness due to shear cracking can be taken into consideration in the model. The concrete model is a smeared crack model such that it does not physically track individual macro cracks. The effect of a crack is indirectly accounted for by its influence on the stress and material stiffness. Once a crack occurs, it is allowed to open and close without any remaining strains resulting in a reduction in the elastic stiffness; a reason why the model is referred to as a damaged elasticity model. The concrete model is presented in the following

- **Cracking**

Cracking and post-cracking are the most important aspects of a concrete model. Cracking occurs when the stress in the biaxial state reaches a crack detection surface (failure surface), as shown in Figure G-2. The characteristics of the failure surface should be carefully considered to control the cracking occurring in the member.

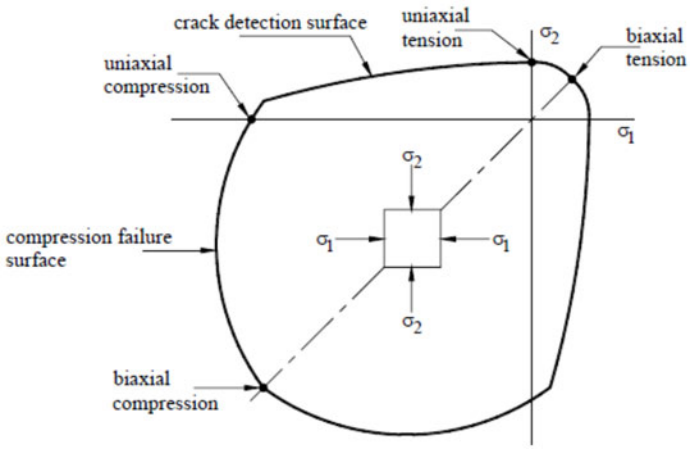

Figure G-2: Yield and failure surfaces “crack detection surface” in plane stress

The shape of the failure surface of the concrete model in ABAQUS is controlled using the command *FAILURE RATIO. Four parameters are defined as detailed below:

*Failure ratio

$\alpha 1$, $\alpha 2$, $\alpha 3$, $\alpha 4$

where

- $\alpha 1$ = is the ratio of the ultimate biaxial compressive stress to the uniaxial compressive ultimate stress
- $\alpha 2$ = is the absolute value of the ratio of uniaxial tensile stress at failure to the uniaxial compressive stress at failure.
- $\alpha 3$ = is the ratio of the magnitude of a principal component of plastic strain at ultimate stress in biaxial compression to the plastic strain at ultimate stress in uniaxial compression
- $\alpha 4$ = is the ratio of the tensile principal stress value at cracking in plane stress, when the other nonzero principal stress component is the ultimate compressive stress value, to the tensile cracking stress under uniaxial tension.

The post-cracking behaviour is described by a tension stiffening model in the sense that a concrete softening relationship is to be defined. The introduction of proper tension stiffening into the model reduces mesh sensitivity, Crisfield (1986). Tension stiffening is available in ABAQUS in two models, as shown in Figure G-3. One model has a post-failure stress-strain relation, while the other has a stress-crack opening relationship using a fracture energy cracking criterion. It is known that the first model may lead to a divergence problems and it is very sensitive to mesh sizes and distribution of cracks along the specimen, (ABAQUS, Inc 2004). If the cracks are distributed uniformly along the concrete member length, the mesh size would not be of a concern in this model. The latter method relies on brittle fracture concepts to define the energy required to open a unit area of crack as a material parameter, Hillerborg et al. (1976). In general, this method is adopted to allay the unreasonable mesh sensitivity concern for many practical purposes. The stress-strain method is more appropriate for reinforced concrete structures in which there is a significant amount of reinforcement, while the fracture energy approach is usually more appropriate when analysing plain concrete or lightly reinforced structures. Many trials showed that the first method leads to more stable solutions in most of the test specimens, and as a result, it is used in this study.

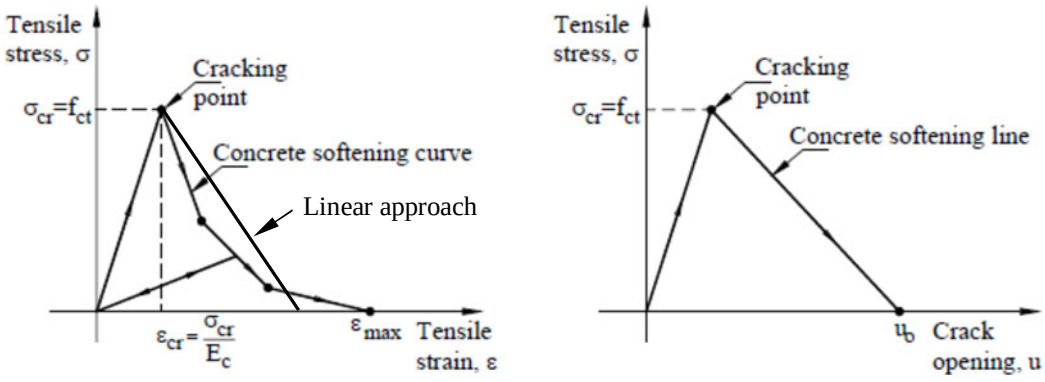

Figure G-3: Concrete softening models (ABAQUS, Inc 2004)

The selection of an appropriate tension stiffening model is not an easy task and usually has an effect on the accuracy of the results. As a starting point, it is suggested in the ABAQUS manual that, when modelling heavily reinforced sections, stress across the crack be reduced to zero at a total strain of about 10 times the strain at failure Hibbit et al. (1995). Previous studies (such as Gilbert and Warner 1978; Kolleger and Mehlhorn 1987; Lin and Scordelis 1975), however, have used different values for ultimate tensile strain, ranging from about 6 to 20 times the strain at first cracking. In the studied case, it is found that a linear softening model with a strain at stress=0 equal 10 times of that at first cracking (default input in ABAQUS) provides an accurate representation of the response in the small scale beams. In the medium scale beams, however, this value is found to be 15 times the strain at first cracking.

- **Compression**

The concrete model in compression requires the definition of a uniaxial compression stress-plastic strain relationship for concrete. This relationship is incorporated in concepts of isotropic hardening and associated flow to determine the response and compressive failure surface in plane stress, as explained previously. In this regard, the Eurocode 2 (2004) uniaxial compressive concrete model is adopted in the FE analyses, as shown in Figure G-4. However, the modulus of elasticity of the ACI 318-08 (2008) is used, for the reasons mentioned in Chapter 3.

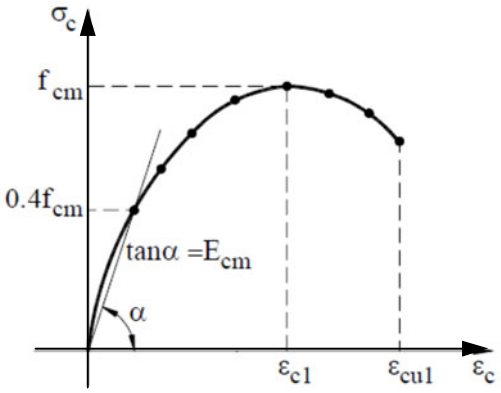

$\sigma_c = f_{cm}\frac{k\eta-\eta^2}{1+(k-2)\eta}$: $\eta = \varepsilon_c/\varepsilon_{c1}$

$\varepsilon_{c1}=0.0007 f_{cm}^{0.31} < 0.0028$

$k=1.05E_{cm}\,\varepsilon_{c1}/f_{cm}$

$E_{cm} = 22(0.1f_{cm})^{0.3} \times 0.9$

$\varepsilon_{cu1}=0.0035$ for $f_{cm} < 58$ MPa

Figure G-4: EC2 Uniaxial compressive stress-strain concrete model (CEN, 2004)

- **Shear Stiffness**

ABAQUS offers the option to reduce the shear stiffness of the concrete member due to cracking by multiplying the elastic shear modulus (G) of untracked concrete by a reduction shear retention factor (ρ). ρ is assumed to have a linear relationship with the strain in a crack and is given by the following equation:

$$\rho = (1 - \varepsilon/\varepsilon_{max}), for\ \varepsilon < \varepsilon_{max}; and\ \rho = 0, for\ \varepsilon \geq \varepsilon_{max} \quad \text{(G-1)}$$

where ε_{max} is the maximum strain developing across a crack

Due to the fact that most of the tested beams fail prematurely at the elastic stage, the developed cracks are considered to have no effect on the shear deformations. Since it does not affect the results, full shear retention is used in the model (ρ=1).

G.4 CONNECTION ELEMENTS

Previous researchers such as Popov (1984), Soroushian et al. (1991) and Reyes (1999) have suggested that the behaviour of reinforcing bars embedded in concrete can be idealised using one-dimensional multi-spring model such that each spring represents the local bond resistance on the bar surface, as shown in Figure G-5. This modelling technique has not only been implemented in ABAQUS FE models, as mentioned earlier, to simulate the bond problem, but also it was used in many other analyses (for example Reyes and Pincheira (1999), Barin and Pincheira (2002), Melek and Wallace (2003), Cho and Pincheira (2004), among others) to capture rotations due to slip of splices at a column base.

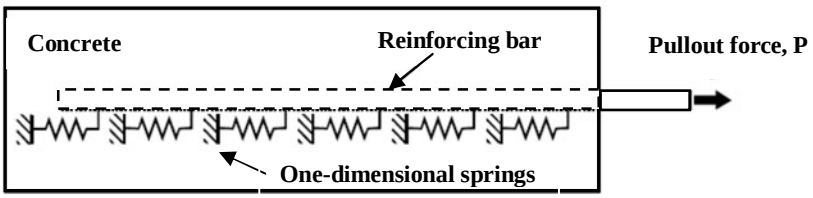

Figure G-5: Uniaxial multi-spring model isolated anchored bar (Soroushian et al., 1991)

ABAQUS offers one-dimensional spring-type elements to simulate the connection between concrete and external bars (truss elements). The SPRING element introduces stiffness between two degrees of freedom without introducing an associated mass. The spring behaviour can be linear or nonlinear. The nonlinear spring behaviour is defined by giving pairs of force–relative displacement values, as seen from Figure G-6. These values should be given in ascending order of relative displacement and should be provided over a sufficiently wide range of relative displacement values so that the behaviour is defined properly. ABAQUS assumes that the force remains constant (which results in zero stiffness) outside the range given. It should be mentioned that a connector-type element is also available in ABAQUS and can be used as an alternative (see ABAQUS manual).

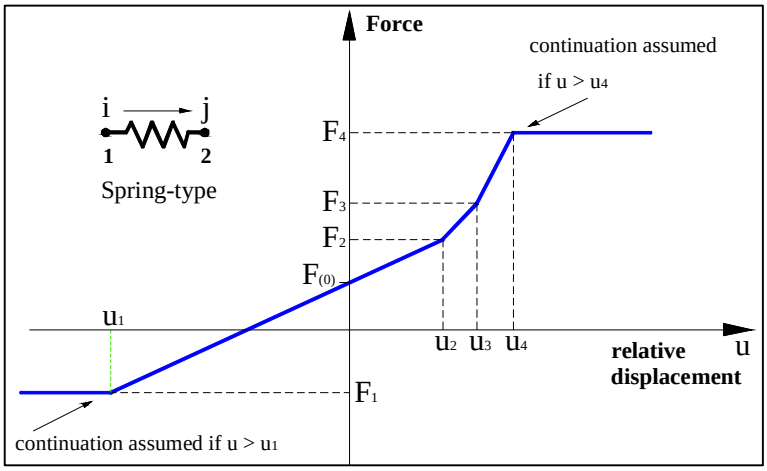

Figure G-6: Nonlinear spring force–relative displacement relationship (ABAQUS, Inc. 2004)

G.5 NONLINEAR ANALYSIS

Due to material nonlinearity and nonlinear behaviour of connection elements in the splice zone, nonlinear analysis is required. Moreover, the development of cracks, caused by the excessive deformations of the connection elements, results in a sudden release of strain energy leading to kinetic effects. Consequently, the analysis becomes highly unstable, especially if many nonlinear connection elements are used.

ABAQUS offers special algorithms to deal with the high nonlinearity. Nevertheless, those solutions have some limitations. Among the available algorithms are the modified RIKS, GENERAL STATIC and STABLIZE algorithms. These were investigated by performing numerous analyses. The load in these analyses is applied in a displacement control fashion at the loading points. It was found that the general static procedure (see ABAQUS manual for more details) provides more stable solutions during concrete cracking, compared to the other loading procedures that did not converge. Therefore, this procedure is adopted in the nonlinear analysis.

Appendix H

JOINT DETAILING

H.1 KUANG AND WONG (2005)

Table H-1: Concrete compressive strength of test units and level of axial load

	Specimen Designation	Failure mode	f'_c MPa	$\frac{P}{A_g f'_c}$
Kuang and Wong (2005)	BS-L	J	30.8	0.16
	BS-L-LS	J	31.0	0.16
	BS-U	J	33.3	0.15

Note
(1) Beam size: 260 × 450 mm;
main bars: 3T20 at top and bottom.
(2) Column size: 300 × 300 mm;
main bars: 4T25;
lap length in BS-L-LS = 935 mm.
(3) Stirrups: T10; 90° hook with 8ϕ
extension.

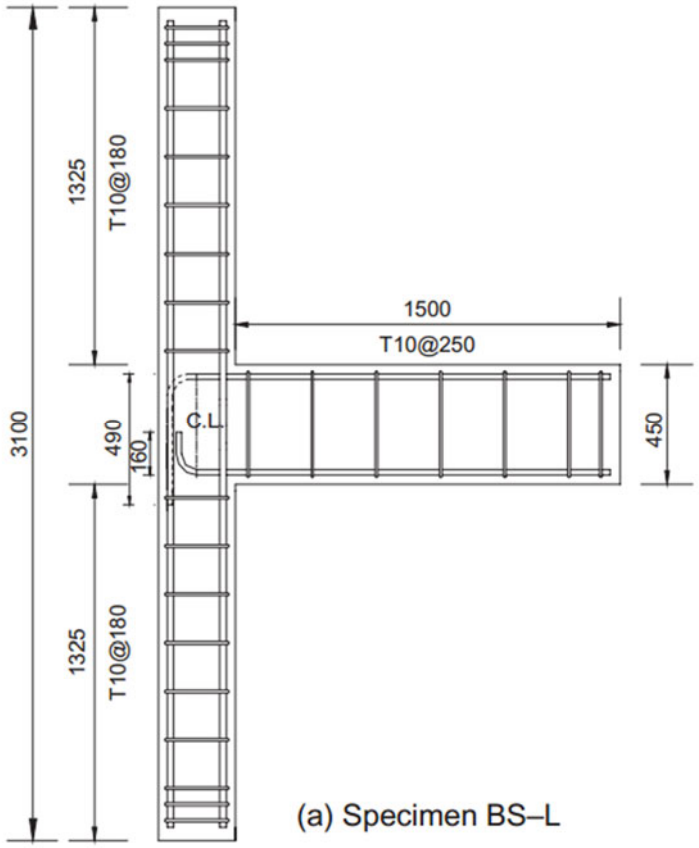

Figure H-1: Test units BS-L: dimensions and reinforcement details (Kuang and Wong, 2005)

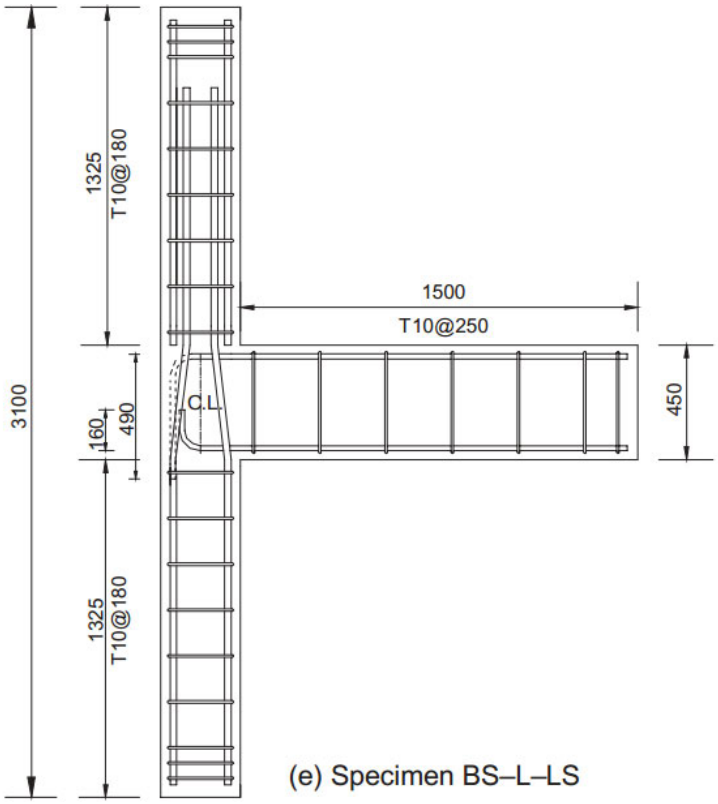

Figure H-2: Test units BS-L-LS: dimensions and reinforcement details (Kuang and Wong, 2005)

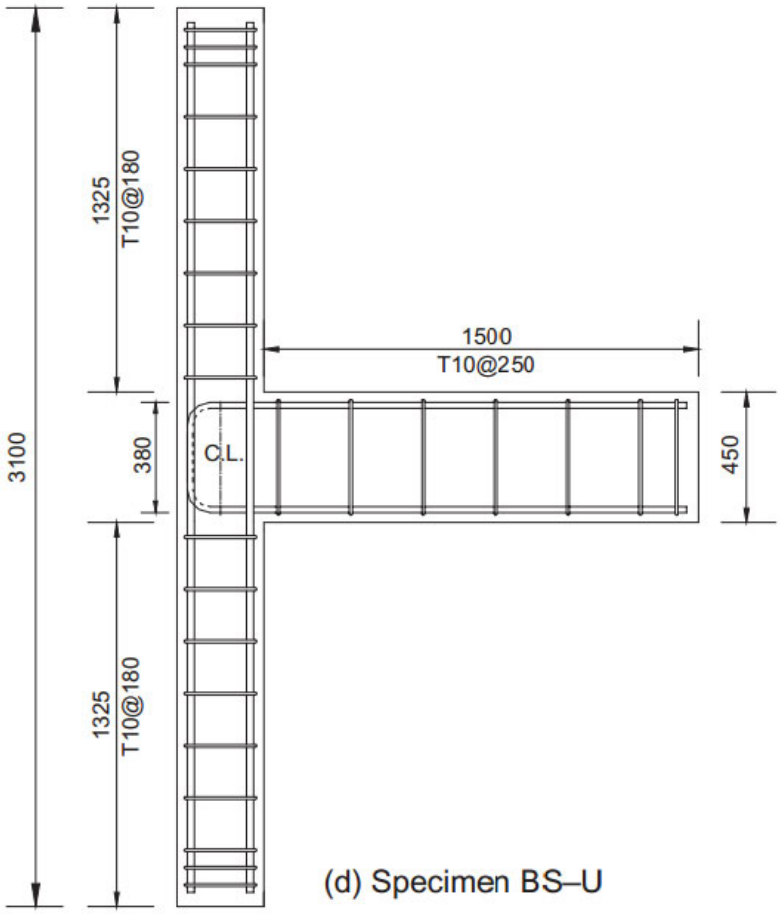

Figure H-3: Test units BS-U: dimensions and reinforcement details (Kuang and Wong, 2005)

H.2 PANTELIDES ET AL. (2002)

Table H-2: Concrete compressive strength of test units and level of axial load

	Specimen	Failure	f'_c	$\frac{P}{A_g f'_c}$
	Designation	mode	MPa	
Pantelides et al. (2002)	3	J	34	0.1
	4	J	31.6	0.25
	5	J	31.7	0.1
	6	J	31	0.25

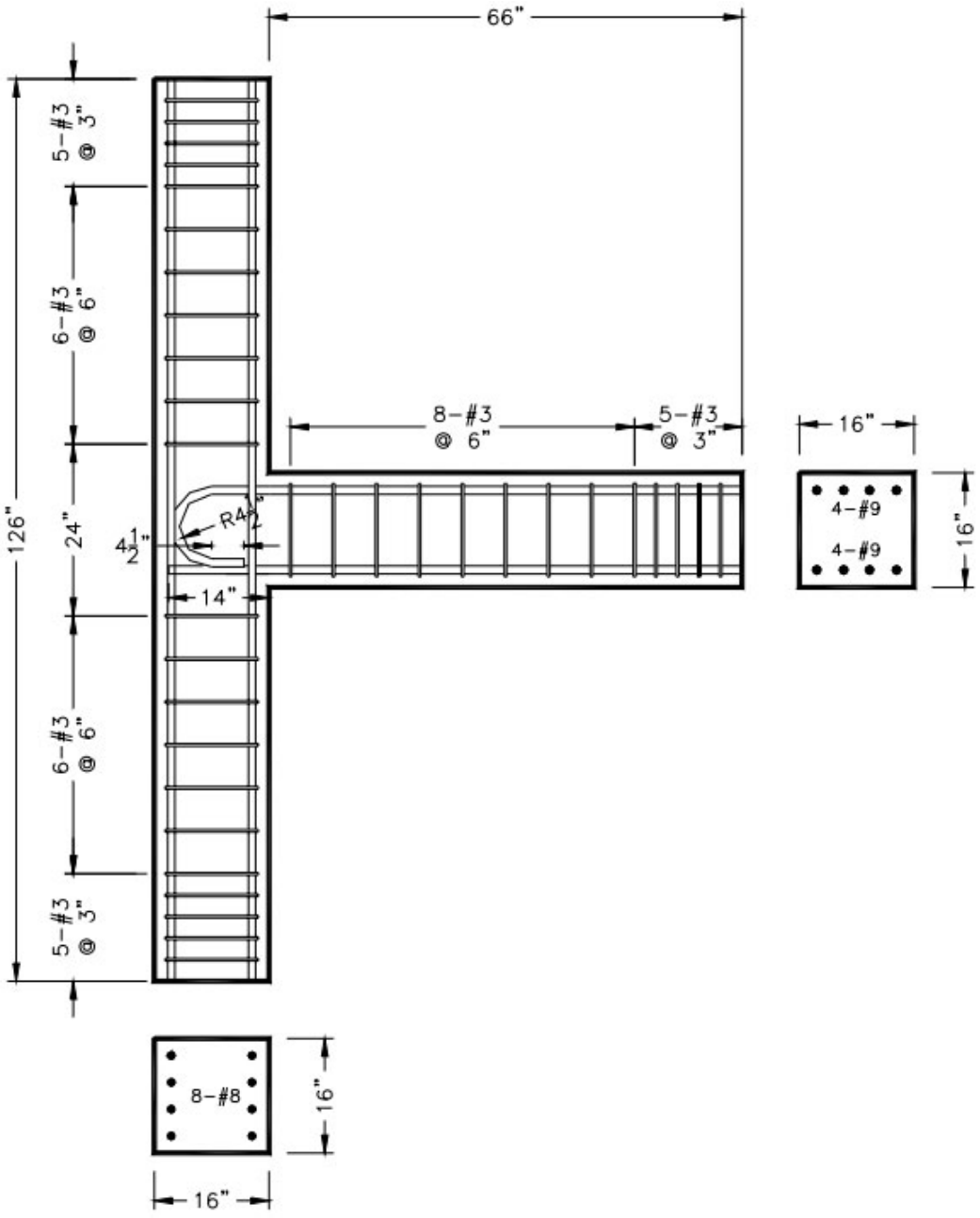

Figure H-4: Test units 3 and 4: dimensions and reinforcement details (Pantelides et al., 2002)

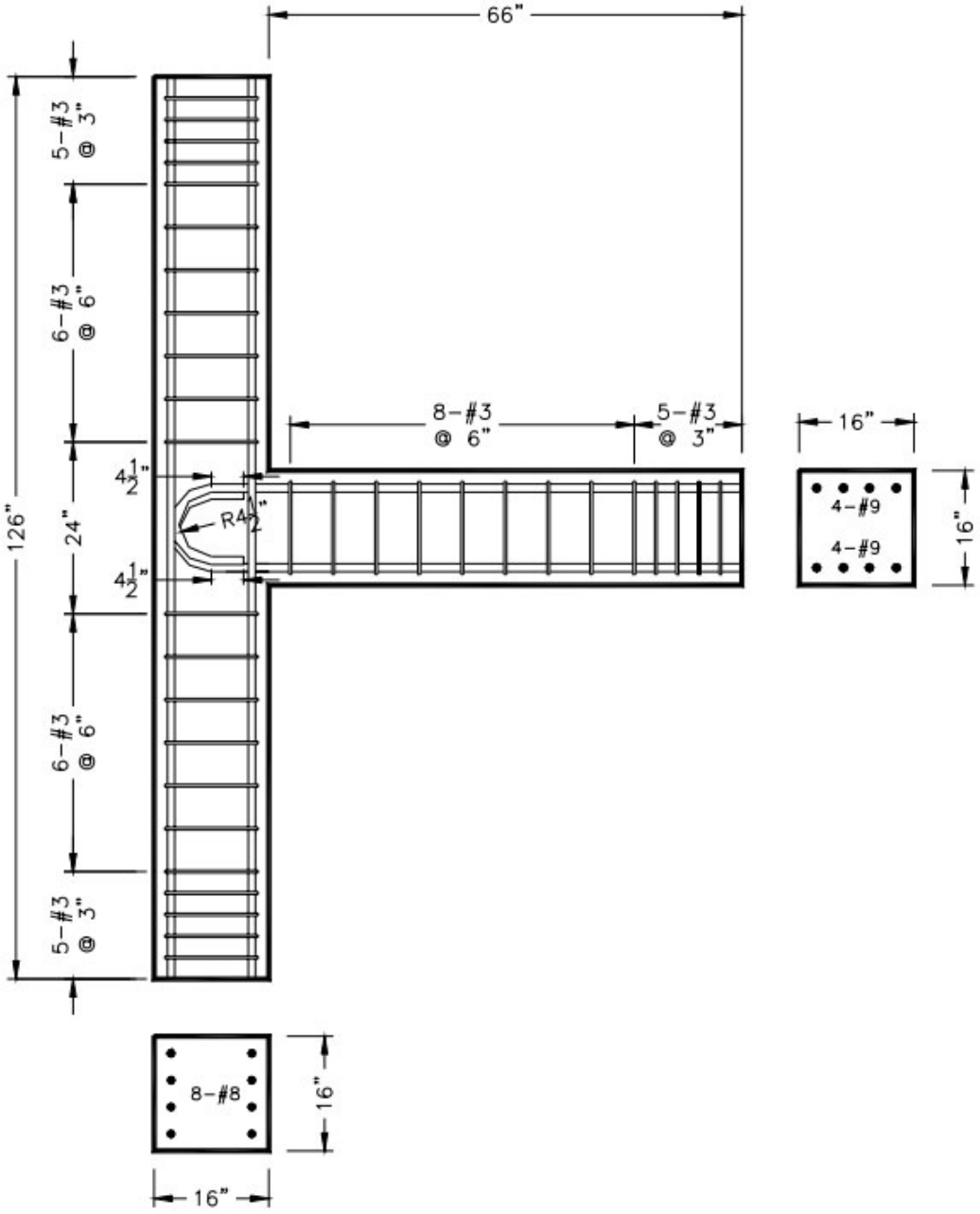

Figure H-5: Test units 5 and 6: dimensions and reinforcement details (Pantelides et al., 2002)

H.3 CLYDE ET AL., (2000)

Table H-3: Concrete compressive strength of test units and level of axial load

	Specimen Designation	Failure mode	f'_c MPa	$\frac{P}{A_g f'_c}$
Clyde et al. (2000)	2	J	46.2	0.1
	6	J	40.1	0.1
	4	J	41	0.25
	5	J	37	0.25

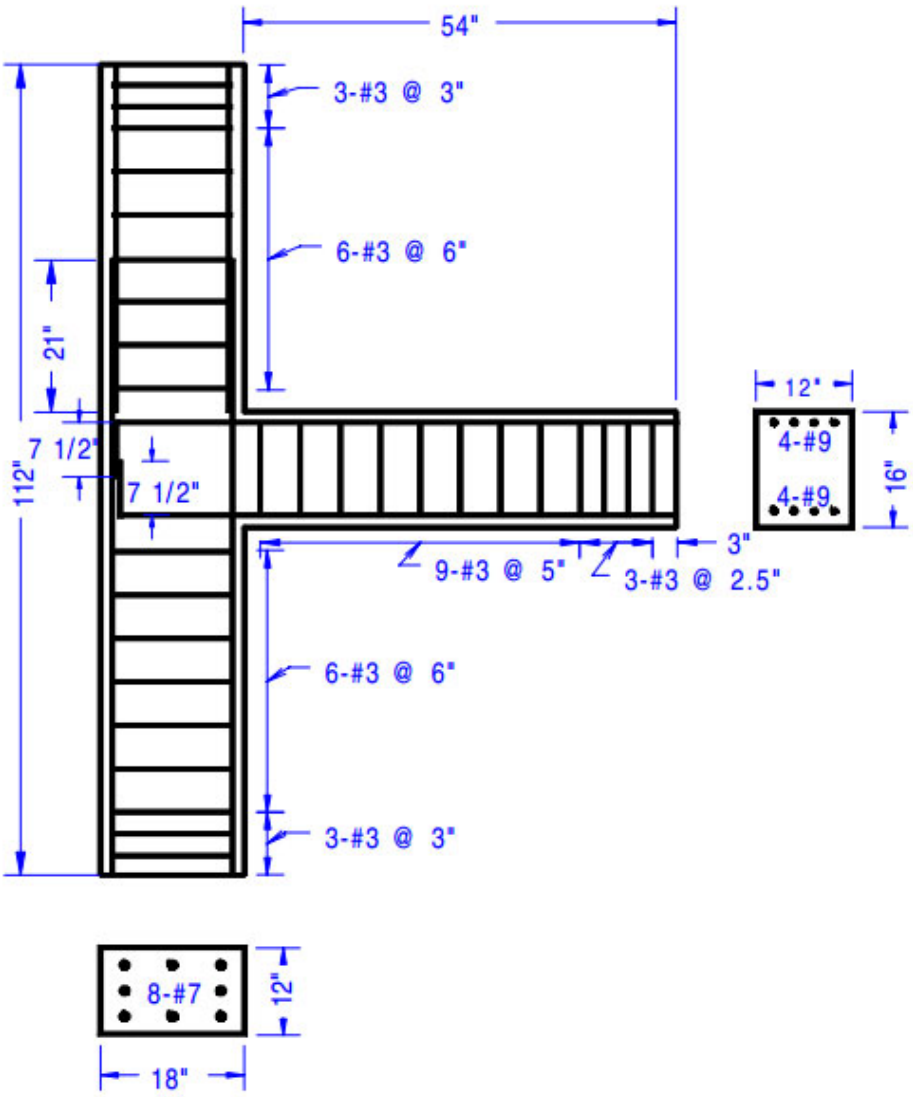

Figure H-6: Specimen dimensions and reinforcement details (Clyde et al., 2000)

Appendix I

DRAIN 2DX - CODES

I.1 STATIC ANALYSIS – JOINT JC-1PTMS (UNITS: kN.m)

```
*STARTXX
  YHPhD12         0 1 0 0
*NODECOORDS
C     1010        0.       0.
C     1110        0.     0.575
C     1210        0.     0.975
C     1310        0.     0.975
C     2010        0.     1.175
C     2014        0.     1.175
C     2018      0.13     1.175
C     2022      0.13     1.175
C     2026      1.58     1.175
C     2030      1.78     1.175
C     2110        0.     1.375
C     2210        0.     1.375
C     2310        0.     1.375
C     2410        0.     1.777
C     3010        0.      2.35
*RESTRAINTS
S 110      1010      1010        10
S 100      3010      3010        10
*ELEMENTGROUP
   15    1    0        0.00063         GROUP 1: 1ST FLOOR COLUMNS
    1    1    1    0    0    0    0    0    1
    5    2       0.5       100
10000     0.0005
```

```
15000     0.001
20000     0.0016
27000     0.0025
19550     0.0035
2300      0.000076
100       0.0007
2    100
555000    0.00231
677000    0.1
  13         1
 0.1       0.000201  S01
 0.1       0.000201  S01
 0.1       0.000201  S01
 0.0       0.000201  S01
 0.0       0.000201  S01
-0.1       0.000201  S01
-0.1       0.000201  S01
-0.1       0.000201  S01
 0.104     0.01352   C01
 0.052     0.01352   C01
 0.0       0.01352   C01
-0.052     0.01352   C01
-0.104     0.01352   C01
   1
 1.0       F01
   1     1010      1110       100    1
*ELEMENTGROUP
  15    1    0        0.00063          GROUP 2: 1st FLOOR COLUMNS
   1    1    1    0    0    0    0    0    1
   5    2       0.5       100
    10000   0.00043
    17610   0.00089
    26190   0.00165
    36450   0.00387
    27250   0.02074
    3000    0.000076
    100     0.00070
2    100
555000    0.00231
677000    0.1
  13         1
 0.1       0.000201  S01
 0.1       0.000201  S01
 0.1       0.000201  S01
 0.0       0.000201  S01
 0.0       0.000201  S01
-0.1       0.000201  S01
-0.1       0.000201  S01
-0.1       0.000201  S01
 0.104     0.01352   C01
 0.052     0.01352   C01
 0.0       0.01352   C01
-0.052     0.01352   C01
-0.104     0.01352   C01
   3
 0.1       F01
 0.8       F01
```

```
 0.1      F01
   1     1110     1210      100    1
   2     2310     2410      100    1
*ELEMENTGROUP
  15    1    0       0.00063         GROUP 2: 2nd FLOOR COLUMNS
   1    1    1    0    0    0    0    0    1
   5    2       0.5       100
10000     0.00050
15000     0.001
20000     0.0016
27000     0.0025
19550     0.0035
2300      0.000076
100       0.0007
2    100
555000    0.00231
677000    0.1
  09         1
 0.1       0.000201  S01
 0.1       0.000201  S01
-0.1       0.000201  S01
-0.1       0.000201  S01
 0.104     0.01352   C01
 0.052     0.01352   C01
 0.0       0.01352   C01
-0.052     0.01352   C01
-0.104     0.01352   C01
   1
 1.0       F01
   1     2410     3010      600    1
*ELEMENTGROUP
  15    1    0       0.00063         GROUP 4: Beam elements
   1    1    1    0    0    0    0    0    1
   5    2       0.5       100
10000     0.00050
15000     0.001
20000     0.0016
27000     0.0025
19550     0.0035
2300      0.000076
100       0.0007
2    100
555000    0.00231
677000    0.1
  14         1
 0.155     0.000201  S01
 0.155     0.000201  S01
 0.155     0.000201  S01
 0.155     0.000201  S01
-0.155     0.000201  S01
-0.155     0.000201  S01
-0.155     0.000201  S01
-0.155     0.000201  S01
 0.16675   0.017342  C01
 0.1       0.017342  C01
 0.03335   0.017342  C01
-0.03335   0.017342  C01
```

```
 -0.1       0.017342  C01
 -0.16675   0.017342  C01
   3
  0.1       F01
  0.8       F01
  0.1       F01
   1     2022      2026        4    1
   2     2026      2030        4    1
*ELEMENTGROUP
   2    1    0        0.00439          stiff
   1    0    1
   1  99000000     0.050     0.104  1.111208   4.   4.   2.    9.0867 0.15 0.01
   1    1    999.54    999.55
   1     1310      2010       700    1    0    1    1
   2     2010      2110       100    1    0    1    1
   3     2014      2018         4    1    0    1    1
*ELEMENTGROUP
  10    1    0        0.00063          GROUP 6: R Spring
   6
   1   58.9E04     0.000       53.       53.       1.0    3    4    1
    -1.0      -1.0
   2   8.00E03     0.000       60.       60.       1.0    3    4    1
    -1.0      -1.0
   3   1.85E03      -1.1       27.       27.       1.0    3    4    1
    -1.0      -1.0
   4   8.47E04     0.016     144.5     144.5       1.0    3    4    1
    -0.5      -0.5
   5   12.2E03     -0.05       73.       73.       1.0    3    4    1
    -0.5      -0.5
   6    4.4E04      0.21     144.5     144.5       1.0    3    4    1
    -1.0      -1.0
   1     2010      2014        04    1
   2     2010      2014        04    2
   3     2010      2014        04    3
   4     2018      2022        04    4
   5     2110      2310       200    5
   6     1210      1310       100    6
*ELEMENTGROUP
  10    1    0        0.00063          GROUP 7: H Spring
   4
   1    1.0E15      0.90    1.0E15    1.0E15       1.0    1    1
   2   1.25E05      0.00      22.6      22.6       1.0    1    1
   3   1.70E04      0.00      25.5      25.5       1.0    1    1
   4   3.95E03      -1.1      11.5      11.5       1.0    1    1
   1     2010      2014        04    1
   2     2018      2022        04    1
   3     2110      2310       200    2
   4     2110      2310       200    3
   5     2110      2310       200    4
   6     1210      1310       100    2
   7     1210      1310       100    3
   8     1210      1310       100    4
*ELEMENTGROUP
  10    1    0        0.00063          GROUP 8: V Spring
   1
   1    1.0E15      0.90    1.0E15    1.0E15       1.0    2    1
   1     2010      2014        04    1
```

```
   2     2018     2022      04   1
   3     2110     2310      200   1
   4     1210     1310      100   1
*RESULTS
NSD   001     2030     2030       0
E     001   4   1   1   1
*NODALOAD
 NLD                          Permanent Loads
S       0  -150.00       0     3010     3010       00
*NODALOAD
 HORZ                          HORIZONTAL LOADS-PUSHOVER
S     0.0       2       0     2026     2026       0
*PARAMETERS
F         0.03
OS  0       0   1   0   0
*STAT                         Static analysis
N    HORZ       1.
D    2026     1010    2     0.001       0.1       100 1100
*STOP
```

I.2 CYCLIC ANALYSIS – JOINT JC-1PTMS (UNITS: kN.m)

```
*STARTXX
 YHPhD12         0 1 0 0
*NODECOORDS
C    1010       0.       0.
C    1110       0.    0.575
C    1210       0.    0.975
C    1310       0.    0.975
C    2010       0.    1.175
C    2014       0.    1.175
C    2018     0.13    1.175
C    2022     0.13    1.175
C    2026     1.58    1.175
C    2030     1.78    1.175
C    2110       0.    1.375
C    2210       0.    1.375
C    2310       0.    1.375
C    2410       0.    1.777
C    3010       0.     2.35
*RESTRAINTS
S 110     1010     1010       10
S 100     3010     3010       10
S 020     2030     2030       00
*ELEMENTGROUP
  15   1   0       0.00063         GROUP 1: 1ST FLOOR COLUMNS
   1   1   1   0   0   0   0   0   1
   5   2      0.5       100
10000     0.0005
15000     0.001
20000     0.0016
27000     0.0025
19550     0.0035
2300      0.000076
100       0.0007
```

```
2    100
555000    0.00231
677000    0.1
  13         1
 0.1       0.000201  S01
 0.1       0.000201  S01
 0.1       0.000201  S01
 0.0       0.000201  S01
 0.0       0.000201  S01
-0.1       0.000201  S01
-0.1       0.000201  S01
-0.1       0.000201  S01
 0.104     0.01352   C01
 0.052     0.01352   C01
 0.0       0.01352   C01
-0.052     0.01352   C01
-0.104     0.01352   C01
   1
 1.0       F01
   1      1010      1110       100    1
*ELEMENTGROUP
  15    1    0        0.00063          GROUP 2: 1st FLOOR COLUMNS
   1    1    1    0    0    0    0    0    1
   5    2       0.5       100
    10000   0.00043
    17610   0.00089
    26190   0.00165
    36450   0.00387
    27250   0.02074
    3000    0.000076
    100     0.00070
2    100
555000    0.00231
677000    0.1
  13         1
 0.1       0.000201  S01
 0.1       0.000201  S01
 0.1       0.000201  S01
 0.0       0.000201  S01
 0.0       0.000201  S01
-0.1       0.000201  S01
-0.1       0.000201  S01
-0.1       0.000201  S01
 0.104     0.01352   C01
 0.052     0.01352   C01
 0.0       0.01352   C01
-0.052     0.01352   C01
-0.104     0.01352   C01
   3
 0.1       F01
 0.8       F01
 0.1       F01
   1      1110      1210       100    1
   2      2310      2410       100    1
*ELEMENTGROUP
  15    1    0        0.00063          GROUP 2: 2nd FLOOR COLUMNS
   1    1    1    0    0    0    0    0    1
```

```
   5   2       0.5       100
10000     0.00050
15000     0.001
20000     0.0016
27000     0.0025
19550     0.0035
2300      0.000076
100       0.0007
2    100
555000    0.00231
677000    0.1
  09          1
 0.1       0.000201  S01
 0.1       0.000201  S01
-0.1       0.000201  S01
-0.1       0.000201  S01
 0.104     0.01352   C01
 0.052     0.01352   C01
 0.0       0.01352   C01
-0.052     0.01352   C01
-0.104     0.01352   C01
   1
 1.0       F01
   1      2410      3010       600    1
*ELEMENTGROUP
  15    1    0        0.00063          GROUP 4: Beam elements
   1    1    1    0    0    0    0    0    1
   5    2       0.5       100
10000     0.00050
15000     0.001
20000     0.0016
27000     0.0025
19550     0.0035
2300      0.000076
100       0.0007
2    100
555000    0.00231
677000    0.1
  14          1
 0.155     0.000201  S01
 0.155     0.000201  S01
 0.155     0.000201  S01
 0.155     0.000201  S01
-0.155     0.000201  S01
-0.155     0.000201  S01
-0.155     0.000201  S01
-0.155     0.000201  S01
 0.16675   0.017342  C01
 0.1       0.017342  C01
 0.03335   0.017342  C01
-0.03335   0.017342  C01
-0.1       0.017342  C01
-0.16675   0.017342  C01
   3
 0.1       F01
 0.8       F01
 0.1       F01
```

```
   1     2022     2026       4   1
   2     2026     2030       4   1
*ELEMENTGROUP
   2   1   0       0.00439         stiff
   1   0   1
   1  99000000     0.050     0.104  1.111208   4.   4.   2.    9.0867 0.15 0.01
   1   1   999.54    999.55
   1     1310     2010      700   1   0   1   1
   2     2010     2110      100   1   0   1   1
   3     2014     2018       4   1   0   1   1
*ELEMENTGROUP
  10   1   0       0.00063         GROUP 6: R Spring
   6
   1   58.9E04     0.000      53.      53.      1.0   3   4   1
     3.0      3.0
   2   8.00E03     0.000      74.      74.      1.0   3   4   1
     3.0      3.0
   3   9.25E02     -1.01      13.      13.      1.0   3   1
   4   8.47E04     0.016     144.5     144.5      1.0   3   4   1
     15       15
   5   12.2E03     -0.05      73.      73.      1.0   3   4   1
     15       15
   6    4.4E04      0.21     144.5     144.5      1.0   3   4   1
     15       15
   1     2010     2014      04   1
   2     2010     2014      04   2
   3     2010     2014      04   3
   4     2018     2022      04   4
   5     2110     2310      200   5
   6     1210     1310      100   6
*ELEMENTGROUP
  10   1   0       0.00063         GROUP 7: V Spring
   4
   1    1.0E15      0.90    1.0E15    1.0E15      1.0   1   1
   2   1.25E05      0.00      22.6      22.6      1.0   1   1
   3   1.70E04      0.00      25.5      25.5      1.0   1   1
   4   3.95E03       0.0      11.5      11.5      1.0   1   1
   1     2010     2014      04   1
   2     2018     2022      04   1
   3     2110     2310      200   2
   4     2110     2310      200   3
   5     2110     2310      200   4
   6     1210     1310      100   2
   7     1210     1310      100   3
   8     1210     1310      100   4
*ELEMENTGROUP
  10   1   0       0.00063         GROUP 8: H Spring
   1
   1    1.0E15      0.90    1.0E15    1.0E15      1.0   2   1
   1     2010     2014      04   1
   2     2018     2022      04   1
   3     2110     2310      200   1
   4     1210     1310      100   1
*RESULTS
NSD   001     2030     2030       0
E     001   4   1   1   1
*NODALOAD
```

```
 NLD                              Permanent Loads
S       0  -150.00        0      3010      3010        00
*DISPREC
 D05          JC.txt     (F14.12)       Cyclic Analysis
90000     1    0    0         1         1 0.010           0.0
*PARAMETERS
F         0.001
OD        0         0    1         0    1         1    0         0    0         0
DC  1     0    0    0
DT   0.010
*DISN                             Dynamic analysis 01
900.0     90000     1
R     D05      1     1
D  1      2     1     2030      2030      00
*REST
*STOP
```

Appendix J

BANDIT DESIGN DETAILING

J.1 SUMMARY OF BUILDING DESIGN DETAILS

The geometry of the frame, as seen in Figure J-1 and Figure J-2, is as follows:

- Total height of the specimen: 6.87m
- Four square columns: 260mm section
- Two square slabs: 120mm thickness and 4.26m width
- Four beams per slab: 260mm width and 400mm thickness for beams in X-directions, and 300 mm thickness for beams in Y-direction

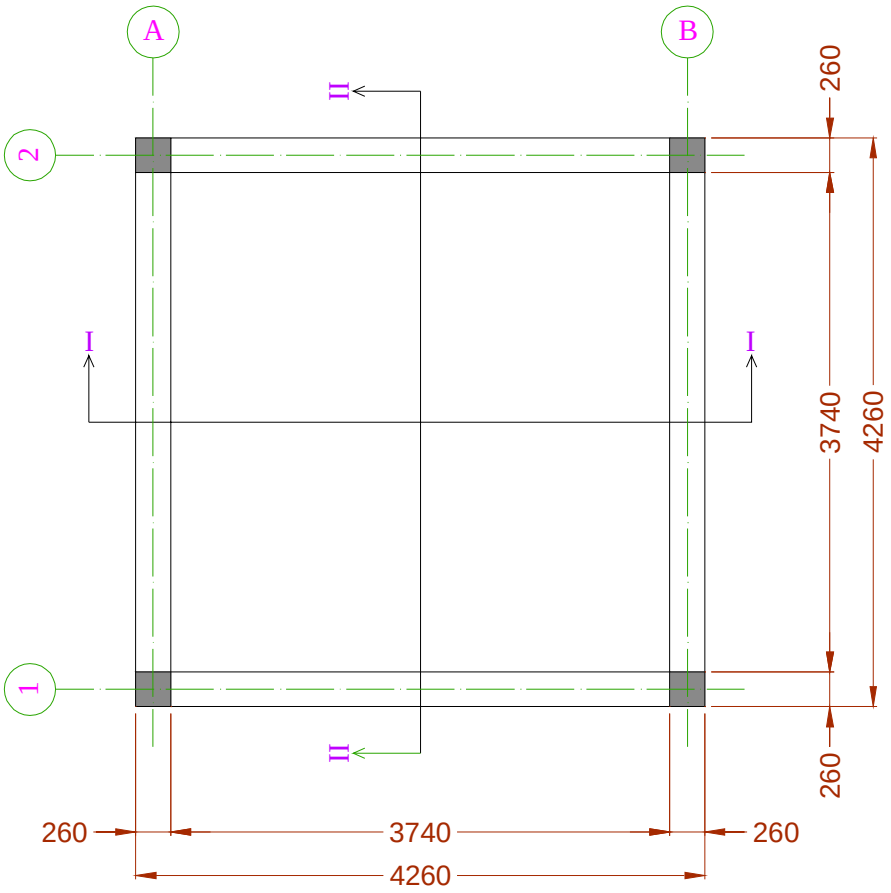

Figure J-1: Plan view of the building

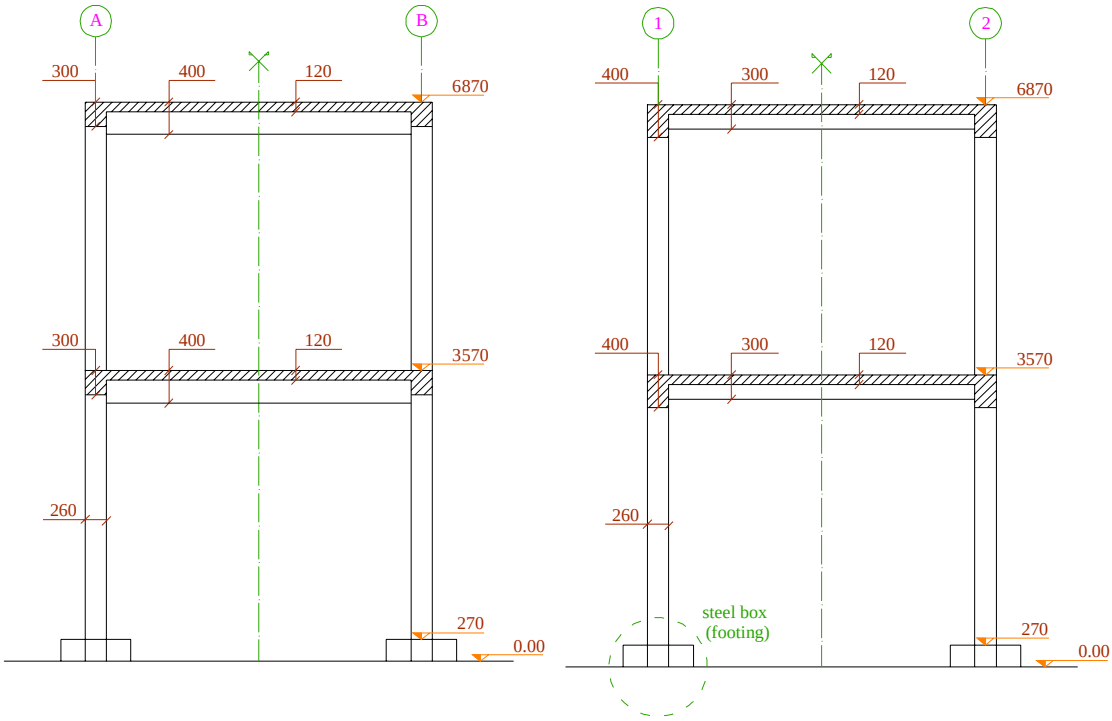

Figure J-2: Section I-I (left) and Section II-II (right) of the building

The self-weight of the structure is around 19 tons. Additional masses were provided to the building for the testing. For the first floor, three steel plates with a mass equal to 4.5 tons each

were fixed under the slab. The detailing of the connection between the mass and the slab was designed to allow the free rotation of the slab, as shown in Figure J-3. In this way the stiffness of the plate does not prevent the slab and subsequently the beams from deforming. For the second floor, the additional mass consisted of a steel plate with a mass of 4.5 tons and twelve concrete blocks with a total mass of 6.5 tons. The concrete blocks were fixed on the plate using the existing peripheral holes of the blocks. Figure J-4 shows clamping of additional masses to the second floor slab.

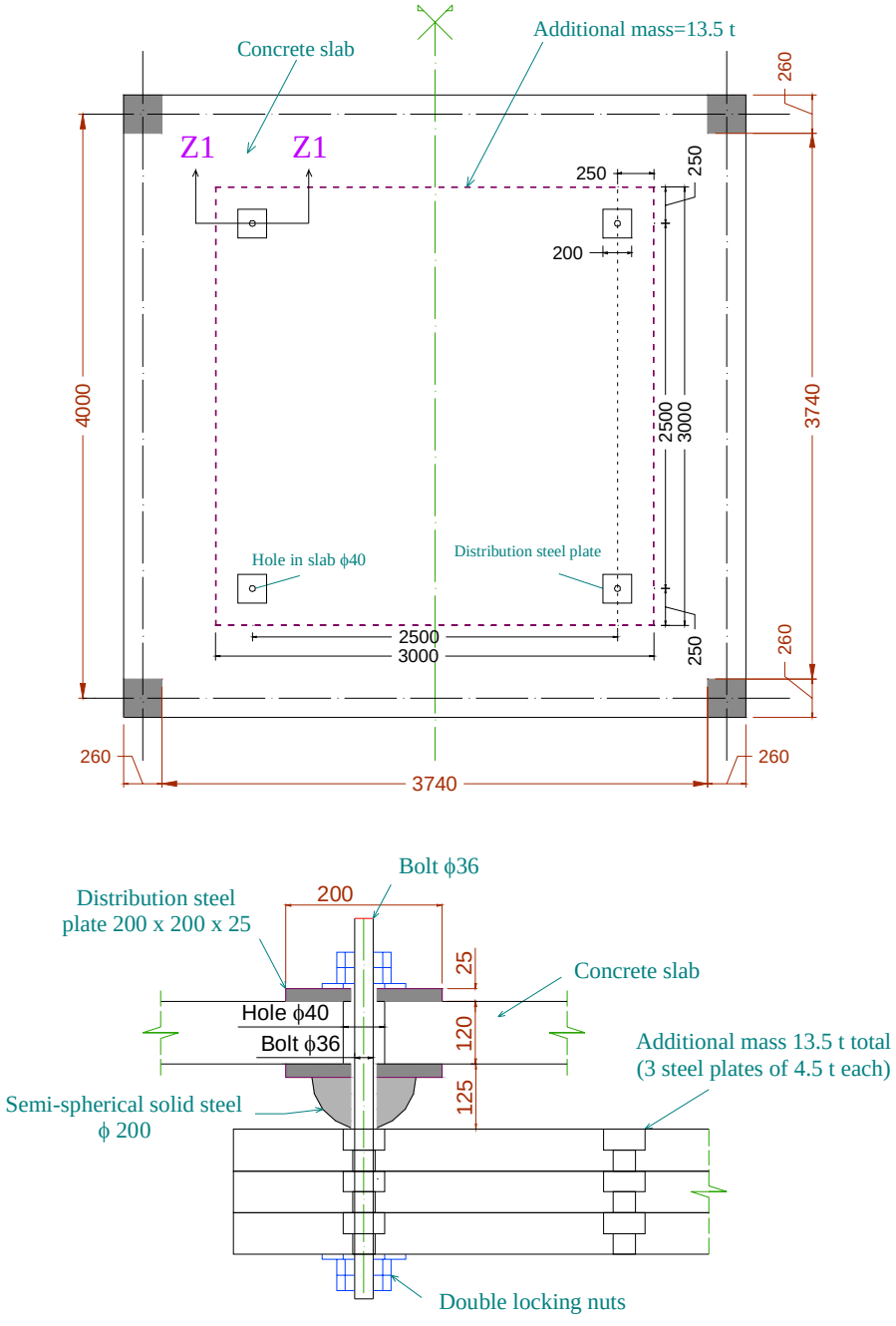

Figure J-3: Clamping of additional masses to 1st floor slab

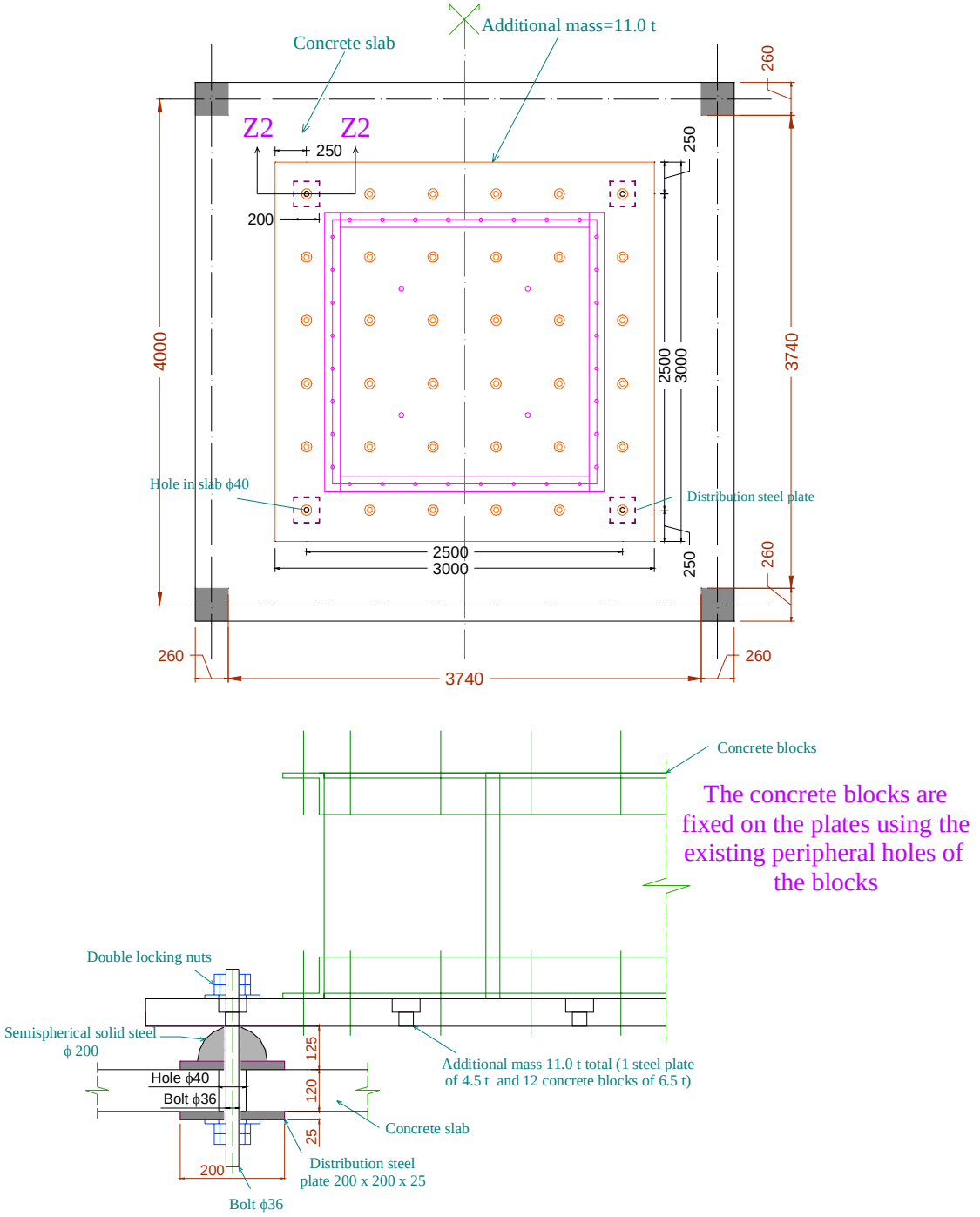

Figure J-4: Clamping of additional masses to 2nd floor slab

The reinforcement details of the members are summarised below and can be seen in Figure J-5 along with a plan view of the frame.

- Longitudinal reinforcement:
  - Columns: 1st floor: 3T14 + 2T14 + 3T14
  - 2nd floor: 2T14 + 2T14
  - Beams: top and bottom: 4T14
- Transverse reinforcement:
  - Columns: ϕ6/200 stirrups

- Beams: ϕ8/250 stirrups

- Slab Reinforcement: steel mesh top and bottom: ϕ10mm – 100x 100mm
- Distance to the centre of reinforcement: 30 mm

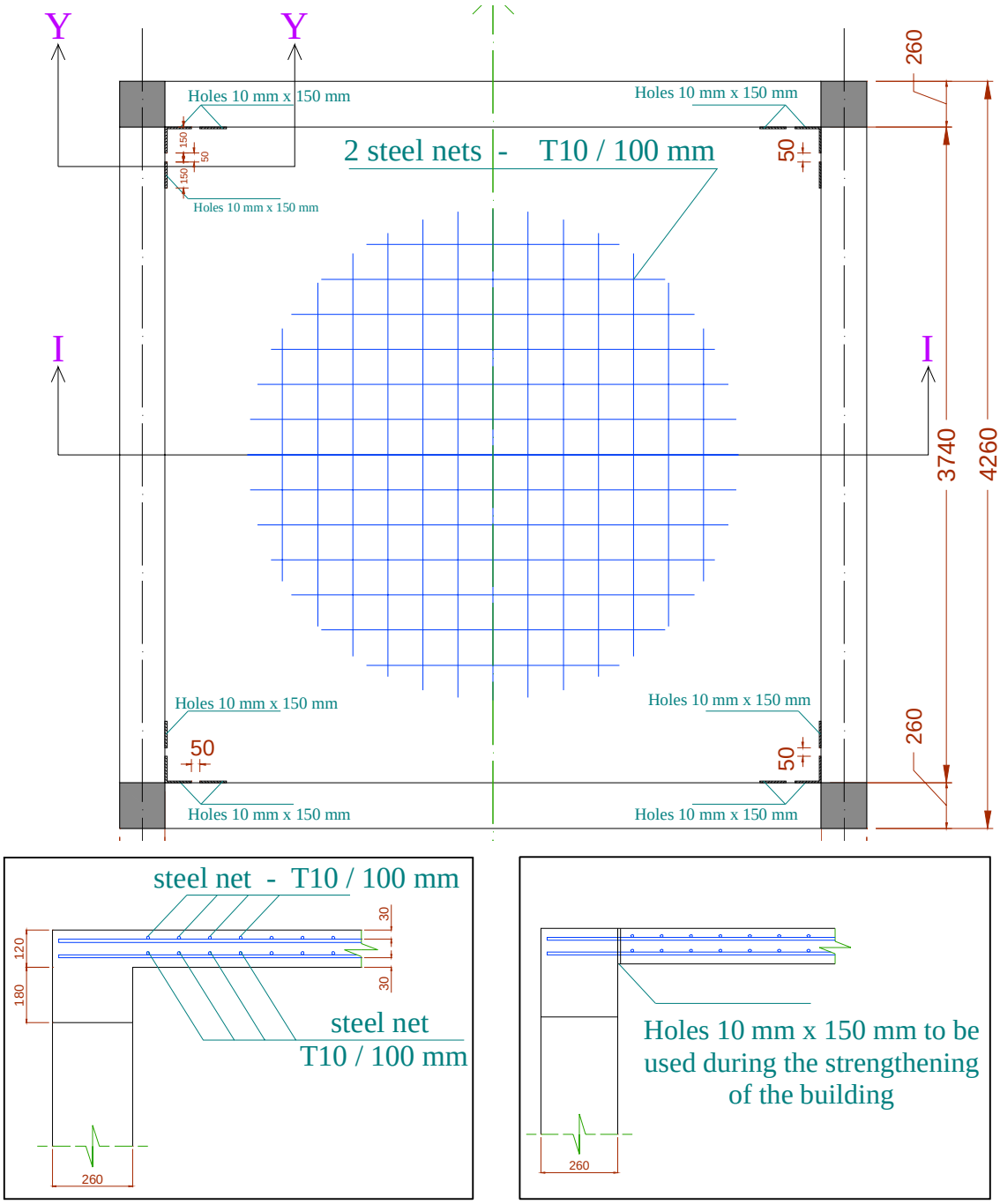

Section Y-Y: reinforcement in slabs Section Y-Y: holes in slabs

Figure J-5: Reinforcement of the slabs

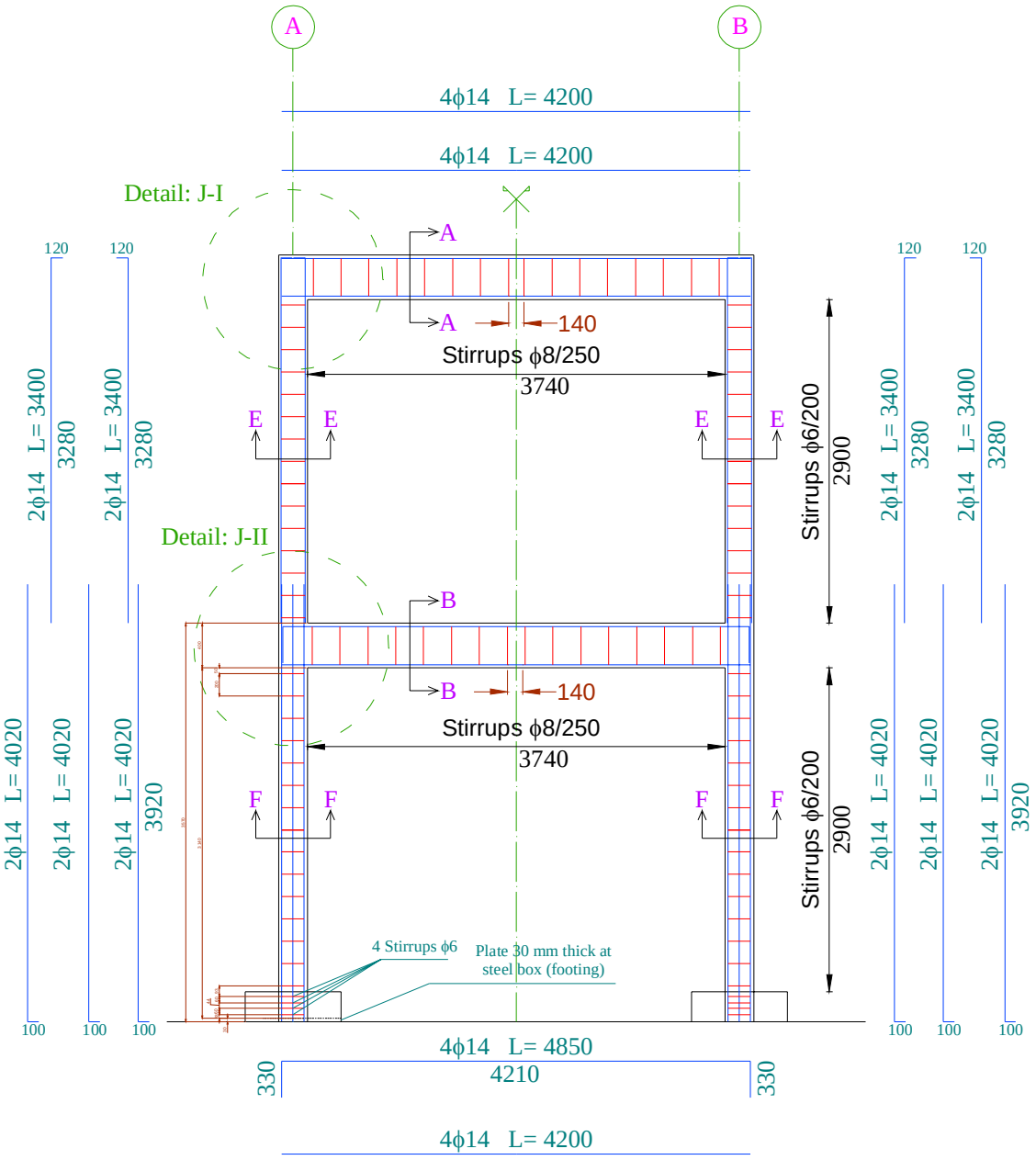

Figure J-6: Frames 1 and 2- reinforcement of beams and columns

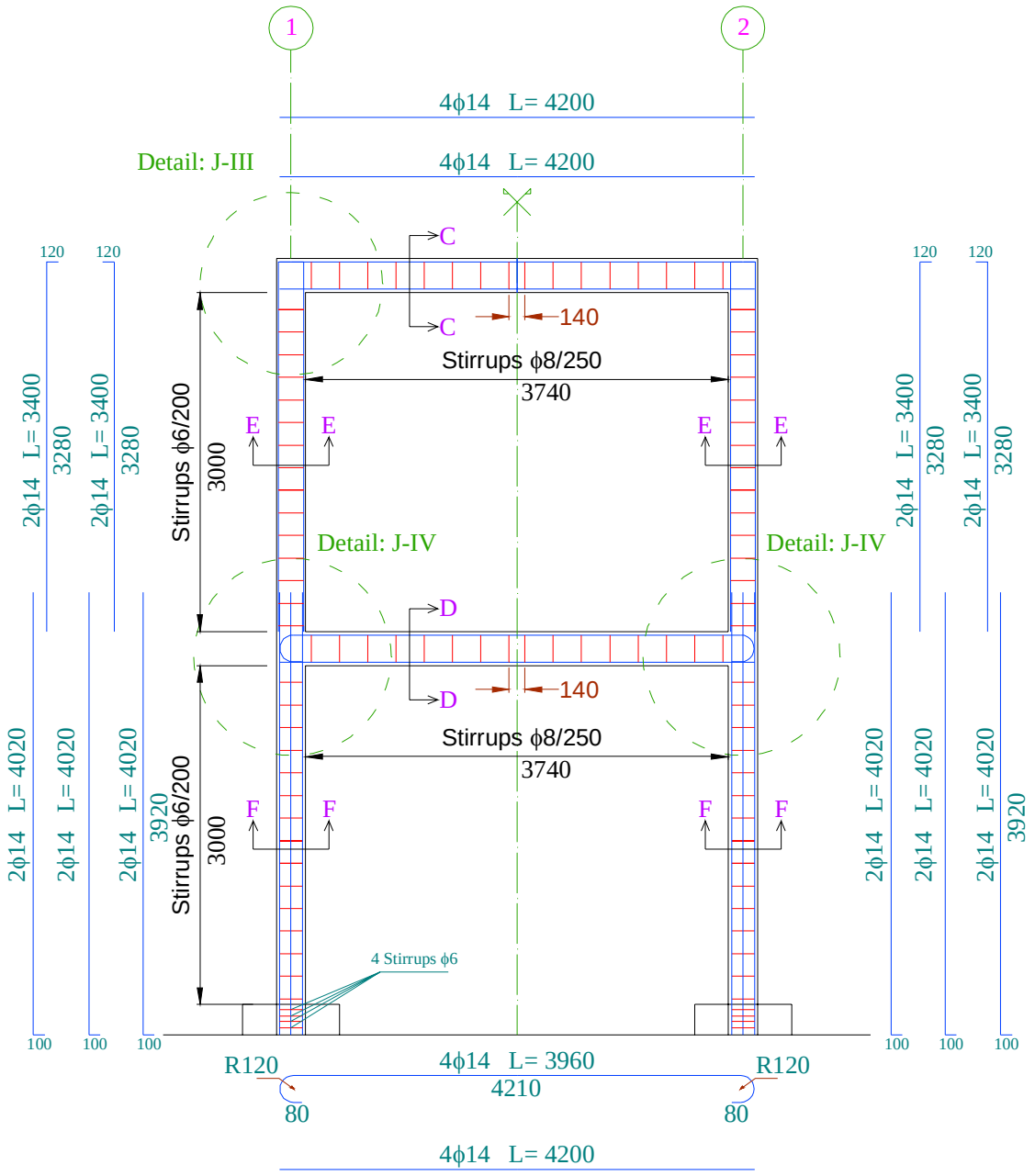

Figure J-7: Frames A and B- reinforcement of beams and columns

J.1.1 Material properties

J.1.1.1 Steel Mechanical Properties

Coupon Tests were performed to determine the mechanical properties of 6, 8, 10 and 14mm diameter bars. The results are shown in Table J-1. Conventional elongation (A%) refers to the elongation at mid-point of the bar where necking occurs. It is suggested that this strain is 2.5 times higher than the ultimate steel strain (Kyriakides, 2007) which is required for the analysis. Three samples were tested for each bar diameter. The standard deviation is given in the same table.

Table J-1: Mechanical properties of reinforcement

	T 6 mm			**T 8 mm**			**T 10 mm**			**T 14 mm**		
	f_y	f_u	A%	f_y	f_u	A%	f_y	f_u	A%	f_y	f_u	A%
	MPa	MPa		MPa	MPa		MPa	MPa		MPa	MPa	
Mean	574	604	18	544	572	15	513	587	20	526	616	19
SD	5.5	8.5	2.0	11.5	9.1	2.5	4.0	8.7	0.6	8.3	2.1	1.0

J.1.1.2 Concrete Mechanical Properties

The mix proportions used for the concrete material are summarised in Table J-2. The target concrete compressive strength was between 10 to 20MPa.

Table J-2: Mix proportions of concrete material

Type	**Constituent**	**Naming**	**Quantity**	**Unit**
Sand 1	0/05 LCH	Chapel GSI	380	Kg
Sand 2	0/4 VIMP	Vimpelles	565	Kg
Aggregates	4/10 VIMP	Vimpelles	945	Kg
Cement	I52LH	CEM I 52,5 N CP2 Le Havre	180	Kg
Adjuvant (agent)	CHR	Chryso Tard CHR	0.5	%CC+CA
Water	EAU DECANT	EAU DECANTEE	220	L

The trial mixes done by the contractor resulted in an average concrete strength of 14.5MPa at the age of 28 days. At the test period (around 120 days), cylinders (160mm diameter × 320mm height) were tested and the results are summarised in Table J-3. The tensile strength was determined by splitting (160mm diameter and 320mm height cylinders) and flexural (prismatic specimens 100×100×500 mm) tests, and the mean results are given in Table J-4.

Table J-3: Test results of cylinders in compression

Floor	**f'_c (MPa)**	**Volumetric weight kg/m^3**	**E_c (GPa)**
1st	32	2200	24.9
2nd	26.5	2167	22.1

Table J-4: Results of splitting and flexural tests

Floor	**f_t (MPa) - flexure**	**f_t (MPa) - splitting**
1st	3.6	2.35
2nd	3.8	2.3

J.1.1.3 Strip Mechanical Properties

The strips used for strengthening had a width of 25 mm and thickness of 0.8mm. The mechanical properties of the strips were obtained by tension tests until failure. Strain gauges were attached to the strip surface to monitor the strains. Figure J-8 shows the test results from the tensile tests. Therefore, the average mechanical properties are as follows: yield stress f_y =1000 MPa; yield strain ε_y =0.004; modulus of elasticity E_s = 250 GPa ; ultimate stress f_u = 1100 MPa; and ultimate strain ε_u = 0.05.

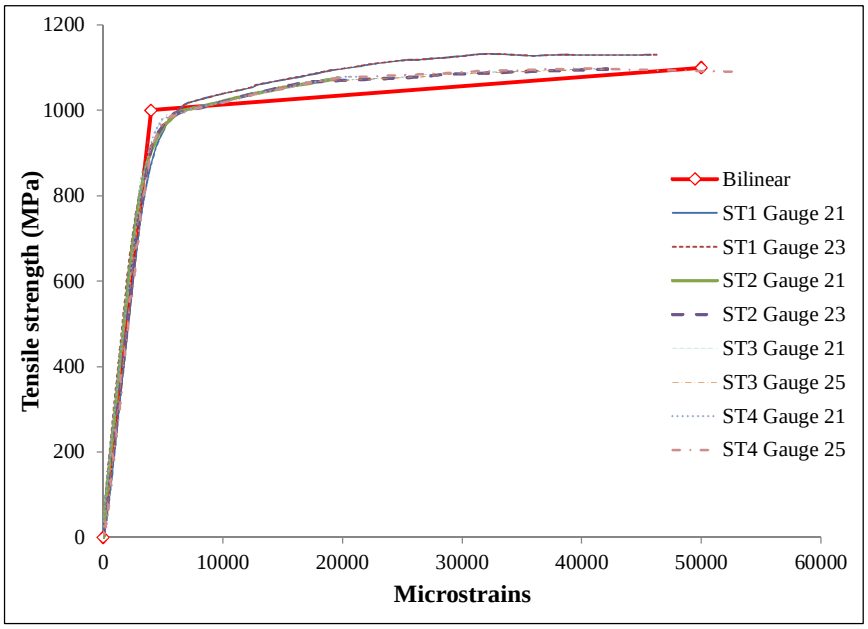

Figure J-8: Mechanical properties of metal strips

J.1.2 Reinforcement detailing at joints

In the current seismic codes of practice such as EC8 (2004) and ACI 318 (2008), adequate anchorage detailing within a joint region is regarded as an essential design requirement in order for the reinforcement to yield and achieve satisfying ductility levels. Moreover, the presence of proper shear reinforcement within the joint area is considered one of the most important detailing to prevent brittle mechanisms and to ensure continuity of beams and columns.

In the building, the reinforcement detailing was very deficient to simulate substandard conditions of design and construction. The detailed drawings and in place arrangement of anchorages at the top of the 1st and 2nd storey joints are shown in Figure J-9 trough Figure J-11.

As can be seen from the figure, the beam bottom bars were inadequately anchored in the joint area with a length of 230mm (16.5 the bar diameter). The top bars were anchored in different ways. For the first floor joints, the top bars were hooked down into the core with L-shaped and C-shaped forms. For the second floor joints, the beam top bars were anchored in a similar way to the bottom bars. The first floor column bars, on the other hand, were spliced with the second floor column bars with a length of 350mm (25 the bar diameter). Two bars of the bottom

columns were discontinued in the second floor. The lateral reinforcement of columns and beams was widely spaced.

No shear reinforcement was provided in the joint area to represent old design and construction defaults. In this case, the joint capacity is expected to be less than the corresponding column and beam capacities.

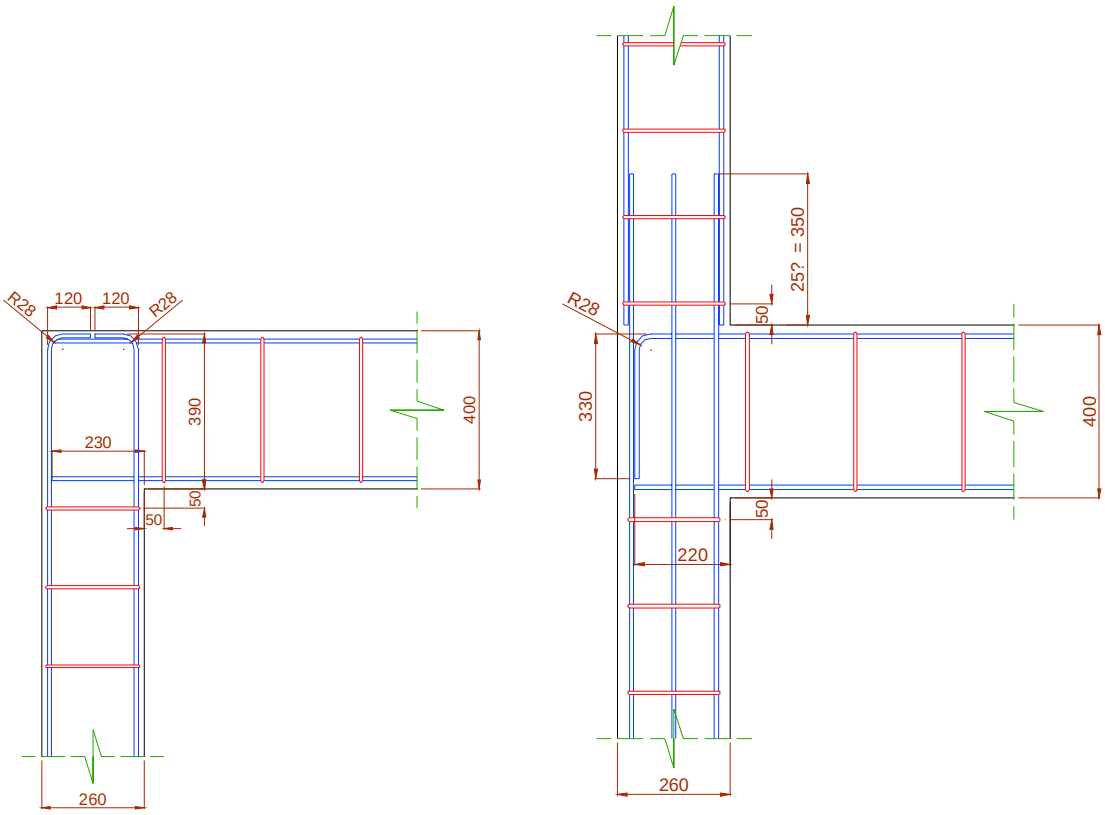

Frame 2: Detail: J-I: anchorage details

Frame 2: Detail: J-II: anchorage details

Figure J-9: Reinforcement detailing of joints of Frame 1&2

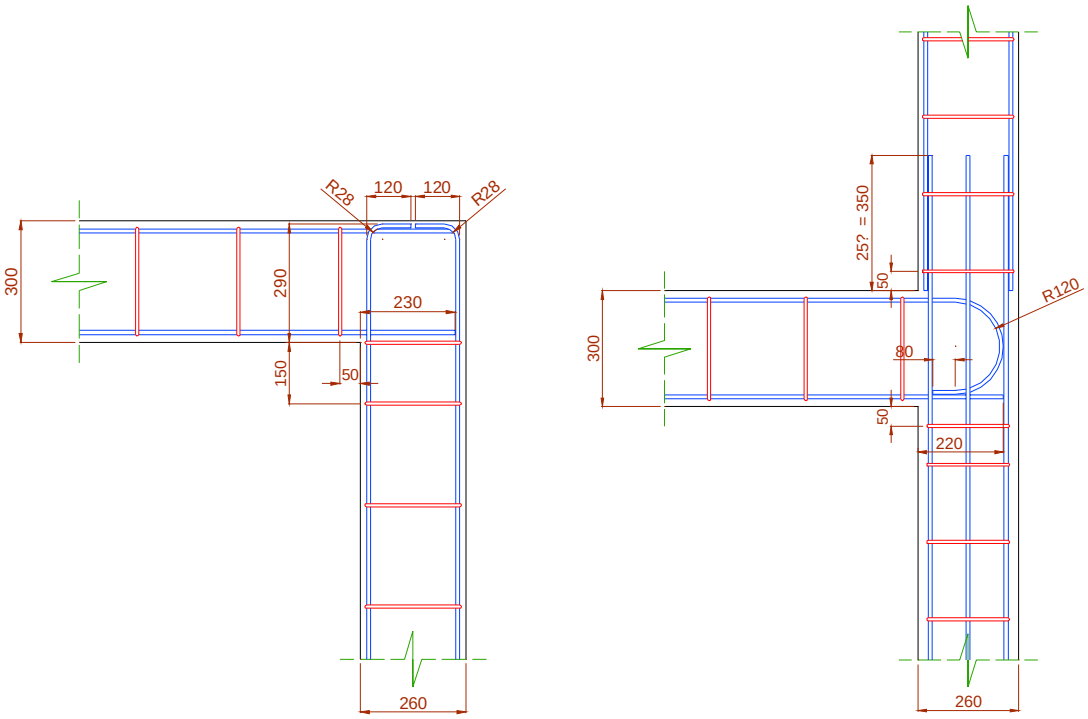

Frame A: Detail: J-III: anchorage details

Frames A&B: Detail: J-IV: anchorage details

Figure J-10: Reinforcement detailing of joints of Frame A&B

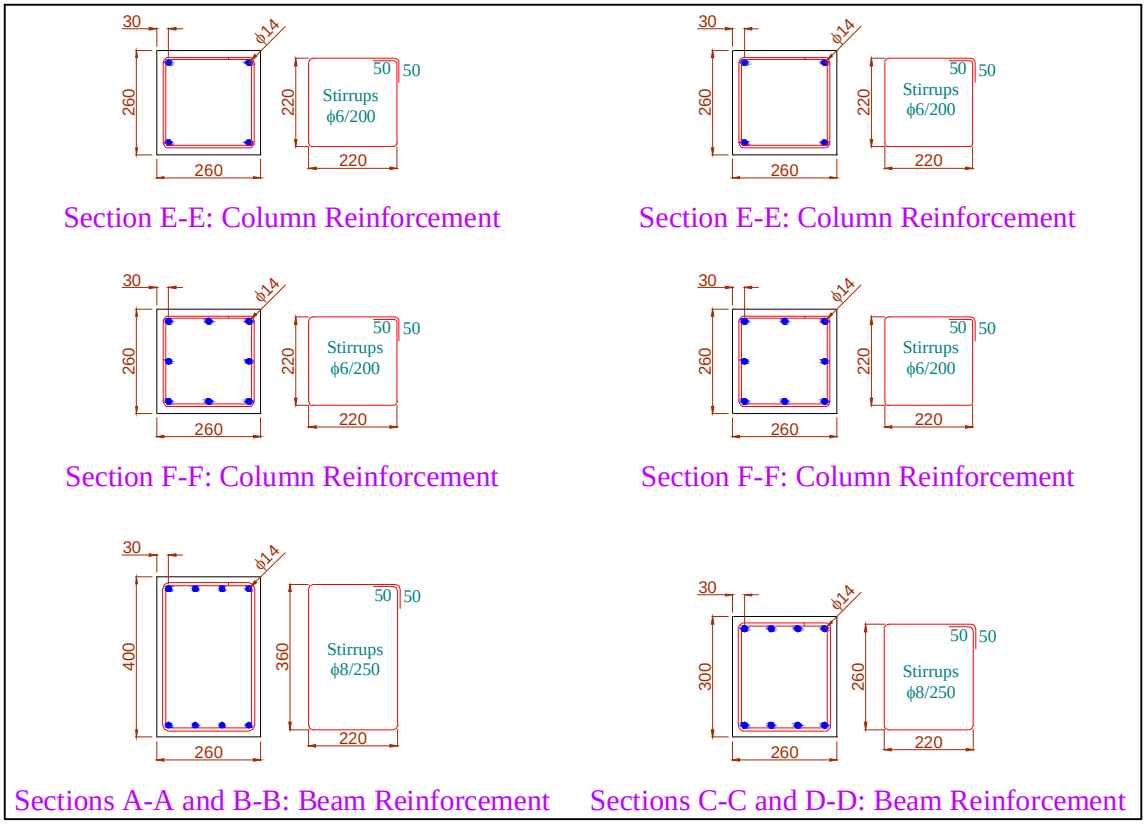

Figure J-11: Reinforcement of beams and columns

At the column base, it is aimed to ensure fully fixed support conditions. The column reinforcement was anchored into a steel box and welded to the base, which served as a foundation. The steel box was 270mm deep and 700mm square in plan and was anchored with the use of 30mm bolts onto the shaking table platform. An additional measure was taken to ensure no rotations at the column ends. That was done through the placement of a horizontal four steel tie bars (Φ16) welded at the sides of the steel box. Figure J-12 shows the geometry of the steel box.

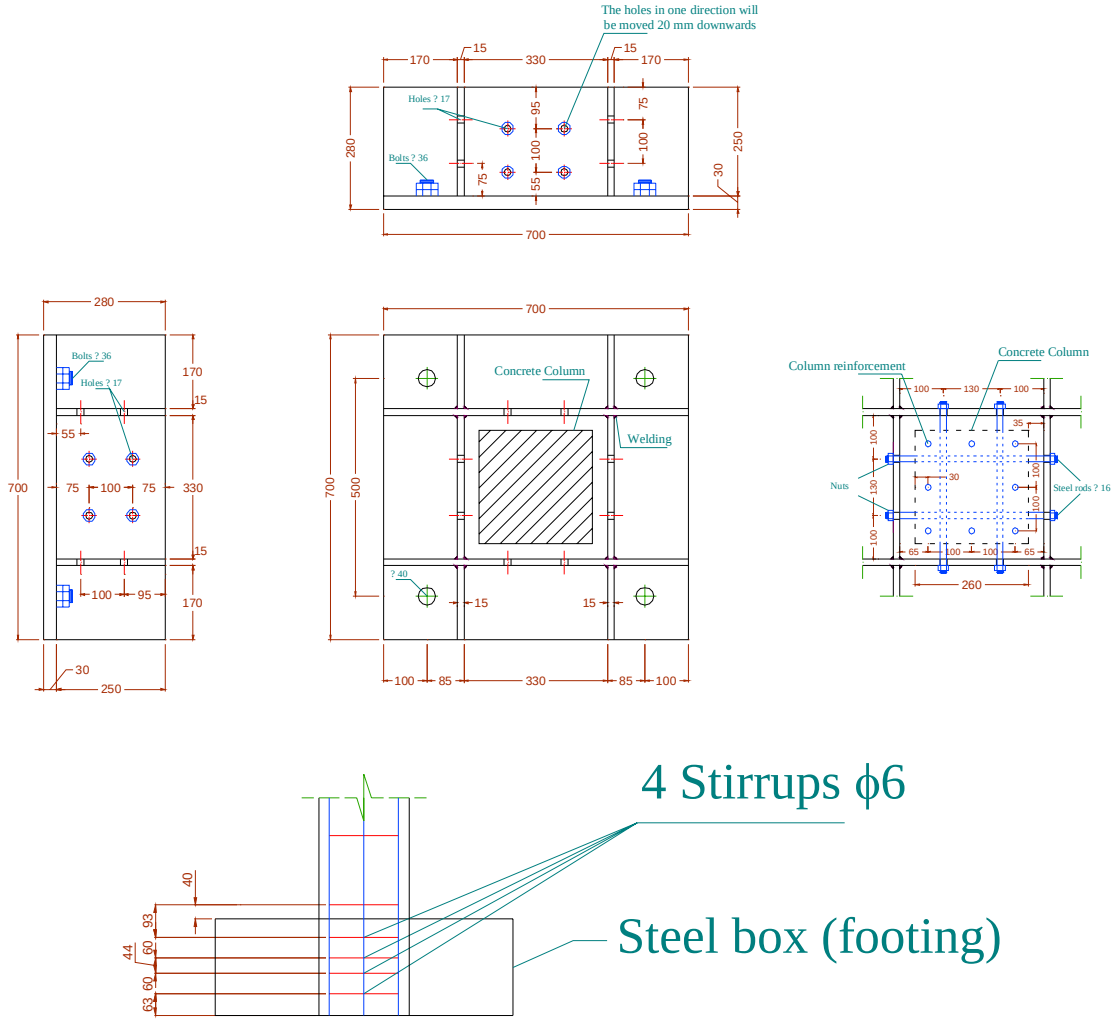

Figure J-12: Geometry of steel box (footing)

J.1.3 Instrumentation

The behaviour of the frame members was monitored both globally and locally. Both force and displacement readings were taken at all nodes. The force at the nodes was computed with the use of capacitive accelerometers whereas the corresponding displacements were read from the LVDT (Linear Variable Differential Transformer) displacement transducers fitted on a retaining wall at one side of the frame. The exact locations of all the transducers are shown in Figure J-13. Strain gauges were also attached to reinforcement to monitor strains during the test.

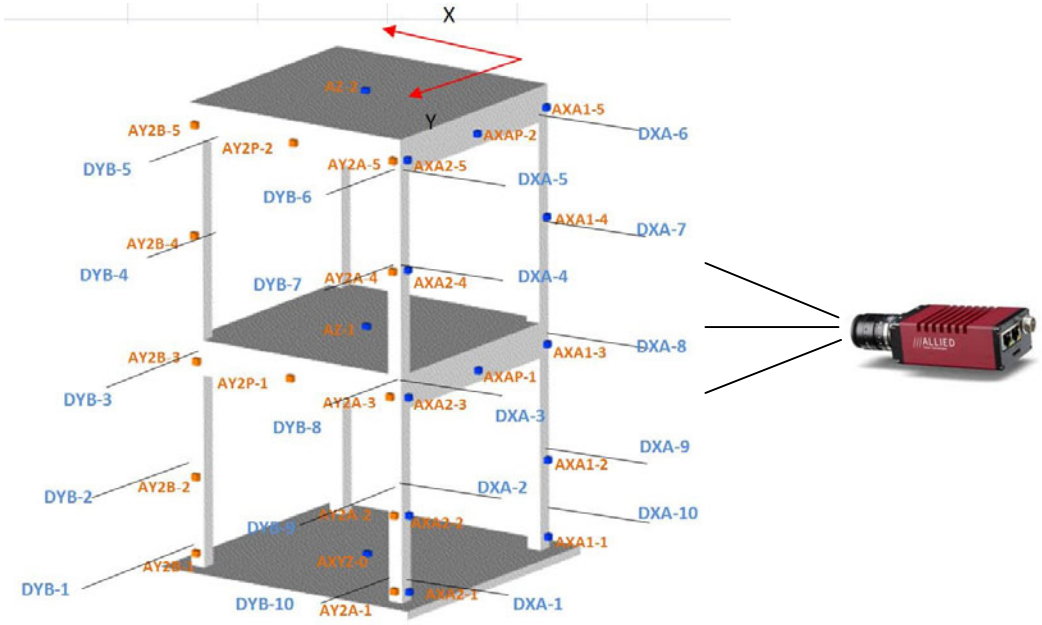

Figure J-13: Displacement & acceleration transducers

Appendix K

BANDIT MODELLING

K.1 DESCRIPTION OF THE MODEL

Because it is symmetrical, the structure is modelled as a 2D frame. DRAIN-2DX is used for the modelling. The columns and beams were modelled using element 15 with connection hinges at the beam/joint interface to simulate bar slippage and at the beam/column-centroid to simulate shear deformations. Using element 15, the beam and column sections are divided into concrete and steel bar fibres. The DRAIN-2DX model for the BANDIT building is shown in Figure K-1.

The mass at each floor is lumped at the side nodes. The mass of each floor comprises the mass of the steel plates in addition to the mass of all structural components. The mass of the 1st floor was calculated at 12.1 tons, whereas it accounted for 10.3 tons for the 2nd floor. Only half of the columns are considered for the 2nd floor. The damping ratios were assumed to be 5% and 2.5% for the 1st and 2nd modes, respectively.

The characteristics of concrete and steel materials used are shown in Figure K-2(a) & (b), respectively. As can be seen from the figures, the concrete material σ-ε behaviour was modelled by defining five points; whereas the steel σ-ε behaviour was defined by an elastic portion until yield and a strain hardening portion until ultimate strength

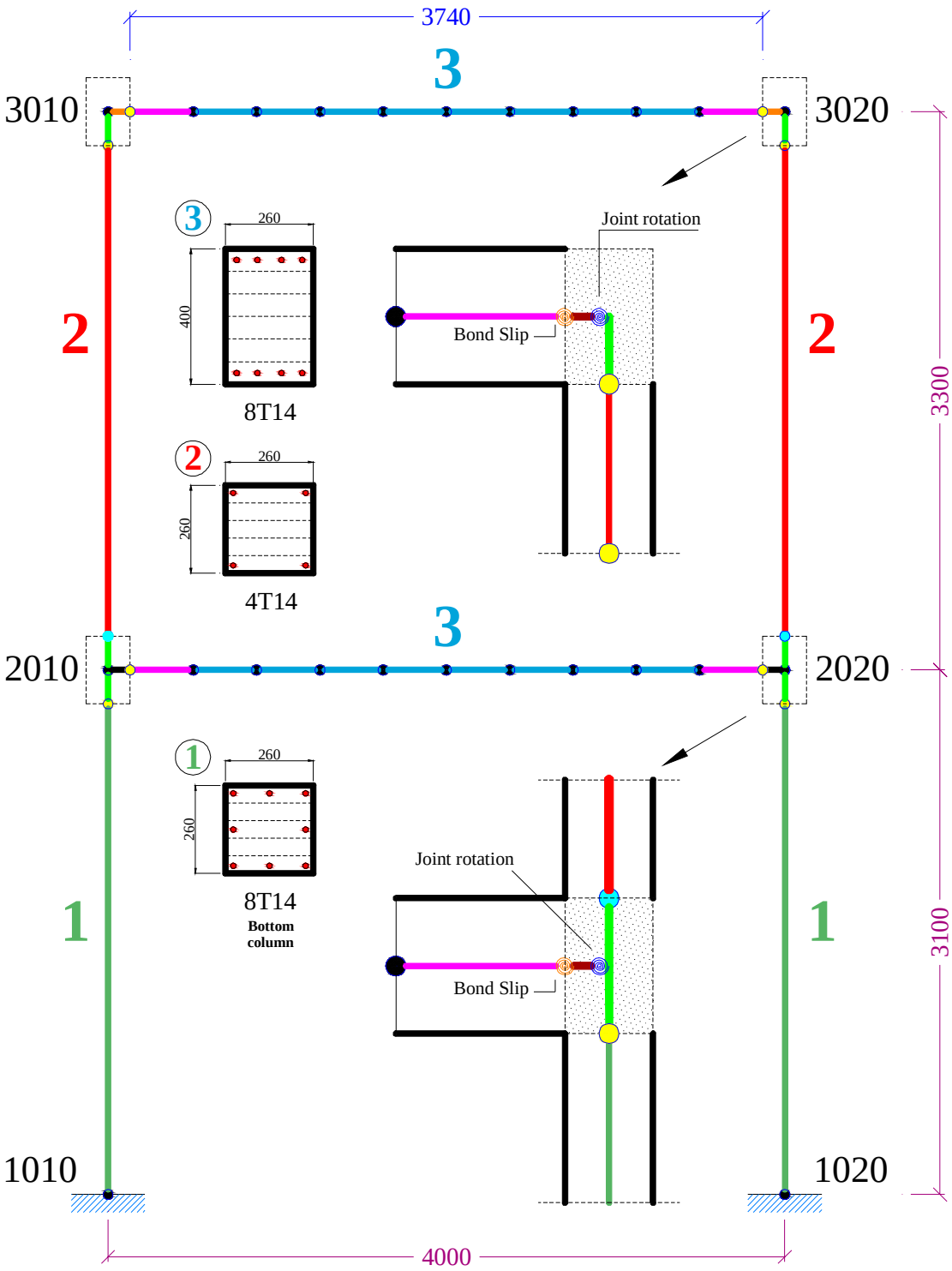

Figure K-1: DRAIN-2DX model for BANDIT building with element 15

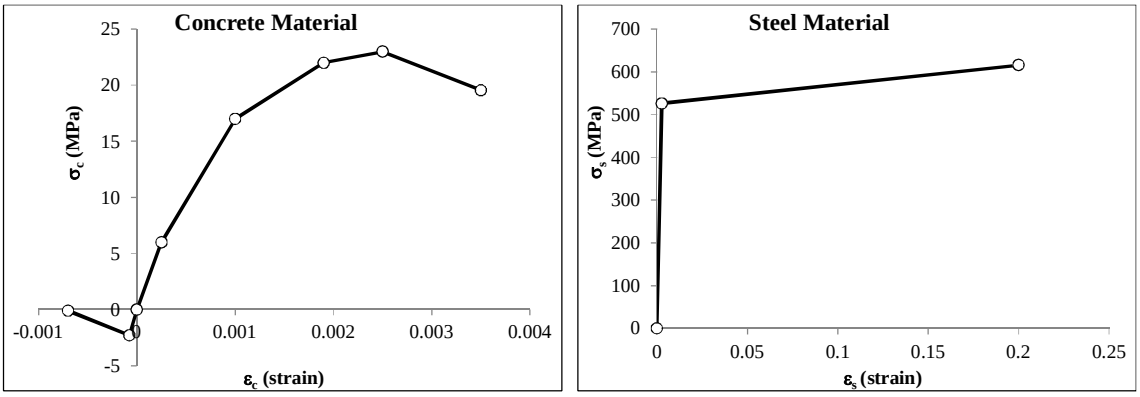

Figure K-2: a) Concrete material model, and b) Steel material model

- ***Modelling of slip***

In E15, slip deformations due to Pullout or Splitting failures can be simulated using connection hinges at element ends. The hinges can be also used to model gaps due to unclosing cracks. The E15 characteristics are shown in Figure K-3.

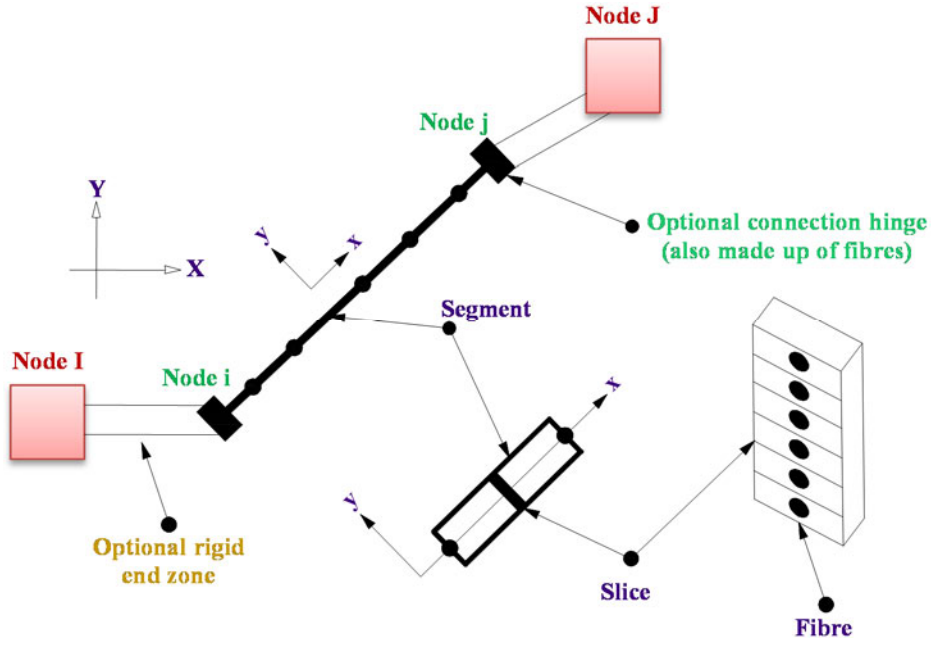

Figure K-3: E15 characteristics

E15 adopts a tri-linear backbone curve to model the pullout deformations. The backbone is normally assigned to pullout fibres at locations of slipping steel bars. Figure K-4 shows a schematic view of a pullout fibre and characteristics of the deformational curve.

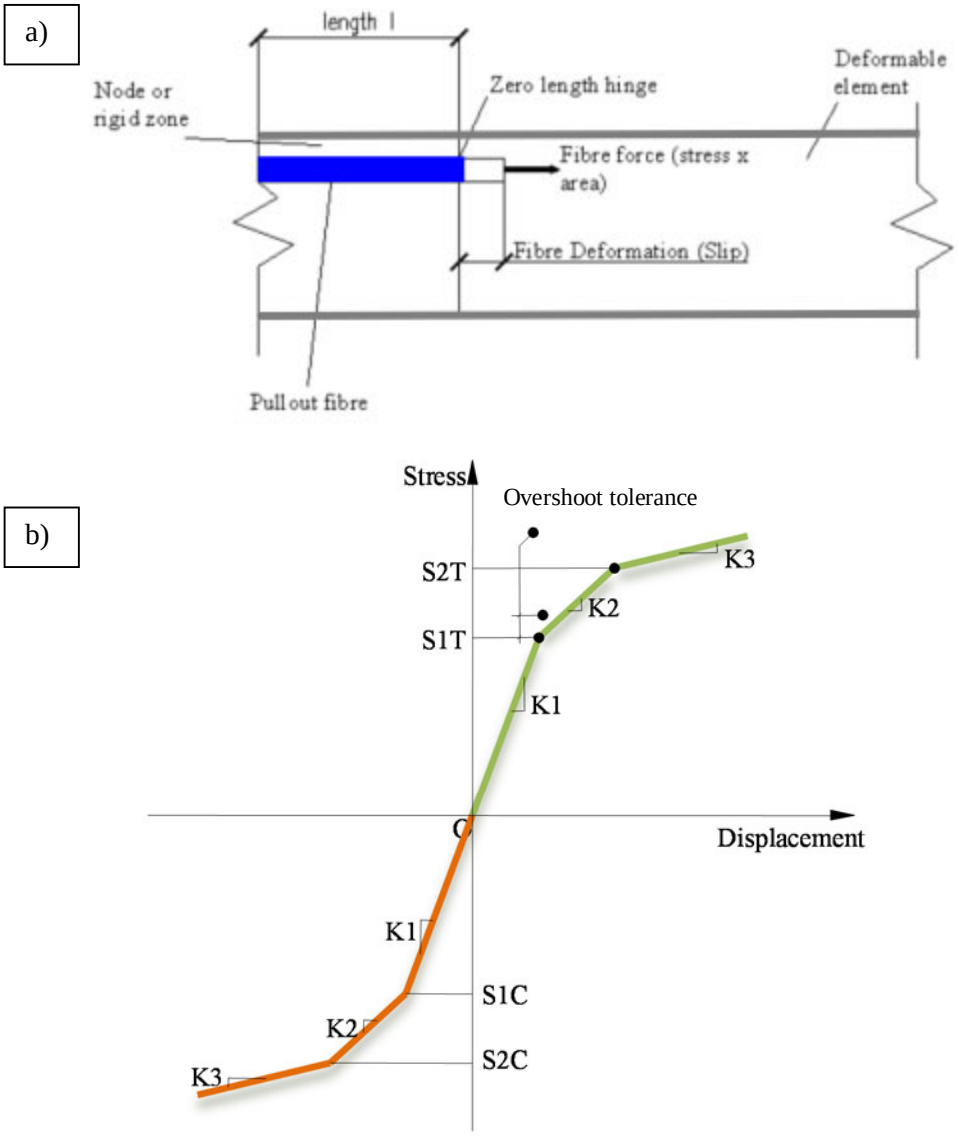

Figure K-4: a) Deformations of a pullout fibre, and b) tri-linear backbone for modelling bar stress-slip

As can be seen from the previous figure, the stress-displacement backbone must be defined both in tension and compression. The input stiffness values are used for both directions, but the strength can differ.

The pullout fibre is capable of incorporating degradation in the unloading/reloading stiffness. In this regard, the backbone curve is decomposed into one linear and two bilinear curves, as shown in Figure K-5(a). The degradation is assigned to the bilinear curves through a factor SDF ranging between 0 and 1, as shown in Figure K-5(b), where 0 means no degradation in the stiffness.

Also, the pullout fibre can account for any strength degradation due to deterioration in bond capacity (see Figure K-6a). Two factors, namely, STDF and SCDF are used to control the

degradation. Both factors can take values between 0 and 1, where 0 means no strength degradation.

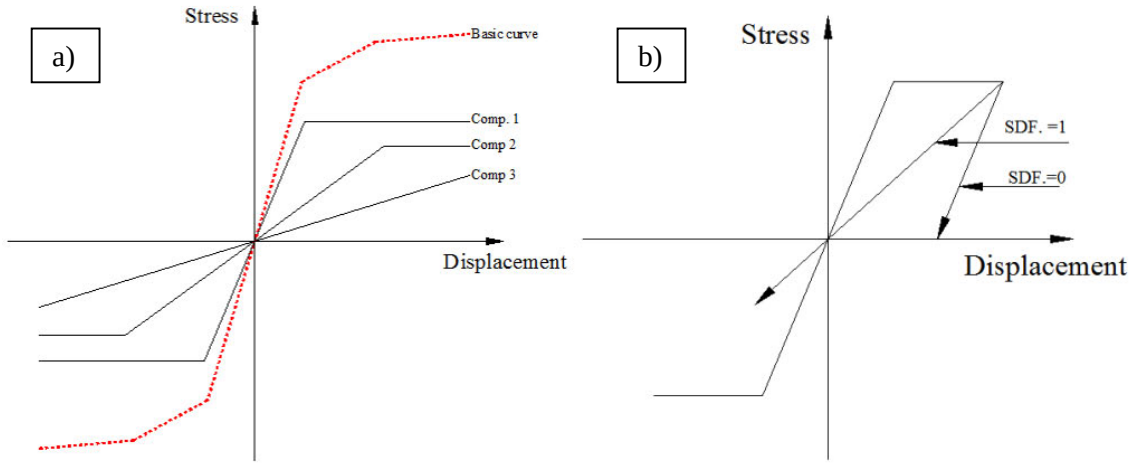

Figure K-5: a) Decomposition of the tri-linear backbone, and b) stiffness degradation rules

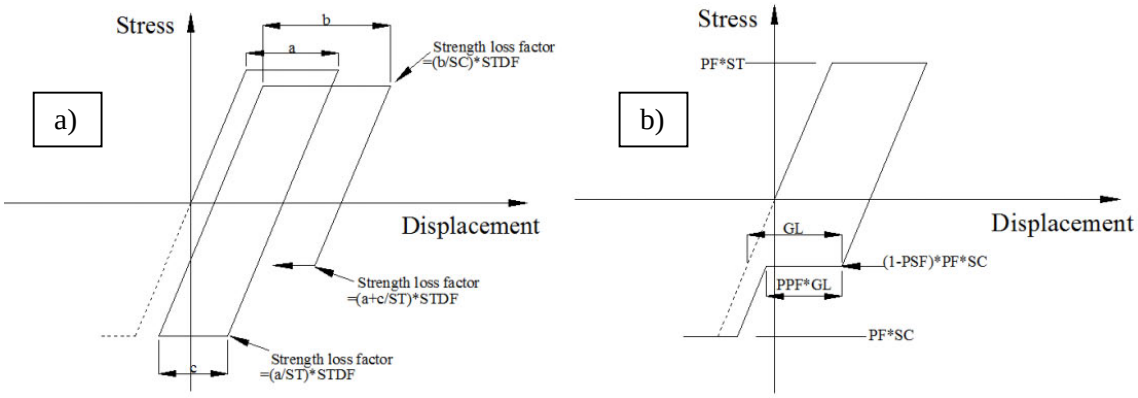

Figure K-6: a) Strength degradation parameters, and b) pinching behaviour

Pinching effect due to gap un-closure near the zero displacement also can be accounted for in the pullout fibre (see Figure K-6b). Three factors are used to control the pinching, namely, pinching factor (PF), pinching strength factor (PSF) and pinching plateau factor (PPF). The PF factor can be assigned values between 0 and 1, where 1 means full pinching. The PSF factor determines the strength where the pinching starts, while the PPF factor determines the length of the pinching plateau. As the PPF value approaches 1, the plateau length enhances until it finally meets the unloading curves.

The bond-slip model adopted for simulating beam bar slippage is Sezen (2003) model. Accordingly, a uniform bond stress of $\sqrt{f'_c}$ is used along the elastic segment of the anchorage length; whereas a bond value of $0.5\sqrt{f'_c}$ is used along the inelastic segment. The anchorage length used for beam anchorages is 235 mm; and thus, no yielding is expected to develop in the bar. The maximum bar stress is calculated at 326 MPa. A slight increase in the value is given thereafter until reaching twice the slip value which corresponds to the maximum stress. This assumption correlates with findings by Hassan (2011). The third segment of the backbone was

assigned a stiffness value of 0.001. Figure K-7 shows the input bar-stress slip curve used for anchorages. The curve is implemented at the beam/column interface. Full degradation parameters are assigned for stiffness degradation, strength degradation and pinching factors.

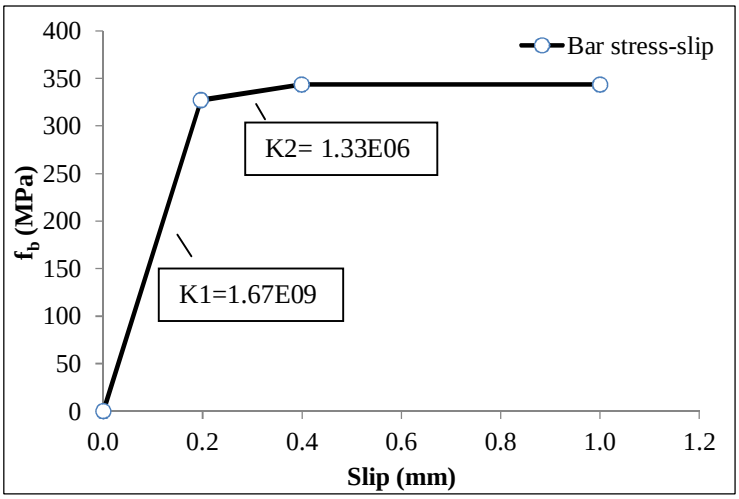

Figure K-7: Input bar stress-slip model

- ***Modelling of Shear***

Shear deformations in the panel zone region can also be simulated using E15. Conventionally, shear deformations are represented by moment-rotation curve derived from shear stress-strain curve. The moment-rotation curve can be transformed into a bar stress-displacement curve through simple considerations. A sectional analysis can be used to transform the moment values into bar stress; whereas shear rotations can be multiplied by (0.7×the beam effective depth) to reproduce displacement values.

The backbone curve suggested by ASCE41-06 is used to model the shear. The shear stress used for first story joints is calculated at $0.67\sqrt{f'_c}$; while for the second story it accounted for $0.33\sqrt{f'_c}$. The first story joints are considered as exterior joints with transverse beams, whereas the second story joints are considered as knee joints. The rotations are calculated at 0.00038 at the maximum stress, 0.0054 at the end of the plateau, and 0.02 at end of the degrading curve.

The moment-rotation curves are generated using an iteration technique following Sharma et al. (2011). The moment-rotation curves were then transformed into bar stress-displacement curves and the final results are shown in Figure K-8. As E15 cannot consider negative degrading slope, small positive values were assigned. The stiffness values calculated are as follows: K1=4.36E09, K2=1.59E06, K3=0.001 for both the exterior and knee joints. It should be mentioned that the use of positive values cannot be taken as a drawback in the modelling, because there is still no evidence that the capacity of the structure was reached or exceeded at 0.15g. The initial findings show that the capacity at 0.15g was just near the maximum. Further examination should be done in this regard by using strain gauge readings to calculate joint shear

strengths and bond capacities, and then implementing the findings in a nonlinear pushover analysis of the structure.

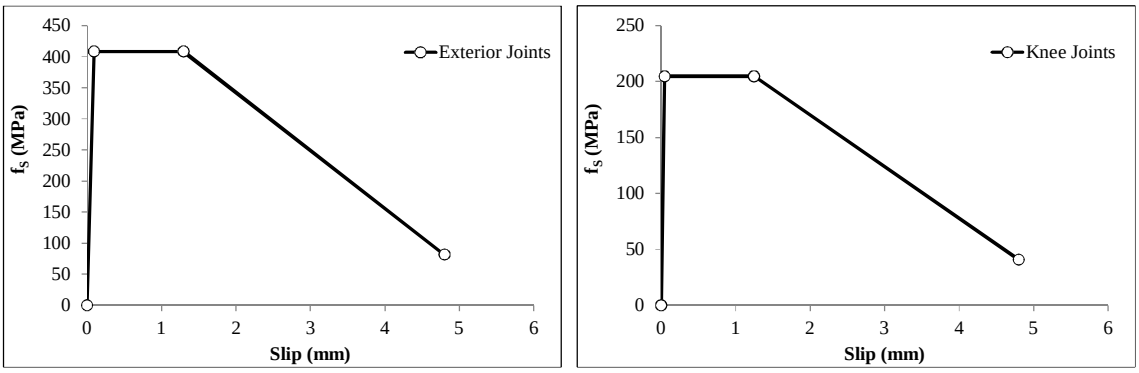

Figure K-8: Bar stress-displacement used at the joint centroid of the exterior and knee joints

REFERENCES: (APPENDICES)

ABAQUS version 6.9. (2009). "Analysis User's Manual." ABAQUS Inc.

ABAQUS version 6.9. (2009). "Theory Manual." ABAQUS Inc.

Achillides, Z., (1998). "Bond behaviour of FRP bars in concrete", PhD Thesis, The University of Sheffield, UK.

American Concrete Institute ACI., (1963). "Building code requirements for structural concrete", ACI Committee 318, Detroit.

ACI Committee 408, (1966). "Bond Stress-The State of the Art", ACI JOURNAL, Proceedings, V.63, No.11, Nov., pp.1161-1188.

ACI 318-71, (1971). "Building Code Requirements for Reinforced Concrete", American Concrete Institute, Detroit, Michigan.

ACI-ASCE Committee 352 (1976). "Recommendations for Design of Beam-Column Joints in Monolithic Reinforced Concrete Structures", American Concrete Institute.

ACI Committee 408, (1979). "Suggested Development, Splice, and Standard Hook Provisions for Deformed Bars in Tension (ACI 408.1R-79)", Concrete International, V. 1, No. 7, July, pp. 44-46.

American Concrete Institute Committee ACI 318-89 (1989). "Building Code Requirements for Reinforced Concrete (ACI 318-89)", American Concrete Institute, Detroit, 351 pp.

ACI Committee 408, (1992). "State-of-the-Art Report: Bond under Cyclic Loads (ACI 408.2R-92 (Reapproved 1999))", American Concrete Institute, Farmington Hills, Mich., 32 pp.

ACI Committee 318, (1995). "Building Code Requirements for Structural Concrete (ACI 318-95) and Commentary," American Concrete Institute, Farmington Hills, Mich., 369 pp.

ACI Committee 224, (1998). "Causes, Evaluation, and Repair of Cracks in Concrete Structures (ACI 224.1R-93 [Reapproved 1998])," American Concrete Institute, Farmington Hills, Mich., 1993, 22 pp.

ACI Committee 503, (1998). "Use of Epoxy Compounds with Concrete (ACI 503R-93 [Reapproved 1998])", American Concrete Institute, Farmington Hills, Mich., 1993, 28 pp.

ACI Committee 408, (2001). "ACI 408.3R: Guide for Lap Splice and Development Length of High Relative Rib Area Reinforcing Bars in Tension and Commentary", American Concrete Institute, Farmington Hills, Mich., 6 pp.

American Concrete Institute Committee ACI318-02. "Building Code Requirements for Reinforced Concrete (ACI 318-02)", ACI 318-95, 99, 02, Detroit, Michigan, 1995, 1999, 2002

ACI Committee 408, (2003). "Bond and Development of Straight Reinforcing Bars in Tension (Reapproved 2012)", Technical Documents, American Concrete Institute, Farmington Hills, Mich.

ACI 318M-08 (2008). "Building Code Requirements for Reinforced Concrete", American Concrete Institute, Detroit, Michigan.

Ahmad, S.H., and Shah, S. P., (1982). "Complete triaxial stress-strain curves for concrete", Journal of the Structural Division, ASCE, Vol. 108, No ST 4, April, pp 728-742.

Ahmad, S., (2011). "Seismic Vulnerability of Non-Ductile Reinforced Concrete Structures in Developing Countries", PhD thesis, the University of Sheffield, Sheffield, UK.

Alcocer, S. M. and Jirsa, J. O., (1993). "Strength of Reinforced Concrete Frame Connections Rehabili-tated by Jacketing", ACI Structural Journal 90(3), 249–261.

Alsiwat, J. M., and Saatcioglu, M., (1992). "Reinforcement Anchorage Slip under Monotonic Loading", Journal of Structural Engineering, ASCE, V. 118, No. 9, Sept., pp. 2421-2438.

Antonopoulos, C. P., and Triantafillou, T. C., (2003). "Experimental investigation of FRP-strengthened RC beam-column joints." J. Compos. Constr., 7(1), 39–49.

Aycardi, L. E., Mander, J. B., and Reinhorn, A. M., (1994). "Seismic Resistance of Reinforced Concrete Frame Structures Designed Only for Gravity Loads: Experimental

Performance of Subassemblages", ACI Structural Journal, V. 91, No. 5, Sept.-Oct., pp. 552-563.

Aycardi, L.E., Mander, J.B., and Reinhorn, A.M., (1994). "Seismic resistance of reinforced concrete frame structures designed only for gravity loads: Experimental performance of sub-assemblages", ACI Structural J., 91(5), 552-563.

Azizinamini, A., Stark, M., Roller, J.J., and Ghosh, S.K., (1993). "Bond Performance of Reinforcing Bars Embedded in High-Strength Concrete", ACI Structural Journal, V.90, No.5, Sept-Oct., pp.554-561.

Azizinamini, A., Chisala, M., and Ghosh, S. K., (1995). "Tension Development Length of Reinforcing Bars Embedded in High-Strength Concrete", Engineering Structures, V.17, No.7, pp.512-522.

Beres, A.; White, R. N.; Gergely, P.; Pessiki, S. P.; and El-Attar, A., (1992). "Behavior of Existing Non-Seismically Detailed Reinforced Concrete Frames" Proceedings of the Tenth World Conference on Earthquake Engineering, Balkema, Rotterdam, pp. 3359-3363.

Barin, B., and Pincheira, J.A., (2002). "INFLUENCE OF MODELING PARAMETERS AND ASSUMPTIONS ON THE SEISMIC RESPONSE OF AN EXISTING RC BUILDING", A report sponsored by the U.S. National Science Foundation, DEPARTMENT OF CIVIL AND ENVIRONMENTAL ENGINEERING UNIVERSITY OF WISCONSIN -MADISON, March, pp187.

Beres, A., El-Borgi, S., White, R. N. and Gergely, P., (1992). "Experimental Results of Repaired and Retrofitted Beam-Column Joint Tests in Lightly RC Frame Buildings', Technical Report NCEER-92-0025, National Centre for Earthquake Engineering Research, State University of New York at Buffalo.

Bertero, V.V., and Bresler, B., (1968). "Behavior of Reinforced Concrete Under Repeated Loading", Journal of the Structural Division, ASCE, V.94, No.ST6, June.

Bertero, V.V., and Popov, E.P., (1977). "Seismic Behavior of Ductile Moment-Resisting Reinforced Concrete Frames", SP-53, Reinforced Concrete Structures in Seismic Zones, ACI, Detroit.

Bertero, V.V., Popov, E.P., and Viwathanatepa, S., (1978). "Bond of Reinforcing Steel: Experiments and a Mech-anical Model", LASS Symposium on Non-Linear Behavior of Reinforced Concrete Spatial Structures, V. 2, pp. 3-17, Darmstadt, West Germany, July.

Biddah, A., Ghobarah, A., and Aziz, T. S., (1997). "Upgrading of Nonductile Reinforced Concrete Frame Connections", Journal of Structural Engineering, ASCE, V. 123, No. 8, Aug., pp. 1001-1009.

Biddah, A., (1997). "Seismic Behaviour of Existing and Rehabilitated Reinforced Concrete Frame Connections", PhD Thesis, McMaster University, Hamilton, Ontario, Canada, 326 p.

Bousselham, A., (2010). "State of Research on Seismic Retrofit of RC Beam-Column Joints with Externally Bonded FRP", Jour composites for construction ASCE January-February 2010, 49-61.

Bracci, J. M., Reinhorn, A. M., and Mander, J. B., (1995). "Seismic Retrofit of Reinforced Concrete Buildings Designed for Gravity Loads: Performance of Structural Model", ACI Structural Journal, V. 92, No. 6, Nov.-Dec., pp. 711-723

Bracci, J. M., Reinhorn, A. M., and Mander, J. B., (1995). "Seismic Resistance of Reinforced Concrete Frame Structures Designed for Gravity Loads: Performance of Structural System", ACI Structural Journal, V. 92, No. 5, Sept.-Oct., pp. 597-609.

Carino, N.J., and Lew, H.S., (1982). "Re-Examination of the Relation Between Splitting Tensile and Compressive Strength of Normal Weight Concrete", ACI JOURNAL, V.79, No.3, May-June, pp.214-219.

CEB-FIP (Mc90) (1993). "CEB-FIP Model Code 1990: Design code. Comite Euro-International Du Beton(Ceb)".

Chinn, J., Ferguson, P.M., and Thompson, J.N., (1955). "Lapped Splices in R.C. Beams", ACI JOURNAL, V.52, No.2, Oct., pp.201-214.

Cho, J.Y., and Pincheira, J.A., (2004). "Nonlinear Modeling of RC Columns with Short Lap Splices", Proceedings of the 13th World Conference on Earth-quake Engineering, Vancouver, British Columbia, Canada.

Choi, O.C.; Hadje-Ghaffari, H.; Darwin, D.; and McCabe, S.L., (1991). "Bond of Epoxy-Coated Reinforcement: Bar Parameters", ACI Materials Journal, V.88, No.2, Mar-Apr., pp.207-217.

Choudhuri, D., Mander, J. B., and Reinhorn, A. M., (1992). "Evaluation of Seismic Retrofit of Reinforced Concrete Frame Structures: Part I—Experimental Performance of Retrofitted Subassemblages", Technical ReportNCEER-92-0030, SUNY/Buffalo.

Clark, A.P., (1950). "Bond of Concrete Reinforcing Bars", ACI JOURNAL, Proceedings V.46, No.3, Nov., pp.161-184.

Clyde, C., Pantelides, C.P., and Reaveley, L.D. (2000). Performance-based evaluation of exterior reinforced concrete building joints for seismic excitation. Pacific Earthquake Engineering Research Center, PEER Report 2000/05, University of California, Berkeley, CA.

Corazao, M. and Durrani, A. J., (1989). "Repair and Strengthening of Beam-to-Column Connections Subjected to Earthquake Loading", NCEER Technical Report No. 89-0013, National Center for Earthquake Engineering Research, State University of New York at Buffalo, NY, 93 p.

Crisfield, M. A., "Snap-Through and Snap-Back Response in Concrete Structures and the Dangers of Under-Integration," International Journal for Numerical Methods in Engineering, vol. 22, pp. 751–767, 1986.

Darwin, D., and Graham, E.K., (1993a). "Effect of Deformation Height and Spacing on Bond Strength of Reinforcing Bars", ACI Structural Journal, V. 90, No. 6, Nov.-Dec., pp. 646-657.

Darwin, D., and Graham, E. K., (1993b). "Effect of Deforma-tion Height and Spacing on Bond Strength of Reinforcing Bars", SL Report 93-1, University of Kansas Center for Research, Lawrence, Kans., Jan., 68 pp.

Darwin D., Mccabe S.L., Idun E.K., and Schoenekase S.P., (1992). "Development Length Criteria: Bars Not Confined by Transverse Reinforcement", ACI Journal, V.89, No. 6, Nov.-Dec., pp. 709-720.

Darwin D., Tholen M.L., Idun E.K., and Zuo J., (1996a). "Splice Strength of High Relative Rib Area Reinforcing Bars", ACI Journal, V. 93, No. 1, Jan.-Feb., pp. 95-107.

Darwin, D., Zuo, J., Tholen, M. L., and Idun, E. K., (1996b). "Development Length Criteria for Conventional and High Relative Rib Area Reinforcing Bars", ACI Structural Journal, V.93, No. 3, May-June, pp. 347-359.

Darwin D., Lutz L.A., Zuo J., (2005). "Recommended provisions and commentary on development and lap splice lengths for deformed reinforcing bars in tension", ACI Structural Journal, 102(6), pp.892-900.

D'Ayala, D., Penford, A. and Valentini, S. (2003), "Use of FRP fabric for strengthening of reinforced concrete beam-column joints", In: 10th International conference on Structural faults and Repair, London.

De Larrard F., Schaller I., and Fuches J., (1993). " Effect of bar diameter on the bond strength of passive reinforcement in high-performance concrete" ,ACI Materials Journal, Vol.90, No. 4, July-Aug, pp. 333-339.

Dorr, K., (1978). "Bond-behaviour of ribbed reinforcements under transversal pressure", Proc., Symp. on Nonlinear Behaviour of R.C. Spatial Structures, Int. Association for Shell and Spatial Strut., Darmstadt, Germany, pp 13-24.

EC2 (2004). "Design of concrete structures-Part 1: General rules and rules for buildings", (BS EN-1992-1-1:200).

EC8, Eurocode No.8, (1993). "Earthquake resistant design of structures", Part 1, General Rules, 2nd Draft, Report CEN/TC250/SC8/N 83.

Eligehausen, R., (1979). "Bond in Tensile Lapped Splices of Ribbed bars with Straight Anchorages", Publication 301, German Institute for Reinforced Concrete, Berlin, 118 pp. (in German).

Eligehausen, R.,(1979). "Lapped splices of tensioned deformed bars with straight ends", Schriftenreihe des Deutschen Ausschusses fur Stahlbe-ton, Wilhelm Ernst & Sohn, Berlin (in German).

Eligehausen R., Bertero V. V., Popov E. P., (1983). "Local bond stress-slip relationships of deformed bars under generalised excitations: tests and analytical model", Technical

Report UCB/EERC-83, Earthquake Engineering Research Center, University of California, Berkeley.

Engindeniz M., Kahn L.F., and Zureick A., (2005). "Repair and Strengthening of Reinforced Concrete Beam-Column Joints: State of the Art", ACI Structural Journal, V. 102, No. 2, March-April, pp 1-14.

Esfahani, M.R., and Vijaya Rangan, B.V., (1998a). "Local Bond Strength of Reinforcing Bars in Normal Strength and High-Strength Concrete (HSC)", ACI Structural Journal, V.95, No.2, Mar-Apr, pp.96-106.

Esfahani, M.R., and Vijaya Rangan, B.V., (1998b). "Bond between Normal Strength and High-Strength Concrete (HSC) and Reinforcing Bars in Splices in Beams", ACI Structural Journal, V.95, No.3, May-June, pp.272-280.

Fafitis, A., and Shah, P.S., (1985). "Predictions of ultimate behaviour of confined columns subjected to large deformations". ACI Journal publ., Vol. 82, No 4, American Concrete Institute, Detroit, July, pp 428-433.

Ferguson, P.M., and Breen, J.E., (1965). "Lapped Splices for High Strength Reinforcing Bars", ACI JOURNAL, V.62, No.9, Sept., pp.1063-1078.

Ferguson, P.M., and Thompson, J.N., (1965). "Development Length for Large High Strength Reinforcing Bars", ACIJOURNAL, V.62, NO.1, Jan., pp.71-94.

Ferguson, P.M., and Thompson, J.N., (1962). "Develop-ment Length for Large High Strength Reinforcing Bars in Bond", ACI JOURNAL, Proceedings V.59, No.7, July, pp.887-922.

Filippou, F.C., (1986). "A Simple Model For Reinforcing Bar Anchorages Under Cyclic Excitations", Journal of Structural Engineering, ASCE, V.112, No.7, July.

Filiatrault, A., and Lebrun, I., (1996). "Seismic Rehabilitation of Reinforced Concrete Joints by Epoxy Pressure Injection Technique", Seismic Rehabilitation of Concrete Structures, SP-160, G. M. Sabnis, A. C. Shroff, and L. F. Kahn, eds., American Concrete Institute, Farmington Hills, Mich., pp. 73-92.

FIP, "Bond of reinforcement in concrete: state-of-art report," Fip Bulletin No. 10, CEB-FIP, Lausanne, Switzerland, 2000.

Frangou, M., (1992). "Repair/strengthening of concreteby lateral post-tensioning", MPhil Thesis, Sheffield University, December.

Frangou, M., Pilakoutas, K. and Dritsos, S., (1993). "Repair/strengthening of columns by a simple localised strengthening technique", Proceedings of the 5th International Conference on

Frangou, M. and Pilakoutas, K., (1994a). "Strengthening of RC columns by lateral tensioning", Proceedings of the Second International Conference on Earthquake Resistant Construction and Design, Berlin, Germany, 15-17 June, pp 841-848

Frangou M., and Pilakoutas K., (1994b). "Novel technique for the repair and strengthening of RC columns", Proceedings of the Fifth U.S. National Conference on Earthquake Engineering, Vol III, Chicago, pp 637-646.

Frangou, M., Pilakoutas, K. and Dritsos, S., (1995). "Structural repair/strengthening of RC columns", Construction and Building Materials Journal, Vol.9, No.5, pp 259-266

Frangou, M., (1996). "Strengthening of concrete by lateral confinement", PhD Thesis, Sheffield University, Sheffield, UK.

French, C. W., Thorp, G. A., and Tsai, W. J., (1990). "Epoxy Repair Techniques for Moderate Earthquake Damage", ACI Structural Journal, V. 87, No. 4, July-Aug, pp. 416-424.

Fujii,S., and Morita, S., (1981). "Effect of Transverse Reinforcement on Splitting Bond Strength", Transactions of the Japan Concrete Institute, V.3, pp.237-244.

Gambarova P.G., Rosati G.P., Zasso B. (1989). "Steel-to-concrete bond after concrete splitting: constitutive laws and interface deterioration", Materials and Structures, 22(5), pp.347-356.

Gambarova, P.G., Rosati, G.P., Schumm, C., (1994). "An elasto-cohesive model for steel-concrete bond", Proceedings of the Europe-US Workshop on Fracture and Damage in Quasibrittle Structures, pp. 557-566.

Gambarova, P.G., Rosati, G.P. (1997). "Bond and splitting in bar pull-out: behavioral laws and concrete-cover role", Magazine of Concrete Research, 49(179), pp. 99-110.

Gerstle, W., Ingraffea, A.R., and Gergely, P., (1982). “Tension Stiffening, A Fracture Mechanics Approach”, Bond in Concrete (P. Bartos, ed.), Applied Science Publishers, London, pp.97-106.

Genesio, G., Akgüzel, U. (2009). "Seismic retrofit for reinforced concrete exterior beam-column joints using a fully fastened metallic haunch solution, Part 1: Feasibility study", Test report, No. WS 212/23 - 09/02. University of Stuttgart, Germany.

Genesio, G., Sharma, A. (2010-1). "Seismic retrofit solution for reinforced concrete exterior beam-column joints using a fully fastened haunch - Part 2-1: As-built joints", Test report, No. WS 221/07 -10/01. University of Stuttgart, Germany.

Genesio, G., Sharma, A. (2010-2). "Seismic retrofit solution for reinforced concrete exterior beam-column joints using a fully fastened haunch - Part 2-2: Retrofitted joints", Test report, No. WS 221/08 - 10/02, University of Stuttgart, Germany.

Genesio, G., Eligehausen, R., Akgüzel, U., Pampanin, S. (2010-2). "Application of post-installed anchors for seismic retrofit of RC frames", 14th European Conf on Earthquake Engineering, Ohrid, Macedonia.

Genesio, G., Eligehausen, R., Sharma, A., and Pampanin, S., (2010). "Experimental and numerical study towards a deformation-based seismic assessment of substandard exterior RC beam–column joints", In: Int. conf. on fracture mechanics of concrete and concrete structures.

Geng, Z.-J., Chajes, M. J., Chou, T.-W., and Yen-Cheng Pan, D.,(1998). “The retrofitting of reinforced column-to-beam connections”, Com-pos. Sci. Technol.,58(8), 1297–1305.

Ghobarah, A., and Said, A., (2001). “Seismic rehabilitation of beam-column joints using FRP laminates”, J. Earthquake Eng., 5(1), 113–129.

Ghobarah, A., and El-Amoury, T., (2005). “Seismic rehabilitation of de-ficient exterior concrete frame joints”, J. Compos. Constr.,9(5), 408–416.

Ghobarah, A., Aziz, T. S., and Biddah, A., (1997). “Rehabilitation of Reinforced Concrete Frame Connections Using Corrugated Steel Jacketing”, ACI Structural Journal, V. 4, No. 3, May-June, pp. 283-294.

Gilbert, R.I., and Warner, R.F., (1978). "Tension Stiffening in Reinforced Concrete Slabs", Journal of Structural Division, ASCE, 104(ST12), 1885-1900.

Giuriani E., Plizzari G., Schumm C., (1991). “ Role of stirrups and residual tensile strength of cracked concrete on bond”, Journal of Structural Engineering, Vol. 117, No.1, January, pp 1-18.

Goto, Y., (1971). “Cracks Formed in Concrete Around Deformed Tension Bars”, ACI JOURNAL, ProceedingsV. 68, No. 4, Apr., pp. 244-251.

Guiriani, E., (1981). “Experimental Investigation on the Bond-Slip Law of Deformed Bars in Concrete”, IABSE Colloquium Delft 1981, IABSE, Zurich, pp.121-142.

Gunja, G.Y., 2005. “Seismic Strengthening of Reinforced Concrete Structures”, MSc dissertation, University of Sheffield, Sheffield, UK.

Gylltoft, K., Ceder-wall, K., Elfgren, L. and Nilsson,G., (1982). “Bond Failure in Reinforced Concrete under Monotonic and Cyclic Loading: A Fracture Mechanics Approach”, SP-75, Fatigue of Concrete Structures, (S.P.Shah, ed.), ACI, Detroit, pp. 269-288.

Hakuto, S., Park, R. and Tanaka, H. (2000). “Seismic load tests on interior and exterior beam-column joints with substandard reinforcing details”. ACI Structural Journal, Vol. 97, No.1, 11-25.

Hamad, B.S., and Itani, M.S., (1998). “Bond Strength of Reinforcement in High-Performance Concrete: The Role of Silica Fume, Casing Position, and Super plasticizer Dosage”, ACI Materials Journal, V. 95, No. 5, Sept.-Oct., pp. 499-511.

Hamad, B.S., Harajli, M.H., and Jumaa, G.,(2001). “Effect of fiber reinforcement on bond strength of tension-lap splices in high-strength concrete”, ACI Struct. J.,98(5), 638–647.

Hamad, B.S., Soudki, K.A., Harajli, M.H., and Rteil, A.A.(2004). “Experimental and analytical evaluation of the bond strength of rein-forcement in FRP wrapped HSC beams”, ACI Struct.J., 101(6), 747–754

Hamad, B.S., Abou Haidar, E.Y., (S), and Harajli, M.H., (2011). “Effect of Fibers on Bond Strength of Hooked Bars in Normal-Strength Concrete”, ACI Structural Journal, Vol. 108, No. 1, Jan-Feb, pp. 42-50

Harajli, M.H., (2004).“Comparison of Bond Strength of Reinforcing Bars in Normal and High-Strength Concrete,” Journal of Materials in Civil Engineering, ASCE, Vol. 16, No. 4, August.

Harajli, M.H., Hamad, B. S., and Rteil, A.,(2004). “Effect of confinement on bond strength between steel bars and concrete”, ACI Struct. J., 101(5), 595–603.

Harajli, M.H., (2009). "Bond stress–slip model for steel bars in unconfined or steel, FRC, or FRP confined concrete under cyclic loading", J Struct Eng; 135(5):509–18.

Harajli, M.H., (2010). “Effect of Steel Fiber Reinforcement on the Bond Behavior between Steel Bars and Concrete under Static and Cyclic Loading: Experimental Evaluations and Analytical Modeling”, Journal of Materials in Civil Engineering, ASCE, Vol. 22, No. 7, July 2010, pp.674-686.

Hassan, E.M., (2011). “Analytical and Experimental Assessment of Seismic Vulnerability of Beam-Column Joints without Transverse Reinforcement in Concrete Buildings”, PhD thesis, University of California, Berkeley, CA.

Hibbit, Karlsson, and Sorensen. (1995). "Analysis of Concrete Structures with ABAQUS", Hibbit, Karlsson and Sorensen Inc., Rhode Island.

Hillerborg, A., M. Modeer, and P. E. Petersson, “Analysis of Crack Formation and Crack Growth in Concrete by Means of Fracture Mechanics and Finite Elements,” Cement and Concrete Research, vol. 6, pp. 773–782, 1976.

Hyatt, T., (1877). "An Account of Some Experiments with Portland-Cement-Concrete Combined with Iron, as a Building Material", Chiswick Press, London, 47 pp.

Ilki, A., Bedirhanoglu, I., Kumbasar, N. (2011). “Behavior of FRP-Retrofitted Joints Built With Plain Bars and Low-Strength Concrete”, ASCE Journal of Composites for Construction, Vol. 15, No.3, pp.1-13.

Indian Standard (IS 456-2000). “Plain and Reinforced Concrete - Code of Practice”, Bureau of Indian Standards, New Delhi.

Johnston, D. W., and Zia, P., (1982). “Bond Characteristics of Epoxy Coated Reinforcing Bars”, Report No. FHWA-NC-82-002, Federal Highway Administration, Washington, D.C., 163 pp.

Karayannis, C. G., Chalioris, C. E., and Sideris, K. K., (1998). “Effectiveness of RC Beam-Column Connection Repair Using Epoxy Resin Injections”, Journal of Earthquake Engineering, V. 2, No. 2, pp. 217-240.

Karayannis, C. G., Chalioris, C. E., and Sirkelis, G. M., (2008). “Local retrofit of exterior RC beam-column joints using thin RC jackets: An experimental study.”Earthquake Eng. Struct. Dyn., 37, 727–746.

Karayannis, C. G., and Sirkellis, G. M., (2008). “Strengthening and rehabilitation of RC beam-column joints using carbon-FRP jacketing and epoxy resin injection. ”Earthquake Eng. Struct. Dyn., 37, 769–790.

Kimura H., Jirsa J., (1992). “ Effects of bar deformation and concrete strength on bond of reinforcing steel to concrete”, International Conference Bond in Concrete from Research to Practice, Riga, Latvia, Vol.1, October, pp 100-109.

Kolleger, J., and Mehlhorn, G., (1987). "Material Model for Cracked RC", IABSE Colloq. on Computational Mechanics of Concrete Structures: Advances and Applications, Delft, 63-74.

Kuang, J. S., and Wong, H. F. (2005). “Effects of beam bar anchorage on beam-column behavior”, Struct. Des. Tall Special Build., 159(2), 115–124.

Kupfer, H. B., and K. H. Gerstle, “Behavior of Concrete under Biaxial Stresses,” Journal of Engineering Mechanics Division, ASCE, vol. 99 853, 1973.

Lee, D. L. N., Wight, J. K., and Hanson, R. D., (1977). “Repair of Damaged Reinforced Concrete Frame Structures”, Proceedings of the Sixth World Conference on Earthquake Engineering, V. 3, New Delhi, India, Jan., pp. 2486-2491.

Lehman D.E., and Moehle J.P., (2000). "Seismic Performance of Well-confined Concrete Bridge Columns", PEER-1998/01. Pacific Earthquake Engineering Research Center, University of California, Berkeley. 316 pages.

Li, B., Pan, T-C., (2011). " Recent Tests on Seismically Damaged Reinforced Concrete Beam-Column Joints Repaired using Fiber-Reinforced Polymers", Conference Paper, PCEE, 14-16 April, Auckland, New Zealand.

Lin, C.S., and Scordelis, A.C., (1975). "Nonlinear Analysis of RC Shells of General Form", Journal of Structural Division, ASCE, 101(ST3), 523-538.

Losberg, A., and Olsson, P.A., (1979). “Bond Failure of Deformed Reinforcing Bars Based on the Longitudinal Splitting Effect of the Bars”, ACI JOURNAL, Proceedings V.76, No.1, Jan., pp.5-18.

Mander, J. B., Priestley, J.N., and Park, P., (1988a). "Theoretical stress strain model for confined concrete", Journal of Structural Engineering, ASCE, Vol. 114, No 8, August, pp 1804-1823.

Mander, J. B., Priestley, J.N., and Park, P., (1988b). "Observed stress-strain behaviour of confined concrete", Journal of Structural Engineering, ASCE, Vol. 114, No 8, August, pp 1827-1849.

Malvar L. J., (1992). “ Bond of reinforcement under controlled confinement”, ACI Materials Journal, Vol. 89, No. 6, Nov-Dec, pp. 593-601

Melek, M., Wallace, J.W., and Conte, J.P., (2003). “Experimental Assessment of Columns with Short Lap Splices Subjected to Cyclic Loads”, Report No. PEER 2003/2004, University of California-Berkeley, Berkeley, CA, 179 pp.

Menzel, C. A., (1952). “Effect of Settlement of Concrete on Results of Pullout Tests”, Research Department Bulletin 41, Research and Development Laboratories of the Portland Cement Association, Nov., 49 pp.

Modena, C., (1992). "Theoretical Prediction of the Ultimate Bond Strength between a Reinforcing Bar and Concrete", Bond in Concrete, Riga Technical University, Riga, Latvia.

Moghaddam, H., Samadi, M., and Mohebbi, S., (2007). "RC MEMBERS STRENGTHENING BY LATERAL POST-TENSIONING OF EXTERNAL METAL STRIPS", International Earthquake Symposium Kocaeu, pp 454-462.

Moghaddam H, Samadi M, Mohebbi S, Pilakoutas K., (2008). “Lateral Post-Tensioned Metal Strips for Strength and Ductility Enhancement of Concrete Columns: Investigation of Size and Shape Effects”, 14th World Conference on Earthquake Engineering (14WCEE), Beijing, China.

Moghaddam, H., Samadi, M., Pilakoutas, K., (2008). "Behavior and modeling of high-strength concrete columns confined by external post-tensioned strips", In: Proceedings of ASCE/SEI structural engineering congress, Vancouver, Canada.

Moghaddam, H., Samadi, M., (2009). "On the effect of ductility of confining material on the concrete ductility", In: Proceedings of ASCE/SEI structural engineering congress, Austin, TX, USA.

Moghaddam, H., Samadi, M., Pilakoutas, K., and Mohebbi, S., (2010). "Axial compressive behavior of concrete actively confined by metal strips; part A: experimental study", Materials and Structures, 15 January.

Moghaddam, H., Samadi, M., and Pilakoutas, K., (2010). "Compressive behavior of concrete actively confined by metal strips, part B: analysis", Materials and Structures, 15 January.

Morita, S., and Kaku, T., (1979). “Splitting Bond Failures of Large Deformed Reinforcing Bars”, ACI JOURNAL’ V.76, No.1, Jan., pp.93-110.

Mosallam, A. S., (2000). “Strength and ductility of RC frame connections strengthened with quasi-isotropic laminates”, Composites, Part B, 31(6–7), 481–497.

Mukherjee, A., and Joshi, M. (2005). “FRPC reinforced concrete beam-column joints under cyclic excitation.” Compos. Struct., 70(2), 185–199.

Nagamoto K., Kaku T., (1992). “Bond behaviour of deformed bars under lateral compressive and tensile stress”, International Conference Bond in Concrete from Research to Practice, Riga, Latvia, Vol. 1, October, pp 69-78.

Orangun, C.O., Jirsa, J.O., and Breen, J.E., (1975). “Strength of Anchored Bars: A Reevaluation of Test Data on Development Length and Splices”, Research Report No. 154-3F, Center for Highway Research, University of Texas at Austin, Austin, Tex., 78 pp.

Orangun, C.O., Jirsa, J.O., and Breen, J.E., (1977). “Reevaluation of Test Data on Development Length and Splices”. ACI JOURNAL, Proceedings V. 74, No. 3, Mar., pp. 114-122.

Pampanin, S., Christopoulos, C., and Chen, T.H., (2006). "Development and validation of a metallic haunch seismic retrofit system for existing under-designedRC frame buildings", Earthquake Engineering and Structural Dynamics 35:1739-1766.

Pantelides, C., Hansen, J., Nadauld, J., and Reaveley, L.D., (2002). "Assessment of Reinforced Concrete Building Exterior Joints With Substandard Details", Technical Report PEER 2002-18, Pacific Earthquake Engineering Research Center (PEER), University of California, Berkeley, CA, May.

Pantelides, C. P., Okahashi, Y., and Reaveley, L. D., (2008). "Seismic rehabilitation of reinforced concrete frame interior beam-column joints with FRP composites", J. Compos. Constr., 12(4), 435–445.

Plizzari G., Deldossi M., Massimo S., (1996). "Experimental study on anchored bars in R.C. elements with transverse reinforcement", Materials and Structures, Vol. 29, November, pp. 534-542.

Popov, E. P., (1984). "Bond and Anchorage of Reinforcing Bars under Cyclic Loading," ACI Journal, 81(4), 340-348.

Powell, G. (1993). "Drain-2DX element description and user guide for element type 01, 04, 05, 08, 09, and 15", version 1.10. Report No. UCB/SEMM-93/18. Department of Civil Engineering, University of California, Berkeley.

Prakash V, Powell GH, Campbell S. (1993). "DRAIN-2DX base program description and user guide", University of California, Berkeley, California.

Prota, A., Nanni, A., Manfredi, G., and Cosenza, E., (2004). "Selective upgrade of under-designed reinforced beam-column joints using carbon fiber-reinforced concrete", ACI Struct. J., 101(5), 699–707.

Rehm, G., and Eligehausen R., (1979). "Bond of Ribbed Bars Under High Cycle Repeated Loads", ACI JOURNAL, Proceedings V.76, No.2, Feb., pp.297-309.

Reyes, O., (1999). "Modeling of Reinforced Concrete Columns with Short Lap Splices Subjected to Earthquakes", MS thesis, University of Wisconsin,Madison, Wis., 108 pp.

Reyes, O., and Pincheira, J.A., (1999). "R/C Columns with Lap Splices Subjected to Earthquake", ASCE Structures Congress, New Orleans, La., pp. 369-372.

Reynolds G. C., Beeby A. W., (1982). "Bond strength of deformed bars", Bond In Concrete, Edited P. Bartos, Applied Science Publishers, London.

Robins, P.J., and Standish, I.G., (1982). "Effect of Lateral Pressure on Bond of Reinforcing Bars in Con-crete", Bond in Concrete (P. Bartos, ed.), Applied Science Publishers, London.

Salloum, Y. A., and Almusallam, T. H., (2007). "Seismic response of interior RC beam-column joints upgraded with FRP sheets—Part I: Experimental study." J. Compos. Constr., 11(6), 575–589.

Sasmal, S., (2009). "Performance Evaluation and Strengthening of Deficient Beam-Column Sub-assemblages under Cyclic Loading", PhD Thesis, Universitaet Stuttgart, Institut für Leichtbau Entwerfen und Konstruieren.

Sezen, H., (2003). "Seismic Behaviour and Modelling of Reinforced Concrete Building Columns" Ph.D. Dissertation. University of California, Berkeley.

Setzler E.J. and Sezen H., (2008). "Reinforcement Slip in Reinforced Concrete Columns", ACI Structural Journal, Vol. 105, No. 3, 280-289

Shah, S.P., and Somayayi, S., (1981). "Bond Stress versus Slip Relationships and Cracking Response of Tension Members", ACIJOURNAL, V.78, No.3, May-June, pp. 217-225.

Sharma, A., Genesio, G., Reddy, G.R., Eligehausen, R., Pampanin, S., and Vaze, K.K. (2010). "EXPERIMENTAL INVESTIGATIONS ON SEISMIC RETROFITTING OF REINFORCED CONCRETE BEAM-COLUMN JOINTS", 14th Symposium on Earthquake Engineering, 14SEE, Paper No. A007, Dec 17-19.

Soretz, S., and Holzenbein, H., (1979). "Influence of Rib Dimensions of Reinforcing Bars on Bond and Bendability", ACI JOURNAL, Proceedings V.76, No.1, Jan., pp. 111-127.

Soroushian P., Choi K-B., (1989). "Local bond of deformed bars with 470 different diameters in confined concrete", ACI Struct J, pp:217–222.

Souroushian, P., Choi, K. B., Park, G. H., and Aslani, F., (1991). "Bond of Deformed Bars to Concrete: Effects of Confinement and Strength of Concrete", ACI Material Journal, 88(3), 227-232.

Tepfers R., (1973). "A theory of bond applied to overlapped tensile reinforcement splices for deformed bars", Publication 73:2, Division of Concrete Structures, Chalmers University of Technology, Goteborg, Sweden.

Tepfers R., (1979). "Cracking of concrete cover along anchored deformed reinforcing bars", Magazine of Concrete Research, Vol. 31, No. 106, Mar., pp 3-12.

Treece, R. A., and Jirsa, J. O., (1989). "Bond Strength of Epoxy-Coated Reinforcing Bars", ACI Materials Journal, V.86, No.2, Mar-Apr., pp.167-174.

Tsonos, A. G., (2001). "Seismic Rehabilitation of Reinforced Concrete Joints by the Removal and Replacement Technique", European Earthquake Engineering, No. 3, pp. 29-43.

Tsonos, A. G., and Stylianidis, K., (2002). "Seismic Retrofit of Beam-to-Column Joints with High-Strength Fiber Jackets", European Earthquake Engineering, V. 16, No.2, pp. 56-72.

Tsonos, A. G., (2008). "Effectiveness of CFRP-jackets and RC-jackets in post-earthquake and pre-earthquake retrofitting of beam–column sub-assemblages", Eng. Struct., 30(3), 777–793.

Vos, E., and Reinhart, H.W., (1982). "Bond-stress Behavior of Deformed Bars, Plain Bars and Strand Under Impact Loading", Bond in Concrete (P. Bartos,ed.), Applied Science Publishers, London, 1982, pp.173-182.

Zsutty, T., (1985). "Empirical Study of Bar Development Behavior", Journal of Structural Engineering, ASCE, V.111, No.1, Jan., pp. 205-219.

Zuo, J., and Darwin, D., (2000). "Splice Strength of Conventional and High Relative Rib Area Bars in Normal and High-Strength Concrete," ACI Structural Journal, V. 97, No. 4, July-Aug., pp. 630-641.